

How an enzyme leverages
electric fields pp. 1456 & 1510

Cancer drug resistance
gets personal p. 1480

Large carnivore populations
recovering in Europe p. 1517

Science

\$10
19 DECEMBER 2014
sciencemag.org

AAAS

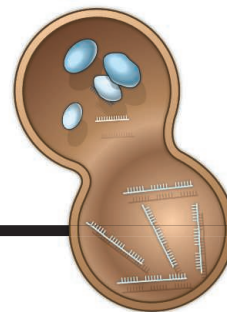
2014

BREAKTHROUGH
of the YEAR



CONTENTS

19 DECEMBER 2014 • VOLUME 346 • ISSUE 6216



1459

MicroRNA maturation
in cancer exosomes

NEWS

IN BRIEF

1434 Roundup of the week's news

IN DEPTH

1436 U.S. FUSION EFFORT MELTS DOWN

Scientific community battles with its federal office *By A. Cho*

1437 SCIENCE AGENCIES MAKE GAINS DESPITE TIGHT U.S. BUDGET

NASA, NSF among 2015 winners in difficult year *By J. Mervis and D. Malakoff*

1439 THE THOROUGHLY BRED HORSE

Genomes from ancient horses show the genetic changes wrought by domestication—and their costs
By A. Gibbons

1440 COSTA RICA'S BIODIVERSITY INSTITUTE FACES FINANCIAL CRISIS

New government rethinks plans to take over INBio's money-losing theme park
By L. Wade

1441 AMBITIOUS CHILDREN'S STUDY MEETS DISAPPOINTING END

After 14 years and \$1.2 billion spent, design and management troubles topple National Children's Study *By J. Kaiser*



1440

INSIGHTS

PERSPECTIVES

1452 FIXING PROBLEMS WITH CELL LINES

Technologies and policies can improve authentication *By J. R. Lorsch et al.*

1454 RETROVIRAL HELP FOR B CELLS

Silent retroviruses present in the human genome help B cells launch a rapid response to pathogenic antigens
By E. K. Grasset and A. Cerutti

► RESEARCH ARTICLE P. 1486

1455 WHAT I CANNOT CREATE, I DO NOT UNDERSTAND

A designed protein transports ions across a membrane *By A. N. Lupas*

► REPORT P. 1520

1456 MORE THAN FINE TUNING

Local electric fields accelerate an enzymatic reaction *By P. Hildebrandt*

► REPORT P. 1510

1458 FOR PEDIATRIC GLIOMA, LEAVE NO HISTONE UNTURNED

Examining histone mutations points to possible therapies for a lethal brain tumor
By O. J. Becher and R. J. Wechsler-Reya

► REPORT P. 1529

1459 MALICIOUS EXOSOMES

Nanovesicles derived from cells of cancer patients carry microRNAs that initiate tumor growth in normal cells
By E. Anastasiadou and F. J. Slack

1461 PROJECTING REGIONAL CHANGE

How accurate are regional projections of climate change derived from downscaling global climate model results? *By A. Hall*

BOOKS ET AL.

1463 THE DIGITAL EINSTEIN PAPERS

Reviewed by A. Robinson

1464 WORKING STIFF

By J. Melinek and T. J. Mitchell, reviewed by Y. Nusinovich

1464 INTERSTELLAR

C. Nolan, director; reviewed by S. Hameed

SPECIAL SECTION

Breakthrough of the Year

WINNER

1442 Comet rendezvous

1443 People's choice

RUNNERS-UP

1444 Cooperative 'bots' don't need a boss

1445 The birth of birds

1445 Youth serum for real?

1446 Chips that mimic the brain

1446 Cells that might cure diabetes

1447 Europe's cave art has a rival

1448 Manipulating memory

1448 Giving life a bigger genetic alphabet

1449 The rise of the CubeSat

OTHER FEATURES

1449 Scorecard for 2014

1450 Areas to watch in 2015

1450 Breakdown of the year: Ebola

1451 Breakdown runners-up

SEE ALSO

► EDITORIAL P. 1433 ► PODCAST ► VIDEO
► sciencemag.org/special/btoy2014/

ON THE COVER

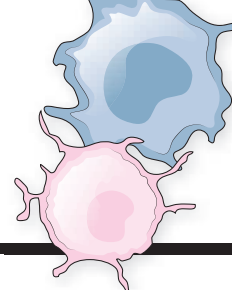


A photo-illustration shows the Philae probe drifting toward comet 67P/Churyumov-Gerasimenko. A landing mishap limited Philae's scientific harvest,

but its parent spacecraft, Rosetta, is giving researchers their first close-up view of a comet as the sun warms and reshapes it. See Breakthrough of the Year page 1442. *Lander:* © ESA/Rosetta/MPS for OSIRIS Team MPS/UPD/LAM/LAA/SSO/INTA/UPM/DASP/IDA; *Comet 67P:* © ESA/Rosetta/Philae/ROLIS/DLR

CONTENTS

19 DECEMBER 2014 • VOLUME 346 • ISSUE 6216



1454 & 1486

Mobilized virome
fights infection

1464 THE SCIENCE OF INTERSTELLAR

By K. Thorne, reviewed by S. Hameed

1465 MELTING AWAY

By C. Seaman

LETTERS

1466 RETRACTION

By G. Lia et al.

1466 ON THE ORIGIN OF FEATHERS

By G. Mayr

1466 RESPONSE

By M.-C. Koschowitz et al.

1467 ERRATA

1467 TECHNICAL COMMENT ABSTRACTS

ASSOCIATION AFFAIRS

1468 MEETING GLOBAL CHALLENGES: DISCOVERY AND INNOVATION THROUGH CONVERGENCE

Integrate biology, physics, engineering,
and social science to innovate

By P. A. Sharp

RESEARCH

IN BRIEF

1476 From *Science* and other journals

RESEARCH ARTICLES

1479 PROTEIN EVOLUTION

Evolution of oligomeric state through
allosteric pathways that mimic ligand
binding T. Perica et al.

RESEARCH ARTICLE SUMMARY; FOR FULL TEXT:

[dx.doi.org/10.1126/science.1254346](https://doi.org/10.1126/science.1254346)

1480 CANCER THERAPY

Patient-derived models of acquired
resistance can identify effective drug
combinations for cancer

A. S. Crystal et al.

1486 HUMORAL IMMUNITY

MAVS, cGAS, and endogenous
retroviruses in T-independent B cell
responses M. Zeng et al.

► PERSPECTIVE P. 1454

REPORTS

1492 ELECTRON TRANSFER

Toward control of electron transfer in
donor-acceptor molecules by bond-
specific infrared excitation M. Delor et al.

1495 PHOTOCHEMISTRY

One-pot room-temperature conversion of
cyclohexane to adipic acid by ozone and
UV light K. C. Hwang and A. Sagadevan

1498 CATALYSIS

Catalytically active Au-O(OH)_x species
stabilized by alkali ions on zeolites and
mesoporous oxides M. Yang et al.

1502 NANOMATERIALS

Element-specific anisotropic growth of
shaped platinum alloy nanocrystals
L. Gan et al.

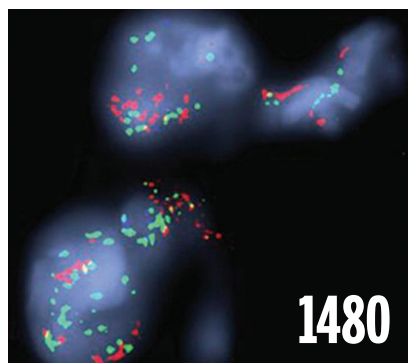
1506 EARTH MAGNETOSPHERE

Direct observation of closed magnetic
flux trapped in the high-latitude
magnetosphere R. C. Fear et al.

1510 BIOPHYSICS

Extreme electric fields power catalysis
in the active site of ketosteroid
isomerase S. D. Fried et al.

► PERSPECTIVE P. 1456



1514 PALEOCEANOGRAPHY

A stagnation event in the deep South
Atlantic during the last interglacial
period C. T. Hayes et al.

1517 CONSERVATION

Recovery of large carnivores in Europe's
modern human-dominated landscapes
G. Chapron et al.

1520 PROTEIN DESIGN

De novo design of a transmembrane
Zn²⁺-transporting four-helix bundle
N. H. Joh et al.

► PERSPECTIVE P. 1455

1525 PROTEIN DESIGN

A designed supramolecular protein
assembly with in vivo enzymatic activity
W. J. Song and F. A. Tezcan

1529 CANCER EPIGENETICS

Use of human embryonic stem cells to
model pediatric gliomas with H3.3K27M
histone mutation K. Funato et al.

► PERSPECTIVE P. 1458

1533 GENE EXPRESSION

Promoter architecture dictates cell-to-
cell variability in gene expression
D. L. Jones et al.

1536 IMMUNE TOLERANCE

Detection of self-reactive CD8⁺ T cells
with an anergic phenotype in healthy
individuals Y. Maeda et al.

DEPARTMENTS

1433 EDITORIAL

Breakthrough to our origins

By Marcia McNutt

► BREAKTHROUGH OF THE YEAR SECTION P. 1442

1586 WORKING LIFE

For the love of ferns

By Karen Perkins

| | |
|-------------------------|------|
| Science Staff | 1432 |
| AAAS News & Notes | 1473 |
| New Products | 1569 |
| Science Careers | 1570 |

SCIENCE (ISSN 0036-8075) is published weekly on Friday, except the last week in December, by the American Association for the Advancement of Science, 1200 New York Avenue, NW, Washington, DC 20005. Periodicals mail postage (publication No. 484460) paid at Washington, DC, and additional mailing offices. Copyright © 2014 by the American Association for the Advancement of Science. The title SCIENCE is a registered trademark of the AAAS. Domestic individual membership and subscription (51 issues): \$153 (\$74 allocated to subscription). Domestic institutional subscription (51 issues): \$1282. Foreign postage extra: Mexico, Caribbean (surface mail) \$55; other countries (air assist delivery) \$85. First class, airmail, student, and emeritus rates on request. Canadian rates with GST available upon request. GST #R1254 88122. Publications Mail Agreement Number 1069624. Printed in the U.S.A. Change of address: Allow 4 weeks, giving old and new addresses and 8-digit account number. Postmaster: Send change of address to AAAS, P.O. Box 96178, Washington, DC 20090-6178. Single-copy sales: \$10.00 current issue, \$15.00 back issue prepaid includes surface postage; bulk rates on request. Authorization to photocopy material for internal or personal use under circumstances not falling within the fair use provisions of the Copyright Act is granted by AAAS to libraries and other users registered with the Copyright Clearance Center (CCC) Transactional Reporting Service, provided that \$30.00 per article is paid directly to CCC, 222 Rosewood Drive, Danvers, MA 01923. The identification code for Science is 0036-8075. Science is indexed in the Reader's Guide to Periodical Literature and in several specialized indexes.

Editor-in-Chief Marcia McNutt

Executive Editor Monica M. Bradford **News Editor** Tim Appenzeller

Managing Editor, Research Journals Katrina L. Kelner

Deputy Editors Barbara R. Jasny, Andrew M. Sugden(UK), Valda J. Vinson, Jake S. Yeston

Research and Insights

SR. EDITORS Caroline Ash(UK), Gilbert J. Chin, Lisa D. Chong, Maria Cruz(UK), Julia Fahrenkamp-Uppenbrink(UK), Pamela J. Hines, Stella M. Hurlley(UK), Paula A. Kiberstis, Marc S. Lavine(Canada), Kristen L. Mueller, Ian S. Osborne(UK), Beverly A. Purnell, L. Bryan Ray, Guy Riddiough, H. Jesse Smith, Jelena Stajic, Peter Stern(UK), Phillip D. Szuroni, Brad Wible, Nicholas S. Wigginton, Laura M. Zahn **ASSOCIATE EDITORS** Brent Grocholski, Melissa R. McCartney, Margaret M. Moerchen, Sacha Vignieri **ASSOCIATE BOOK REVIEW EDITOR** Valerie B. Thompson **ASSOCIATE LETTERS EDITOR** Jennifer Sills **CHIEF CONTENT PRODUCTION EDITOR** Cara Tate **SR. CONTENT PRODUCTION EDITORS** Harry Jach, Trista Wagoner **CONTENT PRODUCTION EDITORS** Jeffrey E. Cook, Chris Filiatreau, Cynthia Howe, Lauren Kmec, Barbara P. Ordway **SR. EDITORIAL COORDINATORS** Carolyn Kyle, Beverly Shields **EDITORIAL COORDINATORS** Ramatoulaye Diop, Joi S. Granger, Lisa Johnson, Anita Wynn **PUBLICATIONS ASSISTANTS** Aneera Dobbins, Jeffrey Hearn, Dona Mathieu, Le-Toua Mayne Flood, Shannon McMahon, Scott Miller, Jerry Richardson, Rachel Roberts(UK), Alice Whaley(UK), Brian White **EXECUTIVE ASSISTANT** Anna Bashkirova **ADMINISTRATIVE SUPPORT** Janet Clements(UK), Michael Crabtree(UK, Intern), Lizanne Newton(UK), Maryrose Madrid, John Wood(UK)

News

NEWS MANAGING EDITOR John Travis **INTERNATIONAL EDITOR** Richard Stone **DEPUTY NEWS EDITORS** Daniel Clery(UK), Robert Coontz, Elizabeth Culotta, David Grimm, David Malakoff, Leslie Roberts **CONTRIBUTING EDITORS** Martin Enserink(Europe), Mara Hvistendahl (Asia) **SR. CORRESPONDENTS** Jeffrey Mervis, Elizabeth Pennisi **NEWS WRITERS** Adrian Cho, John Cohen, Jennifer Couzin-Frankel, Carolyn Gramling, Eric Hand, Jocelyn Kaiser, Kelly Servick, Robert F. Service, Erik Stokstad, Emily Underwood **INTERNS** David Shultz, Jia You **CONTRIBUTING CORRESPONDENTS** Pallava Bagla(South Asia), Michael Balter(Paris), John Bohannon, Ann Gibbons, Sam Kean, Richard A. Kerr, Eli Kintisch, Kai Kupferschmidt(Berlin), Andrew Lawler, Christina Larson(Beijing), Mitch Leslie, Charles C. Mann, Eliot Marshall, Virginia Morell, Dennis Normile(Tokyo), Heather Pringle, Tania Rabesandratana(Brussels), Gretchen Vogel(Berlin), Lizzie Wade(Mexico City) **CAREERS** Jim Austin(Editor), Donisha Adams **COPY EDITORS** Kara Estelle, Nora Kelly, Jennifer Levin **ADMINISTRATIVE SUPPORT** Scherraine Mack

Executive Publisher Alan I. Leshner

Publisher Kent R. Anderson **Chief Digital Media Officer** Rob Covey

BUSINESS OPERATIONS AND ADMINISTRATION DIRECTOR Deborah Rivera-Wienhold **BUSINESS SYSTEMS AND FINANCIAL ANALYSIS DIRECTOR** Randy Yi **MANAGER OF FULFILLMENT SYSTEMS** Neal Hawkins **SYSTEMS ANALYST** Nicole Mehmedovich **ASSISTANT DIRECTOR, BUSINESS OPERATIONS** Eric Knott **MANAGER, BUSINESS OPERATIONS** Jessica Tierney **BUSINESS ANALYSTS** Cory Lipman, Cooper Tilton, Celeste Troxler **FINANCIAL ANALYST** Jeremy Clay **RIGHTS AND PERMISSIONS ASSISTANT DIRECTOR** Emilie David **PERMISSIONS ASSOCIATE** Elizabeth Sandler **RIGHTS, CONTRACTS, AND LICENSING ASSOCIATE** Lili Kiser

MARKETING DIRECTOR Ian King **MARKETING MANAGER** Julianne Wielga **MARKETING ASSOCIATE** Elizabeth Sattler **SR. MARKETING EXECUTIVE** Jennifer Reeves **SR. ART ASSOCIATE, PROJECT MANAGER** Tzeitel Sorrosa **ART ASSOCIATE** Seil Lee **ASSISTANT COMMERCIAL EDITOR** Selby Frame **MARKETING PROJECT MANAGER** Angelissa McArthur **SR. WRITER** Bill Zimmer **PROGRAM DIRECTOR, AAAS MEMBER CENTRAL** Peggy Mihelich **FULFILLMENT SYSTEMS AND OPERATIONS** membership@aaas.org **MANAGER, MEMBER SERVICES** Pat Butler **SPECIALISTS** LaToya Casteel, Javia Flemmings, Latasha Russell **MANAGER, DATA ENTRY** Mickie Napoleoni **DATA ENTRY SPECIALISTS** JJ Regan, Jaimee Wise, Fiona Giblin

DIRECTOR, SITE LICENSING Tom Ryan **DIRECTOR, CORPORATE RELATIONS** Eileen Bernadette Moran **SR. PUBLISHER RELATIONS SPECIALIST** Kiki Forsythe **PUBLISHER RELATIONS MANAGER** Catherine Holland **PUBLISHER RELATIONS, EASTERN REGION** Keith Layson **PUBLISHER RELATIONS, WESTERN REGION** Ryan Rexroth **MANAGER, SITE LICENSE OPERATIONS** Iquo Edim **FULFILLMENT ANALYST** Lana Guz **ASSOCIATE DIRECTOR, MARKETING** Christina Schlecht **MARKETING ASSOCIATES** Thomas Landreth, Minah Kim

DIRECTOR OF WEB TECHNOLOGIES Ahmed Khadr **SR. DEVELOPER** Chris Coleman **DEVELOPERS** Dan Berger, Jimmy Marks **SR. PROJECT MANAGER** Trista Smith **SYSTEMS ENGINEER** Luke Johnson **PRODUCT MANAGER** Walter Jones

CREATIVE DIRECTOR, MULTIMEDIA Martyn Green **DIRECTOR OF ANALYTICS** Enrique Gonzales **SR. WEB PRODUCER** Sarah Crespi **WEB PRODUCER** Alison Crawford **VIDEO PRODUCER** Nguyen Nguyen **SOCIAL MEDIA PRODUCER** Meghna Sachdev

DIRECTOR OF OPERATIONS PRINT AND ONLINE Elizabeth Harman **PRINT PRODUCTION DIRECTOR** Wendy K. Shank **PREFLIGHT MANAGER** Marcus Spiegler **ASSISTANT MANAGER ONLINE** Lisa Stanford **ASSISTANT MANAGER PRINT** Rebecca Doshi **SR. SPECIALISTS** Steve Forrester, Jason Hillman, Antoinette Hodal, Tara Kelly, Anthony Rossen **SPECIALISTS** Jacob Hedrick, Nichole Johnston, Lori Murphy, Kimberley Oster

DESIGN DIRECTOR Beth Rakouskas **ASSOCIATE ART DIRECTOR** Laura Creveling **SR. ILLUSTRATORS** Chris Bickel, Katharine Sutliff **ILLUSTRATOR** Valerie Altounian **SR. ART ASSOCIATES** Holly Bishop, Preston Huey **ART ASSOCIATES** Kay Engman, Garvin Grullón, Chrystal Smith **SR. PHOTO EDITOR** William Douthitt **PHOTO EDITOR** Leslie Blizard

DIRECTOR, GLOBAL COLLABORATION, CUSTOM PUBLICATIONS, ADVERTISING Bill Moran **EDITOR, CUSTOM PUBLISHING** Sean Sanders: 202-326-6430 **ASSISTANT EDITOR, CUSTOM PUBLISHING** Tianna Hicklin: 202-326-6463 **ADVERTISING MARKETING MANAGER** Justin Sawyers: 202-326-7061 **science_advertising@aaas.org** **ADVERTISING MARKETING ASSOCIATE** Javia Flemmings **ADVERTISING SUPPORT MANAGER** Karen Foote: 202-326-6740 **ADVERTISING PRODUCTION OPERATIONS MANAGER** Deborah Tompkins **SR. PRODUCTION SPECIALIST/GRAPHIC DESIGNER** Amy Hardcastle **PRODUCTION SPECIALIST** Yuse Lajiminmuhip **SR. TRAFFIC ASSOCIATE** Christine Hall **SALES COORDINATOR** Shirley Young **ASSOCIATE DIRECTOR, COLLABORATION, CUSTOM PUBLICATIONS/CHINA/TAIWAN/KOREA/SINGAPORE** Ruolei Wu: +86-186 0822 9345, rwu@aaas.org **COLLABORATION/CUSTOM PUBLICATIONS/JAPAN** Adarsh Sandhu + 81532-81-5142 asandhu@aaas.org **EAST COAST/E. CANADA** Laurie Faraday: 508-747-9395, FAX 617-507-8189 **WEST COAST/W. CANADA** Lynne Stickrod: 415-931-9782, FAX 415-520-6940 **MIDWEST** Jeffrey Dembski: 847-498-4520 x3005, Steven Loerch: 847-498-4520 x3006 **UK EUROPE/ASIA** Roger Goncalves: TEL/FAX +41 43 243 1358 **JAPAN** Katsuyoshi Fukumizu(Tokyo): +81-3-3219-5777 kfukumizu@aaas.org **CHINA/TAIWAN** Ruolei Wu: +86-0082-9345

WORLDWIDE ASSOCIATE DIRECTOR OF CAREERS Tracy Holmes: +44 (0) 1223 326525, FAX +44 (0) 1223 326532 tholmes@science-int.co.uk **CLASSIFIED** advertise@sciencecareers.org **U.S. SALES** Tina Burks: 202-326-6577, Nancy Toema: 202-326-6578 **SALES ADMINISTRATOR** Marci Gallun **EUROPE/ROW SALES** Axel Gesatzki, Sarah Lelarge **SALES ASSISTANT** Kelly Grace **JAPAN** Hiroyuki Mashiki(Kyoto): +81-75-823-1109 hmashiki@aaas.org **CHINA/TAIWAN** Ruolei Wu: +86-186 0822 9345 rwu@aaas.org **MARKETING MANAGER** Allison Pritchard **MARKETING ASSOCIATE** Aimee Aponte

AAAS BOARD OF DIRECTORS **RETIRING PRESIDENT, CHAIR** Phillip A. Sharp **PRESIDENT** Gerald R. Fink **PRESIDENT-ELECT** Geraldine (Geri) Richmond **TREASURER** David Evans **SHAW CHIEF EXECUTIVE OFFICER** Alan I. Leshner **BOARD** Bonnie L. Bassler, May R. Berenbaum, Carlos J. Bustamante, Claire M. Fraser, Laura H. Greene, Elizabeth Loftus, Raymond Orbach, Inder M. Verma

SUBSCRIPTION SERVICES For change of address, missing issues, new orders and renewals, and payment questions: 866-434-AAAS (2227) or 202-326-6417, FAX 202-842-1065. Mailing addresses: AAAS, P.O. Box 96178, Washington, DC 20090-6178 or AAAS Member Services, 1200 New York Avenue, NW, Washington, DC 20005

INSTITUTIONAL SITE LICENSES 202-326-6755 **REPRINTS:** Author Inquiries 800-635-7181 **COMMERCIAL INQUIRIES** 803-359-4578 **PERMISSIONS** 202-326-6765, permissions@aaas.org **AAAS Member Services** 202-326-6417 or http://membercentral.aaas.org/discouints

Science serves as a forum for discussion of important issues related to the advancement of science by publishing material on which a consensus has been reached as well as including the presentation of minority of conflicting points of view. Accordingly, all articles published in Science—including editorials, news and comment, and books reviews—are signed and reflect the individual views of the authors and not official points of view adopted by AAAS or the institutions with which the authors are affiliated.

INFORMATION FOR AUTHORS See pages 680 and 681 of the 7 February 2014 issue or access www.sciencemag.org/about/authors

SENIOR EDITORIAL BOARD

A. Paul Alivisatos, Lawrence Berkeley Nat'l Laboratory, Ernst Fehr, U. of Zürich
Susan M. Rosenberg, Baylor College of Medicine, Michael S. Turner, U. of Chicago

BOARD OF REVIEWING EDITORS

(Statistics board members indicated with \$)
Adriano Aguzzi, U. Hospital Zürich
Takuzo Aida, U. of Tokyo
Leslie Aiello, Wenner-Gren Foundation
Judith Allen, U. of Edinburgh
Sonia Altizer, U. of Georgia
Virginia Armbrust, U. of Washington
Sebastian Amigorena, Institut Curie
Kathryn Anderson, Memorial Sloan-Kettering Cancer Center
Peter Andolfatto, Princeton U.
Meinrat O. Andreae, Max-Planck Inst. Mainz
Paola Ariotti, Harvard U.
Johan Auwerx, EPFL
David Awschalom, U. of Chicago
Jordi Bascompte, Estación Biológica de Doñana CSIC
Facundo Batista, London Research Inst.
Ray H. Baughman, U. of Texas, Dallas
David Baum, U. of Wisconsin
Kamran Behnia, ESPCI-ParisTech
Yasmine Belkaid, NIAID, NIH
Philip Benfey, Duke U.
Stephen J. Benkovic, Penn State U.
Carlo Beenakker, Leiden U.
Gabriele Bergers, U. of California, San Francisco
Christophe Bernard, Aix-Marseille U.
Bradley Bernstein, Massachusetts General Hospital
Peer Bork, EMBL
Bernard Bourdon, Ecole Normale Supérieure de Lyon
Chris Bowler, Ecole Normale Supérieure
Ian Boyd, U. of St. Andrews
Emily Brodsky, U. of California, Santa Cruz
Ron Brookmeyer, U. of California Los Angeles (\$) **Christian Büchel**, U. Hamburg-Eppendorf
Joseph A. Burns, Cornell U.
Gyorgy Buzsaki, New York U. School of Medicine
Blanche Capel, Duke U.
Mats Carlsson, U. of Oslo
David Clapham, Children's Hospital Boston
David Clary, U. of Oxford
Joel Cohen, Rockefeller U., Columbia U.
Jonathan D. Cohen, Princeton U.
James Collins, Boston U.
Robert Cook-Deegan, Duke U.
Alan Cowman, Walter & Eliza Hall Inst.
Robert H. Crabtree, Yale U.
Roberta Croce, Vrije Universiteit
Janet Currie, Princeton U.
Jeff L. Dangl, U. of North Carolina
Tom Daniel, U. of Washington
Frans de Waal, Emory U.
Stanislas Dehaene, Collège de France
Robert Desimone, MIT
Claude Desplan, New York U.
Ap Dijksterhuis, Radboud U. of Nijmegen
Dennis Discher, U. of Pennsylvania
Gerald W. Dorn II, Washington U. School of Medicine
Jennifer A. Doudna, U. of California, Berkeley
Bruce Dunn, U. of California, Los Angeles
Christopher Dye, WHO
Todd Ehlers, U. of Tuebingen
David Ehrhardt, Carnegie Inst. of Washington
Tim Elston, U. of North Carolina at Chapel Hill
Gerhard Ertl, Fritz-Haber-Institut, Berlin
Barry Everitt, U. of Cambridge
Ernst Fehr, U. of Zurich
Anne C. Ferguson-Smith, U. of Cambridge
Michael Feuer, The George Washington U.
Kate Fitzgerald, U. of Massachusetts
Peter Fratzl, Max-Planck Inst.
Elaine Fuchs, Rockefeller U.
Daniel Geschwind, UCLA
Andrew Gewirth, U. of Illinois
Karl-Heinz Glassmeier, TU Braunschweig
Ramon Gonzalez, Rice U.
Julia R. Greer, Caltech
Elizabeth Grove, U. of Chicago
Kip Guy, St. Jude's Children's Research Hospital
Takeji Ha, U. of Illinois at Urbana-Champaign
Christian Haass, Ludwig Maximilians U.
Steven Hahn, Fred Hutchinson Cancer Research Center
Michael Hasselmo, Boston U.
Martin Heimann, Max-Planck Inst. Jena
Yia-Wei Hsiang, U. of Cambridge
James A. Hendler, Rensselaer Polytechnic Inst.
Janet G. Hering, Swiss Fed. Inst. of Aquatic Science & Technology
Michael E. Himmel, National Renewable Energy Lab.
Kai-Uwe Hinrichs, U. of Bremen
Kei Hirose, Tokyo Inst. of Technology
David Holdell, U. of Cambridge
David Holder, Imperial College
Lora Hooper, UT Southwestern Medical Ctr. at Dallas
Raymond Huey, U. of Washington
Steven Jacobsen, U. of California, Los Angeles
Kai Johnson, EPFL Lausanne
Peter Jonas, Inst. of Science & Technology (IST) Austria
Matt Kaebberlein, U. of Washington
William Kaelin Jr., Dana-Farber Cancer Inst.
Daniel Kahne, Harvard U.
Daniel Kammen, U. of California, Berkeley
Masashi Kawasaki, U. of Tokyo
Joel Kingsolver, U. of North Carolina at Chapel Hill
Robert Kingston, Harvard Medical School
Eitonne Koechlin, Ecole Normale Supérieure
Alexander Koldobin, Johns Hopkins U.
Roberto Kolter, Harvard Medical School
Alberto R. Kornblihtt, U. of Buenos Aires
Leonid Kruglyak, UCLA
Thomas Langer, U. of Cologne
Mitchell A. Lazar, U. of Pennsylvania
David Lazer, Harvard U.
Thomas Lecuit, IBDM
Virginia Lee, U. of Pennsylvania
Stanley Lemon, U. of North Carolina at Chapel Hill
Ottoline Leyser, Cambridge U.
Marcia C. Linn, U. of California, Berkeley
Jianguo Liu, Michigan State U.
Luis Liz-Marzan, CIC biomaGUNE
Jonathan Losos, Harvard U.
Ke Lu, Chinese Acad. of Sciences
Christian Lüscher, U. of Geneva
Laura Machesky, CRUK Beatson Inst. for Cancer Research
Anne Magurran, U. of St. Andrews
Oscar Marin, CSIC & U. Miguel Hernández
Charles Marshall, U. of California, Berkeley
C. Robertson McClung, Dartmouth College
Graham Medley, U. of Warwick
Yasushi Miyashita, U. of Tokyo
Richard Morris, U. of Edinburgh
Alison Moutsier-Reif, NC State U. (\$) **Sean Munro**, MRC Lab. of Molecular Biology
Thomas Murray, The Hastings Center
James Nelson, Stanford U. School of Med.
Karen Nelson, J. Craig Venter Institute
Daniel Neumark, U. of California, Berkeley
Timothy W. Nilsen, Case Western Reserve U.
Pär Nordlund, Karolinska Inst.
Helga Nowotny, European Research Advisory Board
Ben Olken, MIT
Joe Orenstein, U. of California
Berkeley & Lawrence Berkeley National Lab
Harry Orr, U. of Minnesota
Andrew Oswald, U. of Warwick
Steve Palumbi, Stanford U.
Jane Parker, Max-Planck Inst. of Plant Breeding Research
Giovanni Parmigiani, Dana-Farber Cancer Inst. (\$) **Donald R. Paul**, U. of Texas, Austin
John H. A. Petri, Memorial Sloan-Kettering Cancer Center
Joshua Plotkin, U. of Pennsylvania
Albert Polman, FOM Institute AMOLF
Philippe Poulin, CNRS
David Randall, Colorado State U.
Colin Renfrew, U. of Cambridge
Felix Rey, Institut Pasteur
Trevor Robbins, U. of Cambridge
Jim Roberts, Fred Hutchinson Cancer Research Ctr.
Barbara A. Romanowicz, U. of California, Berkeley
Jens Rostrop-Nielsen, Haldor Topsøe
Mike Ryan, U. of Texas, Austin
Shin-ichi Sakata, Kyoto U.
Shimon Saitoku, Kyoto U.
Miquel Salmeron, Lawrence Berkeley National Lab
Jürgen Sandkühler, Medical U. of Vienna
Alexander Schlier, Harvard U.
Randy Seeley, U. of Cincinnati
Vladimir Shalae, Purdue U.
Robert Siliciano, Johns Hopkins School of Medicine
Joseph Silk, Institut d'Astrophysique de Paris
Denis Simon, Arizona State U.
Alison Smith, John Innes Centre
Richard Smith, U. of North Carolina (\$) **John Speakman**, U. of Aberdeen
Allan C. Spradling, Carnegie Institution of Washington
Jonathan Sprent, Garvan Inst. of Medical Research
Eric Steig, U. of Washington
Paula Stephan, Georgia State U. and National Bureau of Economic Research
Molly Stevens, Imperial College London
V. S. Subrahmanian, U. of Maryland
Ira Tabas, Columbia U.
Sarah Teichmann, Cambridge U.
John Thomas, North Carolina State U.
Shubha Tole, Tata Institute of Fundamental Research
Christopher Tyler-Smith, The Wellcome Trust Sanger Institute
Herbert Virgin, Washington U.
Bert Vogelstein, Johns Hopkins U.
Cynthia Volkert, U. of Göttingen
Douglas Wallace, Dalhousie U.
David Wallace, Weizmann Inst. of Science
Ian Walsmsley, U. of Oxford
David A. Wardle, Swedish U. of Agric. Sciences
David Waxman, Fudan U.
Jonathan Weissman, U. of California, San Francisco
Chris Wikle, U. of Missouri (\$) **Ian A. Wilson**, The Scripps Res. Inst. (\$) **Timothy D. Wilson**, U. of Virginia
Rosemary Wyse, Johns Hopkins U.
Jean Zaenen, Leiden U.
Kenneth Zaret, U. of Pennsylvania School of Medicine
Jonathan Zehr, U. of California, Santa Cruz
Len Zon, Children's Hospital Boston
Maria Zuber, MIT

BOOK REVIEW BOARD

David Bloom, Harvard U. Samuel Bowring, MIT, Angela Creager, Princeton U., Richard Swedder, U. of Chicago, Ed Wasserman, DuPont

Breakthrough to our origins

Long before I dreamed of becoming a scientist, I wondered why Earth was teeming with life, while Mars was a barren, rocky outpost and Venus was shrouded in a dense atmosphere. Somewhere, I read that comets were the reason. Strike a rocky planet with one volatile- and organic-rich comet and an Earth-like environment results. Two comets produce a Venus. No comets: Mars. Of course, this theory was far too simple to explain the differences in the evolution of the inner planets, but no one had ever explored comets up close to know how they might alter a planet's composition and history—until now. Last month, after many years of planning and a decade in transit, the European Space Agency's spacecraft Rosetta reached Comet 67P/Churyumov-Gerasimenko, surveyed landing sites, and deployed its probe, Philae, to execute the first-ever soft landing on a comet's surface (see the News story, p. 1442).

To put into perspective how long Rosetta's 6.4-billion-km journey to 67P took, its launch 10 years ago with an Ariane 5 rocket from French Guiana lagged the launch of Facebook by a month but beat the debut of the iPhone 1 by 3 years. Much of the world held its breath while Philae made its descent and then bounced in the microgravity before landing in a less-than-ideal locale for recharging its solar panels. Although it was disappointing that the tools designed to anchor the lander to the comet did not function as designed, the mission is still likely to achieve most if not all of its objectives, providing important new information on how comets have contributed to the evolution of the solar system. Just last week, we learned that the isotopic ratio of water on comet 67P differs from that found on Earth, ruling out comets from the Kuiper Belt as having delivered water to our planet. For this historic first, we are happy to select the Rosetta

mission as *Science's* Breakthrough of the Year for 2014.

A description of this year's Breakthrough, along with an impressive list of runners-up and other milestones of 2014, can be found on p. 1442. This year's selections also include something new: results of an online poll in which visitors to *Science's* website voted for their favorite advances. As it turns out, the Rosetta mission finished third as the "People's Choice." First place went to

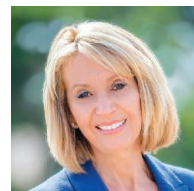
a dramatic feat of synthetic biology: the "engineering" of two novel nucleic acids in the bacterium *Escherichia coli*, thus expanding the genetic alphabet in a living organism by a whopping 50%. Next in line was a spectacular demonstration that the transfusion of blood from young mice to old mice reverses aging in both muscles and brain—effectively a fountain of youth. Already this concept is in clinical trials for treating Alzheimer's patients.

Is it surprising that voters ranked the year's achievements differently from our writers and editors? Not at all. Scientific research is such a huge and multifaceted enterprise, and any attempt to reduce it to a list of greatest hits is bound to be somewhat subjective. Very

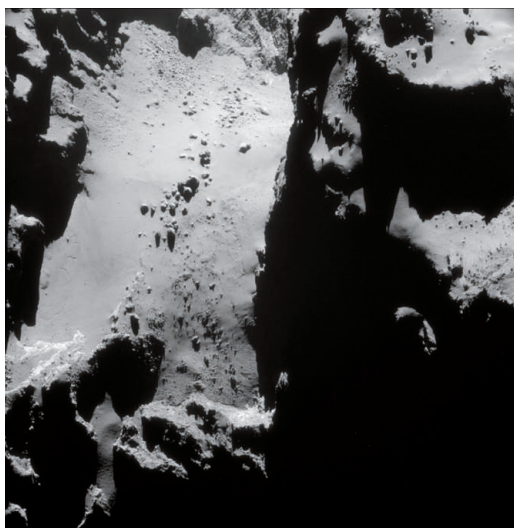
few years can boast a single result that stands decisively out from the pack. As Stephen Jay Gould said about evolutionary history, rewinding the tape and starting all over again might yield a very different result.

There were some 2014 breakdowns, unfortunately. A pair of discoveries vaporized as fast as they appeared: an alleged method for generating pluripotent stem cells (STAP cells) from ordinary cells; and the premature claim that signals detected by the South Pole telescope BICEP2 indicated cosmic inflation during the early universe, just after the Big Bang. But alas, leading this list is the global response to the Ebola epidemic in West Africa: too little, too late. We hope that this tragedy galvanizes efforts by all to stop its spread in the coming year.

—Marcia McNutt



Marcia McNutt
Editor-in-Chief
Science Journals



"Much of the world held its breath while Philae made its descent..."

“The text went from weak to weaker to weakest and it’s very weak indeed.”

Sam Smith, chief of climate policy for the World Wildlife Fund, on last week’s contentious U.N. climate negotiations in Peru.

IN BRIEF

Arizona’s Apache Mountain may soon overlook a copper mine.



Planned mine threatens Apache archaeology

Archaeologists and Native American tribes are protesting legislation to approve a controversial land exchange between the federal government and a copper mining company. Language inserted into the Senate’s defense spending bill, passed last week, would transfer 980 hectares of Arizona’s Tonto National Forest to the company Resolution Copper Mining, which seeks to open a mine there. The land has remained essentially unchanged since the Hohokam people lived there more than 500 years ago, and it contains rare Apache archaeological

sites of value to researchers as well as places sacred to local Native American tribes. It’s right next door to a cliff where Apache warriors plunged to their deaths rather than be taken by the U.S. Cavalry. The bill states that the land will be transferred 60 days after an environmental impact statement has been completed. But some archaeologists say that this language prejudices the environmental review, sidestepping the standard approval process. The bill now awaits President Barack Obama’s signature, and archaeologists think there is little chance of changing or removing the rider. <http://scim.ag/landswap>

AROUND THE WORLD

PubPeer fights to conceal users

DETROIT, MICHIGAN | The postpublication peer-review website PubPeer has moved to quash a subpoena from a scientist who wants to unmask some of its anonymous users. In October, cancer researcher Fazlul Sarkar of Wayne State University in Detroit, Michigan, filed a defamation suit against the users, who pointed out possible image irregularities in some of his papers. He claims their suggestions of misconduct caused the University of Mississippi to rescind a tenured job offer and has

subpoenaed PubPeer for identifying information. Lawyers representing the site now hope to convince a judge that Sarkar’s claim of defamation is invalid. With their 10 December motion to quash the subpoena, they submitted an affidavit from an expert in scientific image analysis, who also found “strong evidence” of image irregularities. <http://scim.ag/pubpeer>

New biodiversity institute

WASHINGTON, D.C. | The Smithsonian Institution announced last week that it will launch a virtual biodiversity genomics

institute to help capture and catalog all the DNA from Earth’s flora and fauna. With the goal of raising \$100 million over the next decade, the Smithsonian’s zoo; natural history museum; and conservation, environmental, and tropical research labs will expand their efforts to collect and store frozen tissue samples, as well as sequence and analyze their DNA. “The Smithsonian is one of the very few institutions around the world that are able to do this,” says Erich Jarvis, a neurobiologist at Duke University in Durham, North Carolina, who coordinated the sequencing of the genomes of 48 bird species. <http://scim.ag/DNAdiversity>

Climate talks yield modest deal

LIMA | After 2 weeks of negotiations (plus 33 hours of overtime), delegates from nearly 200 nations have signed an agreement to reduce their greenhouse gas emissions. The Lima Accord represents the first time that developed and developing countries have all pledged to cut emissions. But many believe the agreement is toothless, in that it doesn't set firm, legally binding requirements for reductions and fails to provide a global metric for measuring progress. The accord, finalized 14 December, will form the basis of the next round of climate negotiations in 2015 in Paris, where delegates hope to reach a binding global agreement to stem climate change.

Sundarbans soiled by oil

MONGLA, BANGLADESH | Nearly 350,000 liters of oil spilled into the world's largest mangrove forest last week after a tanker collided with another vessel. The spill occurred near the Chadpai Wildlife

Sanctuary, part of the 140,000-hectare Sundarbans—a mangrove-rich UNESCO World Heritage Site known for its exceptional biodiversity. The site is one of the country's three sanctuaries for the threatened Irrawaddy and Ganges river dolphins. Experts are concerned about the spill's ecological consequences, especially for the Ganges river dolphin, because the accident occurred within the least disturbed part of its range. <http://scim.ag/sundarspill>

NEWSMAKERS

Three Q's



A U.S. National Academies committee issued a new report last week on the post-doctoral experience. Neurologist **Gregory Petsko** of Weill Cornell Medical College in New York City, who chaired

the committee, told *Science* how its recommendations might be implemented.

Q: The report says that the postdoc is specifically for training researchers, and not for other careers. Is this a fair reading?

A: Exactly. We CANNOT, in my opinion, train too many [science, technology, engineering, and math] Ph.D.s. ... But we can have too many people just defaulting into postdoc positions who don't need to do so.

Q: If postdoc training is advanced research training, does that mean there should be at least a rough equivalence between the number of postdocs trained and the number of research positions available?

A: Maybe, but that's not for us to say. ... But it's certainly true that in a properly functioning labor market, there would be more of an equivalence than there is now.

Q: How would we achieve that equivalence?

A: The simplest way is to raise the minimum postdoctoral salary, thereby reducing demand until supply and demand are more nearly equal. I'm hoping all funders will look at that seriously.

Full interview at <http://scim.ag/PetskoInt>.

BY THE NUMBERS

1

Rank of Facebook's study on secretly manipulating users' emotions via their news feeds, according to Altmetric's analysis of most shared papers of 2014.

\$400
thousand

Size of a new grant from the MacArthur Foundation to expand the website Retraction Watch into a comprehensive database of retracted papers.

88.7%

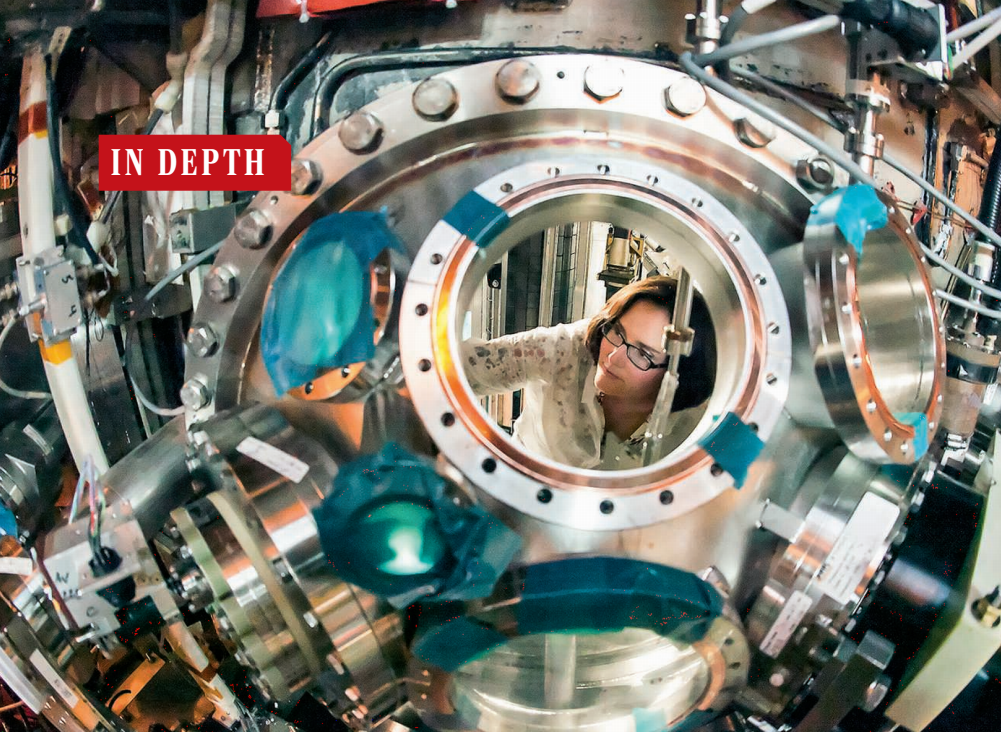
Portion of the Darwin Awards for idiotic behavior won by men, according to a study in *The BMJ*.



An ice floe in McMurdo Sound.

Beauty products blemish Antarctica

Scientists have found trace contaminants from sunscreens, skin products, and medicines in Antarctica's coastal waters—apparently from nearby research facilities. After previous studies detected pollutants, including fuels and flame retardants, some research bases sought to limit their environmental impact. But researchers from the University of Canterbury in New Zealand found new contaminants, at concentrations similar to those measured in cities, in a large swath of McMurdo Bay near the U.S. McMurdo Station and New Zealand's Scott Base. The contaminants, which showed up in clams, fish, and sea urchins, "are endocrine-disrupting chemicals and may impair organismal health," says ecotoxicologist Da Chen of Southern Illinois University in Carbondale. The two agencies that run the bases say they strive to leave as small an environmental footprint as possible.



ENERGY RESEARCH

U.S. fusion effort melts down

Scientific community battles with its federal office

By Adrian Cho

Dysfunctional, broken, in complete disarray: That's how numerous insiders describe the United States' research effort in fusion, which aims to generate energy using the same process that powers the sun. A rift has opened between officials in the Department of Energy's (DOE's) Fusion Energy Sciences (FES) program and the research community it supports. Many scientists say program officials operate opaquely, but the community itself has a reputation for being unmanageable.

The discord has muddled an effort to draw up a strategic plan for the program, due in Congress next month, and it could jeopardize the program's already strained \$505 million annual budget. "When you have to fight for every dollar, it makes it very difficult when you can't even produce a strategic plan," says a Democratic Senate staffer, who calls the planning effort "a failure."

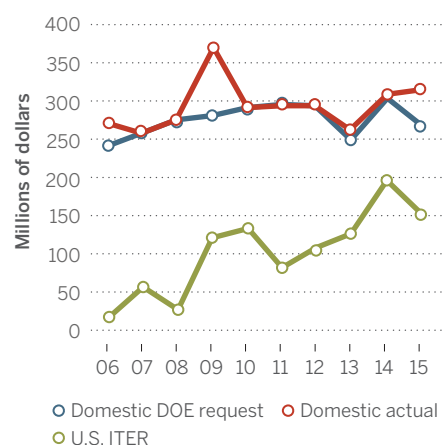
The fusion program has come under intense budget pressure as officials scrounge to pay for the U.S. share of ITER, the gargantuan international experiment to show that controlled fusion can produce more energy than it consumes. Now under construction in France, ITER cost the United States \$199 million in 2014, and DOE officials estimate that its total cost to the United States will be at least \$3.9 billion (*Science*, 18 April, p. 243). With ITER squeezing the rest of

the program, many researchers say that Edmund Synakowski, DOE's associate director for FES, and his staff exclude them from the decision-making process. "He's not a great believer in getting input from the community," says François Waelbroeck, a theorist at the University of Texas, Austin. Synakowski says he's "always a phone call away." But he emphasizes that his role is "to make the tough calls when they need to be made."

The disconnect in the fusion program contrasts with the approach taken in other

As ITER spending grows ...

... spending on domestic research has stagnated, barely keeping up with inflation.



A researcher works on the inside of the doughnut-shaped tokamak at the Princeton Plasma Physics Laboratory.

research programs run out of DOE's \$5.1 billion Office of Science, in which the associate directors strive to guide their communities to develop realistic plans for themselves. For example, a few years ago the U.S. high-energy physics community was perceived as fragmented. So, urged by leaders in DOE's office of high-energy physics, researchers held a 2-year-long series of meetings that informed the ad hoc Particle Physics Project Prioritization Panel (P5), which drew up a road map for the U.S. program (*Science*, 30 May, p. 955). Such a consensus plan "is a great example of what you want to see," says a Republican Senate staffer.

But Synakowski and FES officials aim to write the plan for their community. In January, after years of prodding, Congress demanded that FES draw up the strategic plan that is due next month. In April, DOE officials asked the Fusion Energy Sciences Advisory Committee (FESAC) to form an ad hoc panel to provide input—but not to actually develop the plan. That committee held two 3-day community meetings.

The panel's report, presented to FESAC on 10 October, looked forward 10 years under various tight budget levels. It called for immediately shutting down one of three large fusion devices, or tokamaks, in the United States—the Alcator C-Mod at the Massachusetts Institute of Technology (MIT) in Cambridge—reviving a 2012 DOE plan for shuttering the facility, which Congress reversed. One of two other facilities—the National Spherical Torus Experiment (NSTX) at the Princeton Plasma Physics Laboratory (PPPL) in New Jersey and the DIII-D tokamak at General Atomics in San Diego, California—might be shut down after 5 years. Such closures would enable researchers to start preliminary work on a bigger device, dubbed the Fusion Nuclear Science Facility (FNSF), which would develop the materials and components needed to extract energy from the plasma in a practical power plant.

Even before the report was out, researchers railed against it. The panel included no one from General Atomics, MIT, or PPPL, they noted. Synakowski says such exclusions were necessary to avoid conflicts of interest. Other conflicts of interest left only nine of FESAC's 20 members eligible to vote on the report. Only six voted to accept it.

Complicating matters, Synakowski soon put the kibosh on several of the report's recommendations. On 27 October, at a meeting of the American Physical Society in New Orleans, he told researchers that work toward

the multibillion-dollar FNSF was off the table and that in the next 10 years it would be premature to shut off NSTX or DIII-D. Still, he says the report and previous FESAC studies will inform the plan DOE will deliver to Congress next year.

Some observers say fusion physicists are to blame for failing to make tough choices for themselves. In 2012, DOE asked a panel of researchers to decide which of the three big tokamaks to close if budgets required it. The panel refused to choose, acknowledges Robert Rosner, a theorist at the University of Chicago in Illinois who chaired it. However, that study was requested after DOE announced it intended to shutter the MIT facility. "Being told to take the closure of the MIT machine as a fait accompli completely rubbed people the wrong way," he says.

Regardless of who is to blame, the dysfunction could cause "sponsor fatigue" in the higher levels of DOE and at the White House, says Raymond Fonck, a physicist at the University of Wisconsin, Madison. "In spite of our messianic vision of what we're going to do for energy, there are other things on the federal docket," he says. Recent budget numbers suggest fatigue has already set in. For fiscal year 2015, which began on 1 October, DOE requested \$266 million for domestic fusion work, \$39 million less than the previous year. But Congress reversed those cuts and boosted spending on the domestic program to \$318 million (see right).

Some observers say that the only way to save the domestic fusion program is to pull the United States out of ITER—as Senate budgetmakers have threatened to do. Others say fusion research is a bad fit for the Office of Science and should be moved into its own applied research program within DOE.

Barring such radical moves, FES officials and researchers must get beyond their current impasse. Some observers say that means Synakowski must go. "Until there's a leadership change at FES, they can't work together," says the Democratic Senate aide. "They hate each other so much." The Republican Senate aide is more optimistic: "I genuinely believe Ed is trying, so I would never say that he can't resurrect himself."

Synakowski and researchers agree on one thing: The current planning effort should be the first step. Researchers "desperately want" to expand it into a community-based effort like particle physicists' P5 report, says Steven Zinkle, a physicist at the University of Tennessee, Knoxville, and a planning panel member. Synakowski says he's setting up a series of workshops. Still, he sees their purpose as identifying scientific opportunities, not "making challenging choices." Those divergent views sound like a recipe for further friction. ■

RESEARCH FUNDING

Science agencies make gains despite tight U.S. budget

NASA, NSF among 2015 winners in difficult year

By Jeffrey Mervis and David Malakoff

In Congress, clout still counts. Once the political shenanigans ended and the dust settled, the \$1 trillion 2015 federal budget approved by Congress last week demonstrates that a few lawmakers can still make their voices heard. In a year in which Congress had no new money to play with, that fact was good news indeed for NASA and the National Science Foundation (NSF).

Those agencies received healthy raises thanks in large part to the work of retiring Representative Frank Wolf (R-VA) and Senator Barbara Mikulski (D-MD). The two se-

ingly well, although the largest, the National Institutes of Health, faces an essentially flat budget (see table, p. 1438).

One notable winner was NASA's \$5.15 billion science office. Congress rejected the White House's proposal for a \$179 million cut and instead awarded it a \$93 million raise, to \$5.24 billion. The biggest impacts of that \$272 million turnaround are an additional \$70 million to continue operations of SOFIA, an infrared telescope mounted on a Boeing 747 that NASA had proposed grounding, and \$100 million to accelerate planning for a multibillion-dollar mission to Jupiter's Europa moon, which some researchers believe could harbor life



NASA got \$100 million to plan a mission to Europa that the agency is worried it can't afford.

nior appropriators, who chair the spending panels that oversee NASA and NSF in each body of Congress, have traditionally protected those agencies. (Mikulski also chairs the full Appropriations Committee in the Senate, a position she will relinquish in the new Congress.) And this year their views prevailed in protracted budget negotiations that narrowly averted both another government shutdown and an extension of a spending freeze in effect since the 2015 fiscal year began on 1 October.

Researchers had braced for the worst after a budget deal struck last year allowed for essentially no growth in the discretionary portion of the 2015 budget, which funds most science agencies. Against that backdrop, many research agencies did surpris-

in oceans beneath its icy shell.

Legislators also rejected a proposed \$25 million cut to the Hubble Space Telescope program and added back \$27 million to fund education and public outreach activities carried out by individual missions. Mars exploration also got a boost, as did planning for WFIRST, an infrared survey telescope.

Even so, some space science programs may feel a squeeze as NASA reshuffles money to accommodate Congress's wishes. "There may not be any big losers, but some activities will take a hit," notes Joel Parriott, head of public policy for the American Astronomical Society (AAS) in Washington, D.C. The agency may not be able to advance smaller Discovery-class space probes (which must cost less than \$425 million) and somewhat

larger New Frontiers missions as quickly as it would like, for instance. And it may have to reshuffle funding dedicated to operating and analyzing data from existing missions.

Earth science was the only one of NASA's six major science programs that didn't get any extra help from legislators. Congress accepted the White House's plan for a \$54 million cut, to \$1.77 billion. Mikulski had proposed a \$60 million boost in her version of the NASA spending bill, and Parriott is "a little surprised that the Senate gave up" on her plan. Still, earth science researchers are pleased that the final bill didn't include House of Representatives proposals to terminate or restrict some earth observation missions, which are unpopular with many Republicans.

NASA has long resisted the Europa mission as too expensive when a Mars sample return mission is also in the works. But two of Europa's staunchest supporters sit on Wolf's spending panel, and they have

convinced their boss that the mission deserves his support.

"It's inevitable that we will find life in another world. And when we do, the most likely place to find it first is in the oceans of Europa," says Representative John Culberson (R-TX), who will succeed Wolf.

For Representative Adam Schiff (D-CA), the Europa funds are a boon for NASA's Jet Propulsion Lab in Pasadena, which is in his district, and a message to his party's leader, President Barack Obama. "Each year we've had to beat back proposals from the administration to cut funding," Schiff says. "This is the most resounding statement yet that NASA science is a crown jewel" that needs to be fully funded in the president's upcoming 2016 budget request to Congress.

A bipartisan coalition also reversed a White House plan to remake NASA's education activities. The agency has traditionally allowed mission scientists to run their own education and outreach programs in paral-

lel with agency-wide programs. The administration tried unsuccessfully to end that practice last year as part of a government-wide reshuffling of science education, a move that Congress rejected. This year the administration requested only \$15 million for mission-based activities, but Mikulski added \$27 million, essentially restoring the account to its pre-2014 level.

For advocates of SOFIA, the good news comes with a caveat. The Senate's proposal to spend \$87 million would have allowed scientists to keep upgrading the telescope, exploiting a key advantage of a ground-based instrument. But the final \$70 million allocation likely means no such improvements, notes Joshua Shiode, an AAS policy fellow.

While Congress served NASA with a long list of demands, it gave NSF considerable flexibility to apply its \$172 million increase across research directorates. That's a tribute to the respect for NSF's leadership that Mikulski and Wolf have shown over the years. But legislators were not entirely hands-off. Representative Chaka Fattah (D-PA), the top Democrat on Wolf's spending panel, helped protect the agency's request to double its investment in neuroscience spending as part of the administration's BRAIN Initiative. Wolf made sure that the education directorate received enough of a boost to disseminate lessons learned about improving science in elementary and secondary schools. And NSF received \$3 million for a new program to attract more minority students into science at all levels, although Mikulski had proposed a much more costly initiative that would have given historically black colleges a major role.

When Republicans take control of the Senate in January, Mikulski will lose much of her clout. But her likely successor on both the full Appropriations Committee and the subcommittee that funds NASA and NSF, Senator Thad Cochran (R-MS), is also a big NASA booster and traditionally a supporter of university-based research as well. In the House, Wolf's retirement has opened the door for Culberson, who sees assuming the gavel as an opportunity "to restore the NASA that I remember as a kid growing up in Houston."

Culberson says his twin priorities are "space exploration and scientific research." His ability to achieve those goals will be tested in the fight over the 2016 budget, which promises to be long and bitter. But Culberson is also confident that he can deliver.

"I want to make sure that scientists have what they need," he says. "And if anybody tells me about a hole in NASA's budget, I will plug it." ■

With reporting by Eric Hand.

| Pluses and minuses in budget numbers game | | | | |
|--|--------|--------------|------------|----------|
| Many U.S. science agencies will see increases over 2014 levels that exceed the president's 2015 request. (Figures are in billions of dollars.) | | | | |
| INSTITUTIONS | 2014 | 2015 REQUEST | 2015 FINAL | % CHANGE |
| National Institutes of Health | 29.934 | 30.134 | 30.084 | 0.5% |
| National Science Foundation | 7.172 | 7.255 | 7.344 | 2.4% |
| Research | 5.809 | 5.807 | 5.934 | 2.1% |
| Education | 0.847 | 0.890 | 0.866 | 2.2% |
| DOE Office of Science | 5.066 | 5.111 | 5.071 | 0.1% |
| Basic Energy | 1.712 | 1.807 | 1.733 | 1.2% |
| Bio/Environmental | 0.610 | 0.628 | 0.592 | -3.0% |
| Fusion | 0.505 | 0.416 | 0.468 | -7.3% |
| High Energy Physics | 0.797 | 0.744 | 0.766 | -3.9% |
| Nuclear Physics | 0.569 | 0.594 | 0.595 | 4.6% |
| ARPA-E | 0.280 | 0.325 | 0.280 | 0.0% |
| NIST | 0.850 | 0.900 | 0.864 | 1.6% |
| USGS | 1.032 | 1.073 | 1.045 | 1.3% |
| NASA | 17.647 | 17.641 | 18.010 | 2.1% |
| Science office | 5.151 | 4.972 | 5.245 | 1.8% |
| Earth science | 1.826 | 1.770 | 1.770 | -3.1% |
| Planetary science | 1.345 | 1.280 | 1.437 | 6.8% |
| Astrophysics | 0.668 | 0.607 | 0.684 | 2.4% |
| Heliophysics | 0.654 | 0.669 | 0.662 | 1.2% |
| USDA Agricultural Research | 1.122 | 1.104 | 1.178 | 5.0% |
| NIFA | 1.277 | 1.336 | 1.289 | 0.9% |
| AFRI | 0.316 | 0.325 | 0.325 | 2.8% |
| NOAA Research | 0.427 | 0.462 | 0.446 | 4.4% |
| DOD Basic Research | 2.166 | 2.017 | 2.278 | 5.2% |
| DOD Medical Research | 1.553 | 0.655 | 1.731 | 11.5% |
| DHS S&T | 1.222 | 1.072 | 1.071 | -12.4% |
| EPA S&T | 0.759 | 0.764 | 0.735 | -3.2% |



Thousands of years of breeding have made domesticated horses trainable, like this one in Mongolia.

ANCIENT DNA

The thoroughly bred horse

Genomes from ancient horses show the genetic changes wrought by domestication—and their costs

By Ann Gibbons

From Lipizzaners that perform precise airs to Thoroughbreds that race neck and neck and Clydesdales that haul beer wagons, today's horses are all descendants of wild animals tamed some 5500 years ago on the steppes of Asia. Now, genomes from an ancient stallion and mare reveal how domestication transformed the horse genome, resulting in the beautiful and powerful animals of today—but also leaving horses with flaws of personality and health not found in their wild ancestors.

By comparing the ancient genomes with modern ones, a team of researchers got a before-and-after look at horse domestication. That allowed them to identify the genes that endowed modern breeds with speed, strength, the ability to learn, and a panoply of coat patterns. The work, published this week in the *Proceedings of the National Academy of Sciences*, also reveals the genetic toll of millennia of inbreeding, says lead author Ludovic Orlando, a geneticist at the Natural History Museum of Denmark in Copenhagen. "Modern horses have accumulated more deleterious mutations than horses used to [have] in the wild," he says.

In the past, geneticists had no way to unravel the effects of domestication on the horse genome, because horses lack living wild relatives to serve as genetic proxies for their wild ancestors. (Przewalski's horse

from Mongolia was once thought to represent the predomestic animal, but more recently researchers have suspected it is not a direct ancestor of modern breeds, and it lacks the diversity to reveal horses' genetic history.)

To sample DNA from predomesticated horses, researchers needed to go back in time. Co-author and molecular biologist Beth Shapiro of the University of California, Santa Cruz, traveled to Siberia to gather bits and pieces of animals preserved in permafrost, including bones from a stallion and a mare radiocarbon dated to 16,000 and 43,000 years old, respectively. Working in separate labs, Shapiro and Orlando teased out high-quality sequences from these bones. They compared the ancient genomes with those of five breeds of living horses, as well as a donkey and a Przewalski's horse. As suspected, the Przewalski's horse turned out to be a distant cousin, rather than a direct ancestor, of domesticated horses.

To identify genes that were favored during domestication, Orlando's team looked for genes that came in diverse forms in the ancient horses but were winnowed to just one or two forms in modern breeds, presumably thanks to selection by breeders. The researchers produced a conservative catalog of 125 genes, including a group involved in development of muscles, joints, balance, and coordination. Multiple genes needed for the development of the cardiac

system and metabolism also changed, as did genes for behavior, the response to fear, and learning. This fits with the expectation that ancient people chose more docile, trainable horses, Orlando says.

In many cases, humans appear to have chosen among naturally occurring variations. For example, alleles that give modern racehorses their edge show up in the ancient horses, too, as do several versions of the *ZEAT* gene, which helps determine a horse's height at its withers (shoulders).

But sometimes domestication has favored novel versions of genes. Genes associated with facial shape in Arabians and coat color in all breeds were not found in either ancient horse. "What I really like about this is it's getting to the heart of what humans are selecting for: We are really obsessed with color and novelty," notes evolutionary biologist Greger Larson of the University of Oxford in the United Kingdom.

That obsession is still on view with horses with "leopard spots"—white coats with dark spots, such as those in Appaloosas. A separate ancient DNA study published this month suggests that some ancient breeders prized this rare pattern: DNA from horse bones from an Early Bronze Age site in Turkey shows that the leopard spot allele was unusually common there, according to work published in the *Philosophical Transactions of the Royal Society B*. But the Bronze Age breeding also spread a troubling genetic defect. Animals that inherit copies of the allele from both parents are night-blind, which makes them nervous and timid, especially in the dark.

Domestication had other hidden costs. An apparently selected gene linked to muscle strength is associated with muscular dystrophy in humans and may also cause disease in horses. Those costs likely arose because in creating animals with desirable traits, breeders chiefly mated similar horses to each other. Such inbreeding made it more difficult for natural selection to weed out harmful mutations and allowed bad traits to hitchhike along with favored ones.

The team scanned the ancient and modern horse genomes for changes in specific sites where mutations are usually harmful or even deadly in mammals. Domesticated horses had far more potentially harmful mutations at those nucleotide sites than ancient horses.

Human breeding might not have been the source of the population bottlenecks, Larson and others point out. Climate change or the movement of small herds around the world could also cause inbreeding. Either way, every horse breeder has long known that for all their beauty and power, horses can be fragile. Now we know why. ■



COSTA RICA

Celebrated biodiversity institute faces financial crisis

New government rethinks plan to take over INBio's money-losing theme parks

By **Lizzie Wade**

A pioneering effort to show that preserving tropical biodiversity can pay big dividends is in danger of shutting down. Costa Rica's new government is reviewing a previous administration's plan to save the National Biodiversity Institute (INBio) from crippling debt and has revoked some of its government contracts. Just as INBio is trying to transform itself to achieve a more stable future, it may succumb to the financial problems that have plagued the institute for a decade.

INBio was founded in 1989 to inventory all of Costa Rica's biodiversity. Its financing was based on contracting with pharmaceutical companies and others that hoped to prospect for medicines and other chemicals in the country's plethora of species. Set up as a nongovernmental organization (NGO), INBio promised a model for how developing countries could make money by conserving and exploring their biodiversity. "INBio was the poster child for chemical ecology and conservation," says Jon Clardy, a biological chemist at Harvard University who has worked with INBio in the past.

But it inspired criticism in Costa Rica. Many scientists and academics, especially those based at the University of Costa Rica (UCR) in San Pedro, worried that corporations would take unfair advantage of Costa Rica's natural resources. Others felt that a national institute of biodiversity should be run by the state. Still, a string of Costa Rican presidents heartily supported INBio as

it cut deals with companies such as Merck and succeeded in cataloging about 28% of the country's biodiversity.

Yet the corporate fees collected for granting access to INBio's collection turned out to be insufficient to cope with the financial squeeze that followed. "The strength of the opposition never became visible until INBio got really weak. And by weak, what I mean is that they began to run out of money," says ecologist Daniel Janzen of the University of Pennsylvania, a co-founder of INBio who maintains close ties.

INBio's current crisis can be traced back to 2000, when the institute opened INBioparque, a biodiversity theme park that aimed to attract tourists. INBio borrowed \$7 million to build the park. But "you don't go to Costa Rica to go to Disney World," Janzen says. The money earned by INBioparque and the institute's bioprospecting contracts never came close to covering the new debt. Although the park is a popular educational destination for Costa Rican families and schools, "from a financial standpoint, it was a failure," says Rodrigo Gámez, co-founder of INBio and president of its board of directors.

After loans for the park came due, INBio negotiated a bailout in 2013 in which the Costa Rican government would buy INBioparque's land and transfer INBio's sample collections to the National Museum of Costa Rica in San José. Relieved, INBio began planning to pivot toward a new business strategy based on environmental consulting at home and abroad.

But after UCR professor Luis Guillermo

Solís was elected president of Costa Rica, the new administration balked at the deal. Patricia Madrigal, vice minister of environment, estimates that between purchasing INBioparque's land and assuming responsibility for INBio's collections, the deal would cost the government nearly \$18 million U.S. dollars, at a time when the country has adopted austerity measures to deal with a financial crisis. Her office recently concluded a review of the purchase on INBioparque's land, but the judgment remains under wraps. The bailout "has taken us by surprise, financially and logistically," Madrigal says.

Gámez points out that Madrigal is a long-time critic of INBio; after the bailout was announced last year, she co-wrote an op-ed against the deal with biologist Vivienne Solís, the new president's sister. Gámez sees "a clear intention to shut down the institution" in other government actions, notably the decision by Madrigal's office to revoke INBio's eligibility to administer funds awarded to Costa Rica by the United Nations Development Programme's Global Environment Facility Small Grants Programme. That cuts off one of INBio's few remaining revenue streams. Madrigal says the move is part of a larger anticorruption campaign and that no private organization will be allowed to administer international grants awarded to Costa Rica from now on.

Madrigal underlines that she has no intention to close the institute, nor the power to do so, because it is not a federal agency. "There is no spirit of persecution against INBio," she says.

But Janzen has come to believe that setting up INBio as an NGO was a mistake that left it vulnerable to political whims and unstable funding. If INBio survives by transferring its collection and park into government hands, it may become something closer to the public-private hybrid Janzen now envisions. But it won't be the INBio that he and Gámez founded and that conservationists had looked to with hope. As it stands, "it's a tossup whether an institution that's hit that hard can stay alive," Janzen says. ■

BIOMEDICAL RESEARCH

Ambitious children's study meets disappointing end

After 14 years and \$1.2 billion spent, design and management troubles topple National Children's Study

By Jocelyn Kaiser

In the late 1990s, U.S. researchers trying to understand the complex web of factors that shape child development and health came up with an ambitious idea. They would follow 100,000 children from before birth to age 21, generating an unprecedented trove of biological specimens and data on everything from chemical exposures to psychosocial influences. In 2000, Congress embraced the initiative, known as the National Children's Study (NCS). President Bill Clinton boasted it would "provide critical information" for preventing and curing disease.

Last week, however, that dream died hard. Putting an end to years of organizational struggles and cost concerns, the National Institutes of Health (NIH) pulled the plug on the NCS. The idea is still worthy, an outside review panel told NIH Director Francis Collins, but the project, which has already cost \$1.2 billion, is too flawed to be carried out in a tight budget environment.

Collins announced he is immediately dismantling the NCS, but will redirect some of its \$165 million in funding for 2015 to related research. "This is not killing the study," Collins said at a 12 December meeting of the NIH Advisory Committee to the Director (ACD). "It is discontinuing a study in the form that had been previously contemplated. But it is opening up a much broader array of scientific horizons to try to accomplish those goals, which we all strongly agree are worthwhile."

Researchers involved with the NCS since its inception are not surprised. "The original idea was brilliant. ... But I think [it] was the right decision under the circumstances," says pediatrician Philip Landrigan of the Icahn School of Medicine at Mount Sinai in New York City, one of the researchers who proposed the NCS in the late 1990s. "It's a bittersweet moment," says pediatrician and epidemiologist Nigel Paneth of Michigan State University in East Lansing, a former NCS investigator.

In its original form, the NCS was envisioned as the largest longitudinal study of its kind ever undertaken in the United

States. Planners decided to enroll 100,000 children before birth and investigate a range of hypotheses developed by hundreds of scientists. To assemble a representative sample, they planned to recruit pregnant women by knocking on doors of randomly selected households in about

Rise and fall of the National Children's Study

2000

Congress requests large, long-term child health study

2003

NCS Program Office established at NIH

2004

Scientists dream big: The NCS will recruit a representative sample of 100,000 pregnant U.S. women by knocking on doors in about 100 U.S. counties

2007

Congress approves \$70 million to launch study

2008

IOM endorses sampling plan, but recommends pilot tests

2009

Recruitment begins at academic Vanguard Study sites

2009

NCS director replaced after study's estimated cost balloons to up to \$6.9 billion, more than twice original estimate

2012

To save money, contractors take over 40 academic study sites

June 2014

IOM/NRC report finds design, management problems

December 2014

NIH director cancels study

100 U.S. counties. The U.S. project aimed to collect more detailed data and more specimens than similar studies now under way in Europe and Japan.

In 2007, funding ramped up for the first NCS centers, called the Vanguard sites, which eventually enrolled 5700 children for pilot studies. The recruitment plan proved too cumbersome, however, so the NCS tested other approaches. By 2012, costs were still rising. NIH decided to close the 40 NCS sites at academic institutions and bring in a few large contractors to run the project. The changes sparked an uproar from researchers, who argued that the new design would compromise the study's goals (*Science*, 11 January 2013, p. 133). Congress then called for a review by the Institute of Medicine (IOM) and National Research Council (NRC). That panel's June 2014 report concluded that the NCS had great potential, but found problems with its design and management. Collins responded by putting the NCS on hold and asking a working group of the ACD for advice.

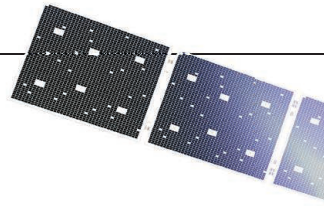
In a report released last week, that group, co-chaired by Philip Pizzo and Russ Altman of Stanford University in Palo Alto, California, agreed with the need to study how exposures early in life affect health. But it concurred with the IOM/NRC panel that there are numerous problems with the NCS and that the project's cost would run into the billions. Despite years of planning, for example, "there is no protocol" for the study, Pizzo said, and developing one could take 18 to 24 months.

Reviewers also concluded that the existing plan for the NCS does not take into account new science, such as the role of the microbiome in health. Nor does it envision making use of new technologies such as social media and electronic medical records that could bring down costs.

The working group agreed with the IOM/NRC report that the study's management team lacks appropriate scientific expertise. The working group's conclusion: The NCS, "as currently outlined, is not feasible."

Collins agreed. NIH will immediately close the NCS program office, which has about 25 staff members, and phase out contracts for the Vanguard Study and other work. But the agency will make existing Vanguard data and biospecimens available to outside researchers.

One bright spot, Collins notes: The 2015 omnibus spending bill approved by Congress last week includes specific language allowing NIH to redistribute NCS funds to institutes for related activities. "That," Paneth says, "would be a very positive outcome" of an otherwise sobering experience. ■



Comet rendezvous

Rosetta's short-lived lander grabbed the headlines, but the ongoing orbital mission is the real news for science *By Eric Hand*

This year's breakthrough captured the public's imagination with a series of hard-won pictures, beamed to Earth from a place beyond Mars. First: an image of a spindly, three-legged thing, framed against the blackness of space, falling toward a comet nearly as black. Would the little Philae lander survive its descent to 67P/Churyumov-Gerasimenko?

Soon, other pictures arrived. One revealed the dusty surface where Philae initially, and briefly, touched down. The lander, equipped with harpoons, screws, and reverse thrusters that didn't work, failed to gain purchase in the surprisingly hard comet crust, and

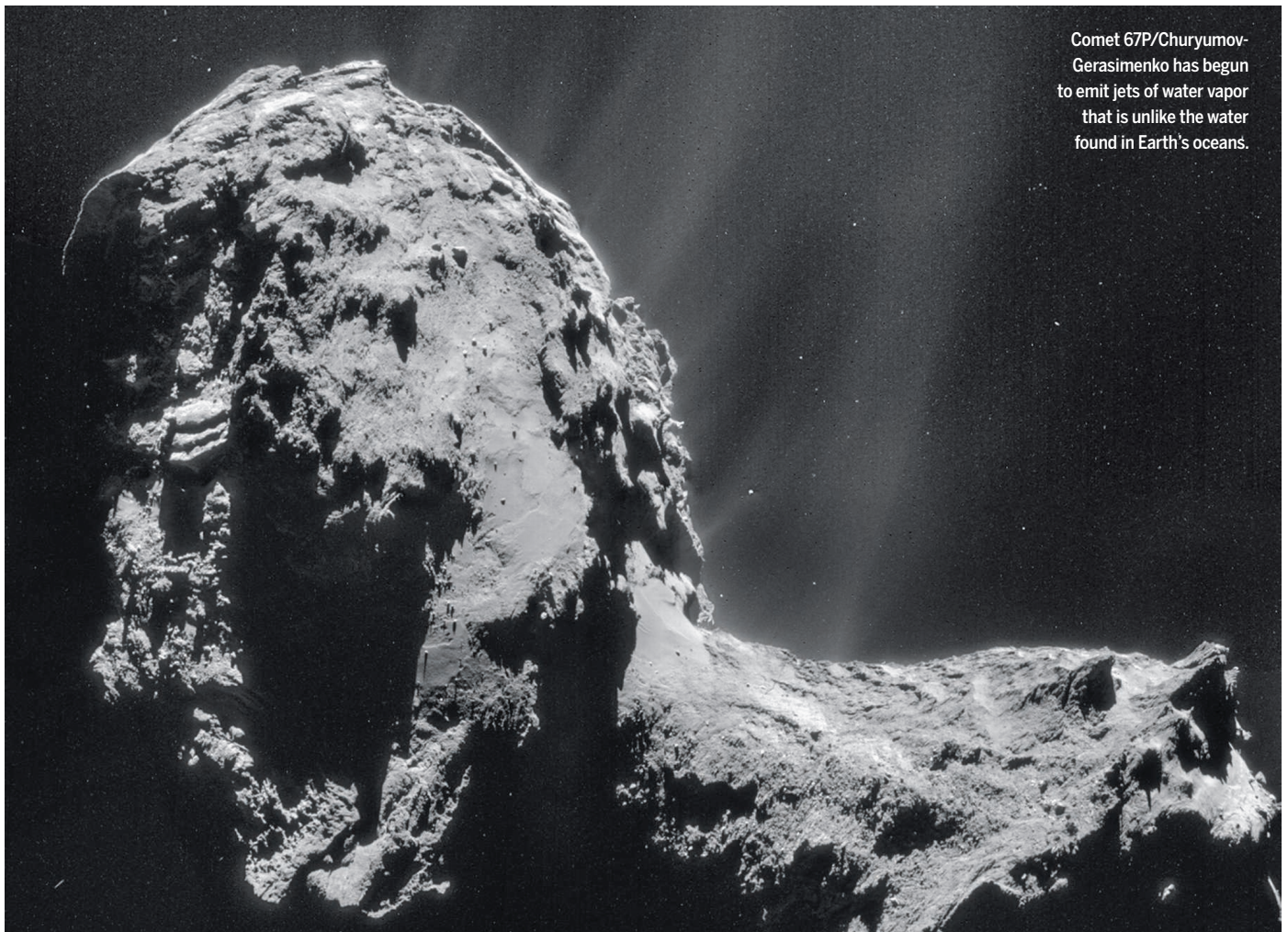
so it rebounded in the barely-there gravity. Then came some disorienting, ominous images. Philae appeared to have come to rest on its side, far from its intended landing spot, in the shadows of a cliff.

Comets are sintered lumps of dust, ice, and organic molecules and do not contain rocks per se. Nevertheless, Philae was caught in a hard place, next to something that looked very much like a rock. With too little sunlight to recharge its batteries, the lander had a feverish 57 hours to gather data before it expired. Philae's anthropomorphized Twitter account mawkishly narrated its final moments. "I'm feeling a bit tired, did you get all

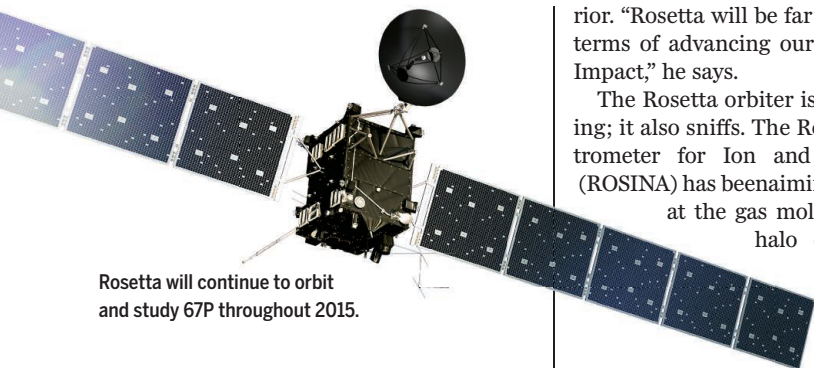
my data? I might take a nap," it said.

Whatever data Philae did manage to return will be significant, not least because 67P is just the seventh place beyond Earth explored by a lander. (Venus, Mars, the moon, Saturn's moon Titan, and two asteroids are the others.) Yet the importance of the landing was largely emotional and symbolic. Mission managers have suggested that 80% of the overall science return would come from Philae's mother ship, Rosetta, which reached the comet in August and has been orbiting it ever since, scrutinizing it from as close as 10 kilometers away. That broader achievement, and the cornucopia of information it is yielding, are what

3



Comet 67P/Churyumov-Gerasimenko has begun to emit jets of water vapor that is unlike the water found in Earth's oceans.



Rosetta will continue to orbit and study 67P throughout 2015.

Science is celebrating as 2014's Breakthrough of the Year.

Merely getting the €1.4 billion mission to the comet was a massive undertaking for the European Space Agency. After launch in 2004, flight engineers put Rosetta through a decade of orbital tricks: Mars and Earth were used as gravitational slingshots to bring the spacecraft in line with the comet's elliptical 6.5-year orbit. When Rosetta caught up with 67P, the comet was still far from the sun and cold. As it plunges sunward, its subsurface ice deposits have begun to sublime, powering jets of gas and dust. Peak activity should come in August 2015 at perihelion, when the comet is halfway between the orbits of Earth and Mars. By watching the jets develop and change, scientists can learn how comets are altered each time they approach the sun. Then, by subtracting those processes, they can turn back the clock and understand how comets formed some 4.5 billion years ago.

Much of Rosetta's power comes from its ability to inspect the comet at close range for months on end. The half-dozen or so previous missions to comets were all flybys that were over in hours. Another ballyhooed flyby of an icy body—NASA's New Horizons mission to Pluto—will whiz past the dwarf planet on 14 July 2015. At its closest, New Horizons will pass Pluto at a distance of 10,000 kilometers, close enough to make out mountain-sized features (with a camera resolution of 12 kilometers per pixel). By contrast, Rosetta's camera can discriminate between objects just centimeters apart. Already, Rosetta has tracked arcs of dust emerging from active jets.

"The breakthrough is yet to come, and it will come from having the orbiter stay with the comet," says Michael A'Hearn, a planetary scientist at the University of Maryland, College Park. A scientist on two of Rosetta's instruments, A'Hearn was also the principal investigator for Deep Impact, a NASA comet flyby that in 2005 lobbed a projectile into the comet Tempel 1 to probe its inte-

rior. "Rosetta will be far more impressive in terms of advancing our science than Deep Impact," he says.

The Rosetta orbiter is not just about seeing; it also sniffs. The Rosetta Orbiter Spectrometer for Ion and Neutral Analysis (ROSINA) has been aiming its spectrometers

at the gas molecules in 67P's thin halo of an atmosphere, called the coma.

In addition to detecting expected gases such as water, methane, and hydrogen, it has started to find rarer species, including formaldehyde and hydrogen cyanide. Getting the list of comets' primordial ingredients is important because many scientists think comets helped jump-start life on early Earth with an infusion of water and organic molecules.

ROSINA has the sensitivity to detect isotopes, too. In one of the most important mission results so far, published online on 10 December in *Science*, the ROSINA team found an exceptionally high ratio of heavy hydrogen (deuterium) to regular hydrogen. Because this D-to-H ratio is so much higher than that found in Earth water, it suggests that comets like 67P—part of a group that hails from the Kuiper belt, a region beyond Neptune—could not have played a major role in delivering water to Earth. The high ratio also buttresses the classical view of where the two main groups of comets formed. In this view, Kuiper belt comets like 67P formed beyond Neptune before being flung farther out into the Kuiper belt by the gravitational influence of Jupiter.

Other comets, with lower D-to-H ratios, formed closer to the sun. There, solar system dynamics gave them an even bigger push, strong enough to scatter them out to an even more distant solar suburb known as the Oort cloud.

Rosetta has its limitations.

It struggles to detect complex chains of organic molecules, such as amino acids, especially on the comet's solid surface. As a result, it is unlikely to tell scientists conclusively whether the organics at the comet's surface are the pristine ingredients that 67P started with, or products of chemical reactions sparked by earlier close encounters with the sun. That's why mission scientists are disappointed that Philae was unable to perform its most ambitious experiment: drilling a sample from below the comet's surface and baking it in an oven for analysis.

Mission managers haven't completely ruled out trying again. As 67P approaches the sun, more light will fall on Philae's

ON OUR WEBSITE

For more on the Breakthrough of the Year, including a video and a podcast, go to <http://scim.ag/breakthru14>.

People's choice

Visitors to *Science*'s website picked their top breakthroughs of 2014. The results:

- 1 Giving life a bigger genetic alphabet **34%**
- 2 Young blood fixes old **32%**
- 3 Comet rendezvous **17%**
- 4 Cells that might cure diabetes **11%**
- 5 An easy cure for hepatitis C **6%**

Since 1996, *Science*'s writers and editors have assembled the Breakthrough of the Year section by holding meetings, revising lists, and even installing a suggestion jar in the office kitchen. This year, we decided to give the public a say. In November, we posted our "long list" of 19 breakthrough candidates online at www.sciencemag.org and let visitors vote on them for 2 weeks. In December, we took the top five semifinalists and posted them for a second, weeklong round of voting.

A science-themed horserace ensued. The Rosetta comet mission—which was making headlines worldwide as the voting began—finished the first round with a healthy lead, garnering more than 16% of the 24,947 votes cast. Next came "Young blood fixes old" with 11% of the votes, followed by "Cells that might cure diabetes" with 10%.

In the second round, things got interesting. "Young blood" took an early lead and looked like a shoo-in. But in a late surge, "Giving life a bigger genetic alphabet" pulled even with the rejuvenated mice. The two results ran neck and neck in the final stages of voting, but the expanded genetic alphabet pulled ahead and won by a nose. The Rosetta mission—*Science*'s own choice—finished third. Kudos to all contestants, and thanks to everyone who cast a vote.

solar panels. In its last tweet, the lander raised the possibility of a resurrection. "My #lifeonacomet has just begun @ESA_Rosetta. I'll tell you more about my new home, comet #67P soon... zzzzz." Regardless of whether Philae wakes up, Rosetta's life at comet 67P has indeed just begun—and it heralds a new age of comet science. ■



Feathers were widespread even among dinosaurs, such as *Kulindadromeus*, that were not closely related to birds.

Cooperative 'bots' don't need a boss

Robots are getting better all the time at working with humans, but this year several teams demonstrated that these machines can also work together, without human supervision. At a time when roboticists are still struggling to improve how well individual robots sense their surroundings and respond to new situations, letting teams of robots execute their own missions may seem premature. But after years of work, researchers have come up with new software and interactive robots capable of cooperating on rudimentary tasks.

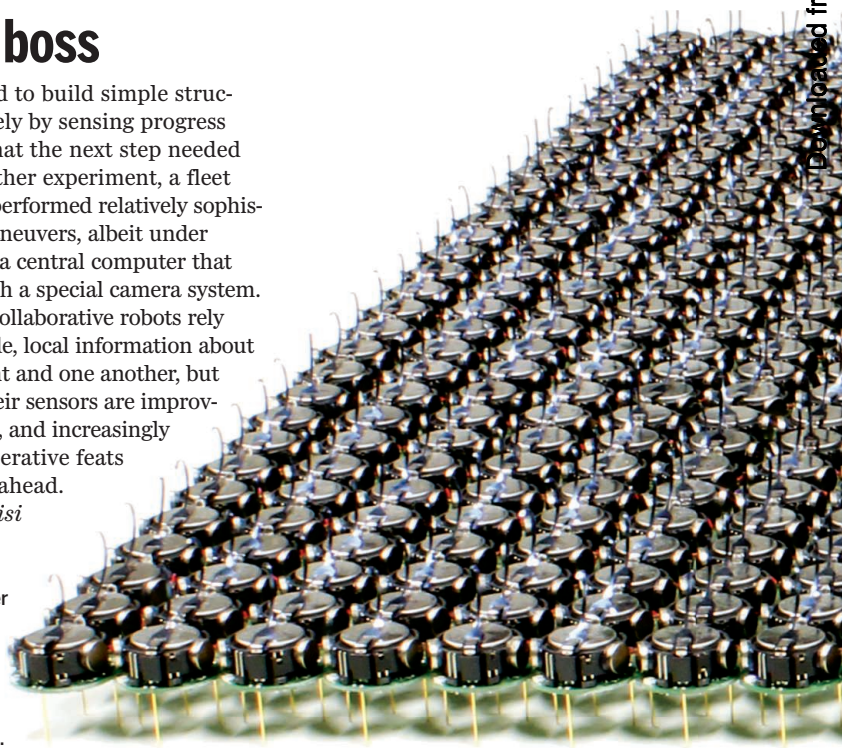
In one study, a thousand robots the size of U.S. quarter coins came together like a marching band to form squares, letters, and other 2D formations. The sheer scale required cheap, easy-to-run robots that could efficiently sense where other robots were. In another project, 10 quadcopters radioed their locations to one another and adjusted their paths to avoid collisions and fly in formation, creating a rotating circle. A third group of robots, inspired by termites,

was programmed to build simple structures cooperatively by sensing progress and inferring what the next step needed to be. In yet another experiment, a fleet of robotic boats performed relatively sophisticated group maneuvers, albeit under the command of a central computer that tracked them with a special camera system.

So far, all the collaborative robots rely on relatively crude, local information about their environment and one another, but both they and their sensors are improving rapidly. More, and increasingly impressive, cooperative feats undoubtedly lie ahead.

—Elizabeth Pennisi

Small, disk-shaped robots that maneuver in formation are just one example of the year's progress in self-organizing machines.



The birth of birds

It took a lot to turn lumbering cousins of *Tyrannosaurus rex* into agile hummingbirds and graceful swans. This year, evolutionary biologists figured out the mode and tempo of the spectacular evolutionary transition from dinosaurs to birds.

Their analyses top off 2 decades of fossil discoveries, primarily in China, showing that birdlike innovations—particularly feathers—emerged repeatedly among dinosaurs, well before the first birds appeared. Feathers, it seems, were not just for flying, but also for insulation, display, or possibly balance.

In 2014, several groups compiled and analyzed data on many dinosaur and early bird fossils as well as on extant birds, to see when other birdlike traits actually appeared. One study compared 850 morphological traits among 150 species; another measured the thickness of leg bones of 426 species. They discovered that the dinosaurs that ultimately gave rise to birds steadily got smaller and finer boned over time.

Once the bird body plan crystallized, new avian species arose quite rapidly, probably because their small size enabled them to find food and shelter that their larger kin could not exploit. Birds took off, but their dinosaur ancestors had given them a running start. —Elizabeth Pennisi

Youth serum for real?

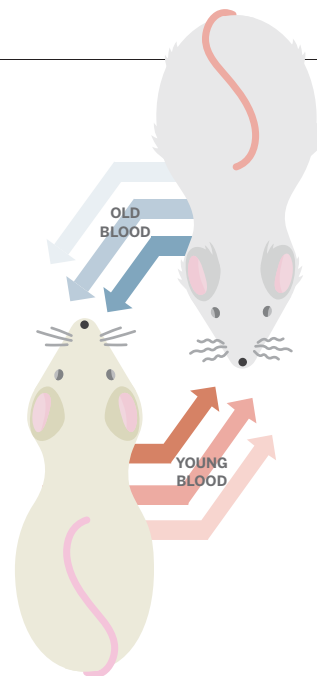
This year, in work with profound implications for aging, researchers showed that blood or blood components from a young mouse can rejuvenate an old mouse's muscles and brain. If the results hold up in people—an idea already in testing—factors in young blood could offer the antidote to aging that humanity has sought as far back as Juan Ponce de León's quest for the Fountain of Youth.

These findings grew out of strange-sounding experiments dating back 150 years, in which researchers sewed together

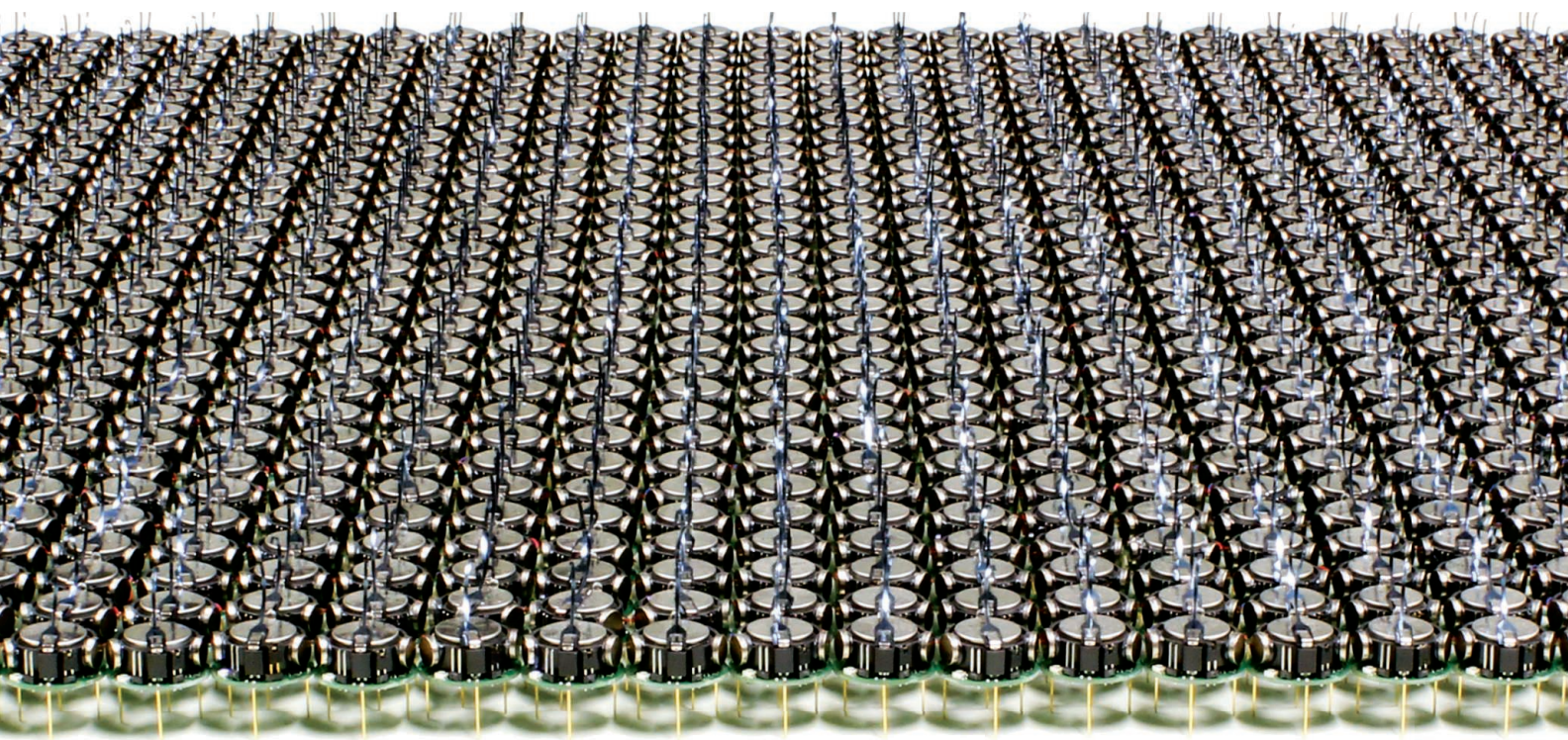
2 the skins of two mice to join their circulation. In the early 2000s, the approach was revived to study stem cells. Researchers found that when they connected the circulation of young and old mice, the muscle stem cells in the old mice were better able to regenerate muscle.

Work published in 2014 strengthened the evidence that something in young blood can reverse multiple signs of aging. One group studied a factor isolated from young mouse blood called GDF11, which had already been shown to rejuvenate the heart. They found that it can also boost the muscle strength and endurance of an old mouse and spur neuron growth in the brain. Another team reported that young blood, or even cell-free blood plasma, bolsters an aging mouse's spatial memory.

Now, in the first clinical trial, 18 middle-aged and elderly Alzheimer's patients are receiving injections of plasma donated by young adults. By this time next year, we may know if young blood can fight one of the most feared diseases of aging. —Jocelyn Kaiser



Old mice thrive when their circulatory systems are linked with those of younger mice, for reasons not yet clear.



Chips that mimic the brain

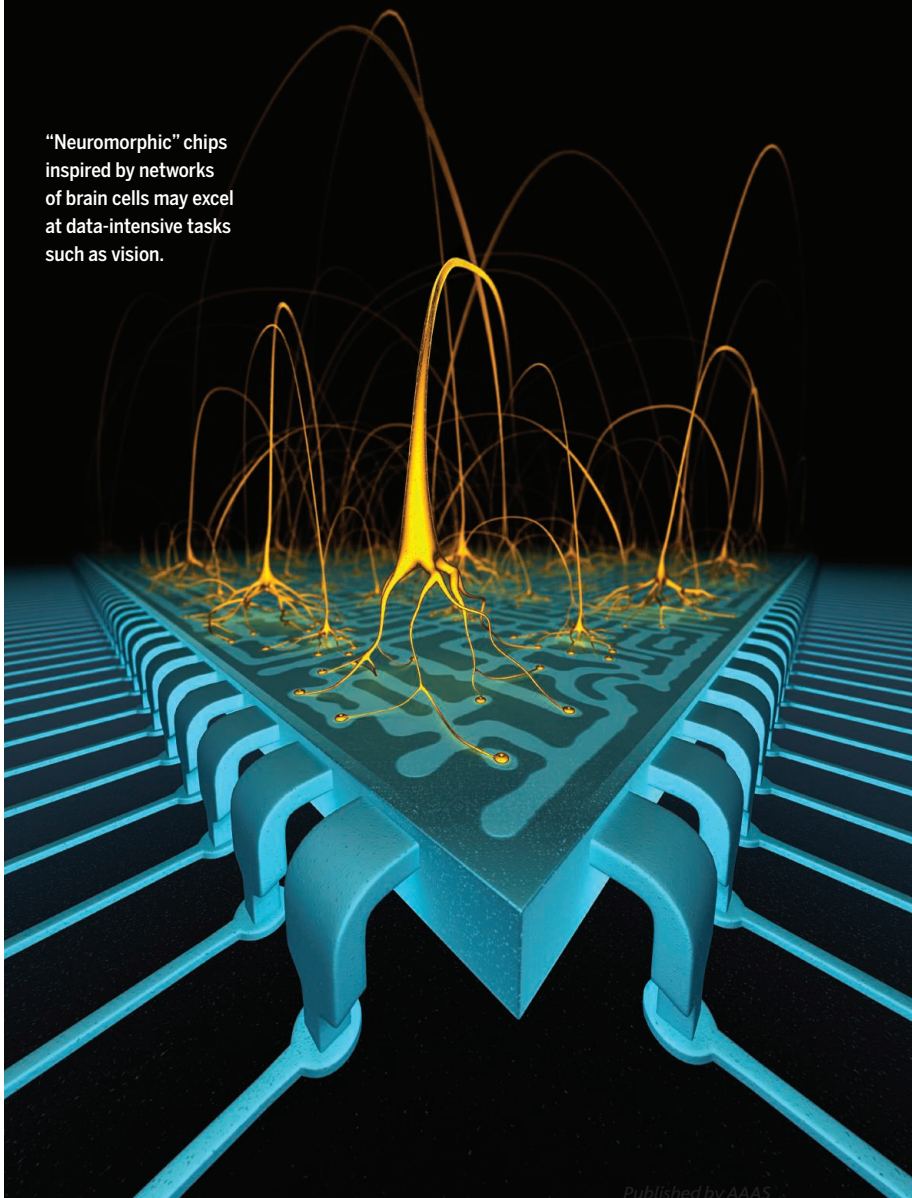
John von Neumann may have finally met his match. Nearly 70 years ago, the Hungarian-born polymath sketched out the basic design of modern computers, with separate processing, memory, and control units. But this year, computer engineers at IBM and other companies rolled out a promising alternative: the first large-scale “neuromorphic” chips, designed to process information in ways more akin to living brains.

Chips based on von Neumann’s architecture excel at carrying out sequences of logical operations, such as those that underlie spreadsheets and word processors. But they struggle with tasks that integrate vast amounts of data, such as vision.

Our brains take a very different approach. Individual neurons communicate with thousands of their neighbors through chemical signals, enabling the brain to process lots of information in parallel. Different brain regions also specialize for greater efficiency.

The brain’s network of 100 billion cells linked by 100 trillion synapses still dwarfs anything neuromorphic chips can muster. But IBM’s new TrueNorth chip includes 5.4 billion transistors and 256 million “synapses,” and the company is working to tile multiple TrueNorths together to build more complex networks. In the future, brainlike processors could transform fields such as machine vision and environmental monitoring, integrating real-time data from sensors from around the globe. —Robert F. Service

“Neuromorphic” chips inspired by networks of brain cells may excel at data-intensive tasks such as vision.



Early artists blew red pigment over their hands to create this cave art on the island of Sulawesi at least 40,000 years ago.

Cells that might cure diabetes

Since the discovery of human embryonic stem (ES) cells, researchers have hoped to wield them against disease. The quest has been frustratingly

4 slow. For more than a decade, for example, labs all over the world have sought to turn ES cells into cells of the pancreas called β cells. β cells respond to rising blood sugar by making insulin, a hormone that allows cells to take up and use glucose. An autoimmune attack that kills β cells leads to type 1 diabetes; replacing them with lab-grown cells might provide a cure.

This year, researchers came closer than ever to that goal, when two groups published methods for growing cells that resemble human β cells.



Europe's cave art has a rival

For decades, visitors have marveled at the prehistoric graffiti that fills the Maros caves on the island of Sulawesi, Indonesia: hand stencils outlined in mouth-blown red paint, mixed with pictures of rare “pig-deer” in red and mulberry hues. This year they evoked an extra measure of wonder. Scientists discovered that the images, thought to be about 10,000 years old, are actually four times older—at least as ancient as the famous cave art in Europe.

The finding could rewrite the history of a key stage in the development of the human mind. People in Africa engraved geometric designs on chunks of hematite and on ostrich eggshells as early as 78,000 years ago. But symbolic art first seemed to blossom between 35,000 and 39,000 years ago in Europe, where artists painted vivid representations of rhinos, horses, lions, and women, notably at Chauvet Cave in France. Some archaeologists argued that the European creative explosion reflected a new leap in human abilities, but others thought the capacity for symbolic expression had already developed in Africa, before modern humans left that continent to populate the world.

The new dates in Indonesia end Europe's monopoly on early symbolic art. By measuring the radioactive decay of uranium in small stalactitelike growths that formed atop the paintings, Australian and Indonesian researchers found that the oldest hand stencil is at least 39,900 years old and the animal paintings at least 35,400. If the numbers are accurate, they suggest that humans in Indonesia independently invented symbolic art as early as Europe's cave painters did—or that modern humans were already sophisticated artists when they spread out of Africa starting about 60,000 years ago. —Ann Gibbons

One approach works with both ES cells and so-called induced pluripotent stem cells—reprogrammed cells that can be made from a patient's skin cells. The recipe is complex, and it takes 7 weeks to convert stem cells into the insulin-producing cells. But researchers can grow 200 million of the β -like cells in a 500-ml flask—in theory, enough to treat a patient. The other method takes 6 weeks and can produce one β -like cell for every two ES cells at the start.

To use the cells to treat type 1 diabetes, researchers need to develop ways of protecting them from the autoimmune reaction that kills β cells in the first place. Meanwhile, the grown-to-order cells give scientists an unprecedented chance to study diabetes in the lab. Researchers have already started to compare β cells made from skin cells of healthy subjects with those made from patients with diabetes, hoping to pinpoint the key differences. —Gretchen Vogel

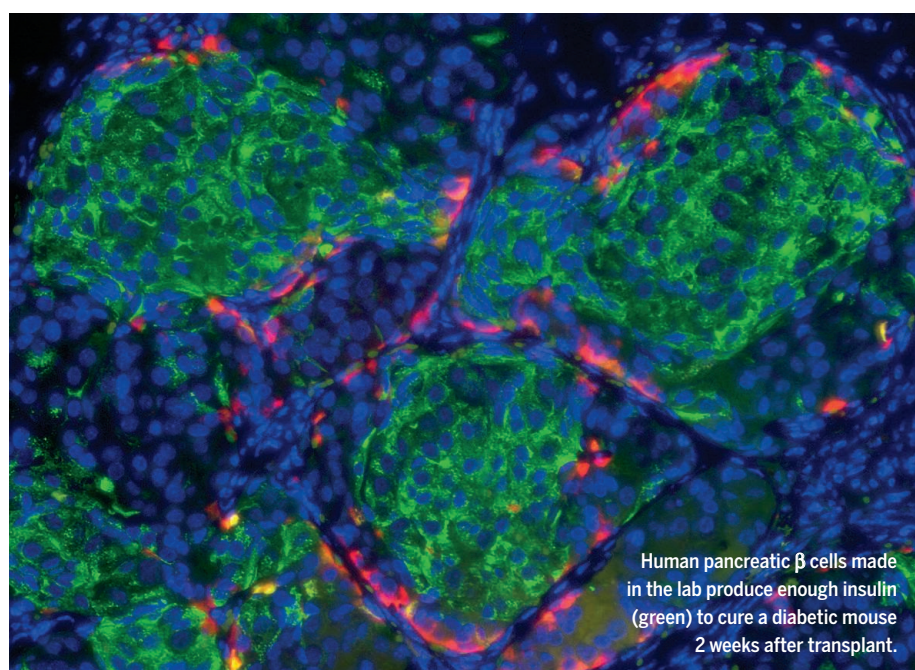


PHOTO: DOUGLAS MELTON

By zapping the brain cells of mice with light, researchers can create, erase, or alter memories.



Manipulating memory

Memory is notoriously malleable. Our recollections fade and take on new meanings; sometimes we remember things that never even happened. But just what is happening in our brain as memories are remodeled remains mysterious.

Recently, however, scientists have started to grasp and tinker with memory's physical basis. Last year, in work evocative of films such as *Eternal Sunshine of the Spotless Mind* and *Inception*, researchers discovered ways to manipulate specific memories in mice using optogenetics, a powerful technique that can trigger nerve cells in animals' brains by zapping them with beams of laser light. In a series of experiments, they showed that they could delete existing memories and "incept" false ones.

This year, researchers went even further: switching the emotional content of a memory in mice from bad to good and vice versa. Under the laser, for example, male mice that had once associated a certain room with being shocked were tricked into acting as though they had once met friendly female mice there instead.

Whether the mice in these experiments actually experienced vivid false memories or just a fuzzy sense of pleasure or fear is unclear. Nor is it clear whether the findings apply to the tricks of memory so familiar to people. Long-sought therapeutic advances, such as treatments for post-traumatic stress disorder, could remain far off. One thing is certain, however: Once considered beyond scientific dissection, memory is finally starting to yield its secrets.

—Emily Underwood

PHOTO: KARL DEISSEROTH, JOHN CARNETT, VIVIANA GRADINARU

Giving life a bigger genetic alphabet

Everywhere on Earth, the genetic code at the heart of living things consists of the same four genetic letters. Everywhere, that is, except in a flask of *Escherichia coli* bacteria on a lab bench in southern California. There, researchers this year engineered the bacteria to incorporate two additional letters into their genetic alphabet. In addition to the natural nucleotides,

in which G pairs with C and A pairs with T, the bacterial DNA includes a novel pair: X and Y.

Researchers around the globe had already devised several pairs of "unnatural" nucleotide bases that, in the test tube, could fit within DNA's double helix. They also managed to get DNA's copying machine, an enzyme known as DNA polymerase, to copy some of these new pairs. But no one had ever made it all happen inside living organisms—until this year.

For now, the new letters in the *E. coli* DNA don't code for anything, but in

principle, researchers could use them to create designer proteins that include "unnatural" building blocks: amino acids beyond the 20 encoded by the bases in normal DNA. Researchers have previously used genetic tricks to do that with natural DNA. But adding the new X-Y combo should make the process far easier. That could be a godsend for makers of medicines and materials. And perhaps not the only one: This year, in a parallel effort to tailor DNA, synthetic biologists also modified its chemistry to create novel catalysts.

Eventually, the expanded genetic code



Two Earth-observing CubeSats (dark oblong objects) shoot from a satellite deployment device on the International Space Station.

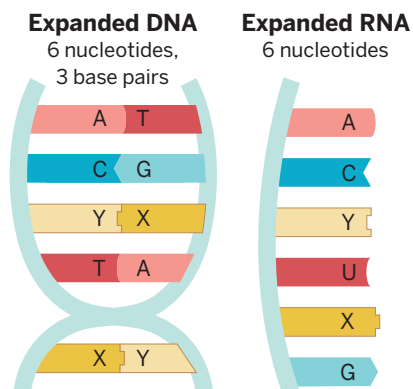
The rise of the CubeSat

A decade ago, CubeSats were just educational tools, a way for university students to place a simple Sputnik in space. Now these 10-centimeter boxes, built with off-the-shelf technology and costing hundreds of thousands of dollars rather than hundreds of millions, have taken off. More than 75 were launched this year, a record. What's more, the little boxes are starting to do real science.

Increased and affordable access to space is driving much of the boom. CubeSats can hitch a ride on commercial or government rockets carrying bigger spacecraft, or they can be pushed out the door of the International Space Station. The rapid-fire launch rate is encouraging something never before seen in space: risk-taking. Designers can tolerate a failure or two and quickly get back in the game. As technology advances, they can also swap in better solar panels, batteries, or processors.

Private money has taken notice, funding companies such as Planet Labs, which is monitoring Earth with a swarm of perennially replaced CubeSats. Their small telescopes take pictures with relatively poor spatial resolution—a few meters—but at frequent intervals. Spy agencies may not be seduced, but Planet Labs' data are plenty useful for monitoring deforestation, urban development, and river changes.

Coming up next: CubeSats that talk to one another while taking measurements. Among other things, such CubeSat constellations will be able to cover more area, faster, or monitor Earth's surface in several wavelengths at once. If they work, CubeSats will have demonstrated not only that small is beautiful, but also that the whole is greater than the sum of its parts. —*Eric Hand*



could also serve a more academic pursuit, enabling researchers to test whether bacteria equipped with the excess letters might evolve novel skills not found in their wild kin. That may sound like a scenario for a dystopian techno-thriller, but the researchers say there's no need to worry: Because unnatural DNA letters don't exist outside the lab, any bacterial escapees would not be able to replicate their artificially expanded genetic instructions and pass them on to their offspring. —*Robert F. Service*

Scorecard for 2014

Every year, the Breakthrough staff picks scientific developments likely to make news in the coming months. The numbers of bars show how last year's forecasts fared; those for 2015 are on page 1450.



SPACE GHOSTS

Last year, physicists with IceCube, a massive neutrino detector deep in the ice at the South Pole, spotted high-energy neutrinos from beyond our solar system. But could IceCube track enough to pinpoint their mysterious sources? We predicted the IceCube team would release search results this year, and in November, it did—but didn't nail down any obvious sources.

CLINICAL GENOMES

Tests that sequence a patient's protein-coding DNA (the exome) or entire genome to uncover disease-causing glitches are fast becoming routine for rare disorders. Whole genome or exome sequencing to identify tumor mutations remains largely a research endeavor, however.

COSMIC HISTORY, WITH A TWIST

We predicted that cosmologists mapping the afterglow of the big bang might spot swirls that would be a telltale sign that in the first sliver of a second the universe underwent an exponential growth spurt called inflation. In March, one team claimed just such a sighting, but by September another had shown that the signal may be entirely spurious (see breakdown runners-up, p. 1451).

BYE-BYE, CHIMPS?

Chimpanzees still live in U.S. research labs, but efforts continue to grant them "legal personhood"—and the right to be free. The Nonhuman Rights Project lost all three of the lawsuits it launched last year to try to free four New York chimps—including two lab chimps—from captivity. This year, it appealed each case and now has its sights set on the state's highest court.

Areas to watch in 2015

Science is a moving target. In addition to looking back on achievements of the previous year, the Breakthrough staff also hazards a few informed guesses about developments likely to make news in months to come.

ARCTIC SEA ICE

As the world heats up, so does research into far-reaching consequences of shrinking Arctic sea ice. Sea ice loss is already known to amplify warming in the region, as the open ocean absorbs more energy from the sun. But what impact the warming Arctic has on lower latitude weather—and whether it is to blame for some of the weather extremes of the past decade, from Asian monsoons to European winters—is still hotly debated. Identifying long-distance connections within the complex dynamics of atmospheric circulation is no easy task. This year, scientists proposed a few patterns to watch, including large-scale Rossby waves and the polar jet stream. In 2015, expect efforts to pin down how they might exert an Arctic influence on weather thousands of miles south.

SOLAR SYSTEM ENCOUNTERS

The year of the comet came in 2014. But 2015 is apt to be the year of the dwarf planet. In March, NASA's Dawn spacecraft will arrive at Ceres, the largest object in the asteroid belt and one that contains a surprising amount of ice. Four months later, in July, NASA's New Horizons spacecraft will speed past Pluto in a brief but momentous encounter. The two icy bodies are twins of a sort. In 2006, the International Astronomical Union upgraded Ceres from an asteroid to a dwarf planet and demoted Pluto from a planet to a dwarf. Some scientists have proposed that both objects were created when icy cometsimals clumped together in the outer reaches of the solar system, then wound up in wildly different places, perhaps tossed there by the gravitational shenanigans of a roving Jupiter. The two missions should go a long way toward sorting out the origin stories.

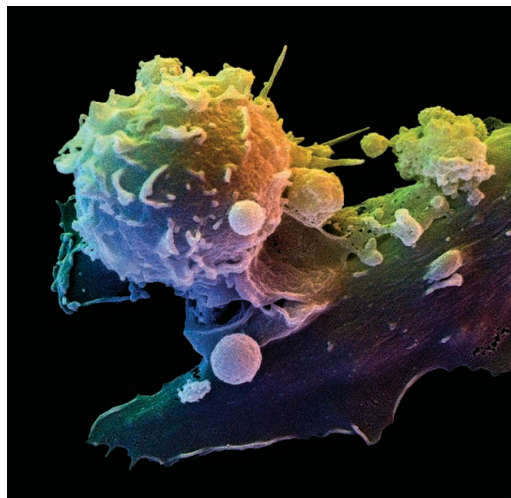
LHC RESTART

Next spring, the Large Hadron Collider (LHC) at CERN, the European particle physics laboratory near Geneva, Switzerland, will power up after 2 years of repairs. In July 2012, the LHC blasted out the Higgs boson, the last piece in physicists'

standard model of the known particles. But some researchers say that if accelerator-based particle physics is to have a future, the massive machine will have to discover something beyond the tried-and-true standard model. Now the LHC is back for another try, at energies expected to be nearly twice as high as in the first run. Look to see whether the LHC finally reaches its design energy—and whether, in the next few years, it discovers new mysteries to sustain the field.

COMBINED IMMUNOTHERAPY

Cancer immunotherapy, *Science's* Breakthrough of 2013, continues to surge as clinical researchers amass evidence that the immune system can be a powerful ally against tumors. One big focus



Combination therapies that help harness T cells and other immune cells in the cancer fight are a key area to watch.

now is mixing and matching treatments: combining two novel immunotherapies, for example, or an immune strategy with a targeted drug, radiation, or chemotherapy. Dozens of clinical trials are under way—ranging from a phase I study in melanoma that combines the recently approved immunotherapy drug ipilimumab with another treatment that slows blood vessel growth, to a phase III trial testing whether ipilimumab and chemotherapy outperform chemotherapy alone in treating lung cancer. The results could make it easier for oncologists to match treatments to patients. But potential toxicity of the new strategies remains a concern.

Breakdown of the year: Ebola

This year, an Ebola outbreak that began in the remote Guinean village of Meliandou grew into a widespread epidemic that has alarmed the entire world. Outpacing efforts to contain it, the virus has ravaged Guinea and neighboring Liberia and Sierra Leone, creating a public health breakdown that Margaret Chan, director-general of the World Health Organization (WHO), described as “likely the greatest peacetime challenge that the United Nations and its agencies have ever faced.”

Ebola outbreaks have flared every few years since the virus was first identified in 1976. Yet until now, containment efforts derailed all outbreaks within a few months and kept them mostly remote and local, limiting the total number of cases to only 2500 or so. This time around, the virus spread across borders and through crowded cities, taking advantage of shaky health systems and a slow, uncoordinated international response to grow into an epidemic that has sickened more than 18,000 people and killed nearly 7000 so far, with isolated cases as far afield as Spain and the United States. “I wonder whether one person in the world could say that he or she predicted this outbreak,” says Bertrand Draguez, the medical director for Doctors Without Borders (MSF) in Brussels. Its future course is equally unpredictable.

After the first case in Meliandou in December 2013, it took 3 months for health officials to realize an Ebola outbreak was under way. MSF quickly sent in teams, and by late March, the virus had spread to four districts in Guinea, and Liberia and Sierra Leone had suspected cases. “We are facing an epidemic of a magnitude never before seen,” MSF warned on 31 March. But over the next month and a half, the outbreak waned and even Guinea’s president declared the situation “well in hand.”

By mid-June, however, the number of cases in the three countries had skyrocketed to 504, surpassing the largest previous outbreak. MSF announced it no longer had enough staff to keep up



Overwhelmed by Ebola in August, Monrovia converted this primary school classroom to an isolation ward. The health care worker is disinfecting a corpse.

with the spread. Wobbly health care systems in the three countries—which long had suffered from political instability, corruption, and staggering poverty—began to collapse. Overwhelmed clinics had no beds for the sick, who returned home and infected others.

The problem still drew little international attention until two American missionary health care workers became infected in late July. On 8 August, WHO declared the epidemic a “public health emergency of international concern.” A month later, U.S. President Barack Obama announced that the country would send in 3000 military troops to help, millions of dollars of aid poured in, and an aggressive push emerged to develop Ebola drugs and vaccines.

Finger-pointing escalated in lockstep with the case counts. WHO and the international community took too long to act. No one effectively coordinated responses. Local governments played ostrich, fudged case reports, and imposed counterproductive quarantines. Frightened health care workers stayed away from work. Affected

communities attacked aid workers and ostracized survivors. Sick people refused to go into isolation or divulge their contacts. Some cultures resisted changing dangerous burial practices.

Over and above those factors, the region’s permeable borders and extensive transportation routes have complicated contact tracing and expanded the epidemic’s reach. More vexing still, the sudden surges of patients in ever-changing locales have meant a constant shortage of trained doctors, nurses, janitors, ambulance drivers, and gravediggers.

“I wonder whether one person in the world ... predicted this outbreak.”

Bertrand Draguez,
Doctors Without Borders

Although Liberia has recently made progress in some places, Draguez, who recently visited 10 Ebola treatment units MSF runs in the three affected countries, says the end is nowhere in sight. “We have to keep on going with the same level of energy for 6 or 8 or even 12 months,”

he warns. Already the Ebola epidemic of 2014 has made it starkly clear that we must move steadily and aggressively against this virus, or it will continue to teach us lessons we do not want to learn.
—Jon Cohen

Breakdown runners-up

Unfortunately, there’s always more than enough bad news to fill this category. A few of this year’s notable flaps, stumbles, and reverses.

STEM CELLS MADE EASY?

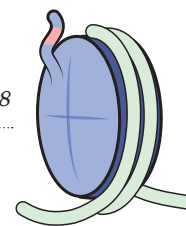
Rarely has so dazzling a claim gone down in flames so quickly. In January, researchers from Japan and the United States published what purported to be an easier, more powerful new method for turning adult cells into stem cells. But within 3 weeks, online commentators spotted questionable images in the two papers. Doubts multiplied as other labs around the world tried and failed to repeat the feat. Lead author Haruko Obokata was found guilty of misconduct, *Nature* retracted the papers, and in a tragedy that shook the field, one co-author took his own life. Officials in Japan radically reorganized the RIKEN institute where most of the work was done, cutting staff from more than 500 to 250.

GLIMPSE OF CREATION?

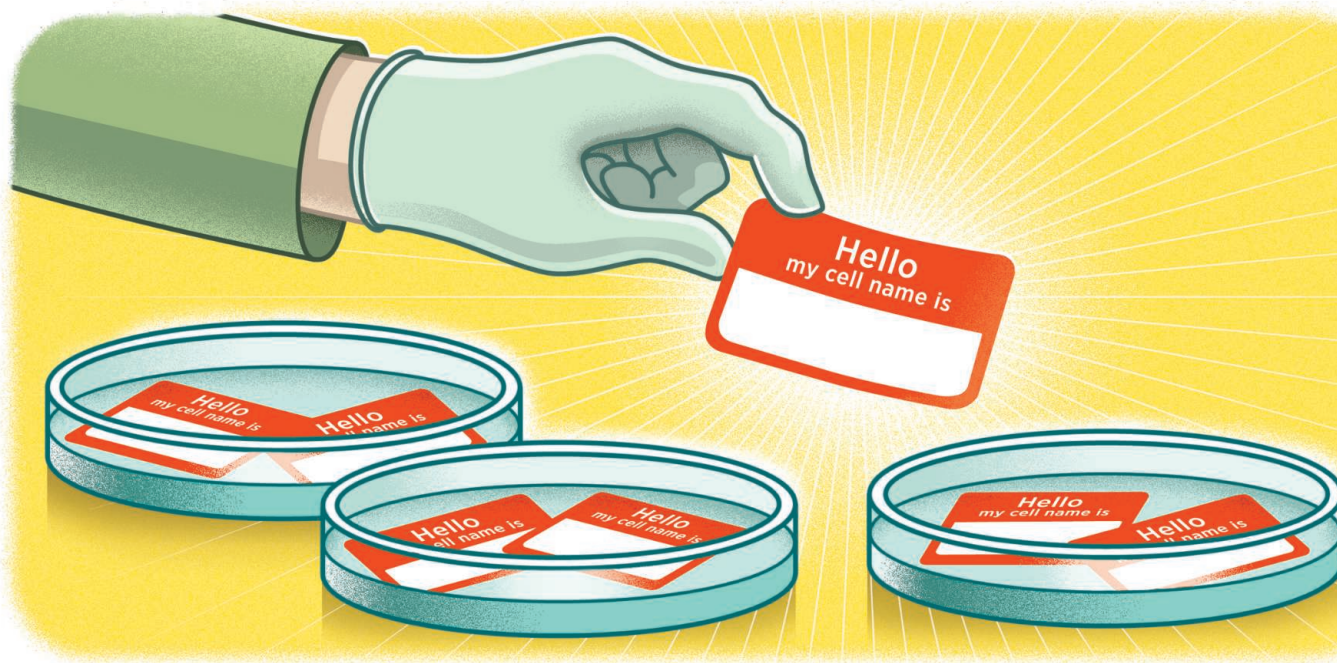
In March, cosmologists working with a specialized telescope at the South Pole called BICEP2 claimed they had spotted in the afterglow of the big bang a sure signal that the newborn universe had undergone a bizarre growth spurt known as inflation. Others suggested the signal could have come from dust within our own galaxy, and in September, researchers with the European Space Agency’s Planck spacecraft showed that most or all of it probably does. The two teams are working on a joint analysis, but the bold claim seems unlikely to hold up.

LAWMAKERS VERSUS NSF

Is the science committee for the U.S. House of Representatives broken or simply doing its job as watchdog? The U.S. research community watched with dismay this year as the committee, led by Representative Lamar Smith (R-TX), pummeled the National Science Foundation and other federal science agencies at hearings, in press releases, and with subpoenas and legislation. Smith says he’s making sure the government spends tax dollars wisely. His actions have captured headlines, but many scientists—remembering the bipartisan, big-picture policy discussions that used to be the panel’s bread and butter—might prefer a return to quiet obscurity.



PERSPECTIVES



CELL BIOLOGY

Fixing problems with cell lines

Technologies and policies can improve authentication

By **Jon R. Lorsch**^{1*}, **Francis S. Collins**²,
Jennifer Lippincott-Schwartz^{3,4}

Despite the important role of cell culture in the study of biology and medicine, evidence has accumulated that cell lines are frequently misidentified or contaminated by other cells or microorganisms. This can be a substantial problem in many fields, such as cancer research, where drugs are

initially tested using a cell line derived from the targeted type of tumor (1). If a drug is tested on the wrong cell line, research can lead to unreliable results, and discovery of effective treatments can be delayed. Even in basic research, use of mistaken cell lines can hinder progress because of variations in cell behavior among different cell types. Given these

POLICY

concerns, developing corrective measures for cell line misidentification and contamination warrants renewed attention.

Since the 1960s, more than 400 widely used cell lines worldwide have been shown to have been misidentified (2, 3). Cells originally thought to have been derived from one tissue type have later been found to be from a different tissue. In some cases, even the species of the cells has been misidentified. A 2011 study of 122 different head and neck cancer cell lines revealed that 37 (30%) were misidentified (4). Analyses of a variety of tissue culture collections and cells sent to repositories for curation and storage from labs in the United States, Europe, and Asia suggest that at least 15% of cell lines are misidentified or contaminated (4, 5).

Misidentified cell lines can create problems at many levels of biomedical research.

For example, studies using just two misidentified cell lines were included in three grants funded by the U.S. National Institutes of Health (NIH), two clinical trials, 11 patents, and >100 papers (6). Nonetheless, the need for validation and accurate reporting of cell line identity does not appear to be widely recognized by researchers; a 2013 study found that fewer than half of cell lines were unambiguously identified in published studies (7).

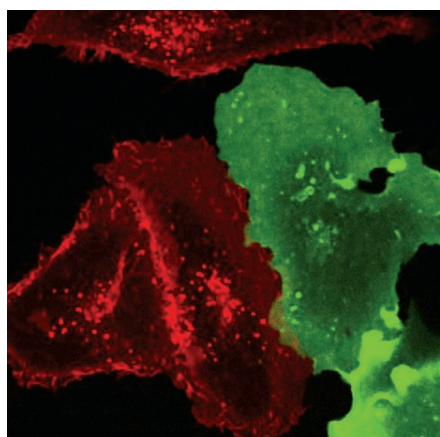
A number of factors contribute to the problems of cell line misidentification and contamination. For example, inadvertently using a pipette more than once when working with different cell lines in culture can lead to cross contamination. If the contaminating cell line divides more rapidly than the original cells, it can quickly dominate the population, changing the identity of the culture. This event often goes undetected because cells from dif-

ferent sources can be morphologically similar (see the photo). Cultured cells can also become contaminated with mycoplasma, viruses, or other microbes, which can alter the cells' behavior. Recent analyses suggest that 5 to 10% of cell culture studies have used cells contaminated with mycoplasma (8, 9). Cell lines in culture can also change over time without any external contamination. As they grow in the lab generation after generation, cells can undergo chromosomal duplications or rearrangements, mutations, and epigenetic changes that alter their phenotypes. Given these factors, in the absence of preventative steps, cell line alteration is inevitable and potentially problematic.

Concerned scientists and research organizations have made efforts to deal with this problem. In 2007, the NIH issued a Guide Notice (10) drawing attention to the misidentification of cell lines and calling on the reviewers of grants and manuscripts to pay special attention to this issue. Despite these efforts, the problem appears to have persisted. The time and cost required for authenticating cell lines likely has been a barrier to widespread adoption of best practices. Shortcomings in training also play a role, as do sociological issues. For example, it is hard for both individual scientists and their fields to accept that their work could be called into question because the wrong cell line was used. For some researchers, the problem may even seem insignificant in the context of their specific research focus; after all, all animal cells have microtubules, motor proteins, and ribosomes, which may lead some scientists to feel that the particular cell type they are studying is irrelevant. These issues may help explain why, even after the misidentification of a cell line has been made public, researchers often continue to publish work attributing the line to its misidentified source [reviewed in (11)].

So what more can we do to address this problem? We believe the biomedical research community—including funding agencies, scientific societies, journals, reagent suppliers, and investigators themselves—needs to give greater focus to the problem of cell line misidentification and must work together to develop new ways to address the complex issues associated with it. A multipronged strategy that combines additional research, alteration of practices, improved training, and investment in the development of new technologies will be necessary.

Some research institutes are urging all



Similar cells, different species. Monkey cells (red) and human cells (green) growing together in culture.

their scientists to fingerprint new cell lines as soon as they arrive in the lab and periodically thereafter. Fortunately, the cost of validating cell lines is falling thanks to improvements in testing techniques. One method, using short tandem repeat (STR) analysis to identify DNA sequences unique to a cell line, is now widely available. This approach is inexpensive and rapid, and there are online databases that allow STR fingerprints to be compared to verify cell line identity. For example, ATCC has an STR database of all of its human cell lines. Although it can authenticate commonly used human cell lines, STR cannot distinguish many lines from other species, and it lacks the resolution needed to identify most genetic changes. It is also a technique that is usually done in core facilities rather than routinely by individual researchers, which presents a barrier to frequent use. Thus, we still need technological improvements to address these problems.

For its part, the NIH is considering several approaches to help catalyze improvements in identifying cell lines and maintaining their integrity. First, grant applicants may be required to provide information on how they intend to address concerns about the identity of their cell lines, the composition of their key reagents, and contamination of their cells, similar to the model organism—sharing plans that are already included in NIH grant applications. Standards and suggested best practices will be developed with the help of academic and industrial researchers, the professional societies, and other organizations and government agencies, such as the American Society for Cell Biology, the Global Biological Standards Institute, and the U.S. National Institute of Standards and Technology.

The NIH is also considering investing in development of improved technologies for cell culture studies, including faster,

cheaper, and easier methods for the validation of cell lines and inexpensive, defined, and controllable media for cell growth. These are areas where reagent suppliers and equipment manufacturers will also need to play a role. In addition, the NIH is exploring funding studies to determine the extent to which variables such as cell type and genetic drift affect the reproducibility and generalizability of biomedical research results. Recently, several components of the NIH launched an initiative to help universities and other organizations enhance training in good laboratory practices (12), an effort in which the professional societies could also be instrumental. Given the global nature of the cell line authentication problem, the NIH will engage additional funding agencies in the United States and around the world to develop concerted approaches to address these and other problems related to reproducibility in cell culture studies and overall rigor of experimental design in life sciences research (13).

The journals and their reviewers also have an important role to play; they can ensure that authors include in published manuscripts data on cell line quality and identity, as well as details about key reagents used in their studies. Some journals have already adopted guidelines and checklists to help make sure these goals are achieved (14), and we urge widespread adoption of these standards. Of course, the authors themselves are ultimately responsible for authenticating their cell lines as rigorously and carefully as possible and for training the next generation of scientists to do the same.

If all of these groups work together, we are confident that the reproducibility and rigor of cell culture studies done will improve. ■

REFERENCES

1. J. N. Weinstein, *Nature* **483**, 544 (2012).
2. A. Capes-Davis et al., *Int. J. Cancer* **127**, 1 (2010).
3. ATCC, The role of ICLAC (International Cell Line Authentication Committee); http://standards.atcc.org/kwspub/home/the_international_cell_line_authentication_committee-iclac/.
4. M. Zhao et al., *Clin. Cancer Res.* **17**, 7248 (2011).
5. R. A. F. MacLeod, H. G. Drexler, *Nature* **439**, 912 (2006).
6. J. J. Boonstra et al., *J. Natl. Cancer Inst.* **102**, 271 (2010).
7. N. A. Vasilevsky et al., *Peer J.* **1**, e148 (2013).
8. S. E. Armstrong, J. A. Mariano, D. J. Lundin, *Biologicals* **38**, 211 (2010).
9. A. O. Olarerin-George, J. B. Hogenesch, *bioRxiv* (2014); <http://biorxiv.org/content/early/2014/07/11/007054>.
10. NIH Guide Notice, NOT-OD-08-017, November 28, 2007; <http://grants.nih.gov/grants/guide/notice-files/NOT-OD-08-017.html>.
11. American Type Culture Collection Standards Development Organization Workgroup ASN-0002, *Nat. Rev. Cancer* **10**, 441 (2010).
12. NIH Guide Notice, RFA-GM-15-006, 28 August 2014; <http://grants.nih.gov/grants/guide/rfa-files/RFA-GM-15-006.html>.
13. F. S. Collins, L. A. Tabak, *Nature* **505**, 612 (2014).
14. M. McNutt, *Science* **346**, 679 (2014).

¹Director, National Institute of General Medical Sciences, Bethesda, MD 20892, USA. ²Director, National Institutes of Health, Bethesda, MD 20892, USA. ³President, American Society for Cell Biology, Bethesda, MD 20814, USA. ⁴National Institute of Child Health and Human Development, Bethesda, MD 20892, USA. *Corresponding author. E-mail: jon.lorsch@nih.gov

IMMUNOLOGY

Retroviral help for B cells

Silent retroviruses present in the human genome help B cells launch a rapid response to pathogenic antigens

By **Emilie K. Grasset¹** and **Andrea Cerutti^{1,2}**

Endogenous retroviruses are footprints left by past retroviral infections that have incorporated viral elements into our genomes (1). They constitute an important component of our virome, the collective genomes from viruses peacefully inhabiting our body (2). These viruses are part of a larger community of commensal and symbiotic microorganisms. The most studied members of this microbiota are commensal bacteria colonizing mucosal organs, including the gut (3). Besides breaking down food and generating nutrients, gut commensals impede the growth of pathogens and stimulate immune system development, including the production of antibodies by intestinal and systemic B cells (4, 5). On page 1486 of this issue, Zeng *et al.* (6) show that endogenous retroviruses can also mobilize B cells to rapidly produce antibodies against pathogenic antigens.

Protein antigens usually elicit antibody production by B cells through a T cell-dependent pathway that involves B cell-T cell interaction in lymphoid follicles (7). Engagement of the B cell receptor (BCR) by discrete protein epitopes, as well as the production of B cell-stimulating factors by T cells, trigger the differentiation of follicular B cells into long-lived memory B cells and plasma cells that produce protective immunoglobulin G (IgG) antibodies (8).

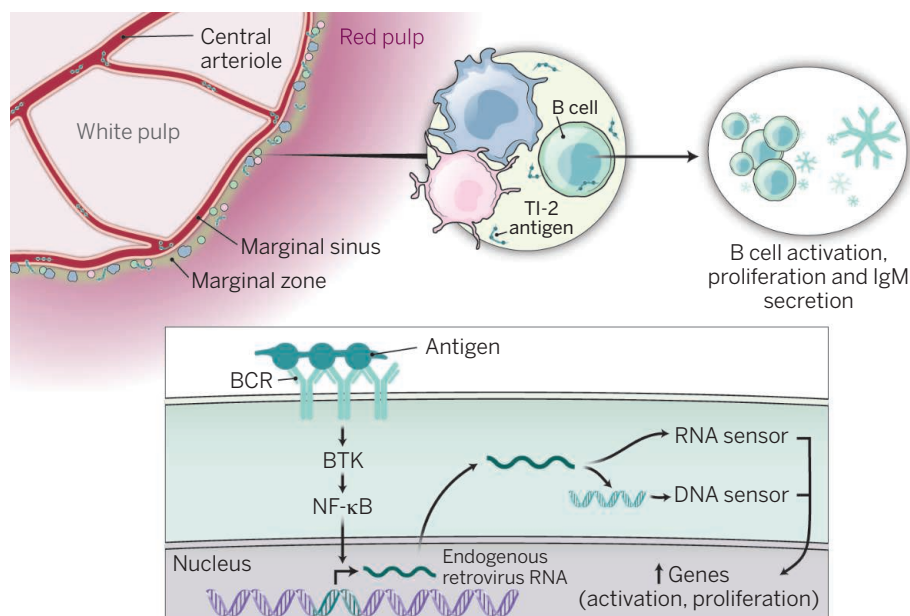
Carbohydrate antigens predominantly activate a T cell-independent pathway that involves extrafollicular B cells positioned in the marginal zone of the spleen (9). In the presence of extensive BCR cross-linking by large polysaccharides called type-2 TI (TI-2) antigens (10), these B cells rapidly differentiate into short-lived plasma cells that secrete protective IgM and some IgG antibodies (11). Despite recent advances (12), the mechanism whereby TI-2 antigens activate marginal zone B cells without help from T cells remains poorly understood.

Zeng *et al.* discovered that BCR cross-linking by TI-2 antigens activates an intracellular signaling cascade that includes Bruton's tyrosine kinase (BTK) and the transcription factor nuclear factor κ B (NF- κ B). NF- κ B transcribes endogenous retroviral DNA, and the resulting viral RNA can activate B cells through two distinct but complementary pathways. In one pathway, the viral RNA triggers an RNA sensor called retinoic acid-inducible gene-1 (RIG-I) and its downstream adaptor mitochondrial antiviral signaling (MAVS). In the other pathway, the viral RNA is reverse transcribed into DNA, which triggers a DNA sensor called cyclic GMP-AMP synthase (cGAS). This protein catalyzes the synthesis of cyclic GMP-AMP (cGAMP), which in turn binds and activates the stimulator of interferon genes (STING). Ultimately, signals from these sensors promote the activation and expansion of antigen-specific B cells, which subsequently differentiate into antibody-secreting plasma cells (see the figure).

Help from endogenous retroviruses appears to be restricted to B cell responses

against TI-2 antigens such as capsular polysaccharides from *Streptococcus pneumoniae* and Pneumovax, a commercial vaccine against *S. pneumoniae*. Whether these retroviruses help both follicular and extrafollicular B cells indiscriminately or specifically target the latter remains unclear. Extrafollicular marginal zone B cells and B-1 cells are innate-like B cells that specialize in mounting "professional" responses to TI-2 antigens (13). Thus, marginal zone B cells and B-1 cells may constitute the main recipient of adjuvant-like signals from endogenous retroviruses. In this regard, it remains to be investigated whether marginal zone B cells and B-1 cells have elevated basal amounts of endogenous retroviruses. Should that be the case, these viruses may contribute to the pre-activation state that characterizes both marginal zone B cells and B-1 cells and accounts for their readiness against blood-borne and mucosal antigens (9).

Although TI-2 antigens stimulate a rapid burst of antibody production, they do not efficiently induce long-term immunological memory, as seen with antigens that stimulate a T cell-dependent pathway of B cell activation. In addition, TI-2 antigens are poorly immunogenic in infants and certain immunodeficient patients. Several strategies circumvent these limitations. Conjugation of TI-2 antigens with proteins or Toll-like receptor agonists enhances systemic but not mucosal antibody responses.



Mobilized virome. Circulating TI-2 antigens are presented by macrophages and dendritic cells to B cells in the marginal zone of the spleen. Extensive cross-linking of the BCR by TI-2 antigens activates a signaling cascade that leads to transcription of endogenous retroviral DNA. The resulting viral RNAs either activate the RNA sensor pathway (through RIG-1 and MAVS) or become reverse transcribed into DNAs that trigger the DNA sensor pathway (involving cGAS and STING). Adjuvant-like signals from both sensors induce the activation and expansion of B cells and their differentiation into antibody-secreting plasma cells.

¹The Immunology Institute, Department of Medicine, Mount Sinai School of Medicine, 1425 Madison Avenue, New York, NY 10029, USA. ²Catalan Institute for Research and Advanced Studies (ICREA), IMIM-Hospital del Mar, Av. Dr. Aiguader 88, 08003 Barcelona, Spain. E-mail: andrea.cerutti@imssm.edu or acerutti@imim.es

The latter may benefit from adjuvant-like signals generated by viral elements (14), including endogenous retroviruses. Even under steady-state conditions, the continuous stimulation of mucosal B cells by commensal antigens might increase the expression of endogenous retroviruses.

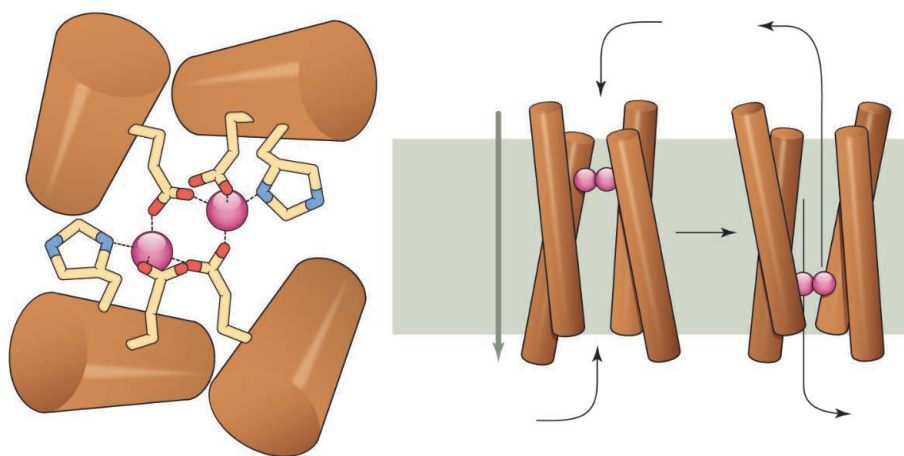
Similar to bacterial polysaccharides, carbohydrates linked to large viral glycoproteins may generate TI-2-like B cell responses (15). Given that certain viral infections stimulate the expression of endogenous retroviruses, adjuvants containing endogenous retroviral sequences may enhance both the magnitude and breadth of neutralizing antibody responses to viruses, including HIV. Thus, a full understanding of our virome may catalyze more efficient strategies to enhance protective humoral responses. However, targeting these viruses with vaccines should be approached with caution, as certain endogenous retroviruses could precipitate or accelerate the development of autoimmunity and cancer as well as the spreading of a preexisting HIV infection. In this context, defining the “virotype” of each individual may be preferable to defining how individual viral strains regulate the immune response. Individual virotypes would define a distinct set of endogenous retroviruses that share target cells, sensors, and downstream transcription factors in an individual (2).

The study by Zeng *et al.* is a reminder that the virome is an integral part of our genetic identity. Thus, deciphering human virotypes may help elucidate the interindividual differences that cannot be explained solely by genetic mutations. Together with the bacterial microbiome, the retrovirome likely shapes both the magnitude and quality of the immune response. Future advances in our understanding of host-virome relationships are bound to generate new insights into the role of these peaceful genome inhabitants in infection, vaccination, inflammatory disease, autoimmunity, and cancer. ■

REFERENCES

1. E. C. Holmes, *Cell Host Microbe* **10**, 368 (2011).
2. H. W. Virgin, *Cell* **157**, 142 (2014).
3. K. Honda, D. R. Littman, *Annu. Rev. Immunol.* **30**, 759 (2012).
4. S. Fagarasan *et al.*, *Annu. Rev. Immunol.* **28**, 243 (2010).
5. J. Z. Oh *et al.*, *Immunity* **41**, 478 (2014).
6. M. Zeng *et al.*, *Science* **346**, 1486 (2014).
7. G. D. Vitoria, M. C. Nussenzweig, *Annu. Rev. Immunol.* **30**, 429 (2012).
8. M. McHeyzer-Williams *et al.*, *Nat. Rev. Immunol.* **12**, 24 (2012).
9. A. Cerutti *et al.*, *Nat. Rev. Immunol.* **13**, 118 (2013).
10. J. J. Mond *et al.*, *Annu. Rev. Immunol.* **13**, 655 (1995).
11. R. Guinamard *et al.*, *Nat. Immunol.* **1**, 31 (2000).
12. G. Magri *et al.*, *Nat. Immunol.* **15**, 354 (2014).
13. F. Martin *et al.*, *Immunity* **14**, 617 (2001).
14. B. Romeu *et al.*, *J. Drug Target.* **20**, 502 (2012).
15. E. Szomolanyi-Tsuda, R. M. Welsh, *Curr. Opin. Immunol.* **10**, 431 (1998).

10.1126/science.aaa3263



A designed ion channel. The ability to reproduce a biological activity in a designed membrane protein, reported by Joh *et al.*, is an essential step in establishing that the underlying principle is understood, as stated succinctly in Richard Feynman's well-known dictum of the title.

PROTEIN DESIGN

What I cannot create, I do not understand

A designed protein transports ions across a membrane

By Andrei N. Lupas

Life today depends on the chemical activity of proteins. Scientists have attempted for decades to understand their intricate structures and diverse chemical activities and to emulate their properties by design. However, designing structured polypeptide chains—a prerequisite for creating functional proteins—has proven extremely challenging. Recent years have seen progress in the design of folded proteins in aqueous solution (1) and of proteins that are catalytically active (2), but the design of membrane proteins remains in its infancy (3). A landmark study by Joh *et al.* on page 1520 of this issue (4) meets two major challenges in the quest to engineer new proteins: the design of a folded membrane protein that performs a biomimetic function.

By the time of the last universal common ancestor of all life on Earth, some 3.5 billion years ago, a tripartite division of labor had emerged among life's macromolecules, with DNA assuming the role of information repository, proteins providing catalytic activity, and RNA mediating between them. All three require defined three-dimensional structures to fulfill their biological roles. But whereas nucleic acids fold spontaneously and recover their structure robustly after denaturation, protein folding is a com-

plicated process that is easily derailed; after denaturation, proteins typically aggregate and have to be degraded and resynthesized.

Rapid advances in engineering nucleic acids have made genetic engineering a routine technology, with a broad range of applications and predictable outcomes. Engineering proteins, on the other hand, turned out to be an altogether more difficult proposition due to what has become known as the protein folding problem: How does an amino acid sequence determine a protein's structure?

Two aspects in particular have made this problem intractable. First, most amino acid chains do not have a folded structure. This may seem counterintuitive, because the chains we typically encounter are those of natural proteins, and most of these are folded. However, screens of polypeptide libraries have shown that fewer than one in a billion exemplars is folded. Second, for the few chains that fold, the free energy of folding is equivalent to just a few hydrogen bonds. Most folded proteins are thus energetically quite close to the unfolded state—a fact illustrated by the disruption that heat shocks of just a few degrees above normal growth temperature can cause. Because

Department of Protein Evolution, Max Planck Institute for Developmental Biology, 72076 Tübingen, Germany. E-mail: andrei.lupas@tuebingen.mpg.de

structure is a prerequisite for chemical activity, protein engineering is still caught up in this problem.

Although a general solution to the protein folding problem would greatly help design, solutions for simplified cases (1, 5), such as for short, idealized, or repetitive polypeptide chains, have nonetheless allowed the field to move forward. Incorporation of sequence patterns conserved in evolution has also been very helpful, as has the use of naturally occurring protein fragments as building blocks. Successful design efforts have not only replicated some natural folds and enzymatic activities, but also generated new folds and catalytic activities (1, 2). As in the well-known dictum by Richard Feynman, "What I cannot create, I do not understand," successful design is also a powerful way to show that a design principle has been understood.

One of the best model systems for protein design is the coiled coil, a fibrous fold formed by two or more helices in parallel or antiparallel orientation curved around a central axis (6). Coiled-coil helices pack

"...Rocker can translocate three to four hydrogen ions in one direction for every Zn^{2+} ion in the other, even against a pH gradient..."

along seams of residues that form regular, geometrically defined interactions; they thus have repetitive sequences of low complexity. They become structured at shorter lengths (often 25 to 30 residues) than do globular folds (typically more than 70 residues) and are more stable. Uniquely among proteins, their structure can be described by parametric equations (the Crick equations) (7), and can thus be computed (rather than simulated, a vastly more laborious process) (4, 5, 8–10). Recent studies, including that by Joh *et al.*, substantially extend the range of engineered coiled-coil forms (4, 9, 10).

Huang *et al.* (9) designed antiparallel bundles of three and four helices that depart from the common coiled-coil sequence periodicity of seven residues by having 18- and 11-residue periodicities, respectively, and are unusually stable. The authors also built a parallel pentameric coiled coil, which marks a transition from bundles with tightly packed cores to barrels enclosing a central, solvent-accessible channel.

The interhelical interactions in coiled-coil barrels involve two seams of residues (rather than one, as in bundles) and are

hence harder to design. Thomson *et al.* (10) classify these complex seams into three types according to their geometry and show that they have understood the principles governing one type by designing penta-, hexa-, and heptameric barrels. On the basis of experiments demonstrating differential chemical accessibility of the channels formed by such barrels (11), they highlight their potential as catalysts.

These channels also have a clear potential for transmembrane solute transport (12). Joh *et al.* now illustrate this by building a membrane-embedded coiled coil that contains two Zn^{2+} binding sites close to its ends. By design, the coiled coil (called Rocker) oscillates dynamically between two states, such that when Zn^{2+} is bound at one site, it is released at the other. By further designing the binding sites such that they can either coordinate zinc ions or hydrogen ions, but not both, Joh *et al.* ensure that these ions are transported in opposite directions. Indeed, they show that Rocker can translocate three to four hydrogen ions in one direction for every Zn^{2+} ion in the other, even against a pH gradient (see the figure). An extensive characterization of the structure and activity of this synthetic antiporter proves the accuracy with which all design goals have been met.

The study of Joh *et al.* convincingly breaks several barriers in protein engineering: taking protein design from the solvent into the membrane, aiming for dynamic properties rather than for stability, and achieving an advanced biomimetic function from first principles, without recourse to screening or directed evolution. The work opens up exciting new avenues for membrane protein engineering, given that most membrane proteins are helical bundles and that Grigoryan and Degradó (13) have provided a general extension of the Crick equations to these structures. It should not be overlooked, however, that extending these advances to other protein folds remains a challenge. ■

REFERENCES

1. N. Koga *et al.*, *Nature* **491**, 222 (2012).
2. G. Kiss, N. Çelebi-Ölçüm, R. Moretti, D. Baker, K. N. Houk, *Angew. Chem. Int. Ed.* **52**, 5700 (2013).
3. J. M. Perez-Aguilar, J. G. Saven, *Structure* **20**, 5 (2012).
4. N. H. Joh *et al.*, *Science* **346**, 1520 (2014).
5. D. N. Woolfson, *Adv. Protein Chem.* **70**, 79 (2005).
6. A. N. Lupas, M. Gruber, *Adv. Protein Chem.* **70**, 37 (2005).
7. F. H. C. Crick, *Acta Crystallogr.* **6**, 685 (1953).
8. P. B. Harbury, J. J. Plecs, B. Tidor, T. Alber, P. S. Kim, *Science* **282**, 1462 (1998).
9. P. S. Huang *et al.*, *Science* **346**, 481 (2014).
10. A. R. Thomson *et al.*, *Science* **346**, 485 (2014).
11. A. J. Burton *et al.*, *J. Am. Chem. Soc.* **135**, 12524 (2013).
12. V. N. Malashkevich, R. A. Kammerer, V. P. Efimov, T. Schultess, J. Engel, *Science* **274**, 761 (1996).
13. G. Grigoryan, W. F. Degradó, *J. Mol. Biol.* **405**, 1079 (2011).

10.1126/science.aaa2721

BIOCHEMISTRY

More than fine tuning

Local electric fields accelerate an enzymatic reaction

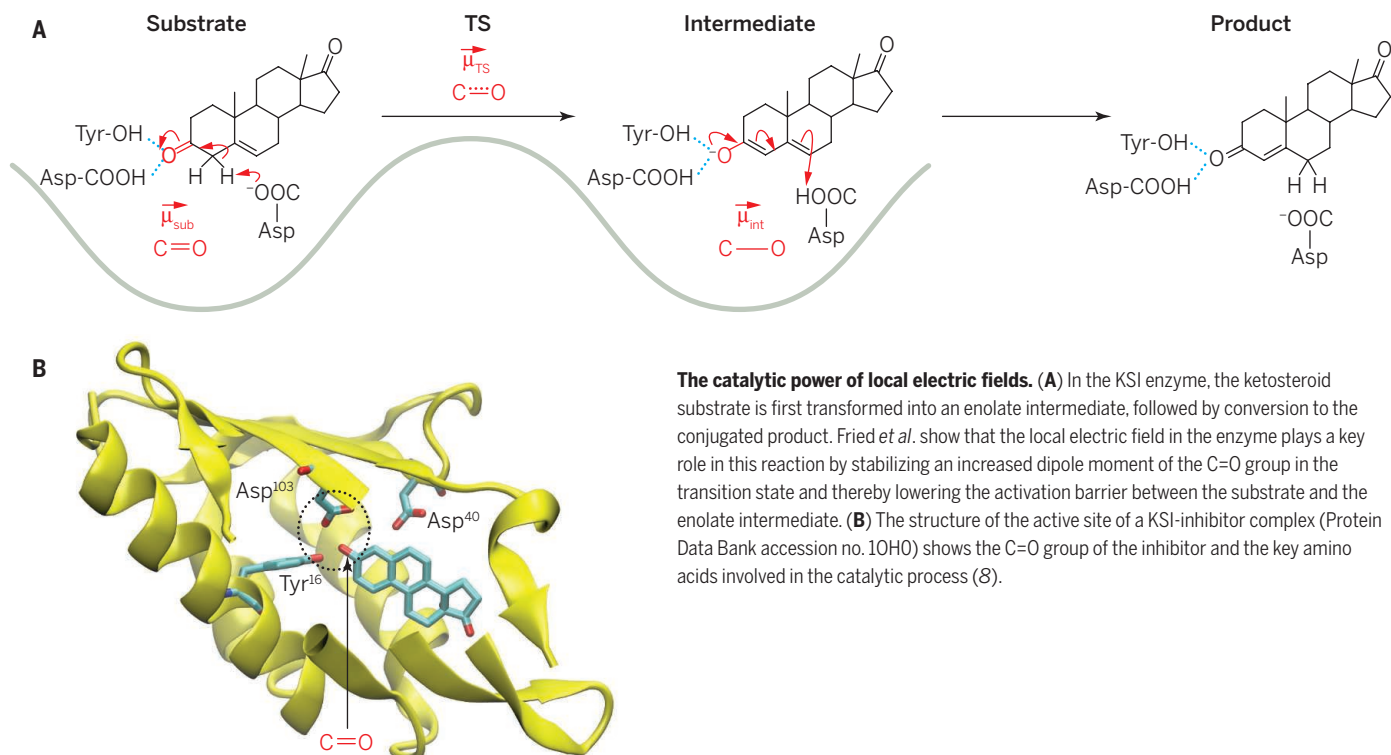
By Peter Hildebrandt

How do electric fields affect enzymatic processes? Binding and crystallographic studies have shown that electrostatic interactions are important in the substrate-binding step that initiates enzyme catalysis. However, for the subsequent steps, experimental data have been limited. The study of electric field effects on the transition state was therefore largely restricted to theory (1). On page 1510 of this issue, Fried *et al.* (2) use a recently developed technique to quantify the electrostatic contribution to the rate-limiting step of an enzymatic reaction. They show that the local electric field accelerates the reaction, a finding that is likely to apply to other catalytic reactions.

The authors exploit the vibrational Stark effect (VSE), which results from the perturbation of molecular vibrational energy levels by the electric field. This effect is particularly strong for the stretching modes of carbonyls and nitriles, which exhibit dipole moments along their bond axes. When such probes are incorporated into proteins through binding of additional ligands or chemical modification of amino acid side chains, the frequency shifts induced by local electric fields can be determined by infrared (IR) spectroscopy (3–7).

Using this technique, Fried *et al.* study the enzyme ketosteroid isomerase (KSI), which catalyzes the isomerization of a group of ketosteroids to their conjugated isomers (8, 9). The reaction cycle involves an enolate intermediate and is associated with substantial changes of the dipole moment of the keto group (see the figure). KSI has one of the highest known unimolecular rate constants in biochemistry. Despite extensive study (9), the mechanistic basis for this high rate and specifically the role of electrostatics remain matters of debate.

The KSI enzyme also binds 19-nortestosterone (19-NT), but this ketosteroid cannot react owing to the position of the C=C double bond. Nevertheless, the C=O group of 19-NT adopts essentially the same position in the active site and experiences the same



The catalytic power of local electric fields. (A) In the KSI enzyme, the ketosteroid substrate is first transformed into an enolate intermediate, followed by conversion to the conjugated product. Fried *et al.* show that the local electric field in the enzyme plays a key role in this reaction by stabilizing an increased dipole moment of the C=O group in the transition state and thereby lowering the activation barrier between the substrate and the enolate intermediate. (B) The structure of the active site of a KSI-inhibitor complex (Protein Data Bank accession no. 1OHO) shows the C=O group of the inhibitor and the key amino acids involved in the catalytic process (8).

hydrogen bond interactions as a reactive substrate. Hence, as for reactive substrates, the C=O bond of the bound 19-NT may be elongated, resembling a putative transition-state structure (see the figure). In this sense, the C=O group of 19-NT is an ideal probe for the electric field environment in the first step of the catalytic reaction.

Fried *et al.* used IR difference spectroscopy to identify the C=O stretching mode of the bound 19-NT on the background of protein signals. When 19-NT is bound to the wild-type (WT) enzyme, the C=O stretching frequency is drastically downshifted compared to the value measured for 19-NT in water. To translate this frequency shift into electric field strength, the authors carried out calibration experiments on 19-NT in different solvents. The analysis provided a linear correlation between the C=O stretching frequency of 19-NT and the electrostatic field.

The authors next examined the frequency shifts of the 19-NT keto function in different mutants of the enzyme. Substitutions for amino acids in the active site led to smaller downshifts with respect to water as compared to the WT protein. These findings confirm that the formation of the enolate is the rate-limiting step of the catalytic cycle. They also show that the local electric field stabilizes an increased dipole moment

“It is very likely that the electric field-dependent acceleration of elementary reactions is a general concept in biological catalysis and perhaps also in chemical catalysis...”

of the C=O group in the transition state, thereby reducing the energy barrier for the formation of the enolate intermediate (see the figure). Assuming that similar electric fields act on the C=O function in the ground and transition state, the authors determine a ~70% electrostatic contribution to the lowering of the activation barrier in the WT enzyme compared to the uncatalyzed reaction in solution.

By reporting quantitative experimental data on the electrostatics of the rate-limiting step—including the contribution of the crucial hydrogen bond interactions—the study is important not only for understanding the enzymatic mechanism of KSI (9). It may also help to elucidate other enzymatic processes involving the attack at polar functional groups. It is very likely that the electric field-dependent acceleration of elementary reactions is a general concept in biological catalysis and perhaps

also in chemical catalysis, as suggested, for instance, for zeolite-based catalytic reactions (10).

Fried *et al.*'s methodology for determining the local electric field is not restricted to enzymatic reactions. VSE spectroscopy may also be applied to other processes involving proteins, particularly those that take place at or in membranes and thus under the influence of additional external electric fields. Here, the key question is how changes of the transmembrane potential can modulate local electric fields to steer or initiate specific processes. Use of model membranes assembled on gold electrodes may allow VSE spectroscopy to be extended to transmembrane proteins; this setup enables control of the transmembrane potential and ensures increased sensitivity of surface-enhanced infrared absorption for signal detection (11). ■

REFERENCES

1. A. Warshel *et al.*, *Chem. Rev.* **106**, 3210 (2006).
2. S. D. Fried, S. Bagchi, S. G. Boxer, *Science* **346**, 1510 (2014).
3. S. G. Boxer, *J. Phys. Chem. B* **113**, 2972 (2009).
4. C. T. Liu *et al.*, *J. Am. Chem. Soc.* **136**, 10349 (2014).
5. H. Jo, R. M. Culik, I. V. Korendovych, W. F. Degrad, F. Gai, *Biochemistry* **49**, 10354 (2010).
6. G. Schkolnik *et al.*, *Chem. Commun. (Camb.)* **48**, 70 (2012).
7. S. D. Fried, S. Bagchi, S. G. Boxer, *J. Am. Chem. Soc.* **135**, 11181 (2013).
8. S. W. Kim *et al.*, *Biochemistry* **36**, 14030 (1997).
9. D. Herschlag, A. Natarajan, *Biochemistry* **52**, 2050 (2013).
10. J. Estephane *et al.*, *J. Phys. Chem. C* **113**, 7305 (2009).
11. J. Kozuch *et al.*, *Phys. Chem. Chem. Phys.* **16**, 9546 (2014).

CANCER

For pediatric glioma, leave no histone unturned

Examining histone mutations points to possible therapies for a lethal brain tumor

By **Oren J. Becher¹** and
Robert J. Wechsler-Reya²

Diffuse intrinsic pontine glioma (DIPG) is an incurable pediatric brain tumor. About 80% of these tumors contain mutations in genes that encode histones (H3.3 or H3.1) (1, 2), proteins that package DNA into chromatin. These mutations, which change lysine 27 to methionine (K27M), are believed to sequester Polycomb repressive complex 2 (PRC2), which normally represses gene expression through histone methylation (see the figure). In the absence of PRC2, genes that should be silent are expressed, which is thought to drive cell transformation (3–5). However, the precise role of histone mutations in tumorigenesis is unclear, and strategies to target the mutations remain elusive. As reported by Funato *et al.* on page 1529 of this issue (6), as well as by Hashizume *et al.* (7), models of K27M-mutant DIPG can be used to elucidate the mechanisms of transformation and to identify new approaches to therapy.

Funato *et al.* created a model of DIPG by differentiating human embryonic stem cells into neural progenitor cells, and then transducing them with a viral vector carrying the gene encoding H3.3K27M. The use of embryonic stem cell-derived neural progenitors to model this type of glioma is noteworthy, as the precise cell of origin for the disease is not known [although a neural progenitor has been proposed as a candidate (8)]. Remarkably, H3.3K27M expression was mitogenic only in neural progenitors derived from embryonic stem cells, and not in undifferentiated embryonic stem cells or astrocytes derived from these cells. This suggests that the histone mutation is oncogenic only in the appropriate cell type.

In studying how H3.3K27M promotes tumorigenesis, Funato *et al.* found that the histone mutation alone was not suffi-

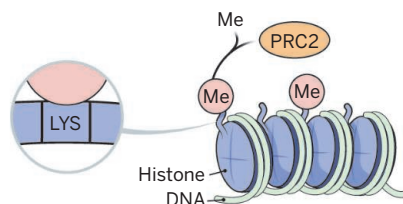
cient to transform neural progenitor cells into tumors. Only when progenitors also expressed an activated form of platelet-derived growth factor receptor A and lacked the TP53 tumor suppressor could they give rise to gliomas after injection into the brainstem of mice. Moreover, even with all three genetic alterations present, the tumors grew slowly and lacked histological features of high-grade glioma (necrosis and vascular proliferation). Although a subset of K27M mutant human DIPGs are low-grade (9), these observations raise the question of what additional mutations, or

what cellular context, may be required for the development of high-grade DIPG.

Although K27M mutant tumors are initiated in neural progenitors, they have an expression profile that resembles the neural plate-neural rosette stage, which precedes the emergence of neural progenitor cells. Based on this, the authors suggest that the K27M mutation acts in part by promoting dedifferentiation to a more primitive, stem-like state. In particular, the authors found that expression of the stem cell-associated genes *LIN28B*, *PLAG1*, and *PLAGL1* is up-regulated by H3.3K27M, and that reducing expression of these genes inhibits tumor cell growth.

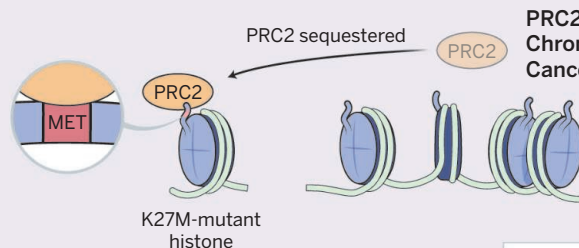
Funato *et al.* also carried out a small-molecule drug screen and discovered that antagonists of menin are potent inhibitors of tumor growth. Menin was originally described as a tumor suppressor in patients with multiple endocrine neoplasia type 1, a disorder characterized by benign tumors in the parathyroid, pancreas, and pituitary glands. It also functions as an oncogenic

Normal



Some histones methylated by PRC2
Chromatin closed
Cancer-promoting genes repressed

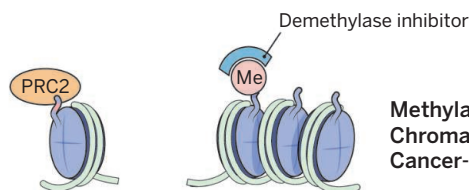
Cancer



PRC2-mediated methylation lost
Chromatin open
Cancer-promoting genes expressed

Gene expression → Tumorigenesis
↓ TP53 function
↑ PDGFR-A activity

Cancer therapy



Methylation maintained
Chromatin closed
Cancer-promoting genes repressed

Histone methylation and tumor growth. K27M histone mutants sequester PRC2, allowing loci that are normally repressed to be activated. Mutant histones cooperate with other mutations [those that inhibit TP53 expression or increase the activity of platelet-derived growth factor receptor A (PDGFR-A)] to promote tumorigenesis. A demethylase inhibitor restores repressive histone marks and blocks tumor growth. Me, methylation

¹Division of Pediatric Hematology-Oncology, Department of Pathology, and Preston Robert Tisch Brain Tumor Center, Duke University, Durham, NC, 27710, USA. ²Tumor Initiation & Maintenance Program, NCI-Designated Cancer Center, Sanford-Burnham Medical Research Institute, La Jolla, CA, 92037, USA. E-mail: rwreya@sanfordburnham.org; oren.becher@duke.edu

cofactor in hematologic malignancies containing mixed-lineage leukemia (MLL) gene fusions (10). In both disorders, menin acts by regulating MLL-mediated histone methylation (11, 12), which may explain why inhibitors of menin counteract the oncogenic effects of K27M mutations. Although the role of menin in DIPG is unclear, these studies suggest it may be an important therapeutic target.

Hashizume *et al.* took a different approach to identify therapies for K27M-mutant DIPG. They hypothesized that the global loss of histone methylation induced by the K27M mutation (and the resulting sequestration of PRC2) is critical for tumor maintenance. The authors used patient-derived DIPG cell lines (established from biopsies and passaged *in vivo*) to evaluate the effects of a K27 demethylase inhibitor on tumor cells. Treatment of H3.3K27M-mutant DIPG cells with this inhibitor increased H3K27 methylation and decreased cell growth. By contrast, treatment of cells harboring wild-type H3.3 or a different histone mutation (H3.3G34R/Y) had little effect. This suggests that global loss of H3K27 methylation may be the primary mechanism of K27M-driven gliomagenesis and raises the possibility that demethylase inhibitors may be valuable therapeutic agents for the disease.

The discovery of K27M mutations was an important step forward in understanding DIPG and promises to yield new approaches to treating the disease. The studies of Funato *et al.* and Hashizume *et al.* take us closer to that goal, creating models that can be used to study DIPG biology and demonstrating that these models can be useful for identifying therapies. It will be interesting to see whether these therapies synergize with one another, or with focal radiation, the standard of care for children with DIPG. Given the dismal prognosis associated with this disease, there will be strong incentive to move them forward into clinical trials. ■

REFERENCES

1. G. Wu *et al.*, *Nat. Genet.* **44**, 251 (2012).
2. J. Schwartzentruber *et al.*, *Nature* **482**, 226 (2012).
3. P. W. Lewis *et al.*, *Science* **340**, 857 (2013).
4. S. Bender *et al.*, *Cancer Cell* **24**, 660 (2013).
5. K. M. Chan *et al.*, *Genes Dev.* **27**, 985 (2013).
6. K. Funato, T. Major, P. W. Lewis, C. D. Allis, V. Tabar, *Science* **346**, 1529 (2014).
7. R. Hashizume *et al.*, *Nat. Med.* **10**, 1038/nm.3716 (2014).
8. M. Monje *et al.*, *Proc. Natl. Acad. Sci. U.S.A.* **108**, 4453 (2011).
9. P. Buczkowicz, U. Bartels, E. Bouffett, O. Becher, C. Hawkins, *Acta Neuropathol.* **128**, 573 (2014).
10. A. Yokoyama *et al.*, *Cell* **123**, 207 (2005).
11. S. K. Karnik *et al.*, *Proc. Natl. Acad. Sci. U.S.A.* **102**, 14659 (2005).
12. Y. X. Chen *et al.*, *Proc. Natl. Acad. Sci. U.S.A.* **103**, 1018 (2006).

CANCER

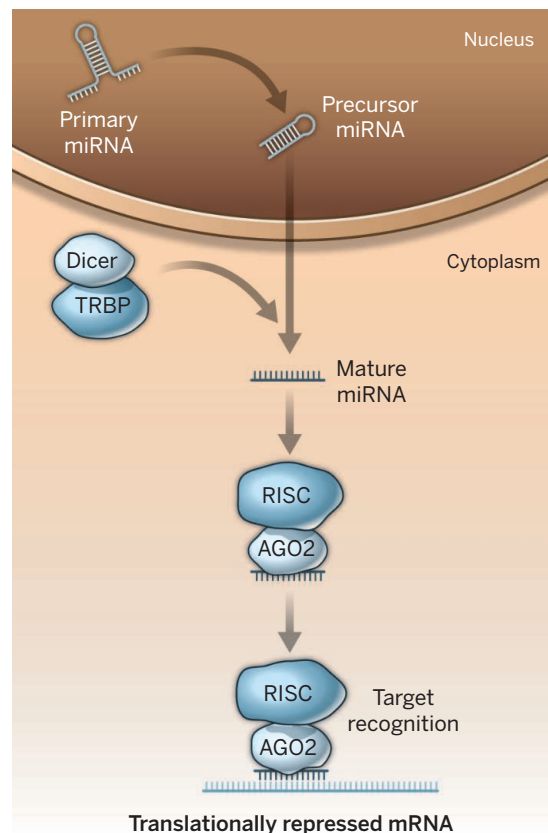
Malicious exosomes

Nanovesicles derived from cells of cancer patients carry microRNAs that initiate tumor growth in normal cells

By Eleni Anastasiadou and Frank J. Slack

Nanovesicles known as exosomes are secreted from a variety of cell types and circulate in biological fluids such as urine and plasma. These exosomes “hijack” membrane components and cytoplasmic contents of these cells and play an important role in intercellular communication, often inducing physiological changes in recipient cells by transferring bioactive lipids, nucleic acids, and proteins (1). These tiny vesicles also have been implicated in a number of human diseases, including cancer, and are becoming an appreciated fundamental aspect of tumor progression and metastasis (2). Recently, Melo *et al.* (3) showed that exosomes from breast cancer cells transfer microRNAs (miRNAs) to normal cells and stimulate them to become cancerous. This potentially expands the mechanisms by which cancer spreads and may provide opportunities to develop exosome-based diagnostics and therapies.

Many physiological processes involve exosomes, such as cell growth, neuronal communication, immune response activation, and cell migration, and in the case of cancer, may transfer angiogenic proteins or oncogenes from one cell to another (4–7). Thus, analyzing the macromolecules harbored by exosomes could have important diagnostic and therapeutic implications. Experimental evidence shows that exosomes mediate interactions between cancer and normal cells. For example, exosomes secreted by breast cancer cells inhibit exosome release from the normal counterparts. These cancer exosomes may trigger extracellular acidity in which cancer cells (but not healthy cells) can survive and which activates hypoxia-dependent angiogenesis during tumor development (1). Exosomes can also induce drug resistance of cancer cells by sequestering chemotherapeutic agents (8); and can stimulate metastasis (2).

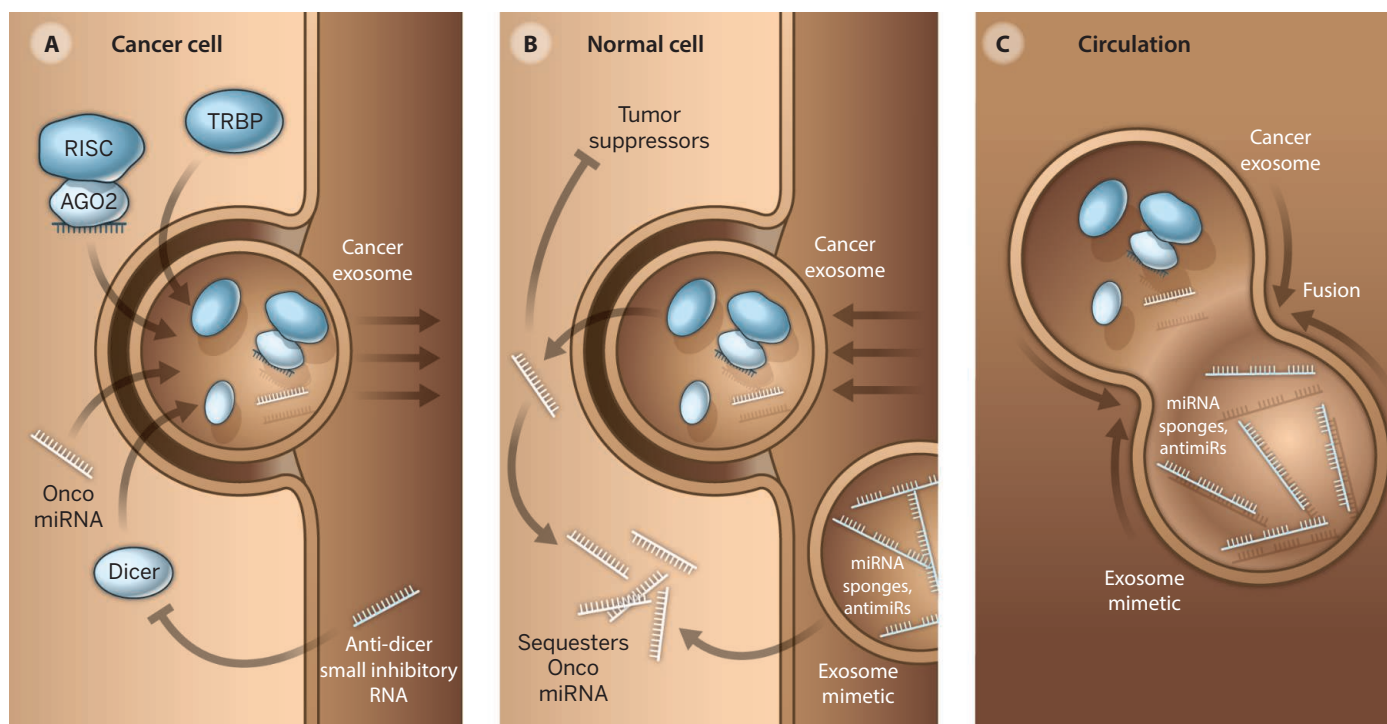


MiRNA biogenesis. MiRNAs combine with AGO2 and other proteins in an RNA-induced silencing complex (RISC) to repress the translation of target mRNAs.

Interestingly, exosomes contain messenger RNA (mRNA) and miRNA that can be transferred to other cells and regulate gene expression of the target cell (9). Likewise, miRNAs are present in apoptotic bodies (small membrane vesicles that are produced by cells undergoing programmed cell death) (10), or they are in the plasma, associated with Argonaute2 (AGO2), the key effector protein of a miRNA-mediated gene silencing mechanism (11). However, miRNAs detected in human serum and saliva are mostly concentrated inside exosomes (12). Virally encoded miRNAs are also found in exosomes, indicating how oncogenic viruses could manipulate the tumor microenvironment (13).

Department of Pathology, Beth Israel Deaconess Medical Center, Harvard Medical School, 330 Brookline Avenue, Boston, MA 02215, USA. E-mail: fslack@bidmc.harvard.edu

10.1126/science.aaa3814



Targeting cancer exosomes. Three possible therapeutic scenarios are shown for targeting tumor-derived exosomes within a cancer cell (A), in a normal recipient cell (B), or in the circulation (C).

The dysregulation of certain miRNAs has been associated with cancer-forming (oncogenic) events and has been identified in numerous types of human cancers. Fabbri *et al.* (14) detected nine miRNAs, including the oncogenic miRNAs (oncomiRs) miR-21, miR-27b, and miR-29a, in nanovesicles derived from supernatants of lung cancer cell lines, but not from normal cells. This suggests a cancer-specific pattern of secreted miRNAs. In particular, Fabbri *et al.* found that tumor-secreted miR-21 and miR-29a can bind to toll-like receptors (TLRs), murine TLR7 and human TLR8, to induce pro-tumoral inflammation that leads to tumor growth and metastasis.

Melo *et al.* (3) reveal a role of exosomes in cell-independent miRNA biogenesis that affects cancer progression. The authors show that only exosomes derived from cancer cells, but not those derived from normal cells, contain key enzymes involved in miRNA biogenesis such as Dicer, TAR (trans-activation response) RNA-binding protein (TRBP), and AGO2 (see the first figure). The exosomes also contain the membrane protein CD43, which plays a role in accumulating Dicer in cancer exosomes. The study also shows that Dicer-containing cancer exosomes process precursor miRNAs into mature miRNAs (including oncomiRs) over time, and upon encounter with normal human mammary epithelial cells induces them to become cancerous. Healthy mammary human epithelial cells formed tumors when they were

injected into mice that were treated with cancer exosomes. Moreover, miRNAs in the cancer exosomes inhibited the expression of their respective mRNA targets—phosphatase and tensin homolog [PTEN, a tumor suppressor protein] and the transcription factor homeobox D10 (HOXD10)—in the recipient epithelial cells. The authors suggest a possible temporal oncogenic “field effect” induced by cancer exosomes that recruits surrounding normal cells to become tumorigenic. The tantalizing results of Fabbri *et al.* and Melo *et al.* merit further investigation in immunocompetent mouse models.

The findings of Fabbri *et al.* and Melo *et al.* could be harnessed to design exosome-based cancer diagnostics and therapeutics. For example, using exosomes as biomarkers in early cancer diagnosis and prognosis might involve detecting the presence of Dicer and mature miRNAs in bodily fluids, which could serve as an additional cancer biomarker without requiring an invasive tissue biopsy. Given the role of oncomiRs such as miR-21 in cancer initiation, progression, and maintenance (15), the findings suggest a new route for anticancer therapy in targeting the malicious exosomes (see the second figure). For example, Dicer could be silenced directly in cancer cells by small interfering RNA. Alternatively, Dicer concentration within the cancer exosomes could be reduced by blocking CD43 expression in tumor cells with a specific monoclonal antibody. This may reduce further processing of oncomiRs from

taking place within the exosomes. Another possibility for therapeutic intervention could be exosome mimetics containing antimiRs or miRNA sponges that either capture the incoming oncomiRs in the recipient cells or fuse with the cancer exosomes and neutralize them while still in circulation.

Gone are the days of considering exosomes as mere “garbage cans” for the cell. We have entered the very early and exciting stage of understanding how cancer cells might use exosomes as drones to assemble and transport a menacing cargo of oncomiRs. Hopefully, evaluation of this phenomenon will spur the development of cancer therapies and broaden our understanding of how cancer spreads. ■

REFERENCES

1. C. Roma-Rodrigues *et al.* *BioMed Res. Int.* **2014**, 179486 (2014).
2. M. T. Le *et al.*, *J. Clin. Invest.* **124**, 5109 (2014).
3. S. A. Melo *et al.*, *Cancer Cell* **26**, 707 (2014).
4. K. Al-Nedawi *et al.*, *Nat. Cell Biol.* **10**, 619 (2008).
5. V. Luga *et al.*, *Cell* **151**, 1542 (2012).
6. H. Peinado *et al.*, *Nat. Med.* **18**, 883 (2012).
7. J. Skog *et al.*, *Nat. Cell Biol.* **10**, 1470 (2008).
8. C. Federici *et al.*, *PLOS ONE* **9**, e88193 (2014).
9. H. Valadi *et al.*, *Nat. Cell Biol.* **9**, 654 (2007).
10. A. Zernecke *et al.*, *Sci. Signal.* **2**, ra81 (2009).
11. J. D. Arroyo *et al.*, *Proc. Natl. Acad. Sci. U.S.A.* **108**, 5003 (2011).
12. A. Gallo, M. Tandon, I. Alevizos, G. G. Illei, *PLOS ONE* **7**, e30679 (2012).
13. D. G. Meekes *et al.*, *Proc. Natl. Acad. Sci. U.S.A.* **110**, 2925 (2013).
14. M. Fabbri *et al.*, *Proc. Natl. Acad. Sci. U.S.A.* **109**, E2110 (2012).
15. P. Medina *et al.*, *Nature* **467**, 86 (2010).

10.1126/science.aaa4024

Projecting regional change

How accurate are regional projections of climate change derived from downscaling global climate model results?

By Alex Hall

Techniques to downscale global climate model (GCM) output and produce high-resolution climate change projections have emerged over the past two decades. GCM projections of future climate change, with typical resolutions of about 100 km, are now routinely downscaled to resolutions as high as hundreds of meters. Pressure to use these techniques to produce policy-relevant information is enormous. To prevent bad decisions, the climate science community must identify downscaling's strengths and limitations and develop best practices. A starting point for this discussion is to acknowledge that downscaled climate signals arising from warming are more credible than those arising from circulation changes.

The concept behind downscaling is to take a coarsely resolved climate field and determine what the finer-scale structures in that field ought to be. In dynamical downscaling, GCM data are fed directly

to regional models. Apart from their finer grids and regional domain, these models are similar to GCMs in that they solve Earth system equations directly with numerical techniques. Downscaling techniques also include statistical downscaling, in which empirical relationships are established between the GCM grid scale and finer scales of interest using some training data set. The relationships are then used to derive finer-scale fields from the GCM data.

Decision-makers as well as scientists in other fields are using downscaled data for regional adaptation planning (1). Unfortunately, the reliability of the information produced by downscaling is often only loosely evaluated, if at all. Meanwhile, some within the climate science community dismiss downscaling (2, 3), rightly pointing out problems with its application, but also casting doubt on cases where it does add value. What can realistically be discovered about climate change at spatial scales smaller than GCM grid spacing?

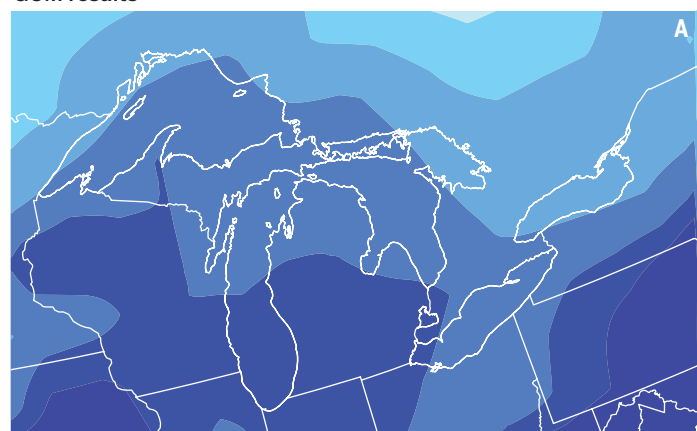
GARBAGE IN, GARBAGE OUT. Climate scientists doubt the quality of downscaled data because they are all too familiar with GCM biases, especially at regional scales.

These biases may be substantial enough to nullify the credibility of downscaled data. For example, biases in certain features of atmospheric circulation are common in GCMs (4) and can be especially glaring at the regional scale.

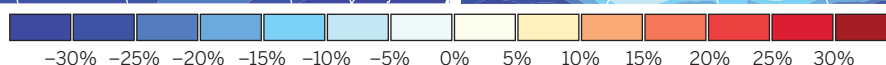
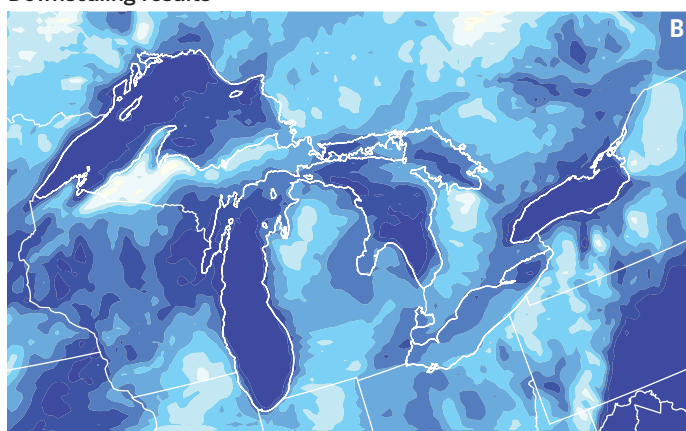
Consider the case of the jet stream, a major circulation feature that brings winter storms to the Northern Hemisphere mid-latitudes. All GCMs simulate the jet stream, but in many of them, its position is only approximately right. Suppose that a particular GCM's mid-latitude jet stream is positioned directly over a mountainous region of interest, whereas in reality, the jet stream is usually found to the north of the region. (In other words, the GCM has a circulation bias.) When that GCM is used to simulate climate change, its circulation signals in the region will inappropriately reflect changes in the GCM's jet stream. A particular downscaling technique might faithfully reproduce smaller scale circulation processes associated with these changes, such as channeling of flow around the region's mountains and through its mountain passes. These downscaled circulation signals may even appear to be realistic. However, the GCM signal being downscaled is linked to a large-scale circulation feature that is not usually found in that region in the real world. In this case, the precision and apparent physical meaning of the downscaled signals are without value. This is an example of the "garbage in, garbage out" argument at the heart of scientific criticism of downscaling (3).

Department of Atmospheric and Oceanic Sciences, University of California, Los Angeles, CA 90095, USA. E-mail: alexhall@atmos.ucla.edu

GCM results



Downscaling results



Modeling regional climate change. Simulated snowfall changes (%) over the North American Great Lakes region by 2050 to 2060 are shown for two cases. (A) Results from CCSM (Community Climate System Model), a global climate model (GCM). (B) Results when the GCM output is downscaled with the Weather Research and Forecasting (WRF) dynamical model (6). In the GCM, snowfall decreases because anthropogenic warming causes a smaller fraction of precipitation to fall as snow. When the GCM is downscaled, snowfall also generally decreases, but with substantial spatial variations. In particular, in areas affected by lake effect snow, the snowfall decrease is almost nonexistent in the regional simulation. Because the lake effect snow can only occur when the lake is unfrozen, a warming climate enhances the likelihood of lake effect snow, largely canceling out the general snow decrease due to a warmer atmosphere. Changes are calculated by differencing the 2050 to 2060 future period and the 1979 to 2001 historical period (6).

SIGNAL IN, SIGNAL OUT. Fortunately, there are regional-scale anthropogenic signals in the GCMs that are not contaminated by regional biases. The best example might be the models' direct thermodynamic responses to anthropogenic forcing, most notably warming. Warming signals arise from hemispheric- to global-scale processes (5). Water vapor, cloud, and surface albedo feedbacks, as well as the ocean's relatively slow heat uptake, are the main factors that shape warming and its spatial distribution. In stark contrast to the circulation example above, there are generally no a priori reasons for excluding a particular GCM's projection of warming at any scale, including the regional scale. It is thus legitimate to ask how that GCM warming signal would be distributed across a region when regional climate dynamics are taken into account through downscaling, and how that warming might affect regional dynamics. This is not "garbage in, garbage out," but rather "signal in," and potentially, "signal out."

Downscaling does not always produce outcomes significantly different from the driving GCM, but in areas of complex coastlines, intense topography, and variations in surface type, regional climate dynamics can profoundly influence how warming signals are distributed across the landscape, and how warming signals, in turn, affect regional climate. For example, Gula and Peltier recently downscaled a GCM climate change simulation dynamically in the Great Lakes region of North America (6). As expected in a warming climate, the GCM projects more precipitation falling as rain rather than snow, with snowfall decreasing by 15 to 30% (see the figure, panel A). Snowfall also decreases overall in the regional model, but along the fringes of the Great Lakes, the changes are almost negligible (see the figure, panel B). The reason is the region's famous lake effect snow, which happens when cold air masses in winter storms become laden with evaporative moisture from still-unfrozen lakes and dump that excess moisture as snow on adjacent land areas. The lake effect is greatly weakened when the Great Lakes freeze. In the future, the lakes are likely to be unfrozen for a larger fraction of the winter, so lake effect snow is possible for more of the winter. In areas where the lake effect operates, this largely cancels out the overall snow decrease caused by a warming climate.

These dynamics are not captured in the



Sierra Nevada, CA. In regions with complex topography, downscaling from GCM data can lead to misleading results.

GCM. But like the most credible features of GCM climate change signals, they have discernible physical origins rooted in basic thermodynamics. Here, downscaling takes a GCM signal shaped by processes much larger than the region itself and then introduces appropriate spatial structure, thus increasing the signal in some places and decreasing it in others, depending on regional climate dynamics.

DOES IT MATTER? The appropriate test of downscaling's relevance is not whether it alters paradigms of global climate science, but whether it improves understanding of climate change in the region where it is applied. The snowfall example above meets that test. In many places, such fine spatial structures have important implications for climate change adaptation. In the urban areas of the United States and Canada most affected by lake effect snow, infrastructure and water resource planning must proceed very differently if lake effect snow is not projected to decrease significantly.

Another recent study further illustrates the implications of spatial detail. When Kumar *et al.* downscaled GCM output over India (7) they found that the high elevation headwaters of the Ganges River warmed by a further 1.0°C by 2100 beyond the warming projected by the GCM. The reason is that well-understood snow albedo feedback effects are not resolved by the GCMs. The effects of this locally elevated warming include advances in snowmelt timing for the Ganges watershed and enhanced evaporative water losses, affecting water resources and water quality for hundreds of millions of people.

In many other regions with complex coastlines and topography (see the photo), downscaling would deepen scientific understanding of climate change. Over half the world's population lives within 200 km of a coast (8), and a similar number

depends on streamflow from mountains for freshwater (9). For these communities, downscaling offers better information about climate change than is available from GCMs alone.

NO SIGNAL UNANALYZED.

The "garbage in, garbage out" problem associated with GCM circulation biases underscores the need for the climate modeling community to continue to reduce those biases. In the meantime, however, demand will continue for information on local circulation changes and their effects on local precipitation. A minimum require-

ment for production of such information is that that only those GCMs whose circulation is reasonably realistic in the region of interest be used for downscaling. Even in this case, the downscaled changes must be analyzed to determine whether they are credible. If they are not, then the original GCM output, however coarse and imperfect, likely represents the current limits of scientific understanding.

Downscaling results can be interpreted with higher confidence when it comes to the warming dimension of climate change. In cases where credible mechanisms exist to explain spatial variations in warming or a warming-related variable in downscaled data, this information will be useful for local planning or interdisciplinary research based on downscaled data. The resulting confidence in regional warming patterns should facilitate understanding of climate change impacts on water resources, ecosystems, fire, public health, transportation, and agriculture. ■

REFERENCES AND NOTES

1. J. J. Barsugli *et al.*, *Eos Trans.* **94**, 424 (2013).
2. Q. Schiermeier, *Nature* **463**, 284 (2010).
3. R. A. Kerr, *Science* **334**, 173 (2011).
4. T. G. Shepherd, *Nat. Geosci.* **7**, 703 (2014).
5. G. Flato *et al.*, in *Climate Change 2013: The Physical Science Basis. Contribution of Working Group I to the Fifth Assessment Report of the Intergovernmental Panel on Climate Change*, T. F. Stocker *et al.*, Eds. (Cambridge Univ. Press, Cambridge/New York, 2013), chap. 9.
6. J. Gula, W. R. Peltier, *J. Clim.* **25**, 7723 (2012).
7. P. Kumar *et al.*, *Sci. Total Environ.* **468-469** (suppl.), S18 (2013).
8. P. Harrison, F. Pearce, *AAAS Atlas of Population and Environment* (American Association for the Advancement of Science and the Univ. of California Press, Berkeley, 2000).
9. M. F. Price *et al.*, Eds., *Mountain Geography: Physical and Human Dimensions* (Univ. of California Press, Berkeley, 2013).

ACKNOWLEDGMENTS

This work was supported by NSF grant EF-1065853.

10.1126/science.aaa0629

Einstein online

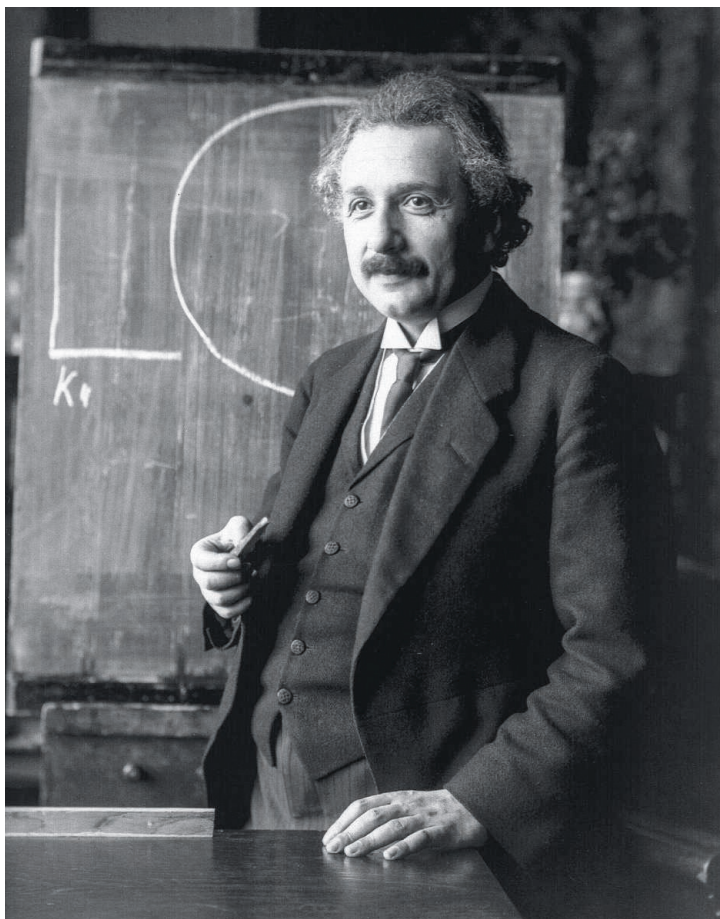
By Andrew Robinson

The goal of the *Digital Einstein Papers* is to provide free online access to *The Collected Papers of Albert Einstein* (1). This ongoing series of print archives currently consists of about 1000 writings, drafts, speeches, notebook and diary entries, lectures, notes, and calculations—both published and unpublished. It also contains Einstein's correspondence: some 12,500 letters written by him and some 16,500 letters written to him. Altogether, the collection contains about 30,000 unique documents, comprising a written legacy comparable in size to that of Napoleon Bonaparte, twice that of Charles Darwin and Gottfried Leibniz, and several times that of Isaac Newton and Galileo Galilei, as noted by Diana Kormos Buchwald, the current director of the Einstein Papers Project, which publishes the print volumes (2).

While marveling at the scope, expert presentation, and astonishing accessibility of the newly digitized papers, I can't help but recall a comment by Einstein himself, who wrote the following aphorism to a friend in 1930: "To punish me for my contempt of authority, Fate has made me an authority myself (3)."

From the time he published the general theory of relativity in 1915, and especially after its astronomical corroboration in 1919, Einstein knew the historical value of even his casual jottings. Indeed, he donated the manuscript of his comprehensive exposition of general relativity to the Hebrew University of Jerusalem for the university's official opening in 1925.

The Collected Papers of Albert Einstein was launched in the United States in the

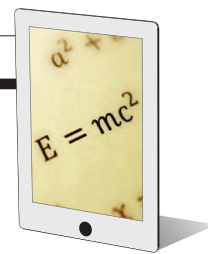


1980s in collaboration with the Albert Einstein Archives at the Hebrew University of Jerusalem. Originally based at Boston University, in 2000 the project moved to the California Institute of Technology, where Einstein worked as a visiting professor in the early 1930s. The first printed volume appeared in 1987. Today, there are 13 volumes, with companion volumes that contain English translations. The current collection spans Einstein's life and career up to 1923. A 14th volume will be published in the spring of 2015, and many more are promised. The forthcoming volumes will cover the last three decades of his life, which included his emigration from Germany to the United States, World War II, and the evolution of nuclear weapons.

Thus far, about 7000 pages, representing 2900 unique documents with dates up to 1923, have been digitized. The contents of each new printed volume will be added to

The Digital Einstein Papers

Princeton University Press.
Launched 5 December 2014;
einsteinpapers.press.
princeton.edu



the online archive roughly 2 years after publication.

Navigating the site is easy and intuitive, whether you wish to read each volume like a printed book or go straight to a document listed in the contents page. Equally effortless is the advanced search facility, which permits the user to search a chosen volume or all 13 volumes for every reference to, say, "light quanta" or Einstein's close friend, physicist Paul Ehrenfest. Still more impressive is the way the documents are linked. At the click of the mouse, each document heading takes the user to either the original version or a high-quality English translation, and hyperlinked footnotes take the user to the document's specific record at the Einstein Archives Online (4). In addition, documents can be printed out as hard copies. It is difficult to imagine what more could be required, even by the most specialized researcher. The new online archive seems to embody Einstein's celebrated remark

"Everything should be made as simple as possible, but not simpler."

But did Einstein actually say these words? If you search the archive with the phrase "as simple as possible," you obtain five results—none of which references this remark. In fact, it seems that no reliable source for it has been located by scholars (5). Perhaps it will be addressed in some authoritative, dismissive footnote of a future volume of *The Collected Papers*.

REFERENCES AND NOTES

1. The Collected Papers of Albert Einstein, www.einstein.caltech.edu/what/published.html.
2. D. Kormos Buchwald, in A. Robinson, *Einstein: A Hundred Years of Relativity* (Abrams, New York, 2005; 2015), Afterword.
3. B. Hoffmann, *Albert Einstein: Creator and Rebel* (Viking, New York, 1972), p. 24.
4. Albert Einstein Archives, www.albert-einstein.org.
5. A. Calaprice, Ed., *The Ultimate Quotable Einstein* (Princeton Univ. Press, Princeton, NJ, 2013), p. 475.

10.1126/science.aaa3615



FORENSIC SCIENCE

The body never lies

By Yevgeniya Nusinovich

With the advent of reality television and the popularity of science-themed shows and museum exhibits, it is becoming increasingly common for the general public to observe things that used to be reserved for trained members of specific professions: surgeries, crime scene investigations, and the like. However, even for people accustomed to the relatively gory images and seemingly realistic procedures they see on television, the new book by pathologist Judy Melinek and writer T. J. Mitchell may come as somewhat of a shock. This book, entitled *Working Stiff: Two Years, 262 Bodies, and the Making of a Medical Examiner*, purports to bring the audience into the real world of a medical examiner, as opposed to the polished and sanitized Hollywood version. This is not a story for the faint of heart, and the reader may find it gut-wrenching in some sections and heartbreaking in others.

The book begins during Melinek's time as a surgery resident, overworked and terrified that she will make a fatal mistake in her sleep-deprived state. Ultimately, she switches career paths, leaving her surgery residency for one in pathology, where the work hours are more manageable and the patients will "still be dead tomorrow." Melinek goes on to complete a fellowship in forensic pathology at the medical examiner's office in New York City.

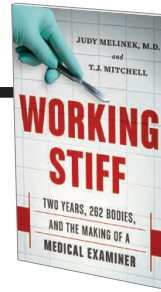
In a large urban setting such as New York City, there is never a shortage of work for a medical examiner, and every day there are autopsies to be done. Death by natural causes, accidents, suicide, and murder are each given a chapter in the book, gradually progressing from the relatively benign to the increasingly macabre.

In addition to her role as a pathologist, we

Working Stiff

Two Years, 262 Bodies, and the Making of a Medical Examiner
Judy Melinek and
T. J. Mitchell

Scribner, 2014. 266 pp.



learn that Melinek also serves as part of the forensic investigation team and is often the first point of contact for bereaved relatives. The latter role becomes especially poignant when we learn of the tragic suicide of Melinek's father, a psychiatrist. At times, the reader feels as though the elder Melinek's ghost is watching over her as she counsels the families of the deceased.

There is more to this book than the regular life of a medical examiner, however. As it happens, Melinek began her fellowship in New York City in the summer of 2001, so she was there to witness one of the darkest chapters in the city's history. The bodies of the almost 3000 people killed in the 9/11 terrorist attacks all had to be processed by the medical examiner's office. Unsurprisingly, the chapter devoted to these events is the longest one in the book and also the most difficult to read. The authors talk about the challenge of identifying victims of whom only small fragments had been recovered. In these cases, Melinek recorded what little details were available—a rim of lavender toenail polish, a gold tooth, an engraved wedding ring—which, together with DNA analysis, would be used to determine each victim's identity. The most compelling part of this chapter is the palpable sense of horror and despair felt by those handling the victims' remains.

Overall, this book admirably accomplishes its goal, showing the reader what it's really like to be a medical examiner. Whether this is something that you can handle is up to you to decide.

FILM

Finding our place among the stars

By Salman Hameed

The blockbuster film *Interstellar* is a stirring defense of space exploration and of our trust in science to get humanity out of trouble. This ambitious movie weaves complex ideas from physics—including relativity, quantum gravity, and higher-dimensional space—into the very fabric of its narrative. With a running time of just under 3 hours, the film manages to tell a gripping story while still getting most of its science right.

Interstellar is set in a near future when blight has destroyed most of the world's crops and food is becoming scarce. The human population has declined precipitously, and humans are in danger of dying out within a generation or two. But a ray of hope comes from space. A wormhole has appeared near Saturn, and a small group of NASA scientists plan to use it to find habitable planets that could serve as humanity's next home.

Wormholes are not new to science fiction, and although there is no scientific evidence that they exist, they are rooted in various solutions to Einstein's theory of general relativity. They also conveniently solve the science fiction author's problem of how to transport characters across vast interstellar—or intergalactic—distances in a relatively short time.

The accuracy of science in the film owes much to one of its executive producers, theoretical physicist Kip Thorne, who has coauthored technical papers on the possibility of traversable wormholes (1, 2). But credit must also go to director Christopher Nolan, who was committed to maintaining a scientifically plausible story line. One example of this collaboration is described in Thorne's wonderfully entertaining companion book *The Science of Interstellar*. It arose when Nolan informed Thorne that the plot required a planet where 1 hour spent on the surface would equal 7 years on Earth. This, according to Nolan, was "non-negotiable." While at first skeptical, Thorne ultimately calculated that such a planet could theoretically exist if it were orbiting close enough



to a supermassive black hole that was rotating close to the maximum speed allowed by physics. Whether moving humanity to this world is a good idea or not is a separate question, but science allows the possibility for such a planet to exist.

Although wormholes are still in the realm of theory and speculation, supermassive black holes do exist and are often found at the centers of galaxies. In chapters 8 and 9, Thorne describes the science that inspired the visual depiction of the black hole in the film. Recalling the first time he saw the film's black hole—Gargantua—he writes, "What a joy it was when I first saw these images! For the first time ever, in a Hollywood movie, a black hole and its disk depicted as we humans will really see them when we've mastered interstellar travel." The results are spectacular to behold in the movie, and Thorne informs the reader that the models

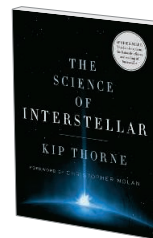
and simulations that helped inspire the images will serve as data in one or more forthcoming technical papers.

One of the best features of the book is its coding system for chapters and subsections into "T" for truth, "EG" for educated guess, and "S" for speculation. For example, much of Gargantua's anatomy is based on broadly accepted theories in physics and, as such, this section is labeled with a "T." The visualization of what one might see inside the black hole, however, is firmly speculative and labeled with an "S."

Clearly, the movie is based in good science; however, it is not without its issues. For example, it decidedly lacks a sense of wonder and curiosity that one would expect to see in a story about exploring new worlds. Similarly, in the imagined future of the film, there seems to be a noticeable lack of internationalism. American flags are fluttering

Interstellar

Christopher Nolan, Director
Paramount Pictures, 2014.
169 minutes.



The Science of Interstellar

Kip Thorne
Norton, 2014.
336 pp.

on planets in another galaxy, and baseball seems to be the sport of choice even in orbital colonies. This is all the more surprising because the movie itself is a result of an international collaboration.

Although *Interstellar* does not have the philosophical sophistication of *2001: A Space Odyssey*, it is still a unique and ambitious film that does not shy away from complex sociological and scientific ideas. Despite its grim premise, the film's message is ultimately one of faith in science and human ingenuity. As agricultural insecurity and resource scarcity become realities in our own 21st-century world, I can't help but hope that the film's main character is right when he states, "We are going to find the way—we always have."

REFERENCES

1. M. S. Morris, K. Thorne, *Am. J. Phys.* **56**, 395 (1988).
2. M. S. Morris, K. S. Thorne, U. Yurtsever, *Phys. Rev. Lett.* **61**, 1446 (1988).

10.1126/science.aaa3646

BOOKS IN BRIEF

Melting Away

A Ten-Year Journey Through
Our Endangered Polar Region

By Camille Seaman

Princeton Architectural Press, 2014, 160 pp.



CAMILLE SEAMAN TRAVELED to the Arctic for the first time in 1999 on a whim. Captivated by its stark beauty and inspired by her Native American heritage, she went on to become an expedition photographer aboard a number of scientific vessels and commercial ships, visiting both the Arctic and Antarctic regions for months at a time over the next decade. Seaman's new book documents the changing polar landscape and the creatures that call these regions home in a series of compelling photographs. The book also features a number of short essays that describe her personal journey as a photographer and advocate for the environment.

10.1126/science.aaa3325



LETTERS

Edited by Jennifer Sills

Retraction

IN OUR REPORT “Polymerase exchange during Okazaki fragment synthesis observed in living cells” (1), a collaboration between the Allemand and Michel labs, we performed single-molecule microscopy experiments to describe the replisome dynamics during replication in *Escherichia coli*. We deduced polymerase exchange from the variation of spot intensity with time, interpreted as specific DNA binding and unbinding of fluorescently tagged components of the replisome. Our recent attempts to repeat these experiments have failed, and we now realize that several issues invalidate the original analyses, including sampling errors, skewed statistical analysis, and miscalculations. The real ratio of significant replisomes (two distinct replisomes per cell) is much less important than stated in the Report, whereas the background (spots due to unbound proteins) is higher. We therefore retract the Report. We apologize to the scientific community for any loss of time and resources caused by this publication.

Giuseppe Lia,¹ Bénédicte Michel,^{2,3*}

Jean-François Allemand^{4,5,6*}

¹Catanzaro, 88100, Italy. ²CNRS, Centre de Génétique Moléculaire, UPR3404, Gif-sur-Yvette F-91198, France. ³Université Paris-Sud, F-91405 Orsay, France. ⁴Laboratoire de Physique Statistique, Ecole Normale Supérieure (ENS), UMR 8550 CNRS, Universités Pierre et Marie Curie et Paris Diderot, Département de Physique, 75231 Paris Cedex 05, France. ⁵Département de Biologie, Institut de Biologie de l'Ecole Normale Supérieure, UMR 8542 CNRS, 75231 Paris Cedex 05, France. ⁶Institut Universitaire de France (IUF) 75005, Paris, France.

*Corresponding authors. E-mail: benedicte.michel@cgm.cnrs-gif.fr (B.M.) allemand@lps.ens.fr (J.-F.A.)

REFERENCE

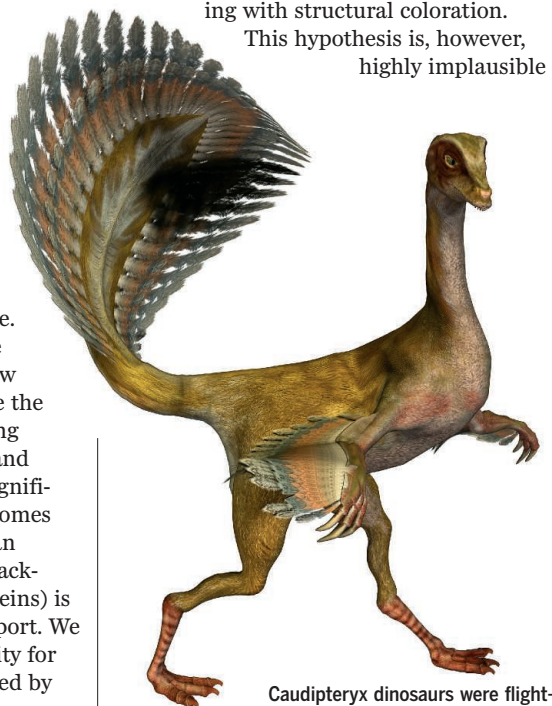
1. G. Lia, B. Michel, J.-F. Allemand, *Science* **335**, 328 (2012); published online 22 December 2011.

On the origin of feathers

FEATHERS ARE ONE of the most characteristic evolutionary novelties of birds, and until recently a broad consensus existed that typical vaned feathers (pennaceous feathers) evolved in an aerodynamic

context to streamline the body and form lift-generating surfaces. Based on the occurrence of essentially modern-type pennaceous feathers in a number of flightless non-avian theropod (“beast-footed”) dinosaurs, Foth *et al.* recently proposed that these feathers originated in a context other than flight (1). In their Perspective “Beyond the rainbow” (24 October, p. 416), M.-C. Koschowitz *et al.* argue that vaned feathers evolved for signaling with structural coloration.

This hypothesis is, however, highly implausible



Caudipteryx dinosaurs were flightless yet had pennaceous feathers.

from an evolutionary point of view.

In most flightless birds, the feather vanes lose their integrity, which indicates that pennaceous feathers evolved to serve aerodynamic functions. In extant birds, signal feathers are usually restricted to small portions of the plumage, which further challenges the hypothesis that pennaceous feathers mainly evolved for display reasons. Moreover, display feathers often do not have a pennaceous structure, but form loose feather bunches or elaborate ornamental structures. Display feathers are almost always restricted to one sex, usually the males. If pennaceous feathers mainly evolved to serve display purposes, why do female birds have exactly the same basic feather morphologies as the males?

Even if some theropods with pennaceous feathers can be shown to have been primarily flightless, the “wing-assisted incline running” hypothesis provides an aerodynamic context for the evolution of feathers in nonflying animals with limbs adapted for running (2). Hypotheses for their evolution in a nonaerodynamic

context are therefore not only evolutionarily implausible but also not necessary to explain their origin.

Gerald Mayr

Senckenberg Research Institute and Natural History Museum Frankfurt, Ornithological Section, D-60325 Frankfurt am Main, Germany.
E-mail: gerald.mayr@senckenberg.de

REFERENCES

1. C. Foth, H. Tischlinger, O. W. M. Rauhut, *Nature* **511**, 79 (2014).
2. K. P. Dial, *Science* **299**, 402 (2003).

Response

MAYR QUESTIONS THE plausibility of our hypothesis that structural color signaling was the initial selective advantage in the evolution of pennaceous feathers. Our hypothesis is grounded in the accepted phylogenetic framework for theropods, which shows that pennaceous feathers evolved before flight (1–3). We thus disagree with Mayr’s suggestion that non-avian, nonflying theropods such as oviraptorosaurs inherited pennaceous feathers from their flying ancestors. Mayr argues that the loss of feather vane integrity in flightless birds indicates that pennaceous feathers evolved for the purpose of flight. However, according to Prum (4), the reduced integrity of the vane in most flightless birds is a variation of the original ancestral pennaceous feather.

Mayr then argues that signaling feathers are localized, whereas in modern birds pennaceous feathers cover the entire body. Yet human visual capability strongly differs from that of birds, and biologically relevant optical cues are not restricted to the plumage that attracts our eye (5). Furthermore, the first known non-avian dinosaurs with planar feathers exhibited them in limited density only on prominent portions of the body (2), consistent with a signaling function.

We agree with Mayr that the “wing-assisted incline running” hypothesis (6) would provide an aerodynamic context for the evolution of pennaceous feathers, but the feathers evolved long before the potential for such behavior. Solitary planar feathers on the anterior extremities could have been gradually added, with respect to more sophisticated signaling, and at the same time incrementally forming lift-generating surfaces: the prerequisite for the transitory stages that resulted in active flight.

Finally, Mayr points out that signaling feathers are “almost always” restricted to one sex, making an initial signaling function difficult to explain. However, intrasexual communication is not fully understood, especially in females (7). We should also

take into account that display structures such as pennaceous feathers make species recognizable to other species.

We emphasize that feathers did not “evolve for” something; rather, their fortuitous appearance was associated with a selective advantage, which resulted in their retention. We argue that their original selective advantage was in signaling, not flight.

Marie-Claire Koschowitz,^{1,2*}

Markus Lambertz,³ Christian Fischer,²

P. Martin Sander^{1,4}

¹Division of Paleontology, Steinmann Institute for Geology, Mineralogy and Paleontology, Rheinische Friedrich-Wilhelms-Universität Bonn, 53115 Bonn, Germany. ²Institute for Zoology and Anthropology, Department of Morphology, Systematics and Evolutionary Biology with Zoological Museum, Georg-August-Universität Göttingen, 37073 Göttingen, Germany. ³Institut für Zoologie, Rheinische Friedrich-Wilhelms-Universität Bonn, 53115 Bonn, Germany. ⁴Dinosaur Institute, Natural History Museum of Los Angeles County, Los Angeles, CA 90007, USA.

*Corresponding author. E-mail: m.koschowitz@uni-bonn.de

REFERENCES

1. M. S. Y. Lee, A. Cau, D. Naish, G. J. Dyke, *Science* **345**, 562 (2014).
2. D. K. Zelenitsky *et al.*, *Science* **338**, 510 (2012).
3. J. Clarke, *Science* **340**, 690 (2013).
4. R. O. Prum, *J. Exp. Zool. Mol. Dev. Evol.* **285**, 291 (1999).

5. M. D. Eaton, *Proc. Natl. Acad. Sci. U.S.A.* **102**, 10942 (2005).
6. K. P. Dial, *Science* **299**, 402 (2003).
7. T. Amundsen, *Trends Ecol. Evol.* **15**, 149 (2000).

ERRATA

Erratum for the Perspective: “Mathematical models for emerging disease” by A. Dobson, *Science* **346**, aaa4792 (2014). Published online 19 December 2014; 10.1126/science.aaa4792

Erratum for the Report: “Proton-catalyzed, silane-fueled Friedel-Crafts coupling of fluoroarenes” by O. Allemann *et al.*, *Science* **346**, aaa4609 (2014). Published online 12 December 2014; 10.1126/science.aaa4609

TECHNICAL COMMENT ABSTRACTS

Comment on “A 12-million-year temperature history of the tropical Pacific Ocean”

Ana Christina Ravelo, Kira Trillium Lawrence, Alexey Fedorov, Heather Louise Ford

Zhang *et al.* (Reports, 4 April 2014, p. 84) interpret TEX₈₆ and U₃₇^{K'} paleotemperature data as providing a fundamentally new view of tropical Pacific climate during

the warm Pliocene period. We argue that, within error, their Pliocene data actually support previously published data indicating average western warm-pool temperature similar to today and a reduced zonal gradient, referred to as a permanent El Niño-like state.

Full text at <http://dx.doi.org/10.1126/science.1257618>

Response to Comment on “A 12-million-year temperature history of the tropical Pacific Ocean”

Yi Ge Zhang, Mark Pagani, Zhonghui Liu

Contrary to our conclusions, Ravelo *et al.* argue that our TEX₈₆-based sea surface temperature (SST) records do not conflict with the supposition of “permanent El Niño-like” conditions during the early Pliocene. We show that the way Ravelo *et al.* treat the existing temperature data perpetuates an inaccurate impression of cooler Pacific warm-pool SSTs and low equatorial temperature gradients in the past.

Full text at <http://dx.doi.org/10.1126/science.1257930>

TECHNICAL COMMENT

OCEANS

Comment on “A 12-million-year temperature history of the tropical Pacific Ocean”

Ana Christina Ravelo,^{1*} Kira Trillium Lawrence,² Alexey Fedorov,³ Heather Louise Ford⁴

Zhang *et al.* (Reports, 4 April 2014, p. 84) interpret TEX₈₆ and U₃₇^{K'} paleotemperature data as providing a fundamentally new view of tropical Pacific climate during the warm Pliocene period. We argue that, within error, their Pliocene data actually support previously published data indicating average western warm-pool temperature similar to today and a reduced zonal gradient, referred to as a permanent El Niño-like state.

Even small changes (≤1°C) in absolute tropical sea surface temperatures (SSTs) have implications for climate conditions both regionally (1) and globally, including climate sensitivity to greenhouse gases (2). Thus, it is crucial to obtain accurate tropical SST

estimates during the warm early Pliocene [5.0 to 3.5 million years ago (Ma)], when atmospheric CO₂ concentrations and extratropical temperatures were, on average, higher than pre-industrial values. SST reconstructions, based on planktonic foraminifera Mg/Ca and biomarker proxy U₃₇^{K'}, indicate two key features of the tropical Pacific (3): average Western Equatorial Pacific (WEP) warm-pool SSTs (4, 5) similar to today and a reduced (but not absent) zonal equatorial SST gradient (4–6). We compile tropical Pacific SST data (4, 6, 7, 8–12) (Table 1) and show, contrary to claims made by Zhang *et al.* (7), that their low-resolution (1 sample per >100,000 years) records,

only appropriate for a cursory characterization of average Pliocene conditions, are largely consistent with previously published data.

The only published data representing the central WEP warm pool is from site 806 (Table 1 and Fig. 1) and indicate average early Pliocene SSTs cooler than today (13): −0.03°C for Mg/Ca, −1.10°C for TEX₈₆, and −0.66°C for U₃₇^{K'}. Because absolute SST estimates are calibration dependent (14–17), a better approach compares proxy measurements and shows that average Pliocene values (0.70 for TEX₈₆, 3.45 mmol/mol for Mg/Ca, and 0.99 for U₃₇^{K'}) are similar to core-top values (0.70 for TEX₈₆, 3.43 mmol/mol for Mg/Ca, and 0.98 for U₃₇^{K'}). Within calibration errors of at least ±1°C (14–17), all proxies concur that the differences between Pliocene and core-top SSTs are negligible (+0.08°C for Mg/Ca, +0.04°C for TEX₈₆, and +0.26°C for U₃₇^{K'}). U₃₇^{K'} is saturated at 29°C (17), but Mg/Ca and TEX₈₆ should detect warmer SSTs if they existed; although potential biases (e.g., changing seawater Mg/Ca and subsurface glycerol dialkyl glycerol tetraether (GDGT) lipid production) need further study, at this point neither Mg/Ca nor TEX₈₆ data provide solid evidence of average warm-pool SSTs substantially warmer than today. Average Pliocene TEX₈₆ SSTs at site 1143 (9°N) of 29.7°C can be explained by an expanded, but not warmer, central warm pool (3); expansion of the tropics during global warming is documented by 21st-century observations (18) and future (19) and Pliocene model simulations (20).

Focusing on long-term smoothed trends, Zhang *et al.* (7) argue that the Pliocene warm pool was substantially warmer relative to today

Table 1. Summary of tropical Pacific SST data. All available data between 3.5 and 5.0 Ma were used to calculate the average Pliocene value, and all available data between 5.0 and 12.0 Ma were used to calculate the average late Miocene value. Modern data are from Simple Ocean Data Assimilation average and standard deviation, calculated from the monthly SST data from 1958 to 2007 (13). Core-top values come from the site location or from nearby sites when available. The calibrations used to calculate SSTs were Dekens *et al.* (16) using the [CO₃^{2−}] dissolution correction for the Mg/Ca data, Müller *et al.* (17) for U₃₇^{K'}, and Kim *et al.* (15) for TEX₈₆. Dashed lines indicate a lack of published data.

| Site | Lat | Lon | Water Depth (m) | SODA avg SST (°C) | SODA Std Dev (°C) | Proxy type | Number of coretops | Coretop avg value ⁱ | Coretop SST (°C) | Pliocene avg value ⁱ (3.5–5.0 Ma) | Pliocene SST (°C) | Pliocene anomaly (rel. to SODA) (°C) | Pliocene anomaly (rel. to coretop) (°C) | Miocene avg value ⁱ (5.0–12.0 Ma) | Miocene SST (°C) | Miocene anomaly (°C) | coretop data reference | paleo-SST data reference |
|-----------------|-------|---------|-----------------|-------------------|-------------------|-------------------------------|--------------------|--------------------------------|------------------|--|-------------------|--------------------------------------|---|--|------------------|----------------------|------------------------|--------------------------|
| South China Sea | | | | | | | | | | | | | | | | | | |
| 1143 | 9.36 | 113.29 | 2772 | 28.40 | 1.00 | U ₃₇ ^{K'} | 1 | 0.97 | 28.06 | 0.99 | 28.80 | 0.40 | 0.74 | --- | --- | --- | 12 | 12 |
| 1143 | 9.36 | 113.29 | 2772 | 28.40 | 1.00 | TEX ₈₆ | 1 ⁱⁱ | 0.73 | 29.41 | 0.74 | 29.70 | 1.30 | 0.29 | 0.76 | 30.40 | 2.00 | 27 | 7 |
| WEP | | | | | | | | | | | | | | | | | | |
| 806 | 0.32 | 159.36 | 2520 | 29.24 | 0.55 | Mg/Ca | 1 | 3.43 | 29.12 | 3.45 | 29.20 | −0.03 | 0.08 | --- | --- | --- | 16 | 4 |
| 806 | 0.32 | 159.36 | 2520 | 29.24 | 0.55 | TEX ₈₆ | 11 ⁱⁱⁱ | 0.70 | 28.10 | 0.70 | 28.14 | −1.10 | 0.04 | 0.75 | 29.87 | 1.77 | 15 | 7 |
| 806 | 0.32 | 159.36 | 2520 | 29.24 | 0.55 | U ₃₇ ^{K'} | 2 ^{iv} | 0.98 | 28.32 | 0.99 | 28.58 | −0.66 | 0.26 | --- | --- | --- | 28 | 7 |
| EEP | | | | | | | | | | | | | | | | | | |
| 1241 | 5.84 | −86.44 | 2027 | 27.80 | 1.01 | Mg/Ca | none | --- | --- | 3.26 | 28.48 | 0.68 | --- | --- | --- | --- | --- | 9 |
| 1241 | 5.84 | −86.44 | 2027 | 27.80 | 1.01 | U ₃₇ ^{K'} | none | --- | --- | 0.97 | 28.11 | 0.31 | --- | --- | 27.93 | 0.13 | --- | 11 |
| 1241 | 5.84 | −86.44 | 2027 | 27.80 | 1.01 | TEX ₈₆ | none | --- | --- | 0.63 | 25.01 | −2.79 | --- | --- | 25.39 | −2.41 | --- | 11 |
| 1338 | 2.50 | −118.00 | 4210 | 25.65 | 1.40 | U ₃₇ ^{K'} | 2 ^v | 0.88 | 25.39 | 0.95 | 27.36 | 1.71 | 1.98 | 0.96 | 27.72 | 2.07 | 28 | 10 |
| 850 | 1.30 | −110.50 | 3786 | 24.51 | 1.74 | U ₃₇ ^{K'} | 2 ^{vi} | 0.89 | 25.53 | 0.93 | 26.70 | 2.20 | 1.17 | --- | --- | --- | 28 | 7 |
| 850 | 1.30 | −110.50 | 3786 | 24.51 | 1.74 | TEX ₈₆ | none | --- | --- | 0.64 | 25.40 | 0.90 | --- | 0.67 | 26.85 | 2.34 | --- | 7 |
| 847 | 0.19 | −95.32 | 3334 | 23.54 | 1.99 | Mg/Ca | none | --- | --- | 3.11 | 27.84 | 4.29 | --- | --- | --- | --- | --- | 4 |
| 847 | 0.19 | −95.32 | 3334 | 23.54 | 1.99 | U ₃₇ ^{K'} | 1 ^{vii} | 0.86 | 24.67 | 0.94 | 27.02 | 3.47 | 2.35 | --- | --- | --- | 29 | 8 |
| 846 | −3.09 | −90.82 | 3296 | 23.75 | 2.36 | U ₃₇ ^{K'} | 1 | 0.82 | 23.55 | 0.93 | 26.99 | 3.23 | 3.44 | --- | --- | --- | 30 | 6 |

ⁱ U₃₇^{K'} and TEX₈₆ values are unitless, and Mg/Ca values are in mmol/mol.
ⁱⁱ coretop from nearby station, 17960, in South China Sea was used.
ⁱⁱⁱ coretops from nearby sites on the Ontong Java Plateau were used.
^{iv} coretops from ERDCBX120 and the 175E transect were used.
^v coretops from PLDS66 and PLDS90 were used.
^{vi} coretop from PLDS68 and PLDS72 were used.
^{vii} coretop from TR163-22 was used.

but in fact show that it was warmer relative to the Quaternary (which includes Pleistocene glacial intervals). Their approach contrasts with a large body of published work, including modeling (20, 21) and observational (5, 8) studies, that compare Pliocene conditions to a modern baseline. This difference in approach is a source of misinterpretation of the TEX_{86} data (7, 22). If one considers TEX_{86} variability, instead of the mean, their approach still misses the profound importance of the data. From 3.5 to 5.0 Ma, TEX_{86} variability is within the $\pm 2.5^\circ\text{C}$ calibration error with minima and maxima straddling the core-top value; this is in stark contrast to CO_2 and climate records from outside the warm pool in which even discrete glacial minima are generally higher than core-top and Pleistocene interglacial values (3).

Unlike the WEP warm pool, the East Equatorial Pacific (EEP) cold tongue was substantially warmer than today during the Pliocene (Fig. 1). This mean state with a reduced zonal SST gradient is referred to as “permanent El Niño-like conditions” and is supported by many data types (5, 23). This term does not imply a lack of variability nor that mean state changes are due to the dynamics that generate interannual El Niño events (3). Rather, it highlights that, like an El Niño event, small changes in the zonal gradient induce major changes in atmospheric circulation with far-field effects. The term “El Padre” is also used to differentiate this Pliocene state from the dynamical El Niño–Southern Oscillation pattern. The Zhang *et al.* (7) data support previous work showing a reduced zonal gradient during the Pliocene.

At EEP site 850, TEX_{86} SSTs are cooler than $U_{37}^{K'}$ SSTs (7); a similar cold bias occurs at site 1241 (Fig. 2A), due to subsurface production of crenarchaeota GDGTs (11). A shallow cool thermocline can explain this cold bias: TEX_{86} apparently records depth-integrated temperature rather than SST. The cold bias likely changed as the thermocline shoaled (24) or as ecosystem structure changed (11) since 5 Ma. At WEP site 806 (Fig. 2B), higher Pleistocene $U_{37}^{K'}$ and Mg/Ca compared to TEX_{86} SSTs may be due to problems with Mg/Ca (7) and/or a cold bias in TEX_{86} that was diminished in the Pliocene when the tropical thermocline was deeper (4, 23–25). Even if regional calibrations can statistically circumvent the TEX_{86} cold bias in the modern ocean (14), they cannot be expected to provide accurate

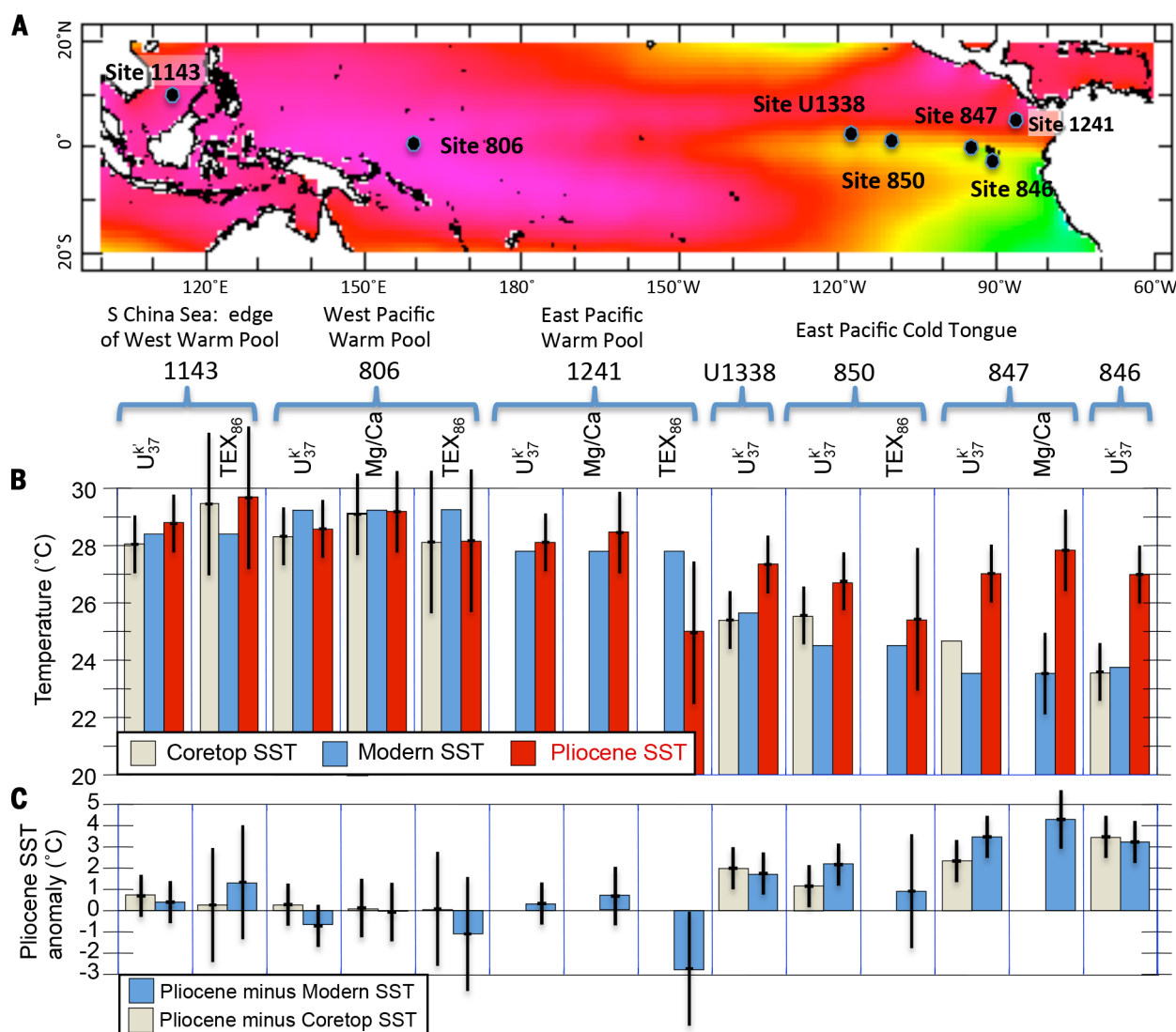


Fig. 1. Spatial pattern of average Pliocene temperature anomalies. (A) Map showing location of sites with published SST data used in this comment, overlain on a map of modern SSTs. (B) Average Pliocene (3.5 to 5.0 Ma) SSTs plotted for each site and each proxy along with the modern annual average SST (13) and with SST estimates made on core tops. (C) SST anomaly calculated as the average Pliocene value minus modern annual average SST and minus the core-top estimate of SST. In (B) and (C), error bars reflect calibration errors: $\pm 2.5^\circ\text{C}$ for TEX_{86} SST (15), $\pm 1.4^\circ\text{C}$ for Mg/Ca SST (16), and $\pm 1.0^\circ\text{C}$ for $U_{37}^{K'}$ (17). See Table 1 for a summary of the calculations.

SST estimates as subsurface temperatures changed through the Pliocene (4, 23–25). Zhang *et al.*'s TEX_{86} data reflect the WEP-EEP depth-integrated temperature difference, but their ability to quantify the surface temperature gradient is tenuous.

To quantify changes in EEP SSTs, we exclude TEX_{86} data (at sites 850 and 1241) because of the clearly documented severe cold bias (11) (Fig. 2A) compared with other available EEP records

(e.g., U_{37}^K). All EEP records show Pliocene SSTs warmer than today (Figs. 1B and 2B). The Zhang *et al.* (7) equatorial data indicate a mean Pliocene WEP-EEP difference of 1.5°C, in agreement with previously published data (Fig. 2C). Given the profound importance of tropical SST, and the fact that biases of all proxy types require additional study, a conservative approach that identifies convergence among data records, and does

not overinterpret the importance of divergent records, is warranted.

The new data (7) confirm previous Pliocene data but provide evidence of Miocene warm-pool temperatures warmer than today (Table 1). Lea (22) states that “the TEX_{86} data support previous evidence that the warm pool responds strongly to radiative forcing,” but in fact, the warm pool was warmer in the late Miocene than in the

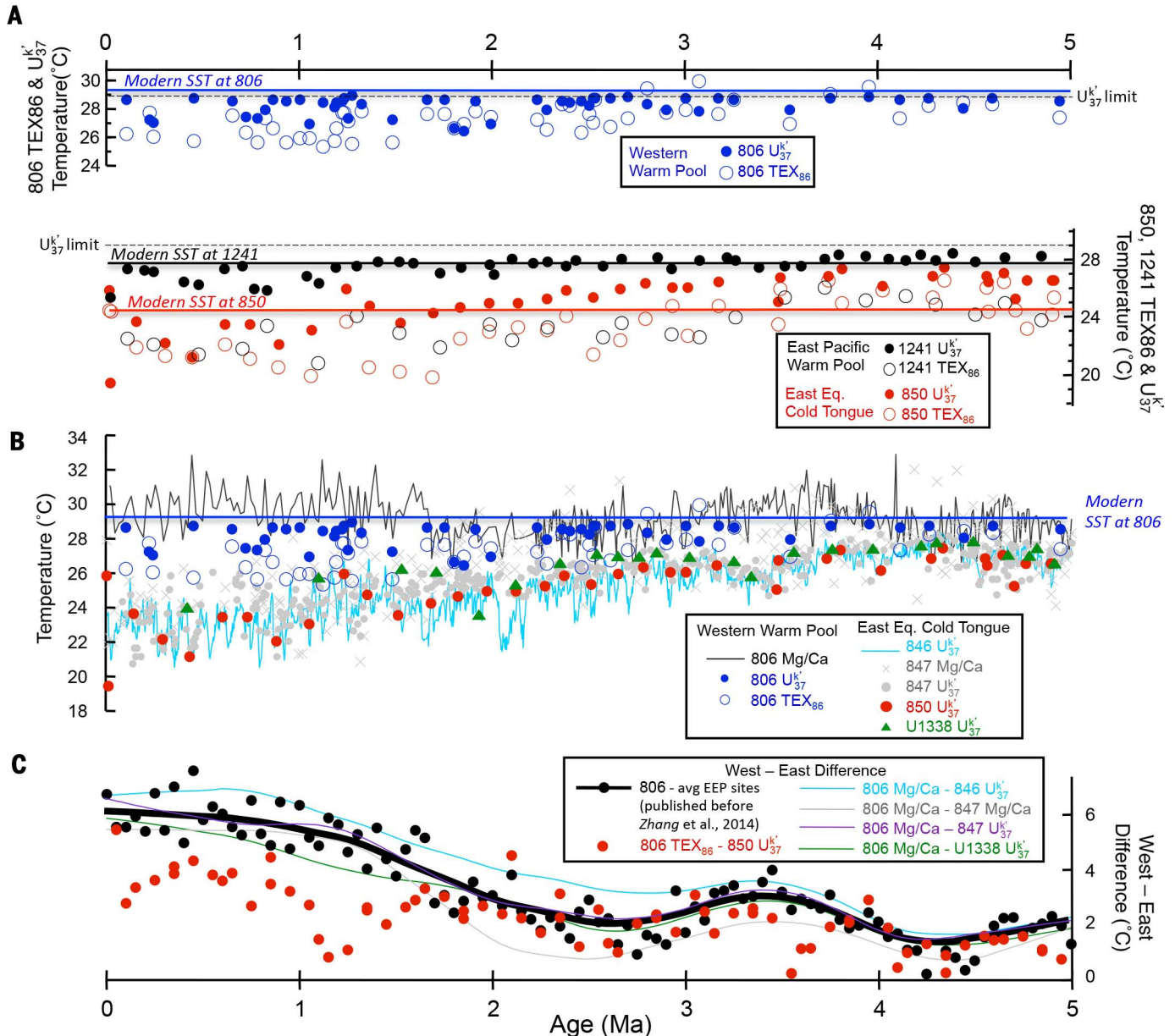


Fig. 2. Tropical Pacific SST records extending from 5 Ma to present. (A) SST records from all sites that have both U_{37}^K and TEX_{86} data: WEP site 806 (7), EEP cold tongue site 850 (7), and Eastern warm-pool site 1241 (11). Solid lines are the modern SST at each site, and dashed lines are the SST limit for the U_{37}^K proxy. The cold bias of TEX_{86} is apparent at all sites but is less severe at site 806 where the thermocline is deepest. **(B)** All records from the WEP and EEP cold tongue excluding site 850 TEX_{86} data because of the severe cold bias due to subsurface production of GDGTs. See Table 1 for references. **(C)** WEP – EEP SST difference calculated by interpolating and resampling all records to

50K resolution and subtracting them from each other. The smoothed curves are generated using a locally weighted least squares (0.25 smoothing parameter) method: (black dots and thick black curve) available Mg/Ca and U_{37}^K data published before Zhang *et al.* (7) [WEP site 806 (4) minus the average of EEP sites 846 (6), 847 (4, 8), and U1338 (10)]; (red dots) new Zhang *et al.* WEP site 806 TEX_{86} minus EEP site 850 U_{37}^K ; (thin colored lines) different combinations of previously published data from WEP and EEP sites. WEP site 806 U_{37}^K data are saturated and therefore are not used to calculate east-west SST difference.

Pliocene, whereas partial pressure of CO₂ was not (26). The new TEX₈₆ data highlight the importance of future research aimed at solving this paleoclimate enigma.

REFERENCES AND NOTES

1. M. Collins *et al.*, *Nat. Geosci.* **3**, 391–397 (2010).
2. T. S. von Deimling, H. Held, A. Ganopolski, S. Rahmstorf, *Clim. Dyn.* **27**, 149–163 (2006).
3. A. V. Fedorov *et al.*, *Nature* **496**, 43–49 (2013).
4. M. W. Wara, A. C. Ravelo, M. L. Delaney, *Science* **309**, 758–761 (2005).
5. H. J. Dowsett, M. M. Robinson, *Philos. Trans. R. Soc. A Math. Phys. Eng. Sci.* **367**, 109–125 (2009).
6. K. T. Lawrence, Z. Liu, T. D. Herbert, *Science* **312**, 79–83 (2006).
7. Y. G. Zhang, M. Pagani, Z. Liu, *Science* **344**, 84–87 (2014).
8. P. S. Dekens, A. C. Ravelo, M. D. McCarthy, *Paleoceanography* **22**, PA3211 (2007).
9. J. Groeneveld *et al.*, *Proc. Ocean Drilling Program: Sci. Results* **202**, 1–27 (2006).
10. G. Rousselle, C. Beltran, M.-A. Sicre, I. Raffi, M. De Rafélis, *Earth Planet. Sci. Lett.* **361**, 412–421 (2013).
11. O. Seki *et al.*, *Paleoceanography* **27**, PA3224 (2012).
12. L. Li *et al.*, *Earth Planet. Sci. Lett.* **309**, 10–20 (2011).
13. J. A. Carton, B. S. Giese, *Mon. Weather Rev.* **136**, 2999–3017 (2008).
14. J. E. Tierney, M. P. Tingley, *Geochim. Cosmochim. Acta* **127**, 83–106 (2014).
15. J.-H. Kim *et al.*, *Geochim. Cosmochim. Acta* **74**, 4639–4654 (2010).
16. P. S. Dekens, D. W. Lea, D. K. Pak, H. J. Spero, *Geochim. Geophys. Geosyst.* **3**, 1–29 (2002).
17. P. J. Müller, G. Kirst, G. Ruhland, I. von Storch, A. Rosell-Melé, *Geochim. Cosmochim. Acta* **62**, 1757–1772 (1998).
18. D. J. Seidel, Q. Fu, W. J. Randel, T. J. Reichler, *Nat. Geosci.* **1**, 21–24 (2007).
19. J. Lu, G. A. Vecchi, T. Reichler, *Geophys. Res. Lett.* **34**, L06805 (2007).
20. W. L. Chan, A. Abe-Ouchi, R. Ohgaito, *Geosci. Model Dev.* **4**, 1035–1049 (2011).
21. A. M. Haywood *et al.*, *Clim. Past* **9**, 191–209 (2013).
22. D. W. Lea, *Science* **344**, 52–53 (2014).
23. A. C. Ravelo, P. S. Dekens, M. McCarthy, *GSA Today* **16**, 4–11 (2006).
24. H. L. Ford, A. C. Ravelo, S. Hovan, *Earth Planet. Sci. Lett.* **355**, 152–161 (2012).
25. A. V. Fedorov *et al.*, *Science* **312**, 1485–1489 (2006).
26. Y. G. Zhang, M. Pagani, Z. Liu, S. M. Bohaty, R. Deconto, *Philos. Trans. A Math. Phys. Eng. Sci.* **371**, 20130096 (2013).
27. G. Jia, J. Zhang, J. Chen, P. Peng, C. L. Zhang, *Org. Geochem.* **50**, 68–77 (2012).
28. M. H. Conte *et al.*, *Geochim. Geophys. Geosyst.* **7**, Q02005 (2006).
29. N. Dubois, M. Kienast, C. Normandeau, T. D. Herbert, *Paleoceanography* **24**, PA4207 (2009).
30. Z. Liu, T. D. Herbert, *Nature* **427**, 720–723 (2004).

ACKNOWLEDGMENTS

We thank all authors who made their published data available to the public. We thank a number of people for helpful discussions and for challenging us to think about the data in critical ways. These people include P. Dekens, A. Paytan, P. Polissar, R. Pancost, J. Tierney, J. Zachos, and two anonymous reviewers. A.C.R. thanks NSF for funding (OCE-1204254). Thanks to go the Integrated Ocean Drilling Program for their role in obtaining deep sea sediments for Pliocene research.

18 June 2014; accepted 20 October 2014
10.1126/science.1257618

PRESIDENTIAL ADDRESS

Meeting global challenges: Discovery and innovation through convergence

Integrate biology, physics, engineering, and social science to innovate

By Phillip A. Sharp

Our awareness of the global nature of major problems facing our planet is relatively new and demands global responses for which neither the scientific community nor the general public is well prepared. To meet such global challenges requires the engagement of people and their leaders from diverse cultures and experiences. While many sectors of society must become involved, the scientific community has a special role in preparing for these challenges. It is impossible to consider here all of the roles of scientists and engineers in this transformation, whether advancing knowledge of nature, translating new insights into innovations, or educating future generations. But few would disagree that in the long term, discovery and innovation are central to effectively meeting these challenges. Yet it is often difficult to link discovery and innovation to their impact because of the years of development required before a discovery matures to a level that can be adopted on a global scale. I highlight below how some organizations are planning to accelerate the transition from discovery to innovation to address some of the great challenges facing society. As an illustration, I discuss the history of the transition from discovery to innovation at the molecular level in life sciences. At the end, I comment on how further convergence of physical, mathematical, engineering, and social sciences with life sciences will accelerate innovation.

The world will be considerably changed by mid-century, but in ways not yet fully clear. Within the lifetime of our children and grandchildren, Earth will have around 9 bil-

lion inhabitants, and each person will need to be fed from a square of arable land about 130 meters on each side (1). Inequities in standards of living between developed and many underdeveloped countries will continue to diminish as the result of modern trade policies and technology, increasing demand for food, energy, and better health care. Increasing connections across the global economy and the expansion of knowledge capital are driving a wave of global entrepreneurs, with emerging nations like India and China showing how innovation-based growth can enable the movement of hundreds of millions

Many view the global challenges facing us as products of past advancements in science.

of people into the global middle class. But as the world is calling for more consumption, we are facing global warming, with increasing accumulation of heat-retaining gases and further stress on environments.

DISCOVERY AND TECHNOLOGY, ENTREPRENEURSHIP, AND INNOVATION Society probably has never been more uncertain about the prospect of a better future. While scientific discovery and technological innovation have enabled innumerable advances, many view the global challenges facing us as products of past advancements in science. It is true that scientific advances and the innovations and corresponding economic growth they have generated are contributors to the global climate challenge we must now overcome. This climate change is connected to, and can increase, the challenges of poverty and disease. In spite of these concerns, innovation-based growth that will enable the movement of hundreds of millions into the global middle class is a given with which we must wrestle. These facts have led to some skepticism in the developed world about whether continued advancement of technology will contribute to a better future.

I believe that some of the concerns about applications of advances in life sciences, such as the adoption of genetically modified organisms (GMOs) and other new technologies, have their source in this skepticism. But I am more convinced than ever that the only avenue to a better future is continued advancements of science that are wisely applied to society. Science-based innovation is tied to the problem, but it is also central to the solution.

Discovery and innovation are means by which science can affect society. But it is important to recognize that innovation is not solely the discovery of new knowledge or the invention of new materials, processes, or devices. The National Innovation Initiative that led to the America Competes Act has a useful definition: Innovation is

the “intersection of discovery, invention and insight leading to the creation of social and economic value.” The connection between discovery and economic growth has never been more apparent. It is widely accepted that innovation is at the heart of economic growth, accounting for approximately half of its expansion over the past 50 years (2). This relationship drives much of the public interest in funding science and the education of students in many nations, which increases the capacity to solve global problems.

The “classical” view in the process of translating science and technology for society is that scientists “discover,” engineers “invent,” and entrepreneurs “innovate.” In the past, scientists viewed these three stages as belonging to properly separated worlds. Vannevar Bush’s 1945 treatise *Science: The Endless Frontier*, which led to the creation of our modern research universities, argued that basic research was the “pacemaker” of technological advance, and therefore investment in research would inevitably yield innovation.

True enough, but to be efficient, the process requires great attention and nurturing. Historically, many universities have had faculties of scientists and engineers with

Phillip A. Sharp is Institute Professor and a faculty member of the Koch Institute for Integrative Cancer Research and the Department of Biology at the Massachusetts Institute of Technology, Cambridge, MA. He was president of AAAS from February 2013 to February 2014. This article is based on the Presidential Address he delivered at the AAAS meeting in Chicago, Illinois, on 13 February 2014.

Cluster of high-tech companies near MIT

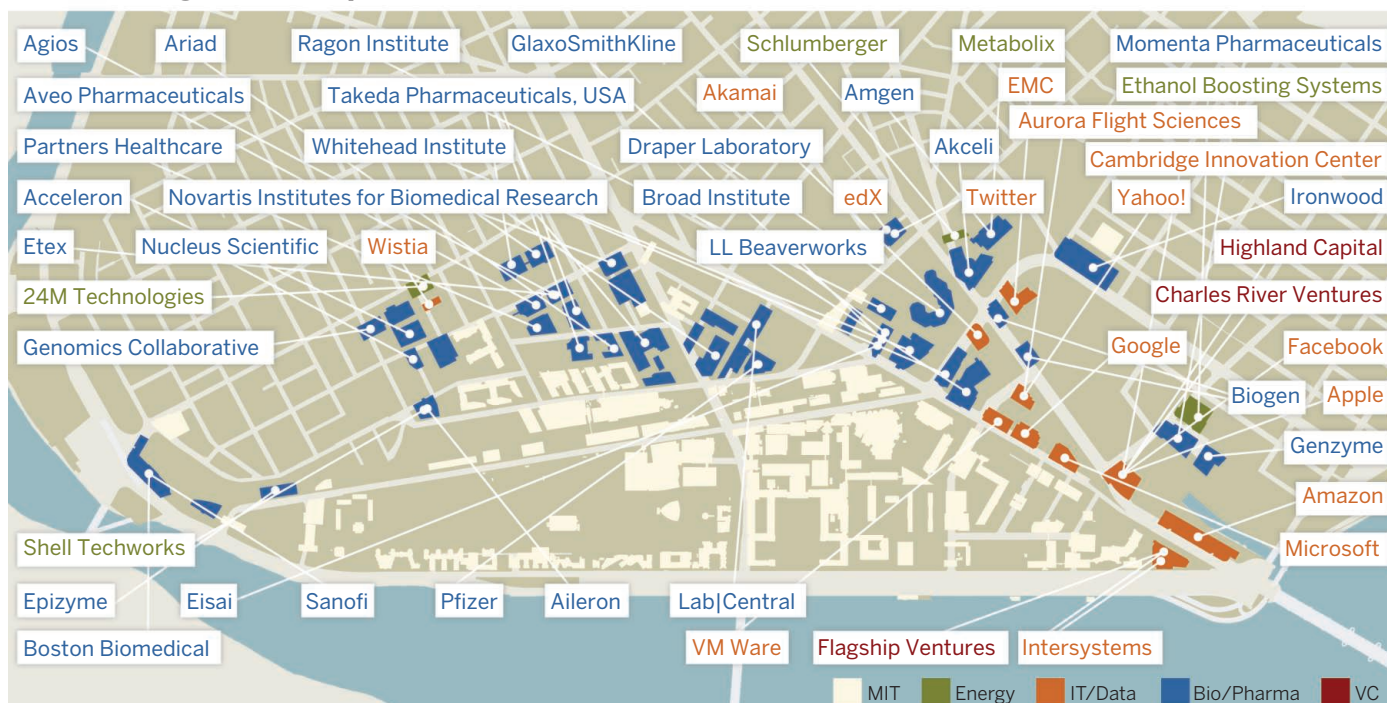


Fig. 1. Cluster of high-tech and related organizations on the boundaries of MIT (source, MIT).

the objective of integrating discovery and invention and educating students in both activities. However, the presence of entrepreneurs on many campuses and the education of students in this subject are recent developments. For example, Ed Roberts of the Massachusetts Institute of Technology (MIT) notes that historically, a third of all MIT alumni have started companies over their 30- to 40-year careers (3). The surprising change in the past decade is that now a third of MIT alumni start companies within 10 years of leaving the campus. Recent graduates of other universities both here and abroad are also engaging in such entrepreneurial activities. In many cases, these startup companies integrate skills that accelerate innovation by combining discovery, invention, and entrepreneurship into a team. Recently, Rafael Reif, president of MIT, suggested an educational need to expand these experiences from alumni to students in science and engineering. This interest in integrating entrepreneurship with training in technology further highlights the relationship between discovery and the economy and the willingness of many public and private research institutes to contribute to economic growth. If discovery is to come to the aid of our great global challenges in climate change, poverty, and disease, we have no choice but to become much better at linking discovery, innovation, and entrepreneurship.

Universities and research institutions are engines of innovation because they are the

major source of discovery, new technology, and scientifically trained people. Technology companies arise on the boundaries of universities for many reasons: Translation of the science is accelerated by the recruitment of recently trained personnel and by consultation with academic scientists involved in discovery and invention; the literal proximity of basic and applied scientists with entrepreneurs fosters conversations and collaborations, accelerating the translation process. This is plainly illustrated in a schematic of the area around MIT in Cambridge, Massachusetts, called the Kendall Square Cluster (Fig. 1). The buildings shown in yellow are on the MIT campus along the Charles River, and around MIT are a large number of high-tech companies. Every blue box is a biopharma company, green is energy, orange is information technology/data, and red is venture capital. Similar clusters are found around campuses in California, Ohio, and many other locations. This immediate proximity of research institutions, high-tech companies, and venture capital highlights the fact that even in this age of the Internet and rapid transport, local interactions are still vital. Leaders across the world recognize this and are establishing research institutes to stimulate local innovation.

LIFE SCIENCES REVOLUTIONS

The history of advances in life sciences at the molecular level and the resulting innovation provides an excellent illustration of discov-

ery and innovation. This history begins in 1953, when Watson and Crick announced the structure of DNA and deduced how genetic information is transmitted when cells divide. This single event, which extended Darwin's theory of evolution and Mendel's discovery of the transmission of genes, took life sciences into a new realm. Just as Newton's principles were the first general statement of the physical mechanistic laws of nature, the discovery of the structure of DNA was the first mechanistic explanation of inheritance in terms of physical laws. The importance of this analogy is that Newton's principles appeared some 200 years before Watson and Crick. Much of the technology of our contemporary economy is built on the laws of Newton. In contrast, life science at the molecular level is very new and will take centuries to mature as an economic force in society.

After the discovery of the structure of DNA, the next 10 years of molecular biology were highlighted by the research of the great French biologists Jacob and Monod, who discovered the steps in the flow of information from DNA to proteins through the intermediate of RNA (Fig. 2). This discovery, along with the elucidation of the genetic code, established how information in DNA is transferred within the cell to synthesize cellular proteins and thus other components.

Another decade passed, during which scientists in academic institutions around the world, motivated by curiosity about the

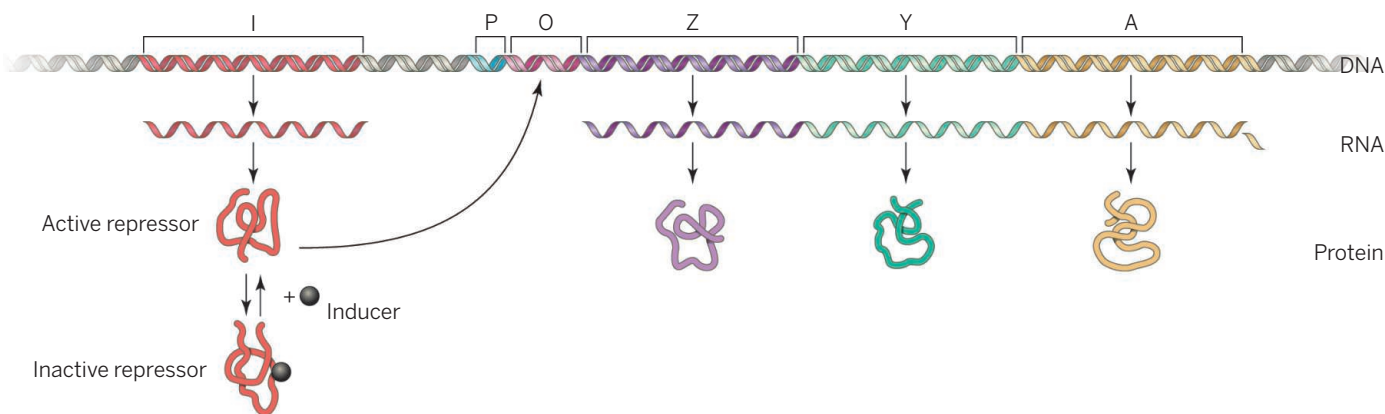


Fig. 2. The original operon model of Jacob and Monod, as proposed for the regulation of the *lac* genes of *E. coli* in 1961 [modified from (4)].

secrets of the gene, investigated biology at the molecular level. This produced three advances in the mid-1970s that changed society: recombinant DNA, DNA sequencing, and chemical synthesis of DNA. In theory and then practice, these discoveries empowered scientists to use all of the complexities of billions of years of evolution to innovate in the creation of new genes and organisms. In the mid-1970s, for the first time in history, life sciences became a synthetic science, much as chemistry had more than a century earlier. Biotechnology, as an innovative industry, arose at this time to translate the new science into products for meeting global needs. The first of these innovations was in health care, where replacement of animal insulin with human insulin benefited diabetics. This was followed by new vaccines, new types of treatments for previously untreatable diseases, and even control of the progression of AIDS by combinations of drugs. It was clear at the earliest stages of biotechnology that it would also contribute to providing new sustainable food sources, energy sources, and materials.

The initial appearance of biotechnology in the late 1970s and early 1980s signaled the transition from the first revolution in life sciences, the discovery of the structure of DNA, to the second revolution, the sequencing of the human genome (Fig. 3). This initiative began in the late 1980s and early 1990s and was completed in the early 2000s, with the draft sequence in 2001 and the complete sequence in 2003. There have been many innovations from the human genome initiative; for example, insights into the genetic causes of cancer and other chronic diseases. However, an often overlooked byproduct of this effort was the development of inexpensive and rapid technology to sequence DNA. With such inexpensive sequencing, we will shortly have in our computers the sequences of billions of genes from most species on our planet,

from the plant, microbial, and animal kingdoms. These genes contain a record of 4 billion years of evolution from shortly after Earth's surface cooled to current times. Some of these genes allow organisms to metabolize an extensive set of compounds for energy, others render cells resistant to pathogens and toxic compounds, and others mediate communication with other organisms to live in a symbiotic relationship. When you picture this vast storehouse of diverse genes with novel functions as a resource for further synthesis of new organisms with innovative capacities, you get a glimpse of society's future.

THE NEXT REVOLUTION: CONVERGENCE
What is the next revolution in life sciences? Many think that an important part of the blueprint for future innovations is the integration, or convergence, of other disciplines with life science. I was fortunate to co-chair,

Note the two parts of this statement. First it acknowledges that recent advances in life sciences have prepared the stage for rapid innovation. In contrast to biologists leading engineers in their research and innovation with genes, biologists “gave” the “gene,” thus empowering engineers in life sciences. The statement also indicates that it is important that biologists and engineers integrate, and together they will create the future. Thus, convergence encompasses engineers and physical scientists applying their knowledge and tools to problems in life science in their own professional domains. An example would be developing new statistics, thermodynamics, and chemistry to explain the origins of life, or developing new computational tools and computer cores to detect signals in vast amounts of clinical data. Convergence is also the collaboration of life scientists with engineers and physical and computational scientists. Hence, the emerging thrust of convergence recognizes the current value and future promise of expanding engagement of these diverse disciplines in life sciences to meet societal challenges.

Convergence is beginning to be recognized in the funding of new U.S. national initiatives, such as in synthetic biology, nanotechnology, and most recently in the Presidential BRAIN Initiative. However, these small but important initiatives are insufficient to capture the promise of convergence. I outline below examples of areas in which larger investment in convergence may have great impact.

Climate change and a future population of 9 billion are a volatile combination for food security. In meeting this challenge, adaptation of plants to a broader range of environments is critical to increase the amount of arable land and distribute production to locations where it is needed to reduce hunger. This should be possible with modern genetic technology and the consideration of agricultural environments

Physicists gave engineers the electron, and they created the IT revolution. Biologists gave engineers the gene, and together they will create the future.

with Tom Connelly of DuPont Corporation, a 2009 National Academy of Sciences report entitled *A New Biology for the 21st Century*. The report emphasized the importance of the convergence of life sciences with engineering, physical, mathematical, and computational sciences in meeting future challenges.

Susan Hockfield, MIT president emeritus, relates this revolution to a historical advance: “Physicists gave engineers the electron, and they created the IT revolution. Biologists gave engineers the gene, and together they will create the future.”

as an ecosystem. Accomplishing this calls us to face the question of the adoption of GMO technology. This technology has proven itself safe and effective in increasing the productivity of agriculture over the past decades. It has now spread beyond a small number of companies and is being developed to improve the nutritional content of plants and protect against rapidly spreading pathogens destroying local crops. In a 2013 article (6), *Technology Review* posed the question, “Can we meet the global food challenge without widespread adoption of GMO plants?” The answer, in my opinion, is “no.”

An important opportunity for meeting the energy challenge of replacing fossil hydrocarbons with a sustainable source is

then expand ecosystem engineering to reduce further damage and restore ecosystem functions. Part of this promise is the application of DNA sequencing to analyze the range of microorganisms in healthy and damaged environments. These organisms are the foundation of the food chain, and shifts in their population will eventually drive change through the surrounding environment. Another part is the development of imaging and detection systems that will report in real time about changes in an ecosystem. In many cases, it will be as easy to collect a lot of information in parallel about an environment as making a measurement of a few constituents. Over time, synthesis of this information can provide profound insights that are actionable.

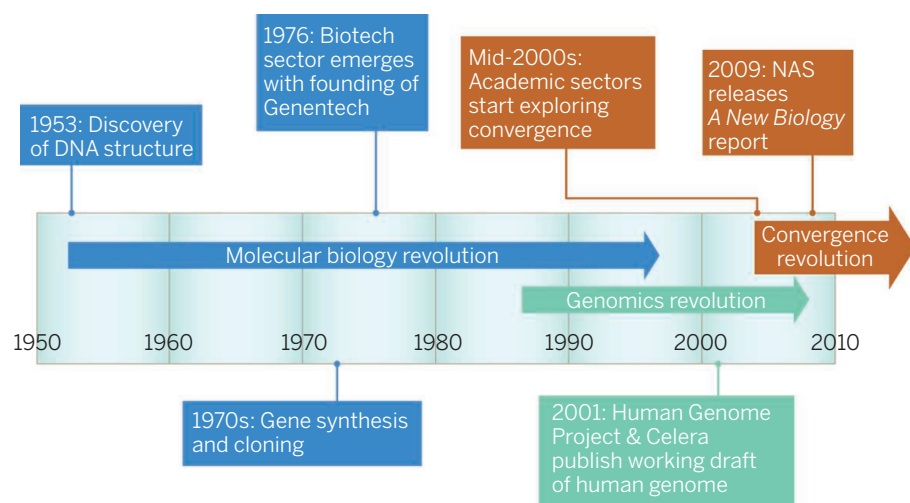


Fig. 3. Timeline: The three life sciences revolutions, leading to convergence [source (5)].

the production of transportation fuels from biomass. As was obvious from the beginning of discussions of alternative energy sources, corn grain, which is used in animal and human nutrition and thus expensive, cannot in the long term be the biomass used in this process. To make a real impact on the energy challenge, many integrated innovative systems need to be developed in which plants are designed specifically to be used as biomass, microorganisms are designed for conversion of this biomass to hydrocarbon-type compounds, and manufacturing processes are engineered for efficient production and distribution. The engineering of integrated synthetic biology and manufacturing processes is rapidly advancing to make this a reality. For example, bio-based polymers are beginning to replace hydrocarbon-based polymers in many consumer products (7).

Convergence will also help meet our environmental challenges. Convergence strategies could help us develop better monitoring for changes in ecosystems and

Increasing the quality of health care in a cost-effective fashion is dependent upon using information technology and advances in life sciences and medicine to assess, inform, and modify lifestyles and better treat individuals. The development of biotechnology is the first step along this path. Merging media, personal communication tools, and the application of medical data to the point of care of individual patients are other important advances. Innovation along these lines will require a broad convergence of social, mathematical, physical, and engineering sciences with the medical, regulatory, and financial communities. For example, if we could use modern genomic technology at the stage of diagnosis to distinguish cancers that will progress to lethality from those that are indolent, it would both improve cancer care and reduce costs.

The promise of convergence is dependent upon continued investment in basic science and translation of the resulting discoveries into innovations. This will not

happen without expansion of current public/private partnerships, with the public sector funding more of the basic research and the private sector funding more of the translational activities. Increase in investment by public agencies needs to happen now. Some of this investment should focus on training the next generation of scientists and engineers. In furthering convergence, this generation of students and fellows would benefit from enhanced communication and collaboration with one another during training in multidisciplinary environments. Another issue that needs to be considered is the limited research funds for engineering and computational scientists to investigate life sciences outside of National Institutes of Health (NIH) support, as many scientists from these domains feel unappreciated by NIH's application and review processes. Government investments in research in many countries, including the United States, have fallen in purchasing power over the past decade. This will result in a slowing of growth in innovation and the economy in the future.

To meet oncoming global challenges, we will need to better link discovery, innovation, and entrepreneurship. In the past, we simply assumed that they would converge as a matter of course, but given their importance, the linkages should be considered more closely. In parallel with strengthening these linkages, we will need stronger cross-discipline integration via the convergence model, joining the life, engineering, social, and physical sciences into common pursuits. This means convergence on both fronts, across the sciences as well as between science and implementation. I end with the following question: “Can we meet future global challenges without such convergence?” I think the answer is “no.”

REFERENCES

1. R. J. Cicerone, Speech at the Fourth Annual Meeting of the STS Forum, Kyoto, Japan (2007); <http://files.stsforum.org/Previous/2007/Speeches/PL105-Cicerone.pdf>.
2. R. M. Solow, The last 50 years in growth theory and the next 10. *Oxford Rev. Econ. Pol.* **23**, 3–14 (2007).
3. Edward B. Roberts, Charles E. Eesley, *Entrepreneurial Impact: The Role of MIT – An Updated Report* (Foundations and Trends in Entrepreneurship, vol. 7, nos. 1–2, 2011), pp. 1–149.
4. G. S. Stent, *Molecular Genetics* (W. H. Freeman, San Francisco, 1971).
5. *The Third Revolution: The Convergence of the Life Sciences, Physical Sciences and Engineering* (MIT White Paper, 2011); <http://dc.mit.edu/sites/dc.mit.edu/files/MIT%20White%20Paper%20on%20Convergence.pdf>.
6. D. Rotman, Why we will need genetically modified foods. *MIT Technol. Rev.*, December 2013; www.technologyreview.com/featuredstory/522596/why-we-will-need-genetically-modified-foods/.
7. M. M. Bomgardner, Biobased polymers. *Chem. Eng. News* **92**, 10–14 (2014); <http://cen.acs.org/articles/92/i43/Biobased-Polymers.html>.



Trellis, the scientific community's new communication platform, will debut in 2015.

Plan to transform AAAS moves full steam ahead

Through a long-range, strategic initiative, AAAS is becoming a more member-focused, digitally oriented organization.

By **Phillip A. Sharp¹** and **Alan I. Leshner²**

Every strong organization should sit back every 10 years and reflect on where it is, where it's going, and how it can best serve its constituents in the future. The world is changing, and as "the voice of science," we at AAAS want to make sure that the organization is maximizing its usefulness to the scientific community and the broader society.

AAAS is in excellent shape from every perspective, making this an ideal time to look forward to the next decade and beyond. Over the past 3 years, we have surveyed our members, clients, readers, and others, and it has become clear that the next iteration of AAAS must do two things: It must adopt a "digital first" mindset to become a multimedia, multiplatform science communication enterprise, rather than a print-centric publisher, and it must listen to its members and undertake activities that better serve their needs.

The AAAS Transformation Initiative, an-

nounced last spring, has completed its initial planning goals, and we are now moving ahead with strong momentum. Further, the AAAS Board has put funding in place to enable this transformation to be carried out over the next 5 years, and results will start becoming outwardly visible within months.

The new, online-only, open-access journal *Science Advances* will debut in February, significantly increasing the volume of high-quality research published by AAAS. Spanning science, technology, engineering, mathematics, and the social sciences, the new digital publication will be a primary focus for new publisher Kent Anderson, who joined AAAS last month, and Editor-in-Chief Marcia McNutt.

All of the *Science* journals are also undergoing a complete digital reorganization,

under the direction of Robert Covey, in the newly created position of digital media officer, and McNutt. The process involves a far-reaching redesign of the *Science* websites and other changes to ensure that all content is created with the Web foremost in mind.

AAAS is also now beta-testing a new science communication platform, Trellis, which will become available to the scientific community within the coming year. This novel online networking platform will better enable participants to connect across disciplines,

affiliations, and geographies to communicate and work together more effectively. Areas of activity will include discipline-crossing topics such as food, water, and energy; "meta-issues" affecting the lives of scientists more broadly; or

newly emerging areas of research.

On the membership front, work is under way to expand AAAS membership by threefold, starting with scientists in both the academic and private sectors and eventually reaching out to the general science-interested public. Under the direction of a Chief Membership Officer to be hired in the coming months, the association is mar-



Phillip A. Sharp



Alan I. Leshner

shaling its considerable resources in areas where members have told us they would like more support and involvement, including advocacy, networking, career support, and volunteering.

A key part of AAAS's mission involves advocating on Capitol Hill and at the state level for sustainable funding for R&D and the responsible use of science in policy. Staff are developing mechanisms to give members many more opportunities to join AAAS in these efforts to speak up for science. For example, a members-only website, to be launched in 2015, will allow members to advocate for research funding and policies that impact the research community. It will provide detailed analyses of S&T legislation, legislative alerts about pending votes or amendments of concern, and mechanisms for contacting policy-makers.

Drawing from expertise across the Association, AAAS is ramping up and better integrating its offerings for scientists at all stages of their careers. The demand for these resources is high: A free AAAS webinar called "Thinking Outside the Lab" drew over 6000 registrants, and the career planning tool called myIDP has 68,000 registered users. Future offerings will include more career-related webinars, a specialized career portal, and networking opportunities for members at local meetings as well as the AAAS Annual Meeting.

This is a time of great creativity and problem-solving at AAAS. It is also the beginning of a fundamental culture shift within the organization, to wholeheartedly embrace a digital-first, member-focused approach. AAAS culture must also become more amenable to innovation, which we are encouraging by setting up a small office to explore and develop new business concepts and other kinds of partnerships.

The Transformation Initiative and the institutional culture change that drives it will be greatly facilitated by the arrival of Rush D. Holt, Ph.D., as AAAS's new chief executive officer. Holt, who was a practicing research physicist and teacher before serving eight terms in the U.S. House of Representatives, will join AAAS this coming February. He will be the ideal next staff leader for the association because of his broad understanding of science and of the issues relating science and the rest of society. ■

¹Chair of the AAAS Board; Institute Professor, Massachusetts Institute of Technology; and Faculty Member of the Koch Institute for Integrative Cancer Research and Department of Biology. ²AAAS Chief Executive Officer and Executive Publisher, Science.

A training ground for innovation

Young entrepreneurs honed their ideas for serving developing societies, at the GIST Tech-I Competition administered by AAAS.

By **Michaela Jarvis**,
in Marrakech, Morocco

Edmund Aienebyona's idea could reduce maternal and infant mortality. Behaylu Abreha's could support the production of animal feed using less land and less water. Felipe Varea's could provide a way to easily and cheaply detect outbreaks of poisonous "red tide" algae. All three of these science- and technology-based innovations could provide jobs and development opportunities in the young entrepreneurs' home countries of Uganda, Ethiopia, and Chile, while improving the lives of people in those countries and beyond.

Yet, each of the ideas needs a support network and funding to become a reality.

Cultivating that type of support network was the impetus behind this year's Global Innovation through Science and Technology (GIST) Tech-I Competition, held 18 to 21 November in Marrakech, Morocco. Initially developed by the U.S. Department of State and organized and run by AAAS, the competition brought together 30 young en-

trepreneurs from 23 developing countries. Eighteen mentors—recruited by AAAS from the front lines of industry, governmental and nongovernmental funding agencies, and science and technology advancement organizations—provided a much-needed forum and training ground for the young innovators.

"In developing countries, most innovative minds are silenced. There's no platform to carry your voice," said Zambian entrepreneur Muchu Kaingu, whose mobile application project aims to "sort out chaos in our communities" by organizing and automating the business activities of merchants, from inventory to pricing to profits. "The human element that the mentors provide, someone to say if you're on the right track, is really important."

"You always love your ideas; you're passionate about them," said Alim Khamitov, who is developing a remotely controlled system to cut down on apartment burglaries in his native Kazakhstan, "so you need input from others. I come here for the experience, to take advantage of the expertise of people in industry. I like the environment,



Cynthia Ndubuisi of Nigeria earned second place in the GIST Tech-I Competition's idea category.

PHOTO: AAAS



2014 GIST Tech-I finalists and mentors

the ecosystem. You can't feel the same thing in Kazakhstan, not even with your team."

The GIST competition began in 2011 as one of the initiatives implemented by the U.S. Department of State to support innovation in the developing world, at the direction of President Barack Obama. Since its inception, participants, who apply for the program and are invited to be finalists through an extremely competitive multi-step selection process, have generated \$80 million in revenue by commercializing their innovations, according to U.S. State Department calculations.

"Scientists and engineers have long been seen as speaking a universal language," said AAAS Chief International Officer Vaughan Turekian, "but globally, more and more entrepreneurs are tapping into science and technology to promote innovation and economic growth."

This year's GIST Tech-I Competition, which was orchestrated by Jennifer Roderick and Cristine Geers of the AAAS International Office, was held at the 5th Global Entrepreneurship Summit in Marrakech, where Vice President Joseph R. Biden made a speech at the opening ceremony about fostering entrepreneurship to drive growth and create jobs.

"When I travel [in Africa and the Middle East] and the entire developing world," Biden said, "I see young people with limitless promise to make not only their countries but the whole world better."

"Fostering entrepreneurship is not just about crafting the right economic policy, or developing the best educational curri-

cula. It's about creating an entire climate in which innovation and ideas flourish."

In 4 days of training and competition, this year's 30 young entrepreneurs worked through exercises designed to help them define and validate their ideas, target their markets, and "pitch" their business propositions. Itzam De Gortari, CEO for a business acceleration organization that identifies and cultivates promising Mexican tech startups, led sessions emphasizing the entrepreneurs' need to focus on the business realities of bringing an idea into the market. "There is no innovation without finding the proper need," he said. "Most startups fail because they didn't develop their markets, not because they didn't develop their products."

Questioning the assumptions the GIST participants had about their innovations caused them to adjust their approaches and even their products, some of them significantly.

"One thing I really enjoyed was when we had to draft the persona of our customer," said Nigerian Cynthia Ndubuisi—whose project brings waste cassava peels to farmers for healthy livestock feed—referring to an important part of the training that focused on defining the customer. "That really helped, because in just doing that, it simplified things so that I can speak to any investor about my business. It made me really think about what my customer wants, and how to get to them."

Mentor Matthew Graham Dyor, CEO at Payboard and former managing director at the Microsoft Accelerator powered by Techstars, called his involvement in GIST Tech-I

an opportunity to give back as "part of the code of entrepreneurship."

"We want to help these young entrepreneurs have a better, more realistic understanding of what they've got going, so that they can translate a passion into an international business that can get customers and investors," Dyor said.

In addition to the support network, the mentoring, the refined perspective on their businesses, and the camaraderie with peers from around the world, the innovators had a chance to win funding. Thirteen winners took home a total of \$68,500 in cash prizes awarded on the quality and presentation of their business propositions, and a number of the contestants said that simply having participated in a program supported by the U.S. Department of State and AAAS will create more opportunities. At least one competitor, Ndubuisi, was approached in Morocco by a representative of the U.S. Agency for International Development, which provides economic assistance in support of U.S. foreign policy objectives.

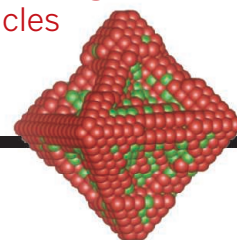
Whatever the exact benefits provided by the program, both young entrepreneurs and mentors expressed commitment to maintain the important network they had established in Morocco, and the young entrepreneurs pledged to bring what they had learned back to their home countries.

"I can serve as a mirror for someone else who has an idea," said Pavel Santos, of the Dominican Republic, who is working on a computer platform that assesses learning style to customize online education, "not to put that idea away, but to make it a reality." ■

RESEARCH

Platinum-rich edges start the growth of metal-alloy nanoparticles

Gan et al., p. 1502



IN SCIENCE JOURNALS

Edited by **Melissa McCartney** and **Margaret Moerchen**



CONSERVATION

Success for Europe's large carnivores?

Despite pessimistic forecasts, Europe's large carnivores are making a comeback. Chapron *et al.* report that sustainable populations of brown bear, Eurasian lynx, gray wolf, and wolverine persist in one-third of mainland Europe. Moreover, many individuals and populations are surviving and increasing outside protected areas set aside for wildlife conservation. Coexistence alongside humans has become possible, argue the authors, because of improved public opinion and protective legislation. — AMS

Science, this issue p. 1517

Education efforts lead to an increase in European brown bear populations.

PHOTOCHEMISTRY

Using ozone below may conserve it above

The accumulation of laughing gas in the atmosphere isn't a laughing matter: Nitrous oxide (N_2O) is a powerful greenhouse gas and a depleter of ozone. The manufacture of nylon releases substantial N_2O as a byproduct during preparation of the precursor adipic acid. Hwang and Sagadevan now demonstrate an alternate route to adipic acid that involves treating cyclohexane with ozone under concurrent ultraviolet irradiation, generating no N_2O .

Thus, ironically, the application of ozone as a chemical reagent could ultimately help conserve its concentration in the atmosphere. — JSY

Science, this issue p. 1495

CANCER THERAPY

Drug resistance, up close and personal

Cancer therapies that target specific genetic mutations driving tumor growth have shown promising results in patients; however, the response is often short-lived because the tumors

acquire new mutations that render them resistant to these therapies. Complicating matters, the mechanism of resistance can vary from patient to patient. To identify drugs most likely to be effective against resistant tumors, Crystal *et al.* established cell lines from the tumors of individual patients after resistance occurred and performed a drug screen and genetic analysis on the cultured cells. This strategy successfully identified drug combinations that halted the growth of resistant tumor cells both in culture and in mice. In the future, pharmacological profiling of

patient-derived cells could be an efficient way to direct therapeutic choices for individual cancer patients. — PAK

Science, this issue p. 1480

PALEOCEANOGRAPHY

A brief hiccup in deep ocean circulation

During the last interglacial period, Antarctic Bottom Water (AABW) formation slowed markedly. This densest ocean water sinks to the bottom of the sea, and its production helps to flush the oceans and eventually to recycle the carbon dioxide (CO_2) that forms from sinking organic matter back into the atmosphere. If the AABW production rate decreases, then CO_2 accumulates at depth, potentially causing a corresponding drop in atmospheric CO_2 concentration. Hayes *et al.* found evidence, in the form of a uranium spike, in deep sea sediments that such a slowdown in AABW formation occurred ~127,000 years ago, which may have caused the atmospheric CO_2 minimum observed at that time. — HJS

Science, this issue p. 1514

IMMUNE TOLERANCE

For the immune system, silence is golden

For the immune system, balance is key. Immune cells must learn to eliminate invading pathogens but tolerate self. A cell type called regulatory T cells (T_{regs}) help to maintain this balance, but how they do so, particularly in humans, is unclear. Maeda *et al.* now report that T_{regs} "silence" T cells with modest reactivity to

self. After culture with T_{regs}, the silenced T cells proliferated very little and produced almost no cytokines in response to antigen. The authors then examined T cells from healthy donors and from people with an autoimmune disease. Only healthy donors harbored silenced T cells, suggesting that if silencing goes awry, autoimmunity may result. — KLM

Science, this issue p. 1536

EARTH MAGNETOSPHERE

How trans-polar arcs transpire above

Auroral arcs within the polar cap are a visual marvel, and they may also indicate trapped energetic plasma in Earth's magnetosphere. Fear *et al.* combined simultaneous observations of both the aurora and signatures of the trapped plasma in Earth's magnetotail to demonstrate one recent instance of this phenomenon. Some researchers have proposed that flux generated by magnetic reconnection might get trapped in the magnetotail lobe, but the standard magnetosphere model does not predict it. This study confirms the idea by taking advantage of a period when the interplanetary magnetic field points northward, a state not yet well understood. — MMM

Science, this issue p. 1506



Aurora displays such as these over Alaska reflect plasma processes in Earth's magnetosphere

PROTEIN DESIGN

Building transmembrane zinc transporters

The ability to design proteins gives insight into the relation between a protein's fold and its function and also provides a path to custom proteins for bioengineering applications. Impressive strides have been made in the design of soluble proteins, but designing membrane proteins remains a challenge. Joh *et al.* achieve a milestone by designing a transmembrane Zn²⁺ transporter (see the Perspective by Lupas). The protein comprises four helices: Two tightly interacting pairs form a weaker interface that facilitates the transport of Zn²⁺ with concomitant reverse transport of protons. — VV

Science, this issue p. 1520; see also p. 1455

IMAGING

Look, pathologists! No lens!

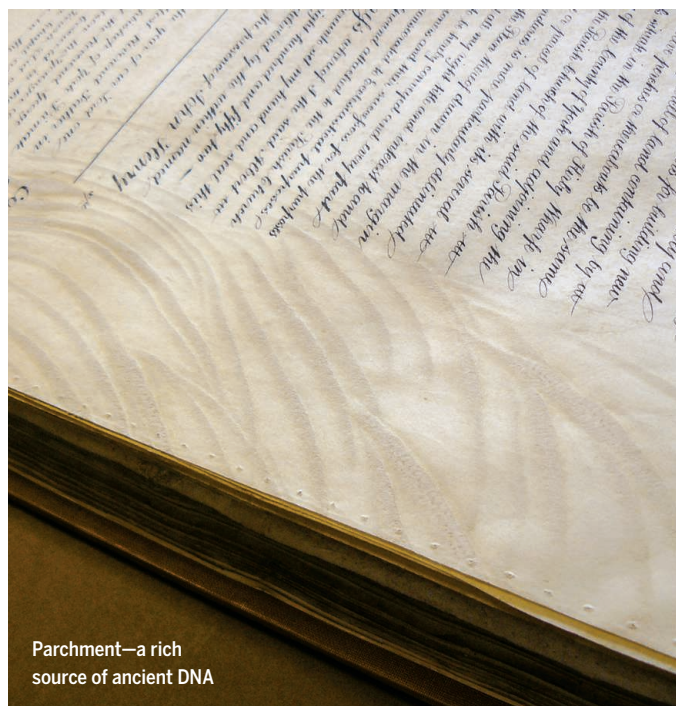
Imaging entire human tissues with a light microscope requires stitching 500+ images together — a digitization process largely confined to advanced laboratories. Greenbaum *et al.* developed a lens-free microscope based on low-cost holographic technology, which enables fields of view a hundredfold larger than conventional technology allows.

This tool employs a small chip and allows for three-dimensional focusing through thick tissue samples. The team imaged human cancer cells, abnormal cells in Pap smears, and sickle cells in whole-blood smears with sufficient resolution and contrast for clinical diagnosis. With its high resolution and speedy readout, the new platform could benefit pathology labs worldwide. — MLF

Sci. Transl. Med. **6**, 267ra175 (2014).

IN OTHER JOURNALS

Edited by **Kristen Mueller** and **Jesse Smith**



Parchment—a rich source of ancient DNA

ANCIENT DNA

Document DNA shows agriculture's course

Finding a good source of ancient DNA can be tough, due to weathering and bacterial contamination. But parchment—made from livestock hides—offers an abundant, well-preserved, and often dated source of DNA, report Teasdale *et al.* The researchers worked with a 2-cm-square piece, but have so refined their sequencing technique that it only requires a tiny sliver of parchment; they hope eventually to do nondestructive testing. These data, they note, can reveal the history of agriculture over the past 700 years. — EP

Philos. Trans. R. Soc. London Ser. B, 10.1098/rstb.2013.0379(2014).

NETWORK BIOLOGY

Meeting the demands of a complex network

Cells face intense metabolic demands. Meeting these demands requires genes to interact in complex networks. But what happens to these networks when the participating genes acquire mutations? To find out, Bajić *et al.* computationally mapped how genes that regulate cellular metabolism interact in yeast lacking specific metabolic enzymes or in yeast that had accumulated

neutral mutations (mutations that did not affect their overall fitness). Their model predicted that deleting specific genes would lead to alternative enzymatic reactions and rewired signaling pathways, depending on the degree of network connectivity. In the case of neutral mutations, their model suggested that network rewiring would occur along with a loss of plasticity. Experimental data supported these predictions. — LMZ

Genome Biol. Evol. 10.1093/gbe/evu255 (2014).

ALSO IN SCIENCE JOURNALS

Edited by Melissa McCartney and Margaret Moerchen

PROTEIN EVOLUTION

Controlling the state of dynamic proteins

Small molecules that change the oligomeric state of proteins by binding to a site distant from the interface are called allosteric. They often act by taking advantage of intrinsic protein dynamics and stabilizing a particular conformation of the protein. Perica *et al.* show that mutations can similarly act at a distance to change protein conformation. They identified 11 mutations in an RNA-binding protein that determine whether it is stable as a dimer or a tetramer. Examination of ancestral sequences showed that the allosteric mutations are part of a downhill adaptation to lower environmental temperatures. This mechanism for modulating the oligomeric state is probably common in evolution. — VV

Science, this issue p. 1479

CANCER EPIGENETICS

Modeling brain cancer from stem to stern

Diffuse intrinsic pontine gliomas (DIPGs) are aggressive brain tumors primarily affecting children. Because the tumors arise in the brainstem, which controls many vital functions, they cannot be surgically excised and are often fatal. To study the pathogenesis of DIPGs—in particular, the role of a histone H3.3 mutation that occurs in 70% of cases—Funato *et al.* developed a new tumor model (see the Perspective by Becher and Wechsler-Reya). They first directed the differentiation of embryonic stem cells into neural progenitor cells. They then introduced a specific combination of genes, including the mutant histone gene, and found that this caused the progenitor cells to acquire features characteristic of cancer cells. During this oncogenic transformation, the cells reverted to a more

primitive differentiation state and displayed altered histone marks at several key regulatory genes. — PAK

Science, this issue p. 1529;
see also p. 1458

HUMORAL IMMUNITY

Endogenous retroviruses trigger B cells

Scattered across our genome are endogenous retroviruses (ERVs), ancient “footprints” of previous viral infections. Scientists do not fully understand their functions, but Zeng *et al.* now report a role for ERVs in mobilizing a particular type of B cell-driven immune response in mice (T cell-independent, TID), which is usually mounted in response to viral capsids or bacterial polysaccharides (see the Perspective by Grasset and Cerutti). Immunizing mice with a model TID antigen elicited an increase in ERV RNA and DNA in the cytoplasm of B cells. Innate immune receptors that recognize cytoplasmic nucleotides then triggered signaling cascades that resulted in the production of immunoglobulin M. — KLM

Science, this issue p. 1486;
see also p. 1454

ELECTRON TRANSFER

Big impact from a well-placed shake

Since the advent of ultrashort laser pulses, chemists have sought to steer reaction trajectories in real time by setting particular molecular vibrations in motion. Using this approach, Delor *et al.* have demonstrated a markedly clear-cut influence on electron transfer probabilities along the axis of a platinum complex. The complex comprised donor and acceptor fragments—which respectively give and take electrons upon ultraviolet excitation—bridged together by triply bonded carbon

chains linked to the metal center. By selectively stimulating the carbon triple-bond stretch vibration with an infrared pulse, the authors could induce substantial changes in the observed electron transfer pathways between the fragments. — JSY

Science, this issue p. 1492

CATALYSIS

Dispersing catalytic gold as widely as possible

In order to maximize the activity of precious metals in catalysis, it is important to place the metal on some support with a high surface area (such as a zeolite) and to maintain the metal as small clusters or even atoms to expose as much metal as possible. The latter goal is more readily achieved with oxides of reducible metals such as cerium or titanium than with the aluminum and silicon oxides that make up most zeolites and mesoporous oxides. Yang *et al.* show that sodium and potassium can stabilize gold along with hydroxyl and oxo groups to create highly active catalysts for the water-gas shift reaction at low temperatures, a reaction that can be useful in applications such as fuel cells. — PDS

Science, this issue p. 1498

becomes the edges and corners for the particles, and the alloying metals deposit to fill in the facets. — PDS

Science, this issue p. 1502

BIOPHYSICS

Stark influence on reaction rates

Enzymes accelerate chemical processes by coaxing molecules into just the right reactive states. Fried *et al.* now elucidate the way the enzyme ketosteroid isomerase pushes its substrate toward product through exertion of a local electric field (see the Perspective by Hildebrandt). First the authors calibrated the shifts in molecular vibrational frequencies, known as Stark shifts, that fields of varying strength impose on a substrate analog; then they measured the vibrational spectrum of that compound in the enzyme's active site. The experiment uncovered an unusually strong field that the local enzyme structure directed to the precise spot where the substrate would react. — JSY

Science, this issue p. 1510;
see also p. 1456

GENE EXPRESSION

Promoters tune gene expression noise

Although cells in a tissue are genetically identical and appear the same, they often exhibit variability in their patterns of gene expression. Organisms may need this to prepare for exposure to varying environmental stresses. Using the tools of synthetic biology, Jones *et al.* construct a wide range of *E. coli* promoters in which the key molecular parameters (such as protein binding and unbinding rates) are systematically varied and compare the resulting expression noise to parameter-free model predictions. This work demonstrates that

expression noise is a tunable parameter, with different gene-regulatory architectures giving rise to different, but predictable, patterns of expression noise.

— BAP

Science, this issue p. 1533

PROTEIN DESIGN

Designing activity at an interface

Enzymes are proteins that are the workhorses of the cell. Designing enzymes with new functions that are also manifested in living systems could be extremely valuable in bioengineering and synthetic biology applications. However, enzyme design is a challenging task and so far has mainly been restricted to repurposing natural enzymes and to in vitro systems. Song and Tezcan started with a monomeric redox protein and introduced mutations that cause it to assemble into a tetramer with catalytic zinc ions in its interfaces. This protein assembly displayed β -lactamase activity, the primary mechanism of antibiotic resistance, and enabled *E. coli* cells to survive ampicillin treatment. — VV

Science, this issue p. 1525

CLIMATE CHANGE

Can regional climate change be predicted?

Global climate models (GCMs) provide broad-brushstroke projections of future climate. These projections lack the resolution required to understand and respond to regional changes. “Downscaling” methods use GCM results as the starting point to model regional climate change. Hall explains that researchers and planners interested in regional adaptation planning should interpret results from such downscaling with care: Climate warming patterns can often be downscaled with confidence, but changes

in atmospheric circulation are much harder to capture. — JFU

Science, this issue p. 1461

CANCER

Menacing exosomes spread cancer

Exosomes are tiny vesicles released from cells that carry proteins, lipids, and nucleic acids: cargo that can affect the biology of recipient cells. In a Perspective, Anastasiadou and Slack highlight recent studies that reveal how these vesicles act as vehicles to spread cancer. Exosomes that are released by cancer cells harbor oncogenic microRNAs (miRNAs), proteins involved in miRNA biogenesis, and miRNAs that induce inflammatory conditions that support tumor growth and metastasis. Such cancer exosomes cause normal cells to form tumors in animal studies. The findings could guide the development of exosome-based diagnostics and therapies for cancer. — LDC

Science, this issue p. 1459

IMMUNOLOGY

Stopping inflammation after infection

In response to microbes, innate immune cells activate the transcription factor NF- κ B, resulting in pro-inflammatory cytokine release. Once an infection has been resolved, NF- κ B signaling must be inhibited to prevent excessive inflammation and tissue damage. Tanaka *et al.* found that this feedback inhibition requires the chaperone protein HSP70, which enabled the breakdown of the NF- κ B subunit p65 in dendritic cells. HSP70-deficient dendritic cells produced more pro-inflammatory cytokines than did wild-type cells, and HSP70-deficient mice had more sustained inflammatory responses to bacterial infection than did wild-type mice. — JFF

Sci. Signal. **7**, ra119 (2014).

self. After culture with T_{regs}, the silenced T cells proliferated very little and produced almost no cytokines in response to antigen. The authors then examined T cells from healthy donors and from people with an autoimmune disease. Only healthy donors harbored silenced T cells, suggesting that if silencing goes awry, autoimmunity may result. — KLM

Science, this issue p. 1536

EARTH MAGNETOSPHERE

How trans-polar arcs transpire above

Auroral arcs within the polar cap are a visual marvel, and they may also indicate trapped energetic plasma in Earth's magnetosphere. Fear *et al.* combined simultaneous observations of both the aurora and signatures of the trapped plasma in Earth's magnetotail to demonstrate one recent instance of this phenomenon. Some researchers have proposed that flux generated by magnetic reconnection might get trapped in the magnetotail lobe, but the standard magnetosphere model does not predict it. This study confirms the idea by taking advantage of a period when the interplanetary magnetic field points northward, a state not yet well understood. — MMM

Science, this issue p. 1506



Aurora displays such as these over Alaska reflect plasma processes in Earth's magnetosphere

PROTEIN DESIGN

Building transmembrane zinc transporters

The ability to design proteins gives insight into the relation between a protein's fold and its function and also provides a path to custom proteins for bioengineering applications. Impressive strides have been made in the design of soluble proteins, but designing membrane proteins remains a challenge. Joh *et al.* achieve a milestone by designing a transmembrane Zn²⁺ transporter (see the Perspective by Lupas). The protein comprises four helices: Two tightly interacting pairs form a weaker interface that facilitates the transport of Zn²⁺ with concomitant reverse transport of protons. — VV

Science, this issue p. 1520;
see also p. 1455

IMAGING

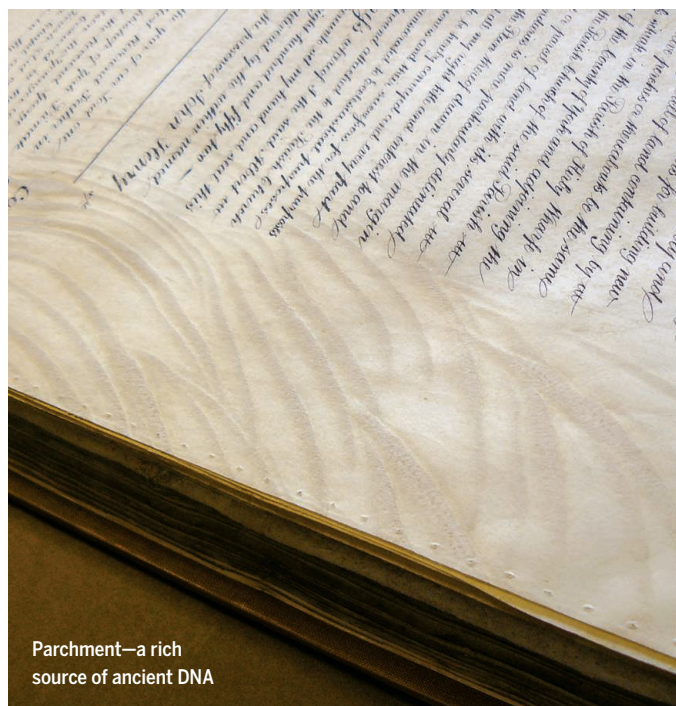
Look, pathologists! No lens!

Imaging entire human tissues with a light microscope requires stitching 500+ images together — a digitization process largely confined to advanced laboratories. Greenbaum *et al.* developed a lens-free microscope based on low-cost holographic technology, which enables fields of view a hundredfold larger than conventional technology allows. This tool employs a small chip and allows for three-dimensional focusing through thick tissue samples. The team imaged human cancer cells, abnormal cells in Pap smears, and sickle cells in whole-blood smears with sufficient resolution and contrast for clinical diagnosis. With its high resolution and speedy readout, the new platform could benefit pathology labs worldwide. — MLF

Sci. Transl. Med. **6**, 267ra175 (2014).

IN OTHER JOURNALS

Edited by **Kristen Mueller**
and **Jesse Smith**



Parchment—a rich source of ancient DNA

ANCIENT DNA

Document DNA shows agriculture's course

Finding a good source of ancient DNA can be tough, due to weathering and bacterial contamination. But parchment—made from livestock hides—offers an abundant, well-preserved, and often dated source of DNA, report Teasdale *et al.* The researchers worked with a 2-cm-square piece, but have so refined their sequencing technique that it only requires a tiny sliver of parchment; they hope eventually to do nondestructive testing. These data, they note, can reveal the history of agriculture over the past 700 years. — EP

Philos. Trans. R. Soc. London Ser. B, 10.1098/rstb.2013.0379(2014).

NETWORK BIOLOGY

Meeting the demands of a complex network

Cells face intense metabolic demands. Meeting these demands requires genes to interact in complex networks. But what happens to these networks when the participating genes acquire mutations? To find out, Bajić *et al.* computationally mapped how genes that regulate cellular metabolism interact in yeast lacking specific metabolic enzymes or in yeast that had accumulated

neutral mutations (mutations that did not affect their overall fitness). Their model predicted that deleting specific genes would lead to alternative enzymatic reactions and rewired signaling pathways, depending on the degree of network connectivity. In the case of neutral mutations, their model suggested that network rewiring would occur along with a loss of plasticity. Experimental data supported these predictions. — LMZ

Genome Biol. Evol. 10.1093/gbe/evu255 (2014).



Scientists used somatic cell nuclear transfer to clone Dolly the sheep

STEM CELLS

Better cloning through expression

One method of generating pluripotent cells for cloning is to transfer the nucleus of a differentiated cell into an oocyte (egg cell) that has had its nucleus removed, a procedure known as somatic cell nuclear transfer (SCNT). However, very few SCNT embryos develop to term. To investigate why, Matoba *et al.* compared gene expression in embryos produced by in vitro fertilization (IVF) and SCNT. They found that SCNT but not IVF embryos repressed certain regions of DNA. Removing this repression enhanced the efficiency of SCNT, suggesting that the expression of one or more of these genes is important for cellular reprogramming. — MDC

Cell **159**, 884 (2014).

NEUROSCIENCE

Neuronal function requires the real deal

Brain slice experiments are a mainstay of modern neuroscience: They allow scientists to probe the molecular details of the brain while keeping brain architecture intact. Scientists usually bathe these slices in artificial cerebrospinal fluid (CSF) instead of CSF obtained from humans. This typically works well, but neurons in brain slices are



Brain slices are an important tool for understanding how neurons work

often quieter than those in intact brains. However, when Bjorefeldt *et al.* replaced artificial CSF with real human CSF, they observed a neuronal activity boost. Pyramidal neurons exhibited lower action potential thresholds and their excitability increased. The authors hypothesized that endogenous neuromodulating

substances in the human CSF increased the excitability of the nerve cells. — PRS

J. Physiol. 10.1113/jphysiol.2014.284711 (2014).

PALEOBIOLOGY

Parasites are rising with the seas

Extrapolating from the fossil record, the prevalence of aquatic parasites should grow along with the extent of anthropogenic climate change. Huntley *et al.* quantified the abundance of pits in nearly 4000 mollusk shells from Holocene Pearl River (China) delta sediments. Pitting is caused by trematodes, or flatworms. Trematode prevalence over the course of ~10,000 years was highest just after the onset of sea-level rise and lowest during maximum flooding. Although a number of variables can change with sea-level rise, parasite prevalence was not statistically explained by changes in salinity or host abundance. — NW

Proc. Natl. Acad. Sci. U.S.A. 10.1073/pnas.1416747111 (2014).

EDUCATION

Translating clicks into efficiency

As the number of web-based resources for science education increases, evaluation of these

websites remains limited. In order to enhance learning experiences, website managers should know how to draw an audience, provide an optimal user experience, and assess any learning that has taken place. Using their own website as an example, Goldsmith *et al.* describe how this evaluation can be done using clickstream analytics. Specifically, the authors determined where their audience came from and what content they did or did not use. With this information, website managers can better allocate their resources to fit their users' needs, making online science education efforts more targeted and efficient. — MM

Ecosphere **5**, 131 (2014).

MATERIALS SCIENCE

The right combination of additives

The formation of ceramic-based materials and composites occurs in nature under mild conditions, aided by a range of organic additives. With this template in mind, Bawazer *et al.* explored whether a combination of organic molecules could be used to make quantum dot assemblies under similar conditions. To discover the right mix, they turned to combinatorial methods paired with genetic algorithms. The recipes that showed the highest

fluorescence intensity became the basis for the next set of experiments. These converged on products that fluoresced after 7 days, and in all three, the same set of four additives was conserved. — MSL

Adv. Mater. 10.1002/adma.201403185 (2014).

PUBLIC HEALTH

The socioeconomics of good sanitation

Diarrheal diseases caused by poor sanitary conditions are a leading cause of childhood mortality worldwide. In Sub-Saharan Africa, improved sanitation has been particularly difficult to implement in rural areas, where the cost to install a latrine toilet is nearly \$190. In a survey of 2000 rural households in Benin, where nearly 95% of the country lacks access to proper sanitation, Gross and Günther found that as much as 50% of the country could have access to latrines if their cost could be reduced to \$50 each. However, the survey also found that cost is not the only socioeconomic factor contributing to poor sanitation, and that sanitation promotion programs should focus on the health security and protection provided by latrines as further reasons to install them. — NW

Water Resour. Res. **50**, 8314 (2014).

RESEARCH ARTICLE SUMMARY

PROTEIN EVOLUTION

Evolution of oligomeric state through allosteric pathways that mimic ligand binding

Tina Perica, Yasushi Kondo, Sandhya P. Tiwari, Stephen H. McLaughlin, Katherine R. Kemplen, Xiuwei Zhang, Annette Steward, Nathalie Reuter, Jane Clarke, Sarah A. Teichmann*

INTRODUCTION: Evolution and design of protein complexes are frequently viewed through the lens of amino acid mutations at protein interfaces, but we showed previously that residues distant from interfaces are also commonly involved in the evolution of alternative quaternary structures. We hypothesized that in these protein families, the difference in oligomeric state is due to a change in intersubunit geometry. The indirect mutations would act by changing protein conformation and dynamics, similar to the way in which allosteric small molecules introduce functional conformational change. We refer to these substitutions as “allosteric mutations.”

RATIONALE: In this work, we investigate the mechanism of action of allosteric mutations on oligomeric state in the PyrR family of pyrimidine operon attenuators. In this family, an entirely sequence-conserved helix that forms a tetrameric interface in the thermophilic ortholog (BcPyrR) switches to being solvent-exposed in the mesophilic ortholog (BsPyrR). This results in a homodimeric structure in which the two subunits are clearly rotated relative to their orientation in the tetramer. What is the origin of this rotation and the change in quaternary structure? To dissect the role of the 49 substitutions between BsPyrR and BcPyrR, we used ancestral sequence

reconstruction in combination with structural and biophysical methods to identify a set of allosteric mutations that are responsible for this shift in conformation. We compared the conformational changes introduced by the mutations to the protein motion during allosteric regulation by guanosine monophosphate (GMP).

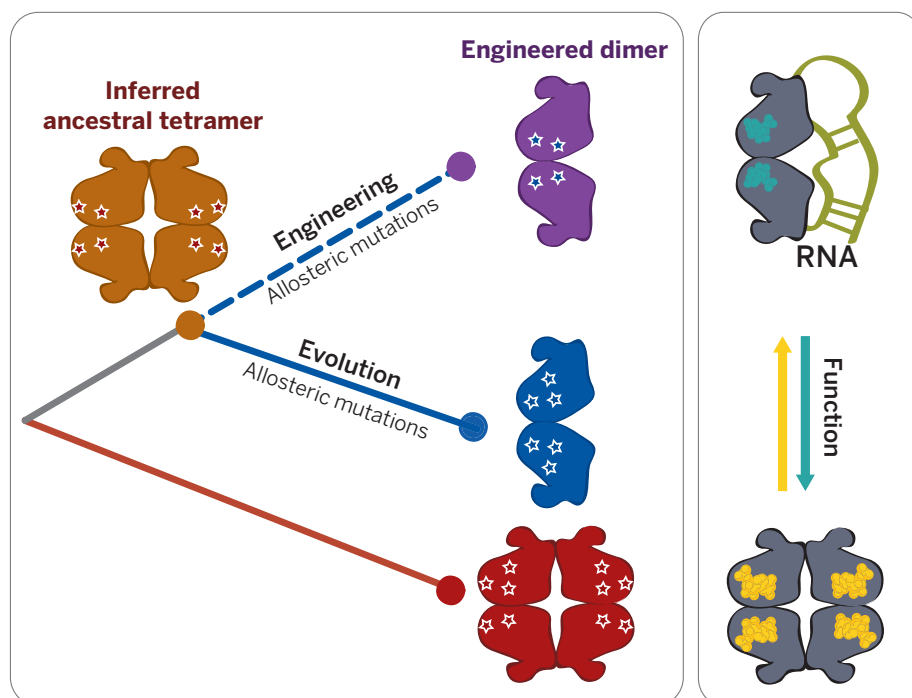
RESULTS: We identified 11 key mutations controlling oligomeric state, all distant from the interfaces and outside ligand-binding pockets. We confirmed the role of these allosteric mutations by engineering a shift in oligomeric state in an inferred ancestral PyrR protein (intermediate in sequence between the extant orthologs). We further used the inferred ancestral states and their mutants to show that the allosteric mutations are part of a downhill adaptation of the PyrR proteins to lower temperatures. We compared the x-ray crystal structures of ancestral and engineered PyrR proteins to the free and

ON OUR WEB SITE

Read the full article at <http://dx.doi.org/10.1126/science.1254346>

proteins to the free and GMP-bound structure of the mesophilic BsPyrR, which shifts its equilibrium from dimer to tetramer upon ligand binding. Binding of the allosteric molecule introduces a change in intersubunit geometry that is equivalent to the evolutionary difference in intersubunit geometry between the dimeric and tetrameric homologs. We further find that the difference in oligomeric state is coupled to the difference in intrinsic dynamics of the dimers. Finally, we used the residue-residue contact network approach to show that the residues corresponding to the allosteric mutations undergo large contact rewiring when the intersubunit geometry and, in turn, oligomeric state change, either by GMP binding or by the introduction of allosteric mutations.

CONCLUSION: We show that evolution employs the intrinsic dynamics of this protein to toggle a conformational switch in a manner similar to that of small molecules. Shifting the relative populations of different states by subtle modifications is a process central to protein function and, as shown here, also to protein evolution. This suggests that we can learn from evolution and design proteins with multiple conformational states. ■



Allosteric mutations change oligomeric state by employing the same conformational dynamics as ligands. PyrR homologs differ by mutations, all of which are outside the tetrameric interface. A subset of these allosteric mutations can be used to engineer a shift in oligomeric state in the ancestral PyrR. Allosteric mutations act by introducing conformational change in a manner analogous to that of the allosteric ligands.

The list of author affiliations is available in the full article online.

*Corresponding author. E-mail: saraht@ebi.ac.uk

Cite this article as T. Perica et al., *Science* 346, 1254346 (2014). DOI: 10.1126/science.1254346

RESEARCH ARTICLE

PROTEIN EVOLUTION

Evolution of oligomeric state through allosteric pathways that mimic ligand binding

Tina Perica,^{1,2*} Yasushi Kondo,² Sandhya P. Tiwari,^{3,4} Stephen H. McLaughlin,² Katherine R. Kemplen,⁵ Xiuwei Zhang,¹ Annette Steward,⁵ Nathalie Reuter,^{3,4} Jane Clarke,⁵ Sarah A. Teichmann^{1†}

Evolution and design of protein complexes are almost always viewed through the lens of amino acid mutations at protein interfaces. We showed previously that residues not involved in the physical interaction between proteins make important contributions to oligomerization by acting indirectly or allosterically. In this work, we sought to investigate the mechanism by which allosteric mutations act, using the example of the PyrR family of pyrimidine operon attenuators. In this family, a perfectly sequence-conserved helix that forms a tetrameric interface is exposed as solvent-accessible surface in dimeric orthologs. This means that mutations must be acting from a distance to destabilize the interface. We identified 11 key mutations controlling oligomeric state, all distant from the interfaces and outside ligand-binding pockets. Finally, we show that the key mutations introduce conformational changes equivalent to the conformational shift between the free versus nucleotide-bound conformations of the proteins.

Proteins diverge during the course of evolution and experience a continuous trade-off between selection for function and stability (1). Gould and Lewontin described how organisms adapt to different competing demands, while at the same time accumulating traits that occur either due to drift or correlations with selected features (2). This view can also be applied to proteins, where mutations of individual residues interact and determine fitness, similar to mutations in genes at the level of organisms (3). Selection is then determined by conditions, both internal (interactions with other macromolecules in the cell) and external (environmental variables such as temperature or pH). Furthermore, due to the difference in the sizes of sequence and structure space, proteins can accumulate destabilizing mutations, as long as they remain stable enough at given conditions (4).

In previous work, we showed that mutations outside protein interfaces are as important for the evolution of quaternary structure (oligomeric state) as mutations directly within interfaces (5). This raised the following question: By what mechanism

do mutations outside interfaces affect their formation? The most likely hypothesis is that these mutations act by changing either protein conformation or conformational dynamics, analogous to the ways in which allosteric ligands introduce conformational change. Thus, we referred to the indirect mutations as allosteric mutations.

Furthermore, the conformational dynamics of proteins enable functional features such as ligand binding and also contribute to evolutionary plasticity; that is, “evolvability.” Protein dynamics are essential for the functions of many proteins (6) and are more conserved at the superfamily level than sequence (7). Selection favors mutations of side-chain interactions that promote acquisition of the folded state. In the same way, selection is stronger on functionally relevant conformations of the entire protein structural ensemble (8). The conformation under the strongest constraint is not the one with the lowest free energy but rather the one most similar to the functional, often ligand-bound state.

The protein family we study here is a group of pyrimidine attenuator regulatory proteins, PyrR, present in the *Bacillaceae* family as well as in some other bacterial species (9). The PyrR family shows clear evidence of mutations acting allosterically with respect to the protein interface. The change from homodimeric to homotetrameric family members is unmistakably brought about by allosteric mutations: Homologs with different oligomeric states share a helix whose surface is 100% conserved in sequence. This helix forms the tetrameric interface in the homotetrameric family members but is solvent-exposed in the dimeric family members.

Bacillaceae live at a wide range of temperatures, to which the PyrR proteins have adapted. At the same time, PyrR is constrained by the need to conserve its double-stranded RNA binding ability and allosteric regulation by nucleotides. PyrR binds to a stem-loop structure in the nascent mRNA of the *pyr* operon, which induces formation of the termination loop and attenuates transcription. Uridine monophosphate (UMP) and guanosine monophosphate (GMP) allosterically regulate binding of PyrR to RNA, reflecting the ratio between purines and pyrimidines in the cell (10, 11) (Fig. 1). As the name suggests, excess pyrimidines, as reflected in UMP binding, attenuate further transcription of the *pyr* operon.

In this work, we use ancestral sequence reconstruction to infer the allosteric mutations that changed the oligomeric state and thermostability in the PyrR family during the course of evolution. We identify 11 allosteric mutations that decrease thermostability in all PyrR proteins but change the oligomeric state only in the context of inferred ancestral PyrR proteins and not in thermophilic PyrR. We show how these mutations affect oligomeric state indirectly, and we describe this allosteric mechanism: The same internal conformational switch in PyrR proteins is toggled by both an allosteric ligand (GMP) and a small number of mutations.

Results and discussion

Close homologs of PyrR have conserved interface amino acids but different oligomeric states

Using size-exclusion chromatography coupled with multiangle light scattering (SEC-MALS) at room temperature and velocity analytical ultracentrifugation (AUC) at 10°C, we observed that the PyrR oligomeric state differs between *Bacillus caldolyticus* and *B. subtilis* homologs and is affected by allosteric regulators such as GMP (Fig. 2). *B. caldolyticus* has an optimal growth temperature of 72°C, and its PyrR (BcPyrR) elutes as one peak corresponding to a tetramer (Fig. 2). Velocity AUC experiments show that the majority of BcPyrR sediments as a tetramer with a minor monomeric species and no apparent dimeric species (fig. S4). *B. subtilis* has an optimal growth temperature of 25°C, and BsPyrR elutes from the size-exclusion column as a broad peak with a range of molecular masses between monomeric, dimeric, and tetrameric oligomeric state (Fig. 2). In the velocity AUC experiment for BsPyrR, two species were observed to sediment, calculated to have molecular masses corresponding to that of a PyrR dimer and tetramer, respectively (fig. S4). Therefore, BsPyrR exists as a dimer in equilibrium with the monomeric and tetrameric species at low micromolar concentrations, which correspond to the physiological range, as the estimated average concentration of PyrR in *B. subtilis* cells is 0.4 μM (12).

BcPyrR and BsPyrR have the highest sequence identity of all PyrR homologs of known three-dimensional structure with different oligomeric states: 73% sequence identity over 180 residues, corresponding to 49 substitutions, most of which are on the solvent-exposed surface of the protein.

¹European Bioinformatics Institute, Wellcome Trust Genome Campus, Hinxton, Cambridge CB10 1SD, UK. ²Medical Research Council (MRC) Laboratory of Molecular Biology, Francis Crick Avenue, Cambridge Biomedical Campus, Cambridge CB2 0QH, UK. ³Department of Molecular Biology, University of Bergen, P.O. Box 7803, N-5020 Bergen, Norway. ⁴Computational Biology Unit, Department of Informatics, University of Bergen, P.O. Box 7803, N-5020 Bergen, Norway. ⁵Department of Chemistry, University of Cambridge, Lensfield Road, Cambridge CB2 1EW, UK.

*Present address: Department of Bioengineering and Therapeutic Sciences, California Institute for Quantitative Biosciences, University of California, San Francisco, 1700 4th Street, San Francisco, CA 94143, USA. †Corresponding author. E-mail: saraht@ebi.ac.uk

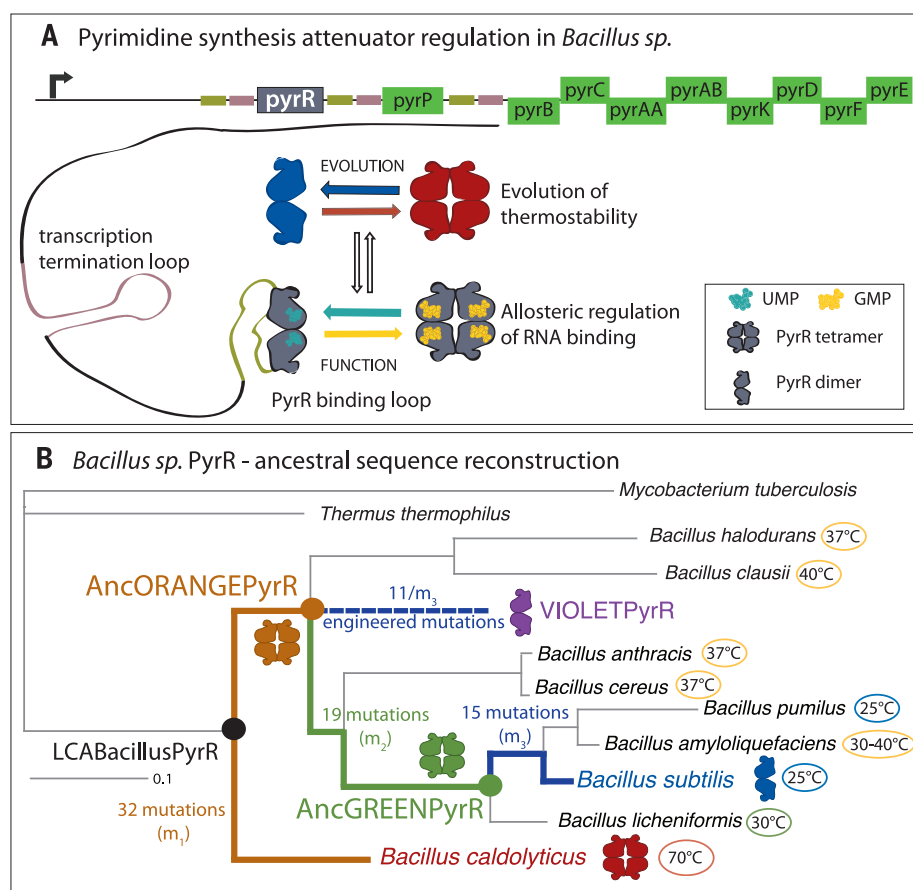


Fig. 1. Function and evolution of the attenuator protein PyrR. (A) Schematic representation of the pyrimidine operon attenuator system in *Bacillus* sp. PyrR binds to the PyrR binding loop as a dimer. UMP allosterically promotes the binding of RNA, whereas the addition of GMP decreases the affinity for RNA (11). Different *Bacillus* species live in various environments and are adapted to different optimal growth temperatures. (B) The phylogenetic tree of *Bacillus* PyrR proteins (inferred using Bayesian MCMC) shows the variety of optimal growth temperatures for different *Bacillus* species: *B. caldolyticus* lives at temperatures higher than 70°C, and at room temperature, its PyrR is a homotetramer. *B. subtilis* optimal growth temperature is 25°C, and at room temperature, its PyrR is in equilibrium between a homodimer and a homotetramer (illustrated here as just a dimer for simplicity). Analysis of the reconstructed ancestral sequences shows that the change from a tetramer to a dimer occurred on the final (blue) branches of the tree, where 15 allosteric mutations (m_3) turn a tetrameric AncGREENPyrR into a dimeric BsPyrR. A subset of 11 of those allosteric mutations ($11/m_3$) also switches the oligomeric state in the context of the ancestral AncORANGEpyrR. LCABacillusPyrR, last common ancestor of the *Bacillus* sp. PyrR.

The residues involved in the tetrameric (dimer-of-dimers) interface are 100% sequence-identical. These interface residues are also probably involved in RNA-binding (13) and, hence, under purifying selection (fig. S2).

A small number of allosteric mutations change the oligomeric state of PyrR

The PyrR protein is present in *Bacillus* species with diverse optimal growth temperatures, as well as the distantly related bacteria *Mycobacterium tuberculosis* and *Thermus thermophilus*, as shown in the phylogenetic tree of this protein family (Fig. 1B). To trace the mutations changing the oligomeric state between the thermophilic BcPyrR (red) and mesophilic BsPyrR (blue), we focused on the two internal nodes in the phylogenetic tree after the split of the BcPyrR from the last

common ancestor of the *Bacillus* sp. PyrR. We reconstructed the most likely ancestral sequences of the internal nodes (14). (See the Materials and methods section for details.) In analogy to the color wheel, we named the two inferred ancestral proteins AncORANGEpyrR and AncGREENpyrR (Fig. 1B).

We used SEC-MALS to reveal that AncORANGEpyrR formed a stable tetramer and that AncGREENpyrR only showed a decrease in the average molecular mass at the lowest concentration (1 μ M), from which we imply a presence of a low concentration of lower-oligomeric state species (Fig. 2). In AUC analysis, both ancestral proteins displayed similar distributions of sedimenting species, as seen for BcPyrR (fig. S4). Therefore, we infer that evolution of the dimeric state occurred toward the terminal branches of

the PyrR phylogenetic tree, between AncGREENpyrR and BsPyrR. There are 12 substitutions and three insertions or deletions (a set of 15 mutations we refer to as m_3) between AncGREENpyrR and BsPyrR (fig. S19). As our goal is to identify the smallest subset of allosteric mutations that clearly change the oligomeric state, we excluded four of these mutations: three insertions or deletions and one substitution [Glu⁴→Gln⁴ (E4Q) (15)], which is a revertant to the same amino acid as in the tetrameric BcPyrR. Two of the insertions or deletions were at each of the termini, and the third one was in a flexible loop. We would not expect these three changes to have a major effect on the structure. Eleven substitutions ($11/m_3$) were different between BsPyrR and all the tetrameric PyrRs (BcPyrR, AncORANGEpyrR, and AncGREENpyrR). To confirm their role in the shift of the oligomeric state, we inserted them into the stable PyrR tetramer AncORANGEpyrR, producing the engineered protein VIOLETPyrR (Fig. 3). The 11 substitutions destabilized the AncORANGEpyrR tetramer: VIOLETPyrR has similar SEC-MALS and AUC profiles as BsPyrR (Fig. 2 and fig. S4). Thus, these mutations, none of which are in the tetrameric interface, shift the oligomeric state through an indirect, allosteric mechanism.

Do these mutations turn any PyrR homolog into a dimer? We grafted the 11 allosteric mutations into the tetrameric BcPyrR, forming the engineered protein PURPLEPyrR. Surprisingly, PURPLEPyrR remains tetrameric, even at the lowest concentration (Fig. 3B and fig. S4). This implies that these 11 allosteric mutations have an epistatic interaction with the 32 m_1 mutations that separate BcPyrR and AncORANGEpyrR. Epistasis between amino acid substitutions is known to be ubiquitous in proteins, as described in multiple recent publications (3, 16, 17).

To pinpoint the key oligomeric state-switching mutations, we further tested the effect of two non-overlapping sets of residues within the 11 allosteric mutations, represented by PLUMPyrR ($3/m_3$) and MAGENTAPyrR ($8/m_3$). We selected the three mutations in PLUMPyrR based on the proximity of these residues to the dimeric interface, expecting them to have the largest effect on the inter-subunit geometry. Both subsets of mutations had independent effects on the oligomeric state (Fig. 3), as the equilibria of both PLUMPyrR and MAGENTAPyrR were shifted toward the dimeric state at the lowest protein concentrations in SEC-MALS, with the appearance of a dimeric species in AUC (fig. S4). This implies that these two small sets of mutations contribute to the oligomeric shift in a cumulative manner.

The 11 mutations that shift the PyrR oligomeric state are part of a downhill adaptation to temperature

Members of the *Bacillus* genus live in dramatically different environments, the most notable difference being ambient temperature. Hobbs *et al.* (18) have shown that the *Bacillus* species have adapted to different temperatures multiple times in evolution. *B. subtilis* (with the

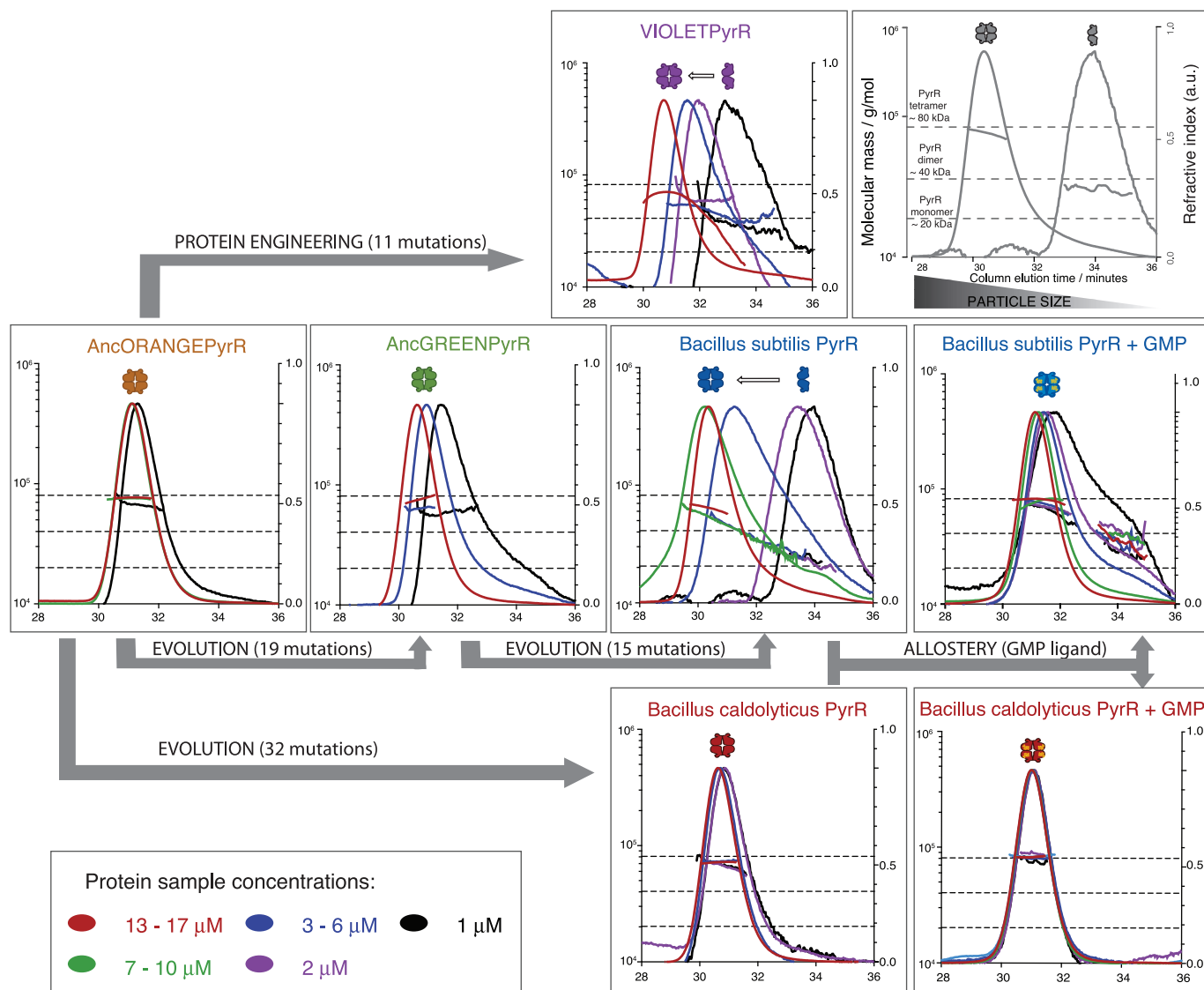


Fig. 2. Analysis of PyrR oligomeric states. Samples of AncORANGEYrR, AncGREENYrR, *B. subtilis* PyrR (BsPyrR), BsPyrR+GMP, *B. caldolyticus* PyrR (BcPyrR), BcPyrR+GMP, and VIOLETPyrR at varying concentrations were separated by size-exclusion chromatography before determination of the excess refractive index and multiangle light scattering (SEC-MALS) from which the molecular masses are determined. Horizontal dashed lines represent the expected masses for monomeric, dimeric, and tetrameric PyrR species, respectively. a.u., arbitrary units.

homodimeric BsPyrR) lives in soil with optimal growth at 25°C, and *B. caldolyticus* (with the homotetrameric BcPyrR) exists in alkaline hot springs with the optimal growth at 72°C (19).

We recorded the circular dichroism (CD) spectra at temperatures from 20° to 90°C for all of our PyrR constructs (Fig. 3C). Their thermal unfolding was irreversible, and all but BsPyrR and PURPLEYrR unfolded in a single phase. This was sufficient to estimate the thermal stability of PyrR proteins along the evolutionary tree. BcPyrR shows no variation in the CD spectra up to 70°C, when it suddenly unfolds cooperatively. BsPyrR, however, exhibits changes in helicity at temperatures as low as 35°C, finally unfolding completely at 75°C. We could not determine from the CD spectra which of the secondary structure changes occur at low temperatures in BsPyrR. However, plotting ellipticity for different wavelengths sug-

gests an exchange between α -helical and β -sheet structure (fig. S5).

AncORANGEYrR thermal unfolding follows the same pattern as that of BcPyrR, with unfolding taking place at 80°C rather than 70°C. This stabilization of 10°C is most probably an artifact of ancestral protein sequence reconstruction, which has been suggested to overestimate protein stability due to a bias toward more stabilizing mutations in the evolutionary substitution models (20). Notably, VIOLETPyrR, which differs from AncORANGEYrR by just the 11 mutations, unfolded at a considerably lower temperature than AncORANGEYrR, whereas PLUMPyrR and MAGENTAYrR have intermediate thermostability (Fig. 3C).

This observation raises the question as to the mechanism for the thermal destabilizing effect of the 11 mutations. They could be affecting thermal

destabilization through the switch in oligomeric state or by changing the polarity of the protein surface. Both residue composition and oligomeric state have been suggested to play a role in protein thermostability (21). A higher oligomeric state is proposed to increase thermostability by burying more residue surface area. It has also been repeatedly observed that thermophilic bacteria have more charged residues and fewer polar residues compared with mesophilic organisms. This bias is especially pronounced when only surface residues are taken into account (22).

To deconvolute whether it is the residue propensity or the oligomeric state that plays the main role in the differences in thermostability of PyrR, we took advantage of the engineered PURPLEYrR, which has the 11 allosteric mutations but is still tetrameric. Although all but the 11 allosteric residues of PURPLEYrR are the same as in the

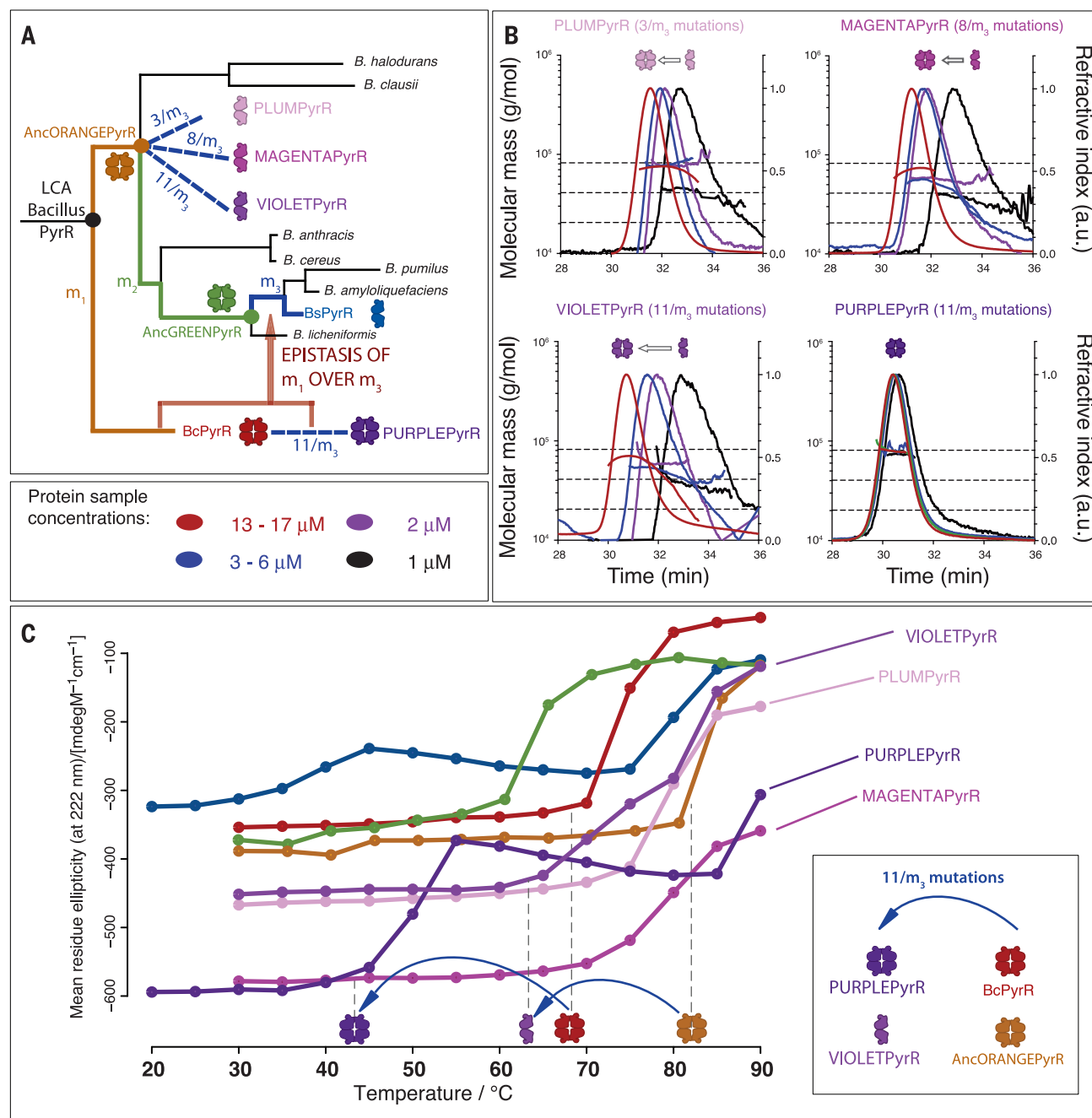


Fig. 3. Allosteric mutations affect oligomeric state and thermostability. (A) Summary of the effects of allosteric mutations on oligomeric state along the PyrR phylogenetic tree. (B) Two nonoverlapping subsets of the 11 allosteric mutations [3/ m_3 mutations (PLUMPyrR) and 8/ m_3 mutations (MAGENTAPyrR)] are enough to overcome the threshold and cause instability of the tetramer sufficient at 1 μ M protein concentrations. All 11 allosteric mutations (11/ m_3) together (VIOLETPyrR) have a larger effect on the stability of the tetramer than the 3/ m_3 and 8/ m_3 individual subsets of mutations. The 11 allosteric mutations change oligomeric state only in the context of AncORANGEpyrR

(or AncGREENyrR), but not in the context of BcPyrR. This is due to the epistasis of (a subset of) m_1 mutations over the m_3 mutations. (C) Oligomeric state and thermostability are coupled in PyrR, but it is the thermophilic propensity of residues, not the oligomeric state, that determines thermostability. Thermal unfolding of PyrR homologs, inferred from CD at 222 nm at temperatures ranging from 30° to 90°C (from 20° to 90°C for BsPyrR and PURPLEPyrR). Loss of CD signal at 222 nm is interpreted as the loss of helicity. The CD signal is plotted as the mean residue ellipticity corrected for protein concentration.

thermophilic BcPyrR, the CD measurements show that tetrameric PURPLEPyrR has decreased thermostability compared with that of BcPyrR. We thus infer that it is the change in thermophilic propensity of surface residues, and not the change in the oligomeric state, that plays a major role in the change of PyrR thermostability.

To dissect this in detail, we bioinformatically define the residue thermophilic propensity as the log ratio of amino acid frequencies between the solvent-exposed surfaces of proteins from thermophilic and mesophilic organisms (22). Thus, we calculated how mutations along the PyrR tree change this thermophilic propensity. As ex-

pected, the mutations increase the thermophilic propensity on the branches from AncORANGE-PyrR toward BcPyrR and decrease toward BsPyrR. Moreover, the largest decrease in thermophilic propensity occurs between AncGREENPyrR and BsPyrR, the branch that also corresponds to the switch toward the dimeric state (fig. S6).

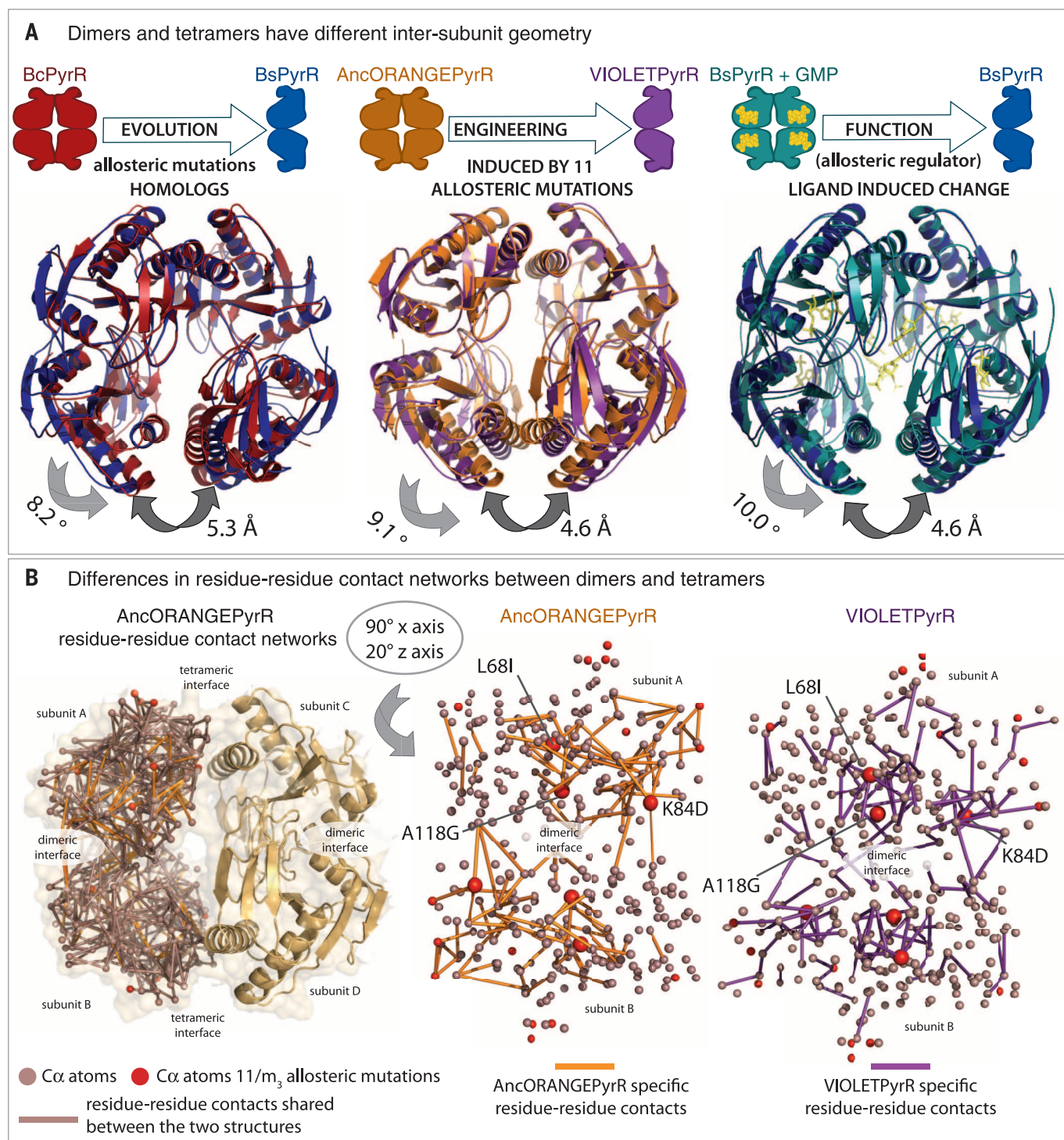


Fig. 4. The difference in oligomeric state is due to a change in intersubunit geometry. (A) Change in oligomeric state through evolutionary variation, functional allostery, or recapitulated by engineering is always coupled to the same difference in intersubunit geometry. The three superimposed pairs of structures are: (i) *B. subtilis* PyrR (BsPyrR; PDB: 1A3C) dimers superimposed on a *B. caldolyticus* PyrR (BcPyrR; PDB: 1NON) tetramer; (ii) VIOLETPyrR dimers superimposed on a AncORANGEpyrR tetramer; and (iii) *B. subtilis* PyrR (BsPyrR; PDB: 1A3C) dimers superimposed on tetrameric *B. subtilis* PyrR in complex with GMP. The intersubunit geometry of free BsPyrR is incompatible with

formation of the dihedral tetramer; however, GMP binding introduces a 10° inter-subunit geometric change, and BsPyrR forms a tetramer. The VIOLETPyrR intersubunit geometry is not compatible with the formation of the tetramer formed by AncORANGEpyrR, and this difference of conformation and oligomeric state is brought about by 11 allosteric mutations. (B) The tetrameric AncORANGEpyrR and dimeric VIOLETPyrR residue-residue contact networks differ by 15% of their contacts. (Orientation of networks can be further explored in movies S1 and S2.) L68I, K84D, and A118G are central hubs and are involved in the majority of contact rewiring between the dimeric and tetrameric networks.

From this, we infer that the 11 allosteric mutations are part of a more general “downhill” adaptation to lower temperatures. Thus, the switch in oligomeric state of free PyrR co-occurs with the evolutionary adaptation to lower temperatures of *B. subtilis* as compared with *B. caldolyticus*. How is this dimer-tetramer switch affected by mutations that are distant from all of the intersubunit interfaces? To answer this question, we investigated the oligomeric states during allosteric regulation by ligands in this protein family.

The allosteric regulators UMP and GMP control oligomeric state

Previous in vivo and biochemical experiments showed that the PyrR binding to the leader RNA sequence (PyrR binding loop) of the *pyr* operon is regulated by small molecules such as UMP and GMP (10, 11). Higher concentrations of pyrimidines increase the affinity of PyrR for the PyrR binding loop and, in turn, attenuate transcription of the pyrimidine synthesis operon. Higher concentrations of purines, on the other hand, decrease the affinity for the binding loop, which in turn increases the transcription of the pyrimidine synthesis operon (9) (Fig. 1). As allosteric regulation usually affects conformational change, we wanted to investigate how GMP and UMP influence PyrR conformation and oligomeric state.

We analyzed the oligomeric state of BsPyrR and BcPyrR by SEC-MALS upon addition of allosteric ligands and observed that both UMP and GMP stabilize the tetrameric state of PyrR (Fig. 2 and fig. S3). This is especially prominent in the case of BsPyrR, where addition of nucleotides shifts the equilibrium toward a higher oligomeric state. The RNA-bound form of PyrR, not investigated here, is likely to be dimeric, based on analytical ultracentrifugation (11) and mutagenesis experiments (13).

This means that the effect of the 11 allosteric mutations is similar to that of RNA and opposite to the nucleotide ligands, which stabilize the tetrameric state. The 11 allosteric mutations are also allosteric with respect to the nucleotide-binding site: Each of the 11 residues is 10 Å or more away from the bound GMP molecules.

Overall, though different ligand-bound and RNA-bound forms of the protein sample both dimeric and tetrameric states, the 11 mutations shift the free-protein equilibrium toward the dimeric state in this landscape of different conformations.

Both mutations and ligands shift oligomeric state by changing intersubunit geometry

To determine the structural changes that occur when the allosteric mutations switch the oligomeric state in the PyrR family, we solved four x-ray crystal structures: AncORANGEpyrR, AncGREENpyrR, VIOLETPyrR, and BsPyrR+GMP (table S2). We then compared these structures to those of BcPyrR and BsPyrR (23, 24).

In our previous work, we hypothesized that evolutionary changes in oligomeric state can arise from difference in intersubunit geometry within a protein complex (5). If this were true for the PyrR

family, we would expect the dimeric structures to have distinct intersubunit geometries as compared to the tetrameric structures.

Superimposing the dimeric BsPyrR on the BcPyrR tetramer shows an 8° rotation around the dimeric interface (Fig. 4A and fig. S1). This conformation of BsPyrR is not compatible with the tetrameric oligomeric state, as the two helices that would form the dimer-of-dimers interface are pulled apart by more than 5 Å. The 11 mutations affect the same difference in conformation. Dimeric VIOLETPyrR and tetrameric AncORANGEpyrR, which differ by the 11 mutations, exhibit the same relative rotations between subunits within the dimer (Fig. 4). The subset of three allosteric mutations introduced into PLUMPyrR from AncORANGEpyrR leads to the same geometric change, where PLUMPyrR has a 9° intersubunit rotation as compared with AncORANGEpyrR (fig. S8).

How does this compare with the difference between free, dimeric BsPyrR and tetrameric GMP-bound BsPyrR? Addition of GMP introduces a 10° rotation, changing the protein conformation into the one compatible with forming the dimer of dimers (Fig. 4). The tetrameric GMP-bound BsPyrR structure is similar to the tetramers formed by free BcPyrR and AncORANGEpyrR (fig. S8). There is a subtle 3.6° subunit rotation around the dimeric interface between the GMP bound form of BsPyrR and AncORANGEpyrR. However, their tetrameric interfaces superimpose almost perfectly, with an average atomic distance difference in the tetrameric interface helices of less than 1 Å.

In summary, homologous dimers all have a similar set of intersubunit geometries, equally different from the intersubunit geometries of tetramers. The tetramers exhibit limited variations in their geometries, all of which are substantially smaller than the differences between the dimers and tetramers. As the geometries of the dimers and tetramers are so clearly distinct from each other, we conclude that the 11 allosteric mutations affect oligomeric state in a manner almost identical to the allosteric ligand GMP.

How does this change in intersubunit geometry come about? This is not immediately evident by inspecting the individual monomeric subunits (fig. S9) or the dimeric interfaces (5) between the dimeric and tetrameric proteins, as they all superpose well. To look for the subtle structural differences that could account for the observed differences in conformation and oligomeric state, we used the residue-residue interaction network approach (25–28). With this approach, the protein structure is reduced to a network in which each node represents a residue and each edge represents a physical interaction between two residues. This allows for an unbiased analysis of structures by using graph theoretical methods, as illustrated in fig. S10.

The tetrameric AncORANGEpyrR and dimeric VIOLETPyrR contact networks differ in ~15% of their contacts, and these differences are non-uniformly distributed around the network (Fig. 4B and fig. S11). To estimate how much each

residue contributes to the difference in residue-residue contacts, we determined the number of contact changes in two shells around the amino acid of interest. To maintain information on residue connectivity, which has been shown to determine residue evolvability (29), we used the absolute number of rewired residue contacts rather than normalizing by total number of contacts. This is because rewiring the contacts of a buried residue with a high connectivity will have a larger structural effect than rewiring a residue with lower connectivity.

Three out of the 11 allosteric mutations (L68I, K84D, and A118G) exhibit dramatic rewiring of contacts (Fig. 4B). Specifically, when comparing AncORANGEpyrR with the dimeric structures (BsPyrR, VIOLETPyrR, and PLUMPyrR), these residues rewire more contacts than the average buried PyrR residue by between one and two standard deviations (fig. S12). L68 and A118 are completely buried in the protein interior, whereas K84 is in the more flexible part of the protein, changing its accessible surface area between different conformations.

Moreover, L68 and A118 are the two residues at the center of the largest rewiring events in the transition from the dimeric BsPyrR to the tetrameric BsPyrR+GMP. This means that the structural changes due to the L68I and A118G mutations mimic the key residue rewiring events that occur upon GMP binding. Thus, the evolutionary mutations and the allosteric ligand GMP share a common mechanism for achieving an identical intersubunit rotation, leading to the same shift in oligomeric state.

The stability difference between PyrR tetramers is coupled to changes in the dynamics of dimeric units

Above we noted that small differences, either via mutation or ligand binding, affect the wiring of residue contact networks. This suggests a small energy difference between the two main conformations of PyrR. Thus, we might expect both of these conformations to be sampled by the vibrational normal modes that describe the intrinsic dynamics of dimeric PyrR.

We compared the similarity of the intrinsic dynamics of different PyrR dimers (both the dimeric PyrRs and the halves of tetrameric PyrRs) by comparing their flexibility calculated with elastic network modeling (ENM) (30). ENM provides a distribution of fluctuations around the equilibrium conformation for each structure, and the overlap of these distributions between different structures can be described by the Bhattacharyya coefficient (BC). We have previously shown that the BC ranges between 0.85 and 1 for members of the same protein family (31). Accordingly, the differences between all PyrR proteins are in this range (between 0.83 and 0.98).

Furthermore, it is clear that the pattern of flexibility is more similar among the three dimers (BsPyrR, VIOLETPyrR, and PLUMPyrR) than the three tetramers (AncORANGEpyrR, PURPLEpyrR +UMP, and BsPyrR+GMP) (Fig. 5A). The BsPyrR dimer and BsPyrR+GMP tetramer had a similarity

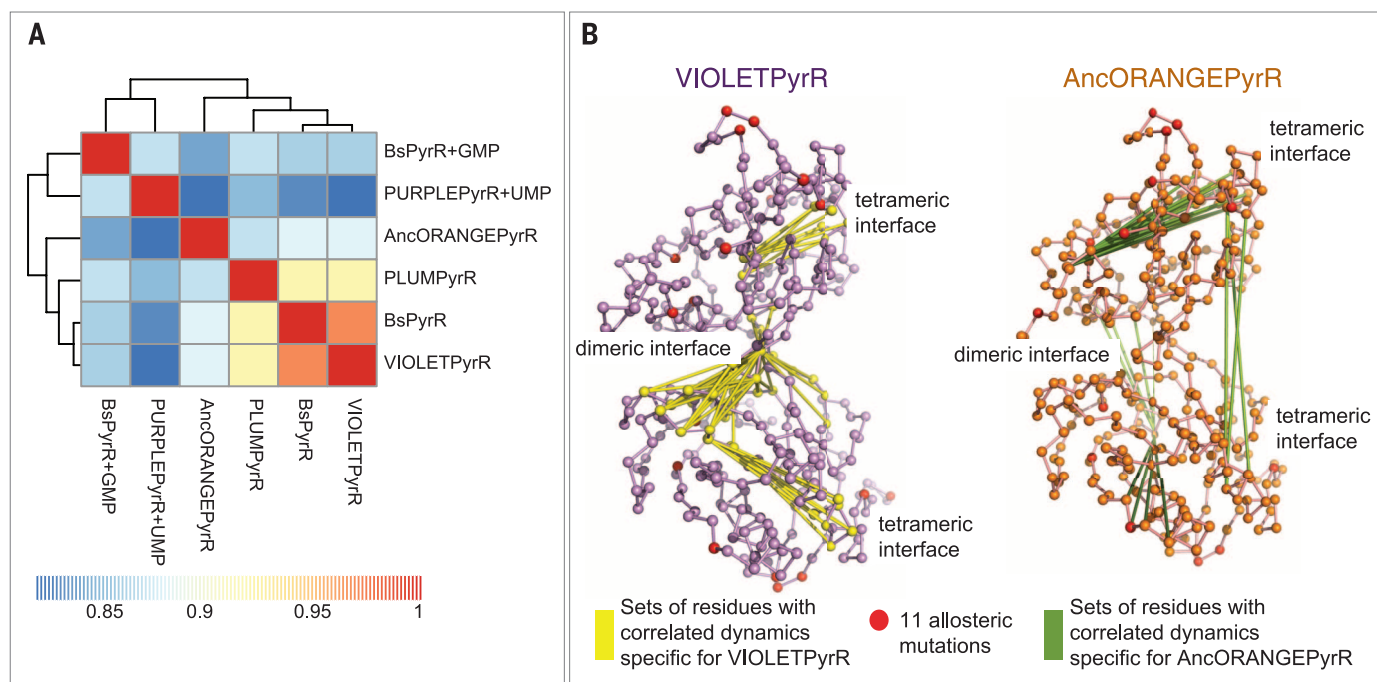


Fig. 5. PyrR intrinsic dynamics and oligomeric state. (A) All PyrR proteins have similar intrinsic dynamics, but the three dimeric proteins are more similar than the tetramers. This difference is most pronounced when comparing the sets of dimeric and tetrameric interface residues with correlated dynamics specific for the dimeric VIOLETPyrR or the tetrameric AncORANGEpyrR. **(B)** Both structures are represented by only their Ca atoms, connected by green or yellow edges if at least one of the residues is involved in either the dimeric or the tetrameric interface and only if the

pair of residues is moving in a concerted, correlated manner in either only the dimeric VIOLETPyrR (yellow edges) or the tetrameric AncORANGEpyrR (green edges). The residues corresponding to the 11 allosteric mutations ($11/\text{m}_3$) are shown in red. The sets of residues with correlation differences shown here have a cluster size of more than three and fall within the correlation difference threshold of 0.1. (Both threshold values were chosen for the sake of clarity; see figs. S16 and S17 for a more exhaustive analysis of the correlation differences.)

score of 0.87, whereas BsPyrR and other dimers (VIOLETPyrR and PLUMPyrR) had higher pairwise similarity scores reflecting more similar dynamics. This illustrates that similarities in intrinsic dynamics among the PyrR proteins are not a simple function of sequence identity, given the fact that BsPyrR+GMP and BsPyrR have the same sequence and VIOLETPyrR is closer in sequence to AncORANGEpyrR than to BsPyrR. The clustering based on the BC score seen in Fig. 5A matches the clustering based on their root mean square deviation (RMSD) (fig. S14). Although BC and RMSD compare different properties of structures, here the structures with the highest BC score also have the lowest RMSD, which confirms that the structural changes are encoded in the intrinsic dynamics of these structures.

It has repeatedly been shown that the conformational difference, either between functional conformations or even homologs, can be sampled by a combination of a few low-frequency normal modes of the protein (32–36). We found that a few lowest-frequency modes of PyrR proteins describe the transition between a tetramer and a dimer, both in the case of the transition being induced by allosteric ligands and by allosteric mutations.

In particular, the mode of the BsPyrR+GMP protein with the second lowest frequency also captured 44% of the transition from this tetramer to the dimeric BsPyrR structure. This mode

is very similar to the three lowest-frequency modes of tetrameric AncORANGEpyrR. The second-lowest-frequency mode of this tetramer also contributes most to the conformational change between AncORANGEpyrR and the dimeric VIOLETPyrR, which differ by just the 11 mutations (fig. S15C). For both tetramers, the transition to the dimer occurs via the low-frequency normal modes that describe the same type of motions in the structure (movies S3 to S5). This mode corresponds to the overall subunit rotation (and translation) required to go from one state to the other, as described in Fig. 4A.

The difference between correlations in residue motions between a dimer and a tetramer were particularly clear when comparing the correlations of dimeric and tetrameric interface residues between AncORANGEpyrR and VIOLETPyrR. In AncORANGEpyrR, the residues from the tetrameric interface exhibit correlations across the subunit and between the two tetrameric interface helices of the two subunits of a dimer, whereas in VIOLETPyrR the majority of the specific correlations are located close to the dimeric interface (Fig. 5B and fig. S16). Furthermore, we observed that the residues corresponding to 3 out of the 11 allosteric mutations (K62P, L68I, and A118G) are within the largest regions that undergo a collective change in intrinsic dynamics from one oligomeric state to the other. The residue corresponding to the V8I mutation also experiences

a notable gain in correlation in both tetramers, related to its proximity to the tetrameric interface and the overall difference seen in that region (fig. S16C). (Details of the statistical analysis of the correlated dynamics are described in the supplementary materials and fig. S17.)

It is important to emphasize that the dynamics were calculated for the dimeric halves of the tetrameric PyrR structures. This means that the observed differences do not stem from the additional residue contacts in the tetrameric (dimer-of-dimers) interface but are solely due to the conformational differences between the dimer and the equivalent half of the tetramer. Thus, the conformational differences between different PyrR proteins are encoded in their intrinsic dynamics, and relatively small effects, such as ligand binding or a small number of strategic mutations, can use these dynamics to toggle an intrinsic conformational switch and change the quaternary structure.

Conclusions

Reconstituting the PyrR sequences and analyzing their biophysical properties enables us to recapitulate the evolutionary history of the family (Fig. 1B). In one part of the phylogenetic tree, PyrR has adapted to remain stable and functional at extremely high temperatures (BcPyrR), whereas in the other part (after the AncGREENPyrR node) the organisms have adapted to life at lower temperatures (25°C). It is known that many proteins

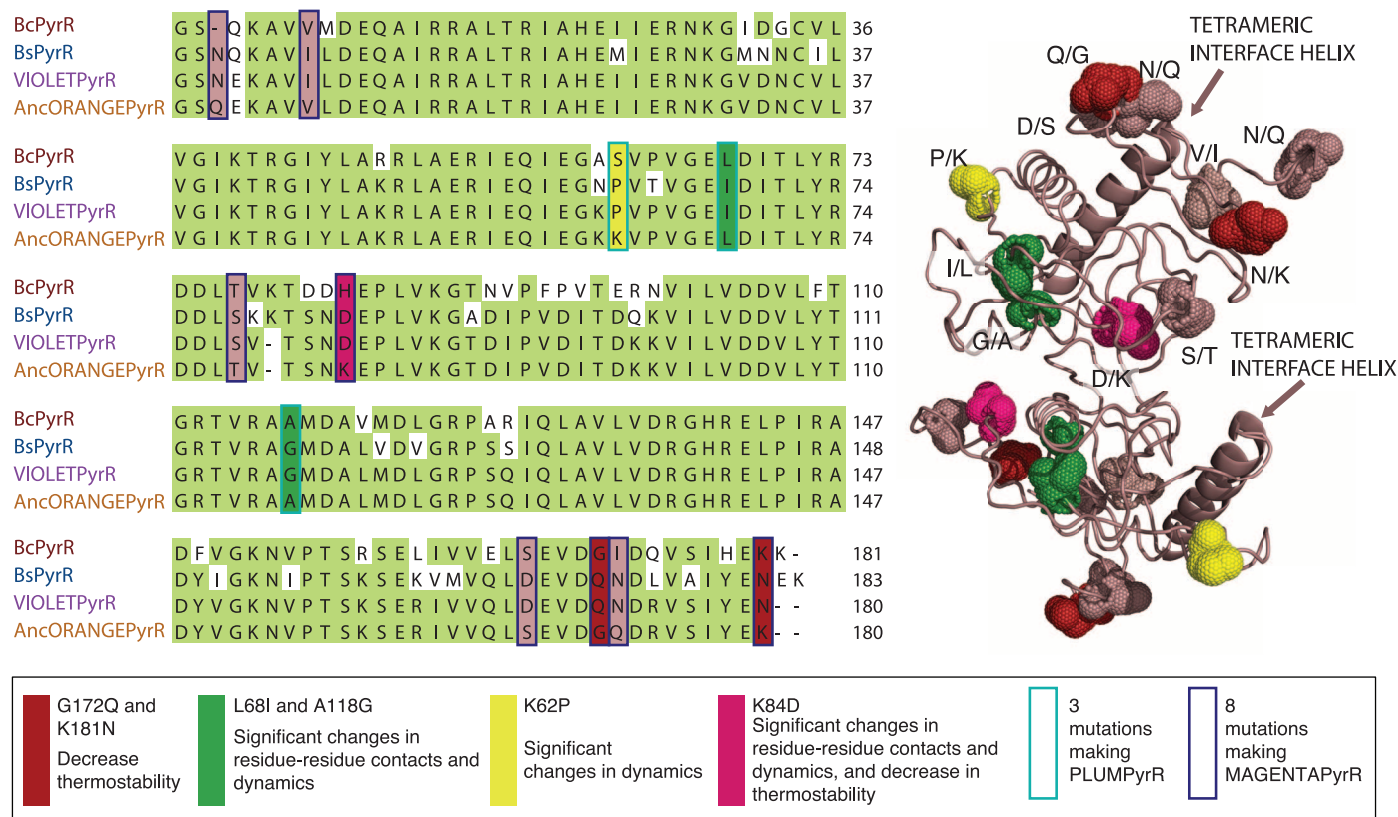


Fig. 6. Summary of mutational mechanisms. A small number of allosteric mutations are responsible for the evolutionary difference in oligomeric state, thermostability, and dynamics of PyrR homologs. We show the mechanism(s) by which each mutation acts, and we summarize similar mutations using the same color scheme.

maintain marginal stability, and one would thus expect the protein stability to reflect the differences in environmental temperatures. This can be explained by the simple fact that the selection pressure for increased stability is relaxed at mesophilic temperatures, meaning that proteins can accumulate destabilizing mutations until they reach marginal stability (4).

However, high stability can come at the expense of increased conformational rigidity, and a protein adapted to be stable at high temperatures may not be flexible enough to perform its function at a lower temperature (37). Whether it was adaptational or simply drift in the case of PyrR, downhill mutations lowered thermostability while at the same time selection for maintaining the RNA binding site and allosteric regulation acted continuously throughout evolution. The accumulated downhill mutations caused small and cumulative changes sufficient to switch oligomeric state in the absence of mutations in the actual tetrameric interface. This change in the stability of the tetramer may have been an evolutionary by-product, demonstrating the power and importance of indirect and structurally allosteric mutations.

We have shown that the change in oligomeric state occurred through an interplay of mutations affecting residue contact networks, intrinsic dynamics, and thermostability. At the same time, for 6 out of the 11 mutations, we were able to estimate relative contributions to each of these properties (Fig. 6). The K84D mutation, which is

in the part of the structure that seems to be disordered in some of the conformations, is predicted to affect all three properties simultaneously. The G172Q and K181N mutations in surface residues are predicted to contribute substantially to the change in thermostability. L68I and A118G are mutations in buried residues at the center of a large residue-residue rewiring event in the transition from dimer to tetramer, both in evolution and ligand binding. Both residues are also part of a region of the protein with highly correlated dynamics. K62P is a mutation in a surface residue, weakly connected to the rest of the structure but part of a region with highly correlated motions where a change has a profound effect on protein dynamics.

Here we showed compellingly how mutations in residues outside the interface can introduce rearrangements that have a knock-on effect on the interface itself. We hope that the importance of mechanisms of allosteric mutations will become increasingly clear with the advancement of methods that accurately predict effects of mutations, as well as methods for engineering proteins with multiple functional conformations.

Materials and methods

Ancestral sequence reconstruction

To reconstruct the ancestral PyrR sequences between the dimeric BsPyrR and the tetrameric BcPyrR, we retrieved all of the PyrR protein sequences from UniProtKB, including the sequen-

ces of two outliers: PyrR from *M. tuberculosis* and *T. thermophilus*. We used MUSCLE (38) to calculate a multiple sequence alignment of the PyrR proteins (fig. S18). We performed Bayesian inference with MrBayes version 3.1 (39). The evolutionary tree topology, branch lengths, and sequences of ancestral nodes were calculated from a PyrR protein alignment by using an estimated fixed-rate evolutionary model. The gaps in the ancestral sequences were determined using the F81-like model for binary data implemented in MrBayes (40). More details can be found in the supplementary materials.

Oligomeric state analysis by SEC-MALS

We resolved the protein samples on a Superdex S-200 10/300 analytical gel filtration column (GE Healthcare) pre-equilibrated with 50 mM Tris pH 7.5, 150 mM NaCl, and 1 mM DTT at 0.5 ml/min. We performed the measurements using an online Dawn Heleos II 18-angle light-scattering instrument (Wyatt Technologies) coupled to an Optilab rEX online refractive index detector (Wyatt Technologies) in a standard SEC-MALS format. We used the ASTRA v5.3.4.20 software (Wyatt Technologies) to determine the absolute molecular mass from the intercept of the Debye plot using Zimm's model (41) and analyzed the light scattering and differential refractive index. We determined the protein concentration from the excess differential refractive index based on dn/dc of 0.186 mg/ml (where dn is the change in refractive

index and dc is the change in concentration). To determine the interdetector delay volumes, band-broadening constants, and the detector intensity normalization constants for the instrument, we used bovine serum albumin as a standard before sample measurement.

X-ray crystallography

All crystallization trials were performed with 15 to 20 mg/ml of protein, and the sample buffer was supplemented with 10 mM $MgCl_2$. AncPURPLE crystallized with 1.2 times excess UMP and BsPyrR with 2 times excess GMP. AncGREENPyrR and BsPyrR were additionally supplemented with 400 mM $(NH_4)_2SO_4$ to obtain crystals. We set up 100-nl protein-drop crystallization trials with the in-house MRC Laboratory of Molecular Biology screen (42). We collected the x-ray diffraction data at the Diamond Synchrotron (Oxford, UK). The data were processed in the CCP4 suite (43). See the supplementary materials for details on crystallization conditions and data processing. All of the structures were solved using molecular replacement with Phaser (44), rebuilt with Coot (45), and refined with Refmac5 (46).

Structural superpositions and intersubunit geometry comparisons

Intersubunit geometries of all PyrR structures (Fig. 4 and fig. S8) were compared as described previously in (5) and are illustrated in fig. S1. We superimposed individual subunits using a sieve-fit approach, described by Arthur Lesk, used notably in (47), and implemented more recently in the Bio3D package for R (48). With sieve-fit, subunits are structurally aligned using only residues that are superposable with a RMSD below 0.5 Å. These residues then define the structural core of the subunit with its corresponding center of mass. We first sieve-fit only subunit A of the complex and then re-sieve-fit the B subunit, noting how much the center of mass needs to deviate from its original position (as an angle of rotation and vector of translation).

Normal mode analysis

We studied the intrinsic dynamics of all PyrR proteins for which we had high-quality structures (meaning solved to a high resolution and not having more than a few residues missing from the structure). These structures were AncORANGE-PyrR, VIOLETPyrR, PLUMPyrR, and PURPLE-PyrR with UMP, as well as the wild-type *B. subtilis* PyrR with and without GMP. We performed the calculations, using the $C\alpha$ atom elastic network model implemented in the Molecular Modeling ToolKit (49), on the dimeric units (dimers and halves of tetramers). The GMP and UMP ligands were modeled into the *B. subtilis* PyrR and the PURPLEPyrR structures by placing dummy nodes at the C4', N9, and N1 or C4', N1, and C4 positions of the bound nucleotides in both subunits, respectively.

To compare the intrinsic dynamics of these structures, we used a structural alignment obtained from MUSTANG (50). The BC (31, 51) was used as a measure of similarity in flexibility, with

a score from 0 (completely dissimilar) to 1 (identical). Furthermore, the correlation matrices were calculated from the 100 lowest-frequency modes (52). (For more details, refer to the supplementary materials.) The conformational overlap analysis of BsPyrR and BsPyrR+GMP, as well as AncORANGE-PyrR with PLUMPyrR and VIOLETPyrR, to obtain the modes that contribute to the transition from the tetrameric state to the dimeric state was done according to Reuter *et al.* (35). We calculated overlaps between the modes of dimeric halves of tetramers and the structural difference vectors between the dimeric half of the tetramer and the corresponding dimer.

Thermostability

We estimated the thermostability of the PyrR proteins by measuring the CD 210- to 260-nm spectrum of each protein over a range of temperatures (from 20° to 90°C). We heated the proteins gradually and continuously (0.2°C per min) and collected the spectrum every 5°C. The proteins were measured at an approximate concentration of 5 μ M. All measurements were done on a Chirascan CD Spectrometer (AppliedPhotophysics). Mean residue ellipticity for each protein at each 5°C temperature point was calculated as the degrees of CD corrected by exact protein concentration and the length of the protein (number of amino acids).

REFERENCES AND NOTES

- N. Tokuriki, D. S. Tawfik, Stability effects of mutations and protein evolvability. *Curr. Opin. Struct. Biol.* **19**, 596–604 (2009). doi: [10.1016/j.sbi.2009.08.003](#); pmid: [19765975](#)
- S. J. Gould, R. C. Lewontin, The spandrels of San Marco and the Panglossian paradigm: A critique of the adaptationist programme. *Proc. R. Soc. London Ser. B* **205**, 581–598 (1979). doi: [10.1098/rspb.1979.0086](#); pmid: [42062](#)
- M. Kaltenbach, N. Tokuriki, Dynamics and constraints of enzyme evolution. *J. Exp. Zool. B Mol. Dev. Evol.* **322**, 468–487 (2014). doi: [10.1002/jez.b.22562](#); pmid: [24522979](#)
- D. M. Taverna, R. A. Goldstein, Why are proteins marginally stable? *Proteins* **46**, 105–109 (2002). doi: [10.1002/prot.10016](#); pmid: [11746707](#)
- T. Perica, C. Chothia, S. A. Teichmann, Evolution of oligomeric state through geometric coupling of protein interfaces. *Proc. Natl. Acad. Sci. U.S.A.* **109**, 8127–8132 (2012). doi: [10.1073/pnas.1120028109](#); pmid: [22566652](#)
- M. Karplus, J. Kuriyan, Molecular dynamics and protein function. *Proc. Natl. Acad. Sci. U.S.A.* **102**, 6679–6685 (2005). doi: [10.1073/pnas.0408930102](#); pmid: [15870208](#)
- S. Maguid, S. Fernández-Alberti, G. Parisi, J. Echave, Evolutionary conservation of protein backbone flexibility. *J. Mol. Evol.* **63**, 448–457 (2006). doi: [10.1007/s00239-005-0209-x](#); pmid: [17021932](#)
- E. Juritz, N. Palopoli, M. S. Fornasari, S. Fernandez-Alberti, G. Parisi, Protein conformational diversity modulates sequence divergence. *Mol. Biol. Evol.* **30**, 79–87 (2013). doi: [10.1093/molbev/ms080](#); pmid: [22396525](#)
- C. L. Turnbough Jr., R. L. Switzer, Regulation of pyrimidine biosynthetic gene expression in bacteria: Repression without repressors. *Microbiol. Mol. Biol. Rev.* **72**, 266–300 (2008). doi: [10.1128/MMBR.00001-08](#); pmid: [18535147](#)
- E. R. Bonner, J. P. D'Elia, B. K. Billips, R. L. Switzer, Molecular recognition of *pyr* mRNA by the *Bacillus subtilis* attenuation regulatory protein PyrR. *Nucleic Acids Res.* **29**, 4851–4865 (2001). doi: [10.1093/nar/29.23.4851](#); pmid: [11726695](#)
- C. M. Jørgensen *et al.*, *pyr* RNA binding to the *Bacillus caldolyticus* PyrR attenuation protein – characterization and regulation by uridine and guanosine nucleotides. *FEBS J.* **275**, 655–670 (2008). doi: [10.1111/j.1742-4658.2007.06227.x](#); pmid: [18190533](#)
- S. Maass *et al.*, Efficient, global-scale quantification of absolute protein amounts by integration of targeted mass spectrometry and two-dimensional gel-based proteomics. *Anal. Chem.* **83**, 2677–2684 (2011). doi: [10.1021/ac1031836](#); pmid: [21395229](#)
- H. K. Savacool, R. L. Switzer, Characterization of the interaction of *Bacillus subtilis* PyrR with *pyr* mRNA by site-directed mutagenesis of the protein. *J. Bacteriol.* **184**, 2521–2528 (2002). doi: [10.1128/JB.184.9.2521-2528.2002](#); pmid: [11948166](#)
- M. J. Harms, J. W. Thornton, Analyzing protein structure and function using ancestral gene reconstruction. *Curr. Opin. Struct. Biol.* **20**, 360–366 (2010). doi: [10.1016/j.sbi.2010.03.005](#); pmid: [20413295](#)
- Single-letter abbreviations for the amino acid residues are as follows: A, Ala; C, Cys; D, Asp; E, Glu; F, Phe; G, Gly; H, His; I, Ile; K, Lys; L, Leu; M, Met; N, Asn; P, Pro; Q, Gln; R, Arg; S, Ser; T, Thr; V, Val; W, Trp; and Y, Tyr.
- J. T. Bridgman, E. A. Ortlund, J. W. Thornton, An epistatic ratchet constrains the direction of glucocorticoid receptor evolution. *Nature* **461**, 515–519 (2009). doi: [10.1038/nature08249](#); pmid: [19779450](#)
- L. I. Gong, M. A. Suchard, J. D. Bloom, Stability-mediated epistasis constrains the evolution of an influenza protein. *eLife* **2**, e00631 (2013). doi: [10.7554/eLife.00631](#); pmid: [23682315](#)
- J. K. Hobbs *et al.*, On the origin and evolution of thermophily: Reconstruction of functional precambrian enzymes from ancestors of *Bacillus*. *Mol. Biol. Evol.* **29**, 825–835 (2012). doi: [10.1093/molbev/msr253](#); pmid: [21998276](#)
- U. J. Heinen, W. Heinen, Characteristics and properties of a caldo-active bacterium producing extracellular enzymes and two related strains. *Arch. Mikrobiol.* **82**, 1–23 (1972). doi: [10.1007/BF00424925](#); pmid: [5025356](#)
- P. D. Williams, D. D. Pollock, B. P. Blackburne, R. A. Goldstein, Assessing the accuracy of ancestral protein reconstruction methods. *PLoS Comput. Biol.* **2**, e69 (2006). doi: [10.1371/journal.pcbi.0020069](#); pmid: [16789817](#)
- M. Robinson-Rechavi, A. Alibés, A. Godzik, Contribution of electrostatic interactions, compactness and quaternary structure to protein thermostability: Lessons from structural genomics of *Thermotoga maritima*. *J. Mol. Biol.* **356**, 547–557 (2006). doi: [10.1016/j.jmb.2005.11.065](#); pmid: [16375925](#)
- S. Fukuchi, K. Nishikawa, Protein surface amino acid compositions distinctively differ between thermophilic and mesophilic bacteria. *J. Mol. Biol.* **309**, 835–843 (2001). doi: [10.1006/jmbi.2001.4718](#); pmid: [11399062](#)
- P. Chander *et al.*, Structure of the nucleotide complex of PyrR, the *pyr* attenuation protein from *Bacillus caldolyticus*, suggests dual regulation by pyrimidine and purine nucleotides. *J. Bacteriol.* **187**, 1773–1782 (2005). doi: [10.1128/JB.187.5.1773-1782.2005](#); pmid: [15716449](#)
- D. R. Tomchick, R. J. Turner, R. L. Switzer, J. L. Smith, Adaptation of an enzyme to regulatory function: Structure of *Bacillus subtilis* PyrR, a *pyr* RNA-binding attenuation protein and uracil phosphoribosyltransferase. *Structure* **6**, 337–350 (1998). doi: [10.1016/S0969-2126\(98\)00036-7](#); pmid: [9551555](#)
- G. Amitai *et al.*, Network analysis of protein structures identifies functional residues. *J. Mol. Biol.* **344**, 1135–1146 (2004). doi: [10.1016/j.jmb.2004.10.055](#); pmid: [15544817](#)
- V. Soundararajan, R. Raman, S. Raguram, V. Sasisekharan, R. Sasisekharan, Atomic interaction networks in the core of protein domains and their native folds. *PLoS ONE* **5**, e9391 (2010). doi: [10.1371/journal.pone.0009391](#); pmid: [20186337](#)
- A. J. Venkatakrishnan *et al.*, Molecular signatures of G-protein-coupled receptors. *Nature* **494**, 185–194 (2013). doi: [10.1038/nature11896](#); pmid: [23407534](#)
- X. Zhang, T. Perica, S. A. Teichmann, Evolution of protein structures and interactions from the perspective of residue contact networks. *Curr. Opin. Struct. Biol.* **23**, 954–963 (2013). doi: [10.1016/j.sbi.2013.07.004](#); pmid: [23890840](#)
- E. Dellus-Gur, A. Tóth-Petroczy, M. Elias, D. S. Tawfik, What makes a protein fold amenable to functional innovation? Fold polarity and stability trade-offs. *J. Mol. Biol.* **425**, 2609–2621 (2013). doi: [10.1016/j.jmb.2013.03.033](#); pmid: [23542341](#)
- K. Hinsen, A. J. Petrescu, S. Dellerue, M. C. Bellissent-Funel, G. R. Kneller, Harmonicity in slow protein dynamics. *Chem. Phys.* **261**, 25–37 (2000). doi: [10.1016/S0301-0104\(00\)00222-6](#)
- E. Fuglebak, J. Echave, N. Reuter, Measuring and comparing structural fluctuation patterns in large protein datasets. *Bioinformatics* **28**, 2431–2440 (2012). doi: [10.1093/bioinformatics/bts445](#); pmid: [22796957](#)
- J. Echave, Evolutionary divergence of protein structure: The linearly forced elastic network model. *Chem. Phys. Lett.* **457**, 413–416 (2008). doi: [10.1016/j.cplett.2008.04.042](#)
- A. Leo-Macias, P. Lopez-Romero, D. Luypan, D. Zerbino, A. R. Ortiz, An analysis of core deformations in protein superfamilies. *Biophys. J.* **88**, 1291–1299 (2005). doi: [10.1529/biophysj.104.052449](#); pmid: [15542556](#)

34. F. Raimondi, M. Orozco, F. Fanelli, Deciphering the deformation modes associated with function retention and specialization in members of the Ras superfamily. *Structure* **18**, 402–414 (2010). doi: [10.1016/j.str.2009.12.015](https://doi.org/10.1016/j.str.2009.12.015); pmid: [20223222](https://pubmed.ncbi.nlm.nih.gov/20223222/)
35. N. Reuter, K. Hinsen, J.-J. Lacapère, Transconformations of the SERCA1 Ca-ATPase: A normal mode study. *Biophys. J.* **85**, 2186–2197 (2003). doi: [10.1016/S0006-3495\(03\)74644-X](https://doi.org/10.1016/S0006-3495(03)74644-X); pmid: [14507684](https://pubmed.ncbi.nlm.nih.gov/14507684/)
36. F. Tama, Y. H. Sanejouand, Conformational change of proteins arising from normal mode calculations. *Protein Eng.* **14**, 1–6 (2001). doi: [10.1093/protein/14.1.1](https://doi.org/10.1093/protein/14.1.1); pmid: [11287673](https://pubmed.ncbi.nlm.nih.gov/11287673/)
37. P. Závodszky, J. Kardos, G. A. Svingor, G. A. Petsko, Adjustment of conformational flexibility is a key event in the thermal adaptation of proteins. *Proc. Natl. Acad. Sci. U.S.A.* **95**, 7406–7411 (1998). doi: [10.1073/pnas.95.13.7406](https://doi.org/10.1073/pnas.95.13.7406); pmid: [9636162](https://pubmed.ncbi.nlm.nih.gov/9636162/)
38. R. C. Edgar, MUSCLE: Multiple sequence alignment with high accuracy and high throughput. *Nucleic Acids Res.* **32**, 1792–1797 (2004). doi: [10.1093/nar/gkh340](https://doi.org/10.1093/nar/gkh340); pmid: [15034147](https://pubmed.ncbi.nlm.nih.gov/15034147/)
39. F. Ronquist, J. P. Huelsenbeck, MrBayes 3: Bayesian phylogenetic inference under mixed models. *Bioinformatics* **19**, 1572–1574 (2003). doi: [10.1093/bioinformatics/btg180](https://doi.org/10.1093/bioinformatics/btg180); pmid: [12912839](https://pubmed.ncbi.nlm.nih.gov/12912839/)
40. J. Felsenstein, Evolutionary trees from DNA sequences: A maximum likelihood approach. *J. Mol. Evol.* **17**, 368–376 (1981). doi: [10.1007/BF01734359](https://doi.org/10.1007/BF01734359); pmid: [7288891](https://pubmed.ncbi.nlm.nih.gov/7288891/)
41. B. H. Zimm, The scattering of light and the radial distribution function of high polymer solutions. *J. Chem. Phys.* **16**, 1093 (1948). doi: [10.1063/1.1746738](https://doi.org/10.1063/1.1746738)
42. D. Stock, O. Perisic, J. Löwe, Robotic nanolitre protein crystallisation at the MRC Laboratory of Molecular Biology. *Prog. Biophys. Mol. Biol.* **88**, 311–327 (2005). doi: [10.1016/j.pbiomolbio.2004.07.009](https://doi.org/10.1016/j.pbiomolbio.2004.07.009); pmid: [15652247](https://pubmed.ncbi.nlm.nih.gov/15652247/)
43. M. D. Winn *et al.*, Overview of the CCP4 suite and current developments. *Acta Crystallogr. D* **67**, 235–242 (2011). doi: [10.1107/S0907444910045749](https://doi.org/10.1107/S0907444910045749); pmid: [21460441](https://pubmed.ncbi.nlm.nih.gov/21460441/)
44. A. J. McCoy *et al.*, Phaser crystallographic software. *J. Appl. Crystallogr.* **40**, 658–674 (2007). doi: [10.1107/S0021889807021206](https://doi.org/10.1107/S0021889807021206); pmid: [19461840](https://pubmed.ncbi.nlm.nih.gov/19461840/)
45. P. Emsley, K. Cowtan, Coot: Model-building tools for molecular graphics. *Acta Crystallogr. D* **60**, 2126–2132 (2004). doi: [10.1107/S0907444904019158](https://doi.org/10.1107/S0907444904019158); pmid: [15572765](https://pubmed.ncbi.nlm.nih.gov/15572765/)
46. G. N. Murshudov *et al.*, REFMAC5 for the refinement of macromolecular crystal structures. *Acta Crystallogr. D* **67**, 355–367 (2011). doi: [10.1107/S0907444911001314](https://doi.org/10.1107/S0907444911001314); pmid: [21460454](https://pubmed.ncbi.nlm.nih.gov/21460454/)
47. M. Gerstein, C. Chothia, Analysis of protein loop closure: Two types of hinges produce one motion in lactate dehydrogenase. *J. Mol. Biol.* **220**, 133–149 (1991). doi: [10.1016/0022-2836\(91\)90387-L](https://doi.org/10.1016/0022-2836(91)90387-L); pmid: [2067013](https://pubmed.ncbi.nlm.nih.gov/2067013/)
48. B. J. Grant, A. P. C. Rodrigues, K. M. ElSawy, J. A. McCammon, L. S. D. Caves, Bio3d: An R package for the comparative analysis of protein structures. *Bioinformatics* **22**, 2695–2696 (2006). doi: [10.1093/bioinformatics/btl461](https://doi.org/10.1093/bioinformatics/btl461); pmid: [16940322](https://pubmed.ncbi.nlm.nih.gov/16940322/)
49. K. Hinsen, The molecular modeling toolkit: A new approach to molecular simulations. *J. Comput. Chem.* **21**, 79–85 (2000). doi: [10.1002/\(SICI\)1096-987X\(20000130\)21:2<79::AID-JCC1>3.0.CO;2-B](https://doi.org/10.1002/(SICI)1096-987X(20000130)21:2<79::AID-JCC1>3.0.CO;2-B)
50. A. S. Konagurthu, J. C. Whisstock, P. J. Stuckey, A. M. Lesk, MUSTANG: A multiple structural alignment algorithm. *Proteins* **64**, 559–574 (2006). doi: [10.1002/prot.20921](https://doi.org/10.1002/prot.20921); pmid: [16736488](https://pubmed.ncbi.nlm.nih.gov/16736488/)
51. E. Fuglebakk, N. Reuter, K. Hinsen, Evaluation of protein elastic network models based on an analysis of collective motions. *J. Chem. Theory Comput.* **9**, 5618–5628 (2013). doi: [10.1021/ct400399x](https://doi.org/10.1021/ct400399x)
52. T. Ichiye, M. Karplus, Collective motions in proteins: A covariance analysis of atomic fluctuations in molecular dynamics and normal mode simulations. *Proteins* **11**, 205–217 (1991). doi: [10.1002/prot.340110305](https://doi.org/10.1002/prot.340110305); pmid: [1749773](https://pubmed.ncbi.nlm.nih.gov/1749773/)

ACKNOWLEDGMENTS

We thank R. L. Switzer (University of Illinois) for the cDNA of *B. subtilis* and *B. caldolyticus* PyrR; E. Natan and D. Gruszka for practical help; C. Vogel, E. Fuglebakk, and N. Tokuriki for helpful discussions and insights; K. Nagai for generous access to his laboratory; and E. Levy, J. Marsh, R. Laskowski, M. Wouters, and B. Lenhard for feedback on the manuscript. Y.K. was supported by the Nakajima Foundation. X.Z. is supported by an Early Postdoc Mobility Fellowship from the Swiss National Science Foundation (grant number PBELP2_143538). J.C. is a Senior Wellcome Trust Research Fellow (grant number 095195). S.P.T. and N.R. are supported by the Bergen Forskningsstiftelse. This work was supported by the MRC, the Lister Research Prize to S.A.T., and a Henry Wellcome Postdoctoral Fellowship to T.P. Coordinates and structural factors have been deposited with the Protein Data Bank (PDB) (accession codes 4P80, 4P81, 4P82, 4P83, 4P84, 4P86, and 4P3K).

SUPPLEMENTARY MATERIALS

www.sciencemag.org/content/346/6216/1254346/suppl/DC1
 Supplementary Methods
 Figs. S1 to S19
 Tables S1 and S2
 References (53–69)
 Movies S1 to S5

3 April 2014; accepted 14 October 2014
 10.1126/science.1254346

RESEARCH ARTICLES

CANCER THERAPY

Patient-derived models of acquired resistance can identify effective drug combinations for cancer

Adam S. Crystal,¹ Alice T. Shaw,¹ Lecia V. Sequist,¹ Luc Friboulet,¹ Matthew J. Niederst,¹ Elizabeth L. Lockerman,¹ Rosa L. Frias,¹ Justin F. Gainor,¹ Arnaud Amzallag,¹ Patricia Greninger,¹ Dana Lee,¹ Anuj Kalsy,¹ Maria Gomez-Caraballo,¹ Leila Elamine,¹ Emily Howe,¹ Wooyoung Hur,^{3,4} Eugene Lifshits,¹ Hayley E. Robinson,² Ryohei Katayama,¹ Anthony C. Faber,¹ Mark M. Awad,¹ Sridhar Ramaswamy,¹ Mari Mino-Kenudson,² A. John Iafrate,² Cyril H. Benes,^{1,*} Jeffrey A. Engelman^{1*}

Targeted cancer therapies have produced substantial clinical responses, but most tumors develop resistance to these drugs. Here, we describe a pharmacogenomic platform that facilitates rapid discovery of drug combinations that can overcome resistance. We established cell culture models derived from biopsy samples of lung cancer patients whose disease had progressed while on treatment with epidermal growth factor receptor (EGFR) or anaplastic lymphoma kinase (ALK) tyrosine kinase inhibitors and then subjected these cells to genetic analyses and a pharmacological screen. Multiple effective drug combinations were identified. For example, the combination of ALK and MAPK kinase (MEK) inhibitors was active in an ALK-positive resistant tumor that had developed a *MAP2K1* activating mutation, and the combination of EGFR and fibroblast growth factor receptor (FGFR) inhibitors was active in an EGFR mutant resistant cancer with a mutation in *FGFR3*. Combined ALK and SRC (pp60c-src) inhibition was effective in several ALK-driven patient-derived models, a result not predicted by genetic analysis alone. With further refinements, this strategy could help direct therapeutic choices for individual patients.

Genotype-based selection of patients for the application of targeted therapies has had a substantial impact on the treatment of cancers. Effective targeted therapies, such as tyrosine kinase inhibitors (TKIs), are widely used to treat patients harboring non-small cell lung cancers (NSCLCs) with activating mutations in *EGFR* (epidermal growth factor receptor) or *ALK* (anaplastic lymphoma kinase) translocations (1–5). However, acquired resistance to these inhibitors eventually develops through a variety of mechanisms, usually within 1 to 2 years [EGFR inhibitors are reviewed in (6) and ALK inhibitors in (7–9)]. In particular, secondary resistance mutations can develop in the oncogene preventing target inhibition by the corresponding TKI (e.g., EGFR T790M or ALK L1196M). Alternatively, resistant cells can develop a compensatory signaling pathway, or

“bypass track,” that reestablishes activation of key downstream proliferation and survival signals despite inhibition of the original oncogene [reviewed in (10)]. As more drugs are developed that effectively overcome secondary resistance mutations in the targeted genes, these bypass track mechanisms of resistance will likely continue to emerge in the clinical setting.

Current efforts to understand resistance often center on two different strategies. One approach is to model the development of resistance in vitro using sensitive cell line models that are exposed to a specific targeted therapy until resistance emerges. A second approach focuses on the genetic analyses of resistant biopsies to identify new genetic anomalies that could be driving resistance. However, both approaches have deficiencies. Although the in vitro-derived resistant cells are amenable to functional studies, it is unknown which models are clinically relevant, and they could never be used to inform treatment decisions for individual patients. Furthermore, there are few genetically appropriate cell lines in existence that could be used to develop such resistant models (e.g., there are less than 10 existing *EGFR* mutant and less than 5 *EML4-ALK* cell lines). Thus, these lines may model only a subset of potential resistance mechanisms. In contrast, studying the genetics of resistant

biopsies has the advantage that the discovered genetic alterations actually occurred clinically. These studies can facilitate the development of hypotheses about what is causing resistance, and even speculation as to how one might treat individual patients. However, since the tissue is nonviable, such hypotheses cannot be directly tested on the resistant tumor cells. Furthermore, many resistant cancers do not harbor genetic abnormalities that clearly point to a treatment strategy. In this study, we describe a discovery platform that integrates the genetics of cancers with acquired resistance with pharmacologic interrogation of cell lines systematically developed from those same resistant patient tumors. This permits the discovery and evaluation of therapeutic strategies for clinically relevant mechanisms of resistance.

Establishment of resistant cell lines from clinical specimens

The ability to develop cell lines directly from patient specimens has been facilitated by recent technological advances, including methodologies developed by Schlegel and colleagues using irradiated feeder cells (11). As shown in table S1, NSCLC cell lines were developed with a ~50% success rate from patient samples (effusions and biopsies), including a 38% success rate from biopsy samples. Of note, the majority of the failures were associated with low cancer cellularity in the sample (see below). For many of these samples, cell viability was established on feeder cells and then transitioned off those cells before characterization and screening. As shown in table S2, the oncogenic mutation (*EGFR* or *ALK*) present in the patient tumor was reliably identified in the derived cell line.

To identify effective drug combinations in these patient-derived models of acquired resistance, we built upon previous work identifying bypass track mechanisms of acquired resistance (10). In this type of resistance, the original driver oncogene and a secondary bypass track redundantly maintain downstream signaling, such as the phosphatidylinositol 3-kinase (PI3K) and mitogen-activated protein kinase (MAPK) pathways, to promote cell survival and proliferation. These cancers are resistant to single-agent inhibition of the primary driver oncogene and are similarly resistant to single-agent inhibition of the acquired bypass track because, in either case, the untargeted pathway maintains downstream signaling. However, simultaneous inhibition of both pathways suppresses downstream signaling, resulting in growth arrest and cell death (fig. S1A) (12–15). Thus, drugs targeting relevant bypass tracks are effective when administered in combination with an inhibitor of the primary driver oncogene but relatively impotent when administered as single agents (fig. S1B). Based on this principle, to discover effective therapeutic strategies and gain insight into the underlying mechanisms of resistance, we performed a screen that combined the original TKI (targeting the driving oncogene) with each of the drugs in an established panel.

¹Massachusetts General Hospital Cancer Center, Department of Medicine and Harvard Medical School, Boston, MA 02114, USA. ²Massachusetts General Hospital Cancer Center, Department of Pathology and Harvard Medical School, Boston, MA 02114, USA. ³Dana-Farber Cancer Institute, Department of Biological Chemistry and Molecular Pharmacology and Harvard Medical School, Boston, MA 02115, USA. ⁴Chemical Kinomics Research Center, Korea Institute of Science and Technology, Seoul, 136-791, South Korea.

*Corresponding author. E-mail: jengelman@partners.org (J.A.E.); cbenes@partners.org (C.H.B.)

We assembled a panel of 76 targeted agents (table S3) directed against a range of key regulators of cell proliferation and survival, including growth factor and development signaling pathways, apoptosis regulators, transcription and protein folding machinery, and DNA damage sensors (table S4). This drug panel included inhibitors of previously identified bypass tracks, as well as several additional clinical targets. The potency of each drug was tested across a 10,000-fold range both in the presence and absence of a fixed concentration of the primary TKI (fig. S2A). Resultant changes in GI50 (the drug concentration necessary to obtain 50% less cells than in the untreated condition) and AUC (area under the dose-response curve) were determined after addition of the primary TKI.

To evaluate the potential of our strategy, we initially examined five previously established models of acquired resistance developed in vitro (i.e., by chronically exposing sensitive cells to TKI in vitro) with known resistance bypass tracks. In these models, the known mechanisms of resistance were identified by our approach with high specificity: For example, in a previously characterized *EGFR* mutant cell line with *MET* amplification (12), the *MET* inhibitors were the sole hits identified in the screen (fig. S2, B and C). In four tested cell lines [HCC827 GR6 (13), HN11 GR (16), SNU638 C1 (17), and H3122 PFR3 (7)], drugs that target known bypass tracks were among those producing the largest shifts in GI50 and AUC (fig. S3, A to D). In the fifth

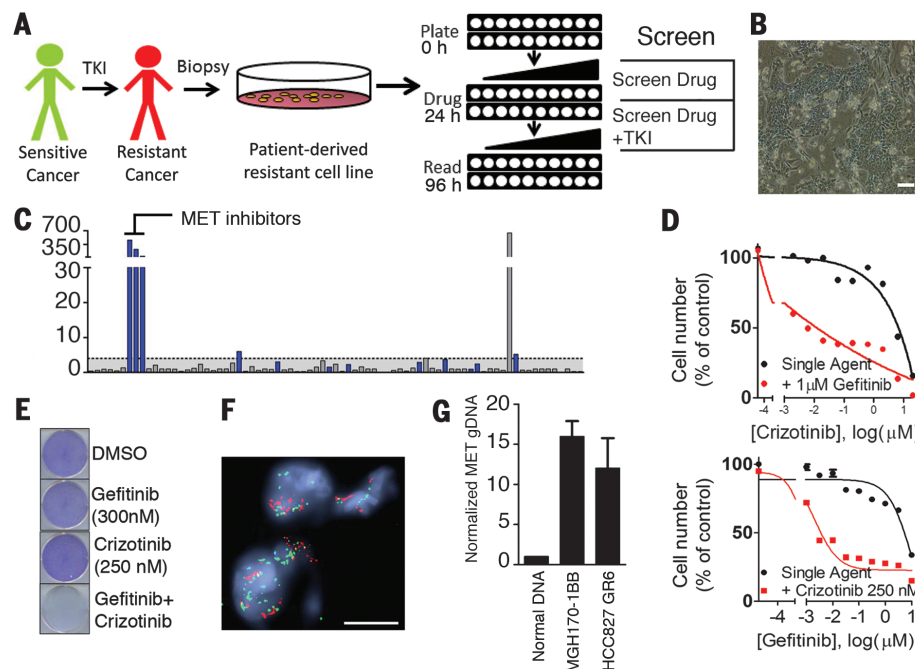
model [A431 GR (16)], the effect of insulin-like growth factor receptor 1 (IGFR1) inhibitors was less marked but recapitulated the previously observed combination effect (fig. S3E). Thus, in these previously investigated models, unbiased screening of a 76-drug panel successfully identified inhibitors of the known bypass tracks. We therefore applied the approach to 55 models of acquired resistance with unknown mechanisms of resistance. Twenty of these models were derived directly from patients who had progressed on either an ALK inhibitor ($n = 9$ models) or an *EGFR* inhibitor ($n = 11$ models). The remaining lines were derived in vitro (table S5). To compare the information yielded by genetic analysis to the pharmacologic interrogation, patient-derived models were also analyzed by next-generation sequencing to identify potential genetic causes of resistance (tables S6 and S7 and databases S1 and S2).

Effective drug combinations in patient-derived resistant NSCLC models

Each of the 55 models of acquired resistance was tested against the panel of 76 compounds in the presence or absence of the inhibitor of the primary target as described above (schema in Fig. 1A). For patient-derived resistance models with gatekeeper resistance mutations in the driver oncogene (i.e., *EGFR* or *ALK*), next-generation inhibitors that overcome those mutations were used as the primary TKI in the combination screen. The results from the initial screening were

analyzed to determine the specific thresholds of GI50 and AUC changes most likely to yield a strong effect on viability and maximize the potential for in vivo efficacy (see Materials and Methods and databases S2 to S4). The process of screening and evaluating hits is demonstrated for the cell line MGH170-1BB in Fig. 1, A to C. These cells were derived from a patient with an *EGFR* mutant lung cancer who had become resistant to multiple lines of *EGFR* TKIs (table S2 and Fig. 1B). The screen clearly identified *MET* inhibitors as hits (Fig. 1C), and *MET* inhibitors effectively resensitized these resistant cells to *EGFR* inhibition (Fig. 1D, top, screen format; bottom, dose response to gefitinib as a single agent or in the presence of a fixed concentration of the *MET* inhibitor crizotinib). The combination of *EGFR* and *MET* inhibitors was synergistic across a range of concentrations tested, with an average of 25% lower viability than predicted by the Bliss independence model for the nine concentrations tested (see table S8 for synergy calculations). Indeed, *EGFR* and *MET* inhibitor combination therapy was effective in eliminating resistant cells (Fig. 1E). Subsequent assessment of a paraffin-embedded biopsy from this patient's cancer demonstrated clear evidence of *MET* amplification (Fig. 1G), and quantitative polymerase chain reaction (PCR) performed on the corresponding MGH170-BB cell line confirmed *MET* amplification (Fig. 1H). Thus, the unbiased pharmacologic interrogation of the cells derived from the patient specimen

Fig. 1. Screen schematic and proof of concept in a patient-derived cell line. (A) Schematic of the screen workflow. Cell line models of acquired resistance were obtained directly from biopsies of patients after the development of acquired resistance to either *EGFR* inhibitor or *ALK* inhibitor in the clinic. Screen drugs were tested as a single agent and in the presence of a single fixed concentration of the primary TKI across 10 concentrations encompassing a 10,000-fold dilution range. After 72 hours, cell viability was determined with CellTiter-Glo. (B) Phase-contrast microscopy of cell line MGH170-1BB, derived from an *EGFR* mutant lung cancer metastatic lesion with acquired resistance to *EGFR* inhibitors. Scale bar, 100 μ m. (C) Representation of screen data for the MGH170-1BB cell line. The y axis represents the fold-change GI50 that resulted with the addition of gefitinib (GI50 single agent/GI50 combination). Each bar is the result for an individual drug. The bars are color-coded blue when the percentage of decrease in AUC from single agent to combination was greater than 10%. Drugs were defined as "hits" when the GI50 shift was > 4 and the AUC change $> 10\%$ (see Materials and Methods). (D) (Top) The *MET* inhibitor crizotinib was more potent in combination with 1 μ M gefitinib (in red) than as a single agent (in black). (Bottom) Crizotinib (1 μ M) resensitizes the MGH170-1BB cells to gefitinib. Error bars, mean \pm SEM. (E) Long-term proliferation assay of MGH170-1BB cells that had been exposed to the indicated drug for 7 days. Cells were stained using crystal violet. (F) Fluorescence in situ hybridization analysis of a biopsy sample from a metastatic bone lesion obtained after the patient had



unequivocally indicated the combination treatment supported by genetic analyses of the patient specimen.

In some instances, pharmacologic interrogation permitted evaluation of the functional relevance of uncharacterized genetic variants. For example, a previously undescribed *FGFR3* variant was identified as a key contributor to resistance in the MGH156-1A cell line derived from a patient with acquired resistance to EGFR TKIs (fig. S4A and table S6). The screen and subsequent follow-up studies clearly indicated that fibroblast growth factor receptor (FGFR) inhibitors resensitized these cells to EGFR inhibitors. The combination also suppressed key signaling events known to regulate proliferation and survival (fig. S4, B to E). Genetic analyses of both the cell line and corresponding biopsy revealed an *FGFR3* mutation, Y649C, located in the tyrosine kinase domain (table S6). Although this *FGFR3* mutation has not been observed previously (www.cbioportal.org/public-portal), it is adjacent to a recurring activating mutation in the kinase domain. Thus, in this model, combining genetic analysis of tumor material and pharmacologic evaluation of cells from the resistant tumor allowed for the identification of actionable therapeutic strategies. Furthermore, this finding demonstrates that FGFR activation is a bona fide mechanism of acquired resistance to EGFR inhibition in this patient.

Among the 60 models screened, 201 hits were identified, for a mean of 3.4 hits per cell line (range 0 to 12). At least one hit was identified in 50 of 60 cell lines (fig. S5 and Fig. 2A). Drugs known to have overlapping specificity were found to have overlapping activity across cell lines, demonstrating robustness of the data set (see, for example, aurora kinase, SRC, and MET inhibitors in Fig. 2, A and B, and fig. S5). Notably, EGFR inhibitors tended to be hits in both ALK- and MET-driven resistant lines, consistent with previously published reports (7, 17). Because re-activation of the PI3K pathway via activating *PIK3CA* mutations and bypass receptor tyrosine kinases (RTKs) has commonly been observed in cancers with acquired resistance (18), it was not surprising that PI3K inhibitors were hits in a subset of resistant cell lines. Importantly, genetic analyses of the cell lines were insufficient to inform which cancers would be sensitive to this combination. Notably, PI3K inhibitors were not sufficient to resensitize to the original TKI in the majority of models tested (Fig. 2A and fig. S5). Other unanticipated drug combinations were identified. In particular, aurora kinase inhibitors were active in combination with EGFR inhibition in a number of *EGFR*-mutant cell lines. Similarly, the Polo-like kinase (PLK) inhibitor (BI2536) was a hit in five EGFR-driven lines. The complete hit profile of each resistant cell line is presented in fig. S6. In the *in vitro* models of acquired resistance (which have a paired sensitive, “parental” cell line from which the resistant cells were derived), we also sought to determine whether resistant models had

developed increased sensitivity to any single-agent treatments compared with the parental cell lines (fig. S7). This analysis revealed that, in the vast majority of cases, resistant models did not acquire sensitivity to single-agent therapies, further supporting the notion of developing combination therapies (fig. S7).

Identification of mechanisms of resistance and combination therapies for ALK-positive lung cancers

Assessment of the patient-derived ALK-positive models identified previously undescribed mechanisms of resistance. The MGH034-2A cell line was derived from a biopsy of a patient harboring an ALK-positive cancer that had become resistant to ceritinib (LDK378), a second-generation ALK inhibitor that was recently approved by the FDA (19, 20) (Fig. 3A). The MAPK kinase (MEK) inhibitor, AZD6244, was a potent hit in combination with ceritinib [Fig. 3, B and C, left panel; synergistic effect with on average 45% less viability than predicted by Bliss (table S8)]. Furthermore, AZD6244 treatment also led to marked resensitization to ceritinib in MGH034-2A (Fig. 3C, right panel). To our knowledge, there have been no previous reports demonstrating that MEK inhibitors resensitize resistant ALK-positive cancer cells to an ALK inhibitor. Furthermore, MEK inhibitor sensitization was not observed in any of the other ALK-positive patient-derived or laboratory-derived models examined in this study (fig. S8A), illustrating the

potential for the present approach to identify patient-specific efficacious combinations. Long-term viability assays revealed that the combination had a potent effect on cell viability, with a marked net decrease in cell number compared to the cell number before drug treatment (Fig. 3D). Accordingly, the combination was required to inhibit PI3K, MAPK, and mammalian target of rapamycin complex (mTORC) activity, as well as to up-regulate BIM (Bcl-2 interacting mediator of cell death) and promote substantial apoptosis (14) (Fig. 3E and fig. S8B). *In vivo*, neither single agent was effective, but the combination resulted in robust tumor regression (Fig. 3F). Importantly, next-generation sequencing (NGS) analysis of the cell line revealed a MAP2K1 K57N mutation (table S7), which has previously been reported as a MEK-activating event in lung adenocarcinoma (21), although neither in conjunction with an activating RTK mutation nor in the setting of acquired resistance to any TKI. Notably, this cell line also harbored a JAK3 V722I variant, an activated allele of JAK3 (22). Despite this, the JAK3 specific inhibitor tofacitinib was not a screen hit (fig. S5) and, furthermore, did not resensitize MGH034-2A cells or other ALK-positive mutant cell lines to ALK inhibition (fig. S9A). Indeed, these cells did not express appreciable levels of JAK3 (fig. S9, B and C). This patient subsequently died, and NGS analysis of 10 resistant lesions acquired at autopsy demonstrated that the MAP2K1 K57N mutation was present in 7 of the 11 lesions (of

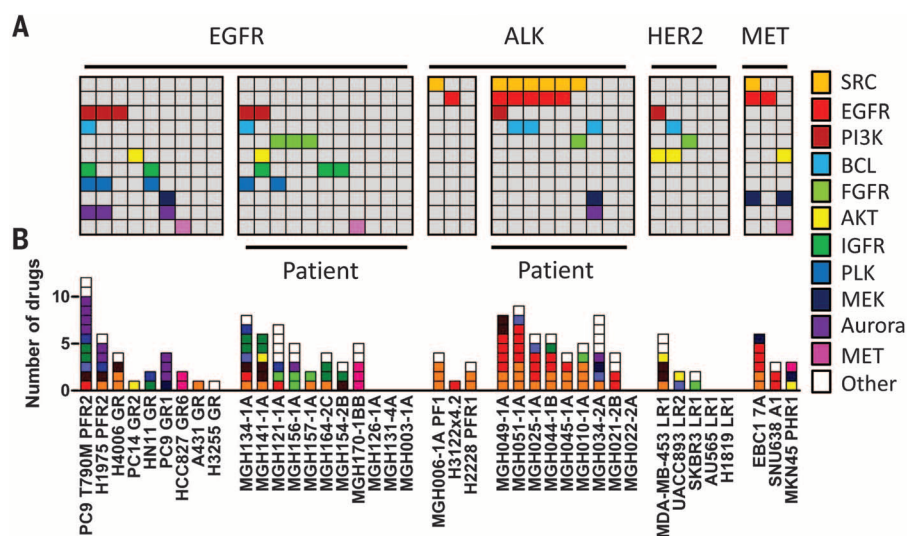


Fig. 2. Representation of selected screen hits in independent resistant models. (A) The patterns of hits across cell lines harboring the indicated oncogene are shown. Each column represents a cell line, and each row represents a target inhibited by the following drugs: Afatinib (EGFR), AZD0530 (SRC), BYL719 (PI3K), ABT-263 [B cell lymphoma (BCL)-2 family], Dovitinib or BGJ-398 (FGFR), MK2206 (AKT), OSI906 (IGFR), BI2536 (PLK), AZD6244 (MEK), AZD1152-HQPA (Aurora kinase B), and MGCD265 (MET). Each drug is color-coded as indicated. (B) The number and profile of all hit drugs for each model. Each box represents a single drug, and the drugs are color-coded by target. The white boxes indicate a hit that corresponds to a drug that is not among the targets listed. For resistant lines derived from a single parental line, only one representative model is presented except in the case of PC9, for which PC9 GR1 and PC9 GR2 are both presented due to the presence of a T790M mutation in PC9 GR2 only.

note, a PIK3CA mutation was identified in one of the other lesions) (Fig. 3H). Importantly, the MAP2K1 K57N mutation was found in the lesions that were rapidly progressing and led to respiratory failure, which caused the patient's death. The autopsy revealed that the JAK3 mutation was a germline variant, supporting the functional data that JAK3 activity was not driving resistance. These results suggest that a combination of MEK and ALK inhibitors may have provided a therapeutic benefit to this patient had these drugs been administered after the cancer had acquired resistance to ceritinib. Importantly, these results also suggest that functional assessment adds information to that provided by genetic analysis alone. Genetic profiling of the tumor alone, as is often performed in the clinic, would not have discriminated between targeting the MAP2K1 K57N mutation and the less consequential JAK3 V722I mutation.

SRC signaling mediates acquired resistance in ALK-positive NSCLC

Multiple SRC family kinase inhibitors were consistently effective across several patient-derived ALK-positive resistant NSCLC models (Fig. 2). In particular, AZD0530 (saracatinib) was a hit in six of nine patient-derived ALK lines tested (Fig. 2A). Models in which AZD0530 was a screen hit had unremarkable sensitivity to single-agent AZD0530, indicating that, as in other cases, these cell lines have not switched to an

entirely different dependency. On the other hand, these resistant ALK-positive cell lines were highly sensitive to AZD0530 in the presence of ALK inhibitors (Fig. 4A). Drug synergism between AZD0530 and ALK inhibitors was also observed (average of 20% less viability than expected across all concentrations for five models retested in triplicate, with maximum differences ranging from 18 to 45% over Bliss (table S8). Two other drugs (dasatinib and KIN001-113) that potentially inhibit SRC family kinases (SFKs) (23, 24) were often hits in models in which AZD0530 was a hit (Fig. 2B and fig. S5). However, due to the more favorable specificity profile of AZD0530 (25), we used this drug in our subsequent studies. Each model in which AZD0530 was a hit (as indicated by arrows in Fig. 4A) was significantly sensitized to ALK inhibition by AZD0530 (Fig. 4B). Notably, other ALK-positive models also demonstrated shifts in sensitivity, with AZD0530 pointing to the possibility of broad involvement of SRC kinases in ALK inhibitor response. Interestingly, AZD0530 was not a hit in any of the mutant EGFR- or HER2-amplified cancers and in only one of nine MET-amplified cancers (fig. S5).

We next aimed to determine the relevant target of AZD0530. Overexpression of the kinase-dead SRC K295R (26), as well as knockdown of SRC alone with either of two short-hairpin RNAs (shRNAs), effectively recapitulated the effect of AZD0530, demonstrating that among AZD0530 targets, including multiple SFKs, SRC inhibition

is sufficient to resensitize cells to ALK inhibition (Fig. 4C). We observed that multiple ALK-positive models were sensitive to both SRC and EGFR inhibitors when combined with an ALK inhibitor. However, the activity of AZD0530 does not appear to be driven by EGFR inhibition directly or indirectly, because AZD0530 did not inhibit EGFR activation in the ALK-positive MGH025-1A cells, which were sensitized by AZD0530 (fig. S10A). Furthermore, some cell lines, such as MGH010-1A, were sensitized by AZD0530 but not EGFR inhibitors (Fig. 2A and fig. S10B). We next examined the effect of combined ALK and SRC inhibition on three resistant ALK-positive models derived from patient biopsies: MGH010-1A and MGH025-A (resistant to crizotinib, no ALK resistance mutations) and MGH049-1A [resistant to ceritinib, no ALK resistance mutations (27)]. In all three models, cells grew at 6 days when treated with either drug as a single agent, but combination treatment resulted in loss of cell viability compared with pretreatment cell number (Fig. 4D) and robust apoptotic cell death (S11A). Consistent with these results, the ALK inhibitor failed to fully inhibit downstream signaling (AKT, MAPK, or S6K) except in the presence of AZD0530 in each of these resistance models (Fig. 5A and fig. S11B).

In each of the patient-derived ALK models in which AZD0530 was effective (including MGH034-2A, which narrowly failed to meet our threshold for hit call for AZD0530), ALK inhibition resulted in robust up-regulation of SRC activity

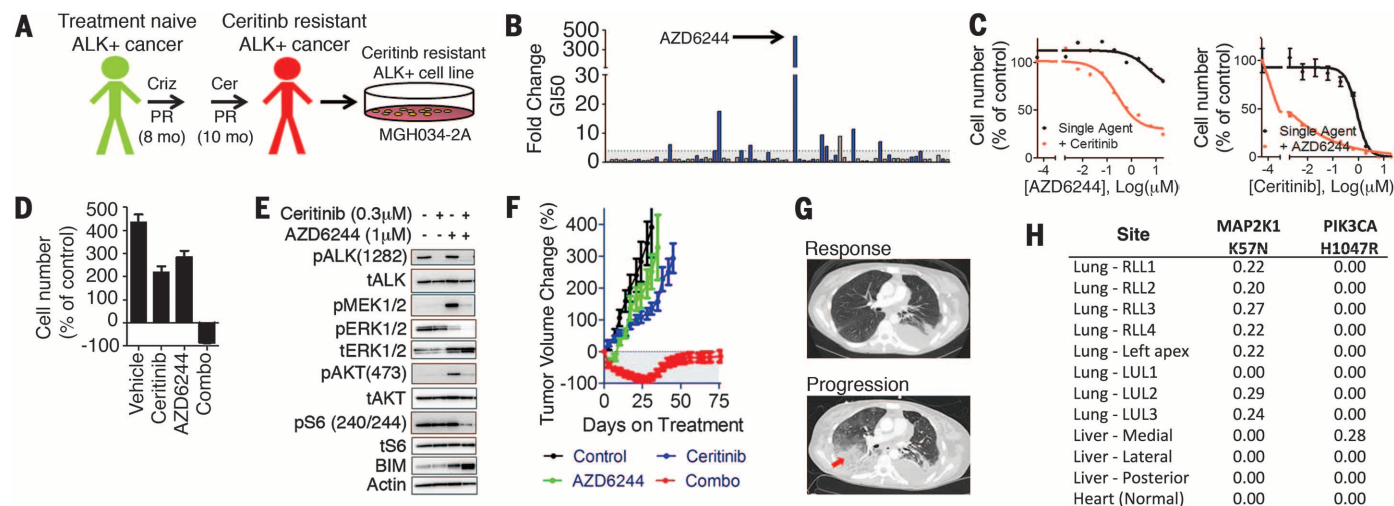


Fig. 3. MEK activation is a mechanism of resistance to ceritinib. (A) Schematic of the derivation of model MGH034-2A. (B) Representation of screen data for the MGH034-2A cell line. The y axis represents the fold-change GI50 that resulted with addition of ceritinib (0.3 μM) (GI50 single agent/GI50 combination). The bars are color-coded blue when the percentage of decrease in AUC from single agent to combination was greater than 10%. (C) (Left) Primary screen data of the effect of ceritinib (0.3 μM) on AZD6244 effect in MGH034-2A. (Right) A dose-response curve to ceritinib is shown in the presence and absence of a fixed concentration of the MEK inhibitor AZD6244 (1 μM). (D) Viability assay of MGH034-2A cells demonstrating the change in cell number after 6 days of treatment with vehicle, ceritinib (300 nM), AZD6244 (1 μM), or the combination of both drugs in comparison with the

number of cells at the initiation of drug exposure. (E) Western blot analysis of MGH034-2A. Cells were treated with vehicle, ceritinib (0.3 μM), AZD6244 (1 μM), or the combination of both drugs for 24 hours. Lysates were analyzed with antibodies to the indicated proteins. (F) Subcutaneous xenografts of MGH034-2A grown in mice were used to determine in vivo efficacy by measuring change in tumor volume when treated as indicated. $n = 6$ mice per group. (G) Axial computed tomography images of the chest demonstrate the patient's disease burden after responding to ceritinib (5.5 weeks on treatment) and at the time of progression on ceritinib (after 9.5 months on treatment). The site of progression in the right lower lobe is indicated by an arrow. (H) Table of allele frequencies for MAP2K1 and PIK3CA mutations discovered at autopsy in the patient.

as measured by the phosphorylation of the SRC substrate Paxillin (Fig. 5B). Thus, ALK inhibition may lead to up-regulation of SRC signaling, perhaps by release of a negative regulatory signal normally coordinating ALK and SRC activities. In contrast, we did not consistently observe an increase in SRC activity as measured by p-Paxillin in EGFR mutant cancers after EGFR inhibitor treatment (fig. S11C), consistent with the absence of efficacy noted with AZD0530 in EGFR mutant cancer. Furthermore, in the *ALK*-positive models, SRC signaling was also up-regulated by inhibition of signaling pathways downstream of ALK. Although the downstream pathways regulated by ALK in individual models vary, the pathway regulated by ALK tended to be the one suppressing SRC signaling. For example, when ALK inhibition primarily affected PI3K signaling but not MEK activity, PI3K inhibition up-regulated SRC signaling (fig. S12A). Moreover, when ALK inhibition suppressed both MAPK and PI3K signaling, SRC signaling was robustly up-regulated by either PI3K or MAPK signaling (fig. S12B). Overall, these results are compatible with a model in which ALK activity suppresses SRC activity broadly in the setting of *ALK*-positive cancers.

To further characterize the effect of ALK inhibition on these models, we performed gene expression analysis on each of the *ALK*-positive patient-derived models in the presence or absence of an ALK inhibitor for 24 hours. The gene ontologies most enriched within genes

whose expression was induced by ALK inhibition were extracellular matrix and basal membrane (Benjamini-Hochberg corrected *P* values 1.75×10^{-4} and 2.31×10^{-4}) (Fig. 5C and data-bases S6 to S8). Because SRC is known to be a focal point of integrin-mediated signaling and the transduction of extracellular signals, these results further support the finding that SRC activity is increased upon inhibition of ALK signaling in *ALK*-positive lung cancers.

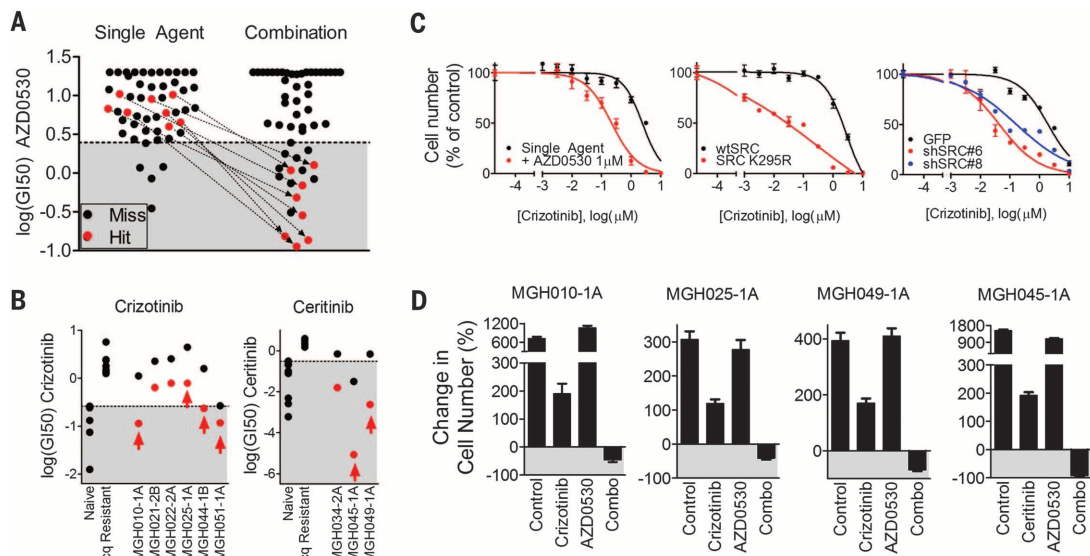
Finally, we tested the efficacy of the combination of ALK TKIs and AZD0530 in vivo using mouse xenograft models. In MGH025-1A (derived from an *ALK*-positive patient who had become resistant to crizotinib), treatment with single-agent crizotinib resulted in tumor progression after 34 days. However, combining AZD0530 and crizotinib resulted in a sustained, profound response for more than 60 days (Fig. 5D). Notably, when AZD0530 was added to the treatment of the xenografts that had progressed on crizotinib, the tumors regressed (fig. S13A). To assess the specificity of AZD0530 for resistant models that demonstrated synergy in the screen, we tested it in the HCC827 GR6 line, which harbors a MET bypass track and was not a hit for AZD0530. In this model, the combination of AZD0530 with gefitinib was ineffective in comparison to gefitinib plus crizotinib (which is a potent MET inhibitor) (fig. S13B). Thus, the effect of AZD0530 appears particular to the models in which combination efficacy was found in the screen.

Because we observed impressive activity of the SFK inhibitors in a large proportion of patient-derived *ALK*-positive resistant models, we also determined whether the combination of ALK inhibitor with AZD0530 might delay the emergence of acquired resistance in a relatively sensitive model. We examined cell line MGH045-1A, a model established from a patient tumor resistant to crizotinib due to the acquisition of a mutation in the ALK kinase domain gatekeeper residue (L1196M) (table S2) (27). Ceritinib, which can overcome the L1196M mutation, was used as the primary TKI in the screen of this cell line, and AZD0530 was a hit (Fig. 2A). The cell line is relatively sensitive to the next-generation ALK inhibitor ceritinib, which can effectively suppress L1196M (27). Over 6 days of treatment in vitro, single-agent ceritinib effectively inhibited growth, but the combination of ceritinib and AZD0530 resulted in near-complete obliteration of cell viability (Fig. 4D). Accordingly, both ALK inhibition and AZD0530 were required to completely suppress key downstream signaling events (fig. S13C). In vivo, single-agent ceritinib slowed tumor growth as previously described (27), but the combination resulted in a more sustained response (fig. S13D). This reinforces the notion that initial treatment combining a SRC and an ALK inhibitor could help induce a more sustained response in patients with *ALK*-positive lung cancer.

Analysis of the discovered mutations identified by the 1000-gene NGS panel in the *ALK*-positive

Fig. 4. SRC inhibition restores sensitivity to ALK inhibitor in multiple models.

(A) Representation of the GI50 of AZD0530 in each screened model as a single agent or in combination with the primary TKI. Models that were hits are color-coded red. The GI50s of cell lines in which AZD0530 scored as hits are connected by an arrow. The shaded area represents the GI50 values among the top 10% sensitive models for single-agent values among all lines screened. (B) GI50 of each *ALK*-positive patient-derived model of acquired resistance to either crizotinib or ceritinib. Control cell line models of sensitivity (MGH006-1A, H3122, SU-DHL-1, KARPAS299, and NB-1) and acquired resistance (MGH006-1A PFR1, MGH006-1A PFR2, H2228 PFR1, H3122 PFR1, H3122 PFR3, and H3122 x4.2) to crizotinib are presented as standards for comparison. Models of sensitivity (H3122, H2228, MGH051-1B, H3122 PFR2, MGH021-2c4, MGH006-1A, MGH026-1A, and MGH039-1A) and acquired resistance (MGH021-5, H3122 LDKR1, H3122 LDKR2, H3122 LDKR2, and H3122 LDKR4) to ceritinib are presented as standards for comparison. The GI50 of each model is presented as a single agent (black) and in combination with AZD0530 (1 μ M) (red). The mean GI50 of the three experiments is presented. Arrows indicate hits identified by the screen. (C) Dose-response curves to crizotinib in model MGH010-1A (crizotinib re-



sistant) are presented. (Left) The dose-response of single-agent crizotinib (black) in the absence or presence of AZD0530 (1 μ M) (red). (Middle) The effect of crizotinib in cells with lentiviral overexpression of either wild-type SRC (black) or kinase-dead SRC (K295R, red). (Right) The effect of lentiviral expression of green fluorescent protein (GFP) (black) or either of two SRC-targeted shRNAs (blue and red). (D) Six-day viability assay of four ALK lines: MGH010-1A, MGH025-1A, MGH049-1A, and MGH045-1A. Each panel presents the percentage of change in cell number after treatment with vehicle, ALK inhibitor (crizotinib 1 μ M or ceritinib 300 nM), AZD0530 (1 μ M), or the combination compared with cell number at the initiation of treatment.

models failed to identify mutations in SRC family kinases and other known regulators of SRC activity (table S7). Thus, the pharmacologic approach identified a drug combination that would not have readily been predicted by DNA sequencing alone.

Discussion

In summary, we have developed cell culture models of acquired resistance to EGFR and ALK inhibition derived directly from patient specimens to rapidly identify combinations that can overcome resistance. These initial studies demonstrated success in developing NSCLC models in 50% of collected specimens. However, we believe that success rates could be further improved by using biopsies acquired specifically for cell line generation. In this study, the biopsies were prioritized for standard pathological analysis, and cell lines were generated from any remaining tissue. As a result, the quality of the specimens was less than ideal. Indeed, in the majority (24 of 39) of the “failures,” the samples we analyzed contained fewer than 20% cancer cells. Despite these obstacles, cell line models were successfully developed in about half of the cases. Thus, if biopsies were isolated primarily

for this purpose, we believe that this methodology could potentially be explored as a diagnostic approach to guide treatment decisions. We also anticipate that this approach will be generalizable to other solid and liquid tumor malignancies.

The robustness of the approach presented here is demonstrated by the success rate of in vivo studies. All five tested models [MGH034-2A (Fig. 3), MGH045-1A (fig. S13), MGH025-1A (Fig. 5D), PC9 PFR2 (fig. S14), and PC9 GR1 (fig. S15)] demonstrated substantial regression in vivo with the discovered active combination. Importantly, this functional assessment of patient-derived samples can provide insights not provided by genetic analysis. For example, the effect of SRC inhibition in resistant *ALK*-positive cancers is not readily predicted by genetic analyses because no mutation was identified in SFKs or their regulators. In addition, our results illustrate how functional assessment of patient-derived cells can complement genetic profiling. For example, FGFR inhibitors were effective in a model with a previously uncharacterized *FGFR3* mutation (fig. S4). In the absence of functional data, the biological consequence of the mutation would have been uncertain.

By interrogating patient-derived models of resistance with this pharmacologic platform, we have discovered several previously undescribed combinations in *EGFR* mutant and *ALK*-positive lung cancers that were validated in follow-up studies and in vivo. We speculate that a similar approach could be explored in the future as a diagnostic test to identify therapeutic strategies for individual patients (under the auspices of an IRB-approved protocol). In the current study, we screened the cells after they became fully established cell lines, which often took 2 to 6 months, a time frame that would make this approach less than ideal as a routine diagnostic test. Nevertheless, the robustness of the results from the current program lays the groundwork for performing screens on viable cells obtained within weeks of a biopsy using newer technologies that would permit screening of the cancer cells while still in the presence of the stroma present in the biopsy. Indeed, it is possible that such functional screens performed on cells derived from a biopsy of a particular patient's resistant cancer might inform the choice of experimental therapies that are most likely to be effective in that patient, advancing toward a future of truly personalized cancer therapy.

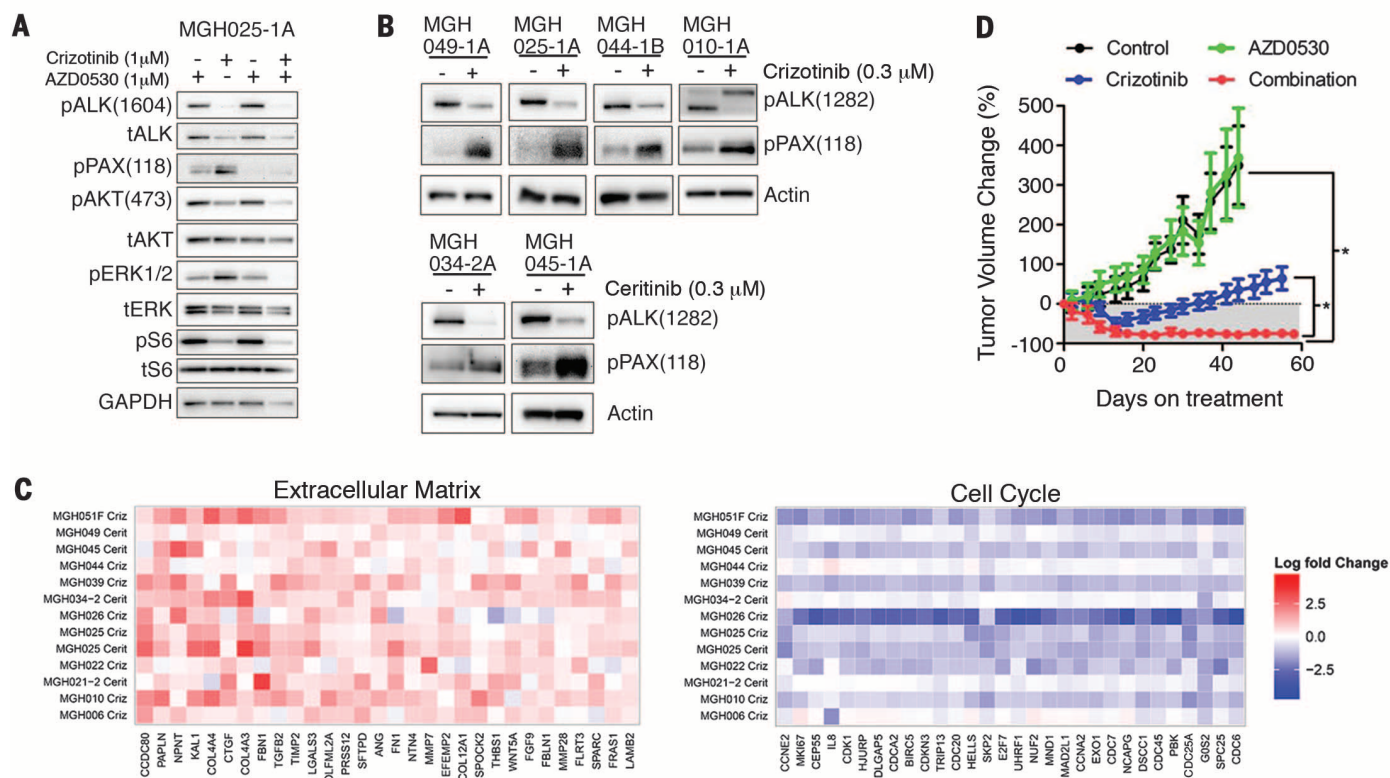


Fig. 5. ALK inhibition and SRC signaling. (A) Western blot analysis of MGH025-1A. Cells were treated with vehicle, crizotinib (1 μM), AZD0530 (1 μM), or the combination of both drugs for 24 hours. Lysates were analyzed with antibodies to the indicated proteins. (B) Western blot analysis of patient-derived resistant *ALK* models treated for 24 hours with crizotinib (300 nM) or ceritinib (300 nM). Lysates were prepared and blotted with the indicated antibodies. (C) Fold-change in gene expression (Log2) upon treatment with the indicated ALK

inhibitor for 24 hours. (Left) Up-regulated genes annotated with the gene ontology (GO) term “extracellular matrix.” (Right) Down-regulated genes annotated with the GO term “cell cycle” (top 30 genes only). (D) MGH025-1A subcutaneous xenografts grown in mice were treated as indicated: vehicle ($n = 4$ mice), crizotinib 25 mg per kg of weight (mg/kg) daily ($n = 6$ mice), AZD0530 50 mg/kg daily ($n = 5$ mice), or the combination of both drugs ($n = 6$ mice). Error bars, mean \pm SEM. * $P < 0.0001$ by Dunn's multiple comparison test.

REFERENCES AND NOTES

1. A. Inoue et al., *J. Clin. Oncol.* **24**, 3340–3346 (2006).
2. E. L. Kwak et al., *N. Engl. J. Med.* **363**, 1693–1703 (2010).
3. R. Rosell et al., *Lancet Oncol.* **13**, 239–246 (2012).
4. L. V. Sequist et al., *J. Clin. Oncol.* **26**, 2442–2449 (2008).
5. A. T. Shaw et al., *Lancet Oncol.* **12**, 1004–1012 (2011).
6. C. R. Chong, P. A. Janne, *Nat. Med.* **19**, 1389–1400 (2013).
7. R. Katayama et al., *Sci. Transl. Med.* **4**, 120ra17 (2012).
8. N. Yamaguchi et al., *Lung Cancer* **83**, 37–43 (2014).
9. J. Tanizaki et al., *Clin. Cancer Res.* **18**, 6219–6226 (2012).
10. M. J. Niederst, J. A. Engelman, *Sci. Signal.* **6**, re6 (2013).
11. X. Liu et al., *Am. J. Pathol.* **180**, 599–607 (2012).
12. J. A. Engelman et al., *Nat. Med.* **14**, 1351–1356 (2008).
13. J. A. Engelman et al., *Science* **316**, 1039–1043 (2007).
14. A. C. Faber et al., *Proc. Natl. Acad. Sci. U.S.A.* **106**, 19503–19508 (2009).
15. M. L. Sos et al., *Proc. Natl. Acad. Sci. U.S.A.* **106**, 18351–18356 (2009).
16. M. Guix et al., *J. Clin. Invest.* **118**, 2609–2619 (2008).
17. J. Qi et al., *Cancer Res.* **71**, 1081–1091 (2011).
18. L. V. Sequist et al., *Sci. Transl. Med.* **3**, 75ra26 (2011).
19. T. H. Marsilje et al., *J. Med. Chem.* **56**, 5675–5690 (2013).
20. A. T. Shaw et al., *N. Engl. J. Med.* **370**, 1189–1197 (2014).
21. J. L. Marks et al., *Cancer Res.* **68**, 5524–5528 (2008).
22. D. K. Walters et al., *Cancer Cell* **10**, 65–75 (2006).
23. M. W. Karaman et al., *Nat. Biotechnol.* **26**, 127–132 (2008).
24. U. McDermott, R. V. Pusapati, J. G. Christensen, N. S. Gray, J. Settleman, *Cancer Res.* **70**, 1625–1634 (2010).
25. L. F. Hennequin et al., *J. Med. Chem.* **49**, 6465–6488 (2006).
26. S. Bagrodia, I. Chackalaparampil, T. E. Kmiecik, D. Shalloway, *Science* **269**, 172–175 (1991).
27. L. Friboulet et al., *Cancer Discov.* **4**, 662–673 (2014).

ACKNOWLEDGMENTS

We thank L. H. Park for direction, redirection, and support; S. R. Vora for continual critical discussion and support; W. Michaud for providing feeder cells and training for the development of patient-derived cell lines; and N. Gray for providing several kinase inhibitors. This study was funded by support from the NIH R01CA137008 (J.A.E.), R01CA164273 (A.T.S. and J.A.E.), 1U54HG006097-01 (C.H.B.), the Wellcome Trust (086357 and 102696, C.H.B.), the National Cancer Institute Lung SP0R P50CA090578 (A.S.C., A.J.I., and J.A.E.), the Department of Defense (L.V.S. and J.A.E.), Conquer Cancer Foundation Young Investigator Award (A.S.C.), Uniting Against Lung Cancer (A.S.C. and A.T.S.), Free to Breathe (A.S.C.), Lungevity (L.V.S. and J.A.E.), National Foundation for Cancer Research (A.T.S.), and Be a Piece of the Solution. J.A.E. is a paid consultant for Novartis, Sanofi-Aventis, AstraZeneca, Chugai, Amgen, Genentech, GSK, Merck, and Pfizer, and he holds equity in Gatekeeper Pharmaceuticals, which has a potential equity interest in T790M inhibitors. J.A.E. also receives research support from Novartis. J.F.G. is a paid consultant for Boehringer Ingelheim. A.T.S. is a paid consultant for Pfizer, Novartis, Ariad, Chugai, Genentech, Roche, and Ignyta. A.J.I. is a Senior Advisory Board member and holds equity in Enzymatics Inc. For gene expression analyses, the raw data are deposited in ArrayExpress (accession number is E-MTAB-783). The normalized data are available at www.cancerrxgene.org/downloads.

SUPPLEMENTARY MATERIALS

www.sciencemag.org/content/346/6216/1480/suppl/DC1
Materials and Methods
Figs. S1 to S16
Tables S1 to S8
Databases S1 to S8
References (28–34)

14 April 2014; accepted 21 October 2014
Published online 13 November 2014;
10.1126/science.1254721

HUMORAL IMMUNITY

MAVS, cGAS, and endogenous retroviruses in T-independent B cell responses

Ming Zeng,¹ Zeping Hu,^{2*} Xiaolei Shi,^{2*} Xiaohong Li,^{1*} Xiaoming Zhan,^{1*} Xiao-Dong Li,^{1,4} Jianhui Wang,^{1,4} Jin Huk Choi,¹ Kuan-wen Wang,¹ Tiana Purrington,¹ Miao Tang,¹ Maggy Fina,¹ Ralph J. DeBerardinis,² Eva Marie Y. Moresco,¹ Gabriel Pedersen,³ Gerald M. McInerney,³ Gunilla B. Karlsson Hedestam,³ Zhijian J. Chen,^{1,4} Bruce Beutler^{1†}

Multivalent molecules with repetitive structures including bacterial capsular polysaccharides and viral capsids elicit antibody responses through B cell receptor (BCR) crosslinking in the absence of T cell help. We report that immunization with these T cell-independent type 2 (TI-2) antigens causes up-regulation of endogenous retrovirus (ERV) RNAs in antigen-specific mouse B cells. These RNAs are detected via a mitochondrial antiviral signaling protein (MAVS)-dependent RNA sensing pathway or reverse-transcribed and detected via the cGAS-cGAMP-STING pathway, triggering a second, sustained wave of signaling that promotes specific immunoglobulin M production. Deficiency of both MAVS and cGAS, or treatment of MAVS-deficient mice with reverse transcriptase inhibitors, dramatically inhibits TI-2 antibody responses. These findings suggest that ERV and two innate sensing pathways that detect them are integral components of the TI-2 B cell signaling apparatus.

Specific antibody production is a hallmark of the B cell response to antigens. T cell-dependent (TD) antibody responses typically elicited by protein antigens require follicular helper T cells for full B cell activation, proliferation, and antibody production. In contrast, T cell-independent (TI) antigens stimulate antibody production in the absence of major histocompatibility complex (MHC) class II-restricted T cell help. TI antigens include the TI type 1 (TI-1) antigens, which engage Toll-like receptors (TLRs) in addition to the B cell receptor (BCR), and TI type 2 (TI-2) antigens, which engage the BCR in a manner that induces extensive crosslinking, leading to BCR activation and immunoglobulin M (IgM) production. TI-2 antigens are large multivalent molecules with highly repetitive structures, such as bacterial capsular polysaccharides and viral capsids (1).

B cell-intrinsic cytosolic DNA and RNA sensing in the TI-2 antibody response

We tested the requirement for innate immune sensing pathways in the antibody response to the model TI-2 antigen 4-hydroxy-3-nitrophenylacetyl-

Ficol (NP-Ficol) by monitoring anti-NP IgM in the serum of mice after immunization (2). C57BL/6J mice mounted a robust NP-specific IgM response by day 4.5 after immunization, which peaked around day 14.5 after immunization (Fig. 1A and fig. S1). Similarly, mice that could not signal via NLRP3, TLR3, TLR7, TLR9, TLR2, TLR4, CD36, MyD88, TICAM1, or IRAK4, all nucleic acid-sensing TLRs (*Unc93b1*^{3d/3d}), or all TLRs (*Ticam1*^{Lps2/Lps2}; *Irak4*^{otiose/otiose}) produced normal levels of NP-specific IgM on day 4.5 after immunization (Fig. 1A). In contrast, *Tmem173*^{gt/gt} mice and *Mb21d1*^{-/-} mice, deficient in the cytosolic DNA-sensing pathway components stimulator of interferon gene (STING) and cGMP-AMP synthase (cGAS), respectively, exhibited suboptimal IgM responses to NP-Ficol on day 4.5 and for up to 30 days after immunization (Fig. 1A and fig. S1). Mice lacking mitochondrial antiviral signaling protein (MAVS), an adaptor for the cytoplasmic RNA-sensing RIG-I-like helicases, also produced diminished amounts of NP-specific IgM (Fig. 1A and fig. S1). Antibody responses to the TI-1 antigen NP-LPS (LPS, lipopolysaccharide) (Fig. 1B), and the TD antigen β -galactosidase (β -gal) encoded by a nonreplicating recombinant Semliki Forest virus (rSFV) vector (3) (Fig. 1C), were normal in STING-, cGAS-, and MAVS-deficient mice.

We evaluated marginal zone (MZ) and B-1 B cell populations in STING-, cGAS-, and MAVS-deficient mice and found no deficiencies in frequencies or numbers (fig. S2 and supplementary text), except in the NP-specific populations after NP-Ficol immunization (fig. S3). Also, NP-Ficol capture by MZ B cells and MZ macrophages was normal in the mutant mice (fig. S4).

We performed adoptive transfer of C57BL/6J, STING-, cGAS-, or MAVS-deficient splenic and

¹Center for the Genetics of Host Defense, University of Texas Southwestern Medical Center, 5323 Harry Hines Boulevard, Dallas, TX 75390-8502, USA. ²Department of Pediatrics and Children's Medical Center Research Institute, and McDermott Center for Human Growth and Development, University of Texas Southwestern Medical Center, 5323 Harry Hines Boulevard, Dallas, TX 75390-8502, USA. ³Department of Microbiology, Tumor and Cell Biology, Karolinska Institutet, Nobels väg 16, SE-171 77 Stockholm, Sweden. ⁴Howard Hughes Medical Institute, Department of Molecular Biology, University of Texas Southwestern Medical Center, 5323 Harry Hines Boulevard, Dallas, TX 75390-9148, USA.

*These authors contributed equally to this work. †Corresponding author. E-mail: Bruce.Beutler@UTSouthwestern.edu

peritoneal B cells into *Rag2*^{-/-} mice and immunized recipient mice with NP-Ficoll one day after transfer. Despite similar reconstitution of the B cell compartment by donor cells (fig. S5), mice that received STING-, cGAS-, or MAVS-deficient B cells produced diminished amounts of NP-specific IgM on day 4.5 after immunization, as compared to mice that received C57BL/6J B cells (Fig. 1D). These data demonstrate that B cell-intrinsic MAVS and cGAS-STING signaling are necessary for antibody responses to TI-2 immunization.

B cell activation by cGAMP

The DNA sensor cGAS binds to cytosolic DNA and catalyzes the synthesis of cGMP-AMP (cGAMP), a cyclic dinucleotide that binds and activates STING, leading to type I interferon production (4). We found that the presence of DNA in the cytoplasm was sufficient to activate C57BL/6J,

but not STING-deficient splenic B cells in vitro (Fig. 2A, fig. S6, and supplementary text). After NP-Ficoll immunization of C57BL/6J mice, cGAMP levels were elevated for at least 10 days in NP-specific B cells relative to levels in non-NP-specific or naïve B cells (Fig. 2, B and C). In vitro cGAMP treatment activated B cells from C57BL/6J but not STING-deficient mice (Fig. 2, D and E), whereas in vivo cGAMP treatment partially rescued NP-specific IgM levels in the serum of cGAS-deficient mice immunized with NP-Ficoll together with cGAMP (Fig. 2F). Thus, cytoplasmic DNA and cGAMP are sufficient to activate B cells in a STING-dependent manner. Human B cells were also activated by cGAMP treatment in vitro (Fig. 2G).

These findings implicate cytosolic DNA sensed by the cGAS-STING pathway in B cell activation by TI-2 antigens. The impaired antibody response of MAVS-deficient mice immunized with NP-Ficoll

(Fig. 1A) suggested that cytosolic RNA may also activate B cells.

ERV transcription and reverse transcription in TI-2 antigen-specific B cells

No exogenous nucleic acid species are known to be introduced into B cells upon BCR engagement by TI-2 antigens, suggesting that endogenous nucleic acids are responsible for activation of the cGAS-STING and MAVS pathways. We hypothesized that RNA and reverse-transcribed DNA derived from endogenous retroviruses (ERVs) or retrotransposons might gain access to the B cell cytoplasm upon BCR signaling. The retroviral life cycle entails the transient localization of RNA and, via reverse transcription, DNA within the cytoplasm (5). Both cGAS-STING (6) and RIG-I-MAVS pathways (7) have been implicated in the sensing of HIV-1 and other retroviruses. We therefore investigated whether ERVs could be induced by TI-2 immunization.

We measured transcript levels of individual ERVs in B cells after immunization of C57BL/6J mice with NP-Ficoll; DNA contamination of the RNA samples was excluded (fig. S7A). Compared to non-NP-specific B cells on day 4.5 after immunization, NP-specific B cells displayed increased expression of multiple ERV mRNAs (Fig. 3A). We found that total RNA isolated from NP-specific B cells was significantly more potent than total RNA from non-NP-specific B cells in activating cytokine and chemokine gene expression in bone marrow-derived macrophages (BMDMs) (fig. S7, B to D). Gene expression induced by NP-specific B cell total RNA was partially dependent on MAVS (fig. S7C); ribonuclease treatment abrogated the effect (fig. S7D). To test the idea that a MAVS-dependent RNA sensing pathway could be activated by ERV RNAs in NP-specific B cells, we used RIG-I immunoprecipitation followed by reverse transcription polymerase chain reaction (RT-PCR) analysis and found that all tested ERV mRNA sequences bound to RIG-I molecules in NP-specific B cells from immunized mice; greater amounts of ERV mRNA were immunoprecipitated with RIG-I from NP-specific B cells than from non-NP-specific B cells (Fig. 3B). We also verified the selective binding of RIG-I to ERV mRNA versus cellular mRNA (fig. S7E).

Reverse transcription of retroviral RNA occurs in the cytoplasm and produces cDNA that can be detected by cGAS (6). Measurement of cytoplasmic ERV DNA (fig. S8A) revealed elevated levels in NP-specific B cells as compared to non-NP-specific B cells from immunized C57BL/6J mice (Fig. 3C). Consistent with this finding, the activity of reverse transcriptase (RT) was up-regulated in NP-specific relative to non-NP-specific or naïve B cells (Fig. 3D). We used inhibitors of RT to determine whether reverse transcription is necessary for B cell activation and antibody production in mice immunized with NP-Ficoll. B cells were cultured in vitro and treated with NP-Ficoll and the RT inhibitors azidothymidine (AZT), nevirapine (NVP), and didanosine (ddI). RT inhibition significantly reduced CD86 and

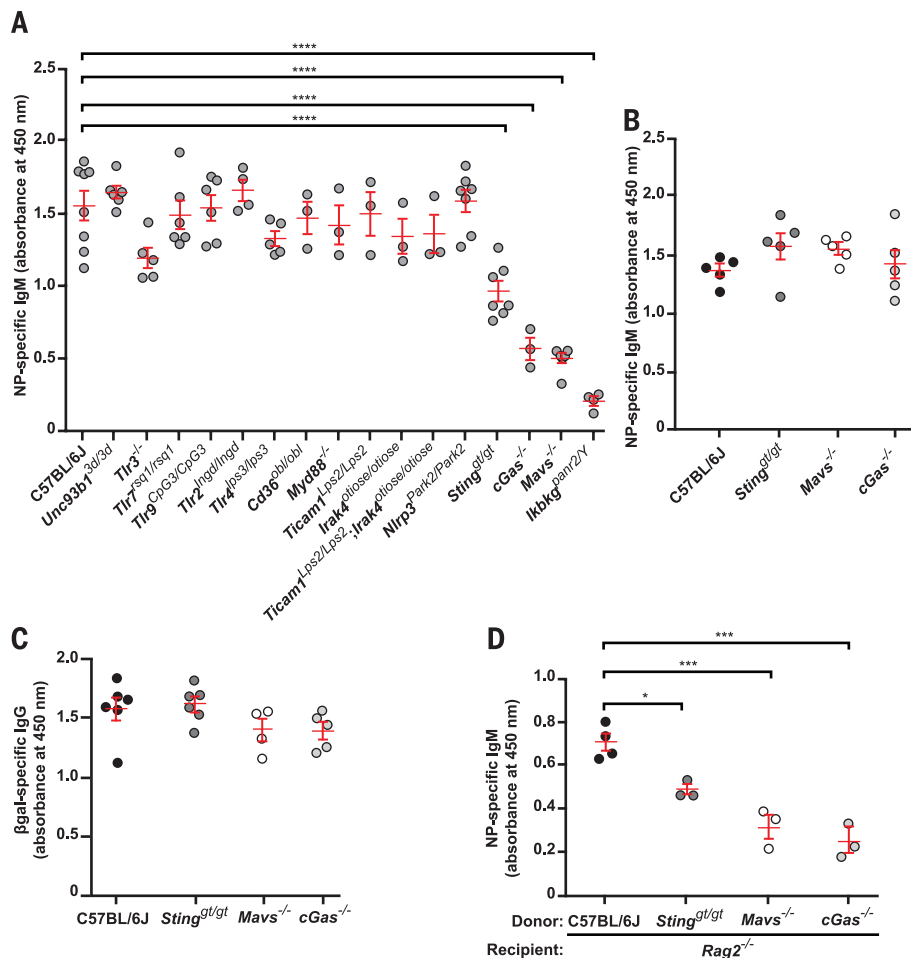


Fig. 1. Cytosolic DNA and RNA sensing pathways are essential for induction of the TI-2 antibody response. (A) Serum NP-specific IgM on day 4.5 after immunization with NP-Ficoll. (B) Serum NP-specific IgM on day 4.5 after immunization with NP-LPS. (C) Serum β-gal-specific IgG on day 14.5 after immunization with rSFV-encoded β-gal. (D) Serum NP-specific IgM on day 4.5 after immunization of *Rag2*^{-/-} mice adoptively transferred 1 day before immunization with splenic and peritoneal B cells from donor mice of the indicated genotypes. Data points represent individual mice. *P* values were determined by one-way analysis of variance (ANOVA) and post hoc Tukey test; in (B) and (C), no significant difference was found between any mutant genotype and C57BL/6J. Results are representative of two or three independent experiments.

GL7 expression in C57BL/6J and MAVS-deficient NP-specific B cells relative to NP-specific B cells without RT inhibition (Fig. 3, E and F).

In vivo, C57BL/6J mice pretreated with AZT and NVP followed by immunization with NP-Ficoll showed varying but significant reductions in ERV DNA levels in the cytoplasm of NP-specific B cells compared to immunized mice treated with vehicle (fig. S8B), which is consistent with the known differential susceptibility of RT enzymes to distinct RT inhibitors (8, 9). C57BL/6J and MAVS-deficient mice treated with RT inhibitors exhibited impaired NP-specific IgM production relative to immunized vehicle-treated mice (Fig. 3G). However, no additive impairment of activation marker expression on NP-specific B cells in vitro, or of NP-specific IgM production in vivo, resulted from RT inhibition in STING-deficient B cells or mice (Fig. 3, E to G). Consistent with these findings, double knockout of MAVS and cGAS reduced NP-specific IgM production to nearly undetectable levels in the serum of immunized mice (Fig. 3H). We also immunized double knockout mice deficient in MAVS and STING and noted that, although reduced as compared to mice lacking either protein alone, residual NP-specific IgM production still occurred, suggesting that cGAS may have functions independent of cGAMP production or that alternate cGAMP receptor(s) remain to be identified (fig. S9). These data suggest that TI-2 immunization activates transcription and reverse transcription to produce ERV mRNAs and cDNAs. These nucleic acids probably then engage the RIG-I-MAVS and cGAS-STING pathways, leading to signaling necessary for B cell activation and antigen-specific antibody production. We note that the potential involvement in TI-2 antibody responses of LINE-1 elements, which are also susceptible to RT inhibition, remains to be tested.

NF- κ B is required for ERV induction and is activated by BCR and MAVS signaling

TI-2 antigens engage the BCR and trigger signaling events, including the activation of Src kinases, the Tec family kinase Btk, and subsequently NF- κ B (10), which is known to activate the transcription of exogenous retroviruses in other cells (11, 12). Because mutations affecting the BCR reduce or eliminate B cells, we investigated the involvement of BCR signaling in the induction of ERVs by measuring ERV mRNA levels in response to BCR engagement by anti-IgM in vitro. Anti-IgM treatment increased activation marker expression (Fig. 4A), caused strong up-regulation of multiple ERV mRNAs (Fig. 4B), and elevated cGAMP (Fig. 4C) in C57BL/6J B cells. Human B cells also up-regulated ERV mRNAs upon treatment with anti-IgM in vitro (Fig. 4D). These data indicate that BCR ligation is sufficient to induce ERV transcription in mouse and human B cells, as well as activation of cGAS in mouse B cells. MAVS- and cGAS-deficient B cells failed to fully up-regulate activation markers in response to anti-IgM (Fig. 4A); these findings are consistent with MAVS and cGAS activation induced by BCR signaling. Downstream from the

BCR, Btk activation is a defining feature of the signaling induced by TI-2 antigens (1). Btk-deficient *xid* mice failed to produce NP-specific IgM on day 4.5 after immunization with NP-Ficoll (Fig. 4E), which is consistent with previously reported data (13). NP-specific B cells from immunized *xid* mice expressed similar levels of ERV mRNAs as non-P-specific B cells from either *xid* mice or from control mice (Fig. 4F). In human B cells in vitro, the BTK inhibitor Ibrutinib blocked both the expression of activation markers (Fig. 4G) and the elevation of ERV transcription induced by anti-IgM (Fig. 4D). These findings demonstrate that Btk is necessary for the induction of ERV mRNAs in mouse B cells by TI-2 immunization, and in human B cells by BCR ligation.

Data from several experiments supported a requirement for NF- κ B in the antibody response to TI-2 immunization, and specifically in the induction of ERV mRNAs. First, NF- κ B-dependent cytokines were up-regulated in NP-specific B cells from C57BL/6J mice immunized with NP-Ficoll, whereas non-NP-specific B cells showed cytokine production similar to that of naïve B cells (Fig. 5A). Second, mutation of NEMO (*Ikkg^{nanR2}*), a component of the IKK complex required for NF- κ B activation, abrogated the NP-specific IgM response of C57BL/6J mice to NP-Ficoll immunization (Fig. 1A). Third, NP-specific B cells from NEMO-deficient mice expressed ERV mRNA levels similar to those of non-NP-specific B cells (Fig. 5B).

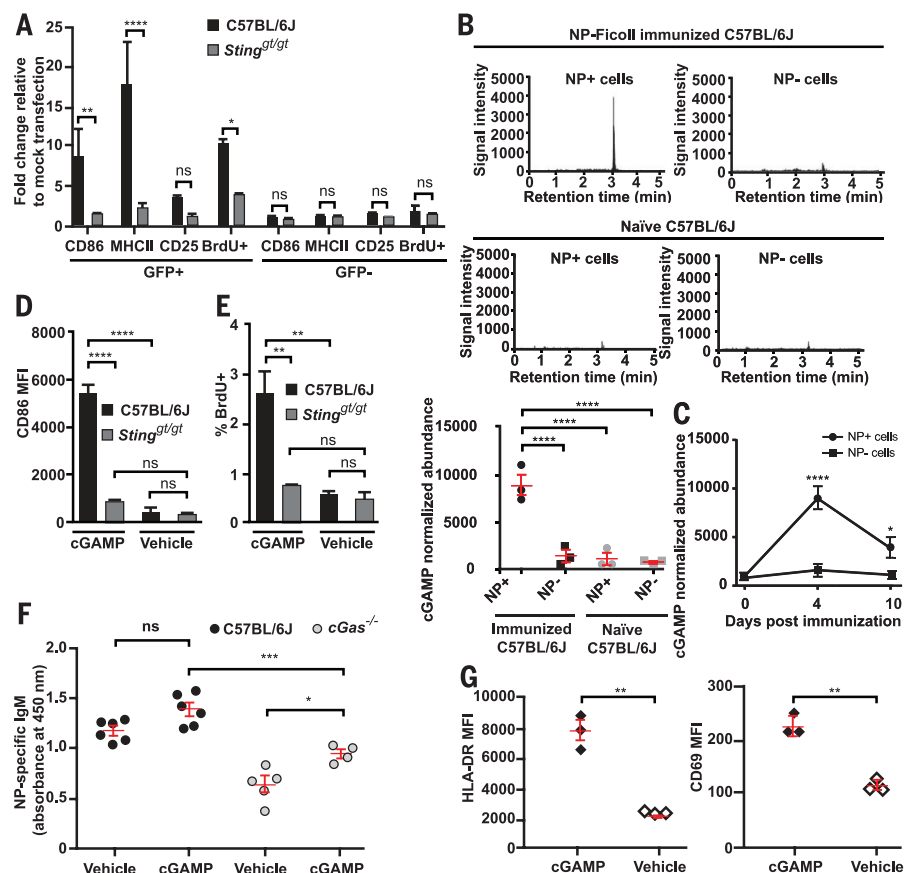


Fig. 2. cGAMP is elevated within antigen-specific B cells after TI-2 immunization and is sufficient to drive B cell activation in vitro and in vivo. (A) CD86, MHC class II, and CD25 expression, and BrdU incorporation by GFP⁺ or GFP⁻ (GFP, green fluorescent protein) splenic CD19⁺ B cells, 36 hours after transfection with a GFP expression plasmid. *N* = 3 C57BL/6J mice and 3 *Sting*^{gt/gt} mice. (B) cGAMP level measured by liquid chromatography–tandem mass spectrometry (LC-MS/MS) in 2×10^5 NP-specific or non-NP-specific splenic CD19⁺ B cells from C57BL/6J mice on day 4.5 after immunization with NP-Ficoll (*N* = 3) or in naïve mice (*N* = 3). Upper panels, chromatograms of cGAMP. Lower panel, cGAMP abundance normalized to cell number for each sample. (C) Time course of cGAMP levels in NP-specific or non-NP-specific B cells from C57BL/6J mice (*N* = 3) immunized with NP-Ficoll. (D and E) CD86 expression (D) or the percentage of BrdU⁺ splenic B cells (E) after treatment with cGAMP or vehicle for 2 days in vitro. *N* = 3 C57BL/6J mice and 3 *Sting*^{gt/gt} mice. (F) Serum NP-specific IgM on day 5 after immunization with NP-Ficoll plus cGAMP or NP-Ficoll plus vehicle. (G) HLA-DR or CD69 expression by human B cells isolated from healthy donor peripheral blood and treated with cGAMP or vehicle for 2 days in vitro. MFI, mean fluorescence intensity. Data points represent individual mice or humans [(B), (F), and (G)]. *P* values were determined by one-way [(A), (B), and (D) to (F)] or two-way ANOVA and post hoc Tukey test (C) or Student's *t* test (G). Results are representative of two or three independent experiments.

Signaling from the BCR, RIG-I-MAVS, and cGAS-STING pathways all activate NF- κ B (10, 14, 15), and we sought to identify which pathway(s) drive NF- κ B activation needed for the TI-2 antibody response. We found that anti-IgM failed to induce ERV mRNAs in NEMO-deficient B cells in vitro (Fig. 4B), suggesting that BCR signaling induces ERV mRNAs via NF- κ B. As we have demonstrated, ERV transcripts trigger a second, sustained wave of signaling via the RIG-I-MAVS and

cGAS-cGAMP-STING pathways that may also require NF- κ B to activate B cells and stimulate antibody production. We evaluated NF- κ B activation by measuring levels of phosphorylated p65 and p105. In response to anti-IgM, C57BL/6J, MAVS^{-/-}, and cGAS-deficient B cells displayed elevated levels of phospho-p65 and phospho-p105 as compared to vehicle-treated cells; however, MAVS-deficient cells showed a diminished level of NF- κ B activation relative to C57BL/6J cells

(Fig. 5C). Analysis of p65 nuclear translocation corroborated these findings (Fig. 5D). Similarly, NP-specific B cells from immunized C57BL/6J, MAVS^{-/-}, and cGAS-deficient mice displayed elevated phospho-p105 relative to non-NP-specific B cells; MAVS deficiency prevented NF- κ B activation to the extent observed in C57BL/6J NP-specific B cells (Fig. 5E). These data suggest that MAVS signaling but not cGAS-STING signaling activates NF- κ B in response to ERV nucleic acids

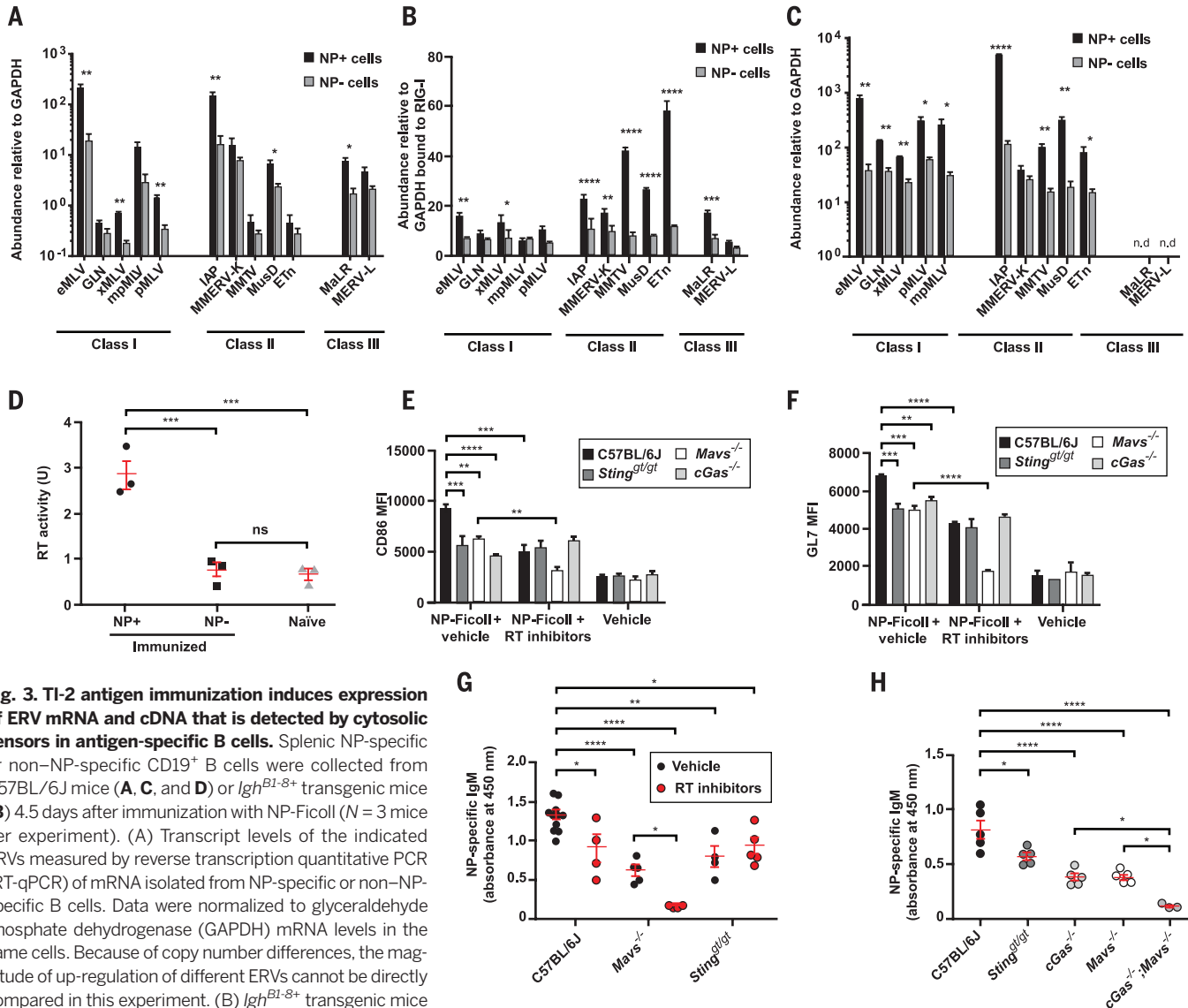


Fig. 3. TI-2 antigen immunization induces expression of ERV mRNA and cDNA that is detected by cytosolic sensors in antigen-specific B cells.

Splenic NP-specific or non-NP-specific CD19⁺ B cells were collected from C57BL/6J mice (A, C, and D) or *Igh*^{B1-8+} transgenic mice (B) 4.5 days after immunization with NP-Ficoll ($N = 3$ mice per experiment). (A) Transcript levels of the indicated ERVs measured by reverse transcription quantitative PCR (RT-qPCR) of mRNA isolated from NP-specific or non-NP-specific B cells. Data were normalized to glyceraldehyde phosphate dehydrogenase (GAPDH) mRNA levels in the same cells. Because of copy number differences, the magnitude of up-regulation of different ERVs cannot be directly compared in this experiment. (B) *Igh*^{B1-8+} transgenic mice express a recombinable variable region derived from an NP-binding antibody in place of the endogenous 3' *Igh*-D element (DQ52) and the *Igh*-J elements. RT-qPCR of the indicated ERV mRNAs immunoprecipitated with RIG-I from NP-specific or non-NP-specific B cells. Data were normalized to the level of GAPDH mRNA bound to RIG-I in the same samples, which represents a nonspecific interaction equivalent in NP-specific and non-NP-specific cells as shown in fig. S7E. (C) qPCR of ERV DNA in the cytoplasmic fraction of NP-specific or non-NP-specific B cells. Data were normalized to GAPDH intronic DNA levels in the same cells. Endogenous ecotropic murine leukemia virus (eMLV) and mouse mammary tumor virus (MMTV) were amplified with primers targeting spliced cDNAs; these species probably represent a minority of the cytoplasmic eMLV and MMTV cDNA levels. (D) RT activity in the

indicated B cells from C57BL/6J mice. (E and F) Splenic CD19⁺ B cells from mice of the indicated genotypes were treated with NP-Ficoll plus RT inhibitors (AZT, NVP, and ddiI) or NP-Ficoll plus vehicle for 2 days, and CD86 (E) or GL7 expression (F) was measured in NP-specific B cells. $N = 3$ mice for each genotype. (G) Serum NP-specific IgM on day 4.5 after NP-Ficoll immunization of mice pretreated for 3 days with RT inhibitors (AZT and NVP) or vehicle. RT inhibitor treatment continued after immunization until measurement of serum IgM. (H) Serum NP-specific IgM on day 4.5 after immunization with NP-Ficoll. Data points represent individual mice [(D), (G), and (H)]. P values were determined by Student's t test [(A) to (C)] or one-way ANOVA and post hoc Tukey test [(D) to (H)]. n.d., not detected. Results are representative of two or three independent experiments.

induced by BCR engagement. The finding that NP-specific B cell RNA from immunized mice transcriptionally activated NF- κ B target genes, including those encoding TNF α , IL-6, MCP-1, and COX-2, in a MAVS-dependent manner (fig. S7, C and D) further supports this conclusion.

cGAS-STING and MAVS signaling in antibody responses to *Streptococcus pneumoniae* capsular polysaccharides

We immunized cGAS-, STING-, MAVS-, or cGAS/MAVS-deficient mice with *Streptococcus pneumoniae* capsular polysaccharides (PSs) 1 and 3 or with the commercial vaccine Pneumovax 23 (PPV-23), containing 23 *S. pneumoniae* polysaccharide antigens. By day 4.5 after immunization, C57BL/6J mice mounted a PS1- and PS3-specific IgM response, which was significantly diminished in cGAS- or MAVS-deficient mice (Fig. 6A). Mice lacking both cGAS and MAVS displayed a further reduction in PS1- and PS3-specific IgM to nearly undetectable levels (Fig. 6A). Similarly, upon immunization with Pneumovax 23, cGAS- or STING-deficient mice produced diminished amounts of PPV-23-specific IgM and IgG as compared to C57BL/6J mice (Fig. 6, B and C). Thus, the requirement for cGAS-STING and RIG-I-MAVS pathways, likely due to their detection of ERV nucleic acids, extends to antibody responses against TI-2 antigens of a clinically important human pathogen.

Discussion

With respect to ERVs, we hypothesize that the following events occur in B cells after TI-2 immunization: (i) ERV proviruses are transcribed, and the resulting unspliced and spliced RNAs are transported to the cytoplasm; (ii) ERV mRNAs are translated to produce RT(s) (Fig. 3D), Env glycoprotein(s) (fig. S10A), and possibly other ERV proteins; (iii) ERV mRNAs are reverse-transcribed to produce cDNAs by one or more of the RT species produced in step (ii); and (iv) ERV mRNAs and cDNAs present in the cytoplasm activate RIG-I and cGAS, respectively (fig. S11). Although retroviruses including HIV-1 and MLV typically proteolytically process RT from the Gag-Pol polyprotein during or after virus budding, RT has also been reported to be active in the precursor form (16, 17); similar ERV-derived precursors may provide the RT activity we measured in NP-specific B cell lysates. Overall, our data support the hypothesis that ERV nucleic acids induced in the TI-2 antigen-activated B cell are sufficient to trigger cytosolic innate sensors, leading to subsequent antibody production by the same cell (fig. S11). However, despite multiple experiments supporting the involvement of ERV nucleic acids, it remains possible that their presence and activity are incidental to other component(s) essential for the activation of MAVS, cGAS, STING, and ultimately TI-2 antibody responses. Determining whether ERV nucleic acids represent a necessary component of the antibody response will require comprehensive inactivation of ERV sequences across the genome.

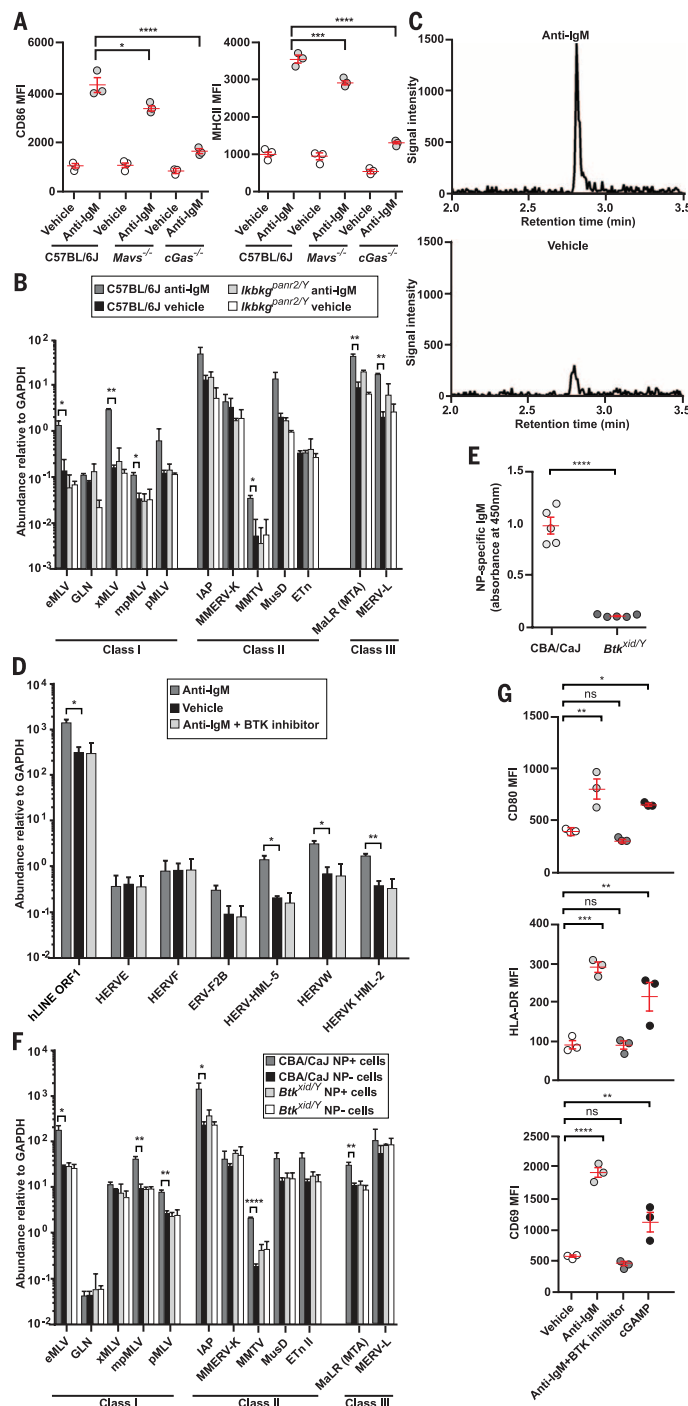


Fig. 4. cGAMP elevation and ERV transcription are induced by BCR signaling. (A to C) Mouse splenic B cells were cultured in vitro and stimulated with anti-IgM or vehicle for 22 hours. (A) CD86 and MHC class II expression. (B) Transcript levels of the indicated ERVs measured by RT-qPCR of isolated mRNA. Data were normalized to GAPDH mRNA levels in the same cells. $N = 3$ mice per genotype. (C) Chromatograms of cGAMP in C57BL/6J B cells measured by LC-MS/MS. $N = 3$ mice. (D) Human B cells from healthy donor peripheral blood ($N = 3$ individuals) were cultured in vitro and stimulated with anti-IgM, anti-IgM + Ibrutinib, or vehicle for 48 hours. Transcript levels of the indicated human ERVs measured by RT-qPCR of isolated mRNA. (E) Serum NP-specific IgM on day 4.5 after immunization with NP-Ficoll. (F) Transcript levels of the indicated ERVs measured by RT-qPCR of mRNA isolated from NP-specific or non-NP-specific B cells. Data were normalized to GAPDH mRNA levels in the same cells. $N = 3$ mice per genotype. (G) Activation marker expression by human B cells treated as in (D), or with 0.06 μ M cGAMP for 48 hours. Data points represent individual mice or humans [(A), (E), and (G)]. P values were determined by Student's t test [(B) and (D) to (F)] or one-way ANOVA and post hoc Tukey test [(A) and (G)]. Results are representative of two independent experiments.

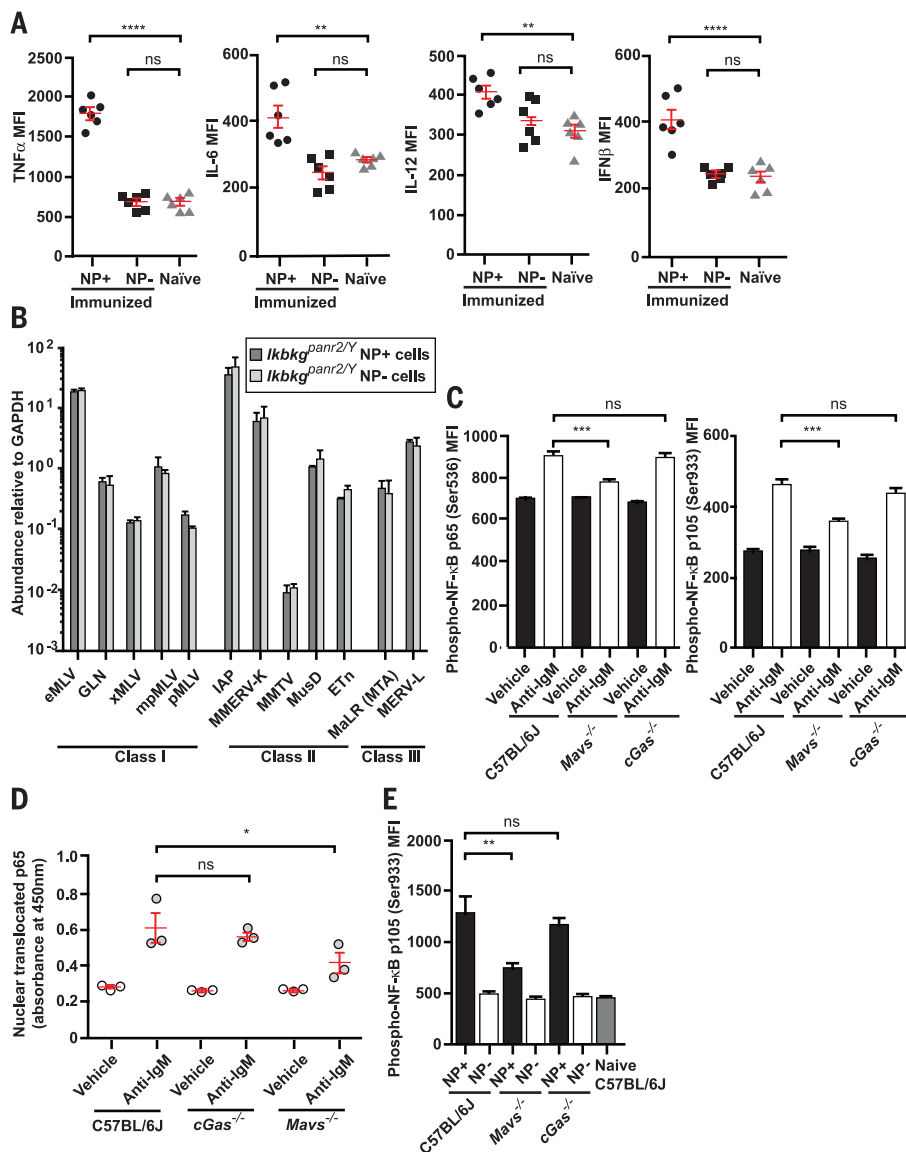


Fig. 5. NF- κ B is required for ERV induction and is activated by BCR and MAVS signaling. (A and B) Splenic NP-specific or non-NP-specific CD19⁺ B cells were collected from mice 4.5 days after immunization with NP-Ficoll. (A) Cytokine expression in the indicated B cells from C57BL/6J mice. (B) Transcript levels of the indicated ERVs measured by RT-qPCR of mRNA isolated from NP-specific or non-NP-specific B cells. $N = 3$ mice. No significant difference was found between NP⁺ and NP⁻ cells for any ERV tested. (C and D) Splenic B cells were cultured in vitro and stimulated with anti-IgM or vehicle for 22 hours. (C) Levels of phospho-p65 (left) and phospho-p105 (right) are shown. $N = 3$ mice. (D) Levels of p65 in the nuclear fraction of cells. (E) Levels of phospho-p105 in splenic NP-specific and non-NP-specific CD19⁺ B cells or naïve B cells on day 6 after NP-Ficoll immunization. $N = 3$ mice per genotype. Data points represent individual mice [(A) and (D)]. P values were determined by Student's t test (B) or one-way ANOVA and post hoc Tukey test [(A) and (C) to (E)]. Results are representative of two independent experiments.

The appropriation of ERV genes for host immunity has often been observed in defense against exogenous retroviruses, as exemplified by *Fv1* (18) and *Fv4* (19). Whereas the host recruits a single ERV-derived gene to counteract one particular step in the life cycle of an exogenous retrovirus, however, it activates a wide range of ERVs in antigen-specific B cells that then serve to trigger intracellular nucleic acid sensors necessary for the TI-2 antibody response. The fate of these ERV nucleic acids remains un-

known. We found in NP-specific B cells from immunized mice that the expression of endogenous murine leukemia virus-specific Env glycoprotein was enhanced (fig. S10A), as was RT activity detected in the supernatants (fig. S10B). Why ERV proteins are produced and how they might come to exist outside the cell during the TI-2 antibody response are open questions.

Recent reports suggest that aberrant cellular accumulation of endogenous retroelement cDNA and its recognition by cytosolic sensors lead to

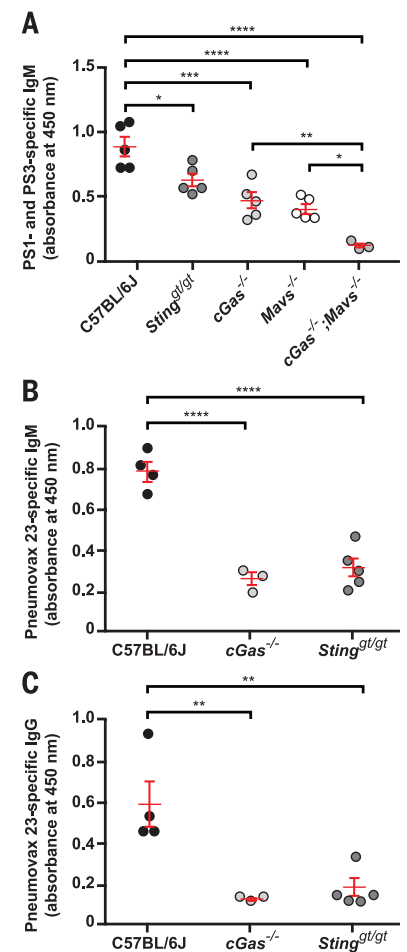


Fig. 6. TI-2 antibody responses to *S. pneumoniae* PS1 and PS3 and to the commercial vaccine Pneumovax 23 require cytosolic DNA and RNA sensing pathways. (A) Serum PS1- and PS3-specific IgM on day 4.5 after immunization with *S. pneumoniae* PS1 and PS3. (B and C) Serum PPV-23-specific IgM (B) and IgG (C) on day 5.5 after immunization with Pneumovax 23. Data points represent individual mice. P values were determined by one-way ANOVA and post hoc Tukey test (A) or Student's t test [(B) and (C)]. Results are representative of two or three independent experiments.

autoimmune disease in mice (20, 21). An association of human autoimmune diseases with ERVs has also been postulated (22). Such diseases may be hypothesized to result from dysregulation of adaptive rather than strictly innate immune activation, in that retroviruses, MAVS, cGAS, and STING serve as components of the normal TI-2 B cell signaling apparatus.

REFERENCES AND NOTES

1. J. J. Mond, A. Lees, C. M. Snapper, *Annu. Rev. Immunol.* **13**, 655–692 (1995).
2. Materials and methods are available as supplementary materials on Science Online.
3. A. S. Hidmark *et al.*, *J. Virol.* **80**, 7100–7110 (2006).
4. X. Cai, Y. H. Chiu, Z. J. Chen, *Mol. Cell* **54**, 289–296 (2014).
5. S. P. Goff, *Nat. Rev. Microbiol.* **5**, 253–263 (2007).
6. D. Gao *et al.*, *Science* **341**, 903–906 (2013).
7. M. Solis *et al.*, *J. Virol.* **85**, 1224–1236 (2011).

8. R. M. Ruprecht, L. G. O'Brien, L. D. Rossoni, S. Nisnoff-Lehrman, *Nature* **323**, 467–469 (1986).
9. S. D. Young et al., *Antimicrob. Agents Chemother.* **39**, 2602–2605 (1995).
10. M. E. Moreno-García, K. M. Sommer, A. D. Bandaranayake, D. J. Rawlings, *Adv. Exp. Med. Biol.* **584**, 89–106 (2006).
11. J. Alcamí et al., *EMBO J.* **14**, 1552–1560 (1995).
12. A. Roulston, R. Lin, P. Beauparlant, M. A. Wainberg, J. Hiscott, *Microbiol. Rev.* **59**, 481–505 (1995).
13. W. N. Khan et al., *Immunity* **3**, 283–299 (1995).
14. X. D. Li et al., *Science* **341**, 1390–1394 (2013).
15. Y. M. Loo, M. Gale Jr., *Immunity* **34**, 680–692 (2011).
16. S. Crawford, S. P. Goff, *J. Virol.* **53**, 899–907 (1985).
17. F. Lori et al., *AIDS Res. Hum. Retroviruses* **4**, 393–398 (1988).
18. S. Best, P. Le Tissier, G. Towers, J. P. Stoye, *Nature* **382**, 826–829 (1996).
19. H. Ikeda, F. Laigret, M. A. Martin, R. Repaske, *J. Virol.* **55**, 768–777 (1985).
20. G. B. Beck-Engeser, D. Eilat, M. Wabl, *Retrovirology* **8**, 91–4690–8–91 (2011).
21. D. B. Stetson, J. S. Ko, T. Heidmann, R. Medzhitov, *Cell* **134**, 587–598 (2008).
22. N. Tugnet, P. Rylance, D. Roden, M. Trela, P. Nelson, *Open Rheumatol. J.* **7**, 13–21 (2013).

ACKNOWLEDGMENTS

We thank L. Evans and F. Malik for the generous gift of the 83A25 antibody; P. Jurek for expert assistance in preparing the figures; and the Children's Medical Center Research Institute Flow Cytometry Facility at the University of Texas Southwestern Medical Center for assistance with cell sorting. The data presented in this paper are tabulated in the main paper and in the

supplementary materials. This work was supported by generous donations from the Lyda Hill Foundation and the Kent and JoAnn Foster Family Foundation; and by NIH grants P01 AI070167 and U19 AI100627 (to B.B.), R01 AI093967 (to Z.J.C.), and R01 CA157996 (to R.D.).

SUPPLEMENTARY MATERIALS

www.sciencemag.org/content/346/6216/1486/suppl/DC1
Materials and Methods
Supplementary Text
Figs. S1 to S11
Table S1
References (23–32)

23 June 2014; accepted 6 November 2014
10.1126/science.1257780

REPORTS

ELECTRON TRANSFER

Toward control of electron transfer in donor-acceptor molecules by bond-specific infrared excitation

Milan Delor,¹ Paul A. Scattergood,¹ Igor V. Sazanovich,^{1,2} Anthony W. Parker,² Gregory M. Greetham,² Anthony J. H. M. Meijer,¹ Michael Towrie,^{2*} Julia A. Weinstein^{1*}

Electron transfer (ET) from donor to acceptor is often mediated by nuclear-electronic (vibronic) interactions in molecular bridges. Using an ultrafast electronic-vibrational-vibrational pulse-sequence, we demonstrate how the outcome of light-induced ET can be radically altered by mode-specific infrared (IR) excitation of vibrations that are coupled to the ET pathway. Picosecond narrow-band IR excitation of high-frequency bridge vibrations in an electronically excited covalent *trans*-acetylide platinum(II) donor-bridge-acceptor system in solution alters both the dynamics and the yields of competing ET pathways, completely switching a charge separation pathway off. These results offer a step toward quantum control of chemical reactivity by IR excitation.

The fundamental process of electron transfer (ET) is central to many light-driven reactions. Light-induced ET in molecules starts by excitation to a so-called Franck-Condon electronic excited state, in which nonzero vibrational levels are usually populated (1–3). The excess vibrational energy is rapidly lost as the excited state relaxes and nuclear rearrangements begin to occur. ET may occur on time scales commensurate with the depopulation of these “vibrationally hot” states, typically 10^{-14} to 10^{-10} s (4), allowing ET to proceed from such nonthermalized states. Previous infrared (IR) spectroscopy studies with vibrational state resolution have shown a significant de-

pendence of ET rates on the vibrational quantum number of the reactant state (5). Taken together, these phenomena offer an enticing strategy to influence ET reactions by exciting vibrations coupled with the ET process, thus perturbing nuclear-electronic (vibronic) interactions, which are known to mediate ET in systems ranging from heterogeneous assemblies to complex biological architectures (6–15). If achieved, this strategy provides a means to alter transition probabilities and ultimately redefine the nature and the yields of products generated in ET processes.

The challenge of directing ET is particularly complex owing to the ultrafast time scales and multicoordinate energy landscape of this class of reactions (3). Because the energies of molecular vibrations lie in the IR region, low-energy IR light can be used to target specific vibrations and potentially affect photoreactivity—an approach successfully implemented in gas-phase photochemistry (16–18). With regard to manipulating photoinduced ET processes, the use of IR light

complements existing strategies employing either chemical modifications—for example, of photosynthetic reaction centers (19)—or nonlinear laser methods (20–22) that use ultrashort pulsed laser light in the ultraviolet (UV) or visible spectral regions.

Control of ET processes using IR excitation is underpinned by a strong theoretical framework pertaining to vibronic interactions in the non-adiabatic (weakly electronically coupled) electron tunneling medium. This framework introduces multiple vibronic coupling pathways between electron donor and acceptor, whereby the interference between the electrons propagating through the different pathways directs ET. Theoretical analyses of vibronic tunneling pathways in model molecules by Beratan and co-workers predicted that in inelastic ET reactions, where a tunneling electron may interact and exchange energy with a bridge-localized vibrational mode, IR driving of pathway-specific vibrations can effectively label and select the ET path (23–25). Such experiments would thus offer the means to control ET reaction outcomes using external IR excitation.

Indeed, vibrational excitation with broadband (~ 120 cm^{-1}) IR pulses that perturbed the H-bonding network linking donor and acceptor molecules was shown to slow down an intermolecular charge-separation process and decrease its yield by $\sim 1.8\%$ (26). These elegant experiments successfully demonstrated the viability of using IR pulses to change the course of an ET reaction.

Our alternative approach to direct ET uses a transform-limited narrowband (~ 12 cm^{-1} , 1.5 ps) (27) IR pulse to achieve mode-specific excitation of intramolecular vibrations directly coupled to ET in a covalently bound donor-bridge-acceptor (DBA) molecular triad. The designed DBA triad **1**, based on a platinum(II)-*trans*-acetylide motif (28, 29), $\text{PTZ-CH}_2\text{-Ph-C}\equiv\text{C-Pt-C}\equiv\text{C-NAP}$ (30), enforces directionality of ET between a powerful electron donor, phenothiazine (PTZ), and an electron acceptor, naphthalene-monoimide (NAP) (Fig. 1A). **1** represents an ideal substrate for IR modulation as the high-frequency $\text{C}\equiv\text{C}$ stretching vibrations of the bridge at ~ 2100 cm^{-1} have previously been identified as the ET reaction coordinate in related Pt(II) acetylides (31) and are sufficiently separated in energy and space from the nearest intense IR absorption [~ 1700 cm^{-1} ,

¹Department of Chemistry, University of Sheffield, Sheffield S3 7HF, UK. ²Central Laser Facility, Research Complex at Harwell, Rutherford Appleton Laboratory, Harwell Science and Innovation Campus, Science and Technology Facilities Council, Chilton, Oxfordshire OX11 0QX, UK.

*Corresponding author. E-mail: mike.towrie@stfc.ac.uk (M.T.), julia.weinstein@sheffield.ac.uk (J.A.W.)

$\nu(\text{C}=\text{O})$ of the acceptor] to ensure selective vibrational excitation.

The photoinduced processes in **1** have been characterized by a combination of time-resolved infrared (TRIR) and electronic transient absorption spectroscopies (30) (see Fig. 1C). The excited-state dynamics are illustrated in Fig. 2, C and D, using TRIR data, collected with a {UV_{pump}; IR_{broadband-probe}} pulse sequence. Absorption of the UV pump partially depopulates the ground electronic state, observed as negative peaks (ground-state bleach), whereas the formation of transient excited states is manifested by positive peaks (excited-state IR absorption) (32).

Electronic excitation of **1** with a 400-nm, ~50-fs UV pump initiates ET from the Pt-acetylide center to the NAP acceptor and populates a vibrationally hot charge-transfer manifold, DB⁺A⁻. This nonthermalized manifold decays over a range of lifetimes from <200 fs to 14 ps, branching over three separate charge transfer pathways (30): forward ET from the PTZ donor, forming the full charge-separated state ³D⁺BA⁻ (10% yield, blue arrows in Fig. 2, main IR-band positions 1550, 1605, and 2105 cm⁻¹), which subsequently decays to the ground state with a 1-ns lifetime; population of a long-lived π - π^* intraligand triplet state of the NAP acceptor, ³A (57% yield, 190- μ s lifetime, red arrows, main IR-band positions 1590, 1638, and 1950 cm⁻¹); and back ET reforming the ground-state DBA (GS, gray arrows in Fig. 2).

Excited-state branching over multiple ET pathways on the picosecond time scale fulfills an

essential requirement to achieve the IR modulation of photoprocesses in **1**. These experiments were performed as follows. Electronic excitation of **1** with a UV pump prepares the vibrationally hot DB⁺A⁻. A tunable narrowband IR pump is then applied at variable time delays t after the UV pump (Fig. 1B), exciting selected vibrations in DB⁺A⁻. The product states generated in all reaction pathways are quantified with a broadband IR probe (~400 cm⁻¹) at variable time delays T . Overall, an ultrafast three-pulse {UV_{pump}; IR_{narrowband-pump}; IR_{broadband-probe}} sequence (33) is applied to **1** to first initiate ET, then selectively excite vibrations in the bridging unit, and finally probe the changes in the charge transfer dynamics and pathways created by the intermediate IR pump (Fig. 1, B and C). The changes in IR absorption were recorded as $\Delta\text{Abs}(\text{IR}_{\text{pumpON}} - \text{IR}_{\text{pumpOFF}})$, thereby solely extracting the effect of the IR excitation.

Figure 2, E to H, shows the effect of exciting the $\nu(\text{C}\equiv\text{C})$ bridging vibration in DB⁺A⁻ on the photoprocesses in **1**. Clear difference signals from all product states that evolve with time indicate that the IR pump has an effect on both the dynamics and on the relative population of transient states (34). When the IR probe arrives at early time delays T after the UV pump (Fig. 2, E and F), the transient IR spectra display pronounced difference signals that indicate a decrease in DB⁺A⁻ (black arrows), and an increase in ³A (red arrows)

and the GS (gray arrows) relative to their population without the IR pump. Thus, IR excitation accelerates charge recombination from the gateway state DB⁺A⁻. The lack of signals associated with the full charge-separated state ³D⁺BA⁻ at early time delays T suggests no acceleration of forward ET from the donor.

The key observation revealed in Fig. 2, G and H, is that difference signals from the product states caused by the intermediate IR pump persist long after the excitation. Thus, at an IR_{pump}: IR_{probe} delay ($T - t$ in Fig. 1B) of ~98 ps ($T = 100$ ps, $t = 2$ ps), the positive signals at 1950, 1638, and 1590 cm⁻¹ indicate that IR excitation increases the population of the ³A state. The negative signals at 2105, 1605, and 1550 cm⁻¹ indicate that less ³D⁺BA⁻ is formed. By $T = 2.2$ ns, most of the ³D⁺BA⁻ (1-ns lifetime) has decayed to the GS. Consequently, the initial decrease in the amount of ³D⁺BA⁻ caused by the IR excitation translates to a lack of ground-state recovery on the nanosecond time scale, resulting in the observed negative GS signals. Thus, the system retains memory of the IR intervention throughout its electronic excited-state lifetime.

The observed IR-modulation effect is mode-specific and is proportional to the IR band intensity of the $\nu(\text{C}\equiv\text{C})$ mode in the DB⁺A⁻ state. This conclusion is based on the following: (i) The magnitude of the effect at different IR-excitation frequencies follows the transient IR-absorption

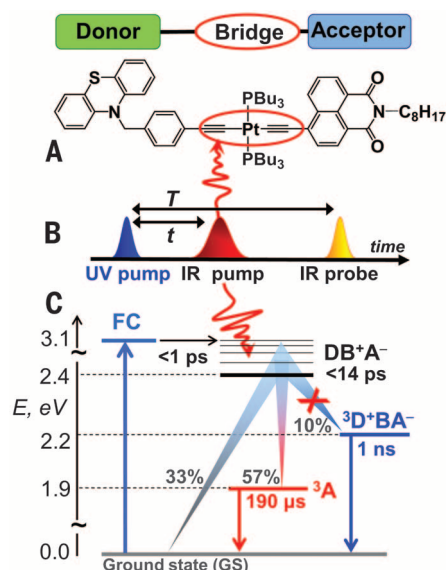


Fig. 1. Schematic of the experiment. (A) DBA triad PTZ-CH₂-Ph-C≡C-Pt-C≡C-NAP (**1**). (B) Pump-pump-probe pulse sequence used in the IR-modulation experiments. (C) The photophysical picture of energetics and dynamics of photoinduced pathways in **1** in CH₂Cl₂ solvent at room temperature. There, the vibrationally hot DB⁺A⁻ manifold branches over three decay pathways to lower electronic states (30); "X" denotes the pathway suppressed by intermediate IR excitation. All figures in the paper follow the same color coding.

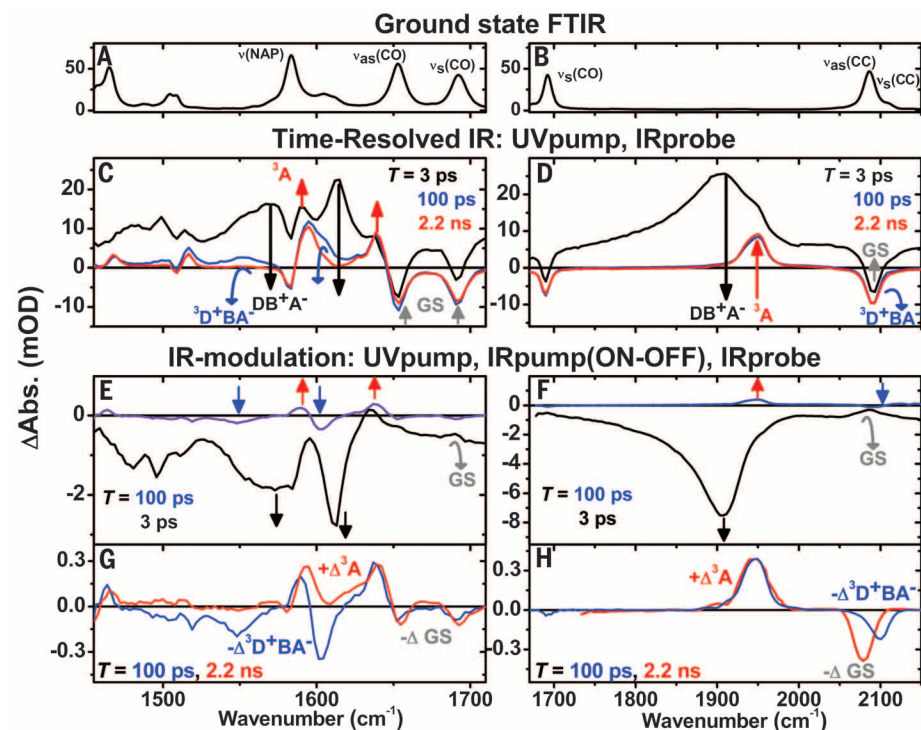


Fig. 2. Excited-state evolution of **1 without and with IR pump in CH₂Cl₂ at room temperature.** (A and B) Ground-state Fourier-transform IR (FTIR) spectra showing vibrational modes before ET is initiated. (C and D) TRIR spectra after 400-nm excitation at representative UV:IR_{probe} delays T . Corresponding kinetics are in fig. S2. (E to H) Difference spectra $\Delta\text{Abs}(\text{IR}_{\text{pumpON}} - \text{IR}_{\text{pumpOFF}})$ at various UV:IR_{probe} delays T with UV:IR_{pump} delay fixed at $t = 2$ ps, and IR-pump at 1908 cm⁻¹ (pulse sequence in Fig. 1B). Arrows indicate formation or decay of a band assigned and color-coded according to the excited states involved; curved arrows represent growth followed by decay of a band.

Fig. 3. Action spectrum of IR modulation, scanning IR-pump frequency, and UV: IR_{pump} delay *t*. (A) Overlay of the normalized TRIR spectrum of **1** at *T* = 3 ps (—) with the relative magnitudes of population change

$\Delta\text{Abs}(\text{IR}_{\text{pumpON}} - \text{IR}_{\text{pumpOFF}})$ for ^3A (1950 cm^{-1}) (circles) and $^3\text{D}^+\text{BA}^-$ (negative projection, 2105 cm^{-1}) (triangles) when scanning the IR pump frequency from 1750 to 1950 cm^{-1} in 10 cm^{-1} steps. (B) Normalized overlay of a TRIR decay trace at 1908 cm^{-1} (—) with $\Delta\text{Abs}(\text{IR}_{\text{pumpON}} - \text{IR}_{\text{pumpOFF}})$ for ^3A (circles) and for the negative projection of $^3\text{D}^+\text{BA}^-$ (triangles) at different UV:IR_{pump} delays *t*. (C) Source spectral data for (B).

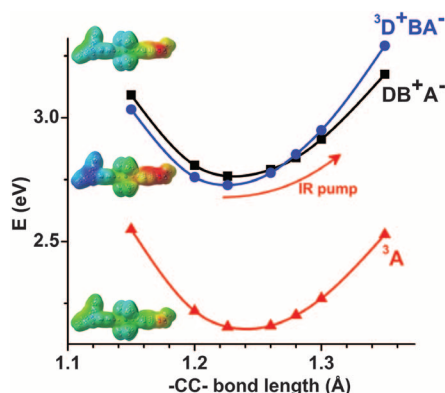
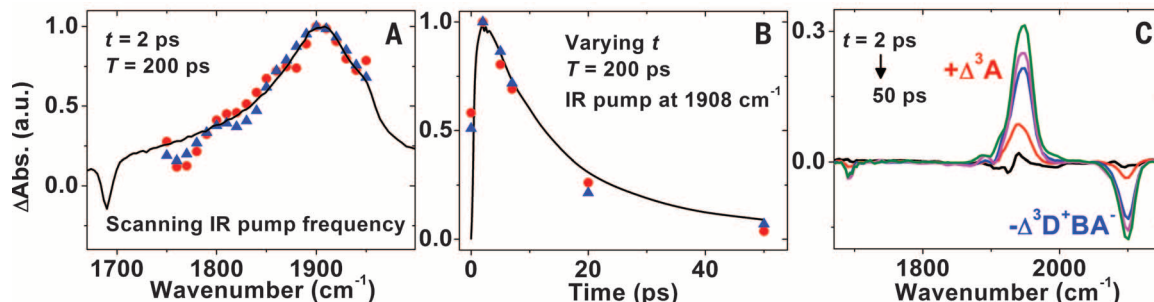


Fig. 4. Calculated potential energy curves and corresponding electrostatic potential maps for **1 in CH_2Cl_2 .** The curves demonstrate a crossing of states at $\text{C}\equiv\text{C}$ bond lengths of the $\text{Pt}\text{C}\equiv\text{C}\text{-NAP}$ (BA) fragment ~ 0.04 Å away from equilibrium. Details are given in fig. S8 and table S1. Electrostatic potential maps illustrate the nature of the excited states by the distribution of electron density upon excitation. Charges are color-coded from -0.1 (red) to $+0.1$ (blue).

profile of the $\nu(\text{C}\equiv\text{C})$ vibration in DB^+A^- (Fig. 3A); (ii) the magnitude of the effect also depends on the UV:IR_{pump} delay used. This dependence follows the decay kinetics of DB^+A^- in TRIR experiments (Fig. 3B); (iii) IR excitation of the acceptor-localized $\nu(\text{C}=\text{O})$ vibration in the same DB^+A^- excited state or of a solvent IR absorption band has no effect (fig. S4), confirming mode specificity and ruling out the influence of local temperature effects.

A quantitative investigation of the effect of the IR excitation revealed that every molecule that absorbs an IR photon has its product states redefined. Without IR excitation, the yield of the full charge-separated state $^3\text{D}^+\text{BA}^-$ is 10% (30). Normalizing to the number of IR photons absorbed by molecules in the gateway DB^+A^- state, we infer that the absolute yield change per IR photon absorbed by the sample is $-10 \pm 1\%$ for the formation of $^3\text{D}^+\text{BA}^-$ and $+10 \pm 1\%$ for ^3A (from 57 to 67%) (35). Thus, within experimental error, the data indicate that the pathway to $^3\text{D}^+\text{BA}^-$ is fully suppressed; forward ET from the donor is completely switched off by selective IR excitation.

In contrast, in a control bridge-acceptor system **2** without the PTZ donor, $\text{Ph-C}\equiv\text{C-Pt(PBu}_3)_2\text{-C}\equiv\text{C-NAP}$ (30, 36), the IR excitation of the $\nu(\text{C}\equiv\text{C})$ in the B^+A^- state influences only the rates of ET, but not the product yields (fig. S7). This difference between **1** and **2** suggests that product yield changes in **1** are due to a process specifically affecting the competitive ET pathways between forward electron transfer from the donor and back electron transfer from the acceptor, i.e., between charge separation and recombination across the bridge.

The observed increased rates of ET from higher vibrational levels of a charge-transfer state in both **1** and **2** are consistent with previous studies on the effect of vibrational quantum state on ET dynamics (5, 37, 38). However, the major changes in product yields and complete suppression of ET in **1** may be better rationalized within the framework of vibronic tunneling pathways (23–25). The charge transfer state DB^+A^- in **1** can be visualized as a vibronic state from which two ET pathways are available: charge recombination and charge separation. Upon IR excitation of the bridging $\text{C}\equiv\text{C}$ oscillator, the latter can exchange energy with a tunneling electron (24) and perturb the interferences governing the two ET pathways, modulating ET propensity nonuniformly across the available paths and in this case achieving the observed elimination of the full charge-separated state. From a more general perspective, when ET is mediated by molecular bridges in donor-acceptor systems (39, 40), the bridge structure and its thermal and nuclear motions modulate ET probability (25, 41) by affecting a number of parameters, including electronic and vibronic coupling interactions, which in turn may be affected by IR excitation (42).

To explore specifically the effect of the IR excitation of the $\nu(\text{C}\equiv\text{C})$ mode in **1** on the relative energies of the excited states involved in ET processes, we performed preliminary time-dependent density functional theory (TD-DFT) calculations for a range of CC distances of the -Pt-CC-NAP fragment (35). The CC distances were varied stepwise across the range ± 0.15 Å from the equilibrium distance calculated for the ground-state geometry, and at each distance the energies of multiple excited states were calculated. The results of these calculations for the lowest

three excited states (Fig. 4) show a $\text{DB}^+\text{A}^-/{}^3\text{D}^+\text{BA}^-$ state crossover at $\text{C}\equiv\text{C}$ bond distances slightly longer than that calculated for the equilibrium geometry. It is therefore feasible that the IR excitation-induced population of a higher vibrational state of the acetylide bridge mode will lead to a transient increase in the average bond length, which could drive the system across this crossover point along the $\text{C}\equiv\text{C}$ reaction coordinate, contributing to the experimentally observed suppression of $^3\text{D}^+\text{BA}^-$ (43).

The above results demonstrate a simple and flexible strategy to influence the outcomes of light-induced electron transfer by IR excitation of intramolecular vibrations and suggest the features of molecular design required to achieve such an effect. We show that ultrafast mode-specific IR excitation of bridge vibrations coupled to electron transfer in a *trans*-acetylide Pt(II) donor-bridge-acceptor system in solution can control competing ET channels and ultimately switch between different product states. Direct experimental observation of such effects provides a test bed for theoretical frameworks and can contribute to the understanding of electron transfer processes under nonequilibrium conditions. Overall, directing charge transfer by vibrational excitation may provide hitherto inaccessible insight into chemical mechanisms, in a step toward quantum control of chemical reactivity.

REFERENCES AND NOTES

1. V. Balzani, *Electron Transfer in Chemistry* (Wiley-VCH, Weinheim, Germany, 2001).
2. R. A. Marcus, N. Sutin, *Biochim. Biophys. Acta* **811**, 265–322 (1985).
3. P. F. Barbara, T. J. Meyer, M. A. Ratner, *J. Phys. Chem.* **100**, 13148–13168 (1996).
4. T. Elsaesser, W. Kaiser, *Annu. Rev. Phys. Chem.* **42**, 83–107 (1991).
5. K. G. Spears, X. Wen, R. Zhang, *J. Phys. Chem.* **100**, 10206–10209 (1996).
6. J. Ulstrup, J. Jortner, *J. Chem. Phys.* **63**, 4358–4368 (1975).
7. J. N. Schrauben, K. L. Dillman, W. F. Beck, J. K. McCusker, *Chem. Sci.* **1**, 405–410 (2010).
8. D. Davis, M. C. Toroker, S. Speiser, U. Peskin, *Chem. Phys.* **358**, 45–51 (2009).
9. D. Devault, Q. Rev. Biophys. **13**, 387–564 (1980).
10. H. B. Gray, J. R. Winkler, *Annu. Rev. Biochem.* **65**, 537–561 (1996).
11. F. D. Lewis et al., *Proc. Natl. Acad. Sci. U.S.A.* **99**, 12536–12541 (2002).
12. C. Bressler et al., *Science* **323**, 489–492 (2009).
13. C. Shih et al., *Science* **320**, 1760–1762 (2008).
14. J. Repp, P. Liljeroth, G. Meyer, *Nat. Phys.* **6**, 975–979 (2010).
15. A. Halpin et al., *Nat. Chem.* **6**, 196–201 (2014).
16. S. Rosenwaks, *Vibrationally Mediated Photodissociation* (Royal Society of Chemistry, Cambridge, 2009).

17. F. F. Crim, *J. Phys. Chem.* **100**, 12725–12734 (1996).
18. B. Arnstrup, N. E. Henriksen, *J. Chem. Phys.* **97**, 8285–8295 (1992).
19. B. A. Heller, D. Holten, C. Kirmair, *Science* **269**, 940–945 (1995).
20. M. Shapiro, P. Brumer, *Rep. Prog. Phys.* **66**, 859–942 (2003).
21. V. I. Prokhorenko *et al.*, *Science* **313**, 1257–1261 (2006).
22. G. M. Roberts *et al.*, *Chem. Sci.* **4**, 993–1001 (2013).
23. S. S. Skourtis, D. H. Waldeck, D. N. Beratan, *J. Phys. Chem. B* **108**, 15511–15518 (2004).
24. D. Xiao, S. S. Skourtis, I. V. Rubtsov, D. N. Beratan, *Nano Lett.* **9**, 1818–1823 (2009).
25. H. Carias, D. N. Beratan, S. S. Skourtis, *J. Phys. Chem. B* **115**, 5510–5518 (2011).
26. Z. Lin *et al.*, *J. Am. Chem. Soc.* **131**, 18060–18062 (2009).
27. To influence ET processes by pulsed IR excitation, both IR excitation and ET should occur on time scales shorter than or comparable to that of vibrational relaxation, i.e., typically a few picoseconds, while the minimum ~1.5-ps IR excitation pulse length is required to achieve the sub-12-cm⁻¹ pulses necessary for selective vibrational excitation. The chemical system and the experimental setup used in this study fulfill these requirements.
28. C. J. Adams *et al.*, *Inorg. Chem.* **47**, 8242–8257 (2008).
29. J. M. Keller *et al.*, *J. Am. Chem. Soc.* **133**, 11289–11298 (2011).
30. P. A. Scattergood *et al.*, *Dalton Trans.* **43**, 17677–17693 (2014).
31. W. M. Kwok, D. L. Phillips, P. K. Yeung, V. W. Yam, *J. Phys. Chem. A* **101**, 9286–9295 (1997).
32. A broad transient signal appears as a baseline offset that decays with the lifetime of the initially formed DB⁺A⁺ excited-state manifold. This signal is due to a broad electronic absorption profile of the initial charge-transfer state that extends into the mid-IR.
33. P. Hamm, M. Zanni, *Concepts and Methods of 2D Infrared Spectroscopy* (Cambridge Univ. Press, Cambridge, 2011).
34. Pumping the C≡C $\nu = 0 \rightarrow 1$ transition with the IR pulse in DB⁺A⁺ is expected to populate $\nu = 1$. A bleach of the $\nu(0 \rightarrow 1)$ band and a corresponding $\nu(1 \rightarrow 2)$ transient signal anharmonically shifted to lower energies are expected, as well as similar signals for vibrational modes coupled to the C≡C mode. These signals are characteristic of two-dimensional IR (2DIR) and transient-2DIR spectra (33), which may use similar experimental setups. However, owing to vibronic interactions between different electronic states in **1**, the IR pump gives rise to signals associated with electronic states other than the pumped DB⁺A⁺.
35. Materials, methods, and additional information are available as supplementary materials on Science Online.
36. In **diad 2**, the excited state populated as a result of 400-nm excitation is B⁺A⁺, an equivalent to the DB⁺A⁺ branching state in **1**. However, in **2** no electron donor is present, and therefore no forward electron transfer is possible.
37. K. G. Spears, *J. Phys. Chem.* **99**, 2469–2476 (1995).
38. Y. Huang, C. T. Rettner, D. J. Auerbach, A. M. Wodtke, *Science* **290**, 111–114 (2000).
39. H. M. McConnell, *J. Chem. Phys.* **35**, 508–515 (1961).
40. M. D. Newton, *Chem. Rev.* **91**, 767–792 (1991).
41. I. A. Balabin, J. N. Onuchic, *Science* **290**, 114–117 (2000).
42. D. N. Beratan *et al.*, *Acc. Chem. Res.* **42**, 1669–1678 (2009).
43. Excitation of the high-frequency $\nu(\text{C}=\text{C})$ mode will affect other vibrations in its vicinity, which may in turn affect the nature and ordering of the excited states. Presently, exploring this multi-dimensional energy landscape is computationally intractable.

ACKNOWLEDGMENTS

We are grateful to M. Newton (Brookhaven National Laboratory), D. Phillips (Imperial College London), A. Orr-Ewing (Univ. of Bristol), D. Clary (Univ. of Oxford), and G. Worth (Univ. of Birmingham) for comments on the manuscript; to I. Rubtsov and R. Schmehl (Tulane University) for discussions; and to the Engineering and Physical Sciences Research Council, Univ. of Sheffield, and Science and Technology Facilities Council for support.

SUPPLEMENTARY MATERIALS

www.sciencemag.org/content/346/6216/1492/suppl/DC1
Materials and Methods
Figs. S1 to S8
Table S1
References (44–57)

29 August 2013; accepted 14 November 2014
10.1126/science.1259995

PHOTOCHEMISTRY

One-pot room-temperature conversion of cyclohexane to adipic acid by ozone and UV light

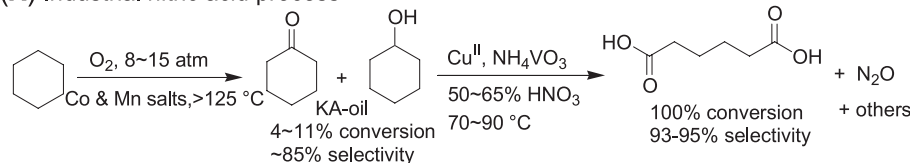
Kuo Chu Hwang* and Arunachalam Sagadevan

Nitric acid oxidation of cyclohexane accounts for ~95% of the worldwide adipic acid production and is also responsible for ~5 to 8% of the annual worldwide anthropogenic emission of the ozone-depleting greenhouse gas nitrous oxide (N₂O). Here we report a N₂O-free process for adipic acid synthesis. Treatment of neat cyclohexane, cyclohexanol, or cyclohexanone with ozone at room temperature and 1 atmosphere of pressure affords adipic acid as a solid precipitate. Addition of acidic water or exposure to ultraviolet (UV) light irradiation (or a combination of both) dramatically enhances the oxidative conversion of cyclohexane to adipic acid.

Adipic acid is a precursor for the synthesis of the nylon-6,6 polymer and, as such, is one of the most important industrial chemical intermediates. More than 3.5 million metric tons of adipic acid were produced in 2013, reflecting a ~5% growth rate per year over the past 5 years (1, 2). Nearly 95% of the worldwide industrial production of adipic acid employed the nitric acid oxidation method (3). The first step is air oxidation of cyclohexane under high temperatures (125° to 165°C) and high pressure (8 to 15 atm) to produce KA oil (i.e., a mixture of cyclohexanone and cyclohexanol) with 4 to 11% conversion and ~85% selectivity (4, 5). In the second step, nitric acid is applied as an oxidant: the conversion is ~100%, and the selectivity for adipic acid is 93 to 95% with some other short-chain acids as side products (see Fig. 1A). The process requires the nitric acid-to-KA oil ratio to be maintained at 40:1. Disadvantages of the current industrial process include low

overall product yield; corrosion of reaction vessels by nitric acid; emission of the ozone-depleting greenhouse gas N₂O; and high energy consumption. It was estimated that ~0.3 kg of N₂O gas is formed per kilogram of adipic acid produced (6, 7). After energy-consuming recovery and recycling, the amount of N₂O gas released to the atmosphere still accounts for ~5 to 8% of annual anthropogenic N₂O emission worldwide (3, 7, 8). Many efforts have been devoted to developing more efficient and environmentally friendly processes for industrial production of adipic acid that avoid the emission of N₂O. In 1998, Sato *et al.* reported a process using H₂O₂ as an oxidant to convert cyclohexene to adipic acid in the presence of a Na₂WO₄ catalyst and the phase-transfer reagent [CH₃(n-C₈H₁₇)₃N]HSO₄. Although the overall adipic acid yield (93%) is very high (9), production of 1 mol of adipic acid requires consumption of 4 to 4.4 mol of H₂O₂. The price of H₂O₂ is ~55% of the price of adipic acid. The requirement of 4 to 4.4 mol of H₂O₂ for production of 1 mol of adipic acid is economically infeasible (7). In addition, other negative factors hinder commercialization of this process, including low availability

(A) Industrial nitric acid process



(B) O₃-UV method

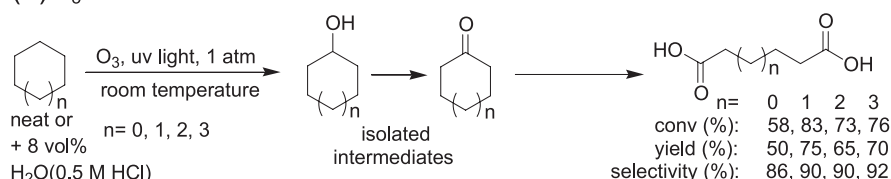


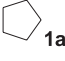
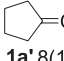
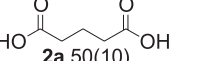
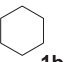
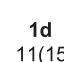
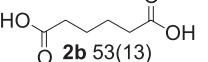
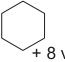
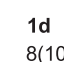
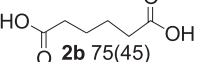
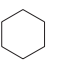

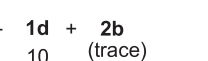
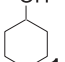
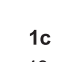
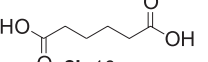
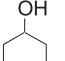

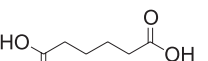
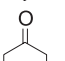
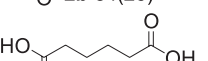
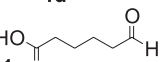
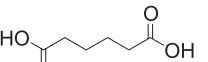
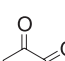
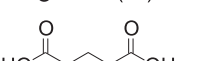
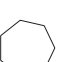
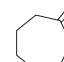
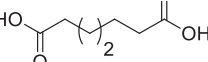
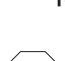
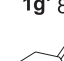
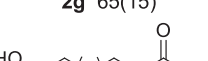
Fig. 1. Comparison of the industrial process and the method presented herein for production of adipic acid. (A) Industrial nitric acid process. (B) O₃-UV method.

of the cyclohexene substrate, poor solubility in water, and challenging recyclability of the catalysts (10–13). Adipic acid can also be produced via a multistep enzymatic conversion of D-glucose via an o-hydroxy phenol intermediate (14). Despite a very high overall yield of 97%, this process requires a large quantity of enzymes and is too costly for commercial production.

Inspired by literature reports that ozone and ultraviolet (UV) irradiation are primarily responsible for oxidative degradation of most hydrocarbons in the atmosphere, we sought to investigate whether both treatments in combination could oxidize cyclohexane, which exclusively contains unactivated sp³ C–H bonds. In a simple experiment, ozone gas was bubbled through neat cyclohexane with concurrent UV irradiation at room temperature. No metal catalyst or solvent was used. After 2 to 8 hours, a solid product gradually precipitated to the bottom of the reaction vessel (see Fig. 1B and fig. S1 for reaction scheme and pictures, respectively). A portion of the liquid cyclohexane evaporated due to the O₃ gas bubbling. The solid oxidation product of cyclohexane was subjected to ¹H nuclear magnetic resonance (NMR) and ¹³C NMR analysis (in deuterated chloroform) for structure characterization and proven to be adipic acid. We further grew single crystals and adopted x-ray crystallography to confirm that the solid precipitate is adipic acid (see fig. S2); our spectroscopic data are consistent with recently reported data (15). The isolated yield of solid adipic acid was ~53 (± 2) mol % at room temperature (an average of three runs, relative to the starting quantity of cyclohexane; the number in parentheses represents the standard error). The mass balance (i.e., all products plus recovered starting materials) was ~63 (± 2) mol %, with the rest of ~37 (± 2) mol % cyclohexane being evaporated as vapor. A stronger UV light fluence and a longer irradiation time generally lead to higher adipic acid yields. When in the presence of 8 volume % aqueous 0.5 M HCl and exposure to ozone–UV irradiation, both the final adipic acid yield and the mass balance could be further improved to ~75 (± 2) mol % and ~84 (± 3) mol %, respectively. The use of a chilled water-methanol condenser (–5° to –10°C) reduced the loss of the starting substrate and intermediates via evaporation and thus improved the mass balance substantially. All experiments were repeated at least three times (see tables S1 to S5). Experimental details can be found in the materials and methods section in the supplementary materials.

Control experiments show that ozonolysis of neat cyclohexane in the dark can also generate 12 mol % yield of adipic acid, and ozonolysis of cyclohexane–8 volume % aqueous 0.5 M HCl in the dark can also result in the formation of 45 mol % yield of adipic acid (see Table 1). Previously, Barletta *et al.* carried out ozonolysis of neat cyclohexane for 1 hour at 10°C in the dark, and derivatization of the final products with “MTBSTFA” (where “MTBSTFA” was not defined). Based on gas-liquid chromatography–mass spectrometry analysis of their ozonolysis products,

Table 1. Substrate scope for oxidative C–H functionalization of cycloalkanes. Neat liquid substrate was used unless otherwise stated. The reactions were carried out either under irradiation by a 100-W Hg lamp (200 mW/cm² at 310 nm), reported first below, or in the dark (reported below in parentheses) at room temperature. The ozone flow rate was 0.45 ml/min. The reactor was connected to a chilled water-methanol circulator condenser (–5° to –10°C) to trap evaporating reactants and intermediates. For substrates with higher freezing points (1c, 1g, and 1h), the temperature of the condenser was set between 5° and 10°C.

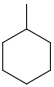
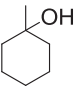
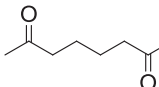
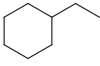
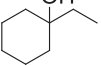
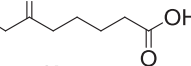
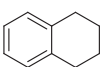
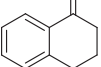
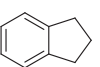
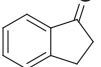
| Substrates | Products %Yield | Time (h) | %Conversion | %Selectivity for 2 | %Mass balance |
|--|---|-------------|-------------|-----------------------|------------------|
|  1a  1a' 8(12) +  2a 50(10) | | 10 | 58(22) | 86(45) | 58(25) |
|  1b  1d + 11(15) |  2b 53(13) | 15 | 64(28) | 84(46) | 64(53) |
|  1b + 8 vol% aqueous 0.5 M HCl  1d + 8(10) |  2b 75(45) | 15 | 83(55) | 90(82) | 83(55) |
|  1c +  1d +  2b 68 15 10 (trace) | | 0.5 | 25 | — | 93 |
|  1c +  1d + 49 40 |  2b 10 | 0.5 | 50 | 20 | 99 |
|  1c +  1d + 10(15) |  2b 84(25) | 8 | 94(40) | 90(63) | 98(96) |
|  1d + 6(65) |  2b 90(30)* | 8 | 90(30) | 99(99) | 96(95) |
|  2b 2.3 M in CCl ₄ |  2b 99(99) | 0.3 | 99(99) | 99(99) | 99(99) |
|  1f 1.0 M in CCl ₄ – 1% H ₂ O |  2a 97(97) | 1.0 | 97(97) | 99(99) | 99(99) |
|  1g  1g' 8(12) +  2g 65(15) | | 15 | 73(27) | 90(56) | 76(60) |
|  1h  1h' 6(12) +  2h 70(20) | | 15 | 76(32) | 92(63) | 85(78) |

*Addition of 8 vol% aqueous 0.5 M HCl to neat cyclohexanone promotes the adipic acid yield from 30 mol% to 45 mol% at room temperature in the dark.

they claimed detection of formation of cyclohexanol and cyclohexanone (16). No adipic acid formation was observed, no ozonolysis of cyclohexane–acidic water result was reported, and no light irradiation was applied in their experiments. Similar dicarboxylic acid products can also be obtained from other cycloalkanes (C_nH_{2n}, where *n* = 5, 6, 7, and 8). For large-ring cycloalkanes, less evaporation occurs, and thus, good yields (65 to 70%) of the dicarboxylic acid products were obtained at room temperature. Upon short-time (0.5 hours) irradiation, a mixture of KA oil (cyclohexanol and cyclohexanone) instead

of adipic acid was obtained (see Table 1). To investigate the reaction mechanism, neat cyclohexanol was used as a substrate for reaction with ozone under UV irradiation. Upon short-time (0.5 hours) ozone treatment under UV irradiation, a mixture of cyclohexanone (major product) and adipic acid (minor product) was obtained. Prolonged UV irradiation led to the formation of a large amount of adipic acid as a solid precipitate (84 mol % isolated yield) along with a small amount of cyclohexanone (10 mol %), suggesting that cyclohexanone was further converted to adipic acid (see Table 1). Indeed, direct ozone treatment and

Table 2. Substrate scope for oxidative C-H functionalization of substituted cycloalkanes. Neat liquid substrate was used unless otherwise stated. The reactions were carried out either under irradiation by a 100-W Hg lamp (200 mW/cm² at 310 nm) or in the dark at room temperature (reported in parentheses). The ozone flow rate was 0.45 ml/min. The reactor for substrates **1i** and **1j** was connected to a chilled water-methanol circulator condenser (−5° to −10°C), but no condenser was used for the **1k** and **1l** substrates due to their high boiling points.

| Substrates | Products %Yield | Time (h) | %Conversion | %Selectivity for 3 | %Mass balance |
|--|---|-------------|-------------|------------------------------|------------------|
|  1i |  2i 10(15) +  3i 70(25) | 5 | 80(40) | 88(63) | 85(60) |
|  1j |  2j 10(12) +  3j 67(23) | 5 | 77(35) | 87(66) | 93(72) |
|  1k |  2k 72(35) | 8 | 72(35) | 94 | 99(99) |
|  1l |  2l 76(38) | 8 | 76(38) | 95 | 99(99) |

UV irradiation of neat cyclohexanone led to the formation of a solid adipic acid precipitate in ~90 mol % yield. The results clearly show that ozone treatment and UV irradiation of neat cyclohexane leads to the formation of cyclohexanol, then cyclohexanone, and finally adipic acid. Measurements of intermediate and product concentrations (by ¹H NMR) during the reaction time course also support the above reaction scheme for the neat cyclohexane-ozone-UV irradiation system (see fig. S3 and discussion therein). The selectivity for adipic acid is nearly quantitative because the intermediates (including cyclohexanol and cyclohexanone) will eventually be converted to adipic acid upon prolonged UV irradiation, and the solid precipitate contains only one product (adipic acid). No short-chain dicarboxylic acids or other products were observed or detected by ¹H NMR measurements.

When substituted cyclohexanes were used as substrates, a similar trend was observed (see Table 2). For example, 1-methylcyclohexanol was obtained as the major product after short-time (2 hours) ozone treatment and UV irradiation of methylcyclohexane, whereas open-chain keto-carboxylic acid emerged as the major product upon prolonged (5 hours) irradiation, with a trace amount of 1-methylcyclohexanol as a minor product (see Table 2). For substrates that have two types of C-H bonds, selective oxidation occurs at methine C-H over methylene C-H bonds and at benzylic C-H over methylene C-H bonds (see Table 2).

It is well established that upon UV (306 to 328 nm) irradiation, ozone decomposes to gen-

erate singlet ¹O₂ and a singlet O(¹D) atom with a quantum yield of 0.79 (17, 18). The singlet O(¹D) atom is highly reactive and can insert into C-H bonds of hydrocarbons to form C-O-H bonds in the gas phase with the conservation of total spin angular momentum (19, 20). Our control experiments show that exposure of cyclohexane to singlet ¹O₂ (by photoirradiation of cyclohexane in the presence of photosensitizers) does not generate adipic acid, suggesting that the formation of adipic acid is mainly due to chemical reactions between atomic O(¹D) with cyclohexane, cyclohexanol, and cyclohexanone. A possible reaction pathway for the neat cyclohexane-ozone-UV system is proposed in fig. S4(i) to account for formation of adipic acid via selective C-H bond oxidation of cyclohexane by O(¹D). First, direct C-H bond insertion of O(¹D) into cyclohexane would lead to the formation of cyclohexanol (21), which is further oxidized by O(¹D) at the weakest methine C-H bond to form a geminal diol, 1,1'-dihydroxycyclohexane. Geminal diols are known to be very unstable and will rapidly undergo dehydration to form stable ketones (22). The bonding energies of methine C-H, methylene C-H, and O-H bonds are ~96, ~99, and ~105 kcal/mol, respectively (23). Insertion of O(¹D) into a C-H bond in cyclohexane requires cleavage of one C-H bond and formation of two bonds (i.e., C-O and O-H), which are exothermic and thermodynamically favored. Subsequent insertion of O(¹D) into the methine C-H bond of cyclohexanol is also thermodynamically favored. Both cyclohexanol and cyclohexanone were isolated as stable intermediates upon short-time UV irradiation

of cyclohexane in the presence of ozone. The conversion of cyclohexanone to adipic acid by reaction with a singlet O(¹D) atom probably proceeds via dihydroxylation at the α-C-H bond adjacent to the ketone functionality, because the α-C-H bond is weaker than other remote methylene C-H bonds.

We also experimentally observed that the addition of acidic water could promote both light and dark conversion of cyclohexane to adipic acid by ozone, as well as improve the mass balance substantially. Both ozone and O(¹D) (generated by UV irradiation of ozone) are reported to react with water to form a hydroxyl radical (·OH) [see eqs. 3 and 4 in fig. S4(ii)] (24, 25). The reaction mechanism is likely to involve hydroxyl radical-mediated selective hydrogen atom abstraction and a peroxidation chain reaction [see proposed mechanism in fig. S4(ii) and discussion therein]. A more detailed discussion of reaction mechanisms can be found in the supplementary text and fig. S4.

Oxidation of cyclohexane by singlet O(¹D) and a hydroxyl radical can occur at any of the 12 equivalent C-H bonds. In the case of later intermediates (i.e., cyclohexanol and cyclohexanone), oxidative C-H bond functionalization seemed to occur exclusively at the weakest α-C-H bond adjacent to the electron-withdrawing hydroxyl or carbonyl site. Note that benzylic C-H (~90 kcal/mol) and methine C-H (~96 kcal/mol) bond strengths are, in general, weaker than that of methylene C-H bonds (~99 kcal/mol) (23). Such site selectivity is unusual because oxidative C-H bond functionalization by electron-deficient oxidants, such as a combination of an organometallic catalyst and H₂O₂, usually occurs at the most remote (or the most electron-rich) C-H bond away from electron-withdrawing groups or directing groups (14, 26–29). The site selectivity here is most likely governed by the singlet spin nature of the O(¹D) atom rather than by its electrophilicity. A similar type of spin-electronic effect governing C-H bond oxidation was also observed in the direct rhodium carbenoid insertion into C-H bonds in tetrahydrofuran and alkanes (29).

Varkony *et al.* previously reported (without discussion of reaction mechanism) that the tertiary C-H site in methylcyclohexane and analogs can be oxidatively converted to 1-methylcyclohexanol by ozone on silica gel at −78°C in the dark with 99.5% conversion and 65% yield (30). A tricopper cluster in tandem with H₂O₂ can oxidatively convert cyclohexane to cyclohexanol and cyclohexanone (31). These processes do not generate dicarboxylic acid as the final product, and their experimental conditions are not suitable for industrial applications. Overall, the process we report here opens up opportunities to oxidatively convert many other inexpensive hydrocarbons to value-added chemicals by using singlet O(¹D) or hydroxyl radical-mediated selective C-H bond functionalization.

REFERENCES AND NOTES

- Y. Wen *et al.*, *Green Chem.* **14**, 2868–2875 (2012).
- "Adipic acid (ADPA): 2014 world market outlook and forecast up to 2018" (Merchant Research and Consulting, Birmingham, UK, 2014).

3. S. Van de Vyver, Y. Roma'n-Leshkov, *Catal. Sci. Technol.* **3**, 1465–1479 (2013).
4. A. Castellan, J. C. J. Bart, S. Cavallaro, *Catal. Today* **9**, 237–254 (1991).
5. A. Chauvel, G. Lefebvre, *Petrochemical Processes: Major Oxygenated, Chlorinated and Nitrated* (Editions Technip, Paris, 1989).
6. L. Schneider, M. Lazarus, A. Kollmuss, "Industrial N₂O projects under the CDM: Adipic acid - A case of carbon leakage?" Working paper WP-US-1006, Stockholm Environment Institute, Somerville, MA, 2010.
7. F. Cavani, J. H. Teles, *ChemSusChem* **2**, 508–534 (2009).
8. R. A. Reimer, C. S. Slaten, M. Seapan, M. W. Lower, P. E. Tomlinson, *Environ. Prog.* **13**, 134–137 (1994).
9. K. Sato, M. Aoki, R. Noyori, *Science* **281**, 1646–1647 (1998).
10. U. Schuchardt *et al.*, *Appl. Catal. A* **211**, 1–17 (2001).
11. M. N. Timofeeva, O. A. Kholdeeva, S. H. Jung, J. S. Chang, *Appl. Catal. A Gen.* **345**, 195–200 (2008).
12. Z. Bohström, I. Rico-Lattes, K. Holmberg, *Green Chem.* **12**, 1861–1869 (2010).
13. Y. Deng, Z. Ma, K. Wang, J. Chen, *Green Chem.* **1**, 275–276 (1999).
14. K. M. Draths, J. W. Frost, *J. Am. Chem. Soc.* **116**, 399–400 (1994).
15. H.-K. Fun, S. Chantrapromma, L.-H. Ong, *Molecules* **19**, 10137–10149 (2014).
16. B. Barletta *et al.*, *Ozone Sci. Eng.* **20**, 91–98 (1998).
17. Y. Matsumi *et al.*, *J. Geophys. Res.* **107**, 10.1029/2001JD000510 (2002).
18. Y. Matsumi, M. Kawasaki, *Chem. Rev.* **103**, 4767–4782 (2003).
19. P. Michaud, R. J. Cvetanovic, *J. Phys. Chem.* **76**, 1375–1385 (1972).
20. T. H. Varkony, S. Pass, Y. Mazur, *J. Chem. Soc. Chem. Commun.* **1975**, 457–458 (1975).
21. M. D. Hoops, B. S. Ault, *J. Mol. Struct.* **929**, 22–31 (2009).
22. I. Ignatyev, M. Montejo, P. G. R. Ortega, J. J. L. González, *Phys. Chem. Chem. Phys.* **13**, 18507–18515 (2011).
23. S. J. Blanksby, G. B. Ellison, *Acc. Chem. Res.* **36**, 255–263 (2003).
24. E. Reisz, W. Schmidt, H. P. Schuchmann, C. von Sonntag, *Environ. Sci. Technol.* **37**, 1941–1948 (2003).
25. B. J. Finlayson-Pitts, J. N. Pitts Jr., *Science* **276**, 1045–1052 (1997).
26. M. S. Chen, M. C. White, *Science* **318**, 783–787 (2007).
27. T. Newhouse, P. S. Baran, *Angew. Chem. Int. Ed.* **50**, 3362–3374 (2011).
28. H. M. L. Davies, T. Hansen, M. R. Churchill, *J. Am. Chem. Soc.* **122**, 3063–3070 (2000).
29. K. Chen, A. Eschenmoser, P. S. Baran, *Angew. Chem. Int. Ed.* **48**, 9705–9708 (2009) and references therein.
30. H. Varkony, S. Pass, Y. Mazur, *J. Chem. Soc. Chem. Commun.* **1974**, 437–438 (1974).
31. S. I. Chan *et al.*, *J. Catal.* **293**, 186–194 (2012).

ACKNOWLEDGMENTS

We are grateful for financial support from the Ministry of Science and Technology, Taiwan. K.C.H. conceived the idea, designed the experiments, and wrote the manuscript. A.S. conducted the experiments. Metrical parameters for the x-ray structures of **2b** and **2g** are available free of charge from the Cambridge Crystallographic Data Centre under accession numbers CCDC 1025098 and CCDC 1025099, respectively. A patent application is pending.

SUPPLEMENTARY MATERIALS

www.sciencemag.org/content/346/6216/1495/suppl/DC1
Materials and Methods
Supplementary Text
Figs. S1 to S6
Tables S1 to S15
References (32–44)
¹H and ¹³C NMR Data
¹H and ¹³C NMR Spectra

6 August 2014; accepted 11 November 2014
10.1126/science.1259684

CATALYSIS

Catalytically active Au-O(OH)_x-species stabilized by alkali ions on zeolites and mesoporous oxides

Ming Yang,¹ Sha Li,² Yuan Wang,¹ Jeffrey A. Herron,² Ye Xu,³ Lawrence F. Allard,⁴ Sungsik Lee,⁵ Jun Huang,⁶ Manos Mavrikakis,² Maria Flytzani-Stephanopoulos^{1*}

We report that the addition of alkali ions (sodium or potassium) to gold on KLTL-zeolite and mesoporous MCM-41 silica stabilizes mononuclear gold in Au-O(OH)_x (Na or K) ensembles. This single-site gold species is active for the low-temperature (<200°C) water-gas shift (WGS) reaction. Unexpectedly, gold is thus similar to platinum in creating –O linkages with more than eight alkali ions and establishing an active site on various supports. The intrinsic activity of the single-site gold species is the same on irreducible supports as on reducible ceria, iron oxide, and titania supports, apparently all sharing a common, similarly structured gold active site. This finding paves the way for using earth-abundant supports to disperse and stabilize precious metal atoms with alkali additives for the WGS and potentially other fuel-processing reactions.

The water-gas shift (WGS) reaction (CO + H₂O → CO₂ + H₂) is an important reaction for hydrogen upgrading during fuel gas processing. Emerging applications in fuel cells require active, nonpyrophoric, and cost-effective catalysts. Along with a new group of platinum catalysts with atomically dispersed Pt sites to maximize activity and catalytic efficiency (1–3), the lower apparent activation energy *E*_a for the WGS reaction (~45 kJ/mol) for gold (Au) versus ~75 kJ/mol for platinum (3–5) can be exploited for low-temperature WGS and other reactions (6, 7). Low-temperature activity is important to avoid multiple-treatment units in practical low-temperature proton-exchange membrane (PEM) fuel cell systems, whereby the deleterious CO should be totally removed for stable, long-term operation. The active Au species in the WGS catalysts are atomic species anchored through –O ligands to different supports such as ceria (3, 8, 9), iron oxide (10–12), lanthana (13), and titania (4), and the number of the active Au sites can be increased through a variety of catalyst preparation protocols. Gold nanoparticles (Au NPs) that can form during catalyst preparation are spectator species in these chemistries (3, 4, 10), in that most of the Au atoms are not activated by the support. Thus, the approach of “cage encapsulation” of Au NPs in mesoporous supports

is not advantageous for the stability of the active (atomically dispersed) Au sites.

Other approaches—for example, AuCl₃ vapor produced by sublimation and introduced into various zeolites (14, 15)—may be used to produce active Au(I)-Cl species for ambient-temperature NO reduction to N₂O by CO. Mohamed and Ichikawa (16) have shown that the Au(I) species are the main active sites for the WGS reaction at temperatures as low as 50°C. Because these sites are not chloride-free (Au-Cl bonds exist) and have weak chemical binding to the zeolites, the Au(I) sites are easily reduced to inactive Au(0) and form Au NPs upon increasing the temperature to only 100°C (16). Similarly, low stability of gold on zeolites was found by Gates and co-workers (17, 18). Careful anchoring of mononuclear Au(III) complexes from organometallic precursors produced chloride-free single-atom Au(III)-O-NaY catalytic centers that were active for CO oxidation but unstable at 25°C and 760 torr, losing ~75% of their initial activity after 15 min on stream (17). Finally, attempts to ion exchange gold in zeolites have been unsuccessful. Thus, gold ions in zeolites tend to be unstable toward aggregation in realistic reaction gas environments at temperatures above the ambient, an issue already understood for other inert supports such as silica or alumina, minimally interacting with gold (19). Hence, it is difficult to determine if the gold catalysts operate through similarly structured Au-O(OH)_x-species on inert supports as in the Au-CeO₂, Au-FeO₂, and Au-TiO₂ systems (20).

To study the nature of the active gold sites on inert supports, it is important to maximize the number of the atomically dispersed gold sites and fully eliminate the formation of Au NPs. Titania is inferior to ceria and iron oxide in that Au NP growth occurs rapidly on its surfaces (21), but with special ultraviolet (UV)-assisted preparation methods, mononuclear Au-O(OH)_x-species

¹Department of Chemical and Biological Engineering, Tufts University, MA 02155, USA. ²Department of Chemical and Biological Engineering, University of Wisconsin-Madison, WI 53706, USA. ³Department of Chemical Engineering, Louisiana State University, Baton Rouge, LA 70803, USA. ⁴Materials Science and Technology Division, Oak Ridge National Laboratory, Oak Ridge, TN 37831, USA. ⁵X-ray Science Division, Argonne National Laboratory, 9700 South Cass Avenue, Argonne, IL 60439, USA. ⁶School of Chemical and Biomolecular Engineering, University of Sydney, NSW 2006, Australia.

*Corresponding author. E-mail: maria.flytzani-stephanopoulos@tufts.edu

Table 1. Composition and reaction activity of supported gold catalysts.

| Sample wt % Au/support | Alkali:gold atomic ratio | | WGS reaction rate at 150°C (10 ⁻⁷ mol H ₂ /g _{cat} s)* | E _a for WGS reaction (kJ/mol) | Surface -OH (μmol/g _{cat} , 50°–350°C)† | Average gold size (nm)‡ |
|---------------------------|-----------------------------|-------------------|---|--|--|----------------------------|
| | Na | K | | | | |
| 0.25 Au/KLTL | – | 1.0 [§] | 1.0 | 46.5 | 34 ± 5 | > 10 |
| 0.25 Au-K/KLTL | – | 11.0 [§] | 8.2 | 49.0 | 174 ± 10 | Atomically dispersed |
| 0.25 Au/ [Si]MCM41 | 0.0 | – | 0.0 | Inactive below 300°C | 20 ± 5 | > 10 |
| 0.25 Au-Na/ [Si]MCM41 | 10.0 | – | 7.9 | 43.6 | 164 ± 10 | Atomically dispersed |

*The kinetics were measured in a simulated reformat gas mixture of 11% CO, 26% H₂O, 7% CO₂, 26% H₂-He (100- to 500-mg sample, steady-state CO conversion <15%). †The total amount of -OH species was titrated by CO TPR (10% CO-He, 30 ml/min, 100 mg, 5°C/min, from 50° to 350°C). ‡Gold nanoparticles larger than 1 nm were determined by HRTEM. The atomically dispersed gold species were imaged by STEM and also fitted by EXAFS. §Value is for the added potassium; it does not include the ion-exchanged potassium in the as-received zeolite KLTL.

can be stabilized on titania up to 1.2 weight % (wt %), and the cations remain stably anchored and active for the WGS reaction from ~ 80° to 250°C (4). Alkali ion addition was investigated in this work as a means to boost further the number of stable mononuclear Au-O(OH)_x-species. This was reported as a successful approach to prepare single-site active Pt-O(OH)_x-(Na or K)_y species on silica and alumina, which were activated at low temperatures (~100°C) for the WGS reaction and were stable to temperatures exceeding 300°C and for many hours (7). Washing of the surfaces could not remove the alkali ions stably associated with the Pt ion through -O linkages. Zugic *et al.* showed that the Pt-O(OH)_x-(Na or K)_y species could be prepared, stabilized, and similarly activated for the WGS reaction on inert (800°C-annealed) carbon nanotube surfaces (2). However, the extension of the platinum findings to gold is neither obvious nor anticipated. A few reports exist on alkali (and alkaline earth) addition to gold to structurally stabilize small Au NPs (1 to 3 nm) on alumina for ambient-temperature CO oxidation (22). Miller *et al.* (19) adopted a NaOH wash to remove the adsorbed Cl ions from the Au/Al₂O₃ catalysts and estimated by extended x-ray absorption fine structure (EXAFS) that the gold was 100% dispersed on these washed samples under mild reduction (up to 200°C) or oxidation (up to 225°C), but their stability under reaction conditions was not reported.

We show how to use alkali addition to activate and stabilize atomic Au for the WGS reaction even on inert zeolite (KLTL) and mesoporous [Si]MCM-41 silica materials. The WGS activity was measured to be comparable to that of Au on reducible oxide supports, and good stability was found up to 200°C (Table 1). The E_a values measured for the reaction over alkali-stabilized gold on the inert supports are all 45 ± 5 kJ/mol, similar to those on the Au-CeO_x, Au-FeO_x, and Au-TiO_x systems (20), indicating that the gold active sites are of similar structure on all support types. It is not straightforward to produce the active alkali-stabilized gold centers on the inert supports, as the alkali ions must interact with the gold, not the support.

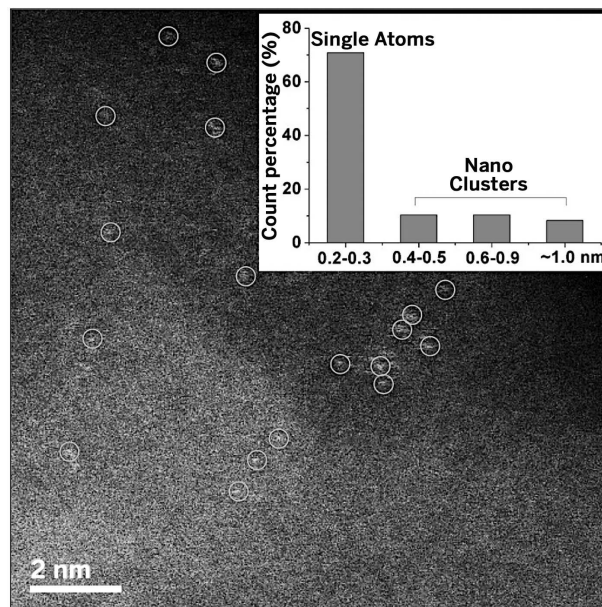


Fig. 1. Aberration-corrected high-angle annular dark-field-STEM images of the 0.25Au-Na/[Si]MCM41 catalyst. The circles are drawn around isolated gold atoms. The size distribution (inset) is based on >150 observed gold species counted from the high-magnification images (recorded at 8 to 10M× original magnification).

Notably, the KLTL-zeolites used here have an abundance of potassium ions (16.8 wt %), but gold addition from a typical precursor (e.g., HAuCl₄) by incipient wetness impregnation (IWI) or deposition precipitation fails to prepare an active catalyst. However, using IWI of KAu(CN)₂ on the KLTL-zeolites followed by solid-state impregnation of KOH (Au:K = 1:10) did form an active Au-K/KLTL catalyst after careful heating [details of the preparation methods are described in the supplementary materials (23)]. In another preparation, a gold sol formed from HAuCl₄ with NaOH (Au:Na = 1:10) at pH ~14 was used to prepare an active Au-Na/[Si]MCM41 catalyst (table S1). For other supports, including a hydrothermally treated alumina in NaOH, see preparation details in the supplementary materials and in fig. S1 and tables S1 and S2.

The preparation protocols show that the requirement for an active catalyst is that the alkali ions are linked to the atomic gold through -O ligands and not merely be present on the support. It has been widely reported that the support

plays a crucial role in the WGS reaction, providing facile dissociation of water molecules to supply -OH species to the vicinal gold sites where CO is adsorbed (24), but the active sites were not resolved. These may still involve just the Au-(OH)_x species attached to the support through -O ligands. We present evidence here for the latter by surrounding the gold atom with a large number (8 to 10) of Na or K ions through -O ligands. The choice of the supporting surface (zeolite, silica, alumina, etc.) is then unimportant for the chemistry.

The lack of sensitivity of E_a for the WGS reaction on the type of support is a strong first indication of a structurally similar gold active site present on all supports. Corroborating this finding, kinetics measurements found that the reaction order for H₂O is 0.7 to 0.8 for all the catalysts (with or without alkali) used in this work (fig. S2), demonstrating that the role of water is common on all the gold catalysts. The alkali addition modifies the support properties at higher temperatures; for example, after a

thermal treatment to 600°C, Amenomiya and co-workers found that alkali-stabilized alumina was activated for the WGS reaction above 400°C with E_a of ~ 80 kJ/mol (25, 26).

CO temperature-programmed reaction (TPR) tests were conducted to titrate the WGS-active hydroxyls on the alkali-stabilized gold sites (up to 350°C) (Table 1, table S2, and fig. S3). The presence of alkali markedly increased the amount of these hydroxyls, and correspondingly the overall WGS activity of the catalyst within the same temperature window. These hydroxyls are regenerable, as shown by consecutive CO-TPR cycles with intermittent rehydration of the catalyst at 25°C (fig. S3). In the absence of gold, the addition of K^+ only provides trace amounts of dry [O] through the surface transformation of -OH to K_2O (27). With the gold present, as in Au-K/KLTL, gold associated with the potassium shows a large amount of CO_2 formation from active -OH species corresponding to a Au:K atomic ratio of 1:8. This was accompanied by the production of a large amount of H_2 (1/2 of CO_2) from the -OH species (fig. S3). Notably, from the samples with fully dispersed gold (0.25Au-K/KLTL and 0.25Au-Na/[Si]MCM41) and earlier reports (4), we found that the total activity is proportional to the number of the surface -OH species, whereas the activity per gold atom (turnover frequency) is the same for all gold catalysts irrespective of the support (fig. S4). The Au-K/KLTL sample also shows good stability in 100 hour-long operation in a reformat-type gas mixture (fig. S5).

Electron microscopy studies revealed that alkali ion addition markedly increased the dispersion of gold on all the inert supports that we investigated in this work (Table 1, Fig. 1, and figs. S6 to S9). For example, 72% of the gold counted in the images was present as isolated atoms away from each other on the surface of the 0.25Au-Na/[Si]MCM41 sample (Fig. 1 and fig. S6). A minority of subnanometer gold clusters present on the same sample did not have the packed gold atom structure of Au NPs. These species appear to comprise a few atoms of gold anchored close to each other but nonaggregated. The presence of the surrounding alkali atoms could not be determined by imaging because of the low contrast of these light elements. EXAFS analysis under in situ conditions for the working catalysts further confirmed that the gold species were atomically dispersed and associated with alkali ions before and after reaction (table S3 and fig. S10). For both the KLTL-zeolite and [Si]MCM41-supported samples, the Na_xO_y linkages to gold effectively reduced the Au-Au coordination number from 11 or 12 to the 3 or 4 range, which means that 100% dispersion of Au had been achieved (19). Although microscopic analysis (transmission electron microscopy or scanning transmission electron microscopy) provides a number-weighted particle distribution, the volume-weighted distribution provided by EXAFS can be heavily skewed by a few large particles (23). Along with the EXAFS results showing an enrichment of the Au-O shell for the alkali-containing samples, in situ x-ray absorption

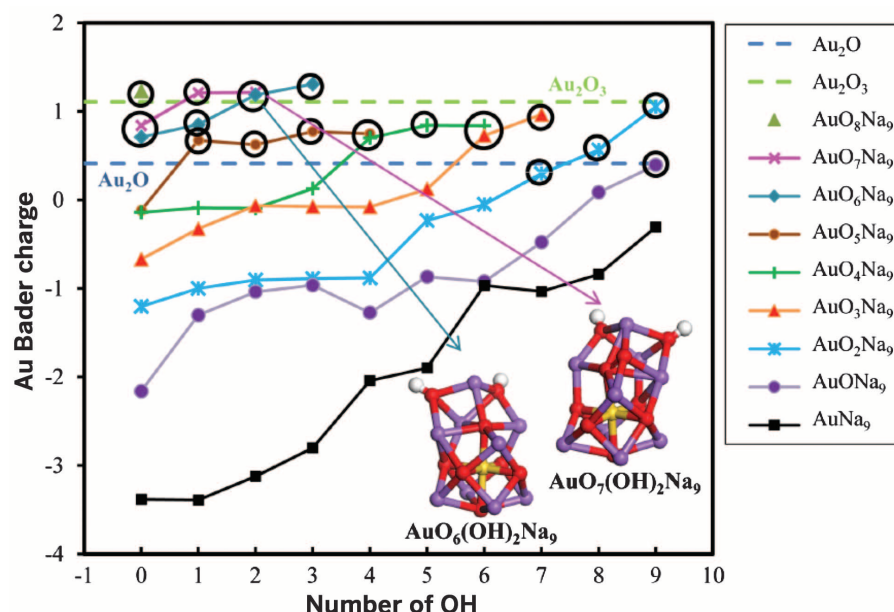


Fig. 2. Bader charge of Au in $AuO_x(OH)_yNa_9$ cluster sites. For reference, the Bader charges of Au in bulk Au_2O (+0.41) and Au_2O_3 (+1.11) are given by the dashed horizontal lines. Au, Na, O, and H atoms are shown with yellow, purple, red, and white spheres, respectively. The clusters shown are examples of promising structural candidates for the WGS active site. The circled data correspond to clusters that have Au oxidation states between that of Au_2O and Au_2O_3 .

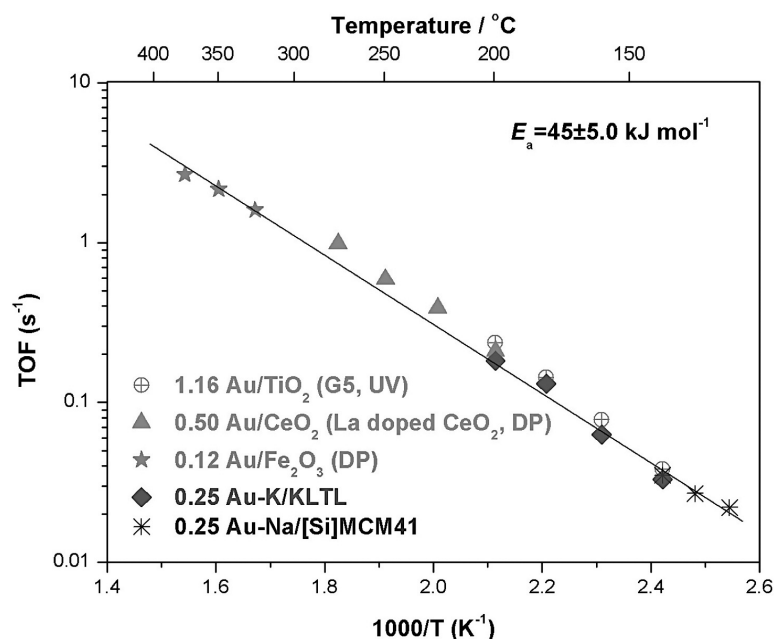


Fig. 3. TOF plot for the WGS reaction over samples with atomically dispersed gold in a reformat-type gas mixture of 11% CO , 26% H_2O , 7% CO_2 , and 26% H_2 -He. The data for the 1.16Au/TiO₂ (G5, UV) sample are from (4), for the 0.50Au/CeO₂ (La doped CeO₂, DP) sample from (8), and for the 0.12Au/Fe₂O₃ (DP) sample from (35). The experimental error for the reaction rate measurements is less than 10%. The R^2 for the linear fit is 0.9927.

near-edge structure spectra (fig. S11) and x-ray photoelectron spectroscopy data (fig. S12) show the cationic nature of the gold species, whereas the alkali-free, catalytically inactive samples con-

tain metallic Au NPs exclusively. The extra K^+ ions stabilizing the Au-O_x site in the Au-K/KLTL sample are different from the ion-exchanged K-O-Al sites in the as-received KLTL zeolite,

but are associated with $-\text{O}$ (28), $-\text{OH}$, and H_2O in their vicinity (29), as indicated by the K_{2p} x-ray photoelectron spectra (fig. S12). These results demonstrate the substantial interaction between gold and potassium through oxygen bonding.

We thus propose a cationic gold-centric active site $[\text{Au}-\text{O}(\text{OH})_x]^-$ species for the WGS reaction that is stabilized by several alkali ions via $-\text{O}-$ linkages. To gain further insights, we used density functional theory (DFT) calculations, performed in the framework of ab initio molecular dynamics (30), by using the VASP code (31) (details of the computational methods are described in the supplementary materials). To create candidate structures for the $\text{Au}-\text{O}(\text{OH})_x-\text{Na}_y$ system, we began by inspecting a series of AuNa_x clusters ($x = 1$ to 10, without oxygen). Out of these, the AuNa_9 precursor was selected for further studies because of its high stability (9 is the maximum number of Na atoms that can fit in a single shell around Au; beyond 9, additional Na atoms must be accommodated in a second shell around the gold atom; see supplementary materials for details) and because its Na:Au ratio closely matches the experimental facts/environment. To create the cationic gold species detected experimentally and to account for the involvement of oxygen in the active site, electron-withdrawing groups (O/OH) were then added to the AuNa_9 cluster, and the Bader charge was calculated (32). For reference, the calculated Bader charges of Au in bulk gold oxides Au_2O and Au_2O_3 (used as references for $\text{Au}(\text{I})$ and $\text{Au}(\text{III})$, respectively) are +0.41 and +1.11, respectively. In a systematic study of cluster sites of the general composition $\text{AuO}_x(\text{OH})_y\text{Na}_9$, several clusters in which the charge of the Au atom is similar to that of Au in bulk Au_2O and Au_2O_3 were identified (the circled models in Fig. 2). To evaluate if any of these structures that feature an oxidized Au atom would be active for WGS, the thermochemical properties relevant to the key steps of WGS (including CO and H_2O adsorption, OH binding, and H_2O activation) were calculated on these candidate $\text{AuO}_x(\text{OH})_y\text{Na}_9$ structures and compared with those on extended Cu(111) and Cu(211) surfaces. As Cu is one of the best low-temperature WGS catalysts, these are the properties that are most relevant to mimic.

Based on both the Bader charge and the thermochemical analysis (see table S4), $\text{AuO}_7(\text{OH})_2\text{Na}_9$, $\text{AuO}_6(\text{OH})_2\text{Na}_9$, $\text{AuO}_3(\text{OH})_7\text{Na}_9$, and $\text{AuO}_2(\text{OH})_9\text{Na}_9$ (structures of the first two clusters on this list are shown in Fig. 2, and the last two are shown in fig. S13) were identified as promising candidates for the active WGS reaction site. Compared with Cu(111), these clusters bind both OH and CO more weakly. These structures (Fig. 2 and fig. S13) share some common geometric features: The $-\text{O}$ ligands bind directly to the central gold atom; OH groups are primarily bound on the many three-fold “ Na_3 ” sites that surround the Au atom; and Na atoms are linked to the Au atom through $-\text{O}$ ligands.

The O/OH groups in the clusters play vital roles in H_2O dissociation. First, O/OH stabilize H_2O binding through hydrogen bonding (33). As a result, H_2O capture should be easier on the clusters than on Au(111). Second, the hydrogen atom released during H_2O dissociation prefers to bind to a surface oxygen atom to form OH, leading to a much more exothermic water dissociation event than on clean Au(111) or Cu(111) surfaces. The more exothermic activation should increase activity for H_2O dissociation. Although CO binding on the gold cation is weak, it is possible. The collocation of adsorbed CO and the $-\text{OH}$ groups bound on the threefold “ Na_3 ” sites that surround the gold atom offers the possibility for facilitating COOH formation, a critical intermediate in the WGS reaction (34). An analog of this structure was recently proposed for single gold atoms stabilized over uncapped oxygen and surrounded by Fe(III) cations on Fe_3O_4 (111) surfaces (12). Notably, the catalytic activity of Au on iron oxide (35) is similar to that of Au in the alkali-stabilized structure reported here, as shown in Fig. 3.

In Fig. 3, we scaled the steady-state reaction rates by the amount of gold loading for the atomically dispersed gold catalysts studied here, and for other gold catalysts reported to comprise only atomic gold on other supports—e.g., after leaching of gold particles—and cast them in terms of a turnover frequency (TOF) in an Arrhenius plot. In addition to the similar E_a values, the closeness of the TOFs over gold catalysts prepared on different supports and from different precursors, and subjected to different treatment methods, is noteworthy. With these findings, we conclude that, being structurally similar as on CeO_2 , Fe_2O_3 and TiO_2 , single-site cationic $\text{Au}-\text{O}(\text{OH})_x^-$ species, stabilized by a number of alkali ions in the form of $\text{AuO}_y(\text{OH})_x(\text{Na}$ or $\text{K})_x$ clusters, may be formed in appreciable amounts on inert supports. These species are highly active for the WGS reaction, the single gold atom maximizing the catalyst efficiency.

REFERENCES AND NOTES

1. Y. Zhai et al., *Science* **329**, 1633–1636 (2010).
2. B. Zugic, S. Zhang, D. C. Bell, F. F. Tao, M. Flytzani-Stephanopoulos, *J. Am. Chem. Soc.* **136**, 3238–3245 (2014).
3. Q. Fu, H. Saltsburg, M. Flytzani-Stephanopoulos, *Science* **301**, 935–938 (2003).
4. M. Yang, L. F. Allard, M. Flytzani-Stephanopoulos, *J. Am. Chem. Soc.* **135**, 3768–3771 (2013).
5. M. Shekhar et al., *J. Am. Chem. Soc.* **134**, 4700–4708 (2012).
6. M. Flytzani-Stephanopoulos, B. C. Gates, *Annu. Rev. Chem. Biomol. Eng.* **3**, 545 (2012).
7. J. M. Thomas, S. Zaghi, P. L. Gai, *Top. Catal.* **54**, 588–594 (2011).
8. Q. Fu, W. Deng, H. Saltsburg, M. Flytzani-Stephanopoulos, *Appl. Catal. B* **56**, 57–68 (2005).
9. R. Si, M. Flytzani-Stephanopoulos, *Angew. Chem. Int. Ed.* **47**, 2884–2887 (2008).
10. W. Deng, C. Carpenter, N. Yi, M. Flytzani-Stephanopoulos, *Top. Catal.* **44**, 199–208 (2007).
11. K. T. Rim et al., *J. Phys. Chem. C* **113**, 10198 (2009).
12. K. T. Rim et al., *J. Am. Chem. Soc.* **134**, 18979–18985 (2012).
13. J. D. Lessard, I. Valsamakis, M. Flytzani-Stephanopoulos, *Chem. Commun. (Camb.)* **48**, 4857–4859 (2012).
14. S. Qiu, R. Ohnishi, M. Ichikawa, *J. Chem. Soc. Chem. Commun.*, 1425–1427 (1992).
15. S. Qiu, R. Ohnishi, M. Ichikawa, *J. Phys. Chem.* **98**, 2719–2721 (1994).

16. M. M. Mohamed, M. Ichikawa, *J. Colloid Interface Sci.* **232**, 381–388 (2000).
17. J. C. Fierro-Gonzalez, B. C. Gates, *J. Phys. Chem. B* **108**, 16999–17002 (2004).
18. J. Lu, C. Aydin, N. D. Browning, B. C. Gates, *Angew. Chem. Int. Ed.* **51**, 5842–5846 (2012).
19. J. T. Miller et al., *J. Catal.* **240**, 222–234 (2006).
20. M. Flytzani-Stephanopoulos, *Acc. Chem. Res.* **47**, 783–792 (2014).
21. G. M. Veith, A. R. Lupini, S. J. Pennycook, N. J. Dudney, *ChemCatChem* **2**, 281–286 (2010).
22. A. C. Gluhoi, X. Tang, P. Margineanu, B. E. Nieuwenhuys, *Top. Catal.* **39**, 101–110 (2006).
23. Supporting materials are available on Science Online.
24. J. A. Rodriguez, S. D. Senanayake, D. Stacchiola, P. Liu, J. Hrbek, *Acc. Chem. Res.* **47**, 773–782 (2014).
25. B. W. Krupay, Y. Amenomiya, *J. Catal.* **67**, 362–370 (1981).
26. Y. Amenomiya, G. Pleizier, *J. Catal.* **76**, 345–353 (1982).
27. W. H. J. Stork, G. T. Pott, *J. Phys. Chem.* **78**, 2496–2506 (1974).
28. R. Sawyer, H. W. Nesbitt, R. A. Secco, *J. Non-Cryst. Solids* **358**, 290–302 (2012).
29. H. H. Huang, X. Jiang, H. L. Siew, W. S. Chin, G. Q. Xu, *Langmuir* **14**, 7217–7221 (1998).
30. S. Nosé, *J. Chem. Phys.* **81**, 511 (1984).
31. G. Kresse, J. Furthmüller, *Phys. Rev. B* **54**, 11169–11186 (1996).
32. G. Henkelman, A. Arnaldsson, H. Jonsson, *Comput. Mater. Sci.* **36**, 354–360 (2006).
33. L. R. Merte et al., *Nat. Commun.* **5**, 4193 (2014).
34. A. A. Gokhale, J. A. Dumesic, M. Mavrikakis, *J. Am. Chem. Soc.* **130**, 1402–1414 (2008).
35. Y. Zhai, thesis, Tufts University (2011).

ACKNOWLEDGMENTS

The financial support by the U.S. Department of Energy, Office of Basic Energy Sciences (DOE-BES) under grant DE-FG02-05ER15730 is gratefully acknowledged. M.Y. thanks H. Luo (Massachusetts Institute of Technology) for some of the surface area and pore structure analysis, C. Wang (Tufts University) for acquiring the XRD data, and B. Reinhart [Argonne National Laboratory (ANL)] for assisting with the in situ XAS experiments. Microscopy research was sponsored in part by a user project supported by the Center for Nanophase Materials Sciences (CNMS), which is sponsored at Oak Ridge National Laboratory (ORNL) by the Scientific User Facilities Division, DOE-BES, and by the U.S. DOE Office of Energy Efficiency and Renewable Energy, Vehicle Technologies Office, Propulsion Materials Program. The XAS research is sponsored by the Advanced Photon Source at ANL under contract DE-AC02-06CH11357. Work at the University of Wisconsin–Madison was supported by DOE-BES, Office of Chemical Sciences. Computational work was performed in part with supercomputing resources from the following institutions: Environmental Molecular Sciences Laboratory (EMSL), a national scientific user facility at Pacific Northwest National Laboratory (PNNL); the Center for Nanoscale Materials (CNM) at ANL; the CNMS at ORNL; and the National Energy Research Scientific Computing Center (NERSC). EMSL is sponsored by the Department of Energy's Office of Biological and Environmental Research located at PNNL. CNM and NERSC are supported by the U.S. Department of Energy, Office of Science, under contracts DE-AC02-06CH11357 and DE-AC02-05CH11231, respectively. Work at Sydney was supported by USyd Early Career Researcher Scheme. The authors declare no conflict of interest.

SUPPLEMENTARY MATERIALS

www.sciencemag.org/content/346/6216/1498/suppl/DC1
Materials and Methods
Supplementary Text
Figs. S1 to S13
Tables S1 to S4
References (36–46)

28 August 2014; accepted 15 November 2014
Published online 27 November 2014;
10.1126/science.1260526

NANOMATERIALS

Element-specific anisotropic growth of shaped platinum alloy nanocrystals

Lin Gan,^{1,3} Chunhua Cui,¹ Marc Heggen,² Fabio Dionigi,¹ Stefan Rudi,¹ Peter Strasser^{1*}

Morphological shape in chemistry and biology owes its existence to anisotropic growth and is closely coupled to distinct functionality. Although much is known about the principal growth mechanisms of monometallic shaped nanocrystals, the anisotropic growth of shaped alloy nanocrystals is still poorly understood. Using aberration-corrected scanning transmission electron microscopy, we reveal an element-specific anisotropic growth mechanism of platinum (Pt) bimetallic nano-octahedra where compositional anisotropy couples to geometric anisotropy. A Pt-rich phase evolves into precursor nanohexapods, followed by a slower step-induced deposition of an M-rich (M = Ni, Co, etc.) phase at the concave hexapod surface forming the octahedral facets. Our finding explains earlier reports on unusual compositional segregations and chemical degradation pathways of bimetallic polyhedral catalysts and may aid rational synthesis of shaped alloy catalysts with desired compositional patterns and properties.

Shape control can be an effective approach for tuning the physical and chemical properties of inorganic nanocrystals (NCs) (1, 2). For metal alloy NCs, shape control offers a flexible means of simultaneously tailoring surface structure and surface composition so as to fine-tune their catalytic properties. For example, owing to the exceptionally high catalytic reactivity of {111}-oriented surfaces, octahedral bimetallic Pt-Ni NCs with their all-{111} orientations have been considered the ultimate “dream electrocatalysts” for the technologically important oxygen reduction reaction (ORR) in

hydrogen fuel cells (3–6). Although a variety of shaped bimetallic Pt alloy NCs such as cubes (7, 8), octahedra (9–14), icosahedra (15), and concave structures (16–18) have been prepared by solution-phase co-reduction of metal precursors, their detailed elemental surface compositions have been largely overlooked and thus remained poorly understood. Contrary to the widely held notion of essentially homogeneous elemental distribution and also contrary to previously theoretically predicted Pt-rich surface composition (19–21), recent studies uncovered an unusual compositional segregation in shaped Pt alloy NCs (22, 23)—for example, Pt-rich frames and Ni-rich facets in Pt-Ni nano-octahedra (22). The elemental distribution resulted in complex structurally corrosive degradation patterns of the alloy octahedra during the ORR electrocatalysis; these patterns proved key to understanding their catalytic activity and stability trajectories.

We address some critical unresolved questions concerning the atomic origins of the complex compositional distribution and segregations in shaped bimetallic NCs. Specifically, how do atoms of different elements self-assemble into the compositionally anisotropic structure during the solution-phase co-reduction? Is the process thermodynamically or kinetically controlled? Although there have been numerous NC growth studies, they tend to focus on monometallic NCs or generally highlight the morphological evolution, not the compositional evolution, during NC growth through the use of transmission electron microscopy (TEM), either ex situ (24, 25) or in situ within a liquid TEM cell (26–29). Typical growth models for shaped monometallic NCs involve the initial nucleation of seeds in the shape of cuboctahedra (the thermodynamically most stable shape); this is followed by a kinetically controlled anisotropic growth, which is induced either through blocking of desired facet orientations by suitable capping ligands or through selective oxidative etching of undesired facets (30). Although these models shed light on the growth of shaped alloy NCs, the compositional evolution at the atomic scale has remained unaddressed, and it is generally assumed that all alloying components follow the same anisotropic growth pathway.

We present an element-by-element study of the growth mechanism of Pt-Ni nano-octahedra using aberration-corrected scanning TEM (STEM) coupled with elemental mapping by electron energy loss spectroscopy (EELS). By tracking both structural evolution and intraparticle composition evolution during the solution-phase growth, we reveal a novel element-specific anisotropic growth mechanism of shaped alloy NCs where different alloying components follow vastly different anisotropic growth pathways. The Pt-rich phase grows first into hexapod-like concave NCs via a ligand-controlled kinetic process. Deposition of a Ni-rich phase into the concave surfaces follows in a thermodynamically controlled step, and finally, Pt-Ni octahedra form with Pt-rich frames and Ni-rich {111} facets. We track the elemental composition trajectory of other

¹Electrochemical Energy, Catalysis and Materials Science Laboratory, Department of Chemistry, Chemical Engineering Division, Technical University Berlin, 10623 Berlin, Germany. ²Ernst Ruska Center for Microscopy and Spectroscopy with Electrons, Forschungszentrum Jülich GmbH, 52425 Jülich, Germany. ³Division of Energy and Environment, Graduate School at Shenzhen, Tsinghua University, 518055 Shenzhen, PR China. *Corresponding author. E-mail: pstrasser@tu-berlin.de

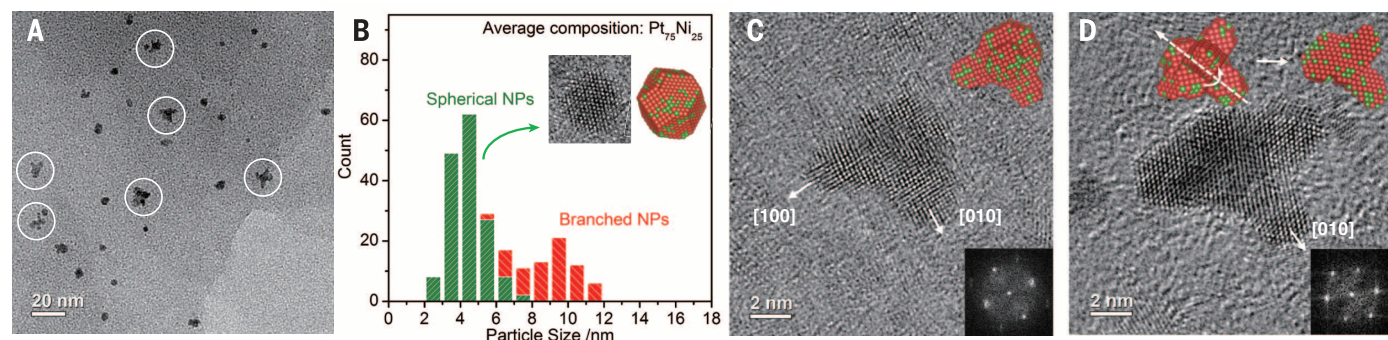


Fig. 1. Characterization of Pt-Ni NCs after 4 hours of reaction time. (A) Typical low-magnification TEM image and (B) particle size distribution, showing smaller near-spherical NCs (~4 nm) and larger branched NCs (~9 nm). They exhibited a Pt-rich average composition of Pt₇₅Ni₂₅. The inset of (B) shows a representative HRTEM image and atomic structure model of the near-spherical cuboctahedral NC. (C and D) HRTEM images and structural models of the branched NCs along the [001] and [101] directions, respectively. The insets show the fast Fourier transform (FFT) patterns to determine the crystallographic directions.

transition metal alloys as well, and conclude that the element-specific growth we observe appears to be responsible for a wide range of shaped Pt alloy NCs. Our finding provides the origin for previously reported unusual compositional segregation and chemical degradations of shaped Pt alloy NCs and enables comprehensive understanding of their entire “life cycle.”

Octahedral PtNi_{1.5} NCs were synthesized by solvothermal reduction of Pt(acac)₂ (4 mmol/liter; acac = acetylacetonate) and Ni(acac)₂ (28 mmol/liter) in 100 ml of dimethylformamide (DMF) at 120°C, where DMF acted as both reducing agent and solvent (12, 22). Unlike other methods requiring capping agents such as oleylamine (9, 10) and polyvinylpyrrolidone (13), no dedicated surfactants were needed to induce the shape-selective growth, leaving clean particle surfaces for catalytic applications. The low-temperature solvothermal synthesis is also slow [up to 42 hours, in contrast to other synthetic reactions that can

complete within several minutes (7, 9)] and allowed us to capture intermediate structures at different growth stages (after 4, 8, 16, and finally 42 hours). The collected NCs were then characterized using a spherical aberration corrected FEI Titan TEM operated at 300 kV for atomic imaging and an FEI Titan STEM (“PICO”) operated at 80 kV for high-angle annular dark field (HAADF) imaging and EELS elemental mapping.

Figure 1 presents the TEM analysis of the Pt-Ni NCs after an initial growth period of 4 hours. Energy-dispersive x-ray spectroscopy (EDX) showed an average composition of Pt₇₅Ni₂₅, suggesting a faster reduction of Pt ions relative to Ni ions, which in turn can be related to a more positive reduction potential of the former. The Pt-rich NCs exhibited two distinct morphologies. One is the near-spherical cuboctahedra around 2 to 8 nm in diameter; the other features a branched structure at larger sizes between 6 and 12 nm (Fig. 1B).

As a typical Wulff polyhedron, a cuboctahedron represents a thermodynamically stable structure at the nucleation stage because of its lowest surface energy. The formation of larger branched NCs, however, indicates a subsequent, kinetically controlled anisotropic growth. High-resolution TEM (HRTEM) images of the branched NCs along two representative orientations (Fig. 1, C and D) suggest an early-stage hexapod structure with asymmetrical arms growing along {100} directions. This asymmetry likely arises from the competition between the anisotropic growth and an opposing surface diffusion/smoothing effect for lowering surface energy, which leads to a dynamic equilibrium between branched and spherical shapes. Once a critical particle size is exceeded (e.g., 6 to 8 nm in Fig. 1B), surface diffusion slows to a point where the anisotropic growth dominates.

Indeed, when extending the reaction to 8 hours, most NCs evolved into the proposed hexapod structure (Fig. 2A), with average size around 11 nm

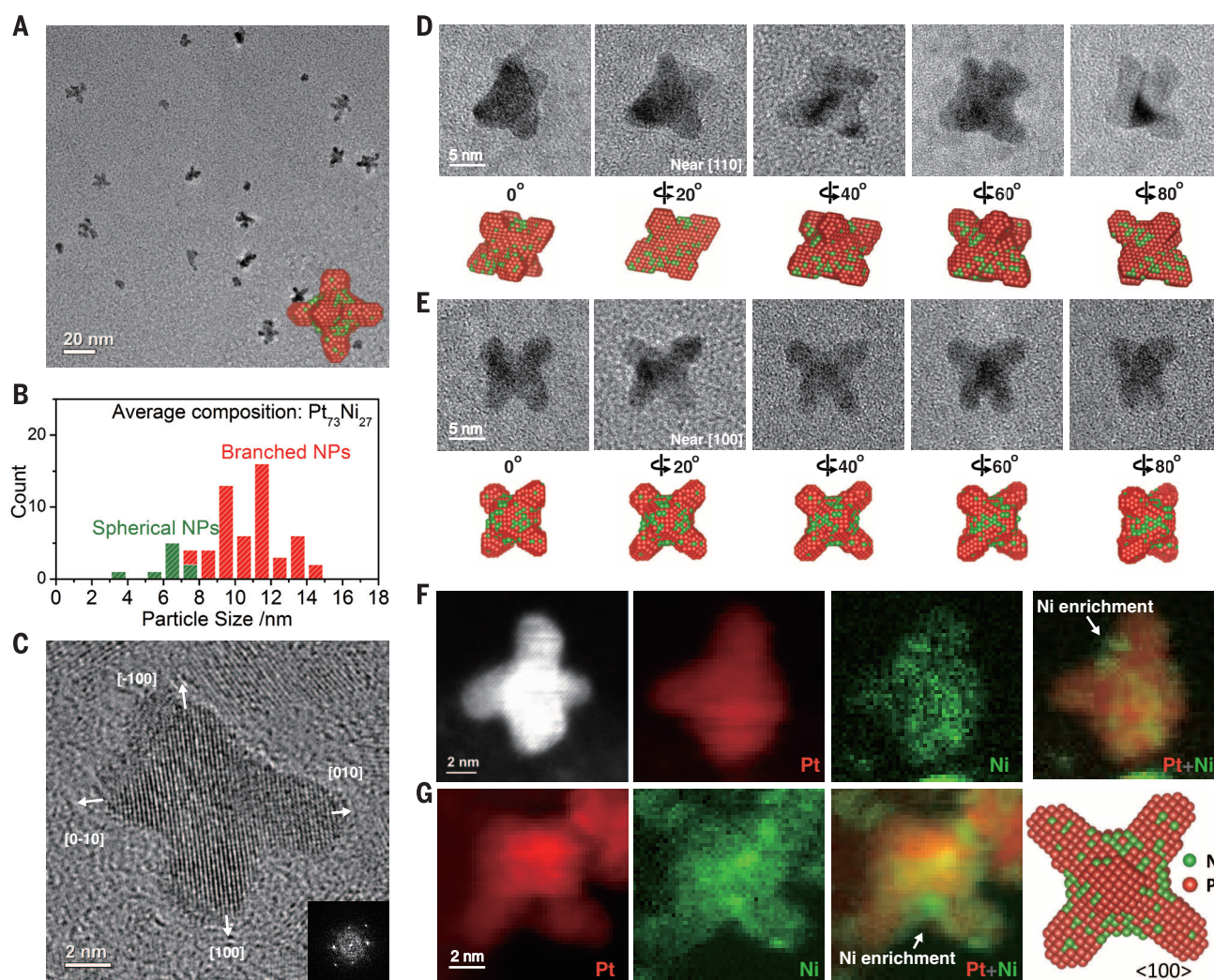


Fig. 2. Characterization of Pt-Ni NCs after 8 hours of reaction time. (A) Typical low-magnification TEM image and (B) size distribution, showing that most of the NCs evolved into branched structures with an average composition of Pt₇₃Ni₂₇. (C) HRTEM image and the corresponding FFT pattern of a branched NC along the [001] zone axis. Inset shows FFT as in Fig. 1, C and D. (D and E) A series of TEM images of two selected hexapods under different tilting conditions, showing one-to-one correspondence with the hexapod structural model. (F and G) HAADF images (red) that mainly represent Pt and EELS spectrum imaging of Ni (green), showing a slight Ni segregation at the concave surface of the Pt-Ni hexapod NCs.

(Fig. 2B). The average composition ($\text{Pt}_{73}\text{Ni}_{27}$) remained nearly unchanged throughout this growth stage, which implies that the growth of a Pt-rich phase along the multipod arms continued to dominate the process. Geometrically, an ideal hexapod NC with six identical arms is most stable when situating on three of the arms on a flat substrate (i.e., along the $[111]$ zone axis), thus showing a three-fold symmetry (18). However, the asymmetrical arms described above led to other projections, such as a crisscross along the $[001]$ zone axis (Fig. 2C). To better understand the 3D morphology, we acquired a series of images at different rotations of selected hexapod NCs (Fig. 2, D and E), with which a hexapod structural model was iteratively compared and refined. Our detailed analysis reveals a striking one-to-one correspondence between the TEM images and the projections of the 3D hexapod model at each rotation angle, which strongly supports our hypothesized growth process of the hexapod NCs.

The anisotropic growth of cuboctahedra into nanohexapods after 8 hours indicates much faster growth along $\langle 100 \rangle$ directions relative to other directions such as $\langle 111 \rangle$. We performed additional controlled syntheses to elucidate the likely mechanistic origin of this extremely anisotropic growth. First, in the absence of any Ni precursor while keeping all other synthetic conditions constant, the obtained pure Pt NCs showed exclusively near-spherical shape (fig. S1A). Thus, the Ni precursor must affect the formation of the hexapod NCs. Second, replacing $\text{Ni}(\text{acac})_2$ by $\text{Ni}(\text{acetate})_2$ resulted in spherical NCs as well (fig. S1B); in contrast, replacing $\text{Ni}(\text{acac})_2$ by $\text{K}(\text{acac})$ again induced an anisotropic growth into branched Pt NCs (fig. S1C). We conclude that the DMF-solvated acetylacetonate ligand plays a critical role in inducing the kinetically controlled anisotropic growth. Specifically, the DMF-solvated acetylacetonate ligand has stronger adsorption on the $\{111\}$ surfaces of preformed cuboctahedra, leading to a faster growth along $\langle 100 \rangle$ directions

and thus forming the hexapods. The presence of adsorbed organic ligands on the hexapod NCs was further evidenced by Fourier transform infrared (FTIR) spectra (fig. S2) and complemented by thermogravimetric analysis (fig. S3).

To gain element-specific insight into the growth mechanism of the hexapod NCs, we characterized their intraparticle composition using aberration-corrected STEM and EELS elemental mapping at 80 KV. As shown in Fig. 2, F and G, for the NCs oriented along two different directions, the HAADF images (red) that mainly represent the distribution of Pt and the EELS mapping of Ni (green) demonstrated slight segregation of Ni at the concave surfaces of the hexapods, whereas Pt was distributed more homogeneously. This result implies a deposition of Ni-rich phase at the concave surfaces of the hexapod NCs (see below).

When the synthetic reaction was extended to 16 hours, a transformation of the hexapod NCs to concave octahedra (Fig. 3A) was observed. Meanwhile, the Ni content of the NCs increased

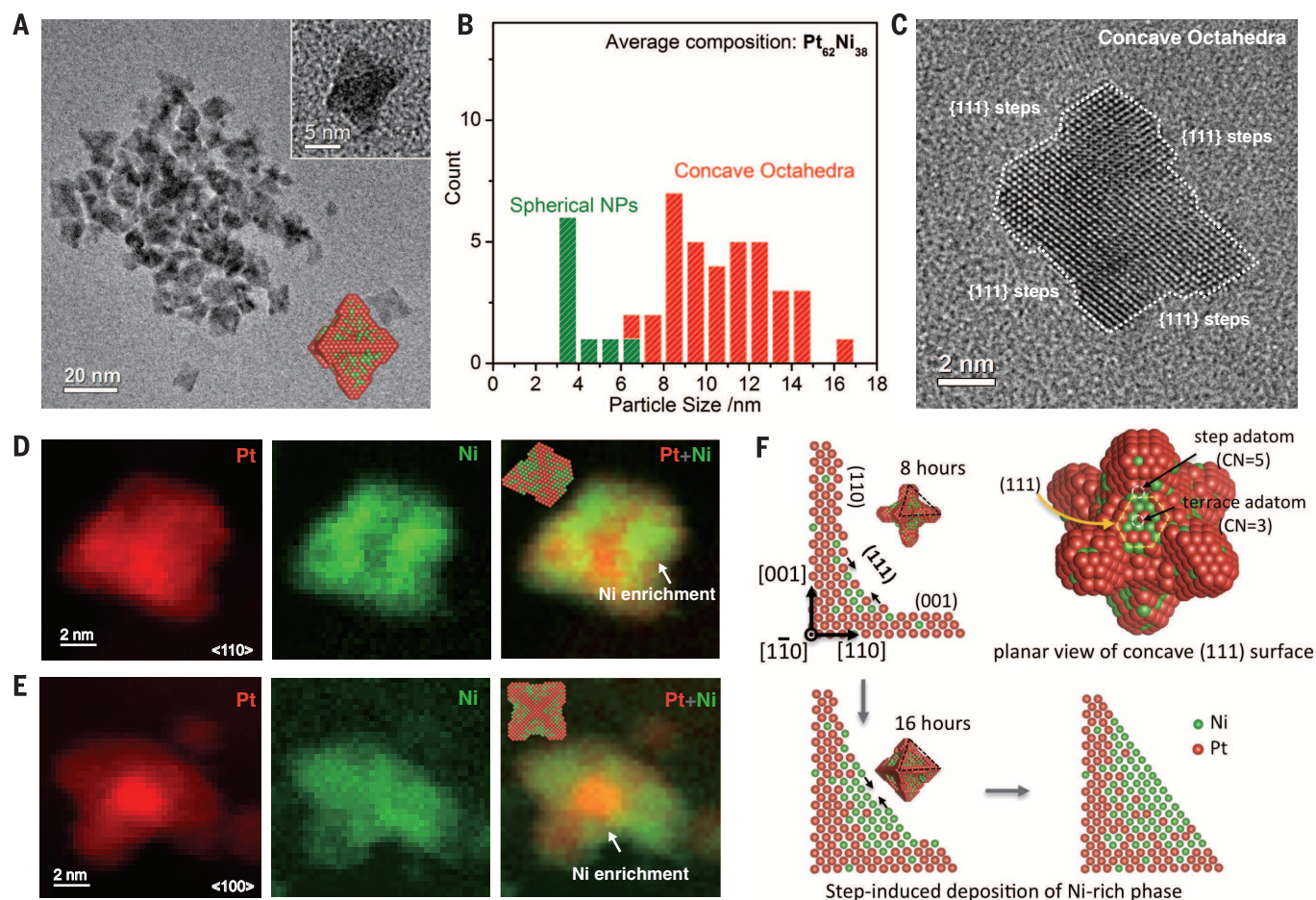


Fig. 3. Characterization of the concave Pt-Ni NCs obtained after 16 hours of growth. (A) Typical low-magnification TEM image (magnified image in inset) showing the concave octahedral shape. (B) Particle size distribution of the dominant concave octahedral NCs with an average composition of $\text{Pt}_{62}\text{Ni}_{38}$. (C) HRTEM image of a concave octahedral NC along the $[110]$ direction, showing the atomic surface steps at the concave $\{111\}$ facets. (D and E) HAADF images (red) that mainly represent Pt and EELS spectrum imaging of Ni

(green) of the concave octahedral Pt-Ni NC along the $[110]$ and $[100]$ directions, respectively. (F) A sketch of the delayed anisotropic growth of Ni-rich phase through a step-induced, layer-by-layer deposition of Ni-rich atoms at the concave $\{111\}$ surfaces of the preformed Pt-rich hexapods. Upper right: Planar view of the concave $\{111\}$ surface. Ni-rich adatoms at the step sites are more energetically favorable than those at the terrace sites because of a higher coordination number (CN).

substantially to $\text{Pt}_{62}\text{Ni}_{38}$ while the NCs maintained their average size (Fig. 3B). These results suggest an accelerated deposition of Ni-rich phase at the concave surfaces; by contrast, the growth of the Pt-rich phase along the hexapod arms (which determined the ultimate particle size) slowed down because of the depletion of the Pt precursor. Figure 3C presents an atomic-scale HRTEM image of a resulting concave octahedral NC along the $[110]$ zone axis. The concave $\{111\}$ surfaces are clearly visible with a high density of atomic steps. The EELS elemental mappings of NCs close to two representative zone axes, $[110]$ (Fig. 3D) and $[100]$ (Fig. 3E), and additional EDX mapping results (fig. S4) give direct evidence of the substantial Ni enrichment at the concave $\{111\}$ facets and the Pt enrichment at the corners.

Although the growth of Pt-rich hexapods after 8 hours was ascribed to the selective capping of DMF-solvated acetylacetonate ligand on the $\{111\}$ surfaces, we doubt that the subsequent deposition of Ni-rich phase at the concave $\{111\}$ surfaces can be explained by another ligand-blocking effect on $\{100\}$ facets. Instead, the atomic steps associated with the concave $\{111\}$ surfaces appear to enable the slow yet steady deposition of the Ni-rich phase through a step-induced, layer-by-layer growth mechanism. In fact, surface defects such as atomic steps, dislocations, and stacking faults have been reported to play important roles in seed-mediated growth of bimetallic and trimetallic core-shell NCs (31, 32). As illustrated in Fig.

3F, the preformed Pt-rich hexapods after 8 hours featured intrinsic $\{111\}$ surface steps at the concave surfaces and $\{100\}/\{110\}$ steps at the side-walls of the arms. Relative to the terrace sites, Ni adatoms energetically prefer the step sites because of a higher coordination number (Fig. 3F, upper right); thus, the process is thermodynamic in nature. Deposition of a Ni atom at the step results in the advance of the atomic step, thereby leading to a continuous, step-induced deposition of primarily Ni atoms. In this context, the side-walls play an important role in providing the initial step sites to induce a layer-by-layer growth of Ni-rich $\{111\}$ facets, as sketched in Fig. 3F. Unlike the previously reported two-pot, two-step, seed-mediated growth of bimetallic core-shell NCs (31, 32), the present anisotropic growth of Pt-rich hexapods was followed by a self-organized slower deposition of a Ni-rich phase on top of the concave $\{111\}$ surfaces. The entire particle formation proceeded spontaneously in a one-pot co-reduction that remained geometrically and compositionally anisotropic. Thus, the current synthesis also enables us to control the extent of concavity by simply controlling the reaction time.

Ultimately, a complete transformation to octahedral Pt-Ni NCs with smooth $\{111\}$ surfaces occurred after a reaction time of 42 hours (Fig. 4A and fig. S5). The Ni average composition increased to $\text{Pt}_{40}\text{Ni}_{60}$, whereas the particle size still increased slightly (Fig. 4B). This change is consistent with a continued, selective anisotropic deposition of an Ni-rich phase at the concave

$\{111\}$ surfaces. As soon as the filling of the Ni-rich phase reaches the top of the hexapod arms and flat $\{111\}$ surfaces form, there are no more step edges available; metal deposition therefore self-terminates and the octahedron is completed. This also accounts for the atomic Ni ratio in the final $\text{Pt}_{40}\text{Ni}_{60}$ octahedra being far below that of the initial metal precursors ($\text{Pt}:\text{Ni} = 1:7$). Elemental STEM-EELS mapping of the octahedral NCs (Fig. 4, C and D) unambiguously shows Ni enrichment at the $\{111\}$ facets versus Pt enrichment at the corners and edges, consistent with our previous finding (22). The Pt enrichment at both the edges and the corners also indicates a refined anisotropic growth trajectory of the Pt-rich phase; that is, the rapid growth of Pt-rich hexapods along $\langle 100 \rangle$ directions was followed by a slower growth along $\langle 110 \rangle$ directions. In contrast, as mentioned above, the growth of the Pt-rich phase along $\langle 111 \rangle$ directions was inhibited because of the selective adsorption of DMF-solvated acetylacetonate ligand on the $\{111\}$ facets.

Our conclusion as to the formation and growth of a Pt-richer phase and a Ni-richer phase on two vastly distinct time scales is fully corroborated by time-resolved XRD patterns (fig. S6). All NCs at different growth stages showed Bragg reflections assigned to a face-centered cubic (fcc) lattice with peaks shifting to higher 2θ values with increasing reaction time, indicating the increase of bulk Ni content in the NCs. Whereas the Bragg reflections of the Pt-Ni NCs growing less than 16 hours showed symmetric Gaussian peaks of a Pt-rich

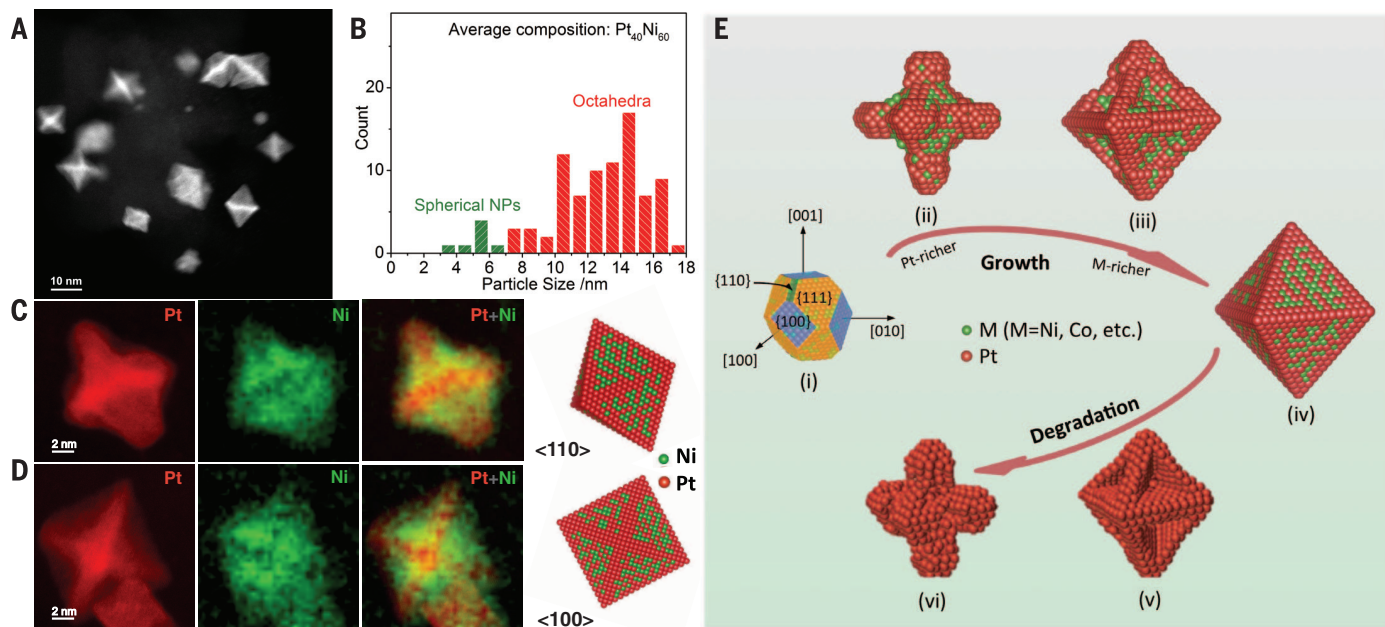


Fig. 4. Characterization of the final Pt-Ni nano-octahedra after 42 hours of reaction time, and overall pathway. (A) A typical low-magnification HAADF-STEM image. (B) Particle size distribution shows dominance of octahedral NCs around 13 nm, with an average composition of $\text{Pt}_{40}\text{Ni}_{60}$. (C and D), HAADF images (red) that mainly represent Pt and EELS spectrum imaging of Ni (green) of the octahedral $\text{PtNi}_{1.5}$ NCs along the $[110]$ and $[100]$ directions, respectively, showing Pt-rich frames along the edges/corners and Ni-enriched facets. (E) Atomic structural models of octahedral Pt bimetallic

alloy NCs (Pt-M ; $\text{M} = \text{Ni, Co, etc.}$) during the solution-phase co-reduction and during the acidic ORR electrocatalysis. (i) Initially formed Pt-rich cuboctahedra. (ii) Rapid growth along the $\langle 100 \rangle$ directions, resulting in Pt-rich hexapods. (iii) A delayed, step-induced deposition of M-rich phase at the concave $\{111\}$ surfaces. (iv) The complete formation of Pt-M octahedra with Pt-rich corners/edges and M-rich facets. (v) Selective etching of the M-rich $\{111\}$ facets during acidic ORR electrocatalysis, leading to Pt-rich concave octahedra. (vi) Degradation of octahedra into Pt-rich hexapods after long-term electrode potential cycling.

fcc phase, the final Pt-Ni octahedra after 42 hours of growth exhibited asymmetric diffraction peaks, implying the coexistence of a Pt-rich phase and a Ni-rich phase.

To demonstrate the general importance of the element-specific anisotropic growth mechanism, we further synthesized Pt-Co NCs by replacing Ni(acac)₂ with Co(acac)₂ while keeping all other conditions unchanged. After 42 hours of reaction time, octahedral PtCo_{1.5} NCs were successfully prepared. By following their morphological and compositional evolution after different growth times (fig. S7), we observed a growth trajectory of the PtCo_{1.5} octahedra similar to that of the PtNi_{1.5} octahedra. The growth of Pt-rich hexapods/concave octahedra before the final formation of Co-rich octahedra again suggests a delayed anisotropic deposition of a Co-rich phase at the concave {111} surfaces. Thus, the element-specific anisotropic growth appears to be an important mechanism for the formation of a variety of shaped Pt alloy NCs in solution-phase co-reduction.

Figure 4E presents a comprehensive, atomic-scale “life-cycle” model of our bimetallic nano-octahedra, including their unusual anisotropic growth pathway and their previously reported degradation pathway during acidic ORR electrocatalysis (22). Our results reveal a previously overlooked element-specific, compositionally anisotropic growth mechanism of shaped Pt alloy NCs, where rapid growth of Pt-rich hexapods/concave octahedra along ⟨100⟩ directions precedes delayed deposition of Ni-rich phase at the concave {111} sites. Whereas the growth of Pt-rich hexapods is a ligand-controlled kinetic process, the step-induced deposition of the Ni-rich phase at the concave surface resembles a thermodynamically controlled process accomplished in a much longer time. The element-specific anisotropic growth provides the origin of our previously reported compositional segregation (Ni-rich facets and Pt-rich corners/edges) and chemical degradation pathway of the Pt-Ni octahedra (22), which underwent a selective etching of the Ni-rich {111} facets and thus activity instability during the ORR electrocatalysis in acidic electrolyte (Fig. 4E and fig. S8). While forming a catalytically active Pt-rich shell, the selective etching of the Ni-rich {111} facets resulted in concave octahedra with the exposure of less active facets such as {100} and {110}. Extended potential cycling further resulted in the re-emergence of Pt-rich hexapods and almost none of the catalytically active {111} surfaces survived, leading to substantial activity degradation. Evidently, the fate of the shaped Pt bimetallic NCs during long-term ORR electrocatalysis is substantially determined by the early stages of their element-specific anisotropic growth during synthesis.

Our results highlight the importance of understanding the element-by-element growth mechanism of shaped alloy NCs. The possibility of controlling the element-specific anisotropic growth modes of such NCs may enable the rational synthesis of Pt alloy nano-octahedra ORR electrocatalysts with desired surface composition (e.g., Pt-rich {111} facets) and sustained high activity.

REFERENCES AND NOTES

1. T. S. Ahmadi, Z. L. Wang, T. C. Green, A. Henglein, M. A. El-Sayed, *Science* **272**, 1924–1926 (1996).
2. N. Tian, Z.-Y. Zhou, S.-G. Sun, Y. Ding, Z. L. Wang, *Science* **316**, 732–735 (2007).
3. H. A. Gasteiger, N. M. Marković, *Science* **324**, 48–49 (2009).
4. V. R. Stamenkovic et al., *Science* **315**, 493–497 (2007).
5. M. K. Debe, *Nature* **486**, 43–51 (2012).
6. G. Wu, K. L. More, C. M. Johnston, P. Zelenay, *Science* **332**, 443–447 (2011).
7. D. Xu et al., *Angew. Chem. Int. Ed.* **48**, 4217–4221 (2009).
8. J. Zhang, J. Fang, *J. Am. Chem. Soc.* **131**, 18543–18547 (2009).
9. J. Zhang, H. Yang, J. Fang, S. Zou, *Nano Lett.* **10**, 638–644 (2010).
10. J. Wu, A. Gross, H. Yang, *Nano Lett.* **11**, 798–802 (2011).
11. M. K. Carpenter, T. E. Moylan, R. S. Kukreja, M. H. Atwan, M. M. Tessema, *J. Am. Chem. Soc.* **134**, 8535–8542 (2012).
12. C. Cui et al., *Nano Lett.* **12**, 5885–5889 (2012).
13. Y. Wu, S. Cai, D. Wang, W. He, Y. Li, *J. Am. Chem. Soc.* **134**, 8975–8981 (2012).
14. S.-I. Choi et al., *Nano Lett.* **13**, 3420–3425 (2013).
15. J. Wu et al., *J. Am. Chem. Soc.* **134**, 11880–11883 (2012).
16. H. Zhang et al., *J. Am. Chem. Soc.* **133**, 6078–6089 (2011).
17. Y. Wu et al., *Angew. Chem. Int. Ed.* **51**, 12524–12528 (2012).
18. X. Liu et al., *Sci. Rep.* **3**, 1404 (2013).
19. E. Christoffersen, P. Liu, A. Ruban, H. L. Skriver, J. K. Nørskov, *J. Catal.* **199**, 123–131 (2001).
20. G. Wang, M. A. Van Hove, P. N. Ross, M. I. Baskes, *J. Chem. Phys.* **122**, 024706 (2005).
21. I. A. Abrikosov, A. V. Ruban, H. L. Skriver, B. Johansson, *Phys. Rev. B* **50**, 2039–2042 (1994).
22. C. Cui, L. Gan, M. Heggen, S. Rudi, P. Strasser, *Nat. Mater.* **12**, 765–771 (2013).
23. C. Chen et al., *Science* **343**, 1339–1343 (2014).
24. J. M. Petroski, Z. L. Wang, T. C. Green, M. A. El-Sayed, *J. Phys. Chem. B* **102**, 3316–3320 (1998).
25. T. Yu, Y. Kim, H. Zhang, Y. Xia, *Angew. Chem. Int. Ed.* **50**, 2773–2777 (2011).
26. H. Zheng et al., *Science* **324**, 1309–1312 (2009).
27. J. M. Yuk et al., *Science* **336**, 61–64 (2012).
28. H.-G. Liao, H. Zheng, *J. Am. Chem. Soc.* **135**, 5038–5043 (2013).
29. H.-G. Liao, L. Cui, S. Whitlam, H. Zheng, *Science* **336**, 1011–1014 (2012).
30. Y. Xia, Y. Xiong, B. Lim, S. E. Skrabalak, *Angew. Chem. Int. Ed.* **48**, 60–103 (2009).
31. Y. Wu et al., *J. Am. Chem. Soc.* **135**, 12220–12223 (2013).
32. Y. Ding, F. Fan, Z. Tian, Z. L. Wang, *J. Am. Chem. Soc.* **132**, 12480–12486 (2010).

ACKNOWLEDGMENTS

Supported by U.S. Department of Energy EERE award DE-EE0000458 via subcontract through General Motors; the Ernst Ruska Center for Microscopy and Spectroscopy with Electrons, Forschungszentrum Jülich GmbH, Germany; and Deutsche Forschungsgemeinschaft (DFG) grants STR 596/4-1 (“Pt stability”) and STR 596/5-1 (“Shaped Pt bimetallics”). We thank the Zentraleinrichtung für Elektronenmikroskopie (Zelmi), Technical University Berlin, for its support of TEM and EDX measurements; N. Erini for carrying out FTIR measurements; and R. Schomack and M. Gleich for analysis of thermal gravimetric data.

SUPPLEMENTARY MATERIALS

www.sciencemag.org/content/346/6216/1502/suppl/DC1
Materials and Methods

Figs. S1 to S8
References (33, 34)

15 September 2014; accepted 19 November 2014
10.1126/science.1261212

EARTH MAGNETOSPHERE

Direct observation of closed magnetic flux trapped in the high-latitude magnetosphere

R. C. Fear,^{1,*} S. E. Milan,^{1,2} R. Maggiolo,³ A. N. Fazakerley,⁴
I. Dandouras,^{5,6} S. B. Mende⁷

The structure of Earth’s magnetosphere is poorly understood when the interplanetary magnetic field is northward. Under this condition, uncharacteristically energetic plasma is observed in the magnetotail lobes, which is not expected in the textbook model of the magnetosphere. Using satellite observations, we show that these lobe plasma signatures occur on high-latitude magnetic field lines that have been closed by the fundamental plasma process of magnetic reconnection. Previously, it has been suggested that closed flux can become trapped in the lobe and that this plasma-trapping process could explain another poorly understood phenomenon: the presence of auroras at extremely high latitudes, called transpolar arcs. Observations of the aurora at the same time as the lobe plasma signatures reveal the presence of a transpolar arc. The excellent correspondence between the transpolar arc and the trapped closed flux at high altitudes provides very strong evidence of the trapping mechanism as the cause of transpolar arcs.

The night side of the terrestrial magnetosphere forms a structured magnetotail, consisting of a plasma sheet at low latitudes that is sandwiched between two regions called the magnetotail lobes (Fig. 1). The lobes consist of the regions in which the terrestrial magnetic field lines are directly connected to the interplanetary magnetic field (IMF),

which is referred to as being topologically “open” (indicated by the dashed gray lines in Fig. 1). Magnetic field lines threading the plasma sheet (solid gray lines in Fig. 1) are not connected to the IMF and are therefore “closed” (1, 2). Topology changes are caused by the process of magnetic reconnection, which drives magnetospheric dynamics when the IMF is southward (1).

Different plasma populations are observed in these regions: Plasma in the lobes is very cool, whereas the plasma sheet is more energetic. The key way to distinguish between open and closed magnetic field lines is that electron distributions on closed field lines may exhibit a double loss cone, in which the distribution peaks perpendicular to the magnetic field (3). This requires the presence of magnetic mirrors on both sides of the observation site; therefore, double loss cones are unambiguous indicators that the magnetic field lines observed by a spacecraft are closed.

A major problem in magnetospheric physics is the adaptation of this picture to times when the IMF is northward. In a recent study (4), Shi *et al.* have reported relatively hot plasma in the lobes, which is unexpected in standard magnetosphere model. The authors attributed the presence of the plasma to direct entry of the solar wind, implying that it should be observed on open magnetic field lines. However, similar observations (5, 6) have previously been interpreted as spatially separated filaments protruding from the plasma sheet into the lobe [though Huang *et al.* noted that no theoretical description existed to explain their presence (6)]. In these studies, the observed plasma has been isotropic, but different magnetic field topologies and interpretations have been inferred due to the absence of evidence of a loss cone.

Another controversy concerns the cause of an auroral configuration called the transpolar arc, which occurs at very high latitudes when the IMF is northward (7, 8). There is no consensus on whether transpolar arcs occur on field lines that are closed (3, 7–10) or open (11–13). Their formation remains the subject of debate, with a range of competing theories (14–20). One mechanism for transpolar arcs is for them to result from the closure of lobe magnetic flux, which then remains trapped in the magnetotail (10); this hypothesis makes a number of predictions that have recently been validated statistically (14, 20). If this is true, a spacecraft situated in the lobe should observe a wedge of closed flux sandwiched within the lobe at high latitudes, well away from the expected location of the plasma sheet.

Virtually all plasma observations of transpolar arcs have come from spacecraft at low altitudes; these observations therefore report the precipitation associated with the arc rather than a direct measurement of the source plasma for the arc. It

has been argued that further examination of in situ observations in the lobes (i.e., at much higher altitudes) is necessary to identify the source plasma and the processes causing transpolar arcs (8). To date, only one study has reported such observations (6), which revealed relatively hot plasma, similar to the atypically hot lobe plasma signatures discussed above (4, 5). The authors concluded that they detected the source plasma for a transpolar arc but that the observed structures were not explained by any existing theory. Here we demonstrate that the presence of this plasma can be explained by the trapped flux mechanism for the formation of transpolar arcs (10) by showing that a double loss cone is observed within the plasma and that the plasma observations correspond extremely well to the back-and-forth motion of a transpolar arc.

On 15 September 2005, the Cluster 1 spacecraft was situated in the southern hemisphere lobe (Fig. 1). An overview of the IMF and the observations made by Cluster 1 is shown as a function of time in Fig. 2. The main period of interest is between 16:00 and 19:00 UT, when the IMF was northward (indicated by a north-south component $B_z > 0$) (Fig. 2A). Before 17:00 and after 19:00 UT, the ions observed were cool (<500 eV) (Fig. 2D), which is consistent with upwelling from the ionosphere and typical of the lobe. However, between 17:00 and 19:00 UT, a much more energetic plasma population was observed (~ 1 -keV electrons and ~ 10 -keV ions) (Fig. 2, C and D), which is comparable to the mean plasma sheet energy when the IMF is northward (27). The electron and ion energies and temperatures (Fig. 2, C to E) are comparable to those reported in previous studies (4–6).

The electron pitch angles observed between 18:15 and 18:45 UT are plotted in Fig. 3A. Cluster 1 observed bidirectional electrons (peaking at pitch angles of 0° and 180°) throughout the interval, except at $\sim 18:36$ UT when the electron distribution was not only more intense but also peaked at pitch angles nearer 90° . Figure 3B shows the pitch angle distribution averaged over 21 s centered on 18:36:43 UT (indicated as “g” in Fig. 3A). The color scale has been selected to emphasize the variations between different pitch angles. The parallel and antiparallel fluxes were approximately half the value observed perpendicular to the magnetic field. This double loss cone is extremely strong evidence that the plasma observed by Cluster was on closed magnetic field lines. The bidirectional electrons observed beforehand (between 18:15 and 18:35 UT) are also consistent with electrons observed on closed magnetic field lines—in typical magnetotail crossings, bidirectional electrons are observed through much of the outer plasma sheet, with double loss cone distributions deep in the central plasma sheet (27). Ion distributions observed at this time are indicative of the occurrence of magnetotail reconnection tailward of the spacecraft (fig. S1).

Simultaneous observations of the Southern Hemisphere aurora on a global scale are available for this period from the far ultraviolet (FUV)

Wideband Imaging Camera (22) on the IMAGE (Imager for Magnetopause-to-Aurora Global Exploration) satellite (Fig. 4A). (The location of IMAGE is also indicated in Fig. 1, and the full sequence of auroral images is shown in movie S1.) In Fig. 4A, the location of Cluster 1 has been mapped onto the Southern Hemisphere ionosphere along the model magnetic field lines (23) of Fig. 2. There is an excellent match between the plasma observations made by Cluster and the location of the transpolar arc relative to the footprint of the spacecraft (see Fig. 2 and movie S1). The second time that the arc intersects the spacecraft footprint [Fig. 4A, panel (g)] corresponds with the time that the highest intensities of energetic plasma were observed by Cluster, which is when the double loss cone was observed in Fig. 3B.

Our observations demonstrate that atypically hot plasma observed in the lobe occurs on closed magnetic field lines and is therefore incompatible with direct entry from the solar wind. The excellent match between the plasma observations and the intersections of the transpolar arc and the spacecraft footprints (d, f, and g in Figs. 2 and 4) confirms that such atypically hot plasma is the source plasma for transpolar arcs. The correspondence between the intersections of the arc and the observation of hotter plasma at two distinct times also demonstrates that the cause of multiple sequential observations of such atypical plasma is the back-and-forth motion of the closed magnetic field lines; that is, they are not necessarily spatially separated filaments, as previously

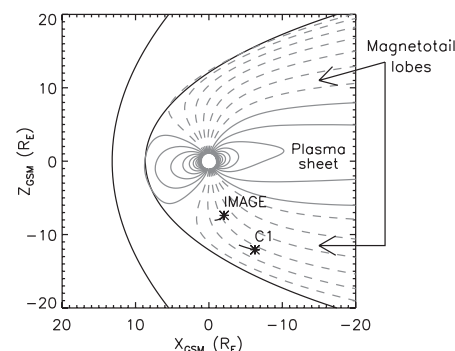


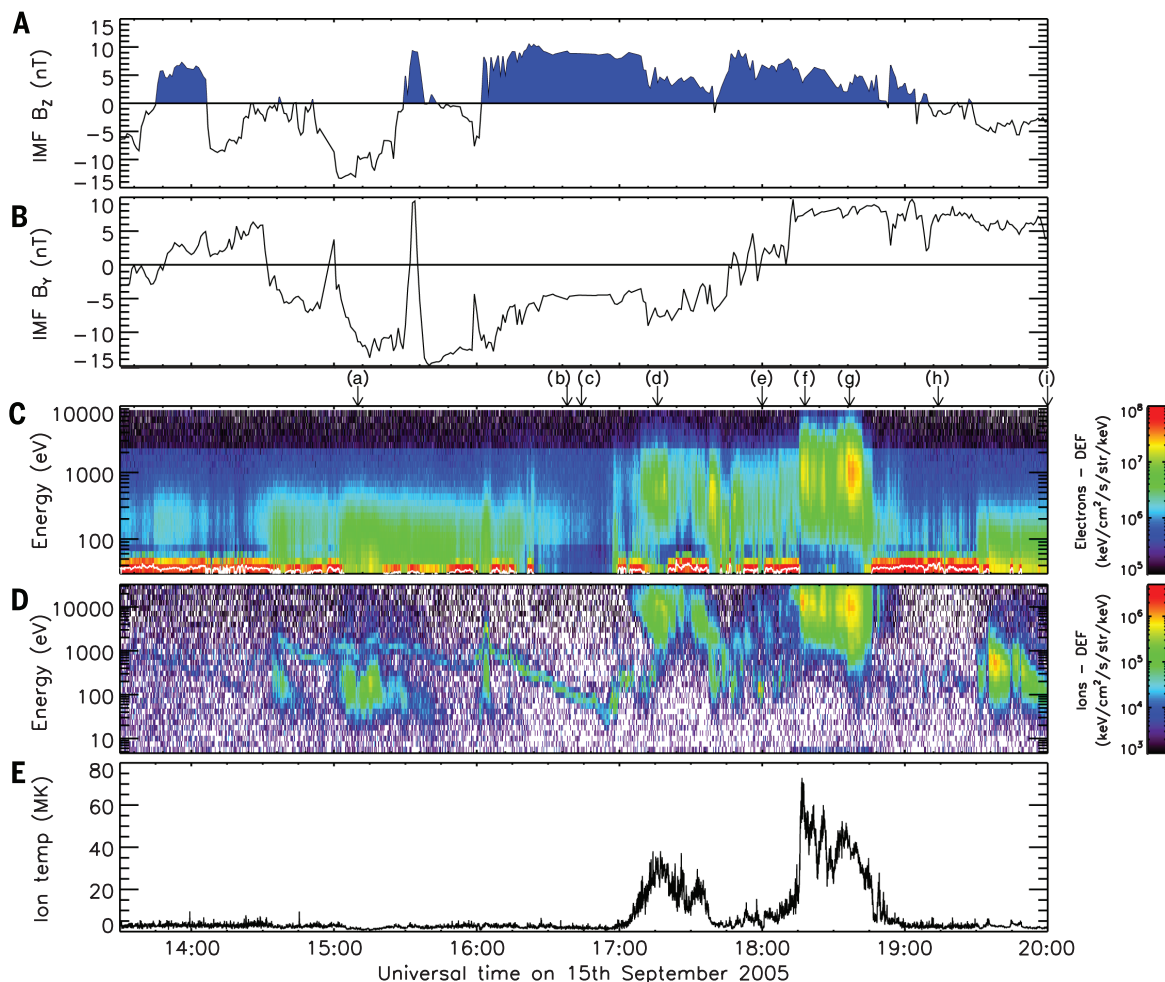
Fig. 1. Locations of the Cluster 1 and IMAGE spacecraft between 17:00 and 19:00 UT on 15 September 2005. Positions are projected into the xz plane of the Geocentric Solar Magnetic (GSM) coordinate system (24), in which the x axis is directed toward the Sun and the z axis is toward magnetic north. Asterisks denote spacecraft locations at 17:00 UT (C1 indicates Cluster 1). Solid black lines indicate model locations for the bow shock and magnetopause; gray lines indicate model geomagnetic field lines from an empirical model (23). The field lines that are expected to be closed are plotted as solid lines, whereas those that would normally be open—and hence connected to the solar wind downtail—are dashed. Cluster 1 was deep inside the lobe, a long way from the expected location of the closed field line region (the plasma sheet). $1 R_E$ is one Earth radius (6400 km).

¹Department of Physics and Astronomy, University of Leicester, Leicester, UK. ²Birkeland Centre for Space Sciences, University of Bergen, Bergen, Norway. ³Belgian Institute for Space Aeronomy, Brussels, Belgium. ⁴Mullard Space Science Laboratory, University College London, Dorking, UK. ⁵Institut de Recherche en Astrophysique et Planétologie (IRAP), UMR 5277, Université Paul Sabatier—Observatoire Midi-Pyrénées, University of Toulouse, Toulouse, France. ⁶IRAP, CNRS, Toulouse, France. ⁷Space Sciences Laboratory, University of California Berkeley, Berkeley, CA 94720, USA.

*Present address: School of Physics and Astronomy, University of Southampton, Southampton, UK. †Corresponding author. E-mail: r.c.fear@soton.ac.uk

Fig. 2. Time series of the interplanetary and magnetospheric conditions. The top two panels show the simultaneous (A)

north-south and (B) dawn-dusk components of the IMF (B_Z and B_Y , respectively) obtained from the OMNI data set (25). The next two panels show the (C) electron and (D) ion populations observed by Cluster 1 in the magnetotail lobes by the PEACE (26) and CIS-HIA (27) instruments, respectively. Both panels contain the differential energy flux (DEF) of the electron or ion population plotted as a function of energy and time. The bottom panel (E) shows the observed ion temperature. Arrows labeled with lowercase letters (a) to (i) indicate selected times of interest.



proposed (5, 6). Although the link with transpolar arcs has previously been suggested (6), the confirmation of the magnetic field topology provides strong evidence that both transpolar arcs and atypically hot lobe plasma observed during periods of northward IMF are caused by the process of magnetic reconnection in the magnetotail, where newly closed lobe flux becomes trapped in the lobe (10). Although other proposed mechanisms could explain the closed nature of the magnetic flux threading the transpolar arc, we are not aware of an alternative mechanism that could explain all of the following points: (i) the observation of the lobe immediately before and after the passage of the arc, (ii) the observed back-and-forth motion of the arc, and (iii) the absence of a change in sign of the IMF B_Y (dawn-dusk) component in the hour before the arc formed (see supplementary text). The reconnection mechanism (10) predicts that closed magnetic flux observed at high latitudes should be similar in most respects to the plasma sheet, because both contain plasma that was originally contained in the lobe but that has since been heated as a result of the contraction of the field lines after their closure. Our observations confirm that the plasma observed at high latitudes is indeed similar to that observed in the plasma sheet. The net effect of this process is an increase

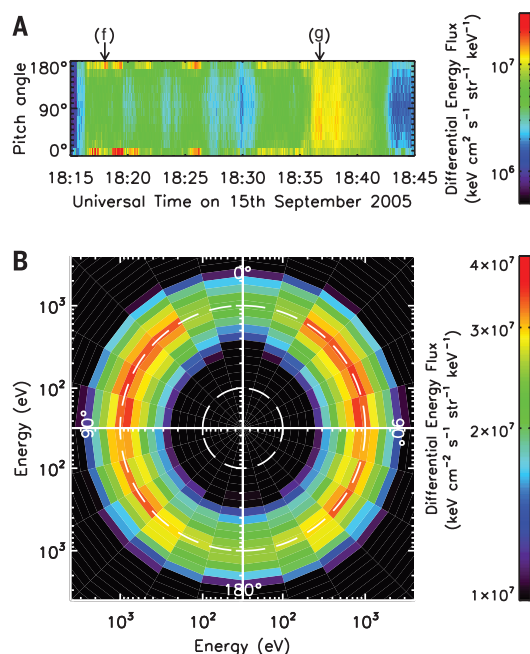


Fig. 3. Electron pitch angle distributions from the hot plasma population.

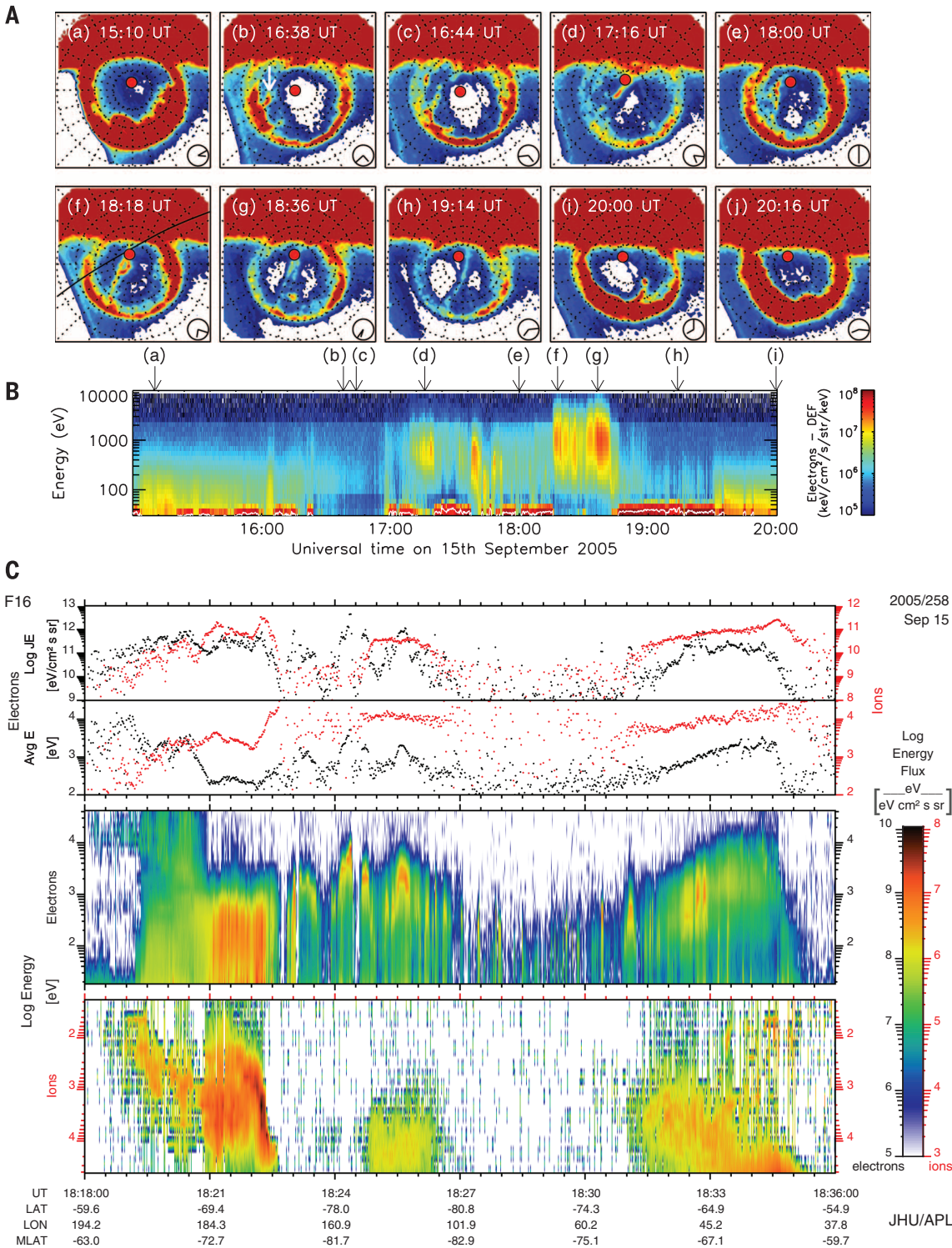
(A) Pitch angle distribution of electrons observed above 100 eV between 18:15 and 18:45 UT. (B) Electron distribution observed at the time of the highest differential energy fluxes observed by Cluster [corresponding to arrow (g) in Fig. 2; also indicated in Fig. 3A]. The distribution has been computed from five consecutive spacecraft spin periods, centered on time (g), and the color scale has been chosen to emphasize the differences in the field-aligned and perpendicular directions.

in the closed fraction of the magnetotail in one narrow local time sector. An interesting consequence is that as this transpolar arc spans the

entire polar cap, the magnetotail is entirely closed in a narrow sector of local time, which highlights the intriguing topology that the

Fig. 4. Summary of the relationship between the auroral and in situ (high- and low-altitude) plasma observations.

(A) Montage of the auroral observations made by the IMAGE FUV Wideband Imaging Camera on 15 September 2005. Each image has been projected onto a grid of magnetic latitude against magnetic local time with local noon at the top and dawn to the right. Panels (a) to (j) show the transpolar arc [indicated by the white arrow in (b)] at different stages of its evolution, with the footprint of the Cluster spacecraft indicated by a red dot. The times corresponding to panels (a) to (j) are also indicated in Fig. 2 and (B) of this figure. At 15:10 UT (a), the aurora conformed to the standard oval configuration, and the Cluster 1 footprint was in the dim region poleward of the main auroral oval (the polar cap), consistent with the location of the spacecraft in the lobe. At 16:38 UT (b), a small feature emerged from the nightside oval (indicated by the white arrow) and subsequently grew into a transpolar arc [(c) to (i)]. The growth and evolution of the arc [(b) to (h)] occurred while the IMF was northward (Fig. 2A). The arc was initially duskward of the footprint of Cluster [(b) and (c)]. At 17:16 UT (d), the arc intersected the spacecraft footprint before retreating duskward again (e); a subsequent and final period of dawnward motion caused the arc to intersect the spacecraft footprint once more [(f) and (g)] and then move past the spacecraft footprint [(h) and (i)]. After the IMF turned southward at 19:10 UT, the arc retreated to the night side of the polar cap (i) and subsequently disappeared (j). **(B)** Electron population observed by Cluster (replotted from Fig. 2C), with labels showing the times corresponding to (a) to (i). There is an excellent correspondence between the times that the uncharacteristic plasma is observed and the times when the transpolar arc intersected the spacecraft footprint [(d), (f), and (g)]. **(C)** Spectrograms of the electron and ion populations observed by the Defense Meteorological Satellite Program (DMSP) F16 satellite at low altitude during a polar cap crossing made between (f) and (g). Ion pre-



cipitation was observed between 18:25 and 18:27 UT, which coincides with the time that the DMSP F16 satellite traversed the arc. [The orbit of the DMSP spacecraft is shown in panel (f) of (A).] The ion and electron precipitation observed at this time is comparable in energy with that observed above the main oval (7, 9) and at high altitudes by Cluster 1 (Fig. 2, C and D), although the electron precipitation observed by DMSP shows signs of further acceleration (inverted “Vs”). In these respects, the precipitation observed by DMSP is typical for transpolar arcs (18). Electron precipitation is observed elsewhere in the polar cap and may be associated with fainter polar cap arcs, presumably on open magnetic field lines.

magnetosphere can attain when the IMF points northward.

REFERENCES AND NOTES

1. J. W. Dungey, *Phys. Rev. Lett.* **6**, 47–48 (1961).
2. J. W. Dungey, in *Geophysics: The Earth's Environment*, C. DeWitt, J. Hieblot, A. Lebeau, Eds. (Gordon and Breach, New York, 1963), pp. 505–550.
3. J. D. Menietti, J. L. Burch, *J. Geophys. Res.* **92**, 7503–7518 (1987).
4. Q. Q. Shi et al., *Nat. Commun.* **4**, 1466 (2013).
5. C. Y. Huang et al., *J. Geophys. Res.* **92**, 2349–2363 (1987).
6. C. Y. Huang, J. D. Craven, L. A. Frank, *J. Geophys. Res.* **94**, 10137–10143 (1989).
7. L. A. Frank, J. D. Craven, J. L. Burch, J. D. Winningham, *Geophys. Res. Lett.* **9**, 1001–1004 (1982).
8. L. A. Frank et al., *J. Geophys. Res.* **91**, 3177–3224 (1986).
9. W. K. Peterson, E. G. Shelley, *J. Geophys. Res.* **89**, 6729–6736 (1984).
10. S. E. Milan, B. Hubert, A. Grocott, *J. Geophys. Res.* **110**, A01212 (2005).
11. D. A. Hardy, W. J. Burke, M. S. Gussenhoven, *J. Geophys. Res.* **87**, 2413–2430 (1982).
12. M. S. Gussenhoven, E. G. Mullen, *J. Geophys. Res.* **94**, 17121–17132 (1989).
13. N. Østgaard, S. B. Mende, H. U. Frey, L. A. Frank, J. B. Sigwarth, *Geophys. Res. Lett.* **30**, 2125 (2003).
14. R. C. Fear, S. E. Milan, *J. Geophys. Res.* **117**, A03213 (2012).
15. A. Kullen, M. Brittner, J. A. Cumnack, L. G. Blomberg, *J. Geophys. Res.* **107**, 1362 (2002).
16. N. Østgaard et al., *J. Atmos. Sol. Terr. Phys.* **69**, 249–255 (2007).
17. A. Goudarzi, M. Lester, S. E. Milan, H. U. Frey, *Ann. Geophys.* **26**, 201–210 (2008).
18. J. A. Cumnack et al., *J. Geophys. Res.* **116**, A02218 (2011).
19. A. Kullen, in *Auroral Phenomenology and Magnetospheric Processes: Earth and Other Planets*, A. Kelling, E. Donovan, F. Bagena, T. Karlsson, Eds. (Geophysical Monograph 197, American Geophysical Union, Washington, DC, 2012), pp. 69–80.
20. R. C. Fear, S. E. Milan, *J. Geophys. Res.* **117**, A09230 (2012).
21. A. P. Walsh et al., *J. Geophys. Res.* **118**, 6042–6054 (2013).
22. S. B. Mende et al., *Space Sci. Rev.* **91**, 271–285 (2000).
23. N. A. Tsyganenko, in *Proceedings of the Third International Conference on Substorms (ICS-3)*, Versailles, France, 12 to 17 May 1996 (SP 389, European Space Agency, Noordwijk, Netherlands, 1996), pp. 181–185.
24. C. T. Russell, *Cosmic Electrodyn.* **2**, 184–196 (1971).
25. J. H. King, N. E. Papitashvili, *J. Geophys. Res.* **110**, A02104 (2005).
26. A. N. Fazakerley et al., in *The Cluster Active Archive - Studying the Earth's Space Plasma Environment*, H. Laakso, M. Taylor, P. Escoubert, Eds. (Springer, Dordrecht, Netherlands, 2010), pp. 129–144.
27. H. Rème et al., *Ann. Geophys.* **19**, 1303–1354 (2001).

ACKNOWLEDGMENTS

Work in the UK was supported by Science and Technology Facilities Council (STFC) Ernest Rutherford Fellowship ST/K004298/1 and STFC grants ST/K001000/1 and ST/K000977/1. R.M. is supported by the Belgian Science Policy Office through the Solar-Terrestrial Center of Excellence. French participation in the Cluster project is funded by the Centre National d'Etudes Spatiales (CNES). IMAGE satellite work at the University of California, Berkeley, was supported through a Southwest Research Institute subcontract under NASA contract NAS5-96020. We acknowledge support from the International Space Science Institute through funding of its International Team on Polar Cap Arcs, and we are grateful for discussions with members of the team. Cluster data were obtained from the Cluster Active Archive (<http://caa.estec.esa.int/caa/>), and the IMAGE FUV data were provided by the NASA Space Science Data Center (<http://nssdc.gsfc.nasa.gov/space/>). The OMNI IMF data were obtained through NASA's CDAWeb (<http://cdaweb.gsfc.nasa.gov/>), for which we acknowledge J. H. King, N. Papitashvili, and the principal investigators of the magnetic field and plasma instruments on the Geotail and Advanced Composition Explorer (ACE) spacecraft. The DMSP particle detectors were designed by D. Hardy of Air Force Research Laboratory, and data were obtained from the Johns Hopkins University Applied Physics Laboratory.

SUPPLEMENTARY MATERIALS

www.sciencemag.org/content/346/6216/1506/suppl/DC1
Supplementary Text

Fig. S1

References (28–38)

Movie S1

12 June 2014; accepted 19 November 2014

10.1126/science.1257377

BIOPHYSICS

Extreme electric fields power catalysis in the active site of ketosteroid isomerase

Stephen D. Fried,^{*} Sayan Bagchi,[†] Steven G. Boxer[‡]

Enzymes use protein architecture to impose specific electrostatic fields onto their bound substrates, but the magnitude and catalytic effect of these electric fields have proven difficult to quantify with standard experimental approaches. Using vibrational Stark effect spectroscopy, we found that the active site of the enzyme ketosteroid isomerase (KSI) exerts an extremely large electric field onto the C=O chemical bond that undergoes a charge rearrangement in KSI's rate-determining step. Moreover, we found that the magnitude of the electric field exerted by the active site strongly correlates with the enzyme's catalytic rate enhancement, enabling us to quantify the fraction of the catalytic effect that is electrostatic in origin. The measurements described here may help explain the role of electrostatics in many other enzymes and biomolecular systems.

Ketosteroid isomerase (KSI) is a small, proficient enzyme with one of the highest known unimolecular rate constants in biochemistry (1, 2), which has prompted extensive study of its mechanism and the catalytic strategies it uses (3–5). In steroid biosynthesis and degradation, KSI alters the position of a C=C double bond (Fig. 1A) by first abstracting a nearby α proton ($E \cdot S \rightleftharpoons E \cdot I$), forming a charged enolate intermediate ($E \cdot I$), and then reinserting the proton onto the steroid two carbons away ($E \cdot I \rightleftharpoons E \cdot P$). The removal of a proton in the first step initiates a rehybridization that converts the adjacent ketone group to a charged enolate, an unstable species that is normally high in free energy and so slow to form. The reaction is therefore expected to produce an increase in dipole moment at the carbonyl bond ($|\Delta\vec{\mu}_{\text{cm}}|$), suggesting that KSI may facilitate this reaction by exerting an electric field (\vec{F}_{enz}) on this bond that stabilizes it in the intermediate form and the preceding transition state (Fig. 1B). Using vibrational Stark effects, we have measured the electric field that KSI exerts on this C=O bond, providing quantitative experimental evidence for the connection between electrostatics and catalytic proficiency.

The frequencies of certain vibrations (such as the C=O stretch) shift in a linear manner with the electric field experienced by that vibration from its environment, a phenomenon known as the linear vibrational Stark effect (6, 7). Through this effect, we have shown that vibrations can be used as probes of local electrostatic fields. The nitrile group has been widely deployed to measure electric fields inside enzymes and their relationship to mutation (8), ligand occupancy (9), or conformational changes over the catalytic

cycle (10). In this study, we have focused on the C=O group of the inhibitor 19-nortestosterone (19-NT) (Fig. 1C), because when 19-NT binds, the C=O group is loaded directly into the catalytic machinery (11, 12). In this way, 19-NT's C=O vibrational (infrared) frequency shift probes the electrostatic environment that the substrate's C=O bond would experience in the active site, except 19-NT cannot react due to the position of the C=C bond.

To calibrate the sensitivity of 19-NT's C=O vibrational frequency to an electric field, we used two complementary approaches. In Stark spectroscopy (Fig. 2, A and B), an external electric field of known magnitude is applied to a frozen glass containing 19-NT, and the accompanying effect on the vibrational spectrum is recorded (7). By fitting the Stark spectrum (Fig. 2B) to derivatives of the absorption spectrum (Fig. 2A), the vibration's difference dipole can be extracted: $|\Delta\vec{\mu}_{\text{C=O}}|f = 1.39 \pm 0.05 \text{ cm}^{-1}/(\text{MV}/\text{cm})$, where f is the local field factor (fig. S1) (6, 7, 13). A vibration's difference dipole is its linear Stark tuning rate; that is, 19-NT's C=O vibrational frequency shifts $\sim 1.4/f \text{ cm}^{-1}$ for every MV/cm of electric field projected onto the C=O bond axis, whether the source of that field is an external voltage (as in Stark spectroscopy) or an organized environment created by an enzyme active site (\vec{F}_{enz}) that we wish to characterize. Whenever an external field is applied to a vitreous sample, vibrational bands will broaden because 19-NT molecules (and their C=O bonds) are randomly oriented with respect to the fixed direction of the external electric field (6, 7). By contrast, a vibrational probe will have a fixed orientation with respect to a protein electric field when bound to a protein, and as such the linear Stark effect then produces spectral shifts instead of broadening. The C=O vibration's Stark tuning rate does not appreciably change when C=O accepts a hydrogen bond (fig. S2), implying that the frequency still responds to fields linearly even when C=O participates in stronger interactions, although those interactions themselves are associated with larger electric fields (14).

Department of Chemistry, Stanford University, Stanford, CA 94305-1052, USA.

^{*}Present address: Protein and Nucleic Acid Chemistry Division, Medical Research Council Laboratory of Molecular Biology, Cambridge CB2 0QH, UK. [†]Present address: Physical and Materials Chemistry Division, National Chemical Laboratory (CSIR), Pune 411008, India. [‡]Corresponding author. E-mail: sboxer@stanford.edu

We also pursued a second approach to calibrate the sensitivity of 19-NT's C=O frequency shifts to electric fields and to assign these frequencies to an absolute field scale: Specifically, we measured 19-NT's vibrational spectrum in a series of solvents (table S1) and examined the correlation of the frequencies with the solvents' reaction fields, estimated by molecular dynamics (MD) simulations (14). As shown in Fig. 2C, 19-NT's C=O band shifts consistently to the red with increasing solvent polarity, from 1690.2 cm^{-1} in nonpolar hexane to 1634.0 cm^{-1} in water, so that the C=O frequency shifts across a 56 cm^{-1} span from solvatochromic effects. The large redshift in water reflects the large electric fields that are created by water's hydrogen bonds (H-bonds). The trend in solvent shifts is strongly correlated with the average electric field that each solvent exerts on the C=O bond (Fig. 2D and fig. S3A); that is, the plot of observed frequency versus computed field is linear ($R^2 = 0.99$) and its slope corroborates the Stark tuning rate measured by Stark spectroscopy. The ~ 2 -fold difference between the slope of this curve [$0.702 \text{ cm}^{-1}/(\text{MV}/\text{cm})$] and the measured Stark tuning rate is consistent with the current understanding of the local field effect ($f \sim 2$), based on other vibrational probes and electrostatic models (text S1) (13, 14). The regression line implies that the frequency variation due to different molecular environments can be well explained as a field effect and suggests that we can model 19-NT's C=O peak frequency in terms of the average electric field experienced by the vibration.

When 19-NT is bound to wild-type KSI, the C=O probe engages in short, strong H-bonds with

Tyr¹⁶ and Asp¹⁰³ (11, 12), and its vibrational frequency reflects the electric field at a primary site of charge rearrangement during KSI's catalytic cycle. Notably, the C=O vibration red-shifts to 1588.3 cm^{-1} (Fig. 3A), 46 cm^{-1} further to the red from the peak frequency in water, implying an extremely large electrostatic field. Attributing the frequency shift to the Stark effect, the linear field-frequency relationship of Fig. 2D maps this frequency value to an ensemble-average electric field of $-144 \pm 6 \text{ MV}/\text{cm}$. Although this highly red-shifted frequency lies outside the known linear range from solvatochromism, additional lines of evidence suggest that the C=O vibrational frequency maintains an approximately linear relationship with the field in this regime; neglect of higher-order terms is expected to result in overestimates of the electric field, but by no more than 10% (fig. S4 and text S2). Not only is the C=O band extremely red-shifted in KSI, it is also extremely narrow (Fig. 3A), suggesting a rather rigid environment (15) that greatly reduces the dispersion in the electric field. This is very different from what is observed in H-bonding solvents like water that exert large, but also highly inhomogeneous, electric fields because solvent H-bonds can assume a broad distribution of conformations (dashed traces in Fig. 3A and fig. S3, B and C) (14). Furthermore, the position of the C=O band in wild-type KSI is situated at the reddest (highest field) edge of the frequencies sampled by the C=O group in water (see the red and dashed traces in Fig. 3A), suggesting that the active site achieves this large field by restricting H-bond conformations to those that are associated with the largest electric fields.

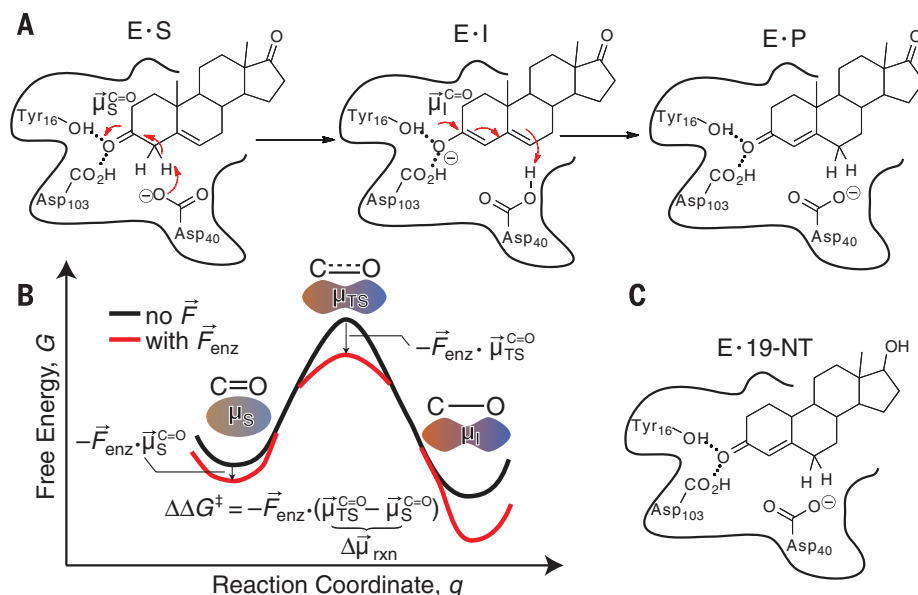


Fig. 1. Catalysis by ketosteroid isomerase. (A) The chemical mechanism of ketosteroid isomerase. In the first step, Asp⁴⁰ removes an α proton from the steroid to form an enolate, stabilized by two H-bonds from Tyr¹⁶ and Asp¹⁰³. This transformation results in an increase of the dipole moment along the C=O bond. E, enzyme; S, substrate; I, intermediate; P, product. (B) Simple model for electrostatic catalysis, illustrating the effect of an electric field from the organized environment of an enzyme active site (\vec{F}_{enz}) on a reaction's activation barrier (ΔG^\ddagger). $\vec{\mu}_{\text{S}}^{\text{C=O}}$, dipole of substrate's C=O bond; $\vec{\mu}_{\text{TS}}^{\text{C=O}}$, dipole of transition state's C=O bond. (C) Complex between KSI and the product-like inhibitor, 19-NT, used in this study to probe electric fields in the KSI active site.

By exploring a series of structurally conservative (but catalytically detrimental) mutants (table S2), we could systematically perturb the catalytic efficacy of KSI and quantitatively evaluate its relationship to the electric field probed by the C=O vibration. In all cases, the assignment of the vibrational bands to 19-NT was confirmed with isotope replacement studies using C=¹⁸O 19-NT (figs. S5 and S6). The H-bond provided by Tyr¹⁶ is known to be essential for KSI's catalysis, as the conservative Tyr¹⁶Phe mutation diminishes KSI's rate by factors of $\sim 10^4$ (11, 16). This single point mutation induced a blue shift from 1588.3 cm^{-1} to 1647.5 cm^{-1} (Fig. 3A), implying a much smaller average electric field. (This change in field magnitude is comparable to that of the change in solvent field between hexane and water.) The Tyr¹⁶Ser mutation (17), although less conservative than the Phe substitution, is actually less detrimental. This observation has been explained by the suggestion that leaving a cavity in Tyr¹⁶'s place allows water to remain in the back pocket of the active site; these water molecules could also H-bond to the steroid substrate, thereby partially compensating for the loss of Tyr¹⁶'s key H-bond (18). Indeed, the C=O stretching frequency in Tyr¹⁶Ser is not as dramatically blue-shifted as it is in Tyr¹⁶Phe. Asp¹⁰³ is the other primary H-bond donor in KSI's active site (Fig. 1A). In the Asp¹⁰³Asn mutant, the H-bonding proton is much less acidic, but N-H and O-H bonds have similar sterics and dipole moments. Consistent with these considerations, the change in electric field and the rate impairment this mutation entails with respect to wild-type are much smaller compared to the other mutants.

Although it is conventionally accepted that KSI uses Tyr¹⁶'s and Asp¹⁰³'s H-bonds to stabilize its transition state (1, 11), these measurements show that the interaction between these H-bonds and the C=O group can be described fundamentally in terms of the electric field they produce. In all the mutants studied, 19-NT's C=O band remains relatively narrow, suggesting that electrostatic rigidity is conferred by KSI's scaffold, rather than by the H-bonding residues. Also, sizable electric fields persist in the KSI active site after removing the critical H-bond donated by Tyr¹⁶ ($-60 \pm 3 \text{ MV}/\text{cm}$), implying that a substantial electrostatic field contribution also arises from the environment fashioned by the enzyme scaffold (Fig. 3B). Nevertheless, that the Tyr¹⁶ H-bond alone contributes a static field of $84 \pm 7 \text{ MV}/\text{cm}$ without an accompanying increase in electric field dispersion makes it quite distinct from water, which donates close to two H-bonds to C=O on average, but taken altogether these H-bonds generate an average field of $\sim 40 \text{ MV}/\text{cm}$ that is also highly heterogeneous (13).

The Asp⁴⁰Asn mutant decreases KSI's catalytic rate by a factor of $\sim 10^6$ (16) but only blue-shifts the C=O vibrational frequency of bound 19-NT by 6 cm^{-1} relative to wild-type KSI (table S2). This behavior strongly contrasts with other mutants studied, which produce blue-shifts commensurate with their deleterious effect on catalysis (Fig. 3B). To explain this

observation, we posit that, whereas the function of Tyr¹⁶ and Asp¹⁰³ is to stabilize the reaction's transition state by exerting electrostatic fields onto the carbonyl moiety, Asp⁴⁰ provides an orthogonal catalytic function (text S3), by acting as the general base in the proton-transfer reaction (Fig. 1A).

When nitrile vibrational probes were placed in other locations around the KSI active site in previous work, frequencies were found well within the range demarcated by the solvent series (9). In other words, the extreme electric field experienced by 19-NT's C=O in wild-type KSI is specific to its precise position in the active site where strong local interactions and the collective effect of the overall enzyme architecture mutually reinforce each other.

A plot of each mutant's apparent activation barrier (calculated from the Michaelis-Menten k_{cat}) (fig. S7A) (16, 18, 19) against its corresponding ensemble-average active-site electric field magnitude (derived from the field-frequency calibration curve in Fig. 2D) reveals a robust linear trend (Fig. 3B; see also fig. S7B). This relationship suggests that electric fields in KSI's active site are intimately linked to catalysis. Moreover, this cor-

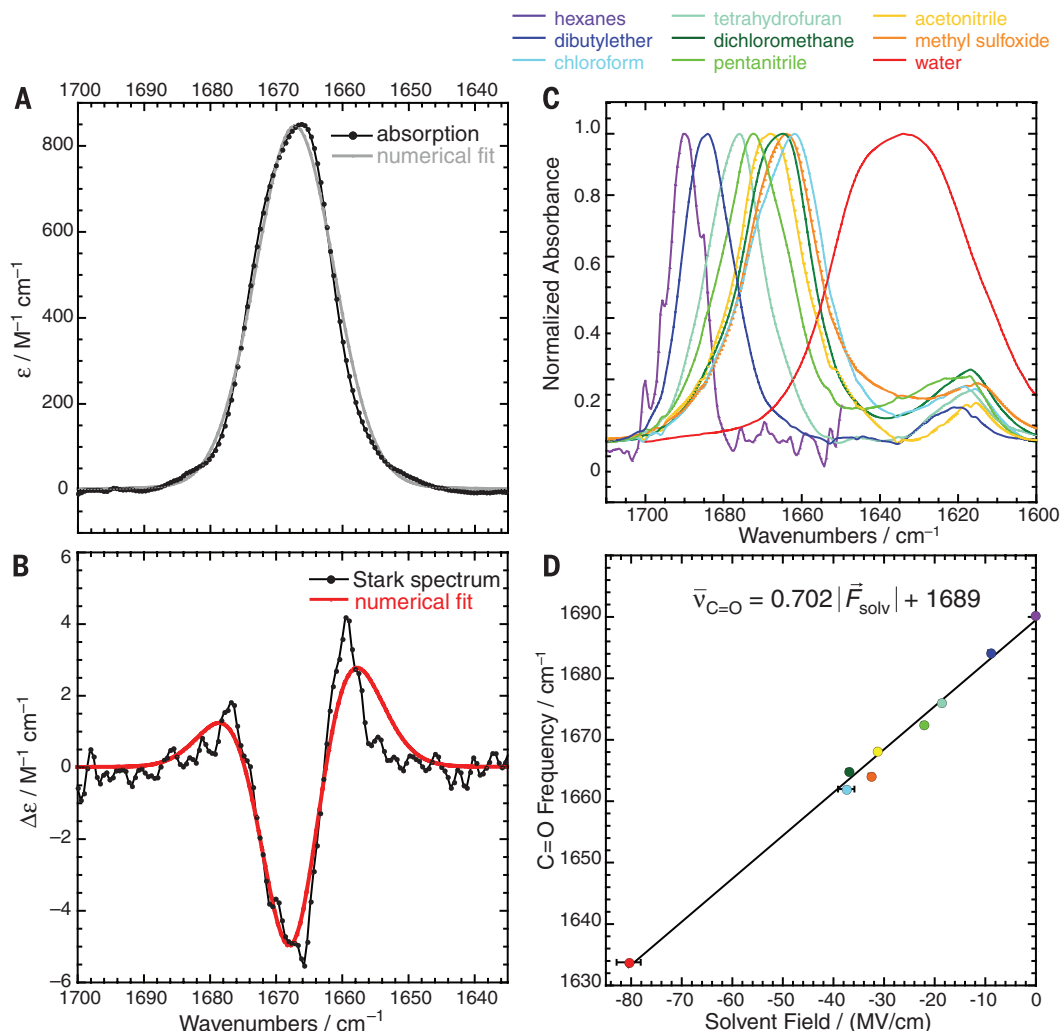
relation can be explained using the simple model for electrostatic catalysis in Fig. 1B. The formation of a transition state generally involves redistribution of electron density, resulting in bonds with larger dipole moments than the analogous bonds in the substrate (e.g., $|\vec{\mu}_{\text{TS}}^{\text{C=O}}| > |\vec{\mu}_{\text{S}}^{\text{C=O}}|$) (20, 21). An electric field will therefore differentially stabilize the transition state in proportion to the reaction difference dipole ($\Delta\vec{\mu}_{\text{rxn}} = \vec{\mu}_{\text{TS}}^{\text{C=O}} - \vec{\mu}_{\text{S}}^{\text{C=O}}$), altering the activation barrier by $\vec{F}_{\text{enz}} \cdot \Delta\vec{\mu}_{\text{rxn}}$ (Fig. 1B). If we make a simplifying assumption that the electric field experienced by the C=O bond is the same in the substrate and transition state, the model can be directly mapped onto the data in Fig. 3B; the slope of the plot (1 D) corresponds to $|\Delta\vec{\mu}_{\text{rxn}}|$, and the intercept (18.8 kcal mol⁻¹) corresponds to the hypothetical activation barrier if KSI contributed no stabilizing electric field. The small value for $|\Delta\vec{\mu}_{\text{rxn}}|$ implies that there is a rather small perturbation in the electrostatic character of the substrate upon activation, consistent with ab initio density functional theory calculations (fig. S7C and table S3). Apparently, the very large field present in the KSI active site is needed to leverage what small charge displacement is associated with the reaction's transition

state. A chemical reaction with a larger charge displacement would consequently be exponentially more accelerated by these electric fields, suggesting that electric field effects may provide a natural framework for explaining the catalysis of more proficient enzymes as well (22).

By comparing the intercept extrapolated to $|\vec{F}_{\text{enz}}| = 0$ from Fig. 3B (18.8 kcal mol⁻¹) to wild-type KSI's activation barrier (11.5 kcal mol⁻¹), we estimate that the active site's electric field contributes 7.3 ± 0.4 kcal mol⁻¹ to KSI's barrier reduction. This corresponds to an $\sim 10^5$ -fold rate enhancement and accounts for 70% of KSI's catalytic speedup relative to an uncatalyzed reference reaction in solution (Fig. 3C and text S3). Moreover, the electrostatic stabilization energy is quite similar to the enthalpic component of KSI's barrier reduction (9 kcal mol⁻¹), suggesting that the thermodynamic manifestation of the electric field effect is enthalpic (23). The active site's suppression of electric field variability, as evidenced by the approximately lifetime-limited linewidth of the C=O vibrational band in all the KSI mutants, is possibly also an important catalytic feature; for example, the Tyr¹⁶Phe mutant produces a smaller average electric field than water (Fig. 3A), although

Fig. 2. Sensitivity of the C=O stretch frequency of 19-NT to electrostatic field. (A) The

absorption spectrum of 19-NT (50 mM) in glassy 2-methyl tetrahydrofuran at 77 K. (B) The Stark spectrum of 19-NT at 1.0 MV/cm, shown as a difference between the field-on and field-off spectra. The Stark tuning rate is related to the second derivative fitting parameter (figs. S1 and S2). (C) Infrared spectra of 19-NT dissolved in organic solvents of various polarities or water; the small peak at 1615 cm⁻¹ is the C=C stretch. (D) Plot of 19-NT's C=O peak frequency, $\bar{\nu}_{\text{C=O}}$ against the calculated solvent electric field, $|\vec{F}_{\text{solv}}|$, the C=O group experiences in each of those solvents (13, 14). The least-squares regression line is $\bar{\nu}_{\text{C=O}} = 0.702|\vec{F}_{\text{solv}}| + 1689$ ($R^2 = 0.99$). Error ranges for frequencies are contained within symbols; for electric fields, error bars report the correlation-adjusted error of the average electric field from 2-ns simulations.



it is still a modest catalyst relative to solution. However, the linear infrared experiments described here cannot directly quantitate this effect.

The remaining catalytic effect beyond electrostatics can likely be attributed to the precise positioning of the general base (Asp⁴⁰) with respect to the proton on the steroid to be abstracted, which is expected to be an entropic effect. From this discussion, we surmise that in enzymatic proton abstraction, electrostatic stabilization and exact positioning of reacting moieties provide the physical basis to achieve enthalpic and entropic contributions to catalysis, respectively; however, contrary to earlier views (24, 25), electrostatic stabilization can be the more important of the two (Fig. 3C).

What is the physical basis for the extreme electric field detected in KSI's active site? Large electric fields arising from Tyr¹⁶ and Asp¹⁰³ are expected when the carbonyl group of the ligand closely approaches the OH groups of these two residues and in a coplanar orientation [as indeed is seen in crystal (3) and solution (12) structures]. Nevertheless, these static structures cannot predict or reproduce the electric fields determined by vibrational Stark effects, likely because structures represent ensemble averages and because electric fields depend sensitively on atomic positions down to resolutions not accessible in most structural data (text S4). Moreover, electric fields calculated from classical MD simulations of the KSI•19-NT complex (text S4) also do not agree

with our experiments (text S4 and fig. S8). Better estimates of active-site electric fields have been obtained with more sophisticated computational models, which have provided a theoretical foundation supporting the link between electric fields and catalysis (10, 21).

Unusual spectral shifts have been observed previously in enzyme active sites (including KSI) (11, 26–28) and have been variously interpreted as implying strain, distortion, or polarization. In contrast, the vibrational Stark effect enables a quantitative connection between spectroscopic observables and a fundamental physical quantity (electric field). As we demonstrate here, these experiments can be applied to measuring the H-bond electric field strength in proteins in functional contexts. Moreover, the electric field description provides a framework to quantify the contributions of specific H-bonding interactions, as well as the overall electrostatic environment with the same units, to give a simple and unified model for electrostatic catalysis (Fig. 1B). That a substantial portion of KSI's catalytic rate enhancement can be explained in terms of its average electric field suggests that the electric field could be a useful design criterion in the ongoing efforts to engineer enzymes with unnatural or enhanced functions. More generally, we anticipate that electric field measurements with functionally relevant vibrational probes will elucidate the physical basis for a broad spectrum of biomolecular and condensed phase interactions and processes.

REFERENCES AND NOTES

1. R. M. Pollack, *Bioorg. Chem.* **32**, 341–353 (2004).
2. D. C. Hawkinson, T. C. Eames, R. M. Pollack, *Biochemistry* **30**, 10849–10858 (1991).
3. D. A. Kraut *et al.*, *PLOS Biol.* **4**, e99 (2006).
4. S. C. L. Kamerlin, P. K. Sharma, Z. T. Chu, A. Warshel, *Proc. Natl. Acad. Sci. U.S.A.* **107**, 4075–4080 (2010).
5. D. Herschlag, A. Natarajan, *Biochemistry* **52**, 2050–2067 (2013).
6. S. G. Boxer, *J. Phys. Chem. B* **113**, 2972–2983 (2009).
7. S. S. Andrews, S. G. Boxer, *J. Phys. Chem. A* **104**, 11853–11863 (2000).
8. A. J. Stafford, D. M. Walker, L. J. Webb, *Biochemistry* **51**, 2757–2767 (2012).
9. A. T. Fafarman, P. A. Sigala, D. Herschlag, S. G. Boxer, *J. Am. Chem. Soc.* **132**, 12811–12813 (2010).
10. C. T. Liu *et al.*, *J. Am. Chem. Soc.* **136**, 10349–10360 (2014).
11. A. Kuliopulos, A. S. Mildvan, D. Shortle, P. Talalay, *Biochemistry* **28**, 149–159 (1989).
12. M. A. Massiah, C. Abeygunawardana, A. G. Gittis, A. S. Mildvan, *Biochemistry* **37**, 14701–14712 (1998).
13. S. D. Fried, L.-P. Wang, S. G. Boxer, P. Ren, V. S. Pande, *J. Phys. Chem. B* **117**, 16236–16248 (2013).
14. S. D. Fried, S. Bagchi, S. G. Boxer, *J. Am. Chem. Soc.* **135**, 11181–11192 (2013).
15. W. Childs, S. G. Boxer, *J. Am. Chem. Soc.* **132**, 6474–6480 (2010).
16. S. W. Kim, K. Y. Choi, *J. Bacteriol.* **177**, 2602–2605 (1995).
17. G. H. Nam *et al.*, *Biochemistry* **40**, 13529–13537 (2001).
18. D. A. Kraut, P. A. Sigala, T. D. Fenn, D. Herschlag, *Proc. Natl. Acad. Sci. U.S.A.* **107**, 1960–1965 (2010).
19. G. Choi *et al.*, *Biochemistry* **40**, 6828–6835 (2001).
20. A. Warshel, *Proc. Natl. Acad. Sci. U.S.A.* **75**, 5250–5254 (1978).
21. A. Warshel *et al.*, *Chem. Rev.* **106**, 3210–3235 (2006).
22. A. Radzicka, R. Wolfenden, *Science* **267**, 90–93 (1995).
23. W. J. Houck, R. M. Pollack, *J. Am. Chem. Soc.* **126**, 16416–16425 (2004).
24. M. I. Page, W. P. Jencks, *Proc. Natl. Acad. Sci. U.S.A.* **68**, 1678–1683 (1971).
25. J. R. Knowles, *Nature* **350**, 121–124 (1991).
26. J. C. Austin, T. G. Spiro, A. Kuliopulos, A. S. Mildvan, *Protein Sci.* **1**, 259–270 (1992).
27. P. R. Carey, P. J. Tonge, *Acc. Chem. Res.* **28**, 8–13 (1995).
28. J. G. Belasco, J. R. Knowles, *Biochemistry* **19**, 472–477 (1980).

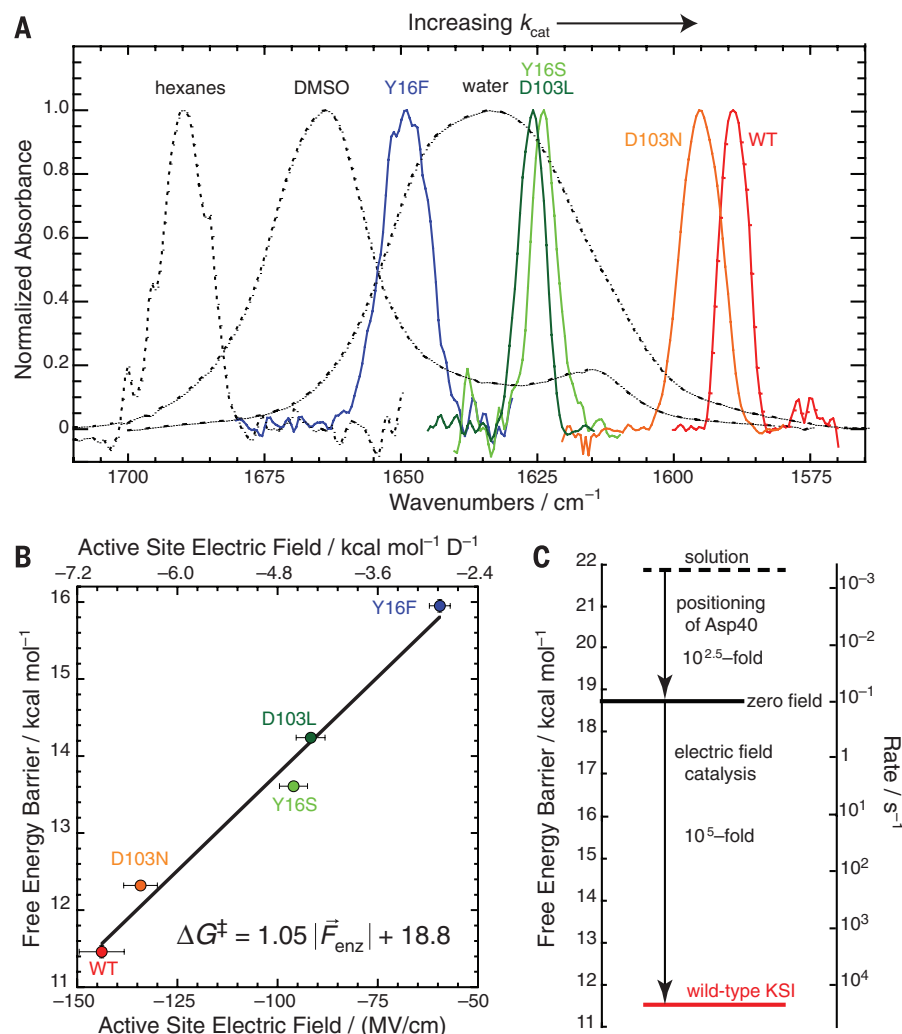


Fig. 3. Contribution of active-site electric fields to KSI's catalytic effect. (A) Infrared spectra of 19-NT bound to the active site of wild-type and mutant KSI (color traces), shown alongside a few spectra of 19-NT in solvents (dotted black traces) as a reference. DMSO, methyl sulfoxide; WT, wild type. **(B)** Plot of enzymatic unimolecular free energy barrier, ΔG^\ddagger , against the electric field, $|\vec{F}_{\text{enz}}|$, 19-NT's C=O group experiences in each of the KSI active sites. Expressing ΔG^\ddagger in kcal mol⁻¹ and $|\vec{F}_{\text{enz}}|$ in units of kcal mol⁻¹ D⁻¹ (upper axis), the least-squares regression line is $\Delta G^\ddagger = 1.05 |\vec{F}_{\text{enz}}| + 18.8$ ($R^2 = 0.98$). Error ranges for free energy barriers are contained within symbols; for electric fields, error bars report both experimental error from vibrational frequency measurements and model error from mapping frequencies to electric fields. **(C)** Relative contribution of KSI's catalytic strategies (electric field effect and general base positioning) to speed up KSI's reaction relative to its rate in solution.

ACKNOWLEDGMENTS

We thank the laboratory of D. Herschlag for providing plasmids of some of the KSI mutants. S.D.F. thanks the NSF predoctoral fellowship program and the Stanford Bio-X interdisciplinary graduate fellowship for support. This work was supported in part by a grant from NIH (grant GM27738). S.D.F. designed the study. S.D.F. and S.B.

performed experiments and collected data. S.D.F. analyzed the data. S.D.F. and S.G.B. discussed results and wrote the manuscript.

SUPPLEMENTARY MATERIALS

www.sciencemag.org/content/346/6216/1510/suppl/DC1
Materials and Methods

Supplementary Text S1 to S4
Figs. S1 to S8
Tables S1 to S3
References (29–70)

8 August 2014; accepted 17 November 2014
10.1126/science.1259802

PALEOCEANOGRAPHY

A stagnation event in the deep South Atlantic during the last interglacial period

Christopher T. Hayes,^{1,2*} Alfredo Martínez-García,³ Adam P. Hasenfratz,³ Samuel L. Jaccard,⁴ David A. Hodell,⁵ Daniel M. Sigman,⁶ Gerald H. Haug,³ Robert F. Anderson²

During the last interglacial period, global temperatures were ~2°C warmer than at present and sea level was 6 to 8 meters higher. Southern Ocean sediments reveal a spike in authigenic uranium 127,000 years ago, within the last interglacial, reflecting decreased oxygenation of deep water by Antarctic Bottom Water (AABW). Unlike ice age reductions in AABW, the interglacial stagnation event appears decoupled from open ocean conditions and may have resulted from coastal freshening due to mass loss from the Antarctic ice sheet. AABW reduction coincided with increased North Atlantic Deep Water (NADW) formation, and the subsequent reinvigoration in AABW coincided with reduced NADW formation. Thus, alternation of deep water formation between the Antarctic and the North Atlantic, believed to characterize ice ages, apparently also occurs in warm climates.

The circulation and biological productivity of the Southern Ocean may help regulate atmospheric CO₂ over millennial to glacial-interglacial time scales (1, 2). Evidence underpinning this view comes largely from study of climate oscillations during ice ages. Here, we report evidence for rapid changes in Southern Ocean circulation during the last interglacial period that is particularly relevant to today's warming climate. Authigenic uranium (aU), a redox-sensitive trace-element proxy for the oxygen content in sediment pore waters (3), reveals a millennial-scale reduction in the ventilation of the deep Southern Ocean around 127,000 years ago, when global temperatures were ~2°C warmer than they are today (4, 5).

Most sediment pore water oxygen concentrations are controlled primarily by the balance between diffusive supply from bottom water and consumption by respiration of sedimentary organic matter. We find evidence in samples from Ocean Drilling Program (ODP) Site 1094 (53.2°S 5.1°E, 2807 m water depth, Fig. 1) for changes in deep water oxygen supply by combining aU mea-

surements with controls on the supply of organic matter to the sediments. In this core, the ²³⁰Th-normalized biogenic opal flux records changes in the vertical rain of organic matter (2, 6). Lateral supply of organic matter by sediment redistribution, or focusing, is assessed by calculating the focusing factor, Ψ (7). For age control during the period surrounding Termination II (T-II), a new sea-surface temperature record from Site 1094, based on the marine lipid index, TEX₈₆^L, was correlated to the Vostok ice core δ D (7, 8) (Fig. 2A, fig. S1, and table S1).

The penultimate glacial period [marine isotope stage (MIS) 6] at Site 1094 is characterized by low export production (Fig. 2B), typical of the Antarctic South Atlantic during ice ages (9). Although substantial sediment focusing occurred during MIS 6 ($\Psi = 4$, Fig. 2C), these glacial age sediments are low in biogenic opal, our proxy of organic carbon export. Given the absence of an enhanced supply of organic carbon to the sea floor (either vertically or laterally), the aU enrichment during glacial MIS 6 (Fig. 2E) must be due to low bottom water oxygen concentrations, consistent with sluggish ventilation of the Southern Ocean during glacial periods (10). This scenario is corroborated by glacial-age aU enrichments observed in other sediment records from the Atlantic (9, 11) and Indian (12) sectors of the Southern Ocean.

During the deglacial period (T-II), export production increased rapidly, with ²³⁰Th-normalized opal fluxes increasing roughly 10-fold (Fig. 2B). Accounting for concurrent changes in sediment focusing, although aU concentrations decreased (Fig. 2E), the mass accumulation rate (MAR) of aU increased from MIS 6 into the earliest part of T-II (Fig. 2D), consistent with an increased load of organic matter to the sea floor enhancing aU deposition. During the course of T-II, export production remained high or even increased, whereas aU MAR gradually decreased (Fig. 2D). We therefore infer that the gradual deglacial decline in aU MAR was driven by increased oxygenation in deep water as a consequence of increased Southern Ocean overturning during T-II.

Against this backdrop of MIS 6-to-T-II changes that are consistent with previous findings, we observed an entirely unexpected feature in the

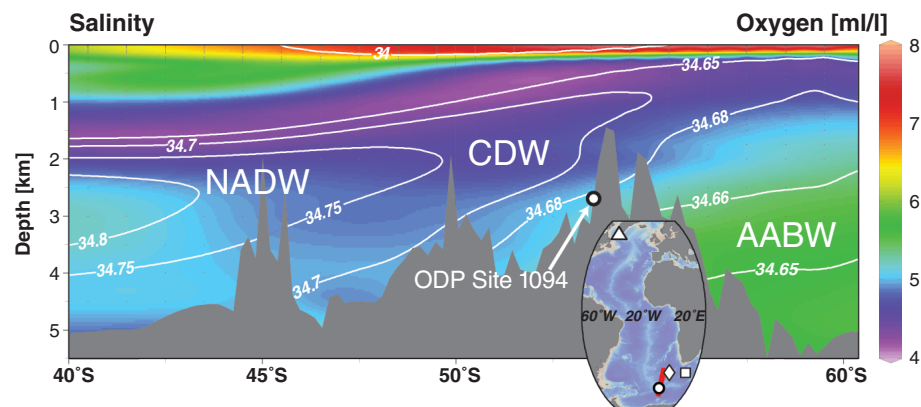


Fig. 1. Vertical section along 5°E in the South Atlantic putting ODP Site 1094 into hydrographic context. Color-mapped oxygen concentrations, with salinity contours overlain, as drawn from the 2009 World Ocean Atlas (30, 31). ODP Site 1094 is marked with a white circle. The inset map indicates the plotted section (red line) and the locations of other cores mentioned in the text: MD03-2664, white triangle; ODP Site 1089, white diamond; and PS2561-2, white square. Figure created with Ocean Data View (odv.awi.de).

¹Department of Earth, Atmospheric and Planetary Sciences, Massachusetts Institute of Technology (MIT), Cambridge, MA 02142, USA. ²Lamont-Doherty Earth Observatory of Columbia University, Palisades, NY 10964, USA. ³Geological Institute, ETH Zürich, 8092 Zürich, Switzerland. ⁴Institute of Geological Sciences and Oeschger Centre for Climate Change Research, University of Bern, 3012 Bern, Switzerland. ⁵Department of Earth Sciences, University of Cambridge, Cambridge CB2 3EQ, UK. ⁶Department of Geosciences, Princeton University, Princeton, NJ 08544, USA.

*Corresponding author. E-mail: cthayes@mit.edu

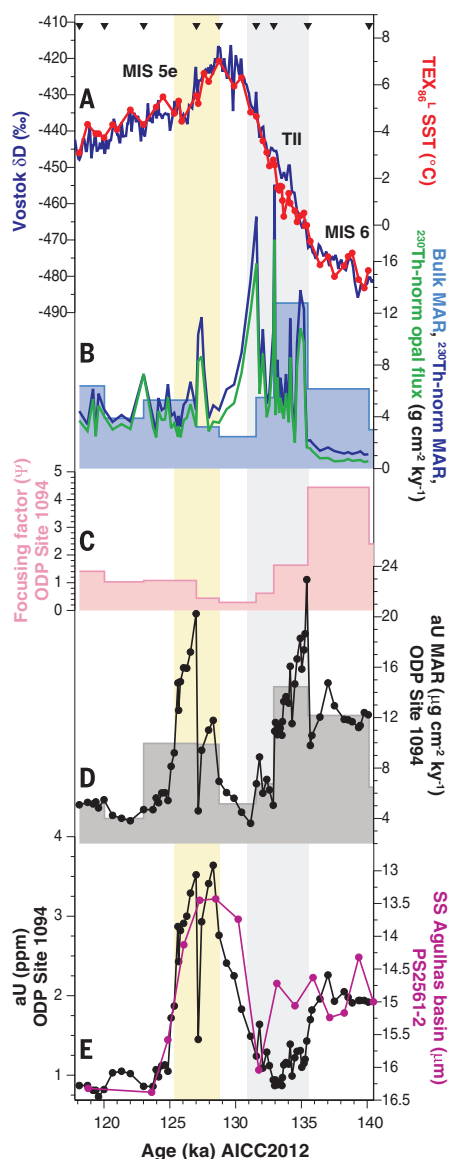


Fig. 2. Records from ODP Site 1094 spanning the penultimate glacial period to the last interglacial. (A) TEX_{86}^{1-} sea-surface temperature (SST) aligned with δD of the Vostok ice core (8, 32). (B) Bulk (square wave) and ^{230}Th -normalized (blue line) mass accumulation rates and ^{230}Th -normalized biogenic opal flux (green line). (C) Focusing factor, the intensity of lateral supply of sediments. (D) Authigenic uranium (aU) accumulation rate calculated as an instantaneous function of the aU concentrations (discrete points) and as interval averages (square wave). (E) aU concentrations from Site 1094 and mean size of sortable silt from Agulhas basin core PS2651-2 (7, 13). Age model tie points for Site 1094 are marked with inverted triangles. Marine isotopostages (MIS) and Termination II (T-II) are roughly indicated and are consistent with available foraminiferal $\delta^{18}\text{O}$ data (25). Gray shading highlights T-II, and yellow shading highlights the authigenic uranium event.

interglacial period MIS 5e: a 3000- to 4000-year spike in aU at 127 ± 1 ka (ka, thousand years ago) (7). Similar peaks in both aU concentration and aU MAR (Fig. 2, D and E; 125 to 129 ka) indicate that the rapid aU enrichment cannot be primarily explained by changes in dilution. Furthermore, the opal flux and focusing factor records (Fig. 2, B and C) show that vertical and lateral supplies of organic matter decreased from T-II to early MIS 5e. This combination of increased aU and reduced organic carbon sedimentation requires that the supply of oxygen to the bottom waters at Site 1094 went

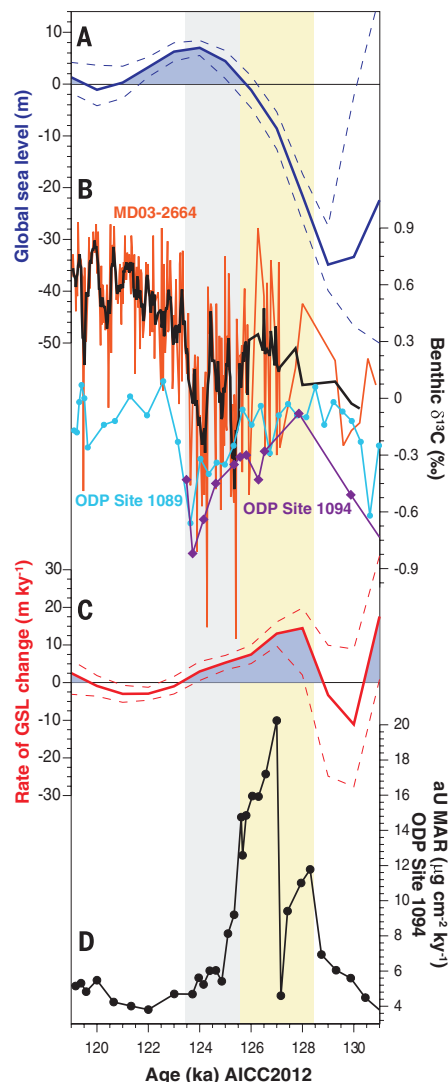


Fig. 3. Seesawing deep circulation events during the last interglacial period compared to changes in global sea level. (A) Estimated record of global sea level (19) and (C) its rate of change (19). Heavy lines mark the median projections of data-based probability density distribution, with dotted lines representing the 16th and 84th percentiles. (B) Benthic foraminiferal carbon isotopic composition from MD03-2664 (24), ODP Site 1089 (25), and ODP Site 1094. (D) Authigenic uranium mass accumulation rate (aU MAR) from Site 1094.

through a minimum around 127,000 years ago.

Today, Site 1094 is bathed by circumpolar deep water (CDW) which, in turn, is composed of contributions, mixed together in the Antarctic Circumpolar Current, from North Atlantic Deep Water (NADW), Indo-Pacific Deep Water (IPDW), and Antarctic Bottom Water (AABW) (Fig. 1). Both NADW and AABW supply oxygen to global deep waters. The last interglacial aU peak at Site 1094 is most simply explained by a reduction in AABW, partly because its formation region is most proximal to Site 1094. This is supported by a record from the abyssal Agulhas basin (PS2561-2, 41.9°S 28.5°E , 4465 m water depth), which contains a notable minimum in sortable silt size during MIS 5e at the time of the aU peak at Site 1094 (Fig. 2E), interpreted as a slow-down of AABW flow (13).

During glacial periods in general and especially during the Antarctic cold intervals preceding Heinrich events, there is evidence for reduced Antarctic productivity, a higher degree of nitrate consumption, and lower atmospheric CO_2 , which taken together suggest reduced Antarctic ventilation of the interior and thus greater deep ocean storage of regenerated carbon (2, 12, 14). aU enrichment during ice ages, such as is evident in the data reported here (Fig. 2), supports this interpretation. Previous authors have postulated a mechanistic link between Antarctic overturning and the strength and position of the global wind belts during glacial periods (15). This hypothesis has been strengthened by the observations that Antarctic productivity changes were coeval with changes in the position of the Intertropical Convergence Zone (ITCZ) (16) and in the strength of the Asian Monsoon (17).

In contrast, the aU spike within MIS 5e occurs in the context of little coherent change in Antarctic productivity (Fig. 2). Neither does the aU event correlate with possible far-field drivers, such as ITCZ migration (16, 17). Given these findings, the mechanism for the MIS 5e event was most likely fundamentally different than the process that reduced Antarctic deep ventilation during ice ages.

Following peak temperatures in Antarctica, global sea-level rose by ~ 20 m in the period 128 to 125 ka (18, 19) (Fig. 3A). Substantial melting at the margins of the Antarctic ice sheet at this time (20) may have freshened Antarctic coastal waters, interfering with the AABW formation that occurs on the Antarctic shelves today. This freshening may also have reached adequately far from shore to reduce deep ocean convection in the Weddell Sea (21). Admittedly, we have no direct evidence for Antarctic melting as the cause of the AABW reduction, and, as described below, other possibilities exist.

Coinciding with the interglacial peak aU accumulation at Site 1094, the brief drop and rebound in atmospheric CO_2 (Fig. 4, B and C, 127 ka) is consistent with increased deep ocean storage of regenerated carbon due to a reduction in AABW formation. Under interglacial conditions, a box model suggests that a shutoff of AABW formation should cause a CO_2 decline of ~ 33 parts per million (ppm) due to increased regenerated

carbon storage and related deep ocean CaCO_3 dissolution (22). However, a partial offset is expected from the CO_2 rise driven by warming of the deep ocean due to the loss of AABW. Given modern deep ocean conditions, AABW shutdown would translate to an ocean interior warming of 1° to 2°C , as NADW becomes the sole ventilator of the abyss, yielding a temperature-driven CO_2 rise of 10 to 20 ppm (23). Taking the difference yields a net CO_2 decline of 13 to 23 ppm, indistinguishable from the range in the reconstructions of the decline, 13 to 24 ppm (Fig. 4B).

The counteracting effect of deep ocean warming may explain why the mid-interglacial AABW shutdown discovered here coincided with a weaker CO_2 decline than has been proposed for ice age

reductions in AABW formation, of 30 to 40 ppm or more (22). During glacial times, reduced Antarctic ventilation may have coincided with climate cooling that prevented deep ocean warming, yielding a greater net CO_2 decline. The 3000- to 4000-year duration of the AABW shutdown during MIS 5e also may have been too short for ocean calcium carbonate dynamics to express the full CO_2 effect that applies to extended glacial periods.

The period 124 to 125 ka, immediately following the aU event at ODP Site 1094, is characterized by a reduction in NADW formation (24), as recorded by benthic foraminiferal $\delta^{13}\text{C}$ in core MD03-2664 (57.4°N , 48.6°W , 3442 m water depth) in the North Atlantic (Fig. 4D). The isotopic signature of this event propagated into the Southern Ocean. Within age model uncertainties, we observe a synchronous decrease in benthic $\delta^{13}\text{C}$ (*Cibicides wuellerstorfi*) of ODP Sites 1089 (25) and 1094 (Fig. 4D). This demonstrates that the reduction of AABW recorded by the aU peak at ODP Site 1094 preceded the reduction in NADW. The phasing suggests that the millennial “bipolar seesaw” in deep water formation between the Antarctic and North Atlantic reconstructed for the last ice age (26) also occurs during warm interglacials.

The climate sensitivity of the wind belts has been proposed as the central connection driving millennial-scale North Atlantic–Antarctic seesaw of the last ice age (15). However, when the aU peak at Site 1094 ended, we are aware of no evidence for an atmospheric teleconnection between AABW and NADW formation. Rather, the coincidence of the reinvigoration of AABW with the reduction in NADW is best explained by changes in deep ocean density (26). With the loss of deep water formation in one hemisphere, the density of the deep ocean declines, leading to a restart or reinvigoration of deep water formation in the other hemisphere on millennial time scales. The reduction in AABW may have encouraged a brief increase in NADW formation at ~ 127 ka (24) and thus spurred additional circum–North Atlantic ice loss, which has been proposed to drive a well-documented reduction in NADW around 125 ka (24). The NADW reduction, in turn, may have driven the reinvigoration of the AABW that is recorded by the end of the aU peak at 125 ka.

As to the cause of AABW reduction at ~ 127 ka, rather than being driven by Antarctic melting, it is possible that this event also originated from a deep ocean density teleconnection, triggered by the interglacial restart of NADW formation. However, the $\delta^{13}\text{C}$ data suggest that NADW formation at ~ 127 ka was not stronger than in the Holocene, which is characterized by deep water formation in both the North Atlantic and the Antarctic. Conversely, Antarctic temperature and sea-level rise were anomalously high before and during the AABW reduction, favoring the Antarctic melting trigger.

Although the South Atlantic stagnation occurred early during the last interglacial, there may be an analogy between this event and the reduction in Southern Ocean ventilation that has occur-

red over the past 40 years, during a much later stage in the current interglacial. Since 1976, deep convection in the Weddell Sea, as identified by polynya formation, has been absent (27), possibly due to anthropogenic warming and an associated freshening of the surface Southern Ocean (28). Such a tendency would be reinforced by coastal freshwater input should Antarctic ice loss accelerate in the coming decades and centuries. In this context, although there is great concern and substantial investigation regarding the potential for reduced NADW formation in the future (29), a marked reduction in AABW formation upon warming would not be unprecedented, in light of the previous interglacial. Moreover, the evidence that the bipolar seesaw in deep water formation (26) also applies to interglacial climate suggests that a global warming-induced reduction in deep water formation in either the North Atlantic or the Southern Ocean would lead to an increase in deep water formation in the other region.

REFERENCES AND NOTES

1. D. M. Sigman, M. P. Hain, G. H. Haug, *Nature* **466**, 47–55 (2010).
2. R. F. Anderson et al., *Science* **323**, 1443–1448 (2009).
3. G. P. Klinkhammer, M. R. Palmer, *Geochim. Cosmochim. Acta* **55**, 1799–1806 (1991).
4. F. Kaspar, N. Kühl, U. Cubasch, T. Litt, *Geophys. Res. Lett.* **32**, L11703 (2005).
5. B. L. Otto-Bliesner, S. J. Marshall, J. T. Overpeck, G. H. Miller, A. Hu, *Science* **311**, 1751–1753 (2006).
6. S. L. Jaccard et al., *Science* **339**, 1419–1423 (2013).
7. See supplementary materials on Science Online.
8. L. Bazin et al., *Clim. Past* **9**, 1715–1731 (2013).
9. M. Frank et al., *Paleoceanography* **15**, 642–658 (2000).
10. L. C. Skinner, S. Fallon, C. Waelbroeck, E. Michel, S. Barker, *Science* **328**, 1147–1151 (2010).
11. Z. Chase, R. F. Anderson, M. Q. Fleisher, *Paleoceanography* **16**, 468–478 (2001).
12. R. François et al., *Nature* **389**, 929–935 (1997).
13. S. Krueger, D. C. Leuschner, W. Ehrmann, G. Schmiedl, A. Mackensen, *Global Planet. Change* **80–81**, 180–189 (2012).
14. R. S. Robinson, D. M. Sigman, *Quat. Sci. Rev.* **27**, 1076–1090 (2008).
15. J. R. Toggweiler, J. L. Russell, S. R. Carson, *Paleoceanography* **21**, PA2005 (2006).
16. K. A. Gibson, L. C. Peterson, *Geophys. Res. Lett.* **41**, 969–975 (2014).
17. H. Cheng et al., *Science* **326**, 248–252 (2009).
18. A. Dutton, K. Lambeck, *Science* **337**, 216–219 (2012).
19. R. E. Kopp, F. J. Simons, J. X. Mitrovica, A. C. Maloof, M. Oppenheimer, *Nature* **462**, 863–867 (2009).
20. C. J. Fogwill et al., *J. Quat. Sci.* **29**, 91–98 (2014).
21. A. L. Gordon, *Nat. Clim. Change* **4**, 249–250 (2014).
22. M. P. Hain, D. M. Sigman, G. H. Haug, *Global Biogeochem. Cycles* **24**, GB4023 (2010).
23. P. Martin, D. Archer, D. W. Lea, *Paleoceanography* **20**, PA2015 (2005).
24. E. V. Gelaasen et al., *Science* **343**, 1129–1132 (2014).
25. D. A. Hodell et al., *Proc. Ocean Drill. Program, Sci. Results* **177**, 1–26 (2003).
26. W. S. Broecker, *Paleoceanography* **13**, 119–121 (1998).
27. A. L. Gordon, M. Visbeck, J. C. Corniso, *J. Clim.* **20**, 2558–2571 (2007).
28. C. de Lavergne, J. B. Palter, E. D. Galbraith, R. Bernardello, I. Marinov, *Nat. Clim. Change* **4**, 278–282 (2014).
29. D. Rayner et al., *Deep Sea Res. Part II Top. Stud. Oceanogr.* **58**, 1744–1753 (2011).
30. H. E. Garcia et al., *NOAA Atlas NESDros. Inf. Serv.* **70** (2010).
31. J. I. Antonov et al., *NOAA Atlas NESDIC* **69** (2010).
32. J. R. Petit et al., *Nature* **399**, 429–436 (1999).
33. R. Schneider, J. Schmitt, P. Köhler, F. Joos, H. Fischer, *Clim. Past* **9**, 2507–2523 (2013).
34. A. Lourdou, J. Chappellaz, J. M. Barnola, V. Masson-Delmotte, D. Raynaud, *Quat. Sci. Rev.* **29**, 1983–1992 (2010).

ACKNOWLEDGMENTS

We acknowledge the Integrated Ocean Drilling Program for providing samples. Data not previously reported are archived at the

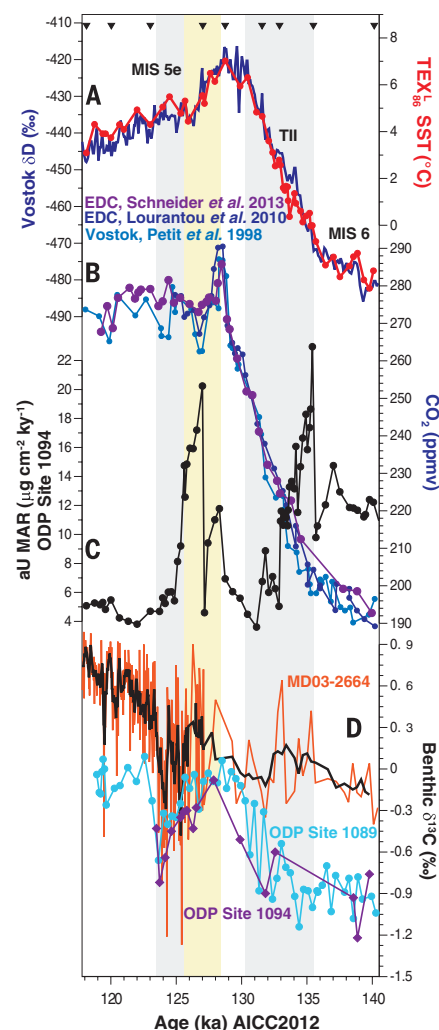


Fig. 4. Records from ODP Site 1094 in the context of atmospheric composition and North Atlantic circulation. (A) TEX_{86}^L SST aligned with δD of the Vostok ice core (8, 32). **(B)** Atmospheric CO_2 from the EPICA Dome C (33, 34) and Vostok (32) ice cores, the spread in which indicates the uncertainty associated with these measurements. **(C)** aU accumulation rate. **(D)** The carbon isotopic composition of benthic foraminifera from MD03-2664, with three-point running means in black, (24), ODP Site 1089 (25), and ODP Site 1094.

U.S. National Climate Data Center (<http://www.ncdc.noaa.gov/paleo/study/17455>) and Pangaea (<http://doi.pangaea.de/10.1594/PANGAEA.839454>) and can be accessed in tables S3 and S4. Financial support was provided by the Comer Science and Education Foundation (CTH/RFA), the W.O. Crosby Fellowship (C.T.H.), Swiss National Science Foundation grants

PZ00P2_142424 (AM-G) and PP00P2_144811 (SLJ), and ETH grant ETH-04 11-1 (SLJ/APH).

SUPPLEMENTARY MATERIALS

www.sciencemag.org/content/346/6216/1514/suppl/DC1
Materials and Methods

Figs. S1 and S2
Tables S1 to S4
References (35–51)

28 May 2014; accepted 21 November 2014
10.1126/science.1256620

CONSERVATION

Recovery of large carnivores in Europe's modern human-dominated landscapes

Guillaume Chapron,^{1,*†} Petra Kaczensky,² John D. C. Linnell,³ Manuela von Arx,⁴ Djuro Huber,⁵ Henrik Andrén,¹ José Vicente López-Bao,^{1,6†} Michal Adamec,⁷ Francisco Álvares,⁸ Ole Anders,⁹ Linas Balčiauskas,¹⁰ Vaidas Balys,¹¹ Péter Bedő,¹² Ferdinand Bego,¹³ Juan Carlos Blanco,¹⁴ Urs Breitenmoser,^{4,15} Henrik Brøseth,³ Luděk Bufka,¹⁶ Raimonda Bunikyte,¹⁷ Paolo Ciucci,¹⁸ Alexander Dutsov,¹⁹ Thomas Engleder,²⁰ Christian Fuxjäger,²¹ Claudio Groff,²² Katja Holmala,²³ Bledi Hoxha,²⁴ Yorgos Iliopoulos,²⁵ Ovidiu Ionescu,^{26,27} Jasna Jeremić,²⁸ Klemen Jerina,²⁹ Gesa Kluth,³⁰ Felix Knauer,² Ilpo Kojola,³¹ Ivan Kos,²⁹ Miha Krofel,²⁹ Jakub Kubala,³² Saša Kunovac,³³ Josip Kusak,⁵ Miroslav Kutal,^{34,35} Olof Liberg,¹ Aleksandra Majić,²⁹ Peep Männil,³⁶ Ralph Manz,⁴ Eric Marboutin,³⁷ Francesca Marucco,³⁸ Dime Melovski,^{39,40} Kujtim Mersini,⁴¹ Yorgos Mertzanis,²⁵ Robert W. Mysłajek,⁴² Sabina Nowak,⁴³ John Odden,³ Janis Ozolins,⁴⁴ Guillermo Palomero,⁴⁵ Milan Paunović,⁴⁶ Jens Persson,¹ Hubert Potočník,²⁹ Pierre-Yves Quenette,⁴⁷ Georg Rauer,² Ilka Reinhardt,³⁰ Robin Rigg,¹² Andreas Ryser,⁴ Valeria Salvatori,⁴⁸ Tomaž Skrbinšek,²⁹ Aleksandar Stojanov,³⁹ Jon E. Swenson,^{3,49} László Szemethy,⁵⁰ Aleksandër Trajçe,²⁴ Elena Tsingarska-Sedefcheva,¹⁹ Martin Váňa,³⁵ Rauno Veeroja,³⁶ Petter Wabakken,⁵¹ Manfred Wöhl,⁵² Sybille Wölfl,⁵³ Fridolin Zimmermann,⁴ Diana Zlatanova,⁵⁴ Luigi Boitani¹⁸

The conservation of large carnivores is a formidable challenge for biodiversity conservation. Using a data set on the past and current status of brown bears (*Ursus arctos*), Eurasian lynx (*Lynx lynx*), gray wolves (*Canis lupus*), and wolverines (*Gulo gulo*) in European countries, we show that roughly one-third of mainland Europe hosts at least one large carnivore species, with stable or increasing abundance in most cases in 21st-century records. The reasons for this overall conservation success include protective legislation, supportive public opinion, and a variety of practices making coexistence between large carnivores and people possible. The European situation reveals that large carnivores and people can share the same landscape.

Large carnivores are among the most controversial and challenging group of species to conserve in our modern and crowded world. There is a deeply rooted hostility to these species in human history and culture, because of perceptions of their negative impacts on human livelihoods (1). Large carnivore abundance and distribution have historically been reduced (2), and their present conservation has become intertwined with broader emotional, political, and socioeconomic issues that further complicate this challenge (3). In addition, large carnivores live at low densities and have large spatial requirements (4). Accordingly, the conservation of viable large carnivore populations needs to be planned and coordinated on very wide scales, often spanning many intra- and international borders [i.e., requiring transboundary management (5)].

The main debate around large carnivore conservation is whether there is enough suitable space

left for viable and ecologically functional populations (6). As the two main drivers of the current biodiversity crisis—human overpopulation and overconsumption—show no sign of reducing, an intuitive forecast could be that large carnivores will persist only in highly managed protected areas (with regular translocations being made to achieve artificial connectivity) or in some remote and uninhabited wilderness areas. This approach derives conceptually from the North American wilderness model that separates people and nature and that has further been adopted in many Asian, African, and neotropical countries (6) (“keeping people and predators apart,” the separation model). The ultimate expression of this approach lies in the southern African propensity to fence protected areas (6). The alternative model, “allowing people and predators together” (coexistence model), following a landscape-scale conservation approach, has rarely been given proper consideration, probably because

it has been deemed a priori to fail because of the existing conflicts between large carnivores and humans. This dichotomy of large carnivore conservation models is analogous to the land-sharing versus land-sparing debate, which is ongoing in a wider biodiversity conservation context (7).

We compiled data about the status (i.e., current and past occurrence and abundance) of large carnivores [brown bears (*Ursus arctos*), Eurasian lynx (*Lynx lynx*), gray wolves (*Canis lupus*), and wolverines (*Gulo gulo*)] in Europe (8). We show that the European continent (considering all continental European countries excluding Belarus, Ukraine, and Russia) is succeeding in maintaining, and to some extent restoring, viable large carnivore populations on a continental scale (Fig. 1 and fig. S1). All mainland European countries except for Belgium, Denmark, the Netherlands, and Luxembourg have a permanent and reproducing occurrence of at least one species of large carnivore (Fig. 1). The total area with a permanent presence of at least one large carnivore species in Europe covers 1,529,800 km² (roughly one-third of mainland Europe), and the area of occasional presence is expanding, as the presence of solitary dispersing wolves has been confirmed in both Denmark and Belgium in recent times.

Brown bears presently occur permanently in 22 countries (485,400 km²) and can be clustered into 10 populations, most of which are native populations (tables S1 to S3). Eurasian lynx presently occur permanently in 23 countries (813,400 km²) and can be clustered into 11 populations, five of them being native populations (tables S5 to S7). Wolves currently occur permanently in 28 countries (798,300 km²) and can be clustered into 10 populations, which are all native (tables S9 to S11). Wolverines, however, are only found in the three Fennoscandic countries, and they permanently occur over a total of 247,900 km² in two populations (tables S13 to S15). Because of the limited biogeographic distribution of wolverines, Fennoscandia is the only region containing all four large carnivore species in Europe (171,500 km²), and could be considered as a large-carnivore hot spot together with southeastern Europe (Dinaric, Carpathian, and Balkan regions) and the Baltics (fig. S2). Three large carnivore species overlap over 593,800 km² in Europe (fig. S2).

Overall, Europe hosts several large and stable populations on the order of thousands of individuals, many medium-sized and increasing populations that number in the hundreds of individuals, and a few small and declining populations with a few tens of individuals. Interestingly, none of the medium or large populations are declining. Brown bears are the most abundant large carnivore in Europe, with an estimated total number around 17,000 individuals, and all population ranges have

been relatively stable or slightly expanding (table S2). Wolves are the second most abundant species, with an estimated total number larger than 12,000 individuals (table S10). Most populations have been increasing or stable during recent years, although the Sierra Morena population (Spain) is on the brink of extinction, with only one pack detected in 2010 (9). In recent years, the larger Iberian population has an uncertain trend, although it seems stable, and the Karelian population has declined (9). The estimated total number of Eurasian lynx is around 9000 individuals (table S6), and most populations have generally been stable in the past decade, although most of the reintroduced populations appear to have stagnated at relatively small sizes, and the Vosges-Palatinian and Balkan lynx populations have declined (9). Finally, the estimated total number of wolverines is 1250 individuals, and both populations are increasing (table S14). Details on large carnivore monitoring methods are given in tables S4, S8, S12, and S16 and (9).

All four large carnivore species are persisting in human-dominated landscapes (fig. S3) and largely outside protected areas. The mean \pm SD human density in areas of permanent large carnivore presence is 19.0 ± 69.9 inhabitants/km² (range: 0 to 1651) for brown bears; 21.8 ± 73.8 inhabitants/km² (range: 0 to 2603) for lynx; 36.7 ± 95.5 inhabitants/km² (range: 0 to 3050) for wolves; and 1.4 ± 5.7 inhabitants/km² (range: 0 to 115) for wolverines (fig. S3). These figures suggest species-specific sensitivities of large carnivores to humans, with wolves being most successful in adapting to human-dominated landscapes (fig. S3). Wolverines are somewhat special, because their distribution is constrained by climatic conditions, which restricts them to northern and high-altitude areas, which have low human population densities (10).

These figures permit cautious optimism for the occurrence, abundance, and trends for large carni-

vores in Europe. The general picture emerging from the current status of large carnivores in Europe is that these species have shown the capacity to survive in human-dominated landscapes, representing an often underappreciated conservation success story. Having high numbers of large carnivores in such landscapes is not exclusive to Europe [the United States has abundant populations of black bears (*Ursus americanus*) and mountain lions (*Puma concolor*)]; however, the largest species, brown bears and wolves, occur in Europe with much higher human densities. For example, Europe hosts twice as many wolves (>11,000) as the contiguous United States [\sim 5500 wolves (11)], despite being half the size (4.3 million km² versus 8 million km²) and more than twice as densely populated (97 inhabitants/km² versus 40 inhabitants/km²).

We believe that the alternative view to the coexistence model (i.e., the separation model), which argues that the largest predators can only survive in protected areas or wilderness, is a consequence of former policy goals to exterminate these species (12). However, our results underline that if the separation model had been applied in Europe, there would hardly be any large carnivore populations at all, because most European protected areas are too small to host even a few large carnivore reproductive units (13).

Whereas large carnivores do not permanently occur in the areas of highest human density in Europe, they have shown an ability to recolonize areas with moderate human densities if they are allowed, and to persist in highly human-dominated landscapes and in the proximity of urban areas (14, 15) in highly fragmented landscapes consisting of forest-farmland mosaics or even agroecosystems. Our results are not the first to reveal that large carnivores can coexist with people (16–18), but they show that the land-sharing model for large carnivores (coexistence model) can be successful on a continental scale.

The reasons for the success of large carnivores in Europe range from coordinated legislation shared by many European countries (19, 20) to context-specific management practices and institutional arrangements. Since the end of World War II, Europe has benefited from stable political institutions ensuring proper law enforcement. The post-communist transition in Eastern European countries was not generally associated with institutional collapse, with the exception of some Balkan countries. This stability created the conditions for securing land tenure and associated rights for activities such as forestry and hunting, which are preconditions for the development of sustainable practices. The rise of environmental movements in the 1970s provided the motivation for various pan-European legislative agreements to emerge that served to promote biodiversity conservation. For example, the Bern Convention, administered by the Council of Europe, covers all countries included in this report, and the Habitats Directive covers all 20 European Union member states with a permanent occurrence of large carnivores. Consequently, the four large carnivore species examined here enjoy some degree of legal protection in all European countries. Large carnivores have also benefited from the socioeconomic changes over the past four decades that led to an improvement in habitat quality. For example, Europe again hosts large populations of wild ungulates (21), which can sustain large carnivore populations. The impact of human land-use activities has also been declining in many areas because of a widespread exodus from rural areas and the associated abandonment of agricultural land (22). These broad patterns are further accompanied by a variety of local, cultural, or regulatory practices making coexistence between large carnivores and people possible (15, 23). One important prerequisite has been to maintain and revive traditional livestock protection measures

¹Grimso Wildlife Research Station, Department of Ecology, Swedish University of Agricultural Sciences, 73091 Riddarhyttan, Sweden. ²Research Institute of Wildlife Ecology, University of Veterinary Medicine, Vienna, Savoyenstrasse 1, 1160 Vienna, Austria. ³Norwegian Institute for Nature Research, Post Office Box 5685 Sluppen, 7485 Trondheim, Norway. ⁴KORA, Thunstrasse 31, 3074 Muri bei Bern, Switzerland. ⁵Biology Department of the Faculty of Veterinary Medicine, University of Zagreb, Heinzelova 55, 10000 Zagreb, Croatia. ⁶Research Unit of Biodiversity (UO/CSIC/PA), Oviedo University, 33600 Mieres, Spain. ⁷State Nature Conservancy of Slovak Republic, Tajovského 28B, 974 01 Banská Bystrica, Slovakia. ⁸CIBIO/InBio, Centro de Investigação em Biodiversidade e Recursos Genéticos, Universidade do Porto, 4485-661 Vairão, Portugal. ⁹Harz Nationalpark, Lindenallee 35, 38855 Wernigerode, Germany. ¹⁰Nature Research Centre, Akademijos 2, 08412 Vilnius, Lithuania. ¹¹Association for Nature Conservation "Baltijos vilkas," Visorui 6A-54, 08300 Vilnius, Lithuania. ¹²Slovak Wildlife Society, Post Office Box 72, 03301 Liptovský Hradok, Slovakia. ¹³Biology Department of the Faculty of Natural Sciences, University of Tirana, Boulevard Zog I, Tirana, Albania. ¹⁴Wolf Project, Consultores en Biología de la Conservación, Calle Manuela Malasana 24, 28004 Madrid, Spain. ¹⁵Centre for Fish and Wildlife Health, Vetsuisse Faculty, University of Bern, Länggassstrasse 122, 3012 Bern, Switzerland. ¹⁶Department of Game Management and Wildlife Biology, Czech University of Life Sciences in Prague, Kamýcká 129, 165 21 Prague, Czech Republic. ¹⁷Ministry of Environment of the Republic of Lithuania, Jakšto 4/9, 01105 Vilnius, Lithuania. ¹⁸Department of Biology and Biotechnologies, University of Rome "La Sapienza," Viale dell'Università 32, 00185 Roma, Italy. ¹⁹Balkani Wildlife Society, Boulevard Dragan Tzankov 8, 1164 Sofia, Bulgaria. ²⁰Lynx Project Austria Northwest, Linzerstrasse 14, 4170 Haslach/Mühl, Austria. ²¹Nationalpark Kalkalpen, Nationalpark Zentrum Molln, Nationalpark Allee 1, 4591 Molln, Austria. ²²Provincia Autonoma di Trento - Servizio Foreste e Fauna, Via Trener no. 3, 38100 Trento, Italy. ²³Finnish Game and Fisheries Research Institute, Viikinkaari 4, 00790 Helsinki, Finland. ²⁴Protection and Preservation of Natural Environment in Albania, Rruga Vangjush Fuxhi 16/1/10, Tirana, Albania. ²⁵Callisto Wildlife and Nature Conservation Society, Mitropoleos 123, 54621 Thessaloniki, Greece. ²⁶Faculty of Silviculture and Forest Engineering, Department of Silviculture, Transilvania University, 1 Beethoven Lane, 500123 Braşov, Romania. ²⁷Forest Research Institute (ICAS) Boulevard Erolor Number 128, Voluntari, Ilfov, 077190 Romania. ²⁸State Institute for Nature Protection, Trg Mažuranića 5, 10000 Zagreb, Croatia. ²⁹University of Ljubljana, Biotechnical Faculty, Jamnikarjeva 101, 1000 Ljubljana, Slovenia. ³⁰LUPUS – German Institute for Wolf Monitoring and Research, Dorfstrasse 20, 02979 Spreewitz, Germany. ³¹Finnish Game and Fisheries Research Institute, Oulu Game and Fisheries Research, Tutkijantie 2E, 90570 Oulu, Finland. ³²Department of Forest Protection and Game Management, Faculty of Forestry, Technical University of Zvolen, T.G. Masaryka 20, 960 53 Zvolen, Slovakia. ³³Faculty of Forestry, University of Sarajevo, Zvezdarska 20, 71000 Sarajevo, Bosnia and Herzegovina. ³⁴Department of Forest Protection and Wildlife Management, Faculty of Forestry and Wood Technology, Mendel University in Brno, Zemědělská 3, 61300 Brno, Czech Republic. ³⁵Friends of the Earth Czech Republic, Olomouc Branch, Dolní náměstí 38, 77900 Olomouc, Czech Republic. ³⁶Estonian Environment Agency, Rõmme tee 2, 51013 Tartu, Estonia. ³⁷Office National de la Chasse et de la Faune Sauvage, ZI Mayencin, 5 Allée de Béthléem, 38610 Gières, France. ³⁸Centro Gestione e Conservazione Grandi Carnivori, Piazza Regina Elena 30, Valderi 12010, Italy. ³⁹Macedonian Ecological Society, Arhimedova 5, Skopje 1000, FYR Macedonia. ⁴⁰Department of Wildlife Sciences, Georg-August University, Büsgenweg 3, 37077 Göttingen, Germany. ⁴¹National Veterinary Epidemiology Unit, Food Safety and Veterinary Institute, Rruga Aleksander Moisiu 10 Tirana, Albania. ⁴²Institute of Genetics and Biotechnology, Faculty of Biology, University of Warsaw, Pawińskiego 5a, 02-106 Warszawa, Poland. ⁴³Association for Nature "Wolf," Twardorzeczka 229, 34-324 Lipowa, Poland. ⁴⁴Latvian State Forest Research Institute "Silava," Rigas iela 111, Salaspils, 2169 Latvia. ⁴⁵Fundación Oso Pardo, Calle San Luis 17, 4° A, 39010 Santander, Spain. ⁴⁶Natural History Museum, Njegoševa 51, 11000 Belgrade, Serbia. ⁴⁷ONCFS-CNERA PAD, Equipe Ours, Chef de Projet, Impasse de la Chapelle, 31800 Villeneuve de Rivière, France. ⁴⁸Instituto di Ecologia Applicata, Via B. Eustachio 10, 00161 Rome, Italy. ⁴⁹Department of Ecology and Natural Resource Management, Norwegian University of Life Sciences, Postbox 5003, 1432 Ås, Norway. ⁵⁰St. István University Institute for Wildlife Conservation, Péter Károly 1, 2103 Gödöllő, Hungary. ⁵¹Hedmark University College, Evenstad, 2480 Koppang, Norway. ⁵²Bavarian Agency of Environment, Hans-Högn-Strasse 12, 95030 Hof/Saale, Germany. ⁵³Lynx Project Bavaria, Trallinga 1a, 93462 Lam, Germany. ⁵⁴Department of Zoology and Anthropology, Faculty of Biology/Sofia University "St. Kliment Ohridski," Boulevard Dragan Tzankov 8, 1164 Sofia, Bulgaria.

*Corresponding author. E-mail: gchapron@carnivoreconservation.org or guillaume.chapron@slu.se †These authors contributed equally to this work.

(livestock-guarding dogs, night corrals, and shepherd herds), as well as to invest in new techniques (electric fences) as an important nonlethal tool to minimize large carnivore depredation on livestock (24).

The most severe challenges for large carnivore conservation are in countries where large carnivores have previously been extirpated, where the adaptations for coexistence have been lost, or where husbandry practices have evolved toward new production schemes. In such contexts, the return of large carnivores can trigger social conflicts. For example, poaching enjoys social acceptance in rural areas of Norway (25), limits the recovery of wolves in Scandinavia (26), and eradicated a reintroduced bear population in Austria (27). In these areas, the practical challenges and economic impacts of carnivore conservation have escalated into social conflicts, where the carnivores have become symbols of wider political divisions between rural and urban populations and between individuals and groups with fundamentally different value orientations and interests.

At present, there is a conjuncture between many policy areas combined with a generally supportive public opinion, so that the positive forces have been prevailing. However, the underlying negative forces are still present and could reemerge as a result of ecological, social, political, or economic changes. There is a need to monitor both the ecological situation and sociopolitical climate to ensure that the current trends are maintained.

The European experience offers hope for wildlife conservation in human-dominated landscapes and is relevant to other areas of the world. Although developing countries may lack many of the institutions and capacities that have enabled large carnivore recovery in Europe, there are other examples of large carnivores persisting and recovering in human-dominated landscapes and even in cities (17, 28, 29). Clearly, the presence of large carnivores in human-dominated ecosystems is associated with modified ecological conditions that deviate from conditions in areas with little human activity. However, the fact that such species

can persist in these novel ecosystems encourages optimism for the conservation of larger and more connected large carnivore populations.

REFERENCES AND NOTES

1. A. Treves, K. U. Karanth, *Conserv. Biol.* **17**, 1491–1499 (2003).
2. W. J. Ripple et al., *Science* **343**, 1241484 (2014).
3. G. Chapron, J. V. López-Bao, *Science (New York, N.Y.)* **343**, 1199–1200 (2014).
4. J. L. Gittleman, S. M. Funk, D. Macdonald, R. K. Wayne, *Carnivore conservation. Conserv. Biol. Ser. (Cambridge)* **5**, 1–675 (2001).
5. J. D. C. Linnell, L. Boitani, *Hystrix* **23**, 80–91 (2012).
6. C. Packer et al., *Ecol. Lett.* **16**, 635–641 (2013).
7. B. Phalan, M. Onial, A. Balmford, R. E. Green, *Science* **333**, 1289–1291 (2011).
8. See materials and methods, figs. S1 to S3, and tables S1 to S16 in the supplementary materials.
9. P. Kaczensky et al., *Status, Management and Distribution of Large Carnivores—Bear, Lynx, Wolf and Wolverine—in Europe* (Report to the EU Commission, Part 1 and Part 2, 2013); http://ec.europa.eu/environment/nature/conservation/species/carnivores/pdf/task_1_part1_statusofcarnivores.pdf and http://ec.europa.eu/environment/nature/conservation/species/carnivores/pdf/task_1_part2_statusofcarnivores.pdf.
10. J. P. Copeland et al., *Can. J. Zool.* **88**, 233–246 (2010).
11. International Wolf Center, *Wolves in the United States*; www.wolf.org/wow/united-states/ (2014).
12. J. D. C. Linnell, J. E. Swenson, R. Anderson, *Anim. Conserv.* **4**, 345–349 (2001).
13. R. Woodroffe, J. R. Ginsberg, *Science* **280**, 2126–2128 (1998).
14. M. Basille et al., *Ecography* **32**, 683–691 (2009).
15. J. V. López-Bao, V. Sazatornil, L. Llana, A. Rodríguez, *Conserv. Lett.* **6**, 448–455 (2013).
16. S. D. Gehrt et al., *Urban Carnivores: Ecology, Conflict, and Conservation* (John Hopkins Univ. Press, Baltimore, MD, 2010).
17. V. Athreya, M. Odden, J. D. Linnell, J. Krishnaswamy, U. Karanth, *PLOS ONE* **8**, e57872 (2013).
18. N. H. Carter, B. K. Shrestha, J. B. Karki, N. M. Pradhan, J. Liu, *Proc. Natl. Acad. Sci. U.S.A.* **109**, 15360–15365 (2012).
19. Council Directive 92/43/EEC of 21 May 1992 on the conservation of natural habitats and of wild fauna and flora (1992); <http://eur-lex.europa.eu/legal-content/EN/TXT/?uri=CELEX:31992L0043>.
20. Convention on the Conservation of European Wildlife and Natural Heritage (1979); <http://conventions.coe.int/Treaty/en/Treaties/html/104.htm>.
21. J. D. C. Linnell, F. E. Zachos, in *Ungulate Management in Europe: Problems and Practices*, R. Putman, M. Apollonio, R. Andersen, Eds. (Cambridge Univ. Press, Cambridge, 2011), pp. 12–53.
22. L. M. Navarro, H. M. Pereira, *Ecosystems (N. Y.)* **15**, 900–912 (2012).
23. E. J. Knott et al., *Eur. J. Wildl. Res.* **60**, 85–97 (2014).
24. J. D. C. Linnell et al., in *Carnivore Ecology and Conservation: A Handbook of Techniques*, L. Boitani, R. A. Powell, Eds. (Oxford Univ. Press, Oxford, 2012), pp. 314–332.
25. K. E. Gangaas, B. P. Kaltenborn, H. P. Andreassen, *PLOS ONE* **8**, e68849 (2013).
26. O. Liberg et al., *Proc. R. Soc. Ser. B* **279**, 910–915 (2012).
27. L. Kruckenhauser, G. Rauer, B. Däubel, E. Haring, *Conserv. Genet.* **10**, 1223–1233 (2009).
28. C. Vynne et al., *PLOS ONE* **6**, e28939 (2011).
29. A. Zimmermann et al., in *Wild Rangelands*, J. du Toit, R. Kock, J. Deutsch, Eds. (Wiley, Oxford, 2010), pp. 129–151.

ACKNOWLEDGMENTS

Shape files of all maps are available in Dryad at this address: <http://doi.org/10.5061/dryad.986mp>. This study was partly funded by European Commission contract 070307/2012/629085/SER/B3. P.K., G.C., J.D.C.L., M.v.A., D.H., H.A., J.V.L.B., and L.B. designed the study; G.C. and J.V.L.B. wrote the paper with help from P.K., J.D.C.L., M.v.A., D.H., H.A., and L.B.; and all authors contributed data.

SUPPLEMENTARY MATERIALS

www.sciencemag.org/content/346/6216/1517/suppl/DC1
Materials and Methods
Figs. S1 to S3
Tables S1 to S16
References (30–258)

17 June 2014; accepted 13 November 2014
10.1126/science.1257553

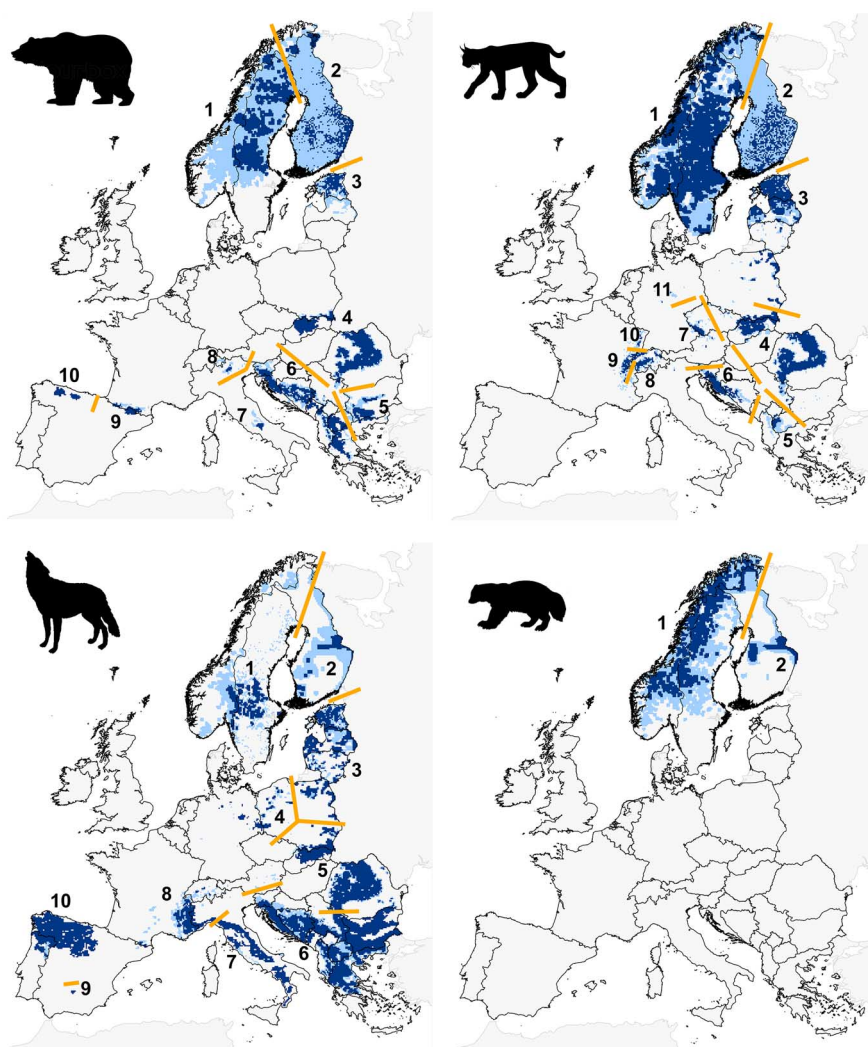


Fig. 1. Distribution of large carnivores in Europe in 2011. Brown bears (top left), Eurasian lynx (top right), gray wolves (bottom left), and wolverines (bottom right). Dark blue cells indicate areas of permanent occurrence, and light blue cells indicate areas of sporadic occurrence. Numbers refers to population identifications in tables S1 to S16. Orange lines indicate boundaries between populations.

PROTEIN DESIGN

De novo design of a transmembrane Zn²⁺-transporting four-helix bundle

Nathan H. Joh,¹ Tuo Wang,² Manasi P. Bhate,¹ Rudresh Acharya,³ Yibing Wu,¹ Michael Grabe,^{1*} Mei Hong,^{2*} Gevorg Grigoryan,^{4*} William F. DeGrado^{1*}

The design of functional membrane proteins from first principles represents a grand challenge in chemistry and structural biology. Here, we report the design of a membrane-spanning, four-helical bundle that transports first-row transition metal ions Zn²⁺ and Co²⁺, but not Ca²⁺, across membranes. The conduction path was designed to contain two di-metal binding sites that bind with negative cooperativity. X-ray crystallography and solid-state and solution nuclear magnetic resonance indicate that the overall helical bundle is formed from two tightly interacting pairs of helices, which form individual domains that interact weakly along a more dynamic interface. Vesicle flux experiments show that as Zn²⁺ ions diffuse down their concentration gradients, protons are antiported. These experiments illustrate the feasibility of designing membrane proteins with predefined structural and dynamic properties.

The de novo design of proteins is an important endeavor that critically tests our understanding of the principles underlying protein folding and function, while also laying the foundation for the design of proteins and molecular assemblies with desired properties. Much progress has been recently demonstrated in the design of water-soluble proteins with a variety of folds (1), and numerous natural proteins have been redesigned to bind metal ions (2) or small molecules (3) or to catalyze mechanistically simple reactions (4–7). However, the design of membrane proteins remains in its infancy (8, 9). To date, the most complex designed membrane proteins contain porphyrins that catalyze transmembrane electron transfer (8), but no designed membrane protein has been experimentally shown to adopt the desired fold at atomic resolution.

Here, we focus on the design of a Zn²⁺ transporter, a goal that presents several challenges. First is to design a membrane protein with a predefined structure and, second, to determine its structure and dynamics at high resolution. Next, the design must precisely position polar ionizable Zn²⁺ ligands, which are ordinarily excluded from a membrane environment. Furthermore, proton-Zn²⁺ antiport requires thermodynamic coupling to link proton binding to changes in metal ion affinity. Finally, we aimed to anticipate and orchestrate dynamics to facilitate ion transport.

Here, we describe a computational strategy for the design of a Zn²⁺ transporter, dubbed Rocker,

to characterize its structure, and demonstrate that it transports Zn²⁺ with concomitant reverse transport of protons. This work demonstrates the feasibility of membrane protein design and suggests that the advances recently reported in the design of water-soluble proteins can now be extended to membrane-spanning structures.

Natural transporters are hypothesized to rock between two or more states in a mechanism known as alternating access (10–12). For example, the multidrug transporter EmrE is a homodimer that is not stable in a single symmetric homodimeric conformation (13). Instead, it rocks between two degenerate asymmetric structures that alternately expose a substrate-binding site to the cytoplasmic and periplasmic sides of the membrane. Many transporters also harness the energy released in the movement of one ion down its concentration gradient to drive the accumulation of a second ion or small molecule. In proton-dependent transporters, protons often compete directly with substrates for binding to ionizable side chains. We sought to design a minimal protein that uses a similar mechanism. Four-helix bundles are capable of transporting protons (14–16) and binding metal ions, so we focused on this fold. Moreover, we previously observed that the Glu side chains in a 4Glu-2His di-Zn²⁺-binding protein were largely protonated, even at neutral pH, in the absence of Zn²⁺, because of the energetic cost of burying negatively charged side chains within the interior of a protein (17). Binding of Zn²⁺ displaces these protons, providing a means to achieve the desired thermodynamic coupling. Moreover, di-metal sites often have bridging water or hydroxide ligands, which could provide kinetically accessible sites for passing protons to the protein ligands as they diffuse through the channel.

We focused on design of a four-helix bundle with the helices inclined by a 10° to 20° angle (Fig. 1, A to D, and fig. S1); if the helices are straight, they diverge from a point of closest

approach to yield a truncated conical shape. However, if they gently curve (as in a coiled-coil), the bundle has a more cylindrical shape. An appropriately designed antiparallel homotetramer might alternate between the two energetically equivalent asymmetric conformations with the wider end at one or the other side of the bundle. The highly symmetric coiled-coil might provide an intermediate state, facilitating movement of ions through the bundle (Fig. 1A). However, the coiled-coil should not be so stable as to kinetically trap the mobile ions. Thus, the process reduces to the design of an energy landscape in which the two degenerate asymmetric states are more stable than the symmetric coiled-coil.

We chose a homotetrameric bundle with two 2His4Glu di-Zn²⁺-binding sites, each site formed by the coalescence of an EXXH motif near the N terminus of two helices and a Glu near the C terminus of the other two helices (Fig. 1, A and B). The symmetric coiled-coil was designed via a stochastic search in the space of Crick parameters (18, 19) to find a backbone conformation that allowed Zn²⁺ binding in a good geometry (20, 21). Moreover, we assured that the helix-helix interfaces would be “designable”; i.e., their backbone geometries should be well represented in a diverse set of native proteins (see fig. S1, E and F, and supplementary methods) (19). The resulting 25-residue-long antiparallel homotetrameric bundle shares no structural similarities with YiiP, the only natural Zn²⁺ transporter with a high-resolution structure (22). YiiP is a hexamer with a single 1His3Asp Zn²⁺ site.

We next created the off-symmetry version of the bundle by straightening helices beyond the boundaries of one metal-binding site, which caused subtle flaring of the bundle (up to 1.7 Å) and distorted the binding site at the opposite end of the oligomer (Fig. 1A). To stabilize this conformation relative to the symmetric coiled-coil, we used a negative design algorithm (23). This was a difficult task, given the high similarity between the structures. Negative design relies in part on introducing interactions to destabilize the symmetric conformation. If the backbone relaxes even subtly in an unanticipated manner, these interactions may become much less destabilizing. Moreover, conformational entropy may be significant for encoding preference for the asymmetric state. To address these issues, we defined configuration-space volume elements around the symmetric and asymmetric structures, and we used VALOCIDY (24) to estimate the free energy in each for the top ~1000 sequences predicted to be asymmetry-selective by initial negative design (NVT ensemble, IMMI force field) (25). The final sequence chosen (Fig. 1C) was the one displaying the largest VALOCIDY-estimated free-energy difference between the two states, while having a sufficiently large pore to permit ion conduction. Residues allowed in design were defined, based on membrane depth using the E_Z potential (table S1) (26, 27). We also required a second-shell H-bond to the metal binding His (28) (see supplementary methods for details).

¹Department of Pharmaceutical Chemistry, Cardiovascular Research Institute, University of California, San Francisco, San Francisco, CA 94158, USA. ²Department of Chemistry, Massachusetts Institute of Technology, Cambridge, MA 02139, USA. ³School of Biological Sciences, National Institute of Science Education and Research, Bhubaneswar, Odisha, India. ⁴Department of Computer Science and Department of Biological Sciences, Dartmouth College, Hanover, NH 03755, USA.

*Corresponding author. E-mail: william.degrado@ucsf.edu (W.F.D.); gevorg.grigoryan@dartmouth.edu (G.G.); meihong@mit.edu (M.H.); michael.grabe@ucsf.edu (M.G.)

The resulting dimer of dimers has two non-equivalent helix-helix interfaces (Fig. 1D); a “tight interface” has a small interhelical distance (8.9 Å) stabilized by efficient packing of small, Ala residues. The geometry of the tight interface is similar to the “alanine coil,” a sequence-structure motif shown to impart thermodynamic stability and structural rigidity in model peptides (29). The “loose interface” has a larger interhelical distance of 12.0 Å packed by large Phe residues. The packing of large apolar residues in membrane proteins provides a much smaller driving force for association than the tight packing of small residues (29–37). Thus, we expected the loose interface to be thermodynamically less stable and geometrically more flexible, which would facilitate the motion of ions through the bundle.

Molecular dynamics (MD) simulations were used to probe the stability and dynamics of the de novo designed structure. We embedded the model structure in a homogenous 1-palmitoyl-2-oleoylphosphatidylcholine bilayer with two Zn^{2+} fully occupying one of the 4Glu-2His sites; the other site was empty as described in the supplement. The fully bound site is electrically neutral when the coordinating residues are in their standard protonation states (charged Glu and neutral His). To explore the role of protonation at the

unliganded site, we carried out four independent simulations exploring different possible charge states (fig. S2, A to C). Qualitatively, all four simulations behave similarly on the 100-ns time scale. The chelated di-zinc site is extremely stable and shows a C α root mean square deviation (RMSD) of about 0.75 Å with very few fluctuations (fig. S2A, right). Water enters the transporter, providing hydration by 10 to 14 water molecules along the lumen between the two binding sites, a desirable feature for ion transport (fig. S2E). Analogous to a hydrophobic gate, bulky aromatic Phe14 adjacent to the Zn^{2+} site appears to partially exclude water.

Next, we examined the distance between the helices in the tight versus loose dimer interfaces. The helices in the tight dimer remain closely packed near the initial structure (red curves, Fig. 1E and fig. S2B). However, the distance between helices in the weak interface increases by as much as 3 Å in three of four simulations (fig. S2B). The separation in the weak dimer interface is most pronounced near the unoccupied metal-binding site. To test the influence of the metal ions on the stability of the structure, we initiated three simulations in which Zn^{2+} was removed from the binding site, with the carboxylates in three different protonation states (table S4). In each simulation, the tight dimer interface remained at a

constant, close distance, whereas the loose dimer interfaces separated by up to 5 Å (fig. S2B). The findings suggest that metal binding is important for stabilizing the tetrameric bundle but not the tightly packed dimer. Although these simulations are much shorter than the time scale required for a transport cycle, they are consistent with the intended design of loose and tight interfaces, each interface with distinct roles in facilitating the positioning of side chains and providing a dynamic waterlike path for ion motion through the center of the transporter.

We used a battery of techniques to define the structural and dynamic characteristics of Rocker. The binding of metal ions and oligomerization was studied in micelles by using analytical ultracentrifugation (AUC) and solution nuclear magnetic resonance (NMR). The structure of the Zn^{2+} -free state was determined at high resolution by x-ray crystallography of Rocker solubilized in both micelles and mono-olein lipidic cubic phase. Finally, the oligomeric state, topology, and Zn^{2+} binding were determined in phospholipid bilayers by solid-state NMR (SSNMR).

AUC showed that Rocker forms tetramers in a Zn^{2+} -dependent manner in dodecylphosphocholine (DPC) micelles. Equilibrium sedimentation curves were well described by an equilibrium between a

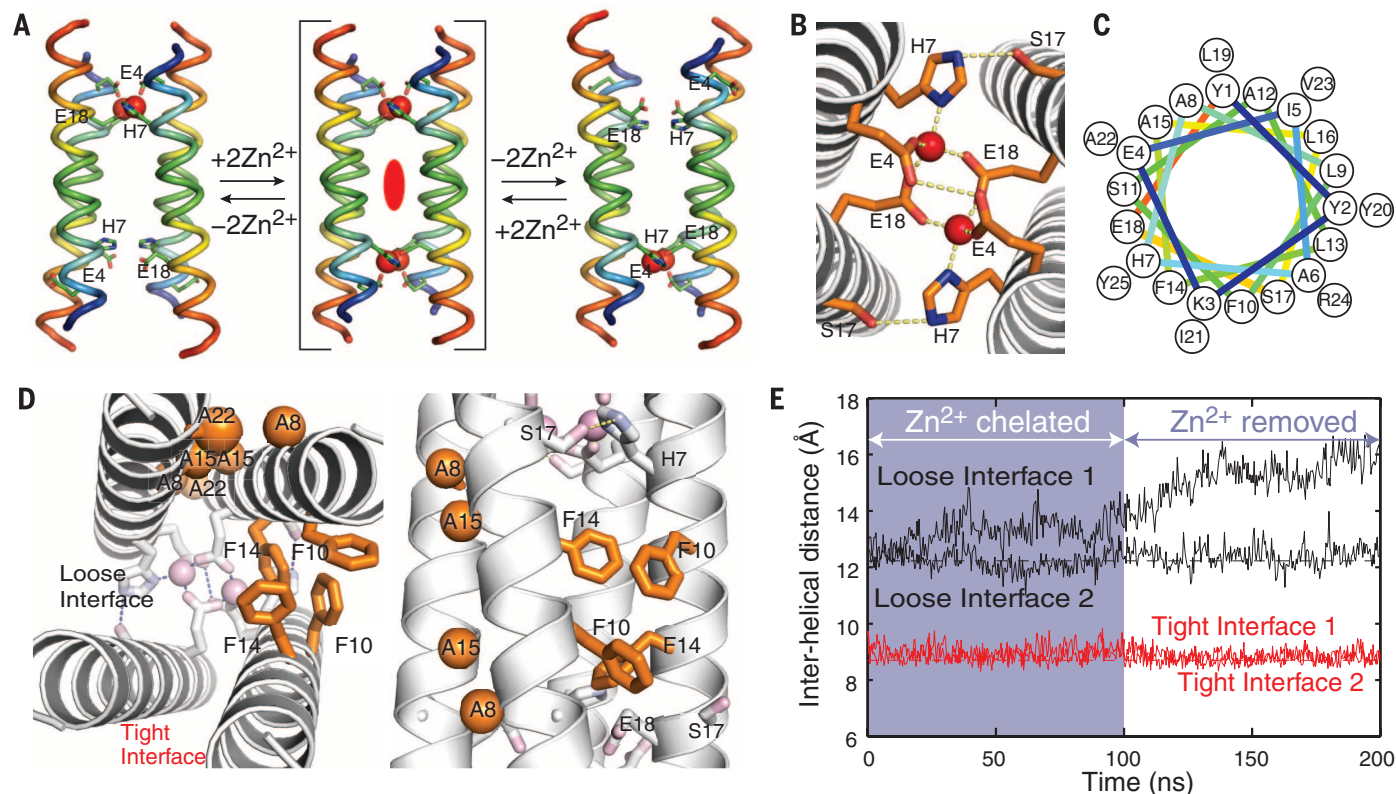


Fig. 1. Computational design and molecular dynamics simulations of Rocker. (A) Schematic of the goal of obtaining conformational exchange between two oppositely oriented symmetry-frustrated states without being trapped in a symmetric state with both sites simultaneously occupied. (B) Metal site consists of a set of ExxH motifs and a single Glu residue from each of the tight dimers. (C) Helical-wheel diagram of Rocker peptide. (D) The re-

packing algorithm placed Ala residues at the tight interface and Phe residues at the loose interface. Empty metal site on the left is omitted for clarity. (E) MD simulation of the design model with two Zn^{2+} ions placed at one metal site show stable interhelical distances for both tight and loose interfaces. Continuing the simulation after removing the Zn^{2+} ions maintained the tight interfaces, but resulted in an increased interhelical distance at the loose interface.

tight dimer and a tetramer (fig. S3). Tetramerization is dominant only at a peptide-to-detergent ratio of 1:200 or higher in this medium, but the addition of excess Zn^{2+} shifted the equilibrium toward the tetrameric state at lower peptide/detergent ratios (supplementary material).

We crystallized Zn^{2+} -free Rocker from micelles, as well as the lipidic cubic phase, in a total of three nonisomorphous space groups and solved structures using data that extended between 2.7 and 2.8 Å (Fig. 2). Only the non- Zn^{2+} form of the protein has crystallized to date. The crystallographic structures solved by molecular replacement show a dimer formed by two tightly packed helices (Fig. 2, A and B). The conformations of the dimer in the three structures are nearly identical (C α RMSDs between 0.60 and 0.84 Å), despite differences in crystal packing. The dimers are composed of straight α helices that interact along the tight interface with tight interdigitation of the small methyl groups of the alanine residues, as in the design. The His and Glu ligands are positioned with the potential to bind metals with a change in rotameric state (Fig. 2, B and C). The observed structure of the dimer is in good agreement with the designed tight dimer (C α RMSD ranges from 2.3 to 2.6 Å). We attribute small deviations from the design to the lack of metal-ligand interactions in the experimental structure. Indeed, in the MD simulations of the Zn^{2+} -free structure, the dimers move 0.8 Å closer to the x-ray structure than the original design (fig. S2C).

The binding stoichiometry for Zn^{2+} was confirmed in solution by titrating Rocker with Zn^{2+} ions in DPC micelles under conditions where it is predominantly tetrameric (peptide/detergent ratio = 1:100). Addition of Zn^{2+} resulted in a decrease in the intensities of aromatic resonances (including the chelating His residue) and an increase in a new set of peaks in the solution NMR spectra (Fig. 3A). The titration plateaus at two Zn^{2+} ions/tetramer. Two sets of peaks in the spectrum indicate that the rate of dissociation and rebinding of Zn^{2+} to the side chains is slower than ~10 ms. Beyond two equivalents, additional shifts are observed, but the change with respect to the Zn^{2+} concentration is more gradual and indicative of much weaker association of the metal ions with a second binding site. This behavior is consistent with the design, which anticipates negative cooperativity between the two sets of di- Zn^{2+} -binding sites.

Previous work with homo-tetrameric peptides shows that they are much more stable in phospholipid bilayers than DPC micelles (32, 33), so we turned to SSNMR to determine the structure and conformational dynamics of Rocker in phospholipid bilayers. One-dimensional (1D) ^{13}C cross-polarization (CP) magic angle-spinning (MAS) spectra of apo-Rocker in dimyristoylphosphatidylcholine (DMPC) bilayers from -40° to 40°C showed a single set of relatively narrow peaks (0.9 ppm C α line widths) per carbon for four ^{13}C -labeled residues (Fig. 3B). The backbone ^{13}C chemical shifts reflect helical structure (fig. S4C). The line widths broaden with increasing temper-

ature, which indicates that the peptide becomes mobile in the liquid-crystalline phase of the membrane. Dipolar coupling measurements yield ^{13}C -H order parameters of 0.84/0.84, 0.73/0.77, and 0.55/0.75 for C α at Ala8/Ala22, L19, and I5 in apo/ Zn^{2+} -bound states, respectively (fig. S4B), and all dephasing curves are asymmetric, which indicates global microsecond-time scale motion in both the apo and Zn^{2+} bound peptides (34, 35). The addition of Zn^{2+} ions had a strong influence on the SSNMR spectra of Rocker. In contrast to the apo sample, the Zn^{2+} -bound sample lacks the L19 α -I5 δ peak and has weaker A8/22-I5 and A8/22-L19 cross peaks, which indicate that Zn^{2+} binding loosens interhelical packing (Fig. 3C). Ion binding also caused noticeable chemical shift changes, which are particularly pronounced at A8 and A22 (Fig. 3C and fig. S4, D and E). Taken together, these results show a single conformation with substantial dynamics on the microsecond time scale and significant Zn^{2+} -dependent structural perturbations.

To determine the oligomeric structure in DMPC bilayers, we conducted a ^{19}F spin diffusion experiment, Centerband-Only Detection of Exchange (CODEX), on Rocker singly labeled with *para*- ^{19}F -phenylalanine (^{19}F -Phe) at position 14 (36, 37). Distance-dependent interhelical ^{19}F - ^{19}F dipolar coupling is manifested as a decay of a ^{19}F spin echo with increasing mixing time. The equilibrium value of the spin echo intensity is $1/n$, where n is the oligomer number of the assembly. The measured ^{19}F CODEX intensities (Fig. 3D and fig. S5) decayed to <0.4, which indicates that the assembly is larger than a dimer. The nonplanar quadrilaterals formed by ^{19}F -Phe modeled in the anticipated tetramer superposed with the crystallographic dimers resulted in excellent fits of the measured decay (Fig.

3D and fig. S5). A C $_4$ symmetrical array of ^{19}F nuclei gave an unsatisfactory fit, which ruled out a square planar model (fig. S5E). These results corroborate an antiparallel tetramer.

Conclusive support for an antiparallel tetramer was obtained from 2D ^{13}C correlation spectra. At a mixing time of 500 ms, cross peaks between L19 and I5 side chains were observed (Fig. 3C). These residues are found along the tight dimer interface, and, together with the ^{19}F -Phe interaction along the loose interface, confirm antiparallel association along both interfaces in bilayers.

Finally, to determine whether the designed peptide is embedded in the lipid bilayer, we measured 2D NMR spectra that correlate the lipid and water ^1H signals with the peptide ^{13}C chemical shifts (38, 39). Lipid-peptide cross peaks were detected at short mixing times (< 36 ms) (fig. S4F), which indicates that the peptide is well inserted into the hydrophobic part of the membrane. The fast spin-diffusion buildup curves for both the lipid and water ^1H peaks (fig. S4G) indicate that the Rocker helical bundle spans the membrane and is well hydrated, likely by both the membrane-surface water and intrachannel water.

Two important characteristics of natural transporters are their substrate-selectivity and their ability to use one substrate's concentration gradient to drive the uphill transport of a second substrate. To test how Rocker meets these criteria, we conducted flux assays in large unilamellar vesicles (LUVs) in which we monitored Zn^{2+} and H^+ influx and efflux using fluorescent indicators (Fig. 4A and supplementary methods).

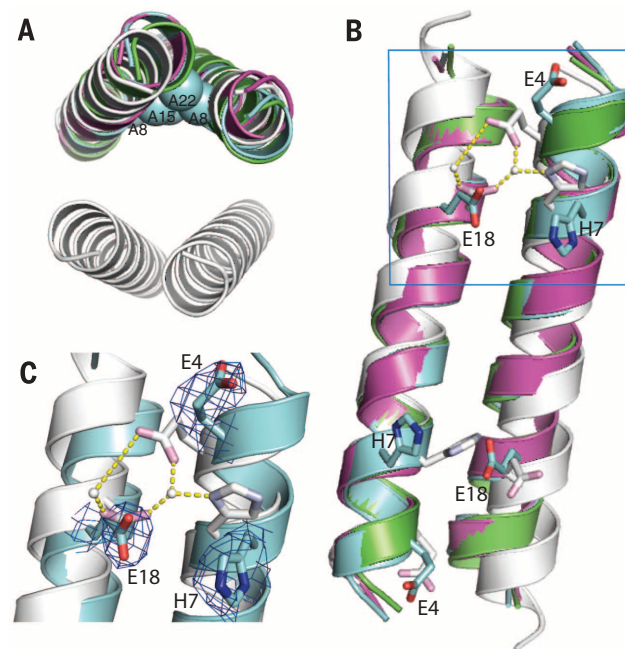
To test ion selectivity, we measured Rocker's ability to facilitate inward metal ion transport down a

Fig. 2. Structure of

Rocker. (A) Axial view of the x-ray crystal structures from three different packing environments (green, cyan, and magenta for space groups of increasing symmetries, P $_4$ 3 $_2$ 2 $_1$, I4 $_1$ 22, and I2 $_1$ 3, respectively) superimposed on the tight dimeric subunit of the design model (white), with the Ala residues (spheres from the cyan structure with highest resolution of 2.7 Å) forming the tight interface as anticipated.

(B) Metal-binding residues (sticks) from the crystal structures can chelate with a change in rotamers without encountering any unfavorable steric interactions within the dimer.

(C) A close-up of the metal site with $2mF_{\text{obs}} - DF_{\text{calc}}$ map contoured at 1.0 σ for the 2.7 Å-resolution structure.



concentration gradient. As expected, Rocker conducts first-row transition metal ions Zn^{2+} and Co^{2+} but not the hard divalent ion, Ca^{2+} , which prefers higher-valent oxygen-rich ligand environ-

ments (Fig. 4B and fig. S6, A and B). Moreover, Ca^{2+} does not influence Zn^{2+} efflux (fig. S6A), and substitution of the Glu ligands to Gln greatly impairs Zn^{2+} efflux (Fig. 4B).

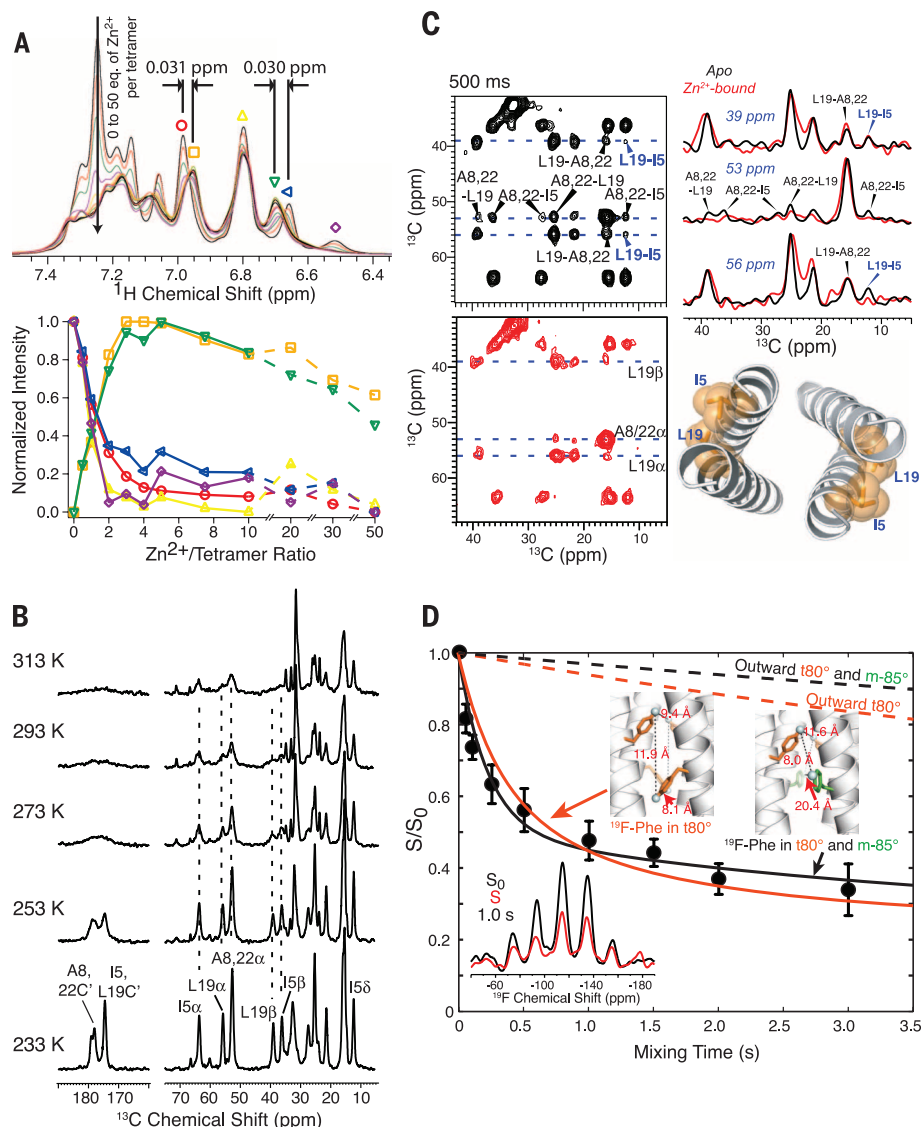


Fig. 3. Evidence for Zn^{2+} binding and tetramerization of Rocker in micelles and lipid bilayers.

(A) ^1H -NMR of Rocker in D_2O and deuterated DPC (at 900 MHz ^1H field) shows significant changes to the side-chain chemical shifts as Zn^{2+} is titrated into the solution. The changes level off when Zn^{2+} reaches two equivalents per tetramer, which indicates the expected binding stoichiometry. (B) 1D ^{13}C CP-MAS spectra of apo Rocker in DMPC bilayers from 233 K to 313 K show invariant peak positions across a wide temperature range, which indicates single species with conformational dynamics in bilayers. (C) 2D ^{13}C - ^{13}C 2D correlation spectra of apo and Zn^{2+} bound Rocker with 500-ms mixing. Relevant 1D cross sections are plotted to compare cross-peak intensities. L19-I5 cross peaks (blue annotations) are observed, indicating antiparallel packing. Compared with the apo sample, the Zn^{2+} -bound sample lacks the L19 α -I5 δ peak in the 56-ppm cross section and has much weaker A8/22-I5 and A8/22-L19 cross peaks, which indicate that Zn^{2+} binding loosens interhelical packing. The proximal L19 and I5 are shown on a structural model of Rocker. (D) ^{19}F CODEX data of DMPC-bound Rocker with *para*- ^{19}F -Phe14 at 220 K and 8 kHz MAS (error bar, SD propagated from signal-to-noise). The CODEX intensity decays to $1/n$ of 0.34, where n is the oligomer number; this indicates that the peptide assembles into a species larger than dimers. The CODEX decay is well fit (solid lines) using ^{19}F - ^{19}F distances found in inward-facing rotamers of Phe14 in an antiparallel tetramer, consistent with the crystal structures. The data rule out outward-facing orientations of Phe14 (dashed lines), which suggests that Glu4 and Glu18 face the pore.

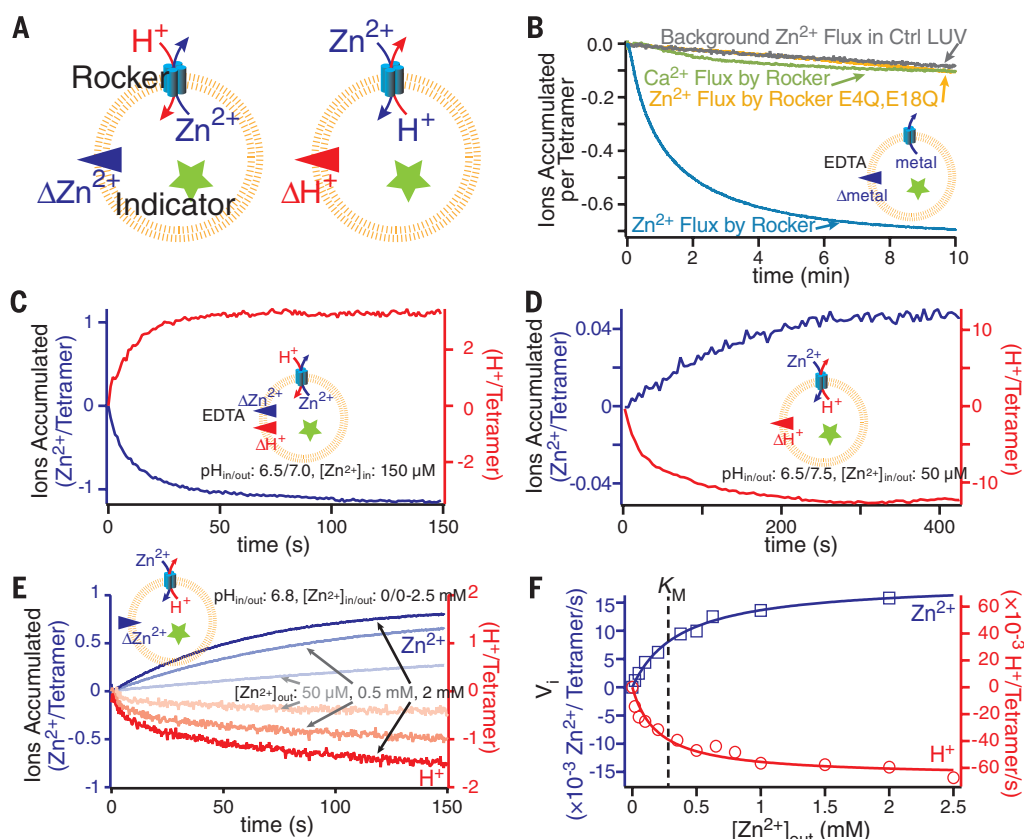
The rate of Zn^{2+} transport into vesicles follows Michaelis-Menten kinetics ($K_M = 280 \pm 90 \mu\text{M}$; $V_{\text{max}} = 1.1 \pm 0.1 \text{ min}^{-1}$). For comparison, the K_M and rate of transport in the natural ZitB Zn^{2+} transporter are $105 \mu\text{M}$ and 142 min^{-1} , respectively (22, 40). From the Irving-Williams (41) series (which approximately predicts the relative affinities of first-row transition metal ions for a given site) and the ligand environment of Rocker, we expected that Co^{2+} should bind less tightly, which could lead to a higher K_M . Also, if ligand exchange is rate-limiting as suggested by the solution NMR spectra (Fig. 3A), the weaker binding affinity might be accompanied by an increase in V_{max} . Indeed, K_M for Co^{2+} increases to $1400 \pm 200 \mu\text{M}$ and V_{max} increases to $470 \pm 40 \text{ min}^{-1}$ (Fig. 4, E and F, and fig. S6B).

We next tested Rocker's ability to cotransport Zn^{2+} and H^+ . Rocker is able to use a Zn^{2+} gradient to drive the transport of protons uphill and into vesicles (Fig. 4C). Cotransport was measured by tracking both the downhill Zn^{2+} flux and the resulting H^+ flux as a function of the internal Zn^{2+} concentration. The rate of proton influx tracks with the rate of Zn^{2+} efflux, with a common K_M of $280 \mu\text{M}$, which indicates that H^+ and Zn^{2+} transport are linked (Fig. 4, E and F). The proton- Zn^{2+} stoichiometry computed from the initial rates is three to four protons per Zn^{2+} . This finding is consistent with the guiding hypothesis that the binding of Zn^{2+} occurs with the concomitant displacement of protons. Moreover, Rocker functioned in a Zn^{2+} -proton antiport assay in the presence of a membrane permeable ion, NO_3^- , which eliminates the accumulation of electrical potentials (fig. S6C).

We also determined that a proton gradient is able to cause accumulation of Zn^{2+} up its own concentration gradient, when the initial concentrations of Zn^{2+} were identical on both sides of the vesicle. However, the efficiency of the process is far less than for the converse: Over 100 protons are transported for every Zn^{2+} transported. This finding suggests that there might be two competing mechanisms: The predominant one is diffusion of protons through Zn^{2+} -bound Rocker; the less-frequent path involves proton binding at the Zn^{2+} site and expulsion of a zinc ion. A possible explanation for the different behavior for Zn^{2+} compared with proton gradients is that the highly polar divalent Zn^{2+} is unable to diffuse through Rocker without binding to the coordination sites, which in turn would require deprotonation of the ligands. By contrast, protons could move along proton wires through the pore without requiring dissociation of the divalent metal ion. A possible reason for the proton-leakiness is the lack of a proton-impermeable hydrophobic gate, which appears to be important for tight coupling in much larger and highly evolved proton-dependent transporters. Future designs will aim to achieve a transporter function similar to that of native proteins. Nevertheless, these findings, along with the very simple structure of Rocker, provide support for the view that

Fig. 4. Antiporter-like function of Rocker.

(A) Examples of liposome flux assays using fluorescent indicators for characterizing the cotransportation function are illustrated. (B) Ion selectivity in Rocker is shown via a Zn^{2+} efflux assay. Rocker can specifically transport Zn^{2+} (blue) but not Ca^{2+} (green), at a level higher than passive leakage (gray). Mutating the first-shell ligands via E4/E18-to-Q substitutions abrogates Zn^{2+} transport (gold). (C) Rocker-mediated, outward $[\text{Zn}^{2+}]$ gradient-driven proton-antiport against an outward pH gradient is shown by measuring net inward proton flux (red, right axis) and the outward Zn^{2+} flux (blue, left axis). (D) Rocker-mediated, H^+ -driven Zn^{2+} antiport under symmetrical Zn^{2+} concentration is shown using both the outward proton flux (red, right axis) and the inward Zn^{2+} flux (blue, left). (E) Representative traces show the dependence of initial rates of transport on the exterior Zn^{2+} concentration. (F) The initial rates of transport of Zn^{2+} and H^+ from panel (E) increase with increasing exterior Zn^{2+} concentration, following Michaelis-Menten kinetics with a K_M of $\sim 280 \mu\text{M}$. (Error values in text are SD propagated from curve fitting.)



transporters may have evolved from very simple pseudo-symmetric precursors (42).

The structural and functional characterization of Rocker indicates that the design community has now passed an important milestone; the first high-resolution structure of a designed membrane protein has been determined through a combination of x-ray crystallography and NMR. Our design strategy combined the strengths of traditional computational design techniques with biophysically motivated conformational ensemble-based reasoning. Although Rocker's activity falls short of natural transporters, it remains significant that function was achieved without high-throughput screening or directed evolution—and bodes well for future investigations in which computational design is combined with these powerful experimental methods.

REFERENCES AND NOTES

- N. Koga et al., *Nature* **491**, 222–227 (2012).
- M. L. Zastrow, V. L. Pecoraro, *Coord. Chem. Rev.* **257**, 2565–2588 (2013).
- C. E. Tinberg et al., *Nature* **501**, 212–216 (2013).
- A. J. Reig et al., *Nat. Chem.* **4**, 900–906 (2012).
- M. L. Zastrow, A. F. A. Peacock, J. A. Stuckey, V. L. Pecoraro, *Nat. Chem.* **4**, 118–123 (2012).
- M. L. Zastrow, V. L. Pecoraro, *J. Am. Chem. Soc.* **135**, 5895–5903 (2013).
- G. Kiss, N. Çelebi-Ölçüm, R. Moretti, D. Baker, K. N. Houk, *Angew. Chem. Int. Ed. Engl.* **52**, 5700–5725 (2013).
- I. V. Korendovych et al., *J. Am. Chem. Soc.* **132**, 15516–15518 (2010).
- J. M. Perez-Aguilar, J. G. Saven, *Structure* **20**, 5–14 (2012).
- S. Radestock, L. R. Forrest, *J. Mol. Biol.* **407**, 698–715 (2011).
- O. Jardetzky, *Nature* **211**, 969–970 (1966).
- P. Mitchell, *Nature* **180**, 134–136 (1957).
- E. A. Morrison et al., *Nature* **481**, 45–50 (2012).
- W. F. DeGrado, Z. R. Wasserman, J. D. Lear, *Science* **243**, 622–628 (1989).
- J. D. Lear, Z. R. Wasserman, W. F. DeGrado, *Science* **240**, 1177–1181 (1988).
- M. Hong, W. F. DeGrado, *Protein Sci.* **21**, 1620–1633 (2012).
- A. Pasternak, J. Kaplan, J. D. Lear, W. F. DeGrado, *Protein Sci.* **10**, 958–969 (2001).
- F. H. C. Crick, *Acta Crystallogr.* **6**, 685–689 (1953).
- G. Grigoryan, W. F. DeGrado, *J. Mol. Biol.* **405**, 1079–1100 (2011).
- C. M. Summa, A. Lombardi, M. Lewis, W. F. DeGrado, *Curr. Opin. Struct. Biol.* **9**, 500–508 (1999).
- A. Lombardi et al., *Proc. Natl. Acad. Sci. U.S.A.* **97**, 6298–6305 (2000).
- Y. Chao, D. Fu, *J. Biol. Chem.* **279**, 17173–17180 (2004).
- G. Grigoryan, A. W. Reinke, A. E. Keating, *Nature* **458**, 859–864 (2009).
- G. Grigoryan, *J. Comput. Chem.* **34**, 2726–2741 (2013).
- F. Lazaridis, *Proteins* **52**, 176–192 (2003).
- A. Senes et al., *J. Mol. Biol.* **366**, 436–448 (2007).
- C. A. Schramm et al., *Structure* **20**, 924–935 (2012).
- C. M. Summa, M. M. Rosenblatt, J. K. Hong, J. D. Lear, W. F. DeGrado, *J. Mol. Biol.* **321**, 923–938 (2002).
- Y. Zhang, D. W. Kulp, J. D. Lear, W. F. DeGrado, *J. Am. Chem. Soc.* **131**, 11341–11343 (2009).
- S. Unterreithmeier et al., *J. Mol. Biol.* **374**, 705–718 (2007).
- D. T. Moore, B. W. Berger, W. F. DeGrado, *Structure* **16**, 991–1001 (2008).
- L. Cristian, J. D. Lear, W. F. DeGrado, *Proc. Natl. Acad. Sci. U.S.A.* **100**, 14772–14777 (2003).
- K. R. MacKenzie, K. G. Fleming, *Curr. Opin. Struct. Biol.* **18**, 412–419 (2008).
- E. R. deAzevedo et al., *J. Chem. Phys.* **128**, 104505 (2008).
- M. F. Cobo, A. Achilles, D. Reichert, E. R. deAzevedo, K. Saalwächter, *J. Magn. Reson.* **221**, 85–96 (2012).
- E. R. deAzevedo, W.-G. Hu, T. J. Bonagamba, K. Schmidt-Rohr, *J. Am. Chem. Soc.* **121**, 8411–8412 (1999).
- J. J. Buffy, A. J. Waring, M. Hong, *J. Am. Chem. Soc.* **127**, 4477–4483 (2005).
- D. Huster, X. Yao, M. Hong, *J. Am. Chem. Soc.* **124**, 874–883 (2002).
- M. Hong, *Structure* **14**, 1731–1740 (2006).
- Y. Chao, D. Fu, *J. Biol. Chem.* **279**, 12043–12050 (2004).
- R. J. P. W. H. Irving, R. J. P. Williams, *J. Chem. Soc.* 3192–3210 (1953).
- M. Rapp, E. Granseth, S. Seppälä, G. von Heijne, *Nat. Struct. Mol. Biol.* **13**, 112–116 (2006).

ACKNOWLEDGMENTS

Authors acknowledge J. Holton and G. Meigs at The Lawrence Berkeley National Laboratory Advanced Light Source 8.3.1; K. Rajashankar, S. Banerjee, and I. Kourinov at Argonne National Laboratory Advanced Photon Source Northeastern Collaborative Access Team for technical support in x-ray data collection; and O. P. Choudhary and J. L. Adelman at the University of Pittsburgh for helpful discussions regarding the simulations. Simulations were carried out in part with XSEDE resources through grant MCB080011 to M.G. This work was supported by NIH F32 GM096727 to N.H.J., The Jane Coffin Childs postdoctoral fellowship to MPB; Ramalingaswami Fellowship from the Department of Biotechnology, India, to R.A.; NIH RO1 GM089740 to M.G.; NIH RO1 GM088204 to M.H.; Alfred P. Sloan Foundation Research Fellowship to G.G.; NIH RO1 GM054616 to W.F.D.; and NSF DMR 1120901 (W.F.D.). The coordinates for the x-ray structures with space groups, P4₃2₁2, I4₂2, and I2₃, are deposited in the Protein Data Bank (PDB) with accession codes, 4P6J, 4P6K, and 4P6L, respectively. The SSNMR structure is deposited in PDB with an accession code, 2MUZ.

SUPPLEMENTARY MATERIALS

www.sciencemag.org/content/346/6216/1520/suppl/DC1
Materials and Methods
Figs. S1 to S6
Tables S1 to S5
References (43–67)

12 September 2014; accepted 21 November 2014
10.1126/science.1261172

PROTEIN DESIGN

A designed supramolecular protein assembly with in vivo enzymatic activity

Woon Ju Song and F. Akif Tezcan*

The generation of new enzymatic activities has mainly relied on repurposing the interiors of preexisting protein folds because of the challenge in designing functional, three-dimensional protein structures from first principles. Here we report an artificial metallo- β -lactamase, constructed via the self-assembly of a structurally and functionally unrelated, monomeric redox protein into a tetrameric assembly that possesses catalytic zinc sites in its interfaces. The designed metallo- β -lactamase is functional in the *Escherichia coli* periplasm and enables the bacteria to survive treatment with ampicillin. In vivo screening of libraries has yielded a variant that displays a catalytic proficiency $[(k_{\text{cat}}/K_m)/k_{\text{uncat}}]$ for ampicillin hydrolysis of 2.3×10^6 and features the emergence of a highly mobile loop near the active site, a key component of natural β -lactamases to enable substrate interactions.

Design and engineering of enzymes not only test our understanding of protein folding and catalysis but can also provide structures and functions that have not been invented by natural evolution (1, 2). Arguably, the rate-limiting step in both the evolution and rational design of enzymes is the de novo creation of three-dimensional protein architectures through extensive non-covalent interactions. Nature often uses pre-existing protein folds, whose active sites can be repurposed for alternative chemistries, as evidenced by the extraordinary functional diversity

of superfamilies such as the TIM barrel proteins (3) and α/β hydrolases (4). Similarly, most enzyme design and engineering efforts have had success by using the active sites of preexisting protein structures (5–11) or by exploiting well-established sequence-folding patterns of α -helical bundles (12, 13) for creating new enzymatic functions.

An alternative route is the construction of catalytic sites in newly formed interfaces between proteins or stably folded domains; indeed, interfacial active sites are frequent among natural enzymes (14). While not benefiting from a preformed scaffold to support an active site, this route is particularly conducive to the introduction of new chemistries, as it is not constrained by the conserved internal structures

of evolved protein folds. The challenge here is that the generation of protein interfaces also requires extensive noncovalent interactions. We (15) and others (16) have shown that construction of new protein interfaces can be aided by coordination by metal ions, which provide large binding energies and have intrinsic chemical properties that can produce nascent enzymatic functions (17). Kuhlman *et al.* recently reported a designed protein dimer stabilized by interfacial Zn ions that catalyzed the hydrolysis of activated esters in vitro (18). Nevertheless, the construction of a novel protein fold or quaternary architecture that displays in vivo enzymatic activity has remained an unmet goal, which would represent an important connection between protein design and synthetic biology (19).

Toward this end, we report an artificial, in vivo active metallo- β -lactamase with interfacial catalytic sites, constructed through the metal-directed self-assembly of a monomeric protein. Rapid evolution of β -lactamase activity is the primary mechanism of antibiotic resistance by bacteria (20) and constitutes an appealing and challenging test case for rational protein design and in-lab evolution. The core catalytic motif of metallo- β -lactamases (a nucleophilic, mono- or di-Zn^{II}-OH₂/OH[−] species) (21) is, in principle, within facile reach for engineering. Moreover, from a practical viewpoint, β -lactamase activity could be readily screenable in bacterial cells, as it is directly linked to their survival.

Previously, Benkovic *et al.* demonstrated that glyoxalase II could be converted into a metallo- β -lactamase by exchange and engineering of active-site loops, enabled by both enzymes sharing a $\alpha\beta/\beta\alpha$ metallohydrolase fold (5). To assemble an artificial metallo- β -lactamase with a different architecture, we used as a building block cytochrome cb₅₆₂ (cyt cb₅₆₂) (22), a

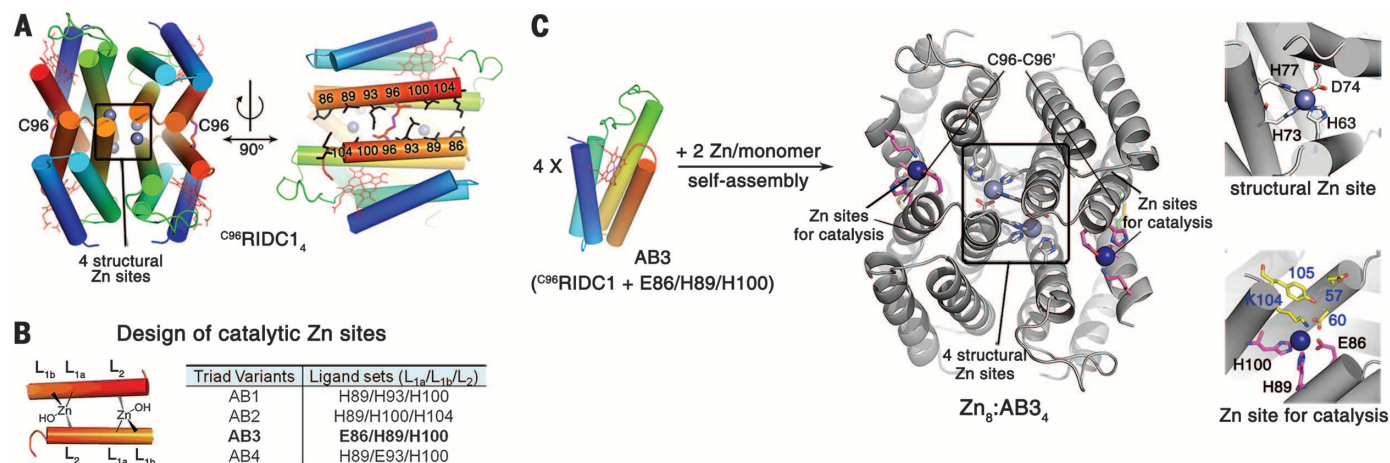


Fig. 1. Structure-guided design of Zn₈:AB3₄. (A) Structure of the tetrameric Zn complex of the self-assembling cyt cb₅₆₂ variant C⁹⁶RIDC1₄ viewed along one of the three twofold rotational symmetry axes. The four α -helical bundle components are rainbow-colored, red to blue from the C to the N terminus. Residues in the disulfide-cross-linked interfaces used for constructing three-coordinate Zn-anchoring motifs are shown as black sticks. (B) List of variants containing triads of Zn-binding residues studied in this work. (C) Crystal structure of Zn₈:AB3₄.

four-helix-bundle redox protein that bears no structural, functional, or sequence homology to any metallo- β -lactamase or hydrolytic enzyme. We previously showed that cyt cb₅₆₂ could be converted through a small number of surface mutations into a variant (^{C96}RIDC1) that self-assembles into a *D*₂ symmetric tetramer through Zn^{II} coordination and a combination of hydrophobic interactions and disulfide bonds (23, 24) (Fig. 1A). A pair of interfaces in this complex (Zn₄:^{C96}RIDC1₄) are cross-linked by Cys⁹⁶-Cys⁹⁶ disulfide bonds. These interfaces present several triads of amino acid positions

that can be used to build the triangular base of a tetrahedral Zn^{II}-OH₂/OH⁻ coordination motif as a hydrolytic site (Fig. 1, A and B, and table S1). Accordingly, we prepared variants of the ^{C96}RIDC1 monomer (AB1-AB4) with combinations of three coordinating residues (His and/or Glu) appropriately placed such that they would self-assemble into tetramers that possess four structural Zn sites in their interiors and four potentially catalytic Zn sites in their interfaces (Fig. 1C).

We examined the Zn binding capacities and oligomerization properties of the AB variants

by inductively coupled plasma optical emission spectroscopy (ICP-OES) and analytical ultracentrifugation (AUC). All variants except AB2 bound two equivalents of Zn^{II} ions per monomer, equaling eight Zn ions per tetramer, as designed (fig. S1A). Among these, AB3 was the only construct that displayed greater than 90% abundance for a tetrameric species (sedimentation coefficient = 4.5S, fig. S1B) upon Zn binding.

The crystal structure of the Zn complex of AB3 (Zn₈:AB3₄), determined at 2.5 Å resolution (Fig. 1C and table S3), confirmed the

Table 1. Summary of hydrolytic activities of the Zn complexes of AB3 variants. The hydrolytic activities were measured in 0.1 M sodium borate buffer (pH 9).

| Variants | <i>p</i> -Nitrophenyl acetate | | | Ampicillin | | | | Substrate selectivity (<i>k</i> _{cat} / <i>K</i> _M , ampicillin)/ (<i>k</i> _{cat} / <i>K</i> _M , pNPA) [‡] |
|--------------|-------------------------------|---|---|---|---|---|--|---|
| | p <i>K</i> _a | <i>k</i> _{cat} (s ⁻¹) | <i>k</i> _{cat} / <i>K</i> _M or <i>k</i> ₂ [*] (s ⁻¹ M ⁻¹) | <i>k</i> _{cat} (min ⁻¹) | <i>k</i> _{cat} / <i>K</i> _M or <i>k</i> ₂ [*] (min ⁻¹ M ⁻¹) | Rate enhancement <i>k</i> _{cat} / <i>k</i> _{uncat} [†] | Catalytic proficiency (<i>k</i> _{cat} / <i>K</i> _M)/ <i>k</i> _{uncat} ^{†‡} | |
| A104AB3 | 9.0(2) | 0.027(8) | 32(8) | ND [§] | 115(3) [*] | ND [§] | 0.7(1) × 10 ⁶ | 0.06(2) |
| A104/G57AB3 | 8.9(2) | 0.019(4) | 29(6) | 3.5(8) | 350(90) | 2.3(6) × 10 ⁴ | 2.3(0.7) × 10 ⁶ | 0.20(4) |
| A104/T105AB3 | 9.2(1) | ND [§] | 6.7(7) [*] | ND [§] | 100(7) [*] | ND [§] | 0.7(1) × 10 ⁶ | 0.25(3) |

^{*}In cases where substrate saturation behavior was not observed, a linear fit was used to obtain a second-order rate constant (*k*₂) instead of *k*_{cat}/*K*_M. [†]The background (uncatalyzed) rate constant for ampicillin hydrolysis was measured to be *k*_{uncat} = 1.5(2) × 10⁻⁴ min⁻¹. [‡]The substrate selectivity was obtained by dividing *k*_{cat}/*K*_M or *k*₂ for ampicillin hydrolysis by that for *p*-nitrophenyl acetate. [§]Cannot be determined owing to lack of substrate saturation behavior.

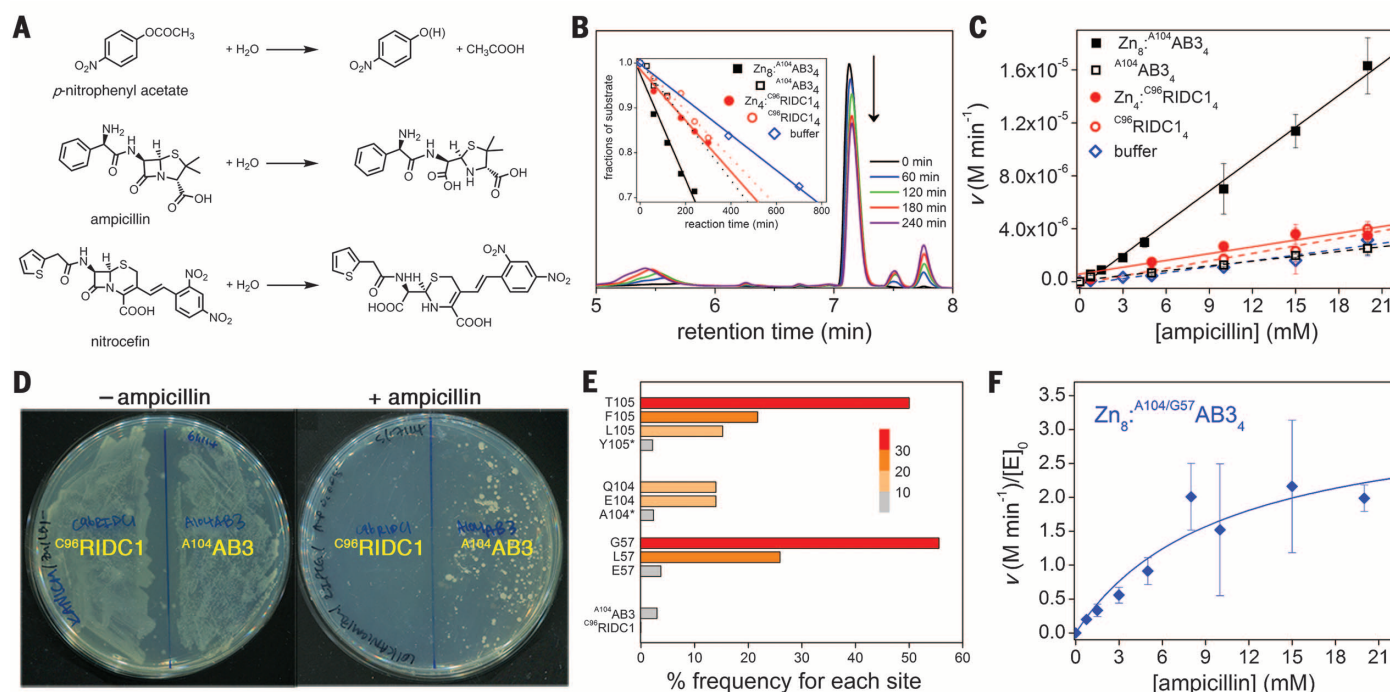


Fig. 2. Investigations of in vitro and in vivo artificial β -lactamase activity. (A) Hydrolytic reactions studied in this work. (B) A representative set of time-dependent HPLC traces, displaying the consumption of ampicillin through the hydrolytic activity of Zn₈:A104AB3₄. (Inset) The plot of fraction of substrate versus reaction time for A104AB3 and ^{C96}RIDC1 in the presence (closed squares or circles) and absence of Zn (open squares or circles). (C) Ampicillin hydrolysis activity of Zn₈:A104AB3₄, metal-free A104AB3₄, Zn₄:^{C96}RIDC1₄, and metal-free ^{C96}RIDC1₄ at var-

ious substrate concentrations. (D) Representative LB/agar plates in the absence (left) and presence (right) of ampicillin (0.8 mg/liter). The left and right halves of each plate are streaked with cells expressing ^{C96}RIDC1 and A104AB3, respectively. (E) In vivo survival frequency (percentage of all colonies) of A104AB3 active-site variants subjected to saturation mutagenesis. Original residues are marked with asterisks. (F) Michaelis-Menten kinetics of Zn₈:A104/G57AB3₄ for ampicillin hydrolysis. Data are mean \pm SD.

formation of the desired tetrameric architecture and the two types of Zn coordination geometries. The overall structure of the tetramer is nearly identical to that of the parent $\text{Zn}_4\text{:}^{\text{C96}}\text{RIDC1}_4$ (fig. S2A). As designed, each of the four peripheral Zn^{II} ions is anchored by Glu⁸⁶ and His⁸⁹ side chains from one monomer and His¹⁰⁰ from another. Unexpectedly, the Lys¹⁰⁴ amine group completes the tetrahedral coordination geometry (fig. S2B).

Hydrolytic activity of $\text{Zn}_8\text{:AB3}_4$ was first evaluated with the chromogenic substrate *p*-nitrophenyl acetate (pNPA, Fig. 2A). $\text{Zn}_8\text{:AB3}_4$ displayed no appreciable activity, because the Lys¹⁰⁴ side chain prevents the formation of the $\text{Zn}^{\text{II}}\text{-OH/OH}_2$ species. However, the K104A mutation yielded a catalytically competent variant, $\text{Zn}_8\text{:}^{\text{A104}}\text{AB3}$ (fig. S3 and Table 1), which we used for subsequent investigations. Hydrolysis rates by $\text{Zn}_8\text{:}^{\text{A104}}\text{AB3}_4$ were measured at pH 9 at different pNPA concentrations, which revealed a Michaelis-Menten behavior with associated kinetic parameters, $k_{\text{cat}} = 0.027(8) \text{ s}^{-1}$ and $k_{\text{cat}}/K_{\text{M}} = 32(8) \text{ s}^{-1} \text{ M}^{-1}$ (fig. S3A). From the plot of $k_{\text{cat}}/K_{\text{M}}$ versus pH, the pK_{a} value of Zn^{II} -bound H_2O was estimated to be 9.0(2) (fig. S3B). At pH = 10, where the tetrameric assembly is largely intact, k_{cat} and $k_{\text{cat}}/K_{\text{M}}$ for pNPA hydrolysis were 0.20(5) s^{-1} and 120(20) $\text{s}^{-1} \text{ M}^{-1}$. These values represent a considerably higher hydrolytic activity relative to synthetic Zn complexes (25) and are in the middle of the range for the most active designed esterases (table S4) (13, 18, 26).

We examined the activity of $\text{Zn}_8\text{:}^{\text{A104}}\text{AB3}_4$ for the hydrolysis of ampicillin, a β -lactam antibiotic (Fig. 2A). This was accomplished by the high-performance liquid chromatography (HPLC) analysis of the reaction mixture and the characterization of the hydrolysis product by electrospray ionization mass spectrometry (ESI-MS) and nuclear magnetic resonance (NMR) (fig. S4). $\text{Zn}_8\text{:}^{\text{A104}}\text{AB3}_4$ hydrolyzed ampicillin (Fig. 2B and Table 1) with a

second-order rate constant of $k_2 = 115(3) \text{ min}^{-1} \text{ M}^{-1}$ (or $1.92 \text{ s}^{-1} \text{ M}^{-1}$) at pH 9, but it did not exhibit saturation behavior even at high (20 mM) substrate concentrations, likely due to the lack of appreciable binding interactions with the antibiotic. Ampicillin hydrolysis was considerably slower in the presence of metal-free $\text{C96}\text{RIDC1}_4$, $\text{Zn}_4\text{:}^{\text{C96}}\text{RIDC1}_4$, and metal-free A104AB3_4 , at rates near to those observed in a buffer solution (Fig. 2, B and C).

We next asked whether β -lactamase activity of $\text{Zn}_8\text{:}^{\text{A104}}\text{AB3}_4$ is also operative within *Escherichia coli* cells and endows them with antibiotic resistance. All cyt *cb*₅₆₂ variants possess an N-terminal leader sequence, which allows them to be translocated to and mature in the *E. coli* periplasm (22). We previously showed that the periplasm is conducive to the quantitative formation of disulfide-mediated cyt *cb*₅₆₂ oligomers, which can successfully compete for Zn^{II} binding in that compartment (27). To determine the oligomeric state of A104AB3 in *E. coli* cells, we extracted the periplasmic contents of the cell pellets via osmotic shock. The extracts were immediately treated with excess iodoacetamide to prevent any uncomplexed A104AB3 from oligomerizing via disulfide-bond formation after extraction. Size-exclusion chromatography of the extracts revealed that ~70% of A104AB3 is tetrameric and contained 2.1(2) Zn equivalents per monomer (fig. S5) and negligible levels of other first-row transition metals (Co, Ni, and Cu). Competition titrations of A104AB3 with the metal-binding indicator MagFura2 (fig. S6 and table S5) confirmed the presence of two distinct types of Zn ions (eight total) with corresponding dissociation constants of 6.7(0.5) nM for one set of four ions and 400(190) nM for the other. These values are comparable to those of natural, periplasmic Zn proteins (28) and explain the quantitative Zn loading of the A104AB3 tetramers in cells.

To test *in vivo* β -lactamase activities, we expressed A104AB3 using *kan*^r/*amp*^r-pET20b(+) vector in BL21(DE3) *E. coli* cells, which were grown on agar/Luria-Bertani (LB) plates containing various amounts of ampicillin. As a control, we used the $\text{C96}\text{RIDC1}$ construct, earlier established as having no appreciable β -lactamase activity (Fig. 2, B and C). *E. coli* cells expressing either $\text{C96}\text{RIDC1}$ or A104AB3 grew unimpeded on the ampicillin-free LB/agar plates (Fig. 2D). However, only those expressing A104AB3 survived ampicillin concentrations in the range of 0.8 to 1.1 mg/liter (Fig. 2D), indicating that $\text{Zn}_8\text{:}^{\text{A104}}\text{AB3}_4$ has sufficient activity in living cells to serve as a basis for *in vivo* selection and optimization of catalytic activity.

For the *in vivo* screening of the synthetic construct, we performed saturation mutagenesis (29) of the four individual amino acid positions that surround the peripheral Zn centers (Glu⁵⁷, Asp⁶⁰, Lys¹⁰⁴→Ala, Tyr¹⁰⁵; Fig. 1C) and thus may form a substrate interaction site. For selection, we fixed the ampicillin concentration in the agar/LB plates at ~1.0 mg/liter and used the frequency of colonies that express a certain AB3 point mutant as a readout for *in vivo* activity (Fig. 2E). Strains expressing the Gly⁵⁷ and Thr¹⁰⁵ point mutants were clear winners, each occurring ~20 times as frequently as the parent Glu⁵⁷ and Tyr¹⁰⁵ and about twice as frequently as the second-most-abundant mutants (fig. S8). In contrast, for position 60, the strain with the parent residue (Asp) displayed the highest frequency, and for position 104, no particular mutant dominated over others. Several other factors besides β -lactamase activity of the mutants may affect their survival frequency, such as codon usage, expression levels, and proper assembly. We therefore individually prepared the Zn-mediated assemblies of each variant and determined their *in vitro* β -lactamase activities (fig. S9). Although there was only a weak correlation between the survival frequencies of the point

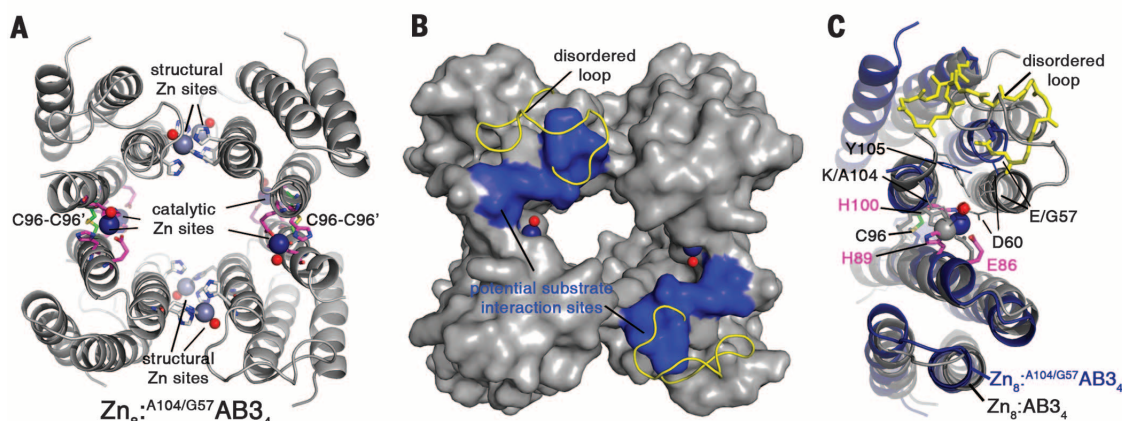


Fig. 3. Crystal structure of $\text{Zn}_8\text{:}^{\text{A104/G57}}\text{AB3}_4$. (A) Cartoon representation of $\text{Zn}_8\text{:}^{\text{A104/G57}}\text{AB3}_4$. Catalytic and structural Zn ions and the coordinating residues are shown as navy and gray spheres, respectively. The Zn-bound water molecules are shown as red spheres. (B) Surface representation of $\text{Zn}_8\text{:}^{\text{A104/G57}}\text{AB3}_4$. Structurally disordered loops are displayed as yellow ribbons. Potential substrate interaction sites consisting of residues 58 to 60 and 104 to 105 are colored in blue. (C) Close-up view of the catalytic Zn sites of $\text{Zn}_8\text{:}^{\text{A104/G57}}\text{AB3}_4$ (navy) overlaid with $\text{Zn}_8\text{:AB3}_4$ (gray) structure. Zn-coordinating residues (Glu⁸⁶, His⁸⁹, and His¹⁰⁰) and the mobile loop are shown as pink and yellow sticks, respectively.

mutants and their β -lactamase activities, the two variants most frequently represented in in vivo screens, $^{A104/G57}$ AB3 and $^{A104/T105}$ AB3, were also the most active in vitro.

AUC and Zn-competition titrations indicated that both $^{A104/G57}$ AB3 and $^{A104/T105}$ AB3 formed Zn-bound tetramers (figs. S10 and S11), with similar binding affinities for Zn as A104 AB3 (table S5). The pK_a of the Zn^{II} -OH/OH₂ active centers was 8.9 for the $^{A104/G57}$ AB3 assembly and 9.2 for the $^{A104/T105}$ AB3 assembly on the basis of their ampicillin hydrolysis activities (fig. S13 and Table 1). The Zn complex of the $^{A104/T105}$ AB3 variant hydrolyzed pNPA with a rate that was $\sim 1/4$ of that of A104 AB3, but its ampicillin hydrolysis activity was essentially the same (Table 1), suggesting that the Y105T mutation may have enhanced interactions with ampicillin. This enhancement was not substantial, however, as the ampicillin hydrolysis rates of the $^{A104/T105}$ AB3 variant were linearly dependent on the substrate concentration over the entire concentration range studied (0 to 20 mM) (fig. S14). In contrast, the $^{A104/G57}$ AB3 variant hydrolyzed ampicillin more than three times as efficiently as both A104 AB3 and $^{A104/T105}$ AB3 and displayed saturation behavior at increased ampicillin concentrations, with a K_m of 10^{-2} M (Fig. 2F), which is consistent with the emergence of a substrate-binding site. The net rate enhancement (k_{cat}/k_{uncat}) and catalytic proficiency [$(k_{cat}/K_m)/k_{uncat}$] of the Zn_8 : $^{A104/G57}$ AB3₄ complex for ampicillin hydrolysis were 23,000 and 2,300,000, respectively, with an increase in selectivity over pNPA hydrolysis by more than threefold relative to Zn_8 : A104 AB3₄ (Table 1).

To examine the formation of a potential ampicillin interaction site and the presence of hydrolytic Zn^{II} -OH/OH₂ centers, we determined the structure of Zn_8 : $^{A104/G57}$ AB3₄ at 2.8 Å resolution (Fig. 3 and fig. S15). Unexpectedly, the tetramer displays a substantially more open architecture compared to Zn_8 :AB3₄ (Fig. 1), ascribed to the elimination of the Lys¹⁰⁴-Zn coordination through the K104A mutation. The peripheral Zn sites show the designed coordination to Glu⁸⁶, His⁸⁹, and His¹⁰⁰, and the Zn-coordinated OH₂/OH⁻ ligand is clearly visible. Although the structural Zn sites of Zn_8 : $^{A104/G57}$ AB3₄ (shown as gray spheres in Fig. 3), which were saturated by protein ligands in the closed Zn_8 : A104 AB3₄ architecture (Fig. 1C), are coordinated by only three protein residues and a solvent molecule, they are substantially buried by Arg⁹², Trp⁹¹, and Trp⁶⁶ side chains (fig. S15) and unlikely to be accessible to ampicillin. The opening of the tetrameric architecture is accompanied by the widening of the interfaces containing the catalytic Zn^{II} -OH₂/OH⁻ centers, but the same set of residues (57, 60, 104, 105) remain in position above the Zn^{II} -OH₂/OH⁻ sites as potential substrate interaction sites. Notably, the long, structured loop near the active site, starting from Ala⁴³ and terminating in residue 57 is completely disordered because of increased conformational freedom by the E57G mutation and the elimination of the

side-chain interactions of Glu⁵⁷ with Lys⁵¹ and Ser⁵⁴. As judged by the packing arrangement of neighboring tetramers in the F222-space-group crystals (65% solvent content), the 43-57 loop is highly mobile and occupies considerable space. Accordingly, binding experiments with 1-anilino-8-naphthalene-sulfonate (1,8-ANS) (fig. S16) suggest that the hydrophobic center of the loop formed by Ala⁴³, Pro⁴⁵, and Leu⁴⁸ in combination with Met⁵⁸ and Tyr¹⁰⁵ side chains has become exposed.

The E57G mutation and ensuing loop mobility above the catalytic Zn^{II} centers have potential implications for substrate binding. Molecular docking simulations with ampicillin suggest that the E57G mutation may open up sufficient room for substrate binding and alleviate charge repulsion with the ampicillin carboxylate group to position the β -lactam ring directly above the Zn^{II} -OH/OH₂ moiety (fig. S15C). Several possible docking modes orient the ampicillin molecule toward the mobile 43-57 loop and within reach for extensive interactions with the loop. Indeed, Zn_8 : $^{A104/G57}$ AB3₄ can also catalyze the hydrolysis of a bulkier β -lactam, nitrocefin (Fig. 2A), whereas the other variants (A104 AB3 and $^{A104/T105}$ AB3) cannot. Although the catalytic efficiency of Zn_8 : $^{A104/G57}$ AB3₄ for nitrocefin hydrolysis [$k_{cat} = 5(1) \times 10^{-4} s^{-1}$, $k_{cat}/K_M = 1.8(6) M^{-1} s^{-1}$] (fig. S17) is considerably lower than for ampicillin and the observed rate enhancement ($k_{cat}/k_{uncat} \sim 160$ -fold) is smaller, the catalytic rate at pH 9 is approximately an order of magnitude higher than that of a known, biomimetic μ -hydroxo-di- Zn^{II} catalyst (30) and comparable to that of a native metallo- β -lactamase, CphA, which possesses a mononuclear Zn^{II} -OH₂/OH⁻ site with pH-independent activity between pH 6 and 9 (31).

In conclusion, we have presented a designed supramolecular protein assembly with in vivo β -lactamase activity, which has allowed its functional screening and optimization via directed evolution. A highly mobile loop near the active site that emerged as an unplanned consequence of in vivo screening is a key feature of natural β -lactamases (32, 33). Our screen was limited to point mutations within a small, nascent active-site pocket. Higher efficiency might be achieved through simultaneous randomization of multiple residues and the enlargement of the active site through loop engineering (34). Moreover, the structural flexibility of the architecture may be used for functional diversification or for engineering allostery (35). Ultimately, Zn_8 : $^{A104/G57}$ AB3₄, a nascent β -lactamase, is only 16 surface mutations away from (i.e., 85% identical to) cyt cb₅₆₂, the parent monomeric redox protein. This illustrates the facility with which protein-protein interfaces nucleated by metal ions lend themselves to creation of new biological structures and functions, whether for rational design or for evolution.

REFERENCES AND NOTES

- G. Kiss, N. Çelebi-Ölçüm, R. Moretti, D. Baker, K. N. Houk, *Angew. Chem. Int. Ed.* **52**, 5700–5725 (2013).

- H. Kries, R. Blomberg, D. Hilvert, *Curr. Opin. Chem. Biol.* **17**, 221–228 (2013).
- R. Sterner, B. Höcker, *Chem. Rev.* **105**, 4038–4055 (2005).
- M. Nardini, B. W. Dijkstra, *Curr. Opin. Struct. Biol.* **9**, 732–737 (1999).
- H.-S. Park *et al.*, *Science* **311**, 535–538 (2006).
- H. K. Privett *et al.*, *Proc. Natl. Acad. Sci. U.S.A.* **109**, 3790–3795 (2012).
- S. D. Khare *et al.*, *Nat. Chem. Biol.* **8**, 294–300 (2012).
- L. Giger *et al.*, *Nat. Chem. Biol.* **9**, 494–498 (2013).
- N. Yeung *et al.*, *Nature* **462**, 1079–1082 (2009).
- P. S. Coelho, E. M. Brustad, A. Kannan, F. H. Arnold, *Science* **339**, 307–310 (2013).
- T. K. Hyster, L. Knörr, T. R. Ward, T. Rovis, *Science* **338**, 500–503 (2012).
- M. Faiella *et al.*, *Nat. Chem. Biol.* **5**, 882–884 (2009).
- M. L. Zastrow, A. F. Peacock, J. A. Stuckey, V. L. Pecoraro, *Nat. Chem.* **4**, 118–123 (2012).
- M. H. Ali, B. Imperiali, *Bioorg. Med. Chem.* **13**, 5013–5020 (2005).
- E. N. Salgado, R. J. Radford, F. A. Tezcan, *Acc. Chem. Res.* **43**, 661–672 (2010).
- B. S. Der *et al.*, *J. Am. Chem. Soc.* **134**, 375–385 (2012).
- W. J. Song, P. A. Sontz, X. I. Ambroggio, F. A. Tezcan, *Annu. Rev. Biophys.* **43**, 409–431 (2014).
- B. S. Der, D. R. Edwards, B. Kuhlman, *Biochemistry* **51**, 3933–3940 (2012).
- K. Channon, E. H. Bromley, D. N. Woolfson, *Curr. Opin. Struct. Biol.* **18**, 491–498 (2008).
- J. F. Fisher, S. O. Meroueh, S. Mobashery, *Chem. Rev.* **105**, 395–424 (2005).
- M. W. Crowder, J. Spencer, A. J. Vila, *Acc. Chem. Res.* **39**, 721–728 (2006).
- J. Faraone-Mennella, F. A. Tezcan, H. B. Gray, J. R. Winkler, *Biochemistry* **45**, 10504–10511 (2006).
- E. N. Salgado, J. Faraone-Mennella, F. A. Tezcan, *J. Am. Chem. Soc.* **129**, 13374–13375 (2007).
- J. D. Brodin *et al.*, *J. Am. Chem. Soc.* **132**, 8610–8617 (2010).
- T. Koike, M. Takamura, E. Kimura, *J. Am. Chem. Soc.* **116**, 8443–8449 (1994).
- C. M. Rufo *et al.*, *Nat. Chem.* **6**, 303–309 (2014).
- A. Medina-Morales, A. Perez, J. D. Brodin, F. A. Tezcan, *J. Am. Chem. Soc.* **135**, 12013–12022 (2013).
- W. Maret, Y. Li, *Chem. Rev.* **109**, 4682–4707 (2009).
- M. T. Reetz, J. D. Carballeira, *Nat. Protoc.* **2**, 891–903 (2007).
- N. V. Kaminskaya, C. He, S. J. Lippard, *Inorg. Chem.* **39**, 3365–3373 (2000).
- M. Vanhove *et al.*, *Cell. Mol. Life Sci.* **60**, 2501–2509 (2003).
- S. D. B. Scrofan *et al.*, *Biochemistry* **38**, 14507–14514 (1999).
- P. E. Tomatis *et al.*, *Proc. Natl. Acad. Sci. U.S.A.* **105**, 20605–20610 (2008).
- D. S. Tawfik, *Science* **311**, 475–476 (2006).
- N. Tokuriki, D. S. Tawfik, *Science* **324**, 203–207 (2009).

ACKNOWLEDGMENTS

We thank D. Rees, T. Ward, N. Gianneschi, S. Cohen, U. Müller, and D. Puerta for helpful discussions. This work was funded by the NSF (CHE1306646 to F.A.T.). Crystallographic data were collected at Stanford Synchrotron Radiation Lightsource, which is supported by the U.S. Department of Energy, Offices of Basic Energy Sciences and Biological and Environmental Research, as well as by the NIH. A description of experimental methods and additional figures and data are provided in the supplementary materials. Coordinate and structure factor files were deposited into the Protein Data Bank under accession numbers 4U9D and 4U9E.

SUPPLEMENTARY MATERIALS

www.sciencemag.org/content/346/6216/1525/suppl/DC1
Materials and Methods
Figs. S1 to S17
Tables S1 to S5
References (36–56)

6 August 2014; accepted 13 November 2014
10.1126/science.1259680

CANCER EPIGENETICS

Use of human embryonic stem cells to model pediatric gliomas with H3.3K27M histone mutation

Kosuke Funato,¹ Tamara Major,¹ Peter W. Lewis,² C. David Allis,³ Viviane Tabar^{1*}

Over 70% of diffuse intrinsic pediatric gliomas, an aggressive brainstem tumor, harbor heterozygous mutations that create a K27M amino acid substitution (methionine replaces lysine 27) in the tail of histone H3.3. The role of the H3.3K27M mutation in tumorigenesis is not fully understood. Here, we use a human embryonic stem cell system to model this tumor. We show that H3.3K27M expression synergizes with p53 loss and PDGFRA activation in neural progenitor cells derived from human embryonic stem cells, resulting in neoplastic transformation. Genome-wide analyses indicate a resetting of the transformed precursors to a developmentally more primitive stem cell state, with evidence of major modifications of histone marks at several master regulator genes. Drug screening assays identified a compound targeting the protein menin as an inhibitor of tumor cell growth in vitro and in mice.

Diffuse intrinsic pontine gliomas (DIPGs) are rare, highly aggressive brainstem tumors primarily affecting children. Over 70% of DIPGs carry somatic mutations in the *H3F3A* gene encoding histone H3.3, leading to a p.Lys27Met amino acid substitution (methionine replaces lysine 27) (1–3). Tumors positive for the mutation are associated with poorer prog-

nosis and diminished survival. Comprehensive whole-genome analyses have shown that the H3.3K27M mutation identifies a distinct subgroup of DIPGs that has substantial overlap with p53 mutations and platelet-derived growth factor receptor, α polypeptide (PDGFRA) amplification (60% and 40%, respectively) (4, 5). These genetic studies have paved the way for investigations of the pathogenesis and treatment of this rapidly fatal tumor. However, tissue access remains a substantial challenge because of the infiltrative nature and sensitive location of the tumor in the brainstem. Key features of K27M-mutated DIPGs are the restricted developmental window during which they emerge [mean age at diagnosis is 8 years (5)] and their specific midline location,

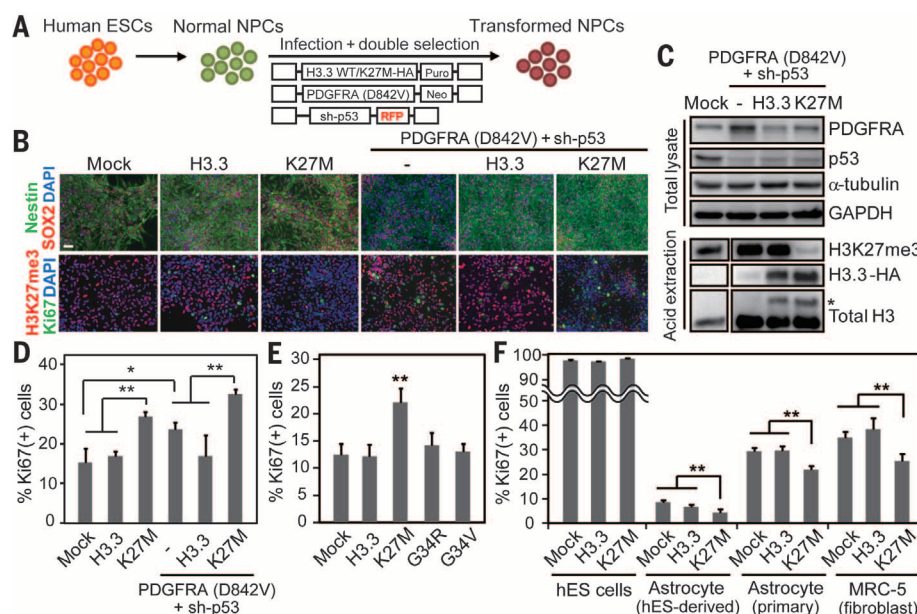
which implicate a developmentally early and anatomically specific cell of origin.

We reasoned that human pluripotent stem cells (hPSCs) (6) might be a valuable model for studying DIPG. These cells provide an attractive platform for functional analysis of oncogenic mutations in a genetically defined human background. In addition, neural differentiation protocols allow the derivation of relevant developmentally early neural stem cells that are often inaccessible; thus, tumorigenesis can be studied in the proper cell context. We first derived early neural progenitor cells (NPCs) from human embryonic stem (hES) cells (H9, WA-09), using the dual Smad inhibition protocol (7). We then co-transduced the cells with lentiviruses encoding (i) a constitutively active form of the PDGFRA in which valine replaces aspartic acid 842 (D842V); (ii), a small hairpin RNA (shRNA) against p53 tagged with red fluorescent protein (RFP); and (iii) a hemagglutinin (HA)-tagged wild-type (WT) or K27M mutant form of histone H3.3 (Fig. 1A). These oncogenes were selected on the basis of their high frequency of expression and/or mutations in K27M-mutated DIPGs (5, 8). After transduction and double selection under puromycin and G418, the cells maintained NPC-like morphology and expression of two NPC marker genes, Nestin and SOX2 (Fig. 1B). Consistent with previous reports (9–11), the expression of H3.3K27M led to a reduction in histone H3K27 trimethylation (H3K27me3), as shown by immunohistochemistry and Western blotting (Fig. 1, B and C). Expression of H3.3K27M alone increased cell proliferation (Ki-67 of ~27% versus 15 to 17%) and total cell number, in comparison to WT H3.3 or mock (empty vector) conditions (Fig. 1D and fig. S1A). Overexpression of constitutively active PDGFRA (D842V) and knockdown of p53 (hereafter referred to as P5) also increased the proliferation of NPCs. The combination of H3.3K27M and P5

¹Department of Neurosurgery, Center for Stem Cell Biology and Brain Tumor Center, Memorial Sloan-Kettering Cancer Center, New York, NY 10065, USA. ²Department of Biomolecular Chemistry, School of Medicine and Public Health, University of Wisconsin, Madison, WI 53715, USA. ³Laboratory of Chromatin Biology and Epigenetics, The Rockefeller University, New York, NY 10065, USA.

*Corresponding author. E-mail: tabarv@mskcc.org

Fig. 1. The impact of H3.3 K27M mutation on neural precursors. (A) hES-derived NPCs were transformed using a combination of lentiviruses encoding H3.3 WT or H3.3K27M, plus PDGFRA and sh-p53. (B) Immunohistochemistry of NPCs transduced with different vector combinations demonstrates maintenance of SOX2 and Nestin expression. DAPI, 4',6'-diamidino-2-phenylindole. Expression of H3.3K27M (K27M) is associated with significantly reduced H3K27 trimethylation mark (H3K27me3). Ki-67 immunopositivity depicts proliferation and is most elevated in the K27M, PDGFRA, and sh-p53 conditions. Scale bar, 50 μ m. (C) Western blotting of transduced NPCs. Total lysates and acid-extracted histones were separated by SDS-polyacrylamide gel electrophoresis and blotted with the indicated antibodies. Asterisk (*) beside higher bands indicates HA-tagged H3.3 transgene. (D) Quantification of Ki-67 immunostaining in transduced NPCs. (E) Proliferation index of NPCs transduced with various H3.3 mutations. (F) Impact of K27M mutation on the proliferation index of various cell lines. Error bars in panels (D) to (F) indicate means \pm SD ($n = 4$ to 5 in each). * $P < 0.05$; ** $P < 0.01$.



was even more effective in increasing the proliferative capacity of the P5 cells, up to a Ki-67 index of >30%. This result was confirmed by using a second independent shRNA against p53 (sh-p53) (fig. S1, B to D). The proliferative effect on neural precursors is specific to H3.3K27M and is not seen in the G34R/V mutations of H3.3 (glycine 34 is replaced by arginine or valine), which are mostly reported in supratentorial glioblastomas (Fig. 1E). It is also highly specific to the cell context, because H3.3K27M expression in undifferentiated hES cells or in differentiated somatic cells—such as hES-derived astrocytes, primary human astrocytes, or MRC-5 human lung fibroblast cells—did not affect proliferation rates and, in some cases, induced senescence (Fig. 1F and fig. S2). Expression of Olig2, reported in DIPGs (4), was increased in both the H3.3K27M and the P5 condition (fig. S3).

We next explored whether the transduced NPCs had acquired features of neoplastic cells. Under low-density culture conditions, all cell groups showed poor survival, with the exception of the P5+H3.3K27M (P5K) cells, which formed robust colonies that grew to confluence, consistent with a neoplastic phenotype (Fig. 2A and fig. S4A). The combination of PDGFRA, sh-p53, and H3.3K27M had a synergistic effect on cell survival. After growth factor withdrawal, the apoptotic cell fraction was higher in the H3.3K27M-expressing cells, in comparison with normal and WT H3.3-expressing NPCs (fig. S4B); this suggests that the proliferative effect imparted by the histone mutation was balanced with an increased apoptotic rate, a phenomenon often associated with premalignant states (12). The introduction of p53

knockdown in the P5K condition abrogated the apoptotic response, and possibly promoting genomic instability as the cells continued to proliferate. The P5 condition also conferred greater efficiency in neurosphere formation, in all groups, including the P5K combination, whereas cells expressing only H3.3K27M were similar to unperturbed NPCs (fig. S4C). These results support a synergistic effect of H3.3K27M and P5 in the oncogenic transformation of NPCs, consistent with the high frequency of comutation of H3.3K27M and mutated p53 in human DIPGs (1, 4, 5).

We also analyzed transduced NPCs for radiation response and migratory capacity. After irradiation, cells transduced with the combination of H3.3K27M and P5 maintained a high proliferation rate despite substantial DNA damage (fig. S4, D to G), a hallmark of cancer cells (13). Expression of H3.3K27M also increased cell migration (fig. S4H) and invasion (fig. S4I) in *in vitro* assays. High migration capacity of tumor cells is a major feature of DIPGs that renders the tumors unsuitable for surgical eradication. There was a near-complete differentiation block in the astrocytic lineage in the P5K cells, despite an extended culture period *in vitro* [normal NPCs acquire a capacity for robust differentiation into astrocytes (glial competence) only after several weeks *in vitro*] (Fig. 2B). Note that neither the P5 nor the H3.3K27M condition alone inhibited differentiation into astrocytes and to some extent differentiation into oligodendrocytes (fig. S5).

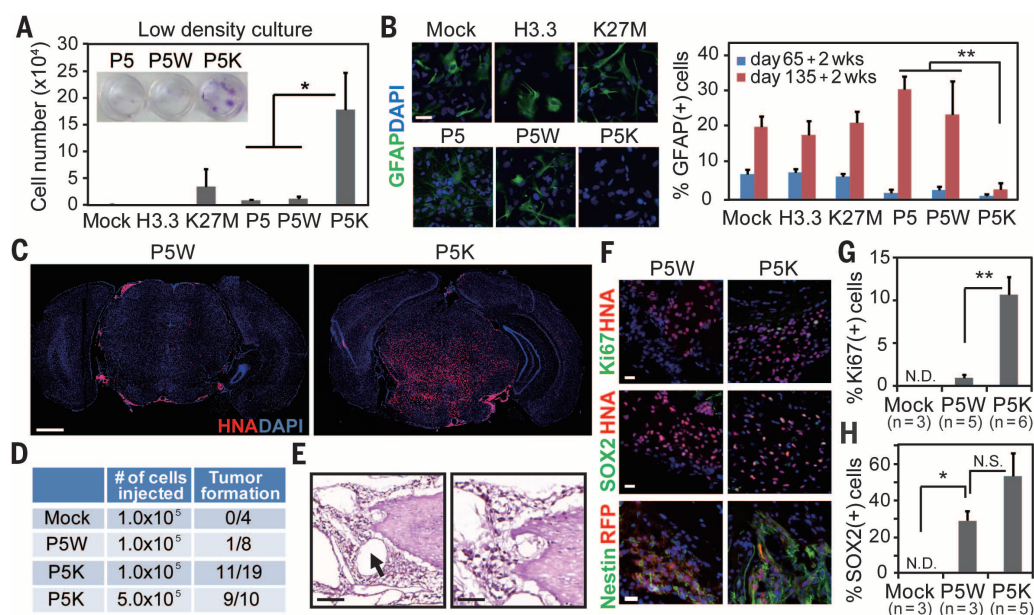
To evaluate tumor formation *in vivo*, we injected transduced NPCs into the brainstem (pons) of immunocompromised mice. Massive brain

tumor formation occurred in the P5K mice, but not in the P5W or mock-injected mice (Fig. 2, C and D). Immunohistochemistry demonstrated human cells infiltrating the pons, with encasement of the basilar artery, microcystic changes, and subarachnoid and subventricular spread, as is often seen in patients with DIPG (fig. S6) (14). Tumor growth was relatively slow, with symptoms and/or substantial tumor volume appearing 3 months after injection of 500,000 cells or 5 months after injection of 100,000 cells. Phenotypic analysis of the tumor cells confirmed expression of the H3.3K27M and sh-p53 constructs (HA and RFP tags in 78% and 76.4% of all human cells, respectively) (fig. S7, A and B), as well as markers of immature NPCs (Nestin, Sox2, and Olig2) and high proliferation rates in the P5K group compared with P5W cells or normal NPCs (10.4% versus 0.7% and 0%, respectively) (Fig. 2, F to H, and fig. S7C). GFAP (glial fibrillary acidic protein) colabeled with tumor cells that had down-regulated H3K27M expression (fig. S7D). Pathologically, the tumors resembled lower-grade DIPGs and not full-blown glioblastomas (GBMs), as determined by the absence of necrosis and microvascular proliferation. We speculate that longer *in vivo* growth periods may be required for the accumulation of mutations leading to a more malignant phenotype. Animals bearing P5W cells showed evidence of a few cell clusters and minimal infiltration in the pons, whereas mock cell injections were associated with minimal cell survival (Fig. 2C).

We next examined gene expression profiles of P5K cells maintained *in vitro* or sorted by fluorescence-activated cell sorting from

Fig. 2. Synergistic effect of K27M and oncogenes in inducing transformation and tumorigenicity of NPCs. (A) Transduced NPCs

were grown at very low density for 4 weeks, and the number of viable cells was counted by trypan blue staining. Crystal violet staining is shown in the inset. P5, P5W, and P5K indicate PDGFRA (D842V) + sh-p53, P5 + WT histone H3.3, and P5 + K27M mutant, respectively. Bars indicate means \pm SD ($n = 4$). (B) Immunohistochemistry and quantification for the glial marker (GFAP) under the differentiation condition. Bars indicate means \pm SD ($n = 4$ to 5). Scale bar, 20 μ m. (C) Transcranial injection of P5K cells into the brainstem of mice led to tumor formation, whereas P5W cells gave rise to isolated cell clusters. Low-magnification immunofluorescence images of representative sections labeled for human nuclear antigen (HNA) and counterstained with DAPI. Scale bar, 1 mm. (D) Summary of transplantation and tumor formation. (E) Light microscopy of hematoxylin and eosin–stained representative section taken from the pons of a mouse bearing P5K tumor demonstrates encasement of the basilar artery (arrow) by tumor cells, microcystic change, and infiltration in the pons. Scale bar, 100 μ m (left panel), 50 μ m (right panel). (F to H) Immunophenotyping of the xenografts. Immunofluorescence images and quantification for HNA, Ki67 (F and G), SOX2 (F and H) and human-specific Nestin (F). Error bars in panels (G) and (H) indicate means \pm SEM ($n = 3$ to 6). Scale bar, 20 μ m. * $P < 0.05$; ** $P < 0.01$; NS, not significant; ND, not detected.



tumor-bearing animals. These profiles were compared with those of patient tumors, including DIPGs with H3K27M or H3G34R/V mutations and adult GBMs without histone mutations (Fig. 3A and fig. S8A). Upon unsupervised hierarchical clustering, the P5K cells from in vitro or in vivo sources clustered closer to the H3K27M group ($P < 4.36 \times 10^{-8}$ and $P < 2.26 \times 10^{-4}$) than the G34R/V or GBMs without histone mutation (fig. S8B). We next analyzed differentially expressed genes among the different NPC groups (Fig. 3B, fig. S8C, and tables S1 and S2). We noted an enrichment in the K27M-expressing cells of a subset of transcripts known to be expressed in neuroepithelial cells at a very early developmental stage—i.e., the neural plate, which precedes the emergence of NPCs. To validate this finding, we derived from public datasets (GEO accession no. GSE9921) (15) gene sets that are uniquely expressed at the neural rosette (early neural plate) stage and the neural precursor stage (L-NSCs), as well as gene sets that are shared between rosette and undifferentiated ES cells. A gene set enrichment analysis revealed a significant correlation between H3.3K27M differentially regulated genes and genes enriched in rosette cells (R-NPCs), but not in normal NPCs (L-NPCs) (fig. S8D). We also found a highly significant intersection of genes that were up-regulated in H3.3K27M cells with those in the rosette or rosette-human ES groups. In contrast, most of the genes that were differentially down-regulated in the H3.3K27M cells

were shared with those in the NPC group (fig. S8E). Reverse transcription with quantitative polymerase chain reaction (RT-qPCR) validated the increased expression of *LIN28B*, *PLAG1*, and *PLAGL1* in hES cells and rosettes and substantial down-regulation of all three genes in normal NPCs. Expression of H3.3K27M in NPCs up-regulated expression levels of the same genes (Fig. 3C). Note that analysis of patient samples revealed that these genes were expressed at higher levels in DIPGs with the H3K27M mutation than in DIPGs with the G34R/V mutation or without either mutation in histone H3.3 (1) (Fig. 3D and fig. S9). Knockdown of *LIN28B* or *PLAG1* led to a significant decrease in cell number and proliferation in P5K cells (fig. S10). These data suggest that expression of mutant H3.3K27M leads to a developmental resetting of neural precursors to a more primitive stem cell state, which in combination with growth factor signaling, results in the acquisition or consolidation of oncogenic features.

We next investigated whether the transcriptional changes in the K27M groups were associated with chromatin modifications. We performed chromatin immunoprecipitation followed by sequencing (ChIP-seq) analysis to map active H3K4me3 and repressive H3K27me3 marks in the P5W and P5K cells. Consistent with previous reports (11, 16), H3K27me3 peaks undergo genomic redistribution in the P5K condition (Fig. 3E). Notably, the genes up-regulated by K27M

had significantly lower levels of H3K27me3 at their gene-body regions in P5K cells in comparison with P5W cells ($P < 3.3 \times 10^{-5}$) (Fig. 3E and fig. S11, A to D). Concomitantly, H3K4me3 peaks remained stable at promoter regions, which implied that K27M may release these genes from the poised state. On the other hand, the genes down-regulated by K27M gained H3K27me3 and lost H3K4me3 marks in P5K cells at their promoter regions (Fig. 3, E and F; fig. S11C; and table S3). Of these, oligodendrocyte differentiation genes *Nkx2.2* and *MBP* were highly marked by H3K27me3, and their expression levels were decreased in the NPCs expressing K27M alone or the P5K combination (Fig. 3E and fig. S11, B and E). Master genes that initiate acquisition of astrocyte cell fate are not fully elucidated in humans and could not be analyzed. We further analyzed a set of genes that gain H3K27me3 marks in P5K and P5W cells by comparing them with reported H3K27me3 or PRC2 target genes in undifferentiated hES cells (17). There was a highly significant intersection of P5K-specific H3K27me3-target genes with H3K27me3-target genes, as well as PRC2-target genes in ES cells ($P < 2.6 \times 10^{-264}$ and $P < 1.7 \times 10^{-219}$) (Fig. 3G and table S4), whereas P5W-specific H3K27me3-target genes have no significant intersection. These data support our hypothesis that the expression of K27M leads to a resetting of neural precursors to a more primitive stem cell state.

Fig. 3. Genomewide analysis of the K27M transformed NPCs.

(A) Hierarchical clustering of microarray data from P5K cells, xenograft-derived P5K cells, and patient tumor samples bearing the K27M or G34R/V mutations (GSE34824) obtained from (1). (B) Principal component analysis (PCA) of microarray data obtained from NPCs transduced with the different H3.3 and oncogene combinations. (C) RT-qPCR demonstrates increased expression levels of *LIN28B*, *PLAG1*, and *PLAGL1* in the P5K cells. Bars indicate means \pm SEM ($n = 4$ to 6). (D) Boxplot shows the expression levels of the genes in patient tumor samples. (E to G) The chromatin landscape of transformed cells. P5K cells showed a global decrease in H3K27me3, but enrichment at the gene body or promoter regions of select genes as shown in representative profiles [(E) H3K4me3 in red and H3K27me3 in blue]. (F) Levels of H3K4me3 and H3K27me3 marks at the promoter region (+1 kilobase to -500 base pairs) of the genes differentially regulated by K27M. P values were calculated by the Wilcoxon rank-sum test. (G) Venn diagrams comparing genes that are marked by H3K27me3 or bound by PRC2. * $P < 0.05$; ** $P < 0.01$; NS, not significant.

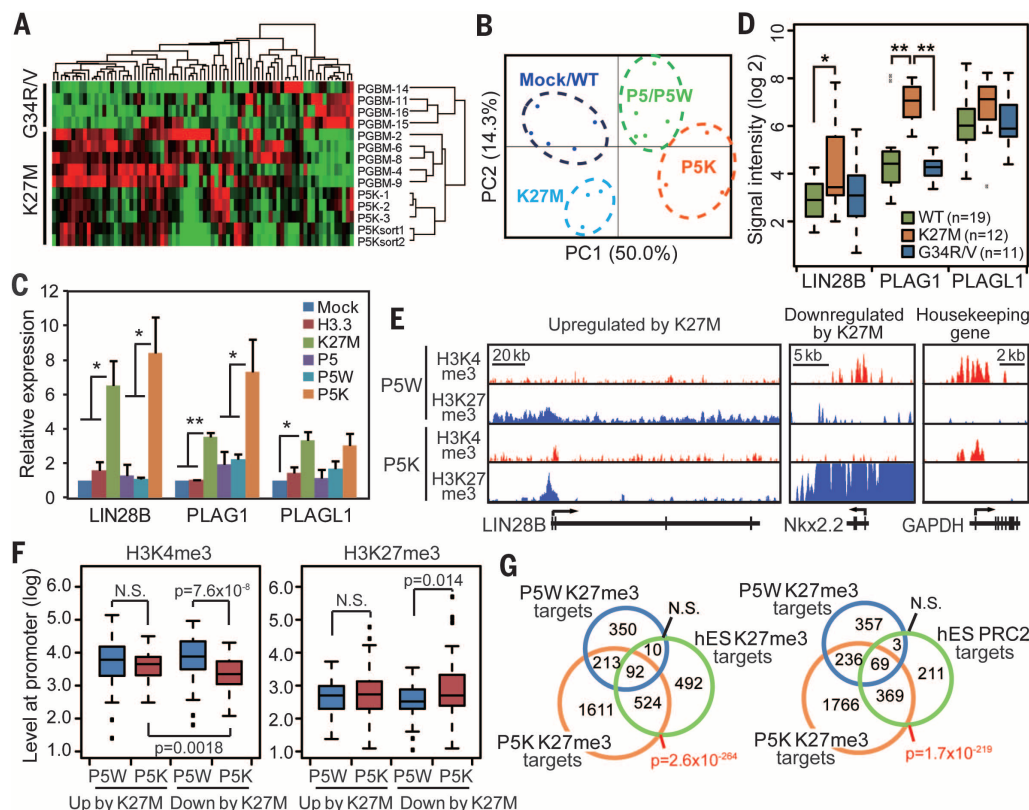
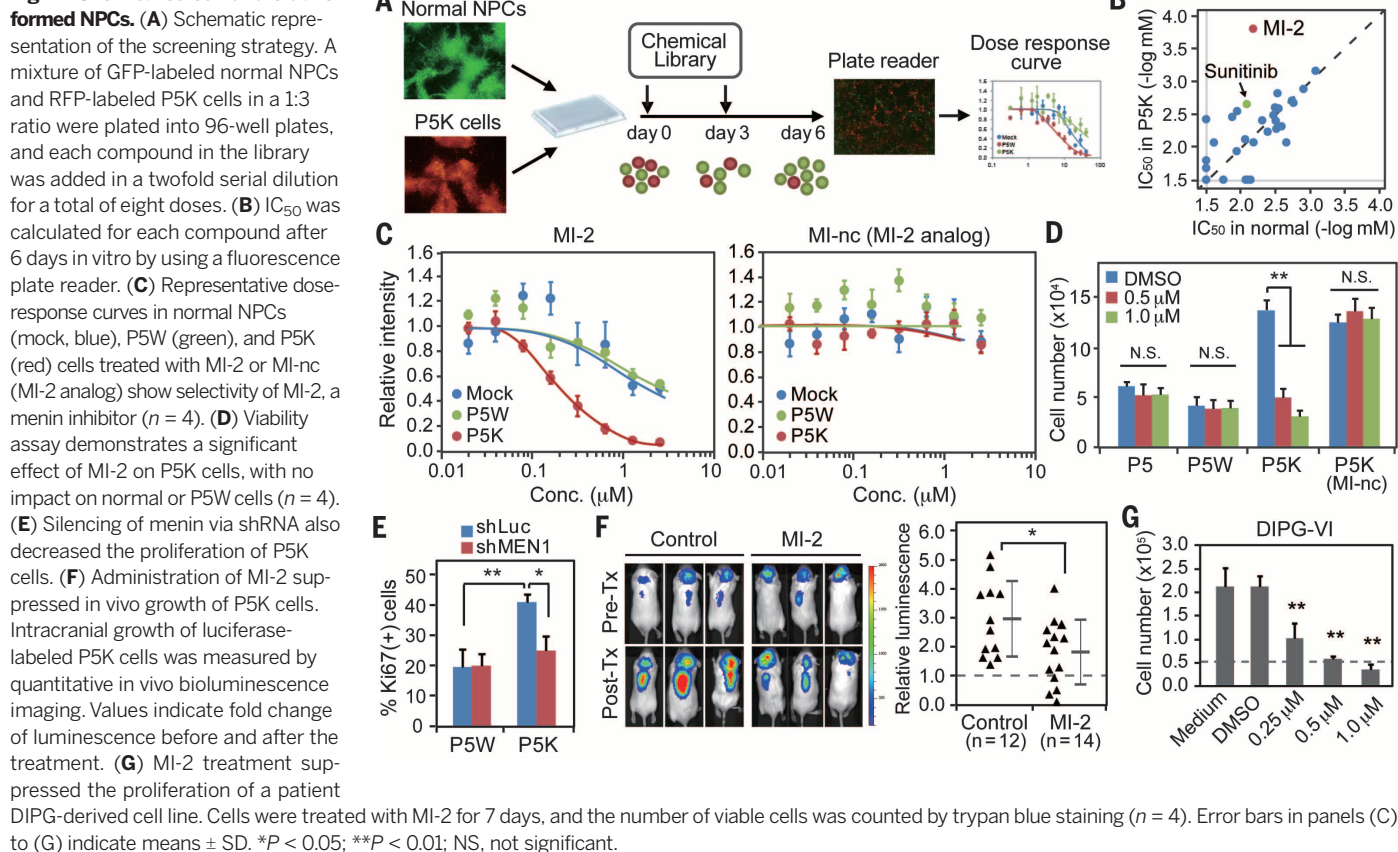


Fig. 4. Chemical screen of the trans-

To explore whether the hES-based tumor model can be used for drug discovery, we performed a chemical screen using a commercially available small-molecule library of compounds that target epigenetic regulators ($n = 80$), such as BET bromodomain inhibitors, deacetylase and demethylase inhibitors, including selective JMJD3 inhibitors (table S5 and the methods section of supplementary materials). Green fluorescent protein (GFP)-labeled normal NPCs and RFP-labeled P5K cells were mixed and seeded onto 96-well plates. Cells were then treated with each compound at eight different concentrations for 6 days, and GFP and RFP fluorescence was quantified by a plate reader (Fig. 4A). The top hit was the menin inhibitor MI-2 (18), which reduced survival of P5K cells at submicromolar concentrations [median inhibitory concentration (IC_{50}) = 155 nM] but had no effect on normal NPCs (Fig. 4B, fig S12A, and table S5). The effect of MI-2 on cell survival was independent of the P5 combination and was restricted to cells with the H3K27M mutation (Fig. 4, C and D) (fig. S12, B to D). shRNA-mediated silencing of the gene encoding menin (*MEN1*) resulted in decreased proliferation of P5K but not P5W cells (Fig. 4E and fig. S12, E to H). It also restored astrocytic differentiation in P5K cells (fig. S12, I and J), which suggests that a common mechanism underlies the major transformation features, i.e., proliferation and impaired differentiation. Menin is expressed in undifferentiated hES cells and rosettes, but its

levels decrease in normal NPCs and astrocytes; however, expression of the P5K combination in NPCs increases menin transcription sixfold (fig S13). Pontine injections of P5K cells transduced with shRNA against menin resulted in significantly reduced tumor formation in mice (fig. S14A). We also tested the impact of systemic treatment with MI-2 on tumor growth in vivo. To this end, we injected P5K cells transduced with a luciferase vector in the brainstem of a large group of mice ($n = 26$), monitored for tumor development via bioluminescence imaging (BLI), then started treatment with intraperitoneal injections of MI-2. Control mice received tumor cell injections in the brain but were treated with dimethyl sulfoxide (DMSO) intraperitoneally. After 4 weeks of drug treatment, the MI-2 group demonstrated significantly smaller tumors by BLI ($P = 0.026$) (Fig. 4F and fig. S14B) in comparison with the DMSO group. We also live-sorted P5K cells from mouse tumors and tested their response to MI-2. The cells exhibited a decrease in cell survival and proliferation and increased apoptosis, similar to P5K cells that were never injected in mice (fig. S15). P5K cells live-sorted from mouse tumors also exhibited a decrease in cell survival when LIN28B or PLAGL1 are silenced (fig. S15H). Finally, we tested MI-2 on cell cultures derived from a patient sample. Cells from a human DIPG positive for the H3.3K27M mutation showed a robust antiproliferative response (Fig. 4G and fig. S16). Menin plays a tumor-

suppressor role in endocrine cancers but is highly oncogenic in mixed lineage-associated leukemias (19, 20). It is a member of the trithorax family histone methyltransferase complex but also interacts with a wide range of proteins and is thought to be involved in transcriptional regulation. Our data suggest that it may be a potential therapeutic target for pediatric gliomas harboring the H3.3K27M mutation.

In summary, using hES cells as a platform to model diffuse intrinsic gliomas, we demonstrate a driver role of the H3.3K27M mutation in the appropriate cell context and developmental window; the model also showed that the altered chromatin landscape induced by H3K27M facilitates the reacquisition of an earlier developmental program with subsequent activation of factors crucial to reprogramming and oncogenesis, such as the micro-RNA binding protein LIN28B (27). A chemical screen identified the menin pathway as a contributor to tumor maintenance, which provides a potential opportunity for therapeutic intervention.

REFERENCES AND NOTES

1. J. Schwartzentruber et al., *Nature* **482**, 226–231 (2012).
2. G. Wu et al., *Nat. Genet.* **44**, 251–253 (2012).
3. J. Zhang et al., *Nat. Genet.* **45**, 602–612 (2013).
4. D. Sturm et al., *Cancer Cell* **22**, 425–437 (2012).
5. D.-A. Khuong-Quang et al., *Acta Neuropathol.* **124**, 439–447 (2012).
6. V. Tabar, L. Studer, *Nat. Rev. Genet.* **15**, 82–92 (2014).

7. S. M. Chambers *et al.*, *Nat. Biotechnol.* **27**, 275–280 (2009).
8. B. S. Paugh *et al.*, *Cancer Res.* **73**, 6219–6229 (2013).
9. P. W. Lewis *et al.*, *Science* **340**, 857–861 (2013).
10. K.-M. Chan *et al.*, *Genes Dev.* **27**, 985–990 (2013).
11. S. Bender *et al.*, *Cancer Cell* **24**, 660–672 (2013).
12. T. D. Halazonetis, V. G. Gorgoulis, J. Bartek, *Science* **319**, 1352–1355 (2008).
13. D. Hanahan, R. A. Weinberg, *Cell* **100**, 57–70 (2000).
14. R. Sethi *et al.*, *J. Neurooncol.* **102**, 121–127 (2011).
15. Y. Elkabetz *et al.*, *Genes Dev.* **22**, 152–165 (2008).
16. P. W. Lewis, C. D. Allis, *Cell Cycle* **12**, 3241–3242 (2013).
17. I. Ben-Porath *et al.*, *Nat. Genet.* **40**, 499–507 (2008).
18. J. Grembecka *et al.*, *Nat. Chem. Biol.* **8**, 277–284 (2012).
19. S. Matkar, A. Thiel, X. Hua, *Trends Biochem. Sci.* **38**, 394–402 (2013).
20. A. Yokoyama *et al.*, *Cell* **123**, 207–218 (2005).
21. S. R. Viswanathan, G. Q. Daley, *Cell* **140**, 445–449 (2010).

ACKNOWLEDGMENTS

K.F. was supported by grants from the Brain Tumor Center and the Center for Stem Cell Biology at Memorial Sloan Kettering Cancer Center; C.D.A. is supported by The Rockefeller University. Funding in part from The Geoffrey Beene Cancer Center, The Starr Cancer Consortium and the New York State Stem Cell Board (NYSTEM). Microarray data generated in this manuscript are deposited in GEO (GSE55541). We thank J. Huse, Sloan Kettering, for the pathology assessment of the mouse tumors, and M. Monje, Stanford University, for the human DIPG line, which is available from her under a material transfer agreement. V.T. and K.F. are coinventors on a patent

application filed by Memorial Sloan Kettering Cancer Center related to the use of the MI-2 drug in tumors and the ES-based modeling system.

SUPPLEMENTARY MATERIALS

www.sciencemag.org/content/346/6216/1529/suppl/DC1
Materials and Methods
Figs. S1 to S16
Tables S1 to S6
References (22–30)

24 March 2014; accepted 5 November 2014
Published online 20 November 2014;
10.1126/science.1253799

GENE EXPRESSION

Promoter architecture dictates cell-to-cell variability in gene expression

Daniel L. Jones,^{1*} Robert C. Brewster,^{1,2*} Rob Phillips^{1,2†}

Variability in gene expression among genetically identical cells has emerged as a central preoccupation in the study of gene regulation; however, a divide exists between the predictions of molecular models of prokaryotic transcriptional regulation and genome-wide experimental studies suggesting that this variability is indifferent to the underlying regulatory architecture. We constructed a set of promoters in *Escherichia coli* in which promoter strength, transcription factor binding strength, and transcription factor copy numbers are systematically varied, and used messenger RNA (mRNA) fluorescence in situ hybridization to observe how these changes affected variability in gene expression. Our parameter-free models predicted the observed variability; hence, the molecular details of transcription dictate variability in mRNA expression, and transcriptional noise is specifically tunable and thus represents an evolutionarily accessible phenotypic parameter.

The single-molecule events underlying gene expression, such as transcription factor binding and unbinding or RNA polymerase (RNAP) open complex formation, are inherently stochastic—a stochasticity inherited by gene expression itself. Over the past decade, theorists have sought to elucidate how changes in molecular kinetic parameters such as transcription factor binding and unbinding rates affect variability in expression (1, 2), whereas experimentalists have measured variability in gene expression at both the mRNA and protein level in prokaryotes and eukaryotes (3–6). Possible phenotypic consequences (4, 7–9) include the intriguing hypothesis that transcriptional noise may increase the fitness of microbial populations by providing phenotypic variability in a population of genetically identical cells (10, 11).

Models of transcription hinge on the molecular details of the promoter architecture (where “promoter architecture” refers collectively to the locations and strengths of transcription factor

and RNAP binding sites governing a particular gene) and make quantitative predictions for the dependence of the variability on these details. For example, two extremely common promoter architectures (12) are shown schematically in Fig. 1A. Here, each rate parameter (r , k_{off}^R , k_{on}^R , and γ) has a physical interpretation (Fig. 1B) as an element that can be tuned independently by genetic manipulation. The effect of promoter architecture on mean levels of gene expression is well established in prokaryotes, where thermodynamic models successfully predict gene expression as a function of promoter architecture (13–15). However, the associated predictions for how transcriptional noise depends on these parameters remain untested in any systematic way. In direct contrast to such models, some high-throughput experiments have culminated in the assertion that the cell-to-cell variability in gene expression is “universal,” dictated solely by the mean level of expression and insensitive to the details of the promoter driving the expression (3, 5, 6).

To confront this divide, we constructed a library of synthetic promoters driving a LacZ reporter in *E. coli* and measured the resulting mRNA copy number distributions using single-molecule mRNA fluorescence in situ hybridization (FISH) (16). Our

approach ensures that differences in promoter sequence between constructs have clear interpretations in terms of the molecular parameters underlying transcription (e.g., transcription factor unbinding rate, basal transcription rate). This allows us to directly compare predictions of models incorporating those parameters with experimentally observed mRNA distributions, and hence to directly link the molecular events underlying transcription with observed variability in gene expression.

For the case of constitutive expression, shown schematically in Fig. 1A, mRNA transcripts are produced and degraded stochastically at rates r and γ , respectively, with constant probability per unit time. It can be shown (17) that the resulting steady-state mRNA copy number distribution is given by a Poisson distribution with mean r/γ . In the following experimental results, we use the Fano factor, defined as the variance divided by the mean, to characterize variability in gene expression. This metric reports the fold change in the squared coefficient of variation ($\text{CV}^2 = \text{variance}/\text{mean}^2$) with respect to a Poisson process, for which $\text{CV}_{\text{Poisson}}^2 = 1/\text{mean}$; hence, $\text{CV}^2/\text{CV}_{\text{Poisson}}^2 = \text{variance}/\text{mean}$. Therefore, the predicted Fano factor for constitutive expression equals 1 identically. However, this analysis is incomplete: The schematics of Fig. 1A represent the dynamics of the stochastic processes (transcription factor binding and unbinding, mRNA degradation, transcription initiation) that contribute to so-called “intrinsic” variability in gene expression, but do not account for the fact that rate parameters such as the repressor binding rate k_{on}^R and transcription rate r are themselves subject to fluctuations due to cell-to-cell variability in repressor and RNAP copy numbers, respectively. Such effects, collectively termed “extrinsic variability,” tend to increase the measured variability (18).

One important contribution to extrinsic noise comes from variability in gene copy number due to chromosome replication (Fig. 2A, bottom panel). It can be shown (16) that the effect of gene copy number variation on the variability in expression is independent and additive to the variability predicted from transcriptional noise, such that

$$\text{Fano} = \underbrace{\frac{\langle m^2 \rangle_1 - \langle m \rangle_1^2}{\langle m \rangle_1}}_{\text{Transcription}} + \underbrace{\frac{f(1-f)}{1+f}}_{\text{Gene copy number}} \langle m \rangle_1 \quad (1)$$

where $\langle m \rangle_1$ is the mean mRNA copy number from a single gene copy, and f is the fraction of

¹Department of Applied Physics, California Institute of Technology, Pasadena, CA 91125, USA. ²Division of Biology, California Institute of Technology, Pasadena, CA 91125, USA. *These authors contributed equally to this work. †Corresponding author. E-mail: phillips@pboc.caltech.edu

the time a cell has two copies of the gene of interest. The first term is simply the promoter architecture-dependent Fano factor of a sin-

gle copy of a gene, whereas the second term is the contribution due to gene copy number variation.

To quantitatively test the predictions of the model for constitutive expression, we measured the mRNA copy number distribution using

Fig. 1. Schematics of the kinetics of transcription for two simple regulatory architectures. (A) Theoretical treatment of two common promoter architectures and the predicted expression (both mean and variability) as a function of the relevant rate parameters. **(B)** Examples of the experimental knobs available for tuning the various model rate parameters: Basal transcription rate r is tuned by RNAP copy number and RNAP binding site affinity (left); repressor binding rate k_{on}^R is tuned by repressor copy number (center); and repressor unbinding rate k_{off}^R is tuned by its binding site affinity (right).

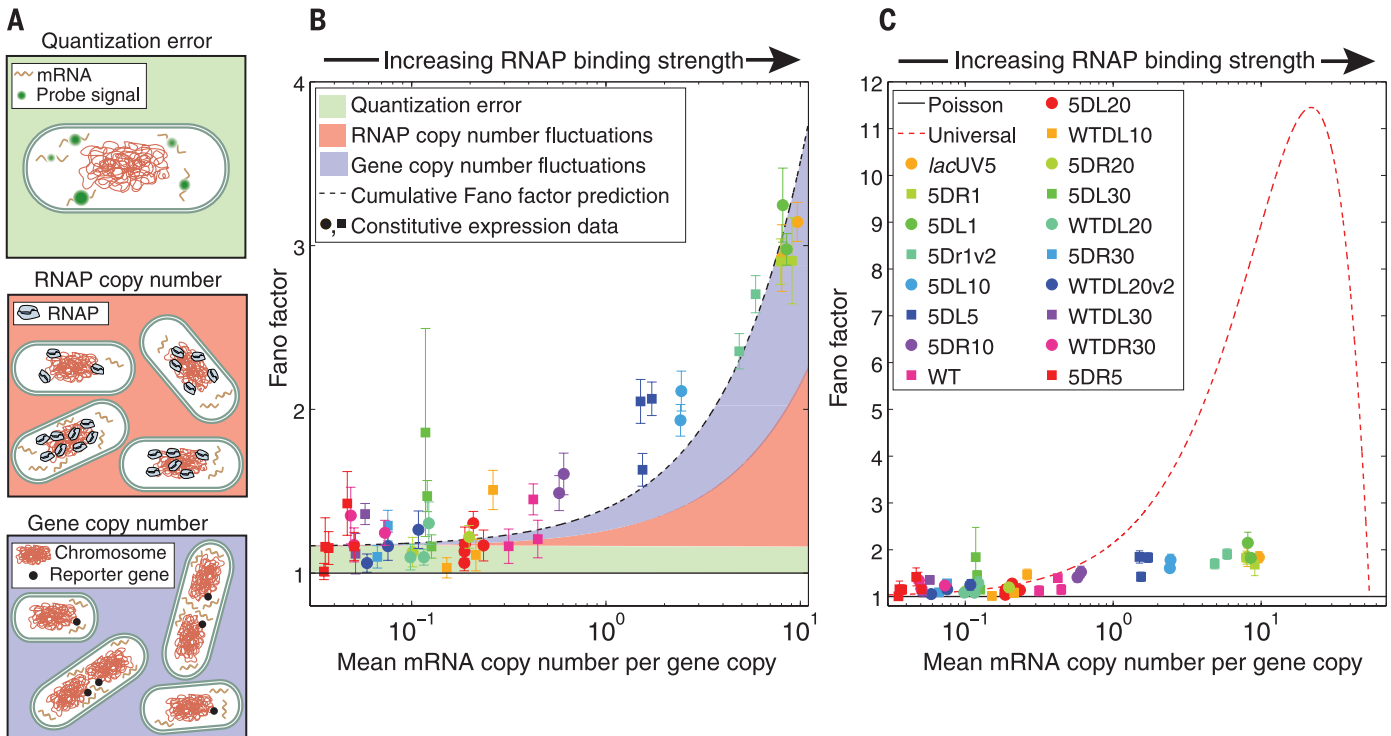
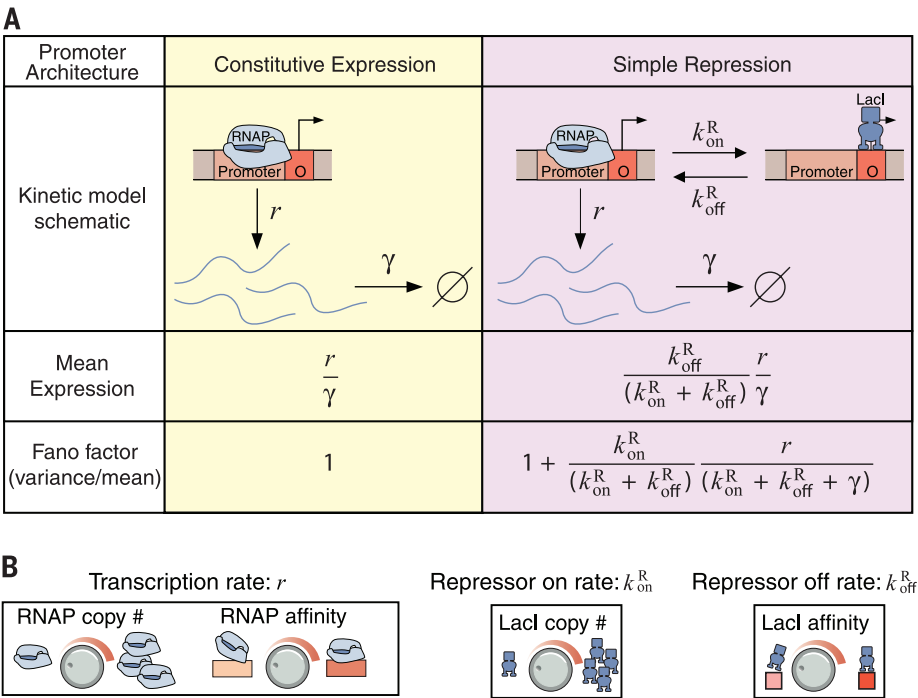


Fig. 2. Variability in gene expression for constitutive expression. (A) Examples of additional noise sources (not accounted for in models of chemical kinetics) present in expression measurements. **(B)** Fano factor (gene copy number variation not subtracted) versus mean expression, plotted for each of 18 constitutive promoters along with estimates of the contributions shown schematically in (A). These factors can account for essentially the entirety of the deviation from Fano = 1. **(C)** Measured Fano

factor for various promoters under constitutive expression, with gene copy number variation subtracted. For reference, the predictions of pure Poissonian production (black solid line) and the “universal noise” curve observed in (5) (red dashed) theories are shown. In (B) and (C), each strain is represented by a unique symbol, and each instance represents repeated measurements with error bars from bootstrap sampling expression measurements of individual cells.

mRNA FISH for 18 unique constitutive promoters (19). In Fig. 2B, we plot the Fano factor versus mean expression for each of this set of promoters (see fig. S9 for full mRNA copy number distributions for each promoter). The solid black line is the prediction resulting from consideration of intrinsic noise alone. The shaded regions represent the effects of what we believe are the three most important additional sources of noise (16). The green shaded region, quantization error, is the variability introduced by our measurement and analysis process. The red shaded region covers the expected contribution from cell-to-cell differences in RNAP copy number; the blue region is the expected contribution from gene copy number variation. Note that the red shaded region is an indirect estimate based on literature sources, whereas the blue and green regions are supported by direct measurements (16). The data and theoretical predictions are in good accord, implying that the dynamics of constitutive transcription are Poissonian with some additional extrinsic noise. In Fig. 2C, we plot the Fano factor minus the predicted gene copy number contribution and observe a quantitative disagreement between the measured noise in expression and the prediction of the “universal” noise model as reported in (5). But to conclusively demonstrate the architecture dependence of the variability, we need to look at alternative regulatory architectures.

To that end, we consider an architecture in which transcription can be blocked by a repressor transcription factor. As shown in Fig. 1A, the promoter transitions from the transcriptionally active (repressor unbound) to inactive state (repressor bound) at rate k_{on}^R , and from the inactive to active state at rate k_{off}^R . The predicted mean expression and Fano factor depend on each of these rates (Fig. 1A, right half); we can tune k_{on}^R by changing the concentration of repressor in the cell, and can tune k_{off}^R by changing the repressor binding site sequence. Note that the predicted relationship between the mean and the Fano factor has a characteristic form depending on which of these rates is being tuned (Fig. 3, A and B, dashed lines).

To test the predicted effect of changing k_{on}^R , we took two of the constitutive promoters described above and placed them under simple repression via a LacI Oid binding site immediately downstream of the promoter (16). The difference in transcription rate for the two constructs is reflected in different values of r/γ . At the same time, we introduced into our cells a genetic circuit enabling inducible control of LacI expression, effectively permitting systematic changes in repressor number. In Fig. 3A, we plot the measured Fano factor as a function of the mean expression over LacI concentrations ranging from ~0 to 50 LacI molecules per cell, for both promoters. In addition, we plot the zero-free-

parameter theoretical prediction for the Fano factor as a function of mean using the measured value of r/γ from the constitutive data and the LacI unbinding rate from (20).

Similarly, we vary k_{off}^R by altering the sequence of the LacI binding site. Holding the RNAP binding site constant (and thus r/γ constant), we created constructs corresponding to four different LacI binding sites (16). At constant repressor concentration (i.e., constant k_{on}^R), tuning mean expression by altering k_{off}^R is predicted to yield a characteristic curve, whereas different repressor concentrations (and hence k_{on}^R values) correspond to distinct instances of this curve. In Fig. 3B, we plot the Fano factor resulting from changing k_{off}^R at each of three different repressor concentrations. We find agreement in the trends between theory and experiment, although this agreement is less good than in the case of tuning k_{on}^R . One possible explanation [reported in (20)] is that changing transcription factor–DNA binding affinity affects the transcription factor–DNA association rate k_{on}^R as well as the dissociation rate k_{off}^R , contrary to our assumption that k_{on}^R is constant along each curve in Fig. 3B. However, the most important outcome of this set of measurements is a demonstration of the qualitatively distinct variability profile when a different set of transcriptional parameters are controlled, illustrating once again the systematic dependence of variability on promoter architecture.

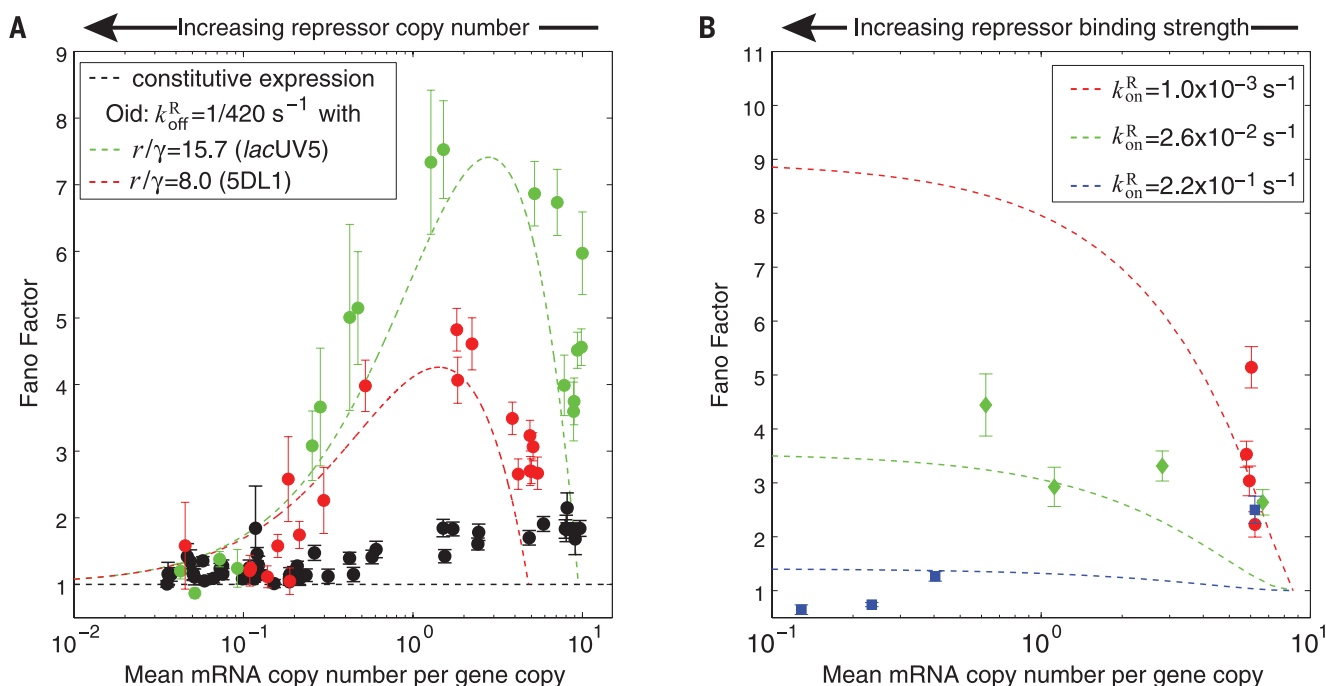


Fig. 3. Variability in gene expression for systematic tuning of repression. (A) Fano factor versus mean mRNA copy number for two promoters (choices of r/γ) while tuning k_{on}^R by inducing LacI to varying levels. For reference, the black data are the constitutive data from Fig. 2. (B) Fano factor versus mean mRNA copy number for *lacUV5* while tuning k_{off}^R by changing repressor binding site identity at fixed repressor copy number; each color represents a different induction condition from red (lowest LacI induction) to blue (highest LacI induction). For both (A) and (B), the

parameter-free predictions from kinetic theory are shown as dashed lines in the corresponding color, holding promoter (r/γ) and (A) repressor binding strength (k_{off}^R) or (B) repressor binding rate (k_{on}^R) constant. In both cases, the Fano factor at a given mean depends on the choice of molecular parameters and agrees with the expectations from theory. The effect of gene copy number variation was subtracted from all data points; error bars result from bootstrap sampling expression measurements of individual cells.

We have shown that transcriptional noise is well predicted by molecularly detailed models for the two most common promoter architectures in *E. coli* as the various genetic knobs are tuned. This agreement is not the result of fitting theory curves to data, because the predicted curves are generated using physical parameter values reported elsewhere in the literature and in that sense are zero-parameter predictions. Earlier reports of “bursty” transcription (5, 21) are based on the observation that the Fano factor is greater than 1 for constitutive mRNA production (as well as direct kinetic measurements). Various explanatory hypotheses have been proposed, including transcriptional silencing via DNA condensation by nucleoid proteins (22), negative supercoiling induced by transcription, or the formation of long-lived “dead-end” initiation complexes (23). Although our data do not rule out these hypotheses, we find that extrinsic noise is sufficient to explain the deviation from Fano = 1 in our constitutive expression data (Fig. 2B). Thus, we find no need to invoke alternative hypotheses to explain the observed “burstiness” of constitutive transcription.

Many interesting earlier experiments make it difficult to interpret differences between promoters and induction conditions in terms of distinct physical parameters because of the wide variety of promoter architectures in play as well as the diverse mechanisms of induction. We have instead taken a “synthetic biology” approach of building promoters from the ground up. By directly controlling aspects of the promoter architecture, our goal has been to directly relate changes in promoter architecture to changes in observed gene expression variability. We believe that this work has demonstrated that mutations in regulatory DNA can alter gene expression noise. This suggests that gene expression noise may be a tunable property subject to evolutionary selection pressure, as mutations in regulatory DNA could provide greater fitness by increasing (or decreasing) variability. Demonstrating the relevance of this hypothesis in natural environments remains an ongoing challenge.

REFERENCES AND NOTES

1. J. Paulsson, M. Ehrenberg, *Phys. Rev. Lett.* **84**, 5447–5450 (2000).
2. A. Sanchez, H. G. Garcia, D. Jones, R. Phillips, J. Kondev, *PLOS Comput. Biol.* **7**, e1001100 (2011).
3. Y. Taniguchi et al., *Science* **329**, 533–538 (2010).
4. W. J. Blake et al., *Mol. Cell* **24**, 853–865 (2006).
5. L. H. So et al., *Nat. Genet.* **43**, 554–560 (2011).
6. H. Salman et al., *Phys. Rev. Lett.* **108**, 238105 (2012).
7. H. Maamar, A. Raj, D. Dubnau, *Science* **317**, 526–529 (2007).
8. A. Eldar, M. B. Elowitz, *Nature* **467**, 167–173 (2010).
9. G. M. Süel, R. P. Kulkarni, J. Dworkin, J. Garcia-Ojalvo, M. B. Elowitz, *Science* **315**, 1716–1719 (2007).
10. M. Thattai, A. van Oudenaarden, *Genetics* **167**, 523–530 (2004).
11. E. Kussell, S. Leibler, *Science* **309**, 2075–2078 (2005).
12. H. Salgado et al., *Nucleic Acids Res.* **41**, D203–D213 (2013).
13. L. Bintu et al., *Curr. Opin. Genet. Dev.* **15**, 125–135 (2005).
14. T. Kuhlman, Z. Zhang, M. H. Saier Jr., T. Hwa, *Proc. Natl. Acad. Sci. U.S.A.* **104**, 6043–6048 (2007).
15. J. M. Vilar, S. Leibler, *J. Mol. Biol.* **331**, 981–989 (2003).

16. See supplementary materials on Science Online.
17. A. Sánchez, J. Kondev, *Proc. Natl. Acad. Sci. U.S.A.* **105**, 5081–5086 (2008).
18. P. S. Swain, M. B. Elowitz, E. D. Siggia, *Proc. Natl. Acad. Sci. U.S.A.* **99**, 12795–12800 (2002).
19. R. C. Brewster, D. L. Jones, R. Phillips, *PLOS Comput. Biol.* **8**, e1002811 (2012).
20. P. Hammar et al., *Science* **336**, 1595–1598 (2012).
21. I. Golding, J. Paulsson, S. M. Zawilski, E. C. Cox, *Cell* **123**, 1025–1036 (2005).
22. A. Sanchez, S. Choubey, J. Kondev, *Annu. Rev. Biophys.* **42**, 469–491 (2013).
23. N. Mitarai, I. B. Dodd, M. T. Crooks, K. Sneppen, *PLOS Comput. Biol.* **4**, e1000109 (2008).

ACKNOWLEDGMENTS

We thank H. J. Lee, C. Wiggins, Y. Lin, X. Zhu, F. Weinert, M. Rydenfelt, R. Milo, H. Garcia, N. Belliveau, and J. Sheung for

useful discussions. Supported by NIH grants DP1 OD000217 (Directors Pioneer Award), R01 GM085286, and 1 U54 CA143869 (Northwestern PSOC Center); La Fondation Pierre Gilles de Gennes (R.P.); and the Donna and Benjamin M. Rosen Center for Bioengineering at Caltech (D.L.J.). Raw microscopy image data are archived in the Phillips laboratory at Caltech and are available upon request.

SUPPLEMENTARY MATERIALS

www.sciencemag.org/content/346/6216/1533/suppl/DC1
Materials and Methods
Supplementary Text
Figs. S1 to S11
Tables S1 to S3
References (24–32)

28 April 2014; accepted 4 November 2014
10.1126/science.1255301

IMMUNE TOLERANCE

Detection of self-reactive CD8⁺ T cells with an anergic phenotype in healthy individuals

Yuka Maeda,¹ Hiroyoshi Nishikawa,^{1*} Daisuke Sugiyama,¹ Danbee Ha,¹ Masahide Hamaguchi,¹ Takuro Saito,¹ Megumi Nishioka,^{1,2} James B. Wing,¹ Dennis Adeegbe,¹ Ichiro Katayama,² Shimon Sakaguchi^{1*}

Immunological tolerance to self requires naturally occurring regulatory T (T_{reg}) cells. Yet how they stably control autoimmune T cells remains obscure. Here, we show that T_{reg} cells can render self-reactive human CD8⁺ T cells anergic (i.e., hypoproliferative and cytokine hypoproducing upon antigen restimulation) in vitro, likely by controlling the costimulatory function of antigen-presenting cells. Anergic T cells were naïve in phenotype, lower than activated T cells in T cell receptor affinity for cognate antigen, and expressed several coinhibitory molecules, including cytotoxic T lymphocyte–associated antigen-4 (CTLA-4). Using these criteria, we detected in healthy individuals anergic T cells reactive with a skin antigen targeted in the autoimmune disease vitiligo. Collectively, our results suggest that T_{reg} cell–mediated induction of anergy in autoimmune T cells is important for maintaining self-tolerance.

Naturally occurring CD25⁺CD4⁺ regulatory T (T_{reg}) cells, which specifically express the transcription factor FoxP3, actively maintain immunological self-tolerance and homeostasis (1). Developmental or functional anomalies of natural T_{reg} cells can cause autoimmune diseases (such as type I diabetes), allergy, and immunopathological diseases (such as inflammatory bowel disease) (2). How T_{reg} cells effectively control potentially hazardous self-reactive T cells in humans remains an open question. In particular, it is unknown whether T_{reg} cell–mediated suppression for a limited period has a critical long-lasting effect on cell fate and antigen reactivity of autoimmune T cells.

To address this issue, we examined proliferation, cytokine production, and cell fate of antigen-

specific CD8⁺ T cells in peripheral blood mononuclear cells (PBMCs) from healthy individuals stimulated in vitro with self-antigen peptide in the presence or absence of natural FoxP3⁺CD25⁺CD4⁺ T_{reg} cells. Melan-A (also known as MART-1) used in the experiments is a self-antigen expressed by normal melanocytes and some melanoma cells and targeted in vitiligo vulgaris, an autoimmune disease of the skin (2–5). In the absence of T_{reg} cells, Melan-A–specific CD8⁺ T cells [detectable by major histocompatibility complex (MHC) tetramers and peptide tetramers] expanded over 10 days from very few cells to a sizable fraction when cultured with peptide-pulsed autologous antigen-presenting cells (APCs) (Fig. 1A) (6). Natural T_{reg} cells, which appeared to be activated by endogenous self-peptides and class II MHC on autologous APCs (7–9), suppressed the expansion of Melan-A tetramer–positive (Tet⁺) CD8⁺ T cells in a dose-dependent manner. Similar stimulation with irrelevant peptide NY-ESO-1, another self- and tumor antigen, failed to induce Melan-A/Tet⁺CD8⁺ T cells. In cultures containing T_{reg} cells,

¹Experimental Immunology, Immunology Frontier Research Center (IFREC-WPI), Osaka University, Osaka 565-0871, Japan. ²Department of Dermatology, Graduate School of Medicine, Osaka University, Osaka 565-0871, Japan.

*Corresponding author. E-mail: shimon@ifrec.osaka-u.ac.jp (S.S.); nisihiro@ifrec.osaka-u.ac.jp (H.N.)

we noted an accumulation of Tet⁺CD8⁺ T cells that had divided once and then stopped further proliferation. This proliferation-aborted population increased in ratio, whereas the population under multiple cell divisions reciprocally decreased, in proportion to the number of added T_{reg} cells. The proliferation-aborted cells had significantly lower tetramer staining intensity than the cells that had vigorously proliferated in the absence of T_{reg} cells (peak a versus b in Fig. 1A, Fig. 1B, and fig. S1). The staining intensity of T cell receptor- $\alpha\beta$ (TCR- $\alpha\beta$) chains was equivalent in both populations, which indicated that the lower tetramer staining intensity was not due to downmodulation of TCR but to lower TCR affinity for the Melan-A peptide, as supported by significantly lower ratios of tetramer versus TCR- $\alpha\beta$ staining

intensities (Fig. 1C). Functionally, they produced reduced levels of cytokines such as interferon- γ (IFN- γ), tumor necrosis factor- α (TNF- α), and interleukin 2 (IL-2) (Fig. 1, D and E), despite the addition of exogenous IL-2 to maintain cultured T cells. Furthermore, upon secondary stimulation, they remained hypoproliferative and produced very low amounts of cytokines (fig. S2). Thus, antigenic stimulation under T_{reg} cell-mediated suppression allows responder T cells with relatively low affinity TCRs for a self-antigen to divide once but prevents their further proliferation, which drives them into a profoundly and stably hypoproliferative and cytokine-hypoproducing state, which can be immunologically defined as “anergy” (10–13).

In contrast with anti-Melan-A responses, CD8⁺ T cells from the same donor, who had detectable

serum anticytomegalovirus (CMV) immunoglobulin G (IgG) antibody, had CMV peptide-specific T cells with a memory phenotype (fig. S3, A to D). CMV-specific CD8⁺ T cells, whether they were in a naïve or memory cell fraction, vigorously proliferated and produced inflammatory cytokines even at a high T_{reg}-to-responder T cell ratio, with no significant differences in CMV tetramer staining intensity among CD8⁺ T cells proliferating in the presence or absence of T_{reg} cells (fig. S3, E to H). However, high numbers of T_{reg} cells completely inhibited the proliferation of polyclonally activated naïve CD8⁺ T cells without allowing a single cell division (fig. S4). The nondividing CD8⁺ T cells proliferated as actively as nonsuppressed cells upon restimulation after removal of T_{reg} cells.

Collectively, T_{reg}-cell dosage, the immunological states of responder T cells (e.g., in a naïve or memory state), and their TCR affinity for cognate antigen contribute to T_{reg} cell-mediated induction of anergy. This is an active process and differs from a mere naïve nonproliferative state.

Microarray gene expression analysis revealed that activated or anergic Tet⁺CD8⁺ T cells or Tet⁺CD8⁺ T cells obtained from T_{reg}-absent or -present cell cultures were substantially different in gene expression profiles (Fig. 2A). As the most striking differences, the transcription of *CTLA4*, encoding the coinhibitory molecule CTLA-4 (14), was significantly up-regulated, whereas *BCL2*, encoding the apoptosis-inhibiting molecule B cell lymphoma-2 (BCL-2) (15), was down-regulated in anergic CD8⁺ T cells, as confirmed by quantitative reverse transcription polymerase chain reaction (RT-PCR) (Fig. 2B). There were no significant differences in the expression of *PDCDI* encoding the coinhibitory molecule PD-1; the genes encoding the anergy-related molecules *GRAIL*, *CBL-B*, and *EGR-2* (16–19); *BAT3*, *TBX21*, and *EOMES*, putative markers for exhausted CD8⁺ T cells (20, 21); and *p27KIP1*, a cyclin-dependent kinase inhibitor. Anergic CD8⁺ T cells did not express FoxP3 (Fig. 2B and fig. S5A). The majority (>90%) of anergic CD8⁺ T cells expressed both CTLA-4 and the chemokine receptor CCR7, which differed from the phenotype of activated or naïve CD8⁺ T cells (Fig. 2, C and D, and fig. S5, B to D) (22, 23). Functionally, during secondary stimulation of anergic Tet⁺CD8⁺ T cells with Melan-A peptide-pulsed APCs after removal of T_{reg} cells, antibody blockade of CTLA-4 and PD-1 at doses enhancing cytokine production by activated conventional T cells failed to rescue proliferation resistance or cytokine hypoproduction of anergic CD8⁺ T cells (fig. S5E) (24). Addition of a high dose of IL-2 induced apoptosis in restimulated Tet⁺CD8⁺ T cells rather than abrogating their hyporesponsiveness. Nevertheless, anergic CD8⁺ T cells were not in the process of immediate apoptosis (fig. S6), despite their lower *BCL2* expression than activated T cells (Fig. 2B). Thus, anergic CD8⁺ T cells induced by T_{reg} cell-mediated suppression are distinct from activated or naïve T cells in gene and protein expression profiles. They also appear to be different from “exhausted” CD8⁺ T cells, which develop as PD-1⁺ hypoproliferative and cytokine-hypoproducing cells

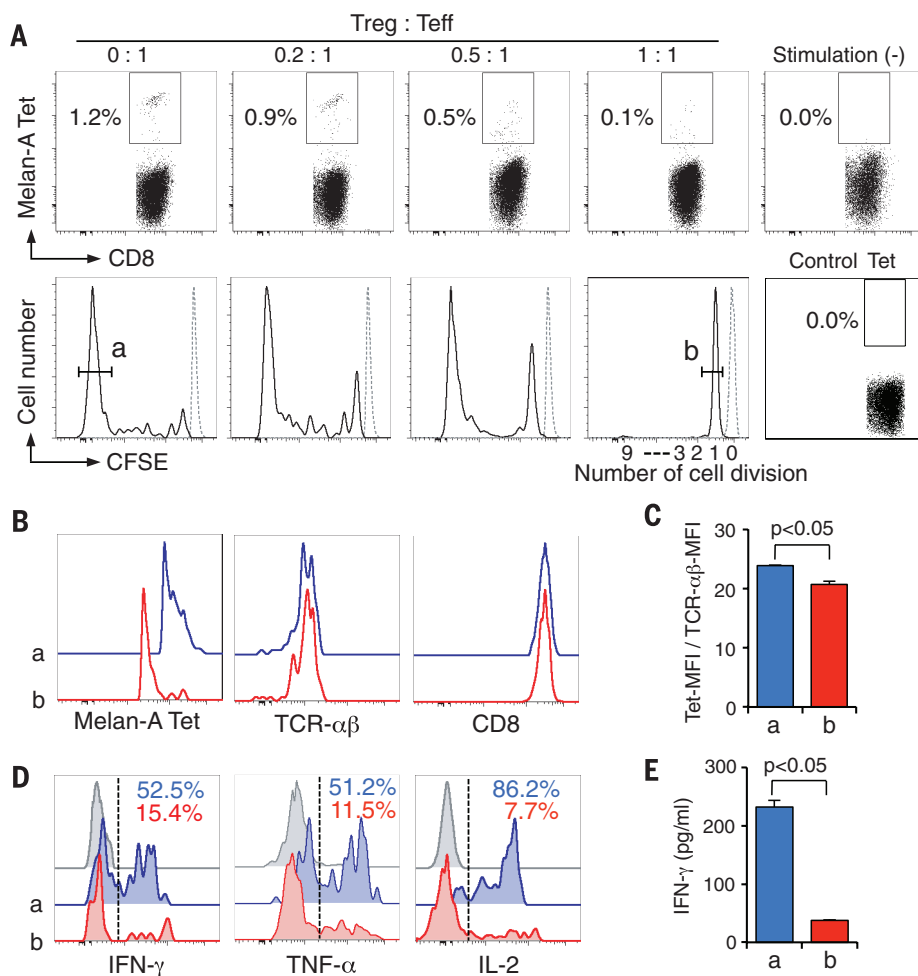


Fig. 1. Natural T_{reg} cells render low-affinity self-reactive CD8⁺ T cells anergic upon antigen stimulation. (A) Melan-A-specific CD8⁺ T cell induction. CFSE-labeled CD8⁺ T cells of HLA-A*0201⁺ healthy individuals were stimulated by T cell-depleted, γ -irradiated, and Melan-A₂₆₋₃₅ peptide-pulsed APCs with graded numbers of CD25^{high}CD4⁺ T_{reg} cells for 10 days (6). Dotted lines mean Tet⁺CD8⁺ cells showing no CFSE dilution. Control tet: NY-ESO-1₁₅₇₋₁₆₅/HLA-A*0201 tetramer. T_{eff} refers to CD8⁺ effector T cells. (B) Tet, TCR- $\alpha\beta$, and CD8 staining of Tet⁺CD8⁺ T cells. Results in (A) and (B) are representative of 10 independent experiments. (C) Relative tetramer staining intensities, calculated as mean fluorescence intensity (MFI) of Tet/MFI of TCR- $\alpha\beta$ staining of Tet⁺CD8⁺ T cells ($n = 5$). (D and E) Cytokine production of Tet⁺CD8⁺ T cells by intracellular staining (D) and enzyme-linked immunosorbent assay (E) (6). Representative result of three independent experiments. The labels a and b in (B) to (E) mean the cell accumulations like a or b in (A). Error bars indicate means \pm SEM. The significance was assessed by Student's two-tailed paired t test.

in chronic viral infections and in tumor tissues, because exhausted CD8⁺ T cells are reportedly CCR7⁺, CD45RA⁺, and BAT3⁺, and their exhaustion can be rescued by a PD-1-blocking antibody (21, 24–26).

T_{reg} cells suppress the activation and/or proliferation of responder T cells (27), at least in part, by down-regulating the expression of the costimulatory molecules CD80 and CD86 on APCs (fig. S7A) (28, 29). To determine whether low expression or down-modulation of CD80 and CD86 on dendritic cells (DCs) was responsible for the induction of antigen-specific anergic CD8⁺ T cells, we stimulated carboxyfluorescein succinimidyl ester (CFSE)-labeled CD8⁺ T cells with autologous immature or mature DCs pulsed with Melan-A

peptide in the presence of graded amounts of CTLA-4-immunoglobulin (CTLA-4Ig), which blocked CD80 and CD86 (fig. S7B) (30). In contrast to the vigorous proliferation of Tet⁺CD8⁺ T cells cultured with mature DCs, the majority of Tet⁺CD8⁺ T cells generated with immature DCs, and some with mature DCs with a high dose (100 µg/ml) of CTLA-4Ig, were proliferation-aborted after one cell division (Fig. 3A). The proliferation-aborted T cells (peaks c and d in Fig. 3A) were lower than proliferating T cells in Melan-A tetramer staining intensity (Fig. 3B), and highly expressed CTLA-4 and CCR7 (fig. S7, C and D); they formed a discrete CTLA-4/CCR7 double-positive population (Fig. 3C and fig. S7E). They produced significantly lower amounts of IFN-γ,

TNF-α, and IL-2 compared with Tet⁺CD8⁺ cells, having proliferated in culture with mature DCs (fig. S7F). Similar to peptide stimulation, polyclonal antibody against CD3-specific monoclonal antibody (mAb) stimulation of CTLA-4⁺ naïve CD8⁺ T cells in the presence of CTLA-4Ig produced cells that were proliferation-aborted after one cell division (fig. S8A). Notably, increasing CTLA-4Ig dose proportionally intensified CTLA-4 expression by the aborted cells, while stably maintaining their high CCR7 expression (fig. S8, A and B). Taken together, antigen presentation with low CD80 and CD86 costimulation is able to drive CD8⁺ T cells to differentiate into CTLA-4⁺CCR7⁺ anergic cells. DCs with moderate CD80 and CD86 reduction can concurrently generate both

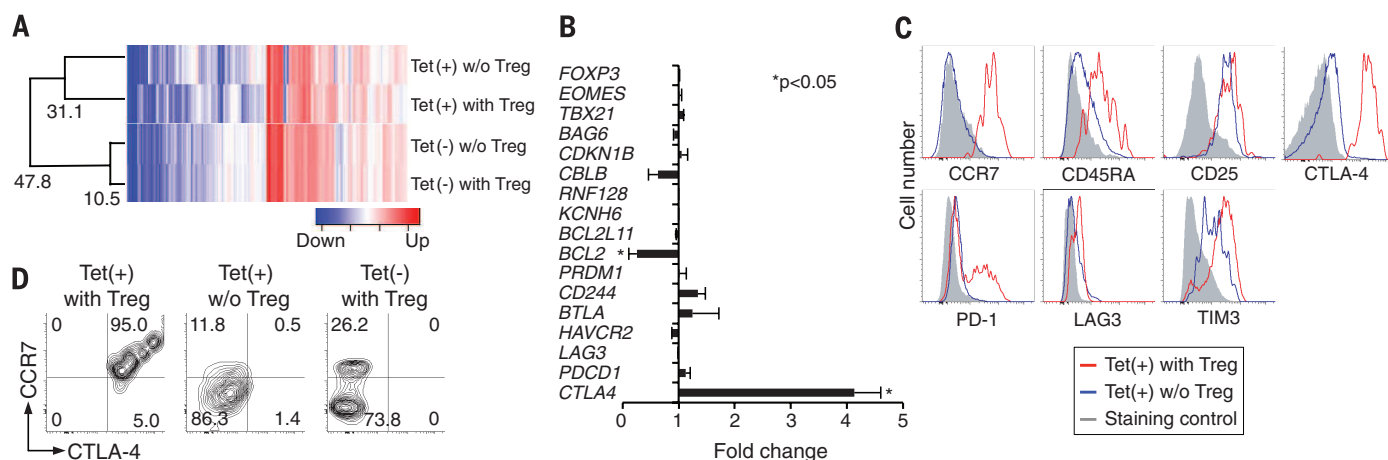


Fig. 2. Distinct phenotype and function of anergic CD8⁺ T cells produced by T_{reg} cell suppression. (A) Global mRNA expression profile. Tet⁺CD8⁺ T cells induced at CD8⁺ T cells: T_{reg} cell ratios of 1:0.5 and 1:0 were subjected to microarray analyses. Gene expression reportedly associated with CD8⁺ T cell function was compared among the indicated four groups and expressed as a heat map. Correlation distances shown were calculated by h-clust (6). Representative of two independent experiments. (B) mRNA expression measured by

quantitative real-time PCR. Fold changes of mRNA level as [Tet(+)/with T_{reg}] versus [Tet(+)/without T_{reg}] in five independent experiments are shown. Error bars indicate means ± SEM. (C and D) Expression of cell surface molecules by Tet⁺CD8⁺ T cells induced at CD8⁺ T cells: T_{reg} cell ratios, 1:1 and 1:0. Representative histogram staining pattern (C) and contour plot staining pattern of CTLA-4 and CCR7 (D). Data are representative of five independent experiments (*n* = 10). The significance was assessed by Student's two-tailed paired *t* test.

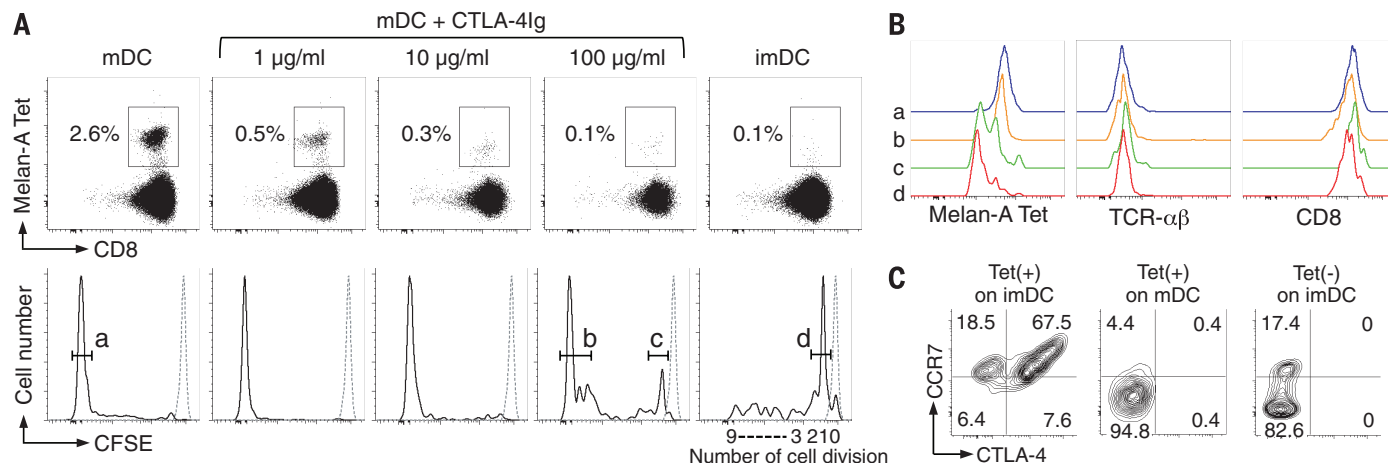


Fig. 3. DC expression of CD80 and CD86 controls the generation of CTLA-4⁺CCR7⁺ low-affinity anergic self-reactive T cells. (A) Melan-A-specific CD8⁺ T cell induction. CFSE-labeled CD8⁺ T cells of HLA-A*0201⁺ healthy individuals were stimulated with γ-irradiated, Melan-A₂₆₋₃₅ peptide-pulsed monocyte-derived immature or mature DCs. CTLA-4Ig was added into mature DCs cultures at indicated concentrations (6). (B) Tet, TCR-αβ, and CD8 staining intensity of Tet⁺CD8⁺ T cells shown in (A). (C) Representative contour plot staining pattern of Tet⁺ or Tet⁺CD8⁺ T cells shown in (A) for CTLA-4 and CCR7. Data in (A) to (C) are representative of five independent experiments.

activated T cells and anergic T cells, in part, depending on TCR affinity.

The above *in vitro* findings prompted us to ask whether healthy individuals harbored such anergic self-reactive CD8⁺ T cells. Direct *ex vivo* staining of CD8⁺ T cells in PBMCs of healthy donors ($n = 10$) for Melan-A peptide and MHC tetramer, with CD8⁺ T cells from vitiligo patients ($n = 10$) as a positive control, revealed that a small number of Tet⁺CD8⁺ T cells were indeed present in healthy individuals and constituted ~0.03% of CD8⁺ T cells in PBMCs, which contrasted with high percentages (~0.1%) in vitiligo patients (Fig. 4, A and B) (6). Two-thirds of the former had a naïve

(CCR7⁺CD45RA⁺) phenotype, whereas the majority of the latter had an effector or memory phenotype (Fig. 4C and fig. S9A) (4, 5). The Tet⁺CD8⁺ T cells from healthy individuals had significantly lower tetramer staining intensity than those from vitiligo patients (Fig. 4, D and E). They expressed CTLA-4 at higher levels than Tet⁺CD8⁺ T cells from vitiligo patients or Tet⁺CD8⁺ T cells from healthy individuals, or activated CD8⁺ T or natural T_{reg} cells (Fig. 4F and fig. S9, B to D), and ~90% of the Tet⁺CD45RA⁺CD8⁺ cells were double positive for CTLA-4 and CCR7 (Fig. 4G and fig. S9B). Functionally, Tet⁺CD8⁺ T cells directly prepared from healthy donors scarcely

produced IFN- γ , TNF- α , or IL-2, contrasting with active cytokine production by naïve Tet⁺CD8⁺ T cells (Fig. 4H) or Melan-A-specific CD8⁺ T cells from vitiligo patients (4, 37).

To determine further the function of these anergic T cells, we cocultured CTLA-4⁺ and CTLA-4⁻ fractions of naïve (CCR7⁺CD45RA⁺) CD8⁺ T cells from healthy individuals and assessed the proliferative activity of Tet⁺CD8⁺ T cells present in each fraction (Fig. 4I). The CTLA-4⁺ fraction, which constituted less than 10% of naïve CD8⁺ T cells in healthy donors, contained the majority (~95%) of Melan-A Tet⁺CD8⁺ T cells before stimulation (Fig. 4, I to K). These CTLA-4⁺Tet⁺ cells were

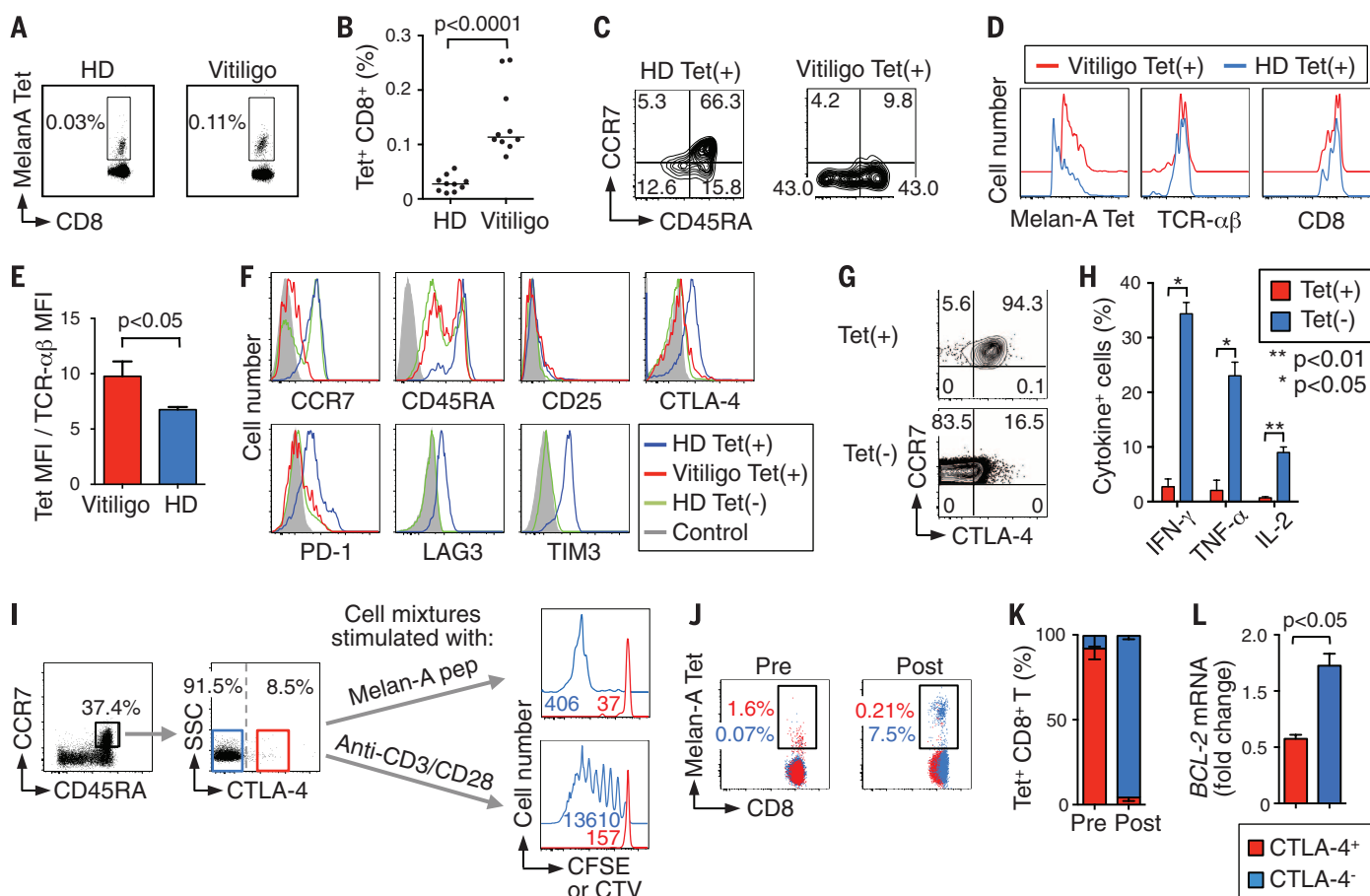


Fig. 4. Detection of low-affinity anergic self-reactive CTLA-4⁺CCR7⁺CD8⁺ T cells in healthy individuals. (A) Melan-A-Tet⁺CD8⁺ T cells in PBMCs of a healthy donor (HD) and a vitiligo patient. (B) Percentages of Tet⁺CD8⁺ T cells in HDs and vitiligo patients ($n = 10$). (C) CCR7 and CD45RA expression by Tet⁺CD8⁺ T cells in an HD and a vitiligo patient. (D) Tet, TCR- $\alpha\beta$, and CD8 staining intensity of Tet⁺CD8⁺ T cells in an HD and a vitiligo patient. (E) Ratios of MFI of tetramer staining to MFI of TCR- $\alpha\beta$ staining in Tet⁺CD8⁺ T cells in HDs and vitiligo patients ($n = 4$ each). (F) Expression of cell surface molecules by Tet⁺ or Tet⁻CD8⁺ T cells in a representative HD and a vitiligo patient. (G) Representative staining for CTLA-4 and CCR7 of Tet⁺ or Tet⁻ cells in CD45RA⁺CD8⁺ T cells of an HD. Data shown in (A), (C), (D), (F), and (G) are representative of four independent experiments. (H) Cytokine production by Tet⁺CD8⁺ T cells in HDs assessed by intracellular staining with CCR7⁺CD45RA⁺Tet⁺CD8⁺ T cells as control. Data summarize four independent experiments. (I) Proliferation and cytokine production of CTLA-4⁺ or CTLA-4⁻ naïve CD8⁺ T cells in HDs. CCR7⁺CD45RA⁺CD8⁺ T cells

from HD PBMCs were further separated into CTLA-4⁺ and CTLA-4⁻ cells, labeled with Cell Trace Violet (CTV) or CFSE, respectively, mixed at a 1:1 ratio, stimulated with Melan-A₂₆₋₃₅ peptide-pulsed APCs for 10 days (top) or CD3/CD28-specific mAb for 5 days (bottom), and assessed for proliferation by CTV or CFSE dilution (red and blue, respectively) (6). Numbers in right two figures represent the numbers of cells in each cell fraction. SSC, side scatter. (J) Representative tetramer staining of the cell mixtures before (Pre) and after (Post) Melan-A₂₆₋₃₅ peptide stimulation for 10 days. Numbers represent percentages of Tet⁺CD8⁺ cells in the CTLA-4⁺ or CTLA-4⁻ fraction (red and blue, respectively). (K) Percentages of Tet⁺CD8⁺ T cells in the CTLA-4⁺ (red) or CTLA-4⁻ (blue) fraction in the cell mixtures before (Pre) and after (Post) cell culture as shown in (I) and (J). (L) BCL2 mRNA expression of CTLA-4⁺CCR7⁺CD45RA⁺Tet⁺CD8⁺ and CTLA-4⁻CCR7⁺CD45RA⁺Tet⁺CD8⁺ T cells measured by quantitative real-time PCR. Data in (I) to (L) are representative of at least three independent experiments. Error bars indicate means \pm SEM. The significance was assessed by Student's two-tailed paired *t* test.

hypoproliferative, low in *BCL2* expression, and prone to die upon Melan-A stimulation (Fig. 4, I to L). In contrast, the CTLA-4⁻ fraction, which initially contained fewer than 5% of total Tet⁺CD8⁺ T cells, gave rise to proliferating Tet⁺CD8⁺ T cells, which made up ~95% of total Tet⁺CD8⁺ T cells after stimulation (Fig. 4, I to K). In addition, polyclonal stimulation of the cell mixtures with CD3-specific and CD28-specific mAb revealed that the CTLA-4⁺ fraction as a whole was hypoproliferative (Fig. 4I) and cytokine hypoproducing (fig. S9E), in contrast with active proliferation and cytokine production of the CTLA-4⁻ fraction.

These results collectively indicate that healthy individuals harbor at least two distinct populations of self-reactive CD8⁺ T cells: one that is functionally anergic and expresses CTLA-4 and CCR7 and another that is CTLA-4⁻ and naïve in function and phenotype. The latter, especially those with high-affinity TCRs, may become activated and expand upon self-antigen stimulation in the absence or reduction of natural T_{reg} cells, as shown in Fig. 1A.

Thus, anergic self-reactive T cells, which are phenotypically distinct from other T cells, are physiologically present in the immune system. They appear to be generated, at least in part, as a result of T_{reg}-mediated suppression, which can determine cell fate of responder T cells (i.e., activated, anergic, or ignorant) upon antigenic stimulation, depending on the number and suppressive activity of T_{reg} cells, the TCR affinity and differentiation states of responder T cells, and the condition of APCs. This T_{reg}-dependent switching of re-

sponder T cell fate can be a key target in controlling autoimmunity and tumor immunity, as illustrated by our analysis of Melan-A-specific immune responses, as well as a variety of other physiological and pathological immune responses.

REFERENCES AND NOTES

1. S. Sakaguchi, *Nat. Immunol.* **6**, 345–352 (2005).
2. P. G. Coulie et al., *J. Exp. Med.* **180**, 35–42 (1994).
3. Y. Kawakami et al., *Proc. Natl. Acad. Sci. U.S.A.* **91**, 6458–6462 (1994).
4. G. S. Ogg, P. Rod Dunbar, P. Romero, J. L. Chen, V. Cerundolo, *J. Exp. Med.* **188**, 1203–1208 (1998).
5. M. J. Pittet et al., *J. Exp. Med.* **190**, 705–716 (1999).
6. Materials and methods are available as supplementary materials on Science Online.
7. M. Itoh et al., *J. Immunol.* **162**, 5317–5326 (1999).
8. C. S. Hsieh, H. M. Lee, C. W. Lio, *Nat. Rev. Immunol.* **12**, 157–167 (2012).
9. T. Yamaguchi et al., *Proc. Natl. Acad. Sci. U.S.A.* **110**, E2116–E2125 (2013).
10. M. K. Jenkins, R. H. Schwartz, *J. Exp. Med.* **165**, 302–319 (1987).
11. R. H. Schwartz, *Annu. Rev. Immunol.* **21**, 305–334 (2003).
12. F. Macián, S. H. Im, F. J. García-Cózar, A. Rao, *Curr. Opin. Immunol.* **16**, 209–216 (2004).
13. A. D. Wells, *J. Immunol.* **182**, 7331–7341 (2009).
14. A. H. Sharpe, G. J. Freeman, *Nat. Rev. Immunol.* **2**, 116–126 (2002).
15. P. E. Czabotar, G. Lessene, A. Strasser, J. M. Adams, *Nat. Rev. Mol. Cell Biol.* **15**, 49–63 (2014).
16. N. Anandasabapathy et al., *Immunity* **18**, 535–547 (2003).
17. M. S. Jeon et al., *Immunity* **21**, 167–177 (2004).
18. D. L. Mueller, *Nat. Immunol.* **5**, 883–890 (2004).
19. Y. Zheng, Y. Zha, G. Driessens, F. Locke, T. F. Gajewski, *J. Exp. Med.* **209**, 2157–2163 (2012).
20. M. A. Paley et al., *Science* **338**, 1220–1225 (2012).
21. M. Rangachari et al., *Nat. Med.* **18**, 1394–1400 (2012).

22. F. Sallusto, D. Lenig, R. Förster, M. Lipp, A. Lanzavecchia, *Nature* **401**, 708–712 (1999).
23. M. A. Williams, M. J. Bevan, *Annu. Rev. Immunol.* **25**, 171–192 (2007).
24. D. L. Barber et al., *Nature* **439**, 682–687 (2006).
25. S. D. Blackburn et al., *Nat. Immunol.* **10**, 29–37 (2009).
26. E. J. Wherry, *Nat. Immunol.* **12**, 492–499 (2011).
27. E. M. Shevach, *Immunity* **30**, 636–645 (2009).
28. K. Wing et al., *Science* **322**, 271–275 (2008).
29. O. S. Qureshi et al., *Science* **332**, 600–603 (2011).
30. J. A. Bluestone, E. W. St. Clair, L. A. Turka, *Immunity* **24**, 233–238 (2006).
31. K. S. Lang et al., *J. Invest. Dermatol.* **116**, 891–897 (2001).

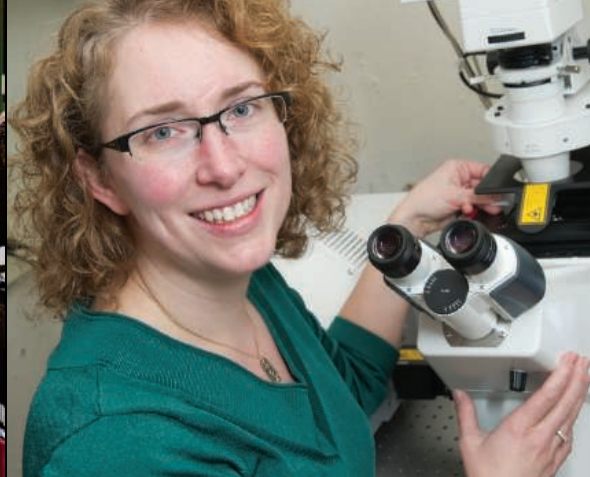
ACKNOWLEDGMENTS

We thank Y. Tada, K. Teshima, and Y. Funabiki for technical assistance. The data presented in this paper are tabulated in the main paper and in the supplementary materials. Microarray data are deposited in GSE63129. This study was supported by Grants-in-Aid for Specially Promoted Research (to S.S., no. 20002007) and for Scientific Research (i) (to S.S., no. 26253030) and (ii) (to H.N., no. 23300354 and 26290054) from the Ministry of Education, Culture, Sports, Science, and Technology of Japan; Core Research for Evolutional Science and Technology (CREST) from Japan Science and Technology Agency (to S.S.); Health and Labor Sciences Research Grants, Research on Applying Health Technology (H24-Clinical Cancer Research-general-006 to H.N.) from the Ministry of Health, Labor, and Welfare, Japan, the Cancer Research Institute CLIP grant to H.N. All authors have no competing financial interest.

SUPPLEMENTARY MATERIALS

www.sciencemag.org/content/346/6216/1536/suppl/DC1
Materials and Methods
Supplemental Text
Figs. S1 to S9
References (32–37)

21 October 2014; accepted 20 November 2014
10.1126/science.aaa1292



Northeastern University, a global, experiential, research university, seeks an enterprising and energetic leader for the position of **Provost and Senior Vice President for Academic Affairs.**

Northeastern is a university on the move. Since 2006, it has hired 442 new tenure-line faculty and will add 200 more by fall 2017. Over the past eight years, external research funding has more than doubled, and today the university is home to eight national research centers. Construction is currently under way for a new 220,000-square-foot Interdisciplinary Science and Engineering Complex.

The world's recognized leader in cooperative education—the integration of classroom study with professional experience—Northeastern's undergraduate enterprise has never been stronger.

The university continues to receive a record-breaking number of applications each year, and the mean two-part SAT score of this year's freshman class is 1413. Students now have opportunities to work, study, and conduct research in 128 countries.

Today, Northeastern is a top-ranked national university with a focus on innovation in higher education. In addition to its main campus in Boston, regional campuses in Charlotte and Seattle (and in Silicon Valley this January) form the basis of a new Global Network designed to expand the reach of Northeastern's education and research.

The university's finances are strong, its location is highly attractive for students and faculty alike, and it possesses the space for continued growth. Above all, Northeastern has the leadership, momentum, and ambition to maintain its impressive trajectory.

Working closely with the president and a highly collaborative senior leadership team, Northeastern's next provost will leverage the university's energy and lead the deans and faculty, as well as Northeastern's academic programs and distinctive learning model, to the forefront of global higher education.

northeastern.edu

Northeastern University has retained the services of Isaacson, Miller to assist with this search. Nominations, applications, and inquiries should be sent in confidence to: John Isaacson, Chair, Heather Brome, Senior Associate; Isaacson Miller, Inc., 263 Summer Street, 7th Floor, Boston, MA 02210. To apply, please visit www.imsearch.com/5169

Northeastern University is an Equal Opportunity, Affirmative Action Educational Institution and Employer, and Title IX University. Northeastern University particularly welcomes applications from minorities, women, and persons with disabilities. Northeastern University is an E-Verify Employer.



Northeastern University

Fidelity amplified.

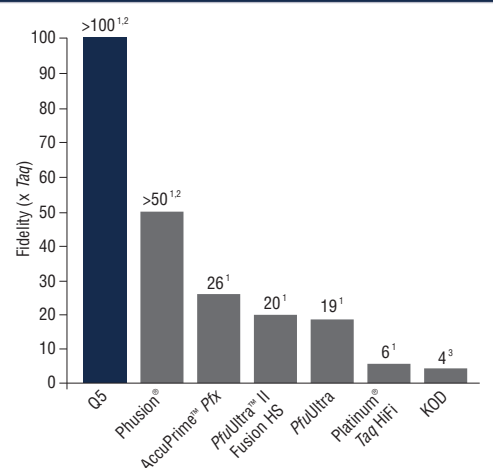
Q5[®] High-Fidelity DNA Polymerase

Q5 High-Fidelity DNA Polymerase sets a new standard for both fidelity and performance. With the highest fidelity amplification available (>100X higher than *Taq*), PCR with Q5 DNA Polymerase results in ultra-low error rates. Its unique buffer system provides superior performance for a broad range of amplicons, regardless of GC content. Q5 DNA Polymerase represents the finest in fidelity.

Request a free sample*
at www.Q5PCR.com

NEW ENGLAND BIOLABS[®], NEB[®] and Q5[®] are registered trademarks of New England Biolabs, Inc. PHUSION[®] is a registered trademark and property of Thermo Fisher Scientific. Phusion[®] DNA Polymerase was developed by Finnzymes Oy, now a part of Thermo Fisher Scientific. PFUULTRA[™] is a trademark of Agilent Technologies, Inc. PLATINUM[®] is a registered trademark of Life Technologies, Inc. ACCUPRIME[™] is a trademark of Life Technologies, Inc.

The highest fidelity amplification available



¹ PCR-based mutation screening in *lacZ* (NEB), *lacI* (Agilent) or *rpsL* (Life)

² Due to the very low frequency of misincorporation events being measured, the error rate of high-fidelity enzymes like Q5 is difficult to measure in a statistically significant manner. Although measurements from assays done side-by-side with Taq yield Q5 fidelity values from 100-200 X Taq, we report ">100X Taq" as a conservative value.

³ Takagi et al (1997) Appl. Env. Microbiol. 63, 4504-4510.

Anhui Sanlian University

One of the first private universities in China
The first private university in Anhui Province

As a private university approved by the Ministry of Education of PRC, Anhui Sanlian University (ASU) has devoted herself to public welfare. The University has thirty undergraduate specialties such as prevention engineering of road traffic accident, digital media technology and nursing etc., and three collaborative innovation centers including traffic safety, service robot and digital art.



ASU warmly invites universities and institutions at home and abroad to collaborate with us to set up:

1. a Joint Traffic Safety Research Center;
2. a Joint Robot Research Center.

ASU warmly invites high-quality educational resources from abroad to collaborate with us to set up an International Nursing College.

[Http://www.slu.edu.cn](http://www.slu.edu.cn) E-mail: yb@slu.edu.cn

[Http://weibo.com/ahsanlian](http://weibo.com/ahsanlian) Fax: 86+0551+63830755 Phone: 86+0551+63830766





Congratulations to the 2014 Winners

Larry Smarr

**Black Holes and
Supercomputing**

R. Preston McAfee,
Paul Milgrom, and
Robert Wilson

Auction Design

Saul Schanberg, Cynthia
Kuhn, Gary Evoniuk, and
Tiffany Field

Rat and Infant Massage

The Golden Goose Award honors federally funded researchers whose work may have seemed odd or obscure when it was conducted but which led to major breakthroughs and significant societal benefit.

**Nominations for 2015 are
now being accepted.**

www.goldengooseaward.org



Join the Conversation!

Twitter is a great way to connect with AAAS members and staff about the issues that matter to you most. Be a part of the discussion while staying up-to-date on the latest news and information about your personal member benefits.

**Follow us @AAASmember
and join the conversation
with #AAAS**



The Art and Science of Traditional Medicine

Part 1: TCM Today – A Case for Integration



Sponsored by



北京中医药大学
BEIJING UNIVERSITY OF CHINESE MEDICINE



香港浸會大學
HONG KONG BAPTIST UNIVERSITY



This is the start of something big.

ScienceAdvances |  AAAS
SIGNIFICANT RESEARCH, GLOBAL IMPACT

Introducing *Science Advances* – the new, online-only, open-access journal from *Science* and AAAS. Find out how you can be among the first authors published at **scienceadvances.org**.



Contents

In this first installment of a three part series, “The Art and Science of Traditional Medicine,” we present a series of articles making a case for the integration of traditional Chinese medicine (TCM) into modern medical practice. From the new WHO Traditional Medicine Strategy to the application of systems biology in studying TCM, we aim to highlight the potential for creating an integrated, network-based health care system. The next two issues will cover herbal genomics and highlight the importance of quality control, standardization, regulation, and safety for traditional therapies. An overview of indigenous medicines in Europe, Africa, the Middle East, India, and the Americas will also be provided.

Editorial Team

Tai-Ping Fan, Ph.D. (Guest project editor)
University of Cambridge, UK

Josephine Briggs, M.D.
National Center for Complementary & Alternative Medicine, NIH, USA

Liang Liu, M.D., Ph.D.
Macau University of Science & Technology, Macau SAR, China

Aiping Lu, M.D., Ph.D.
Hong Kong Baptist University, Hong Kong SAR, China

Jan van der Greef, Ph.D.
University of Leiden and TNO, The Netherlands

Anlong Xu, Ph.D.
Beijing University of Chinese Medicine, China

Editor: Sean Sanders, Ph.D.

Assistant Editor: Tianna Hicklin, Ph.D.

Proofreader/Copyeditor: Yuse Lajiminmuhip

Designer: Amy Hardcastle

Bill Moran, Global Director
Custom Publishing
bmoran@aaas.org
+1-202-326-6438

Ruolei Wu, Associate Director, Asia
Custom Publishing
rwu@aaas.org
+86-186-0082-9345

Forewords

- S2 **Supporting the integration and modernization of traditional medicine**
Margaret Chan, M.D.
- S3 **A middle way for traditional medicine**
Alan Leshner, Ph.D.
Science/AAAS
- S4 **Message from the editorial team**

Articles

- S5 **The WHO Traditional Medicine Strategy 2014–2023: A perspective**
- S7 **A global scientific challenge: Learning the right lessons from ancient healing practices**
- S10 **East is East and West is West, and never the twain shall meet?**
- S13 **Zheng: A systems biology approach to diagnosis and treatments**
- S16 **Integrated network-based medicine: The role of traditional Chinese medicine in developing a new generation of medicine**
- S19 **The hunt for antifibrotic and profibrotic botanicals**
- S21 ***i*-Needle: Detecting the biological mechanisms of acupuncture**
- S23 **Purinergic signaling in acupuncture**

The content contained in this special, sponsored section was commissioned, edited, and published by the *Science*/AAAS Custom Publishing Office. It was not peer-reviewed or assessed by the Editorial staff of the journal *Science*; however, all manuscripts have been critically evaluated by an international editorial team consisting of experts in traditional medicine research selected by the project editor. The intent of this section is to provide a means for authors from institutions around the world to showcase their state-of-the-art traditional medicine research through review/perspective-type articles that highlight recent progress in this burgeoning area. The editorial team and authors take full responsibility for the accuracy of the scientific content and the facts stated. Articles can be cited using the following format: [Author Name(s)], *Science* **346** (6216 Suppl), Sxx-Sxx (2014).



Supporting the integration and modernization of traditional medicine

Nearly a quarter of all modern medicines are derived from natural products, many of which were first used in a traditional medicine context.

Traditional medicine (TM) holds great potential to improve people's health and wellness. It is an important, yet often underestimated, part of health care. TM is found in almost every country in the world and the demand for its services is increasing every day. TM can contribute to addressing a number of global health challenges of the 21st Century, in particular in the area of chronic, noncommunicable diseases and population aging.

TM is often seen as more accessible, more affordable, and more acceptable to people and can therefore also represent a tool to help achieve universal health coverage. It is commonly used in large parts of Africa, Asia, and Latin America. For many millions of people, often living in rural areas within developing countries, herbal medicines, traditional treatments, and traditional practitioners are the main—and sometimes the only—source of health care. The affordability of most traditional medicines makes them all the more attractive at a time of soaring health care costs and widespread austerity.

In wealthy countries, TM meets an additional set of needs. People increasingly seek natural products and want to have more control over their health. They turn to TM to relieve common symptoms, improve their quality of life, and protect against illness and diseases in a holistic, nonspecialized way.

Incidentally, nearly a quarter of all modern medicines are derived from natural products, many of which were first used in a traditional medicine context. TM is thus a resource for primary health care, but also for innovation and discovery.

However, TM needs rigorous, scientific data to demonstrate its efficacy. It also needs evidence-based standards for quality and safety evaluation to support its appropriate regulation. I am happy to see included in this special feature of *Science* magazine, a series of perspectives on TM from a global team of experts, and would like to encourage more views to be shared and more robust research to be conducted in the area of TM in the future.

The general situation concerning the global use of TM was recently disseminated through the WHO Traditional Medicine Strategy 2014–2023. It makes clear that, to move into mainstream medicine on an equally trusted footing, TM needs a stronger evidence base. The need for stronger regulatory control covers not only the products, but also extends across the practice and practitioners. Updating and enhancing the strategy has allowed WHO to acquire a better understanding of how to boost the global integration of TM into health systems, to benefit individuals seeking the right care, from the right practitioner, at the right time.

The two systems of traditional and Western medicine need not clash. Within the context of primary health care, they can blend together in beneficial harmony, taking advantage of the best features of each system and compensating for certain weaknesses in each as well. In an ideal world, TM would be an option, a choice, offered by a well-functioning, people-centred health system that balances curative services with preventive care. The challenge is to give TM its appropriate place in an integrated health system, to help all practitioners understand its unique and valuable contribution, and to educate consumers about what it can and cannot do. In other words, we need to modernize this rich resource and cultural heritage, and put it in its proper place in today's world.

Margaret Chan, M.D.
Director-General, World Health Organization



A middle way for traditional medicine

Traditional medicine researchers are applying modern 'omics and the latest technologies in an attempt to standardize traditional treatments.

In discussions surrounding traditional healing techniques, a common perception is that those in the West most often take a reductionist approach to medicine, breaking down the body into ever-smaller parts in order to understand its inner workings. In the East, by contrast, medical practitioners are seen to take a more holistic view, regarding the body as a complex, integrated system and treating it as such.

At some point in the past, these two philosophies were certainly at odds. However, this seems less so to be the case today. The line between Eastern and Western medicine is blurring as “alternative” healing practices such as acupuncture, meditation, and yoga have become popularized in the West, and as evidence-based science finds a foothold in the East, particularly in the realm of drug discovery and development.

The rise of systems biology as a discipline, starting around five decades ago but gaining sharply in acceptance and popularity in the last 20 years, has created a slow but unambiguous shift in the Western research paradigm. Reductionism, although still a respected philosophy, is no longer consistently the preeminent methodology of choice in biological research. Researchers around the world are coming around to the notion that, while we can learn much from understanding the finest details at a molecular level, particularly when it comes to treating disease, a deeper knowledge of the interactions between systems and networks is essential.

Conversely, taking a purely holistic approach can produce its own challenges. This is particularly true when quality control of medicinal products and reproducibility of results comes into question. No matter the weight of historical, anecdotal data, drug regulatory agencies such as the U.S. Food and Drug Administration (FDA) will not allow new therapeutics for human treatment without verifiable scientific evidence. Although there are many challenges inherent in meeting this requirement, traditional medicine researchers are applying modern 'omics and the latest technologies in an attempt to standardize traditional treatments, especially through identification and isolation of bioactive compounds and careful analysis of their levels and activities in various herbal remedies.

In Buddhism, the Middle Way is described as the route to enlightenment—a path found by balancing opposing views, accepting neither extreme, but rather investigating both sides and finding a middle ground. Perhaps a Middle Way can be found for traditional medicine, one that takes the best of East and West and brings them together for the benefit of all.

Alan Leshner, Ph.D.
CEO, AAAS
Executive Publisher, *Science*

Integrating traditional medicine into modern health care



Tai-Ping Fan, Ph.D.
(Guest project editor)
University of Cambridge,
UK



Josephine Briggs, M.D.
National Center for
Complementary &
Alternative Medicine,
NIH, USA



Liang Liu, M.D., Ph.D.
Macau University of
Science & Technology,
Macau SAR, China



Aiping Lu, M.D., Ph.D.
Hong Kong Baptist
University,
Hong Kong SAR, China



Jan van der Greef, Ph.D.
University of Leiden and
TNO,
The Netherlands



Anlong Xu, Ph.D.
Beijing University of
Chinese Medicine,
China

Almost every culture has its distinct herbal traditions, each with its indigenous plants and unique practices. But one premise unites them all—herbs have remarkable properties that make them a source of potentially powerful medicines.

Thanks to early explorers like Marco Polo (1254–1324), *materia medica* has been travelling between East and West for centuries. It is now important for us to harness the traditional medicines from across the globe. In Britain, the rich history of traditional medicine use was given credence in the early 1500s by the Herbalists Charter of Henry the VIII (1491–1547). His contemporary in China, Li Shizhen (1518–1593) was a great naturalist who spearheaded a 40-year research project that led to the publication of *Bencao Gang Mu*, a pharmacopoeia and also a treatise on botany, zoology, mineralogy, and metallurgy.

To make the case that traditional medicine has valuable insights for modern society, an independent editorial team was gathered consisting of experts in a range of topics related to traditional medicine research. This team compiled a unique collection of state-of-the-art perspectives from global experts on traditional medicine research, the first installment of which is presented in this special feature. Further exciting articles will be published early in 2015.

We have chosen traditional Chinese medicine (TCM) to illustrate the art and science behind the ancient practice of holistic healing, and how the good practices of quality control, pharmacology and toxicology testing, carefully designed clinical studies, and proper regulation are applicable to all traditional medicines.

This first issue introduces the WHO Traditional Medicine Strategy (2014–2023), highlighting the global scientific challenges and showing how a systems biology approach can be applied to diagnosis, leading to integrated network-based medicine. Recent advances in mechanistic studies of acupuncture are also discussed. Some of the exciting areas in TCM research include the therapeutic potential of herbal remedies against influenza, cancer, diabetes, and cardiovascular diseases; the exploration of gut microbiota-targeted dietary interventions against chronic inflammation; and the study of the biological activities of complex polysaccharides present in medicinal plants. Chemogenomics and network pharmacology have been applied to predict molecular targets and decipher the mechanisms of action of pure compounds or phytocomplexes found in combinatorial herbal formulas. A better understanding of the philosophy of synergetic interactions of *Jun*, *Chen*, *Zuo*, and *Shi* classes of Chinese *materia medica* used in traditional formulations has led to a simplified *Jun-Shi* compatibility drug discovery strategy model.

Evaluating the safety of herbal medicines is critical to their wider acceptance as valid therapeutic agents. Integrated toxicological approaches have been successfully applied in this area, for instance to identify antifibrotic and profibrotic substances in certain medicinal plants. As research into the broader application of traditional medicine continues, newer 'omics technologies and poly-pharmacokinetics will also play an increasing role in bridging the gap between the personalized approach of Chinese medicine theory and modern clinical research methodology.

Acknowledgments

We are particularly grateful to Zhu Chen, vice-chairman of the Standing Committee of the National People's Congress of the People's Republic of China for inspiring us to undertake this project, to WHO Director-General Margaret Chan and her team, Commissioner Guoqiang Wang of the State Administration of Traditional Chinese Medicine, and AAAS CEO Alan Leshner for their vision and support for this special feature. Thanks are also due to all authors, referees, advisors, and sponsors for charting the journey ahead to translate ancient traditional medicines into the therapies of tomorrow.

The WHO Traditional Medicine Strategy 2014–2023: A perspective

Authors:

Zhang Qi^{1*} and
Edward Kelley²

There has been a continuing demand for, and popular use of, traditional and complementary medicine (T&CM) worldwide. In some developing countries, native healers remain the sole or main health providers for millions of people living in rural areas. For instance, the ratio of traditional health practitioners to citizens in Africa is 1:500, whereas the ratio of medical doctors to citizens is 1:40,000 (1). In the Lao People's Democratic Republic, 80% of the population live in rural areas, with each village being serviced by one or two traditional health practitioners (2). Over 100 million Europeans are currently users of T&CM, with one-fifth being regular users; a similar proportion choose health care that includes T&CM (3). According to a national survey in China, practitioners of traditional Chinese medicine received 907 million visits from patients in 2009, which accounts for 18% of all medical visits to surveyed institutions. Further, the number of traditional Chinese medicine inpatients was 13.6 million, or 16% of the total in all hospitals surveyed (4).

In a few countries, certain types of traditional medicine (TM) have been completely integrated into the health care system, including China, the Democratic People's Republic of Korea (North Korea), the Republic of Korea (South Korea), India, and Vietnam. In China, for instance, traditional Chinese medicine and conventional medicine are practiced alongside each other at every level of the health care service, and public and private insurance cover both forms of treatment (Box 1).

In many other countries, T&CM is partially integrated into the national health system, while in some countries there is no integration at all.

Recent changes, emerging challenges, and needs

Much has changed since the last World Health Organization (WHO) global strategy document was released in 2002. More and more countries are coming to accept the contribution that T&CM can make to the health and well-being of individuals and the comprehensiveness of their health care systems. In the period 1999 to 2012, the number of member states of WHO with national policies covering TM has increased significantly. This includes countries better regulating herbal medicines or creating national research institutes to study T&CM (5).

Governments and consumers are becoming more open to broader aspects of T&CM practices and to considering them as an integrated part of health service delivery. In Africa, the number of national regulatory frameworks increased from one in 1999/2000 to 28 in 2010 (6). Across the Atlantic, the Ministry of Health in Brazil has developed a national policy on integrative and complementary practices (7), while in the eastern

Mediterranean region, five member states report having regulations specifically for T&CM practitioners (5). Member states in the southeast Asia region are now pursuing a harmonized approach to education, practice, research, documentation, and regulation of TM (5); in Japan, 84% of Japanese physicians use *Kampō* (Japanese traditional medicine) in daily practice (8). In Switzerland, certain complementary therapies have been reinstated into the basic health insurance scheme available to all Swiss citizens (9).

Despite significant advances, the regulation of T&CM products, practices, and practitioners is not occurring at an equal pace (5). Member states report that faster progress is being made in the regulation of herbal medicines, while that for T&CM practices and practitioners is lagging. Of concern is that the safety, quality, and efficacy of T&CM services cannot be assured if there is not appropriate regulation of practices and practitioners. This situation presents a serious challenge for many member states, where a lack of knowledge and experience exists regarding the formulation of national policy, leading to weak or absent regulation and a lack of proper integration of T&CM services into the health service delivery system. It also reflects the need of all member states to push WHO to update its global strategy on TM.

The WHO Traditional Medicine Strategy: 2014–2023

Responding to the needs and challenges identified by member states and building on the work done under the *WHO Traditional Medicine Strategy 2002–2005* (10), the updated strategy for the period 2014–2023 devotes more attention than its predecessor to health services and systems, including T&CM products, practices, and practitioners. The key objectives of the updated strategy are summarized below.

Objective 1: *To build the knowledge base for active management of T&CM through appropriate national policies.* There is a great diversity of products, practices, and practitioners in T&CM. The first strategic step towards achieving this objective is to understand and recognize the role and potential of T&CM. The strategy recommends that member states acknowledge and appraise, in detail, which types of T&CM are used by their populations and devise their own country profile for T&CM practices. As the marketplace for T&CM becomes more global, harmonization and cooperation will become more important.

The second strategic step under this objective recommends that member states strengthen knowledge generation, collaboration, and sustainable use of T&CM resources, including intellectual and natural resources.

Objective 2: *To strengthen quality assurance, safety, proper use, and effectiveness of T&CM by regulating T&CM products, practices, and practitioners.* The first strategic element under this objective is to recognize the role and

Materials that appear in this section were not reviewed or assessed by *Science* Editorial staff, but have been evaluated by an international editorial team consisting of experts in traditional medicine research.

¹Coordinator, Traditional and Complementary Medicine Unit, Service Delivery and Safety Department, World Health Organization, Geneva, Switzerland

²Director, Service Delivery and Safety Department, World Health Organization, Geneva, Switzerland

*Corresponding Author: zhangqi@who.int

importance of product regulation. The emphasis should be on the monitoring and implementation of established regulations of TM products. Since herbal medicines are now used internationally, products often used in parts of the world other than that in which they were originally grown, developed, or manufactured. This highlights the importance of considering different legislative frameworks in different countries, and ensures that information on quality and safety is shared so that products are used appropriately.

The second strategic direction is to recognize and develop T&CM practice and practitioner regulations for education and training, skills development, services, and therapies. As more countries develop policies and regulatory frameworks, there is a need to evaluate their effectiveness and identify ways in which challenges regarding practice and practitioner regulations can be addressed by benchmarking against appropriate reference standards.

Objective 3: *To promote universal health coverage by integrating T&CM services into health care service delivery and self-health care.* One of the most significant questions raised about T&CM in recent years is how it might contribute to universal health coverage by improving service delivery in the health system, particularly primary health care. A first step is to capitalize on the potential contribution of T&CM to improve health services and health outcomes. Mindful of the traditions and customs of peoples and communities, member states should consider how T&CM might support disease prevention or treatment as well as health maintenance and health promotion. This process should be consistent with safety, quality, and effectiveness standards and in line with patient choice and expectations. Based on each country's realities, it is recommended that models for integrating T&CM into national health systems should be explored.

Next, it is important to ensure that consumers of T&CM can make informed choices about self-health care. In many member states, self-selection of T&CM products accounts for a large part of the T&CM market. Education of consumers, together with ethical and legal considerations, should support and shape the key aspects of informed choice for T&CM intervention.

The WHO resolution WHA67.18 urges member states to adapt, adopt, and implement the *WHO Traditional Medicine Strategy 2014–2023* as a basis for national T&CM programs or work plans and to report to WHO on progress in implementing the strategy. The resolution also encourages WHO to support member states in the implementation of the strategy in the coming decade (11).

Conclusions

Around the world, T&CM continues to grow in popularity. Progress in the regulation of T&CM is gaining momentum, even as that of T&CM practices and practitioners advances at a somewhat slower pace. Safety, quality, and effectiveness of T&CM services is paramount, but cannot be ensured if appro-

BOX 1. Traditional medicine health service integration in China.

In China, there are about 440,700 health care institutions providing TM services, with 520,600 patient beds, including all levels of TM hospitals and general hospitals, clinics, and health stations in urban and rural areas. About 90% of general hospitals include a TM department and provide TM services for all patients. TM medical institutions are governed by the same national legislation on medical institutions as conventional medical institutions. TM practitioners are allowed to practice in both public and private clinics and hospitals. The public is free to choose their preferred form of health care services, or follow the advice of their doctors (12).

priate regulation of practices and practitioners is not in place. The goals of *WHO Traditional Medicine Strategy 2014–2023* are to support member states in harnessing the potential contributions of T&CM to health, wellness, people-centred health care, and universal health coverage, while also promoting safe and effective use of T&CM through the regulation, research, and integration of T&CM products, practices, and practitioners into the health system, as appropriate.

It should be emphasized that given the great diversity of products, practices, and practitioners in T&CM among the member states, it is important to enhance international communication and collaboration in sharing knowledge and practices, in developing and exchanging scientific knowledge and training programs, and in sharing experiences in developing

and implementing policies and regulations. Also, as the marketplace for T&CM becomes more globalized, the quality, safety, proper use, and efficacy of T&CM in different nations need to be harmonized and standardized utilizing evidence-based science.

References

1. A. A. Abdullahi, *African J. Trad., Comp. and Altern. Med.* **8**, 115 (2011).
2. Lao Ministry of Health and World Health Organization. *Health Service Delivery Profile, Lao PDR, 2012* (Compiled in collaboration between WHO and Ministry of Health, Lao PDR, 2012), http://www.wpro.who.int/health_services/service_delivery_profile_laopdr.pdf.
3. European Information Centre for Complementary & Alternative Medicine (<http://www.eiccam.eu/home.php?il=1&l=eng>).
4. State Administration of Traditional Chinese Medicine, *Report of a survey on T&CM basic situation in 2009* (2011).
5. WHO Traditional Medicine Strategy 2014–2023 (World Health Organization, Geneva, 2013), pp. 15–56.
6. World Health Organization, *Progress report on decade of traditional medicine in the Africa region* (WHO African Region (AFRO), Brazzaville, 2011).
7. Retrieved from http://bvsms.saude.gov.br/bvs/publicacoes/pn_pic_access_expansion_initiative.pdf.
8. E.C. Moschik *et al.*, Usage and Attitudes of Physicians in Japan Concerning Traditional Japanese Medicine (Kampo Medicine): A Descriptive Evaluation of a Representative Questionnaire-Based Survey. *Evidence-Based Complementary and Alternative Medicine*. **2012**, (Article ID 139818, 13 pgs, 2012).
9. Swiss Confederation, *Five CAM methods eligible for reimbursement under specific conditions for a provisional period of six years.* (2011; www.bag.admin.ch/aktuell/00718/01220/index.html?lang=de&msg-id=37173).
10. *WHO Traditional Medicine Strategy 2002–2005* (World Health Organization, Geneva, 2002).
11. World Health Organization, *WHO Governing Body Documentation Official Records*, <http://apps.who.int/gb/or/>.
12. Government of China, National Bureau of Statistics of China. *China Statistical Yearbook 2011: Chinese Medicine (1987–2010)* (The State Administration of Traditional Chinese Medicine, China, 2011).

A global scientific challenge: Learning the right lessons from ancient healing practices

Author:
Josephine P.
Briggs

Health is a fundamental human value. Consequently, most cultures have sought after and used a broad range of healing practices. In both developed and developing economies, the practices of modern medicine exist side-by-side with traditional approaches and alternative remedies. For many living in developing economies, traditional healers and herbal remedies are the only source of available health care. In contrast, developed economies typically use these approaches as an optional complement to modern medicine, driven by patient preference. However, in both China and India, the ancient medical traditions—traditional Chinese medicine and Ayurvedic medicine—have flourished either in parallel or integrated with advanced modern care. Currently, in North America and Europe certain ancient healing practices—such as acupuncture, traditional Chinese medicine, massage, and meditation—have generated increasing interest and are seen as gentler, “low-tech” complements to conventional care.

The persistence of such traditional practices in these settings suggests we have much to learn from them. Modern scientific methods can offer means to examine traditional practices. In this brief perspective, a few examples of traditional remedies are discussed to illustrate the issues we face in thinking about the intersection between modern medicine and traditional healing practices.

Malaria and botanical-based therapies

About half of the pharmaceuticals developed over the last two decades and approved by the U.S. Food and Drug Administration (FDA) were either natural products, synthetic derivatives, or had at their core a prototype molecule derived from a natural product (1). Continuing to development therapeutics from natural sources is imperative for finding new treatments, and healing traditions can provide insight into such resources. Moreover, many modern therapeutics exploit the ability of plants to synthesize a wide range of small molecules of great variety and complexity. Plant-based medicines remain important sources of therapeutics for much of the world's population, and plant-derived products remain a major source of new therapeutic small molecules.

Treatment of malaria is a case in point. Modern malaria treatment started with the discovery of *Cinchona* (Rubiaceae) bark, which was reportedly being used in South American native traditional healing practices and was brought back to Europe by Jesuit missionaries in the 17th century. Until the mid-1990s, virtually all treatments for malaria were molecular entities based on the terpenoid structure of the *Cinchona*

alkaloids. This includes quinine, chloroquine, and the synthetic derivative mefloquine. The alkaloids are abundant in *Cinchona* bark, up to 15 percent by weight, and quinine itself can represent half or more of the alkaloid content (2). Simple tea extracts of *Cinchona* bark have substantial antimalarial activity. Quinine-based compounds remain critical for both the treatment of malaria and for prophylaxis, but the emergence of resistance, particularly for *Plasmodium falciparum*, has created enormous urgency to develop new agents.

The next chapter in the development of antimalarial therapy belongs to *Artemisia annua*—a vigorous weedy annual which is widespread throughout the world (Figure 1A). *Artemisia annua* is known in Chinese herbal tradition as *qinghao* and as sweet wormwood in Europe. The development of artemisinin-based antimalarials represents one of the great recent victories for ethnomedicine. The discovery was a complex team effort, initially led by the Chinese, later bringing in Western nonprofit and governmental entities and pharmaceutical companies (3, 4). The story illustrates how healing traditions can point scientists in a direction to find new medicines, but also exemplifies how challenging developing therapeutics from plants can be.

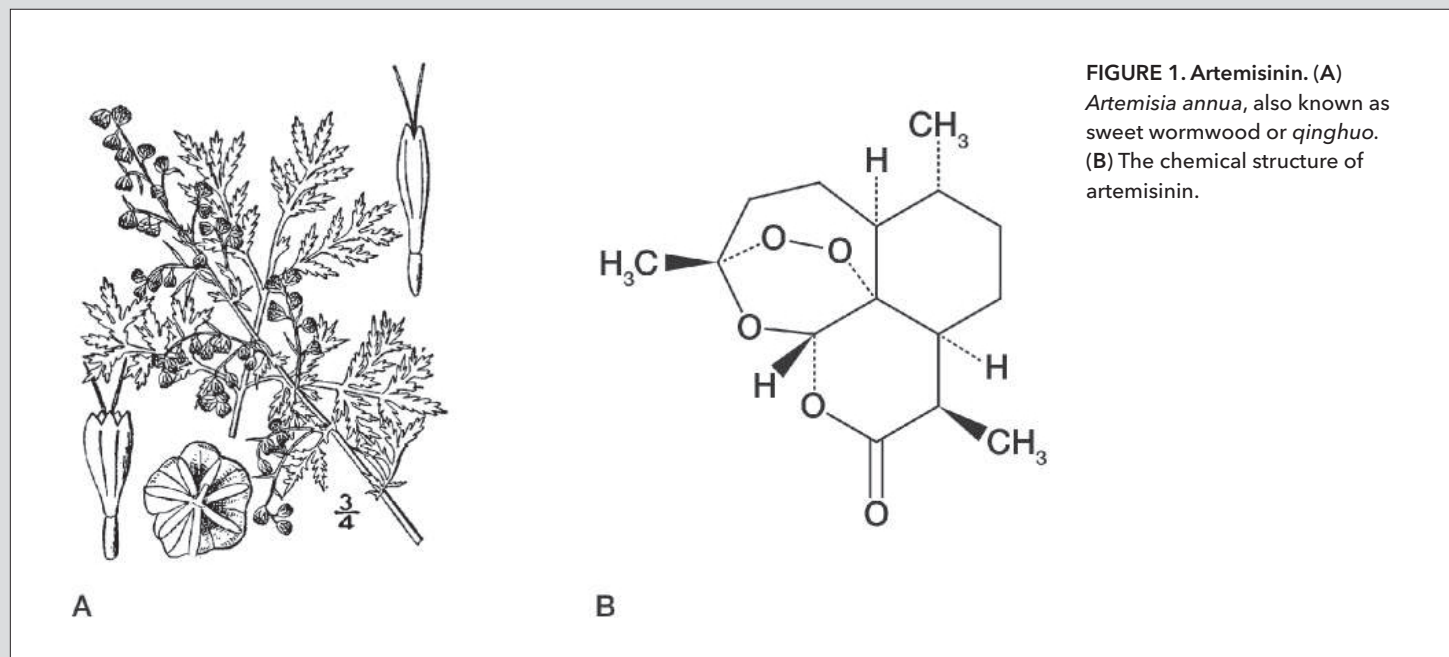
The Chinese government funded a major screening effort, Project 523, which was undertaken to test a large number of herbs, using a mouse model of malaria. Using a labor intensive methodology, they studied thousands of herbs, hundreds of extraction “recipes,” and had hundreds of hits. Moving from these hits to the initial isolation and characterization of a bioactive compound required enormous persistence. The effort to find a new treatment could easily have failed; the reports suggested that drug responses were fleeting at times and difficult to reproduce. However, a gentle extraction method that maintained activity of the active principle was finally developed by Tu YouYou (3). In contrast with the *Cinchona* alkaloids, artemisinin (Figure 1B) is present in only low concentrations, sometimes as low as 0.05% by weight (2). Additionally, it is detected only in *Artemisia annua*, but not in other *Artemisia* species. Its unusual endoperoxide structure is critical for activity, but is relatively unstable under many extraction conditions. Nevertheless, the effort succeeded, yielding a small molecule that is now the cornerstone of malaria treatment.

Acupuncture and chronic pain

Acupuncture is an integral part of Asian medical traditions, where it is widely used in traditional practice settings and its efficacy in relieving pain is taken as a given; however, acupuncture's introduction into American and European health care settings, while welcomed by many patients and providers, has encountered substantial skepticism from medical professionals. A sizable number of clinical trials have been implemented to explore its value, many of which are focused on pain management. These have included both

Materials that appear in this section were not reviewed or assessed by *Science* Editorial staff, but have been evaluated by an international editorial team consisting of experts in traditional medicine research.

Director, National Center for Complementary and Alternative Medicine
National Institutes of Health, Bethesda, MD
briggsj@mail.nih.gov



efficacy and effectiveness trials. Efficacy trials generally compare acupuncture to a sham control designed to be indistinguishable to the subject from traditional acupuncture. The typical sham controls use the same ritual, the same practitioner reassurance, and the same counter-irritant effect of needles or pressure points as the comparison group (although the needles may be replaced with non-penetrating devices and the insertion points chosen do not lie on treatment meridians). Effectiveness trials typically compare a subject's response to different treatments, which are randomly assigned and include either acupuncture or standard care.

A recent, systematic review of 29 trials, with approximately 18,000 study participants, resulted in some clear conclusions: The magnitude of acupuncture's effect depends upon which group is used for a comparison (5). Specifically, when acupuncture was compared to no acupuncture (in effectiveness studies), the benefit appears to be quite sizable, approximately 50% reduction in pain severity. In contrast, when acupuncture is compared to a sham treatment (in efficacy studies), more modest effects are observed (Figure 2). Although statistical significance is achieved, the reduction in pain severity is not as substantial, typically only 20%. Based on this analysis, it seems reasonable to conclude that needling itself may be contributing to acupuncture's pain-reducing effects, and that the overall benefit is heavily dependent on context—on the reassurance and expectation produced by the acupuncture ritual.

What does this mean for clinical practice? Here, the arguments erupt. Is a contextual effect (some would call it a placebo) that relieves pain and reduces the need for medication an acceptable form of treatment? This is still, for many Western practitioners, a quandary to which there is no simple answer. Building a better biological understanding based on the neuroscience of pain may provide some common ground. As we learn more about the central pain circuits, the mechanisms underlying acupuncture's

effects—specific and nonspecific—can also be teased out. Acupuncture appears to modulate the central circuitry for pain (6), partially from the peripheral actions of adenosine (7) and partially from the centralized actions of endorphins (8). Moreover, there may be overlap in the descending pain circuits recruited by the specific and contextual effects.

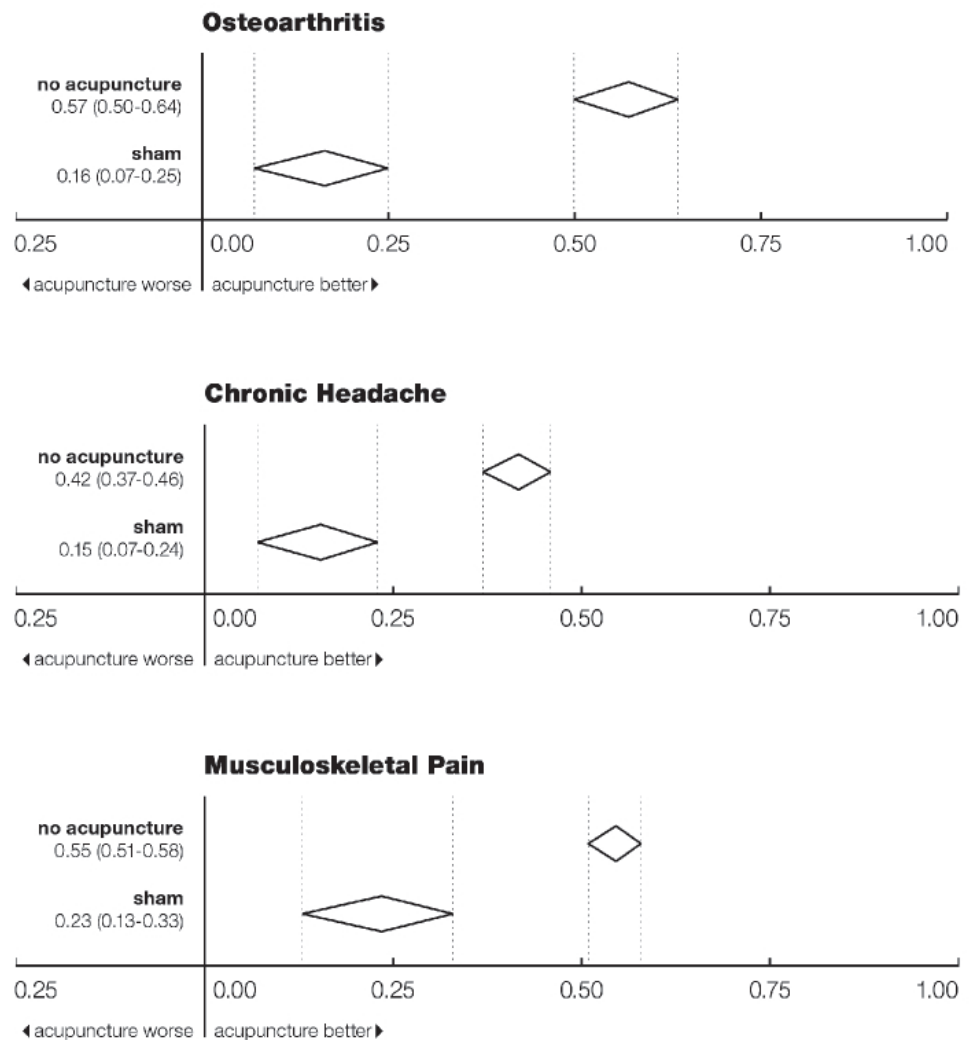
Ultimately the goal of the research is clear. We need better treatments for pain without the sedative, narcotic, and addictive effects of the available drugs. Understanding this ancient tradition is a good place to turn for insights that will improve pain treatment.

Traditional versus modern medical systems

A major difference between resource intensive and resource poor environments is the extent to which common complaints of daily living are viewed as medical problems requiring intervention, help, and treatment. Medicalization has been defined as, "the process by which human conditions and problems come to be defined and treated as medical conditions, and thus become the subject of medical study, diagnosis, or treatment" (9). As health care providers in resource-intensive environments, we often take for granted the medicalization of a wide range of complaints—sadness, worry, fatigue, musculoskeletal discomforts, and even restless legs—as necessary and normal.

Comparisons of traditional and modern health systems challenge these assumptions. Modern medicine has created a set of symptoms-based diagnostic categories for a range of common problems that differ greatly from those in traditional health systems. Diagnostic criteria, based on symptoms and limited physical findings but lacking laboratory diagnostic criteria, have been developed for a variety of physical complaints, such as chronic fatigue syndrome and chronic functional pain syndromes such as fibromyalgia, interstitial cystitis, vulvodynia, and chronic prostatitis. These diagnostic categories carry clinical insights about symptoms that cluster together, and sometimes patients can benefit. The

FIGURE 2. Acupuncture effects compared with controls. The results of a meta-analysis of 29 high-quality randomized clinical trials of acupuncture are shown for three conditions. Differences in the average standardized mean (with 95% confidence intervals) for treatment relative to control is shown. When compared to no treatment, acupuncture produces striking improvement; however, when compared to sham treatments, the effect is more modest (5).



diagnoses may provide some clarity and community support. Nevertheless, although there is some evidence for efficacy of pharmaceutical treatments for some such conditions, often these disorders respond inconsistently or poorly to available treatments. There is also clinical concern that sometimes these diagnoses can contribute to an expectation of chronic functional impairment.

Traditional diagnoses often emphasize a temporary imbalance and promote an expectation that the subject will return to health. Although many patients with these conditions seek alternative remedies, most of the evidence of benefit is anecdotal. In resource-poor environments, people almost certainly suffer from the same set of symptoms, and anecdotally, at least, these complaints may sometimes be effectively addressed through the care of traditional healers. We are currently supporting a small number of trials that address whether the emotional and social support of interventions such as tai chi (10), yoga, or mindfulness-based meditation may capture some of the benefit of the healing traditions. Clearly, Western medicine does not have all the answers,

and systems of care that allow thoughtful integration of healing traditions with modern medicine may offer help to troubled patients.

References

1. D. J. Newman, G. M. Cragg, *J. Nat. Prod.* **70**, 461 (2007).
2. P. M. Dewick, *Medicinal Natural Products: A Biosynthetic Approach*. (Wiley, New York, ed. 3, 2009). pp. 335-336.
3. Y. Tu, *Nat. Med.* **17**, 1217 (2011).
4. D. G. Dalrymple, *Artemisia annua, Artemisinin, ACTs and Malaria Control in Africa: Tradition, Science and Public Policy*. (Politics and Prose Bookstore, Washington, DC, 2012).
5. A. J. Vickers et al., *Arch. Int. Med.* **172**, 1444 (2012).
6. J. Kong et al., *Neuroimage* **47**, 1066 (2009).
7. T. Takano et al., *J. Pain* **13**, 1215 (2012).
8. J. S. Han, *Neurosci. Lett.* **361**, 258 (2004).
9. Medicalization entry. Wikipedia. Accessed at: <http://en.wikipedia.org/wiki/Medicalization> on June 21, 2014.
10. C. Wang et al., *NEJM* **363**, 743 (2010).

East is East and West is West, and never the twain shall meet?

Authors:

Yan Schroën^{1,3},
Herman A. van
Wietmarschen^{1,2}, Mei
Wang^{1,5},
Eduard P. van Wijk^{1,4},
Thomas Hankemeier⁴,
Guowang Xu^{1,6},
Jan van der
Greef^{1,2,4,5*}

Western medicine and Chinese medicine developed within the context of different cultures and perspectives of the natural world. The more reductionistic approach of Western biomedical sciences has generated tremendous knowledge of anatomy, physiology, histology, genetics, and biochemistry, while the phenomenological approach of Chinese medicine has produced a more holistic understanding of biology. The two concepts are complementary, and combining them to optimally balance detail and context could generate a highly rewarding step forward for medicine.

A diversity of perspectives on life and consciousness has developed across humanity's different cultures. In the Western Hemisphere, a key development was the affirmation by Greek Ionian scholars such as Thales, Pythagoras, and Archimedes that it was not gods, but rather laws of nature, that create and organize our reality. The modern concept of the laws of nature emerged in the seventeenth century through the work of scholars such as Kepler and Galileo, with the most notable contributions coming from Newton and from Descartes, who emphasized a duality between the mind and the physical body.

Philosophers have pondered whether more than one set of laws was possible. It seems that our conception of natural laws may depend on our approach to understanding reality. Hawking and Mlodinow introduced the notion of model-dependent realism, which posits that a physical theory or worldview is a model with a set of rules that connects the elements of the model to observations (1). That is, in the words of Hawking and Mlodinow, "There is no picture- or theory-independent concept of reality," and every model is only an approximation of reality.

The modern Western scientific model arose in the context of historical and cultural developments that enabled philosophical pursuits and provided fertile ground for philosophers of science. A different approach to understanding reality and the laws of nature arose in Eastern cultures, such as China. Both models can be considered valid, each with its own model-dependent realism.

The modern Western scientific model arose in the context of historical and cultural developments that enabled philosophical pursuits and provided fertile ground for philosophers of science. A different approach to understanding reality and the laws of nature arose in Eastern cultures, such as China. Both models can be considered valid, each with its own model-dependent realism.

Bridging the gap

Although there are many similarities between the Greek and Chinese concepts of health and medicine, the medical systems that arose in the West and in the East are quite distinct. Most notably, a highly reductionist, detailed view dominates in the West, whereas a more phenomenological, descriptive, and systems-based view holds sway in China. In recent decades, Western systems thinkers have started to combine

theories from a variety of disciplines, developing an expanded systems view of medicine. Systems thinking, and in particular systems biology, have been recognized as the scientific bridge between Western medicine and traditional medicine models, including traditional Chinese medicine (TCM) (2, 3).

Figure 1 illustrates how systems-based theories can bridge Eastern and Western models, as well as connecting ancient and modern ideas. The left forward image shows a dynamic correlation network of interactions between various genes, proteins, and metabolites. This nodal network reflects the particularized understanding of the complexity of biochemical pathways and the dynamic organization of the body that characterize Western biomedical science. The right forward imagery is a drawing of the Taoist Inner Landscape. In keeping with ancient Taoist tradition, the drawing provides a poetic description of the complex relationships among the various organ functions of the body. The background of the figure merges two very well-known, almost archetypical, symbols of systems thinking: the Vitruvian Man (*Le proporzioni del corpo umano secondo Vitruvio*) and the *Taiji* (太极, the literal translation of which is "great pole"). The Vitruvian Man is by Leonardo da Vinci, a visionary and pioneer of the evidence-based scientific view of the universe. A man is pictured within a square, which reflects the terrestrial aspect of humanity, and a circle, which represents the spiritual realm. The *Taiji* (often called the Yin-Yang symbol in the West) represents the Eastern, Taoist tradition of systems thinking. It depicts a dynamic relationship between the two components of a duality that encompasses the known universe. Interestingly, the *Taiji*, which symbolizes humanity as part of an eternal universe, has all the properties of a fractal.

Amalgamation in action

Figure 2 depicts an amalgamation of Western and Eastern medical systems, a process that we call systems medicine. The left side of the figure shows a simplified, hierarchical view of molecules being organized into cells, with further consolidation into tissues, organs, and, ultimately, a whole organism. This illustrates the bottom-up approach practiced in Western biomedical sciences. It has produced a tremendous amount of knowledge of anatomy, physiology, cells, genes, and biochemistry. It has also created physicians with highly specialized, albeit arguably fragmented, knowledge. In the Western scientific model, data are collected to generate information, knowledge, and, ultimately, a form of wisdom. By contrast, traditional medical systems, most prominently TCM, have focused on gaining a holistic understanding of systems, and on applying that wisdom in a top-down manner in the search for knowledge, information, and data that may increase the understanding of

Materials that appear in this section were not reviewed or assessed by *Science* Editorial staff, but have been evaluated by an international editorial team consisting of experts in traditional medicine research.

¹Sino-Dutch Centre for Preventive and Personalized Medicine, P. O. Box 360, 3700 AJ, Zeist, The Netherlands

²TNO, P.O. Box 360, 3700 AJ, Zeist, The Netherlands

³Oxriver, Education and Research, Diessenseweg 51, Hilvarenbeek, The Netherlands

⁴Division of Analytical Biosciences, LACDR, Leiden University, P.O. Box 9502, 2300 RA Leiden, The Netherlands

⁵SU BioMedicine, Utrechtseweg, Zeist, the Netherlands

⁶Dalian Institute of Chemical Physics, Chinese Academy of Sciences, Dalian, China

*Corresponding Author: jan.vandergreef@tno.nl

the web of life. Somewhere in the middle these two world-views meet and this nexus has the potential to yield a valuable combination in which detail and context are optimally balanced.

One way to bridge the two worldviews is through unification of diagnosis, based on an integration of the collections and arrangements of symptoms and signs. Western biomedical advances offer a plethora of biomarkers that can be detected and measured with advanced equipment, while Chinese medicine contributes knowledge about the dynamic relationships among signs and symptoms. The right side of Figure 2 provides an example of this inter-relationship for rheumatoid arthritis (RA). In Chinese culture, RA is classified as a "*Bi Zheng*," a so-called painful obstruction syndrome. In TCM diagnosis every condition is primarily distinguished according to eight basic principles: External-Internal, Heat-Cold, Excess-Deficiency, and Yin-Yang. Figure 2 focuses on the Cold-Heat differentiation.

The signs and symptoms of RA are universally represented across peoples independent of culture, although variations in concepts and emphasis can be seen. In TCM, RA patients can be subdivided based on the predominance of "hot" versus "cold" symptoms. Examples of "hot" symptoms, as illustrated in Figure 2, are thirst, fever, irritability, restlessness, warm feeling, dry mouth, and pain that is relieved by cold, while "cold" symptoms include clear urine, sharp pain, stiff joints, and pain that is relieved by warmth. This systemic approach may help biomedical researchers to distinguish biological subtypes of RA in a manner that could lead to personalization of medical care; firstly, through more personalized lifestyle advice, and in the long term, through the application of modern biomedical technology in studies of RA subtypes. Ultimately, recognizing the particular individualized presentation of RA across different patients based on a systemic approach may improve treatment choices and outcomes.

Recently, research teams have begun the process of integrating Western and Eastern notions of medicine for RA. For example, Van Wietmarschen and colleagues (4) used a questionnaire to differentiate distinct "cold" and "hot" RA subtypes. These two patient groups display differences in the regulation of apoptosis, in CD4+ T cell gene expression levels, and in plasma and urine metabolite profiles. In another study, 11 acylcarnitine metabolite variants associated with differences in muscle breakdown was used to distinguish between the "cold" and "hot" RA subtypes (5).

In similar recent work on pre-diabetes, Wei and colleagues

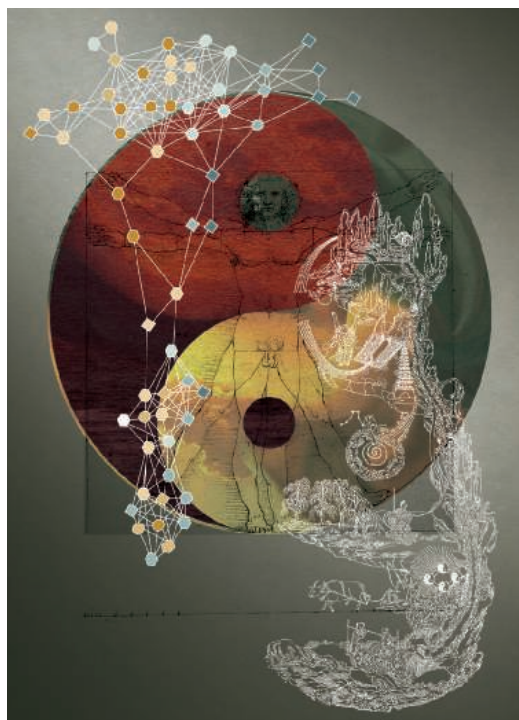


FIGURE 1. An artist impression of the ancient and modern bridge between Chinese and Western medicine.

(6) examined blood and urine samples from patients categorized by Chinese subtypes of pre-diabetes, namely *qi* and yin deficiency with or without dampness, and *qi* and yin deficiency with stagnation. Numerous sugar and amino acid level differences were recorded, indicating that the subtypes are characterized by variation in carbohydrate metabolism and renal function.

Several other studies have also shown that biological mechanisms can be correlated with TCM-based groupings in patients diagnosed in Western medical systems (7-10).

The path ahead

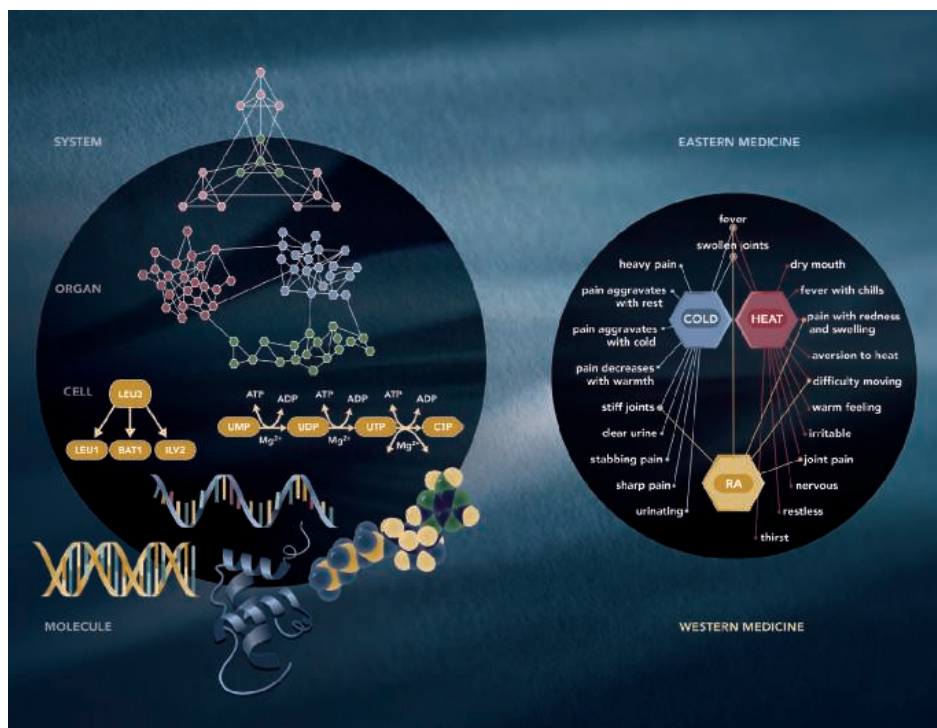
In the above studies, TCM subtyping and Western diagnostic criteria coincided. This suggests that symptom pattern questionnaires could reliably standardize the segregation of patients into TCM subgroups (11). The comprehensive symptom questionnaire used in the RA study was based on the TCM perspective of arthritis as a bi-syndrome. Following completion of the question-

naire, the data was subjected to a principal component analysis, revealing one principal component related to the concepts of "internal" and "external," plus another related to "cold" and "hot" (11). These findings support the contention that TCM concepts have a basis in actual biological variation among patients. The current challenge is to uncover non-linear relationships between the diagnostic symptom clusters revealed by the questionnaire results.

We believe that Western diagnostics would benefit greatly from the integration of broader knowledge of relationships between symptoms, including consideration of TCM descriptions of syndromes. TCM descriptions offer potential directions for detailed, explanatory biomedical research, bringing us closer to a biopsychosocial model of health in which more and more relationships between diseases, psychology, and behavior are uncovered (12). Arguably, the dearth of understanding of the dynamics of systems presents the greatest opportunity for improvement in Western health care diagnostics. It is a topic that will only grow in importance as the focus in health care shifts from the treatment of acute disease to the long-term management and prevention of chronic diseases. Among the more promising developments that may improve our understanding of system dynamics are the application of nonlinear dynamic modeling techniques to the study of coherent oscillations in the brain (13), examination of the synchronization of physiological rhythms such as heart beat and breathing rhythms (14), and the study of metabolic processes that show oscillatory behavior (15). Another

FIGURE 2. Systems medicine.

A hierarchical systems view on human biology (left)—scientific studies in Western medicine develop typically via a biochemistry/pathway bottom-up approach, while in Chinese medicine, a top-down dynamic symptom relationship approach is more common. The right image illustrates the diagnostic bridge between symptom relations in Chinese Medicine bi-syndrome (top) and Western medicine (bottom) for rheumatoid arthritis.



intriguing area being examined is the coherent, spontaneous ultra-weak photon emission patterns of organisms (16, 17). Recent work suggests that photon distribution dynamics may provide insights into regulatory coherence at a high systems level (18, 19). Indeed, these coherent light functions may be directly involved in communication in addition to influencing biochemical networks (20, 21).

It should also be clear that modern quantitative technologies developed in the West have a great deal to offer to Chinese diagnostics. Especially relevant are methodologies that provide information about the large-scale organization of systems as well as the dynamics of such organization (Figure 2).

Integration of Western and Chinese medicine thinking has enormous potential for synthesizing modern technological and social innovation. Although Chinese and Western medicine are perceived as wholly distinct paradigms today, they are poised to merge in the arena of personalized systems medicine, wherein patients can take a greater role in managing their own health and wellness. Human-human relationships are critical for diagnosis and intervention in a biopsychosocial context, with health care providers supporting patients through an empathic coaching role. The integration of Western and Chinese medicine can be much more than the sum of the parts: it can accelerate the shift from disease management to health promotion that is presently taking place in health care systems around the world. Although, as Kipling states in the opening lines of his famous poem, "East is East and West is West" (22), at least in the realm of diagnostic medicine, these two world cultures have met.

References

1. S. Hawking, L. Mlodinov, *The Grand Design* (Bantam Press, New

York, 2010).

2. M. Wang et al., *J. Phytother. Res.* **19**, 173 (2005).
3. J. van der Greef, H. van Wietmarschen, Y. Schroën, M. Wang, T. Hankemeier, G. Xu., *Planta Med.* **76**, 1 (2010).
4. H. van Wietmarschen et al., *J. Clin. Rheumatol.* **15**, 330 (2009).
5. H. van Wietmarschen et al., *PLOS ONE* **7**:e44331 (2012).
6. H. Wei et al., *Mol. Biosyst.* **8**, 1482 (2012).
7. S. Li et al., *IET Syst. Biol.* **1**, 51 (2007).
8. C. Matsumoto, T. Kojima, K. Ogawa et al., *Evid.-Based Compl. Altern. Med.* **5**, 463 (2008).
9. B. Patwardhan, G. Bodeker, *J. Altern. Compl. Med.* **14**, 571 (2008).
10. Q. Wang, S. Yao, *Am. J. Chin. Med.* **36**, 827 (2008).
11. H. van Wietmarschen et al., *PLOS ONE* **6**:e24846 (2011).
12. G. Engel, *Science* **196**, 129 (1977).
13. G. Buzsáki, A. Draguhn, *Science* **304**, 1926 (2004).
14. L. Glass, *Nature* **410**, 277 (2011).
15. J. Bass, J. S. Takahashi, *Science* **330**, 1349 (2010).
16. F. A. Popp, L. Belousov, *Integrative Biophysics: Biophotonics* (Kluwer Academic Publishers, Dordrecht 2003).
17. R. van Wijk, *Light in Shaping Life: Biophotons in Biology and Medicine* (Ten Brink, Meppel, 2014).
18. R.P. Bajpai, E. P. A. van Wijk, R. van Wijk, J. van der Greef, *J. Photochem. Photobiol. B.* **129** 6 (2013).
19. R. van Wijk, E. P. A. van Wijk, H. A. van Wietmarschen, J. van der Greef, *J. Photochem. Photobiol. B.* **5**:1011 (2013).
20. G. Albrecht-Buehler, *Proc. Natl. Acad. Sci. USA* **102** 5050 (2005).
21. D. Fels, *PLOS ONE* **4**, e5086 (2009).
22. R. Kipling, *The Ballad of East and West* (Sterling Publishing Co. Inc., New York, 1889).

Acknowledgments

The authors thank Charlotte Lokin for producing the artwork shown in Figure 1.

Zheng: A systems biology approach to diagnosis and treatments

Authors:
Yonghua Wang and
Anlong Xu*

Traditional Chinese medicine (TCM) is an ancient medical practice system which emphasizes regulating the integrity of the human body and its interrelationship with natural environments. As a key concept in TCM, *Zheng* (meaning syndrome or pattern) is the overall physiological and/or pathological pattern of the human body in response to a given internal and external condition, which usually is an abstraction of internal disharmony defined by a comprehensive analysis of the clinical symptoms and signs gathered by a practitioner using inspection, auscultation, olfaction, interrogation, and palpation of the pulses (1). Correctly identifying the *Zheng* is fundamental for the diagnosis and treatment of diseases.

to systems level is important for advancing the identification and treatment of these syndromes, and for providing more objective and quantitative diagnostic criteria.

Zheng-guided disease research

In Western medicine, a disease is a particular abnormal and pathological condition that affects part or all of the human body and is often construed as a medical condition associated with specific symptoms. By contrast, *Zheng* puts forth a very different definition of a disease and encompasses all of the symptoms a patient presents.

Because of the highly interconnected nature of the human interactome, it is difficult to study different diseases at the molecular level completely independent of one another (3), and this issue also applies to *Zhenges*. Moreover, *Zhenges* are dynamic with changing boundaries, overlapping symptoms,

FIGURE 1. Using systems pharmacology and systems biology approaches for understanding TCM *Zheng* can help bridge the gap between herbal medicines and diseases. Se, face color; Xing, body shape; She, tongue texture; Mai, pulse.



Moreover, *Zheng* has been historically applied as the key pathological principle guiding the prescription of herbal formulas (Figure 1).

A lack of research on *Zheng* has left us with little understanding of its underlying biology or the relationships between different *Zhenges*, diseases, and drugs. Moreover, there have been attempts to integrate *Zheng* differentiation with modern biomedical diagnostic methods, though these efforts have not achieved the desired results (2). Many well-known herbal recipes, such as Liu Wei Di Huang Wan and Jin Kui Shen Qi Wan, have long been used for the clinical treatment of *Zheng* disorders; however, *Zheng*-guided treatments are still scarce due to the lack of evidence-based interpretations of syndromes and treatment efficacies. Thus, investigating the biological basis of *Zhenges* from a molecular

and a multiscale nature, which makes them difficult to understand at a biological and mechanistic level. Thus, we propose that a comprehensive *Zheng* map be constructed that links together all the *Zhenges* based on their molecular and cellular relationships. Further, we suggest creating the “Zhengome” as a new ‘omics field, in which a network is the basic research unit used to investigate the hierarchy present in the human body, from the molecular to the systems level. A comprehensive understanding of the Zhengome requires us to bring together multiple sources of evidence, from shared genes to protein-protein interactions, shared environmental factors, common treatments, and phenotypic and clinical manifestations, in order to capture the relationships between the different *Zhenges*.

Zheng uses the Yin-Yang, exterior-interior, cold-heat, and deficiency-excess definitions to describe patients’ conditions, which are then managed by *Zheng*-specific recipes (Figure 1). Modern ‘omics techniques combined with bioinformatics and bionetwork models through a systems biology approach have

Materials that appear in this section were not reviewed or assessed by *Science* Editorial staff, but have been evaluated by an international editorial team consisting of experts in traditional medicine research.

School of Basic Medical Sciences, Beijing University of Chinese Medicine, Beijing, China
*Corresponding Author: xuanlong@bucm.edu.cn

been applied to investigate the differences between *Zhenges* and to identify novel biomarkers. For instance, rheumatoid arthritis (RA) patients differentiated on the basis of “hot” and “cold” *Zhenges* have been shown to be associated with different underlying genomic and metabolomic profiles, with the RA hot group showing more apoptotic activity than the cold group (4). Additionally, Li et al. used a network-based computational model to understand *Zheng* in the context of the neuro-endocrine-immune network and found that cold and hot *Zhenges* were closely related to a metabolism-immune imbalance (5). Wang and colleagues investigated the urine metabolome of patients with jaundice syndrome and its two subtypes of Yang Huang (acute) and Yin Huang (chronic), and identified several biomarker metabolites (6). However, most of the current studies have relied on only one or two approaches for molecular profiling and have lacked an efficient method to integrate data obtained at different ‘omic levels. These studies also did not look at combining the analysis of molecular data with clinical variables, possibly missing an opportunity to generate more convincing conclusions. Considering the limitations of past studies, future efforts should integrate an analysis for all levels of ‘omics (e.g., genomics, transcriptomics, epigenomics, and proteomics) data from a large number of patient samples for different *Zhenges* and include an investigation of the prognostic and therapeutic utilities of the data as a whole. Moreover, combining these molecular data with patients’ clinical information could provide evidence-based theoretical interpretations for *Zhenges* and enable an assessment of *Zheng*-based therapeutic approaches.

Zhenges may change dynamically during disease progression. Differentiating the specific *Zheng* involved in each stage of a disease could provide valuable guidance for prescribing a dynamic therapeutic recipe. Using dynamic network modeling, a disease process can be conceptualized as spatio-temporal changes in network structures. The changes associated with a *Zheng* under dynamic therapy can be used to identify the key factors in the dynamic biological networks. Appropriate network perturbation models and subsequent robustness and topology analysis could help unveil potential disease-related genes or therapeutic targets involved in a disease’s progression or evolution (7). The relationships between the different aspects of a disease (e.g., main symptoms versus complications) in a specific *Zheng* as well as the psychological, social, and even environmental factors should be taken into account during the modeling and simulation process in order to uncover the dynamic nature of complex diseases. Combining a *Zhengome* approach with dynamic modeling has the potential for establishing an accurate and quantitative *Zheng* research model, as well as for creating a new system for performing disease research.

***Zheng*-driven drug discovery**

Despite considerable progress in genome, transcriptome, proteome, and metabolome-based high throughput screening methods and in rational drug design, drug discovery often encounters considerable costly failures that challenge the fidelity of the modern drug discovery system. *Zheng*-driven drug discovery has shown tremendous success for traditional drug discovery throughout Chinese medicine’s history. However, since this concept is completely new to Western

medicine, it is no easy task to incorporate *Zheng*-driven drug discovery into modern drug discovery workflows.

Here, we propose the “*Zheng* to TCM” and “TCM to *Zheng*” strategies within the framework of systems pharmacology to investigate biological systems and develop new therapeutics (Figure 2). The first strategy, *Zheng* to TCM, proposes developing a pipeline from *Zheng* diagnoses to TCM drugs, including differentiating *Zhenges*, identifying *Zheng*-related diseases and the associated genes and proteins, reverse targeting of drug effects, constructing and analyzing network/systems, and finally identifying effective herbal medicines (8). In effect, this strategy can be considered a reverse targeting and screening approach that is designed to uncover drugs from natural products that can target multiple *Zhenges* or related diseases. The goal of this method is to help researchers identify the active components within medicinal plants and multi-ingredient synergistic herbal formulas or drug combinations (9). In fact, this novel strategy has already been successfully applied in a *qi*-blood study, where we identified the active compounds in the *qi*-enriching and blood-tonifying herbs, their targets, and the corresponding pathways involved in the treatment of *qi* and blood deficiency syndromes (8).

The second strategy, TCM to *Zheng*, consists of a whole-system evaluation process starting with herbs or herbal formulas and culminating in identifying the *Zhenges*. This process includes the initial collection and classification of herbal medicines; screening the ingredients for absorption, distribution, metabolism, excretion, and toxicity (ADME/T); performing targeted drug screenings and tissue localization; constructing and analyzing networks; and finally identifying *Zhenges*/diseases (10). Using this strategy, it is possible to identify novel multitarget drugs in natural products (11). One particularly striking example is the systematic analysis of blood stasis and *qi* deficiency syndrome in coronary heart disease and the herbal drugs used to treat the syndromes. The results indicate that the herbs for eliminating blood stasis have pharmacological activity that acts to dilate blood vessel, improve the microcirculation, reduce blood viscosity, and regulate blood lipid, while *qi*-enhancing herbs have the potential for enhancing energy metabolism and anti-inflammatory activity (12). The TCM to *Zheng* strategy can also help to elucidate the pharmacological effectiveness of herbs and formulas.

In our ongoing work investigating Pi-deficiency syndrome (PDS) in the context of *Zheng*, we are analyzing patient samples using the sequencing alternative polyadenylation sites (SAPAS) method, RNA sequencing (13), lipid metabolomics, proteomics, and transcriptomics in order to decipher the pathogenesis and complex responses of the human body to PDS. From a drug development perspective, we plan to systematically investigate the *Si Jun Zi* decoction, a widely used herbal recipe for PDS, within the framework of the “TCM to *Zheng*” strategy, so as to understand why this recipe can regulate the immune response, stimulate blood circulation, and adjust gastrointestinal digestive functions. Despite the progress in *Zheng*-guided drug discovery, its future success requires the integration of multidisciplinary technologies, together with further innovations in these technologies, to facilitate the understanding of multifactorial diseases and the development of new therapies.

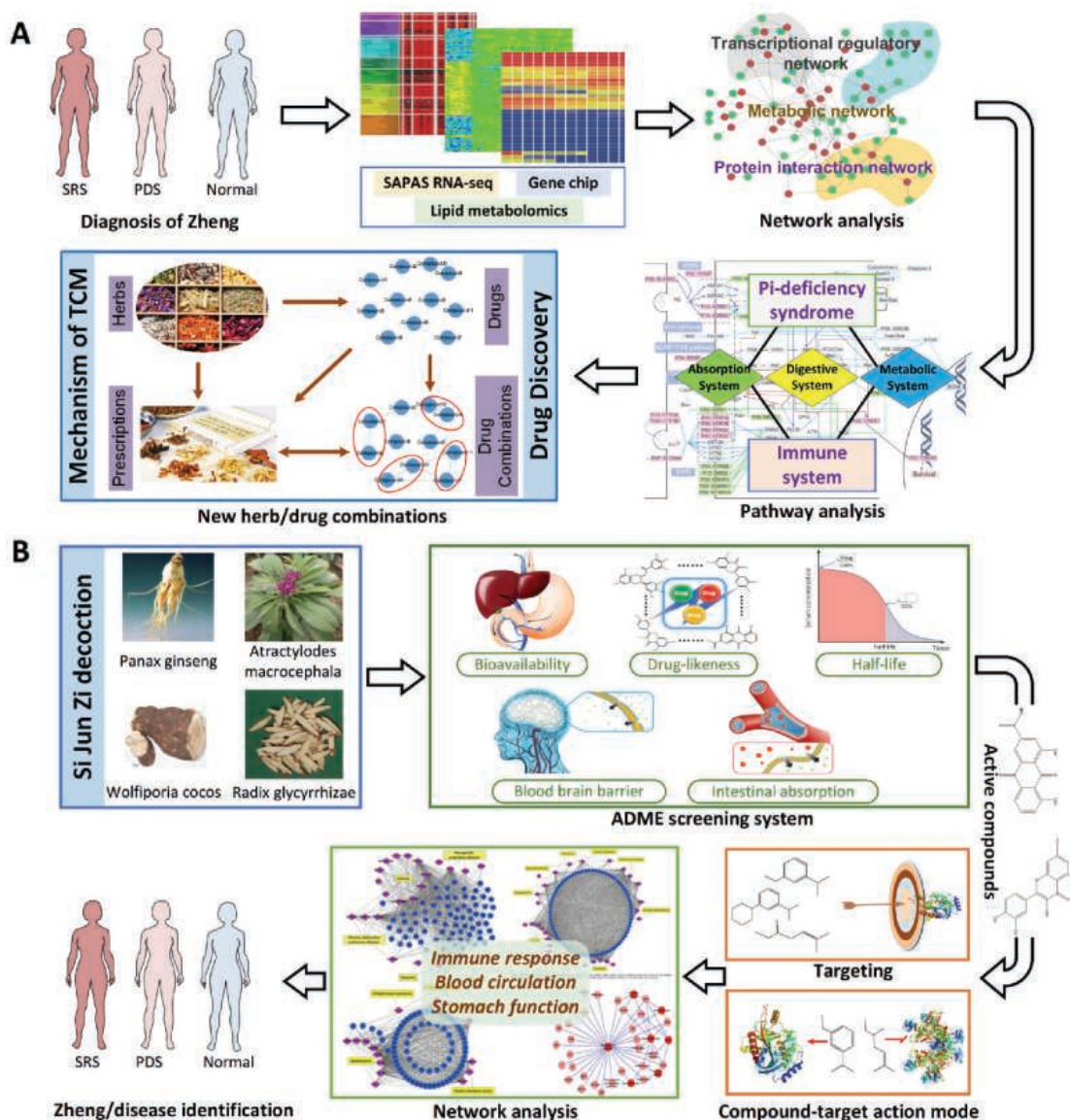


FIGURE 2. Zheng-driven drug discovery using Pi-deficiency syndrome and Si Jun Zi decoction as examples. (A) A “Zheng to TCM” procedure can build a pipeline from Pi-deficiency syndrome (PDS) to new effective herb/drug combinations by integrating ‘omics data, network and pathway analysis, and pharmacokinetic evaluation technologies. SRS, Shi-Re syndrome, is a positive control for PDS. (B) An example of a “TCM to Zheng” strategy consisting of an entire evaluation process from Si Jun Zi decoction (SJZD) to PDS through a systems pharmacology strategy including text mining, ADME/T (absorption, distribution, metabolism, excretion, and toxicity) screening, target identification, and network analysis to reveal the underlying mechanisms of SJZD activity and build new diagnostic methods for PDS.

References

1. F. Cheung, *Nature* **480**, S82 (2011).
2. A. Lu, M. Jiang, C. Zhang, K. Chan, *J. Ethnopharmacol.* **141**, 549 (2012).
3. A. L. Barabasi, N. Gulbahce, J. Loscalzo, *Nat. Rev. Genet.* **12**, 56 (2011).
4. H. van Wietmarschen *et al.*, *J. Clin. Rheumatol.* **15**, 330 (2009).
5. S. Li *et al.*, *IET Syst. Biol.* **1**, 51 (2007).
6. X. Wang *et al.*, *Mol. Cell. Proteomics* **11**, 370 (2012).
7. P. Csermely, T. Korcsmaros, H. J. M. Kiss, G. London, R. Nussinov, *Pharmacol. Therapeut.* **138**, 333 (2013).
8. J. Liu *et al.*, *Evid. Based Compl. Alt. Med.* **2013**, 938764 (2013).
9. P. Li *et al.*, *J. Ethnopharmacol.* **151**, 93 (2014).
10. C. Huang *et al.*, *Brief. Bioinform.* **15**, 710 (2014).
11. C. Zheng *et al.*, *Mol. Diversity* **18**, 621 (2014).
12. W. Zhou, Y. Wang, *J. Ethnopharmacol.* **151**, 66 (2014).
13. Y. G. Fu *et al.*, *Genome Res.* **21**, 741 (2011).

Integrated network-based medicine: The role of traditional Chinese medicine in developing a new generation of medicine

Authors:

Elaine Lai-Han Leung,
Vincent Kam-Wai
Wong, Zhi-Hong Jiang,
Ting Li, Liang Liu*

According to the philosophy of traditional Chinese medicine (TCM), health is the state of harmony between individual internal physiological networks (IPNs) and external environmental networks (EENs). Aberrant interactions between and within these networks cause complex diseases. TCM is grounded in these holistic principles, integrating philosophies from art and science; it stresses the maintenance of balance, or homeostasis, between the systems of the body and nature.

We believe that this kind of network-based holistic approach to medicine offers a useful counterpoint to today's biological reductionism-based thinking. We champion integrated network-based medicine (INBM) which takes a systems approach to understanding the individual's body as a whole, as opposed to relying on discrete components such as gene mutations, in order to explain illness (1). Built on the principles of IPNs and EENs, INBM offers a comprehensive medical system that integrates fundamental theories, diagnostic methods, and therapeutics based on a holistic and dynamic network-based approach.

The INBM system

Reductionist approaches to medicine, such as phenotype-based and target-based biomedicine (TBBM), are limited by their failure to consider the interactive nature of the human body and its environment. TBBM often views a disease as a tissue/organ-based condition that presents a single target for treatment, such as the elimination of a pathogen or the suppression of a disease-associated molecular target. This narrow focus can miss a broader range of pathogens and targets within the physiological and environmental networks.

It may also overlook potentially useful global network effects that an intervention may have. For example, metformin was originally regarded solely as an anti-diabetic drug that inhibits the mitochondrial respiratory chain and activates the 5' adenosine monophosphate-activated protein kinase pathway, resulting in inhibition of gluconeogenesis and the lowering blood glucose levels (2). Recently, a novel anti-cancer effect of metformin was identified by studying the

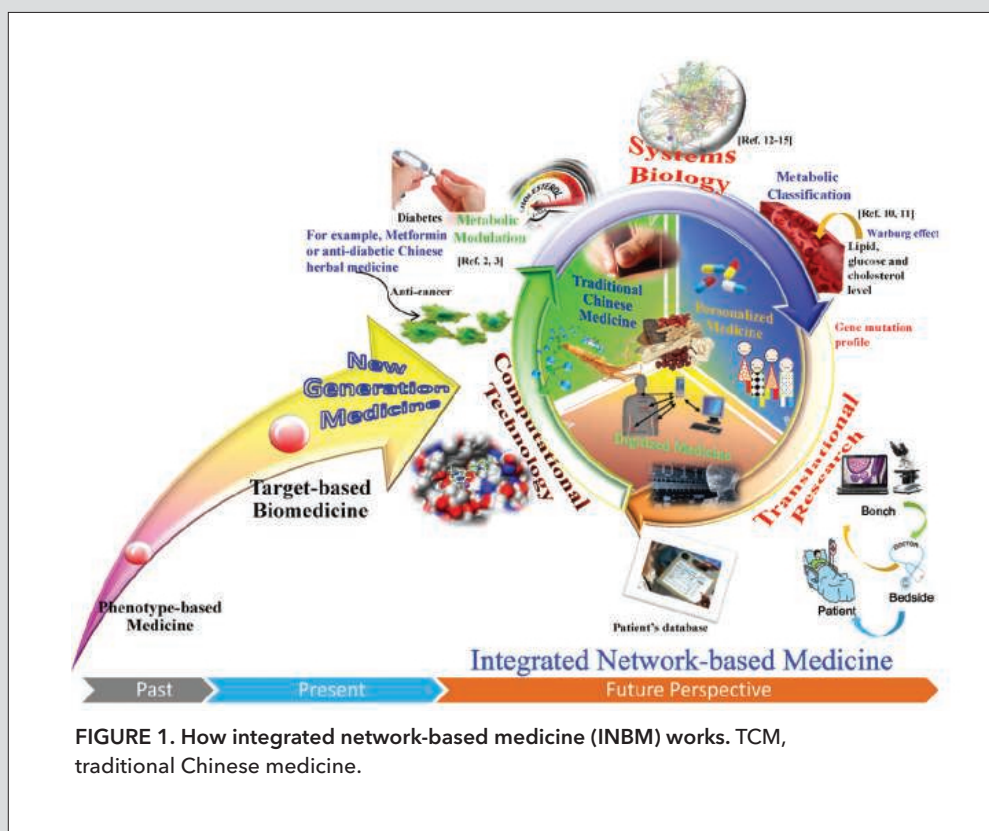


FIGURE 1. How integrated network-based medicine (INBM) works. TCM, traditional Chinese medicine.

overall impact of drug on the glucose metabolic network (3). This has raised the possibility that the drug will have new therapeutic uses (4). Efforts to focus on a single target can also have deleterious effects on the body's overall system. An example is indomethacin, a conventional Western-medicine drug. Indomethacin exerts an anti-inflammatory effect by inhibiting prostaglandin E2 (PGE2) synthesis (5), but this suppression of PGE2 also affects a receptor for mucus secretion, leading to gastric mucosa damage (6, 7). A holistic view of the body's network of connections will anticipate such

Materials that appear in this section were not reviewed or assessed by *Science* Editorial staff, but have been evaluated by an international editorial team consisting of experts in traditional medicine research.

State Key Laboratory of Quality Research in Chinese Medicine, Macau University of Science and Technology, Macau, China
*Corresponding Author: lliu@must.edu.mo

S17

development of CHMs can be combined with digitalized medicine advances such as systems biology techniques, computational technologies, and translational research to provide the foundation for a “personalized” INBM strategy. Our proposal for a new personalized approach to cancer treatment provides just one example of the use of CHM for a network-based treatment. We have recently investigated two CHMs, *Panax ginseng* and *Rhizoma Coptidis*, and found that they inhibit cancer growth, prompting us to investigate the effects of these herbs on cancer cell metabolism. Using profiling methods such as liquid chromatography, mass spectrometry, and nuclear magnetic resonance, we found alterations to the glucose and fatty acid metabolic pathways at a network level (10, 11). We therefore speculate that metabolic biomarkers could be used to identify subgroups of patients with lipid- and glucose-related metabolic disorders. These patients are likely to benefit most from the herbs’ active compounds. The approach could be further refined by the application of ‘omics technologies to optimize the synergistic effect of the herbal remedies (12–15). With clinicians and basic researchers working together to create a database of personal therapeutic responses, continual improvements to herbal formulations would become possible.

From TBBM to INBM

How do we turn the INBM system from an idea into a practice? One major step forward would be the systematic quantitative and qualitative analysis of individual CHM components. Such a database would help define parameters for the combination treatments. One requirement is to identify, monitor, and control the major metabolic pathways, as altering a key molecular switch could have unintended, amplified effects on the entire network. A number of studies have begun to identify the specific network effects of various CHM-extracts or CHM-derived chemicals, including red yeast rice, *Tripterygium wilfordii* Hook. F., *Ganoderma lucidum*, San Miao Wan, arsenic sulfide, astragaloside IV, *Artemisia capillaris* Thunb, *Radix Angelica Sinensis*, Realgar-Indigo naturalis formula, and quinolones (11–16). In another example from our own work, we recently found that an active component from *Ampelopsis grossedentata* targets a novel drug-binding site on IKK- β kinase. The use of this ingredient in combination with dexamethasone suppresses inflammation in mice and reduces one of dexamethasone’s side-effects: shrinkage of the thymus (17). We have also investigated matrine, an alkaloid found in *Radix Sophorae Flavescentis*. This small molecule can activate the Ca²⁺-NFAT (nuclear factor of activated T cells) pathway, resulting in anergy (immune unresponsiveness), suggesting that it may be useful for treating autoimmune disorders (18).

Further investigation of network connections revealed that the CHM components PAB, saikosaponin d, and shikonin inhibit IKK- β and NF- κ B pathways simultaneously, while NFAT activation can be triggered by matrine. As shown in Figure 2, the overall impact is to trigger immunotolerance (19–21). A number of other studies have also demonstrated network-based effects in inflammatory diseases and cancer with CHM compounds such as PHY906 (22), curcumin (23), and berberine (24).

In conclusion, the development of INBM will enhance our medical and health care system, and TCM has an important role to play in building the foundation for the approach. The route from TBBM to INBM has obstacles, from unraveling the crosstalk of multiple molecular pathways to understanding CHM’s network effects, to digitalizing the large amounts of data. Nevertheless, TCM—and our ancestors’ wisdom—offers us a blueprint for establishing and implementing an INBM system for the betterment of humankind.

References

1. H. J. Federoff, L. O. Gostin, *JAMA* **302**, 994 (2009).
2. G. Rena, E. R. Pearson, K. Sakamoto, *Diabetologia* **56**, 1898 (2013).
3. D. Li, *J. Diabetes* **3**, 320 (2011).
4. R. J. Dowling, M. Zakikhani, I. G. Fantus, M. Pollak, N. Sonenberg, *Cancer Res.* **67**, 10804 (2007).
5. S. G. Rhind, G. A. Gannon, M. Suzui, R. J. Shephard, P. N. Shek, *Am. J. Physiol.* **276**, R1496 (1999).
6. P. Kalinski, *J. Immunol.* **188**, 21 (2012).
7. T. J. Weber, T. J. Monks, S. S. Lau, *Am. J. Physiol.* **273**, F507 (1997).
8. W. L. Hsiao, L. Liu, *Planta Med.* **76**, 1118 (2010).
9. C. T. Keith, A. A. Borisy, B. R. Stockwell, *Nat. Rev. Drug Discov.* **4**, 71 (2005).
10. R. J. DeBerardinis, C. B. Thompson, *Cell* **148**, 1132 (2012).
11. M. Journoud, P. J. Jones, *Life Sci.* **74**, 2675 (2004).
12. F. F. Costa, *Drug Discov. Today* **19**, 433 (2014).
13. J. van der Greef et al., *Planta Med.* **76**, 2036 (2010).
14. Q. Y. Zhang et al., *Proc. Natl. Acad. Sci. U.S.A.* **106**, 3378 (2009).
15. J. Zhao, P. Jiang, W. Zhang, *Brief. Bioinform.* **11**, 417 (2010).
16. J. Sendzik, M. Shakibaei, M. Schafer-Korting, H. Lode, R. Stahlmann, *Int. J. Antimicrob. Ag.* **35**, 366 (2010).
17. Z. Q. Liu et al., *J. Pharmacol. Sci.* **99**, 381 (2005).
18. T. Li et al., *Biol. Pharm. Bull.* **33**, 40 (2010).
19. T. Li et al., *J. Cell. Biochem.* **108**, 87 (2009).
20. T. Li, F. Yan, R. Wang, H. Zhou, L. Liu, *Evid. Based Compl. Alt. Med.* **2013**, 379536 (2013).
21. V. K. Wong, H. Zhou, S. S. Cheung, T. Li, L. Liu, *J. Cell. Biochem.* **107**, 303 (2009).
22. W. Lam et al., *Sci. Transl. Med.* **2**, 45ra59 (2010).
23. A. Koeberle, O. Werz, *Drug Discov. Today*, Epub ahead of print (2014), doi: 10.1016/j.drudis.2014.08.006.
24. Z. Li, Y. N. Geng, J. D. Jiang, W. J. Kong, *Evid. Based Compl. Alt. Med.* **2014**, 289264.

The hunt for antifibrotic and profibrotic botanicals

Authors:

Qihe Xu^{1*},
Yibin Feng²,
Pierre Duez³,
Bruce M. Hendry¹,
Peter J. Hylands⁴

The U.S. government estimates that 45% of deaths in the United States can be attributed to fibrotic diseases,

which are characterized by tissue scarring and often lead to chronic organ failure (1). Over the past several decades, researchers have investigated the underlying mechanisms involved in fibrosis and successfully pinpointed a number of possible drug targets, such as molecular mediators and effector cells. Moreover, a number of exceedingly potent and selective compounds against such targets have been developed, although many have fallen short of expectations (2). For example, the only antifibrotic drug registered in Europe and the United States, pirfenidone, has shown beneficial effects in patients with idiopathic pulmonary fibrosis and fibrotic kidney diseases; however, evidence for its efficacy lies in modest functional improvements, although its clinical efficacy on fibrosis remains elusive (3–5). On the other hand, a number of herbal medicinal products, such as those used in traditional Chinese medicine (TCM), have been reported as modulators of fibrosis, but definitive, comprehensive scientific evidence of botanicals as safe and effective antifibrotic therapeutics is lacking.

Botanicals: A double-edged sword

Botanicals are an important source of antifibrotic activities. For example, halofuginone, a derivative of febrifugine isolated from *Dichroa febrifuga* Lour., and curcumin from *Curcuma longa* L., are reportedly antifibrotic (6–8); silymarin, a standardized mixture of flavolignans from milk thistle [*Silybum marianum* (Linn.) Gaertn.], has been widely used as a hepatoprotective and antifibrotic agent in chronic liver diseases (9, 10). Fuzheng Huayu, a formula widely used in China to prevent and reverse hepatic fibrosis, has recently completed a Food and Drug Administration (FDA)-approved phase II trial in the United States (11, 12).

To discover and compare inflammation-independent antifibrotic activities, we have developed high throughput cellular models of fibrosis to visualize and quantify excessive accumulation of total collagens (a gold standard for clinical diagnosis of fibrosis) and the subsequent disruption of cell monolayers (resembling fibrosis-induced disruption of a tissue's architecture) (13). Using this in vitro platform, we have established the direct antifibrotic activities of five active compounds, 11 individual

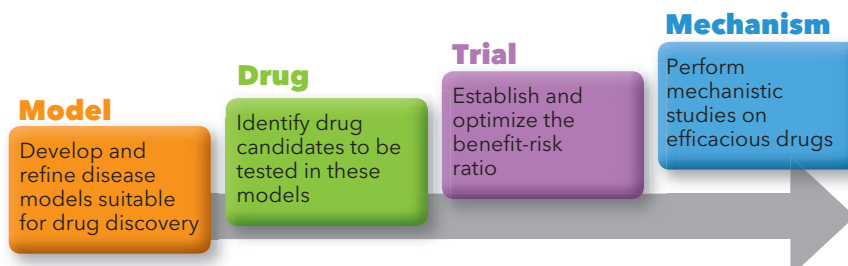


FIGURE 1. Steps proposed for an efficacy-based drug development strategy, particularly well-suited for studying antifibrotic botanicals.

herbs, and 16 herbal formulae (14, 15).

We found that Fuzheng Huayu and *Salvia miltiorrhiza* Bunge (SMB) root, a main component of Fuzheng Huayu, display the most potent in vitro antifibrotic activities among all the formulae and herbs that were tested (14). Besides, in a recent systematic review on clinical treatment of chronic hepatitis B—which took into account 138 trials, 62 proprietary traditional drugs, and 16,393 patients—SMB and its extracts were pinpointed among the top five herbal entities reported to have the most potent antifibrotic activities (16).

In contrast, some botanicals are suspected of causing fibrosis. Herbs have been regularly reported as being associated with chronic liver damage, from Africa to Asia and across the world (17–21). In clinical reports from Beijing and Shanghai, for example, herbs accounted for 21%–53.6% of drug-induced liver injury (18, 22, 23). In one of these same studies, biopsy findings indicated that liver fibrosis is not uncommon in patients with herb-associated liver injury (18).

Herbs have also been reported to be associated with fibrosis of the heart, mesentery, and kidney (24). For example, mesenteric fibrosis has been associated with long-term consumption of formulae containing *Gardenia jasminoides* Ellis fruits in Japanese patients and renal fibrosis is now well known to be induced by some *Aristolochia* taxa and other species containing aristolochic acids (AAs) (25–27). Once reported for medicinal use across a number of different regions, AA-containing plants are now recognized as a worldwide health threat and banned in most Western countries due to their association with AA nephropathy (AAN), including Balkan endemic nephropathy, which results from consuming grains contaminated by *Aristolochia* seeds (27). In vitro and in vivo studies indicate that many other herbs are associated with renal fibrosis. Notable examples include *Dioscorea villosa*

Materials that appear in this section were not reviewed or assessed by *Science* Editorial staff, but have been evaluated by an international editorial team consisting of experts in traditional medicine research.

¹Department of Renal Sciences, Division of Transplantation Immunology and Mucosal Biology, MRC Centre for Transplantation, King's College London, London, U.K.

²School of Chinese Medicine, The University of Hong Kong, Hong Kong SAR, China

³Department of Therapeutical Chemistry and Pharmacognosy, Université de Mons, Mons, Belgium

⁴Institute of Pharmaceutical Science, King's College London, London, U.K.

*Corresponding Author: qihe.xu@kcl.ac.uk

L. rhizome, an herb commonly used in Australia to treat symptoms of menopause and rheumatoid arthritis (28), and *Leonurus japonicus* Houtt., an herb commonly used in TCM for gynecology and obstetrics (15, 29). Additionally, we previously found that ethanolic extracts from unprocessed main roots of *Aconitum carmichaeli* Debx. have potent in vitro profibrotic activities (15)—this is likely clinically relevant since consumption of *Aconitum* species is known to cause acute renal failure and has been recently linked to end-stage renal disease (ESRD) in a case report by the U.K. Medicines and Healthcare Products Regulatory Agency (30).

The impact of identifying and avoiding exposure to profibrotic botanicals is profound. For instance, about one-third of the Taiwanese population consumed AA-containing herbs between 1997 and 2003 (31), and AAN previously accounted for up to 10% of all ESRD in Taiwan (32). The banning of AA-containing herbs, together with other efforts such as public-awareness campaigns, education of patients, funding for research into chronic kidney disease, and provision of integrated care, has turned Taiwan into one of the few regions with retarded increase of ESRD incidence (33).

Moving forward

Due to the contradictory and complex roles botanicals play in fibrotic diseases, there is an urgent need for studies that investigate the efficacy, safety, and good practices for botanical-based remedies.

Since fibrotic diseases are multifactorial conditions and botanicals are typically multitarget entities, an efficacy-based strategy is particularly well-suited for studying antifibrotic botanicals (Figure 1).

Such a strategy is highly dependent on disease modeling. It is worth emphasizing that innovation is needed to develop high-quality in silico, in vitro, and in vivo models that can facilitate the investigation of antifibrotics and detect profibrotic activities.

Because evidence-based medicine is a relatively new concept in many countries (34), many clinical reports on herbal treatment of fibrotic diseases are criticized for poor quality. Diseases for which the literature has been recently reviewed include liver fibrosis (35, 36), pulmonary fibrosis (36), multiple sclerosis (36), and adhesive small bowel obstruction (37). An efficacy-based strategy ultimately demands high-quality clinical trials to prove antifibrotic effects and invites interregional cooperation on pharmacovigilance of profibrotic botanicals, which is challenging due to the insidious nature of fibrosis and the variability in the distribution channels and legal status of botanicals across regions (38, 39).

Finally, traditional use is only an indication but certainly not a proof of either safety or efficacy (40). To harness and understand botanicals both as potential antifibrotic therapeutics and for the prevention of fibrotic diseases, future research and innovation must focus on efficacy and safety, and must be built on and contribute to good practices, which we have recently defined at length (41). Development and refinement of good practices, however, can only be achieved with sustainable funding.

References

1. T. A. Wynn, *Nat. Rev. Immunol.* **4**, 583 (2004).
2. S. L. Friedman, D. Sheppard, J. S. Duffield, S. Violette, *Sci. Transl. Med.* **5**, 167sr1 (2013).
3. P. W. Noble et al., *Lancet* **377**, 1760 (2011).
4. K. Sharma et al., *J. Am. Soc. Nephrol.* **22**, 1144 (2011).
5. M. E. Cho, D. C. Smith, M. H. Branton, S. R. Penzak, J. B. Kopp, *Clin. J. Am. Soc. Nephrol.* **2**, 906 (2007).
6. M. Pines, I. Vlodavsky, A. Nagler, *Drug. Dev. Res.* **50**, 371 (2000).
7. D. Punithavathi, N. Venkatesan, M. Babu, *Br. J. Pharmacol.* **131**, 169 (2000).
8. R. Bruck et al., *Liver Int.* **27**, 373 (2007).
9. N. D. Freedman et al., *Aliment Pharmacol. Ther.* **33**, 127 (2011).
10. F. Wei et al., *Eur. J. Clin. Microbiol. Infect. Dis.* **32**, 657 (2013).
11. P. Liu, *Chin. J. Integr. Med.* **18**, 398 (2012).
12. Z. Xu, *Nature* **480**, S90 (2011).
13. Q. Xu, J. T. Norman, S. Shrivastav, J. Lucio-Cazana, J. B. Kopp, *Am. J. Physiol. Renal Physiol.* **293**, F631 (2007).
14. Q. Hu et al., *Nephrol. Dial. Transplant.* **24**, 3033 (2009).
15. Q. Xu et al., in *Recent Advances in Theories and Practice of Chinese Medicine*, X. Kuang Ed, (Intech, Rijeka, 2012), p. 337.
16. T. Zhan, X. Wei, Z. Q. Chen, D. S. Wang, X. P. Dai, *J. Tradit. Chin. Med.* **31**, 288 (2011).
17. B. J. Auerbach et al., *PLOS ONE* **7**, e41737 (2012).
18. R. T. Lai et al., *Zhonghua Gan Zang Bing Za Zhi* **20**, 185 (2012).
19. J. B. Wang et al., *PLOS ONE* **6**, e24498 (2011).
20. J. Y. Wang et al., *Liver Int.* **34**, 583 (2014).
21. R. Teschke, J. Schulze, A. Schwarzenboeck, A. Eickhoff, C. Frenzel, *Eur. J. Gastroenterol. Hepatol.* **25**, 1093 (2013).
22. F. Q. Hou, T. L. Wang, X. Liu, N. Huo, G. Q. Wang, *Hepatogastroenterology* **57**, 554 (2010).
23. G. D. Zhou et al., *Zhonghua Gan Zang Bing Za Zhi* **15**, 212 (2007).
24. D. H. Connor, K. Somers, A. M. Nelson, P. G. D'Arbela, R. Lukande, *Trop. Doct.* **42**, 206 (2012).
25. K. Hiramatsu et al., *Aliment Pharmacol. Ther.* **36**, 575 (2012).
26. K. Nomura et al., *Nihon Shokakibyō Gakkai Zasshi* **109**, 1567 (2012).
27. M. R. Gökmen et al., *Ann. Intern. Med.* **158**, 469 (2013).
28. K. Wojcikowski, H. Wohlmuth, D. W. Johnson, G. Gobe, *Food Chem. Toxicol.* **46**, 3122 (2008).
29. R. Sun, X. Wu, J. Liu, L. Sun, L. Lv, *Pharmacology and Clinics of Chinese Materia Medica* **21**, 28 (2005).
30. MHRA warns of the dangers of taking unlicensed herbal medicines containing aconite. 2013, <http://www.mhra.gov.uk/Safetyinformation/Generalsafetyinformationandadvice/Herbalmedicines/Herbalsafetyupdates/Allherbalsafetyupdates/CON263932>
31. S. C. Hsieh, I. H. Lin, W. L. Tseng, C. H. Lee, J. D. Wang, *Chin. Med.* **3**, 13 (2008).
32. F. L. Lin Wu et al., *Nephron. Clin. Pract.* **120**, c215 (2012).
33. V. Jha et al., *Lancet* **382**, 260 (2013).
34. J. Wang, *Lancet* **375**, 532 (2010).
35. F. Cheung et al., *Chin. Med.* **7**, 5 (2012).
36. J. Liu, in *The Fundamentals of Fibrosis, and the Prevention and Treatment of Fibrosis in Traditional Chinese Medicine*, J. Niu, C. Ben, Eds. (People's Health Press, Beijing, 2008), p. 31.
37. T. Suo et al., *Cochrane Database Syst. Rev.* **5**, CD008836 (2012).
38. EMA, EMA publication EMA/322570/2011 Rev. 3, 2013, http://www.ema.europa.eu/docs/en_GB/document_library/Report/2011/05/WC500106706.pdf
39. T. P. Fan et al., *J. Ethnopharmacol.* **140**, 568 (2012).
40. Q. Xu et al., *BMC Complement Altern. Med.* **13**, 132 (2013).
41. H. Uzuner et al., *J. Ethnopharmacol.* **140**, 458 (2012).

Acknowledgments

The authors thank Kidney Research UK and the European Commission for their funding support, and Professor Chih-Wei Yang (Chang Gung Memorial Hospital and Chang Gung University College of Medicine, Taiwan) and Professor Joëlle Nortier (Erasmus Hospital, Université Libre de Bruxelles, Brussels, Belgium) for their expert advice in the preparation of this manuscript.

i-Needle: Detecting the biological mechanisms of acupuncture

Authors:

Christine Nardini^{1,2*†},
Sandro Carrara^{3*†},
Yuanhua Liu²,
Valentina Devescovi²,
Youtao Lu²,
Xiaoyuan Zhou²

A long standing obstacle to the (full) integration and acceptance of acupuncture in conventional medicine lies in the difficulty of reconciling traditionally defined categories (acupoints, meridians, and energy flow or *qi*) with anatomical structures and biochemical

pathways. Additionally, a unified scientific theory to explain the diverse effects of acupuncture (from pain control to immunomodulation) is lacking, despite important advances in the association of purinergic signaling with the effects of acupuncture on pain control. As new technologies simultaneously offer enhanced capacities to explore breadth (using 'omics) and depth (using nanobiochips) of biochemical events, we propose the innovative conjugation of these approaches into an intelligent needle (*i*-needle) as a means to overcome the abovementioned limitations.

Acupuncture is being widely debated in the medical community as a potential alternative or complementary treatment for many diseases (1). There are numerous challenges to achieving a consensus over the use of acupuncture in a medical environment, including: filling the gap in knowledge about the underlying molecular mechanisms of acupuncture, and (re)interpreting traditional categories (such as acupoints, meridians, and *qi*) and therapeutic indications within an evidence-based medicine framework. Important questions aimed at increasing our understanding of the molecular effects of needle stimulation have been posed, mostly regarding pain control (2), functional recovery of tissue (3), and immunomodulation (4), with remarkable work done as to the correlation of pain control with purinergic signaling (5, 6). Using 'omics-based technology and network representations, researchers have successfully mapped the molecular underpinnings of traditional categories (7). More generally, the holistic method used in acupuncture, which has long been difficult to reconcile with the scientific reductionist viewpoint, has recently been found to be compatible with a systems biology approach (8).

'Omics-based techniques are diverse and allow for the screening of targets from nucleic acids (DNA-sequencing, RNA-sequencing) to proteins and metabolites (mass spectrometry/liquid chromatography, nuclear magnetic resonance) and their heterogeneous interactions (chromatin immunoprecipitation-sequencing), to name just the major technologies. Recently, whole new areas of exploration have been opened with metagenomics and metatranscriptomics where the host-microbiome relationship can be analyzed systemically and in situ. Further, rapidly decreasing costs are permitting researchers to prefigure relatively high spatial (different body regions and tissues) and temporal resolution. Here, we propose to

integrate such highly resolved molecular, temporal, and spatial data to reveal the molecular signaling pathways that flow from the tip of the needle to the disease/injury site.

Understanding the biochemical signaling pathway that the mechanical rotation of an acupuncture needle sets into motion (9) is an important starting point. Mechanosensing and mechanotransduction are widespread in biology with well-assessed relevance in embryonic development, i.e., type 1 epithelial-mesenchymal transition (EMT) (10). Their roles, however, have not been well explored under the broader definition of EMT (11)—which includes events such as wound healing (type 2 EMT) and cancer (type 3 EMT)—despite promising therapeutic results when mechanical stimulation is locally applied (12). Acupuncture needle stimulation (9) and low level laser therapy (13) are among the triggers that have been shown to initiate a series of synergistic events, including calcium waves, ATP fluxes (purinergic signaling), and changes in reactive oxygen and nitrogen species concentration, known to initiate healing (14, 15). The homeostatic effects of type 2 EMT include local changes in purinergic signaling, inflammation control, regeneration, and remodeling at the site of injury. By contrast, acupuncture is recommended for systemic diseases like rheumatoid arthritis (1) and is thought to act in a more global fashion.

Using the framework we propose here, we can investigate the long range, systemic effects of mechanotransduction by building on what has already been reported about the wound healing process, including the presence of peripheral markers of EMT (16).

To explore the long range effects of acupuncture, multiomic analysis of molecular events—occurring proximally (acupoint), distally from the stimulation point (target organ), and systemically (blood and gastrointestinal microbiome)—can be used to construct a spatial analysis (17). This information can then be enriched with data about the temporal onset of early gene expression, in addition to later time points (Figure 1A) to construct a systems biology view (network) of the biochemical events.

To build such networks and identify new targets for diagnosis and therapy, computational analysis must bring together the different 'omics approaches (Figure 1B), coupled with the requisite temporal and spatial resolution of the data (19). This type of network approach can identify the most important molecules from the thousands to tens-of-thousands of interactions and hundreds-to-thousands of molecules analyzed, also taking into account distal factors that might play a role in causing or modulating the pathologies.

Furthermore, the identification of additional markers is made possible with a complementary approach to the high

¹Lazzari, Bologna, Italy

²Group of Clinical Genomic Networks, Key Laboratory of Computational Biology, CAS-MPG Partner Institute for Computational Biology, Shanghai Institutes for Biological Sciences, Shanghai, China

³Bio/Interfaces Group, Integrated System Laboratory, EPFL-École Polytechnique Fédérale de Lausanne, Switzerland.

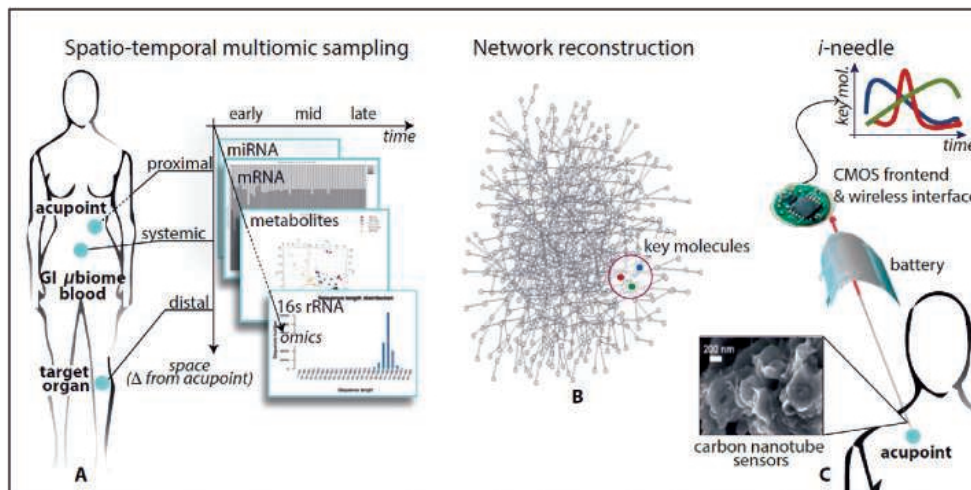
*Corresponding Authors: christine.nardini.rsrc@gmail.com (C.N.) and sandro.carrara@epfl.ch (S.C.)

†These authors contributed equally to this work

Materials that appear in this section were not reviewed or assessed by *Science* Editorial staff, but have been evaluated by an international editorial team consisting of experts in traditional medicine research.

FIGURE 1. Elements of the i-needle. (A) A variety of 'omics techniques can be used to monitor molecular progress across body sites and over time. The pictured model shows the spatiotemporal multi-'omic sampling of the molecular flow of events over the therapy's delivery, from early molecular activation at the acupoint to the peripheral bloodstream and gastrointestinal (GI) microbiome (μ biome) to ultimately reach the target organ. (B) Multi-'omic systems biology enables the identification of a network of

events, allowing interpretation of acupuncture in terms of a biochemical signaling flow that alters the whole system (body/patient). Network analysis and simulations allow identification of molecules that can be monitored as markers of the progress of the therapy (18). (C) Diagram showing carbon nanotube (CNT)-based sensor integration to continuously monitor the therapy-induced biochemical progression. Sensors are mounted on an energy-autonomous device that is able to transmit information remotely and in real-time.



throughput and low sensitivity of these 'omics analyses. This can be imagined in the form of a nanobiochip that is the size and shape of an acupuncture needle (hence, an "intelligent" needle or *i*-needle) (Figure 1C).

Toward this end, we recently created a proof-of-principle miniaturized platform, integrating revolutionary carbon nanotubes and nanographite petals, which can monitor five endogenous human metabolites using highly sensitive and selective nanobiosensors (20). The electronics needed to acquire and transfer the detected signal have already been sufficiently miniaturized (21) and can be powered by ultrathin polymer-based batteries (22) currently available on the market and able to meet the energy demands of the proposed *i*-needle (~80–130 μ Ah).

The challenge for the realization of the *i*-needle has already moved from the miniaturization to the integration step (23). Progress has already been made, based on recent reports of the measurement and transmission of temperature, pH, and endogenous metabolite data using single-platform enzyme-carbon nanotube hybrid sensors (24, 25).

Conclusions

Overall, it is our hope that this research can provide a more unified approach to understanding the complex nature of patient responses to acupuncture—including effects as diverse as the control of pain, degeneration, and inflammation—and to addressing fundamental issues in acupuncture treatment, such as the frequency of delivery, developing more precise therapeutic indications, and establishing proper "dosage" guidelines. These steps will undoubtedly encourage acceptance of acupuncture as a complementary and/or alternative personalized treatment, with important application in a wide variety of areas including pain control, and degenerative and chronic inflammatory diseases, among others.

References

1. WHO, *Acupuncture: review and analysis of reports on controlled clinical trials*. (WHO, Geneva, Switzerland, 2002), <http://apps.who.int/iris/handle/10665/42414>.
2. G. Burnstock, *Med. Hypotheses* **73**, 470 (2009).
3. Y. Ding et al., *BMC Neurosci.* **10**, 35 (2009).
4. Y. Liu et al., *PLOS ONE* **8**, e51573 (2013).
5. N. Azorin et al., *Exp. Dermatol.* **20**, 401 (2011).
6. W. Z. Tu et al., *Neurochem. Int.* **60**, 379 (2012).
7. H. van Wietmarschen et al., *J. Clin. Rheumatol.* **15**, 330 (2009).
8. J. Jia et al., *J. Ethnopharmacol.* **140**, 594 (2012).
9. H. M. Langevin, N. A. Bouffard, G. J. Badger, D. L. Churchill, A. K. Howe, *J. Cell. Physiol.* **207**, 767 (2006).
10. A. Mammoto, T. Mammoto, D. E. Ingber, *J. Cell Sci.* **125**, 3061 (2012).
11. R. Kalluri, R. A. Weinberg, *J. Clin. Invest.* **119**, 1420 (2009).
12. V. W. Wong, S. Akaishi, M. T. Longaker, G. C. Gurtner, *J. Invest. Dermatol.* **131**, 2186 (2011).
13. E. Takai, M. Tsukimoto, H. Harada, S. Kojima, *Radiat. Res.* **175**, 358 (2011).
14. J. V. Cordeiro, A. Jacinto, *Nat. Rev. Mol. Cell. Biol.* **14**, 249 (2014).
15. G. C. Gurtner, S. Werner, Y. Barrandon, M. T. Longaker, *Nature* **453**, 314 (2008).
16. M. Mildner et al., *PLOS ONE* **8**, e60103 (2013).
17. S. E. Winter, C. A. Lopez, A. J. Baumler, *EMBO Rep.* **14**, 319 (2013).
18. P. Tieri, X. Zhou, L. Zhu, C. Nardini, *Front. Cell Dev. Biol.*, **2**, Epub before print (2014), doi: 10.3389/fcell.2014.00059.
19. B. Kholodenko, M. B. Yaffe, W. Kolch, *Sci. Signal.* **5**, re1 (2012).
20. I. Taurino et al., *Nano Letters* **14**, 6 (2014).
21. J. Yoo, L. Yan, S. Lee, Y. Kim, H.-J. Yoo, *IEEE Journal of Solid-State Circuits* **45**, 178–188 (2010).
22. H. Nishide, K. Oyaizu, *Science* **319**, 737 (2008).
23. T. E. Kiazor, *Philosophical Transactions of the Royal Society A: Mathematical, Physical and Engineering Sciences* **372**, 20130105 (2014).
24. A. Cavallini, C. Baj-Rossi, S. Ghoreishizadeh, G. De Micheli, S. Carrara, *Biomedical Circuits and Systems Conference (BioCAS), 2012 IEEE*, pp. 124 (2012).
25. S. Carrara, A. Cavallini, S. Ghoreishizadeh, J. Olivo, G. De Micheli, in *IEEE Sensors conference*, (2012), pp. 28–31.

Purinergetic signaling in acupuncture

Author:
Geoffrey Burnstock

The proposed role of purinergetic signaling in the physiological basis of acupuncture was first presented in 2009. Data showing that ATP is released from keratinocytes and other skin cells during acupuncture treatments lends weight to this hypothesis. ATP in turn activates P2X3 receptors on the sensory nerves in the skin, which then transmit those messages to motor neurons in the brain stem that control autonomic functions and modulate nociceptive activities. Here, we review and describe the recent evidence for purinergetic signaling underlying acupuncture effects and propose ways to further test this hypothesis.

Introduction

It has been well established that adenosine 5'-triphosphate (ATP) is an intracellular energy source in cellular biochemistry. In 1970, Burnstock et al. suggested that ATP acted as a nonadrenergic, noncholinergic neurotransmitter in the gut (1), and in 1972 he named the extracellular actions of ATP, "purinergetic signaling" (since ATP is a purine nucleotide), and formulated the purinergetic signaling hypothesis (2).

In 2009, Burnstock proposed that purinergetic signaling could be involved in the physiological mechanisms mediating acupuncture effects. This hypothesis suggested that mechanical deformation of the skin by needles or application of heat or electrical current leads to the release of large amounts of ATP from keratinocytes, fibroblasts, and other cell types in skin (Figure 1). The released ATP then activates P2X3 ion channel receptors on sensory nerves within the skin and tongue that transmit messages via sensory ganglia and the spinal cord to the brain stem and hypothalamus. These brain regions contain motor neurons that control autonomic functions, including cardiovascular, gastrointestinal, respiratory, and urinogenital activities—common targets of acupuncture treatments. These sensory neuron messages also modulate the pathways that lead to centers in the cortex responsible for conscious awareness of pain and other central nervous system activities, including sleep regulation (3). A number of subsequent studies have been published that also implicate purinergetic signaling in various aspects of acupuncture, detailed below.

Materials that appear in this section were not reviewed or assessed by *Science* Editorial staff, but have been evaluated by an international editorial team consisting of experts in traditional medicine research.

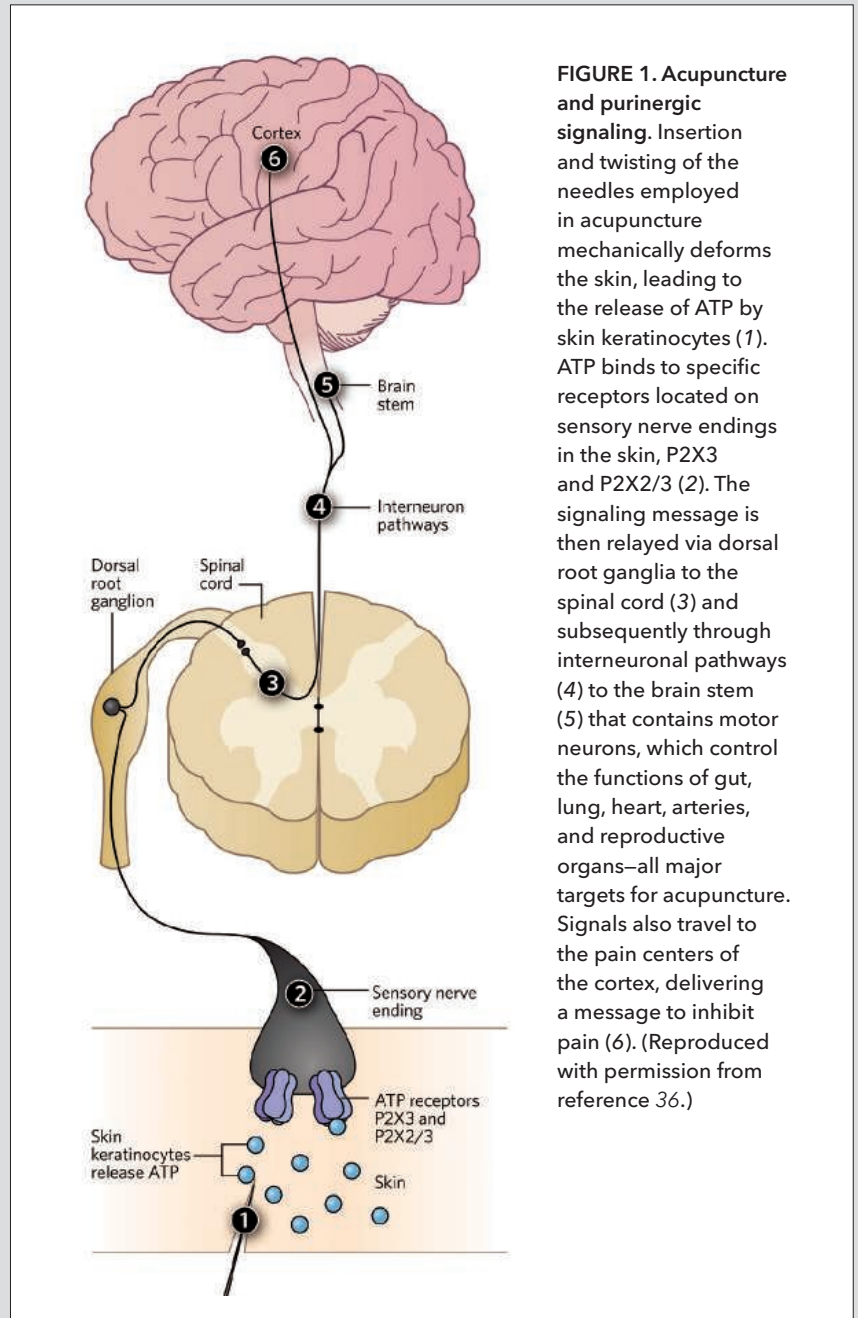


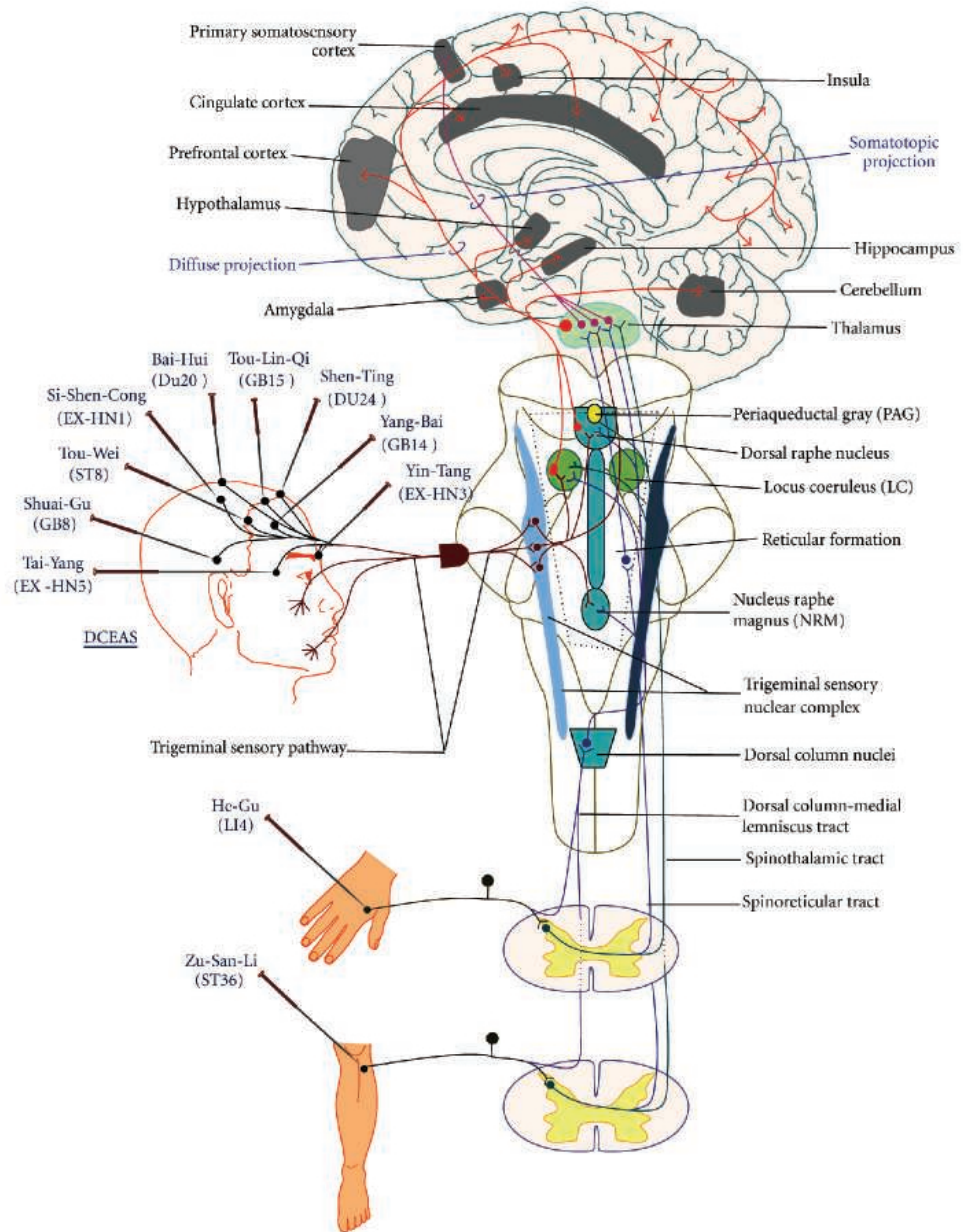
FIGURE 1. Acupuncture and purinergetic signaling. Insertion and twisting of the needles employed in acupuncture mechanically deforms the skin, leading to the release of ATP by skin keratinocytes (1). ATP binds to specific receptors located on sensory nerve endings in the skin, P2X3 and P2X2/3 (2). The signaling message is then relayed via dorsal root ganglia to the spinal cord (3) and subsequently through interneuronal pathways (4) to the brain stem (5) that contains motor neurons, which control the functions of gut, lung, heart, arteries, and reproductive organs—all major targets for acupuncture. Signals also travel to the pain centers of the cortex, delivering a message to inhibit pain (6). (Reproduced with permission from reference 36.)

Supporting evidence for the hypothesis

Studies that have established the components involved in the purinergetic signaling pathway include: (i) release of ATP (in response to mechanical or chemical stimulation)

Autonomic Neuroscience Centre, University College Medical School, London, UK, and Department of Pharmacology and Therapeutics, The University of Melbourne, Melbourne, Australia
g.burnstock@ucl.ac.uk

FIGURE 2. Schematic illustration of the central neural pathways that carry afferent (sensory) neural impulses following acupuncture treatment from various parts of the body. Brain areas that commonly respond in neuroimaging studies to acupuncture stimulation are indicated with gray shadow. DCEAS: dense cranial electroacupuncture stimulation. (Reproduced from 28, with permission from Hindawi Publishing Corporation.)



from keratinocytes (4-6) and possibly from Merkel cells, which contain high levels of ATP (7, 8); ATP has also been shown to be released from keratinocytes upon heating (9); (ii) immunohistochemical data demonstrating the presence of P2X3 receptors on sensory nerve fibers in the skin (10-12) and tongue (13); (iii) in an isolated tongue/lingual nerve preparation, mechanical activation of the tongue with De Frey hairs was shown to result in a discharge in the lingual sensory nerve fibers that was mimicked by ATP activation and blocked by P2X3 receptor antagonists (14); and (iv) both presynaptic inhibition via adenosine A_1 and P2Y receptors, and enhancement via P2X and A_{2A} receptors at synapses in

the central nervous system have been reported (15).

Subsequent papers have built upon and extended evidence in support of purinergic signaling underlying acupuncture effects. Several studies have associated the skin cells affected by acupuncture techniques with purinergic signaling. For example, ATP has been shown to be released from human keratinocytes in response to mechanical stimulation by hypo-osmotic shock (16), as well as from keratinocytes in response to heat (17). Additionally, mast cells, which accumulate around the acupuncture needles, also release ATP in response to mechanical stimulation (18). Another skin cell type, human subcutaneous fibroblasts, can

also release ATP in response to bradykinin and histamine (19, 20). Tsutsumi et al. demonstrated that mechanical stimulation can evoke the propagation of calcium waves between human keratinocytes, induced by ATP and activation of P2Y₂ receptors (21, 22), which is consistent with the earlier results from Koizumi et al. (5). Tuina (traditional therapeutic massage) and moxibustion (a traditional Chinese medicine therapy using a moxa, often made from dried mugwort, either used as a fluff or processed into a cigar-shaped stick; it can be used indirectly, with acupuncture needles, or burned on to the patient's skin) may also act via the purinergic signaling pathway (23). Papers describing the release of ATP from human epidermal keratinocytes via connexin hemichannels and vesicles involving vesicular nucleotide transporter have recently been published (24–26). A 2010 study has claimed that adenosine, following breakdown of released ATP during acupuncture, can act as a prejunctional inhibitor of neurotransmission via A₁ receptors, resulting in anti-nociceptive actions (27). Valuable reviews are available describing the neural pathways from different skin regions to structures in the brain stem and higher brain centers. These pathways are important because different acupuncture sites may activate different neural pathways impinging on specific nuclei in the brain stem that control autonomic functions potentially modulated by acupuncture (Figure 2) (28, 29).

Purinergic signaling and electroacupuncture

Electroacupuncture is a form of acupuncture where a small electric current is passed between pairs of acupuncture needles. This is thought to augment traditional acupuncture and is believed to be particularly helpful in treating pain.

The supraspinal antinociception effect of electroacupuncture has been associated with P2X3 receptor activation in the midbrain periaqueductal gray region (30). Moreover, the analgesic effect of electroacupuncture on chronic neuropathic pain has been shown to be mediated by P2X3 receptors in rat dorsal root ganglion neurons (31). Following these studies, electroacupuncture was shown to result in a reduced expression of P2X3 and P2X2 receptors in the dorsal root ganglion of rats with chronic neuropathic pain (32) and visceral hypersensitivity (33). Electroacupuncture at *He-Mu* points can also reduce P2X4 receptor expression in colon and spinal cord in visceral hypersensitivity (34). Moreover, in a review by Lin et al., the neuroprotective effects of acupuncture were reported to act via increasing brain derived neurotrophic factor (BDNF) expression via stimulation of ATP (35).

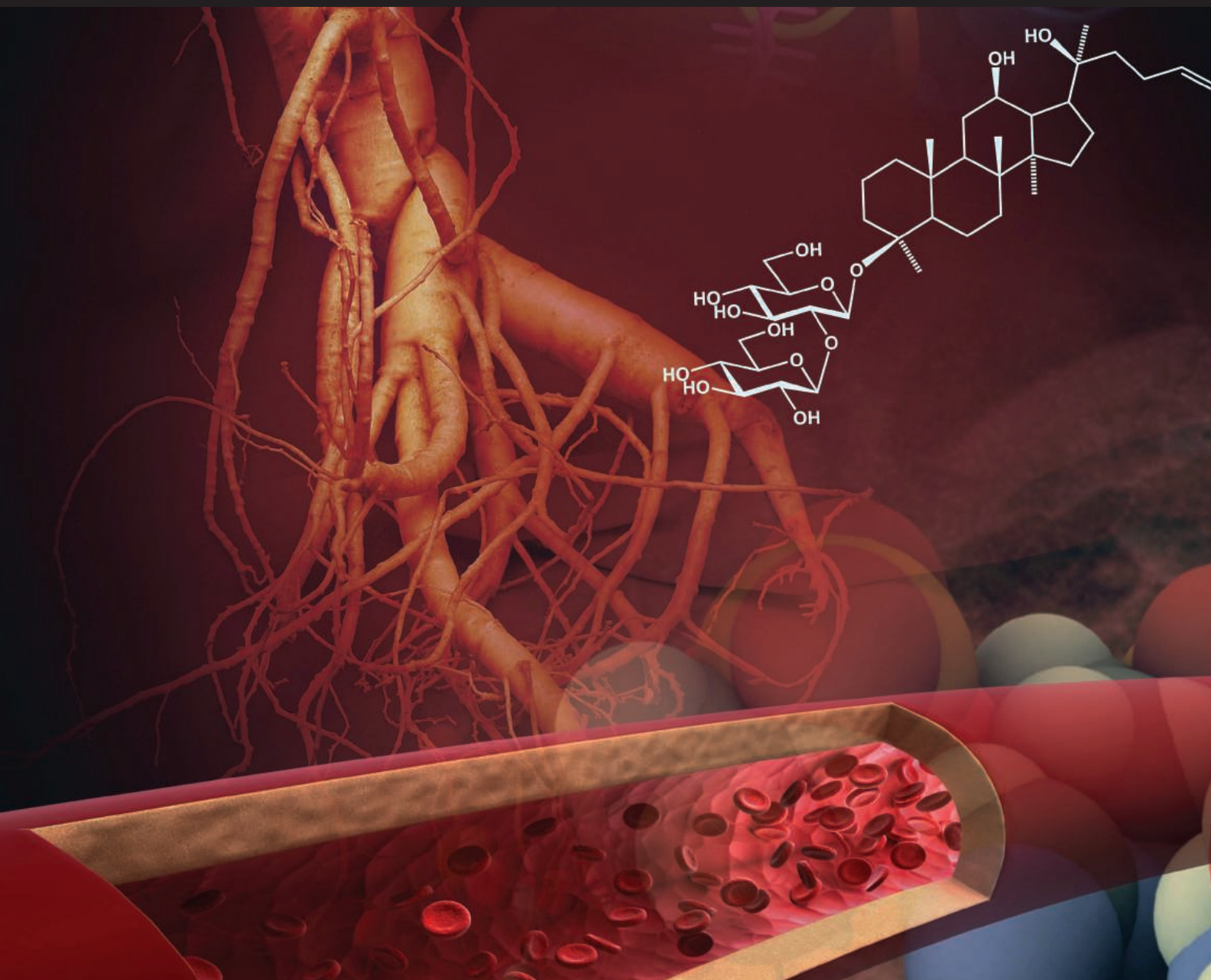
Conclusions

Evidence in support of the hypothesis of purinergic signaling mediating the physiological mechanisms underlying acupuncture effects has been accumulating over recent years. To help further test this hypothesis, I propose that experienced acupuncturists focus on acupuncture sites that induce effects that can be quantified, such as an

increase or decrease in heart rate or blood pressure, and identify specific neurons that are activated in the brain using noninvasive scanning techniques. If acupuncture-induced effects can be identified and quantified, researchers could then test whether ATP mimicks the responses and if P2X3 receptor antagonists block the effects. Moreover, we suggest that researchers conduct experiments recording responses from sensory neurons in the skin and tongue in animal models and distinguish between low-threshold fibers involved in acupuncture and high-threshold fibers that mediate nociception, as well as recordings from the motor nerves in the brainstem responsible for autonomic functions.

References

1. G. Burnstock, G. Campbell, D. Satchell, A. Smythe, *Br. J. Pharmacol.* **40**, 668 (1970).
2. G. Burnstock, *Pharmacol. Rev.* **24**, 509 (1972).
3. G. Burnstock, *Med. Hypotheses* **73**, 470 (2009).
4. N. Mizumoto, M. E. Mummert, D. Shalhevet, A. Takashima, *J. Invest. Dermatol.* **121**, 1066 (2003).
5. S. Koizumi et al., *Biochem. J.* **380**, 329 (2004).
6. H. E. Burrell et al., *J. Biol. Chem.* **280**, 29667 (2005).
7. R. Crowe, M. Whitear, *Cell Tissue Res.* **190**, 273 (1978).
8. M. Silberstein, *Med. Hypotheses* **75**, 272 (2010).
9. S. Mandadi et al., *Pflugers Arch.* **458**, 1093 (2009).
10. E. J. Bradbury, G. Burnstock, S. B. McMahon, *Mol. Cell. Neurosci.* **12**, 256 (1998).
11. G. Burnstock, *Br. J. Anaesth.* **84**, 476 (2000).
12. M. Taylor, J. C. Peleshok, A. Ribeiro-da-Silva, *J. Comp. Neurol.* **514**, 555 (2009).
13. X. Bo et al., *Neuroreport* **10**, 1107 (1999).
14. W. Rong, G. Burnstock, K. M. Spyer, *J. Physiol.* **524**, 891 (2000).
15. G. Burnstock, *Physiol. Rev.* **87**, 659 (2007).
16. N. Azorin et al., *Exp. Dermatol.* **20**, 401 (2011).
17. J. R. Gifford, C. Heal, J. Bridges, S. Goldthorpe, G. W. Mack, *J. Physiol.* **590**, 6403 (2012).
18. L. Wang et al., *Evid. Based Complement. Alternat. Med.* **2013**, 350949 (2013).
19. R. Pinheiro et al., *Cell Commun. Signal.* **11**, 70 (2013).
20. R. Pinheiro et al., *J. Biol. Chem.* **288**, 27571 (2013).
21. M. Tsutsumi et al., *Cell Tissue Res.* **338**, 99 (2009).
22. M. Tsutsumi et al., *Skin Res. Technol.* **16**, 146 (2010).
23. L. Fan, L. M. Yin, *J. Acupunct. Tuina Sci.* **12**, 125 (2014).
24. T. P. Barr et al., *PLOS ONE* **8**, e56744 (2013).
25. T. Takahashi et al., *J. Invest. Dermatol.* **133**, 2407 (2013).
26. K. Inoue et al., *J. Invest. Dermatol.* **134**, 1465 (2014).
27. N. Goldman et al., *Nat. Neurosci.* **13**, 883 (2010).
28. Z. J. Zhang, X. M. Wang, G. M. McAlonan, *Evid. Based Complement. Alternat. Med.* **2012**, 429412 (2012).
29. Q. Q. Li et al., *Evid. Based Complement. Alternat. Med.* **2013**, 267959 (2013).
30. Z. Xiao et al., *Brain Res.* **1330**, 31 (2010).
31. W. Z. Tu et al., *Neurochem. Int.* **60**, 379 (2012).
32. R. D. Cheng et al., *Chin. J. Integr. Med.* **19**, 374 (2013).
33. Z. Wang et al., *Neural Regen. Res.* **8**, 802 (2013).
34. X. Guo et al., *Neural Regen. Res.* **8**, 2069 (2013).
35. D. Lin et al., *Int. J. Mol. Sci.* **15**, 3234 (2014).
36. G. Burnstock, *The Scientist* **25**, 24 (2011).



**The American Association for
the Advancement of Science**
1200 New York Avenue NW
Washington, DC 20005



The content contained in this special, sponsored section was commissioned, edited, and published by the *Science*/AAAS Custom Publishing Office. It was not peer-reviewed or assessed by the Editorial staff of the journal *Science*; however, all manuscripts have been critically evaluated by an international editorial team consisting of experts in traditional medicine research selected by the project editor. The intent of this section is to provide a means for authors from institutions around the world to showcase their state-of-the-art traditional medicine research through review/perspective-type articles that highlight recent progress in this burgeoning area. The editorial team and authors take full responsibility for the accuracy of the scientific content and the facts stated. Articles can be cited using the following format: [Author Name(s)], *Science* **346** (6216 Suppl), Sxx-Sxx (2014).



Automated Microplate Reader

The new Synergy HTX Multi-Mode Microplate Reader is offered as an entry-level multi-mode reader to automate UV-Vis absorbance, fluorescence, luminescence, and AlphaScreen/AlphaLISA assays in 6- to 384-well microplates in 2 μ L samples with BioTek's Take3 Micro-Volume plates. The unique dual-optics design results in superior filter based top and bottom fluorescence-, luminescence-, and monochromator-based absorbance measurements for maximum applications versatility. Synergy HTX's modularity allows upgrading over time and the powerful Gen5 software controls all functionality while providing data analysis for many applications within one powerful yet intuitive package. Synergy HTX has linear and orbital shaking and 4-Zone incubation to 50°C with condensation control to minimize plate lid condensation. These features, plus an available dual reagent dispenser, make Synergy HTX an ideal platform for biochemical and cell-based applications like nucleic acid quantification, cell growth, and toxicity assays, kinetic enzyme-linked immunosorbent assay, and inject/read assays. Workflows can be further automated with the Bio-Stack Microplate Stacker or third-party automation.

BioTek Instruments

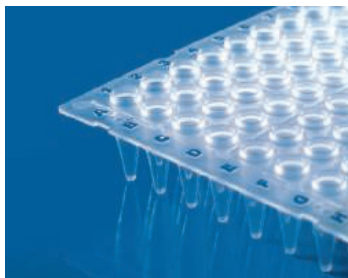
For info: 888-451-5171
www.biotek.com

Environmental Sample Evaporation

The EZ-2 ENVI is designed for gentle evaporation of volatile environmental samples and is proven to give excellent recovery and reproducibility. The fully automated system can concentrate a number of samples at the same time and provide protection from cross contamination and bumping. The ingenious patented design of SampleGenie enables the EZ-2 ENVI to productively concentrate environmental samples to less than 1ml without losing any volatile analytes. Years of experience in solvent evaporation and sample purification have culminated in a smart sample evaporator that saves you time and delivers optimal performance and solvent recovery. Running an EZ-2 ENVI evaporator is as simple as 1, 2, 3. Just load your samples, select maximum safe temperature for samples, select solvent type and hit start. Autostop, when dry or concentrated, means the EZ-2 offers truly unattended operation. Requiring no peripherals for operation the compact EZ-2 ENVI fits neatly onto a laboratory bench or into a fume hood.

Genevac

For info: +44-(0)-1473-240000
www.genevac.com/environmental



PCR Plastics

BrandTech Scientific, Inc. announces a new line of high-quality polymerase chain reaction plastics for standard and low-profile thermal cyclers. These products are made in one of the world's largest cleanroom facilities of its kind and are produced with the newest production technologies, raw materials, and quality testing. They have unique blue alpha-numeric coding and cut corner for easy well identification and handling resulting in more efficient workflow. Extra-thin and uniform walls combined with a rigid upper deck results in more optimal heat transfer and sturdiness for use with robotic equipment. Standard profile plates can now be sealed with cap strips using a unique capping and decapping tool. Low-profile non-skirted and half-skirted plates (0.15 mL) are available for use with popular thermal cyclers such as the Applied Biosystems 9800 Fast, 7900 HT, and 7500 Fast, BIORAD CFX96, and Eppendorf Mastercycler systems.

BrandTech Scientific

For info: 888-522-2726
www.brandtech.com

Raman Spectroscopy Software

Featuring a new 3-D surface and volume display module, LabSpec 6.3 is fully compatible with high-resolution confocal volume maps acquired with HORIBA's range of Raman microscopes. With full control of map rotation, transparency, filtering, and slicing, it is now very easy to view the internal chemical structure of complex heterogeneous samples. Topographic images from the range of combined Raman-AFM (Atomic Force Microscopes) and TERS (Tip-Enhanced Raman Spectroscopy) systems can also be rendered by the module, benefiting from full 3-D surface display with superimposed chemical distribution maps. Innovation and improvements throughout the software also include fully customizable templates for fast personalized reporting, the OneClick easy Raman acquisition tool, and the addition of Partial Least Squares to its multivariate analysis line-up. It also retains the advanced Raman-Particle characterization capabilities of the ParticleFinder module. LabSpec 6 is simple yet powerful software, which allows researchers to handle advanced analytical functionalities in multi-user environments.

HORIBA Scientific

For info: 732-494-8660
www.horiba.com/labspec6

Compound Data Visualization Software

Sentira is a new desktop application that provides dynamic data visualization and analysis of compound data. Applicable across all fields of chemistry, Sentira enables users to quickly find patterns in compound data, visualize structure-activity relationships (SAR) and elegantly present and report findings. Researchers can intuitively review and interpret compound data sets from large screening libraries to individual chemical series. Sentira provides a comprehensive range of plots, all with extensive and fully customizable features. Multiple plots can be created side-by-side, all dynamically linked to each other and the underlying data set, enabling quick identification of important relationships between compound properties. Flexible tools for SAR and matched pair analysis, coupled with a link to the underlying compound structures, affords insightful and intelligent compound data analysis. Sentira's simple design and user-friendly environment provides data management tools to perform calculations, merge, sort, filter, and tag data sets.

Optibrium

For info: +44-(0)-1223-815900
www.optibrium.com

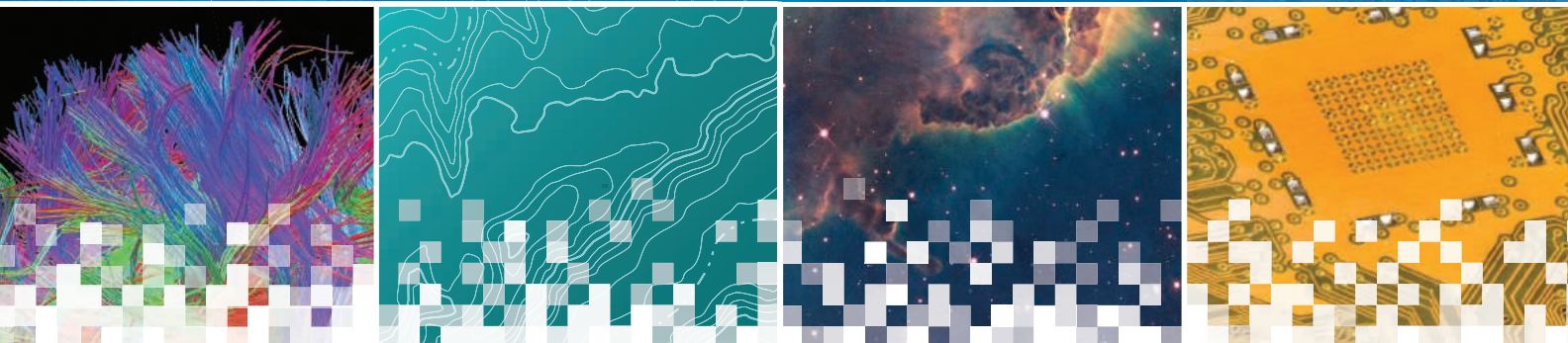
Electronically submit your new product description or product literature information! Go to www.sciencemag.org/products/newproducts.dtl for more information.

Newly offered instrumentation, apparatus, and laboratory materials of interest to researchers in all disciplines in academic, industrial, and governmental organizations are featured in this space. Emphasis is given to purpose, chief characteristics, and availability of products and materials. Endorsement by *Science* or AAAS of any products or materials mentioned is not implied. Additional information may be obtained from the manufacturer or supplier.

AAAS | 2015 ANNUAL MEETING

12–16 FEBRUARY • SAN JOSE, CA

INNOVATIONS, INFORMATION, AND IMAGING



Thank you to our sponsors

AAAS, publisher of *Science*, thanks the sponsors and supporters of the 2015 Annual Meeting



Johnson & Johnson



Genentech
A Member of the Roche Group



the Lemelson foundation
improving lives through invention



for its generous support of
the Science Journalism Awards

www.aaas.org/meetings



EVERYTHING COUNTS

BUT NOTHING COUNTS LIKE THE COUNTESS® II FL AUTOMATED CELL COUNTER

You see the potential in every sample, in every cell.
In your work, simplicity, affordability, and flexibility
mean more time for discovery.

Count cells in a whole new light with the
quantifiably brilliant Countess® II FL Automated
Cell Counter.



Everything counts at lifetechnologies.com/countessII

life
technologies

For Research Use Only. Not for use in diagnostic procedures. © 2014 Thermo Fisher Scientific Inc. All rights reserved. All trademarks are the property of Thermo Fisher Scientific and its subsidiaries unless otherwise specified. C0012648 1114

A Thermo Fisher Scientific Brand



There's only one **Science**

Science Careers Advertising

For full advertising details, go to ScienceCareers.org and click For Employers, or call one of our representatives.

Tracy Holmes

Worldwide Associate Director
Science Careers
Phone: +44 (0) 1223 326525

THE AMERICAS

E-mail: advertise@sciencecareers.org
Fax: 202 289 6742

Tina Burks

Phone: 202 326 6577

Nancy Toema

Phone: 202 326 6578

Marci Gallun

Sales Administrator
Phone: 202 326 6582

Online Job Posting Questions

Phone: 202 312 6375

EUROPE / INDIA / AUSTRALIA / NEW ZEALAND / REST OF WORLD

E-mail: ads@science-int.co.uk
Fax: +44 (0) 1223 326532

Axel Gesatzki

Phone: +44 (0) 1223 326529

Sarah Lelarge

Phone: +44 (0) 1223 326527

Kelly Grace

Phone: +44 (0) 1223 326528

JAPAN

Katsuyoshi Fukamizu (Tokyo)

E-mail: kfukamizu@aaas.org
Phone: +81 3 3219 5777

Hirofumi Mashiki (Kyoto)

E-mail: hmashiki@aaas.org
Phone: +81 75 823 1109

CHINA / KOREA / SINGAPORE / TAIWAN / THAILAND

Ruolei Wu

Phone: +86 186 0082 9345
E-mail: rwu@aaas.org

All ads submitted for publication must comply with applicable U.S. and non-U.S. laws. *Science* reserves the right to refuse any advertisement at its sole discretion for any reason, including without limitation for offensive language or inappropriate content, and all advertising is subject to publisher approval. *Science* encourages our readers to alert us to any ads that they feel may be discriminatory or offensive.

Science Careers

FROM THE JOURNAL SCIENCE **AAAS**

ScienceCareers.org



DANA-FARBER
CANCER INSTITUTE

Assistant/Associate Professor, Cancer Precision Medicine

The Department of Medical Oncology at the Dana-Farber Cancer Institute (DFCI) invites applications for a full-time position. Appointment at the Assistant or Associate Professor level at Harvard Medical School will be commensurate with academic accomplishment. This individual will develop an independent, laboratory-based translational research program. The application of "liquid biopsy" approaches (e.g., circulating tumor cells or cell-free DNA) is of particular interest. Expertise in hematologic malignancies is a plus, though investigators with solid tumor expertise may also apply. The successful candidate will join the newly-formed Center for Cancer Precision Medicine and either the Division of Molecular and Cellular Oncology or the Division of Hematologic Neoplasia. The research program will also interface closely with ongoing translational research within the Departments of Pathology, Radiology and Surgery at the Brigham and Women's Hospital. Candidates with an interest in isolation and comprehensive genomic/molecular characterization of circulating tumor cells or cell-free DNA from cancer patients are especially encouraged to apply. Prior experience in team-based cancer genomics projects is a plus. The candidate must have an MD and/or PhD and a proven track record of outstanding laboratory research.

The candidate will work principally at the Dana-Farber Cancer Institute and the Brigham and Women's Hospital, while also collaborating closely with the Broad Institute of Harvard and MIT. Salary and benefits will be competitive with other institutions. Candidates should be board certified or board eligible in Internal Medicine and Medical Oncology. Dana-Farber Cancer Institute is an NCI-designated Comprehensive Cancer Center.

Interested candidates must submit a curriculum vitae, a research plan and 3 letters of reference to: Levi A. Garraway, MD, PhD, Director, Center for Cancer Precision Medicine, Dana-Farber Cancer Institute, 450 Brookline Avenue, Boston, MA 02215. Please send submissions via email to: ccpmsearch@partners.org



HARVARD
MEDICAL SCHOOL



BRIGHAM AND
WOMEN'S HOSPITAL

We are an equal opportunity employer and all qualified applicants will receive consideration for employment without regard to race, color, religion, sex, national origin, disability status, protected veteran status, or any other characteristic protected by law.

Boston, MA



Northeastern

Associate/Full Professor Pharmacology

Department of Pharmaceutical Sciences

The Northeastern University Bouvé College of Health Sciences' Department of Pharmaceutical Sciences seeks candidates for a full-time tenured faculty position at the associate or full professor level. The Department has strengths in neuropharmacology, immunology, medicinal chemistry, pharmaceuticals, imaging, drug discovery, development and delivery, and it seeks candidates able to complement, collaborate, and expand these areas of strength. Qualified candidates must hold a Ph.D. in pharmacology or related specialty field and will have an extramurally-funded research program in one of the areas of pharmacology named above. Applicants with transferable funding will be given priority.

To apply, visit <http://apptkr.com/553476>

Northeastern University is an Equal Opportunity/Affirmative Action, Title IX, and an ADVANCE institution. Minorities, women, and persons with disabilities are strongly encouraged to apply. Northeastern University is an E-Verify employer



**THE UNIVERSITY
OF QUEENSLAND**
AUSTRALIA

SCHOOL OF CHEMICAL ENGINEERING

FACULTY OF ENGINEERING, ARCHITECTURE AND INFORMATION TECHNOLOGY

THE UNIVERSITY OF QUEENSLAND, BRISBANE, AUSTRALIA

POSTGRADUATE FELLOWSHIP IN CHEMICAL SCIENCE AND ENGINEERING

The role To explore innovative routes for the production of chemicals, specifically bromine as an oxidant, without co-producing carbon dioxide.

Remuneration AUD\$86,850 – \$103,125 p.a., plus 17% superannuation. Fixed-term, one year, full-time appointment at Academic Research Level B.

Applications close 15 February 2015
Job No. 496741

To apply: Go to www.uq.edu.au/uqjobs to obtain a copy of the position description and application process. UQ is an equal opportunity employer.

IN A COMPANY HELPING THE WORLD'S POPULATION BE WELL...

WE EMBARK ON A JOURNEY TO REVOLUTIONIZE PROCESS DESIGN AND DEVELOPMENT

We are dedicated to scientific excellence and fearless problem-solving. Our vision is to translate breakthroughs in fundamental biomedical research into meaningful new therapeutics that improve and extend the lives of people, worldwide.

At Merck Research Laboratories, our team members are specialists in their fields who come together to advance drug discovery and development.

We are currently recruiting scientists with specialization in the areas of biocatalysis and flow chemistry to work within our Process Chemistry department. Candidates must have a PhD in chemistry or chemical engineering and 0-10 years of industrial or other relevant professional experience.

Job Opportunities – Rahway, NJ

BIOCATALYSIS GROUP

PRE000452 Senior Scientist, Chemistry

CHE004216 Associate Principal Scientist, Chemistry

FLOW CHEMISTRY

CHE004182 Associate Principal Scientist, Chemistry

www.merck.com/careers

Merck is an equal opportunity employer, M/F/D/V – proudly embracing diversity in all of its manifestations.





西南大学

Faculty Positions Available in Southwest University, Chongqing, China

Southwest University invites applications from home and abroad for faculty positions at any level—assistant to full professors in ALL areas. Candidates must have a doctor's degree and exceptional research accomplishments in relevant research fields. Competitive packages including set-up and research funds as well as attractive salaries and benefits will be provided to all successful candidates. Distinguished candidates who have outstanding track record in research area and already got professor position abroad could be recruited through the national Recruitment Program of Young Experts or the national "One Thousand Talents Program". Successful applicants will be offered great support and a series of favorable policies in career development and personal well-being, including academic teaming, research platform, housing and children's education.

Southwest University is a comprehensive and national key university of the "211" project directly under the Ministry of Education. It is located in Chongqing. The university currently comprises 55 undergraduate programs, 46 master's programs, 21 doctor's programs, 22 postdoctoral research stations, 3 national key disciplines, 3 key disciplines with national support, 37 provincial key disciplines, 1 state key laboratory, and 10 key laboratories of Ministry of Education or Agriculture. Among its 2,700 faculty and staff members, there are 1 member of the Chinese Academy of Sciences, 2 members of Chinese Academy of Engineering, 8 professors in National "One Thousand Talents Program", 7 "Chang Jiang Scholars", 2 recipients of National Science Fund for Distinguished Young Scholars, 2 chief scientists of National "973" research Projects, and 13 professors in "BaiQianWan Talents Program". The university got more than 700 national research projects and the research projects and funds increased by 33% per year in the past five years.

Further information is available at <http://renshi.swu.edu.cn/rcgzbgs/> or from the address: The Talents Recruitment Office, Southwest University, Beibei, Chongqing 400715, P. R. China. Please kindly send applications or nominations in the form of an application letter enclosing a current CV to rencai@swu.edu.cn.



Faculty Position Available at China University of Petroleum in Qingdao

China University of Petroleum (UPC) is a national key university directly affiliated with the Ministry of Education and a member of the "211 Project" and "985 innovation platform for preponderant discipline" universities. Honored as "the cradle of scientific and technological talents for petroleum industry", UPC is an important base of training high-level talents for the petroleum and petrochemical industry and has already developed into a multi-disciplinary, well-rounded university focusing on petroleum and engineering.

UPC now has two campuses in Shandong Province, one in Qingdao and one in Dongying. Qingdao Campus, the main and new campus, is located in Qingdao which enjoys a high reputation for its charming scenery and favorable climate. We warmly welcome scientific and technological elites all over the world to join us and build our university into a national renowned, high-level, research-oriented institute with its petroleum-related disciplines reaching the world's first-class level.

UPC provides eligible talents with a good academic environment and excellent working and living conditions.

①. Tenured professor of well-known overseas universities or experts and scholars who have published a thesis as the original author in "Science" or "Nature" can be recruited as a high level professor at UPC, and will be offered 2 million RMB settling-in allowance or housing subsidy and 3-8 million RMB scientific research and academic funds after the evaluation.

②. Experts or scholars who have a high academic reputation and are qualified leader in certain disciplines can be recruited as a high level or regular professor, and will be offered 1 million RMB settling-in allowance or housing subsidy and 1-3 million RMB Scientific research and academic funds after the evaluation.

③. Youth talents who qualify for China's "Youth 1000 Talents projects" can be offered 0.5 million RMB annual salary, 1.5 million RMB settling-in allowance or housing subsidy and 1-3 million RMB scientific research and academic funds.

④. Youth talents who receive the position as postdoctoral, assistant professor, associate professor or have a PhD from a famous overseas university or research institution can be offered higher treatment than similar talents in China.

Further information is available at <http://rsc.upc.edu.cn>

Contact us:

Tel: 0086-532-86981808; 86981806

E-mail: teacher@upc.edu.cn



西南交通大学
Southwest Jiaotong University

Southwest Jiaotong University, P.R.China
Anticipates Your Working Application

Southwest Jiaotong University (SWJTU), founded in 1896, situates itself in Chengdu, the provincial capital of Sichuan. It is a national key multidisciplinary "211" and "985 Feature" Projects university directly under the jurisdiction of the Ministry of Education, featuring engineering and a comprehensive range of study programs and research disciplines spreading across more than 20 faculties and institutes/centers. Boasting a complete Bachelor-Master-Doctor education system with more than 2,500 members of academic staff, our school also owns 2 first-level national key disciplines, 2 supplementary first-level national key disciplines (in their establishment), 15 first-level doctoral programs, 43 first-level master programs, 75 key undergraduate programs, 10 post-doctoral stations and more than 40 key laboratories at national and provincial levels.

Our university is currently implementing the strategy of "developing and strengthening the university by introducing and cultivating talents". Therefore, we sincerely look forward to your working application.

More information available at <http://www.swjtu.edu.cn/>

I. Positions and Requirements

A. High-level Leading Talents

It is required that candidates be listed in national top talents programs such as *Program of Global Experts*, *Top Talents of National Special Support Program*, "*Chang Jiang Scholars*", *China National Funds for Distinguished Young Scientists* and *National Award for Distinguished Teacher*.

Candidates are supposed to be no more than 50 years old. The limitation could be extended in the most-needed areas of disciplinary development.

Candidates who work in high-level universities/institutes and reach the above requirements are supposed to be no more than 45 years old.

B. Young Leading Scholars

Candidates are supposed to be listed in or qualified to apply for the following programs:

• *National Thousand Young Talents Program*

• *The Top Young Talents of National Special Support Program (Program for Supporting Top Young Talents)*

• *Science Foundation for the Excellent Youth Scholars*

Candidates should have good team spirit and leadership, outstanding academic achievements, broad academic vision and international cooperation experience and have the potential of being a leading academic researcher.

C. Excellent Young Academic Backbones

Candidates under 40 years old are expected to graduate from high-level universities/institutes either in China or other countries. Those who are professors, associate professors and other equal talents from high-level universities/institutes overseas could be employed as professors and associate professors as well.

D. Excellent Doctors and Post Doctoral Fellows

Candidates under 35 years old are supposed to be excellent academic researchers from high-level universities either in China or other countries.

II. Treatments

The candidates will be provided with competitive salaries and welfares that include settling-in allowance, subsidy of rental residence, start-up funds of scientific research, assistance in establishing scientific platform and research group as well as international-level training and promotion. As for outstanding returnees, we can offer further or specific treatments that can be discussed personally.

III. Contact us:

Contacts: Ye ZENG & Yinchuan LI

Telephone number: 86-28-66366202

Email: talent@swjtu.edu.cn

Address: Human Resources Department of SWJTU, the western park of high-tech zone, Chengdu, Sichuan, P.R.China, 611756

<http://www.swjtu.edu.cn/>



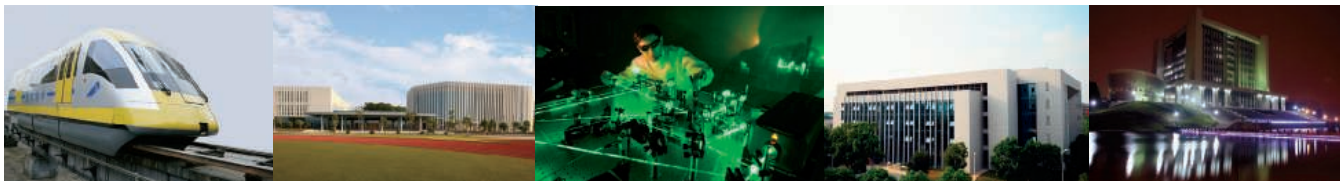
大连理工大学
DALIAN UNIVERSITY OF TECHNOLOGY

Faculty Positions in DUT

Dalian University of Technology (DUT) is located in the beautiful coastal city of Dalian, in northeastern China's Liaoning Province. It is a national key university of the "211" and "985" project directly under the Ministry of Education.

DUT is seeking to recruit excellent expert, scholars (i.e. The Recruitment Program of Global Experts, The Plan for Recruiting 1,000 Professorship for Young Talent, Changjiang Scholar Distinguished Professors and Changjiang Scholar Guest Professors) and faculties from both home and abroad. Qualified applicants of professors, associate professors and lecturers are required to be under the age of 45, 40, 35 separately, and have obtained a PhD degree in a nation(world)-renowned university or academy of Chinese Academy of Sciences. DUT will provide a good academic environment, competitive salaries at international levels. Potential candidates are encouraged to send your application letter enclosing a current CV to Jiailing or ZhangYan(zhaopin@dlut.edu.cn), indicating in the email subject with "academy + position + applicant's name".

For more details, please visit the website: <http://rc.dlut.edu.cn/>



国防科学技术大学

National University of Defense Technology

CALLS FOR TALENTS ALL OVER THE WORLD

The National University of Defense Technology (NUDT) is a comprehensive national key university under the dual supervision of the Ministry of Defense and the Ministry of Education as designated by Project 211 and Project 985. The University is located in Changsha, a magnificent city enjoying thousands of years of history. Over the past 60 years, NUDT has accomplished a large number of advanced scientific achievements, among which listed the Galaxy series and Tianhe series of supercomputer systems, Beidou Satellite Navigation System, Medium and Lower Speed Maglev, Core Routers and Unmanned Vehicles. The University has played an important part in building an innovation oriented country. After Tianhe-1 Supercomputing System, developed by NUDT, shocked the world as the first Chinese supercomputer topping the TOP500 list of fastest supercomputers, Tianhe-2 has retained the supremacy of TOP500 for 4 times and reigned as World's Best Supercomputer since 2013.

In order to accelerate the establishing of a leading university, NUDT now welcomes outstanding scholars and technicians all over the world to our multidisciplinary faculty positions.

Positions Available

1.1000-Talent Plan

The Innovative Talents Long Term Program

This program aims at recruiting world-class scholars under age 55 if in a field of natural sciences, or under 60 in a field of humanities and social sciences as full-time professors at NUDT. Applicants should have acquired doctoral degree(s) and have worked either as professors or at equivalent positions in world-renowned overseas universities or research institutes.

Successful applicants should spend at least 9 months per year undertaking research and teaching on NUDT campus for 3 consecutive years after being selected for the Program.

The Innovative Talents Short Term Program

This program aims at recruiting world-class scholars under age 55 if in a field of natural sciences, or under 60 in a field of humanities and social sciences as part-time professors at NUDT. Applicants should have acquired doctoral degree(s) and have worked either as professors or at equivalent positions in world-renowned overseas universities or research institutes.

Successful applicants should spend at least 3 months per year undertaking research and teaching on NUDT campus for 3 consecutive years after being selected for the Program.

Foreign Experts Program of 1000-Talent Plan

This program is designed for world-class scholars of non-Chinese ethnicity under age 65. Applicants should have worked either as professors or at equivalent positions in world-renowned overseas universities or research

institutes. Successful applicants should spend at least 3 months per year undertaking research and teaching on NUDT campus for 3 consecutive years after being selected for the Program.

1000-Young-Talent Program

This program is one type of "1000-Talent Plan" especially for young scholars under age 40. Generally, applicants should have official teaching or research positions in world-renowned overseas universities or institutes. Three or more years of overseas post-doctoral research experience is required if the doctoral degrees were acquired overseas, while five or more years required if degrees obtained in Mainland China. Special offers are granted to those who have made distinguished research achievements.

2.Chang Jiang Scholars Program

Distinguished Professors

Applicants should be under age 45 if in a field of natural sciences, or under 55 in a field of humanities and social sciences. Applicants should have worked either as associate professors (or with above academic titles), or at equivalent positions in world-renowned universities or research institutes.

Chair Professors

Applicants should have worked either as professors or at equivalent positions in world-



renowned overseas universities or research institutes. Successful applicants should spend at least 2 months per year undertaking research and teaching on NUDT campus for 3 consecutive years after being selected for the Program.

3.University Distinguished Guest Professors

Applicants should be academicians of CAS or CAE, or have worked either as professors or at equivalent positions in world-renowned overseas universities or research institutes, and should have outstanding contribution to their domains of specialties or with world recognized achievements. Successful applicants should spend at least 3 months per year undertaking research and teaching on NUDT campus for 3 consecutive years after being selected for the Program.

4.Elite Young Scholars

This program is designed for the great cohort of innovative and promising scientific minds under age 40, willing to work at NUDT as full-time faculty. Applicants should have obtained doctoral

degrees at world-renowned overseas or domestic universities or research institutes, willing to exert their strength and passion for research excellence and self-fulfillment.

Research Fields in Demand

Physical Oceanography
Marine Meteorology
Data Assimilation
Marine Information Engineering
Underwater Acoustic Engineering
Oceanic Circulation
Numerical Modeling of Marine Hydrodynamics
Aerospace Propulsion Theory and Engineering
Materials Science and Engineering
Mechanics
Statistics
Atomic and Molecular Physics
Condensed Matter Physics
Quantum Communication
Quantum Information
Network Science
Synthetic Biology
Mechanical Engineering
Control Science and Engineering
Instrument Science and Technology
Satellite Navigation and Positioning
Space-based Information Acquisition and Processing
Management Science and Engineering
Applied Mathematics
Computer Science and Technology
Software Engineering
Microelectronics and Solid-State Electronics
Optical Engineering
Physical Electronics
Foreign Languages and Literature
Philosophy
International Relations

Salary and Support

Successful applicants will be offered sufficient research support, adequate laboratory space, highly competitive salary, startup funding and social benefits, and extensive opportunities for collaboration both within NUDT and with partner institutions. Relocation or establishment of your own research team will be supported.

Contact Us

All the position demands are long-term effective. Any further inquiries will be welcomed via emails. Interested applicants are invited to submit documents including a cover letter, a CV, a brief future research plan, 2 recommendation letters, 3 pieces of representative works to our Talent Affairs Office:

Tel: +86-731-84572217

Fax: +86-731-84572217

E-mail: rcb@nudt.edu.cn

Address: Talent Affairs Office, Human Resources Department, National University of Defense Technology, 137 Yanwachi Street, Changsha, Hunan, People's Republic of China.



Overseas Talent Recruitment by China Medical University

China Medical University (CMU) is currently the only medical university that has not merged into a comprehensive university and was formerly under the direct administration of the Ministry of Health. It is located in Shenyang City of Liaoning Province.

China Medical University has 29 schools, divisions and faculties, which are School of Basic Medical Science, School of Public Health, School of Forensic Medicine, (International) School of Nursing, School of Pharmacy, International Education School, School of Humanities and Social Sciences, School of Clinical Medicine, First College of Clinical Medicine, Second College of Clinical Medicine, Fourth College of Clinical Medicine, School of Stomatology, Division of Medical Imaging, Division of Ophthalmology, Division of Pathology, Division of Medical Informatics, Division of Biomedical Engineering, Division of Sports Medicine, Division of Medical Laboratory Science, Division of Biological Science and Biological Technology, Division of Medical Psychology and Mental Health, Division of Cell Biology, Faculty of Science and Engineering, Graduate School, Vocational and Technical College, School of Distance Education, School of Continuing Education (Adult Education), Laboratory Animal Center. CMU is entitled to award degrees in medicine, education, science, engineering, philosophy and management, and doctorate degrees can be awarded in the following six disciplines: basic medical sciences, clinical medical sciences, biology, stomatology, public health and preventive medicine, and nursing. It has set up 56 doctorate-degree awarded specialties and 67 master's degree awarded specialties. CMU has 5 national key disciplines, which are internal medicine (respiratory disease), dermatology and venereology, surgery (general surgery), internal medicine (endocrine and metabolic disease), and occupational and environmental health. It also has 1 national key discipline (cultivating): medical imaging and nuclear medicine. In addition, CMU has 6 first-class provincial characteristic disciplines: biology, basic medical sciences, clinical medical sciences, stomatology, public health and preventive medicine, and nursing.

To speed up the pace of development, China Medical University recruits all levels of professionals at home and abroad, including leading talents, academic leaders and backbones, post-doctoral scientific research backbones. Outstanding professionals all over the world are welcome to join in the university and jointly strive for constructing a domestic first-class and internationally well-known medical university.

I. Recruitment Requirements

(I) Basic Requirements

1. Good academic ethics, rigorous scientific research attitude, healthy psychological quality and teamwork spirit
2. Consistent with our university's talent introduction demands, including research direction, professional skill level, educational level, etc.

(II) Specific Requirements for Different Levels

1. Leading talents: Internationally well-known professors or distinguished scholars recognized in the same field, having high academic attainments, taking the leading position internationally in terms of academic level, obtaining internationally recognized important achievements, being capable of building interdisciplinary collaboration and leading relevant disciplines up to internationally advanced level.
2. Academic leaders: doctorate degree, associate professor or above in an overseas famous university or research institution, being generally under the age of 55, having relatively high academic attainments in a discipline, being in the top among the young and middle-aged scholars in this discipline field in terms of academic attainments, having obtained internationally advanced or domestic leading academic achievements, being capable of striving for and chairing national key research projects and important international cooperation projects, and being able to lead this discipline up to internationally advanced level.
3. Academic backbones: doctorate degree from an overseas university, being generally 45 years old or below, having the title of assistant professor or above in an overseas university or research institution, being capable of mastering the development frontier of this discipline, having obtained certain

academic achievements, being able to apply for and chair international cooperation or national research projects, being capable of leading a certain research direction to an internationally advanced level.

4. Excellent doctoral graduates or post-doctoral outbound personnel: possessing overseas doctorate or the doctorate from a domestic first-class university, having at least one uninterrupted year of experience of overseas study or cooperative research, being generally 35 years old or below, having several publications in SCI Journals as the first author or the corresponding author, being capable of applying for and taking over national scientific research projects.

II. Supportive Conditions Provided

Providing a remuneration that equals to or higher than that of other domestic same-level universities, providing favorable conditions in terms of professional title, salary, scientific experiment supporting funds, housing, team construction, etc.

III. Ways of Job Application

The applicant can apply to our university by self-recommendation or expert recommendation. Applicants may directly contact us for detailed recruitment matters (see below for contact information), or visit our website for relevant recruitment information. The recruitment announcement is long-term effective since the date of release.

Please send to the designated e-mail the application materials including a curriculum vitae and scientific projects, patents, academic papers and academic research achievements of the recent five years, a list of other honors and the certificate copies, etc.

IV. Contact information

Contact: Hu Xia E-mail: job@cmu.edu.cn

Zhao Xin Email: cmuhr@cmu.edu.cn

Tel: +86-24-23262650 +86-24-31900982

Fax: +86-24-23251769

Address: Talent Exchange Service Center of China Medical University

No.130, Bei'er Road, Heping District, Shenyang City, Liaoning Province.

Web Site: www.cmu.edu.cn www.cmu.edu.cn/hr





Faculty Positions Chemical and Biological Engineering

The Physical Sciences and Engineering (PSE) Division (<http://pse.kaust.edu.sa>) at King Abdullah University of Science and Technology (KAUST) invites qualified applicants to apply for faculty positions at all ranks (Assistant, Associate and Full Professor) in the Chemical and Biological Engineering program.

KAUST offers superb research facilities which includes the BioScience and Bioengineering and Analytical Core laboratories, generous assured research funding and internationally competitive salaries. The science produced in PSE focuses on understanding, modeling and manipulating matter at all scales (nano, meso and macroscopic levels), in all forms (bulk, thin films, divided colloids, fluid flows, the earth as system, etc.) and in interaction with external stimuli (light, heat, fluids, stresses, etc.). The knowledge produced serves to help design and engineer cutting-edge materials, technologies and systems.

The Chemical and Biological Engineering program offers opportunities to develop real-world solutions to global challenges by leveraging basic discoveries in the chemical and biological sciences. The successful candidate will focus his/her research in the following areas of expertise:

Process Modeling and Design

- Solid academic/industrial background
- Conduct design, optimization and cost analysis of membrane and conventional separation processes
- Teach advanced principles of process design and control.

Advanced Water Treatment Processes/novel Membranes (Senior-level Position)

- Background and strong knowledge in the water industry
- Expertise in industry and academia

Biomolecular Engineering (Senior-level Position)

- Development and leadership of the Biomolecular Engineering program
- Well-established research in areas such as biomaterials, tissue engineering, bioprocess engineering or biomedical engineering

Reactor Design and Process Engineering (Position Open in Kaust Catalysis Center: <http://kcc.kaust.edu.sa>)

- Specialize in heterogeneous or photo catalysis
- Scale up reactors in the field of water splitting, high temperature catalytic processes and processes for air-sensitive catalysts
- Expertise in academia, industry or both

Applicants should have a proven track record to establish a high-impact research program, and should have a commitment to high-quality teaching at the graduate level.

To learn more about the PSE Division and complete the online application form, visit <http://apptrkr.com/546570>. Application requirements include the following:

- Updated curriculum vitae with a full list of publications
- Statement of research
- Statement of teaching interests
- Contact details of at least four potential referees.

Applications received by January 31, 2015 will receive full consideration. Positions will remain open until filled.

www.kaust.edu.sa



The University Hospital of Basel and the Faculty of Medicine of the University of Basel wish to recruit, to the new, **professorship funded by the Gertrude von Meissner Foundation** at the Institute for Pathology in the University of Basel, a

Professor of Paediatric Osseous and (Soft tissue) Tumours (not tenured)

The duties in this post comprise the clinical-pathological assessment of osseous and (soft tissue) tumours, in close cooperation with the Osseous Tumour Reference Centre also located in the University Hospital of Basel Pathology Department, university-level teaching and research in particular. The main focus of the translational research is the characterisation of molecular-genetic changes in paediatric osseous tumours, during the course of which cooperation and synergies with existing research groups within the Faculty's specialisms of oncology and/or stem cells should be utilised or created. The foundation professorship is initially offered for a limited period of 5 years, after which further funding may be possible.

The applicant must fulfil the following requirements:

Official designation of Specialist in Pathology or an equivalent qualification. Experience in the clinical-pathological diagnosis of osseous and soft tissue tumours. Habilitation or equivalent qualification. An internationally-recognised track- record in carrying out of research into the field of osseous and soft tissue tumours. Evidence of successful competitive external funding. Enjoyment and commitment to modern university-level teaching.

Courses in the Faculty of Medicine are taught in German.

The University of Basel stands for excellence through diversity and advocates equal opportunities and family-friendliness. The University endeavours to increase the proportion of women in professorial positions and therefore particularly welcomes applications from women.

If you require further information, please contact the Chair of the Appointments Committee, Prof. Dr. Reinald Brunner, (Tel. +41 61 704 2802, reinald-g-h.brunner@unibas.ch) and University Hospital of Basel Senior Consultant in Pathology, Prof. Dr. Markus Tolnay (Tel. +41 61 328 6896, E-Mail markus.tolnay@usb.ch).

Applications must be submitted by February 7, 2015. Information concerning the documents to be submitted can be found on the homepage at <http://medizin.unibas.ch/> under Dekanat/Bewerbungen.

Please send the documents, exclusively in 5 PDF files as described in the Guidelines, to bewerbungen-medin@unibas.ch.



Federal Ministry
of Education
and Research



"Bernstein Award" 2015 Young Scientists Research Award in Computational Neuroscience

The German Federal Ministry of Education and Research (BMBF) has established the "National Network for Computational Neuroscience" with six high-performing "Bernstein Centers for Computational Neuroscience" as the major structural elements.

The "Bernstein Award" is equipped with up to 1.25 Mio Euros in the form of a grant over a period of five years. It will be awarded to a highly qualified young researcher, considering the candidates' verifiable research profile in the field of Computational Neuroscience and the scientific concept for a future young research group. Young researchers can apply for their own position and group. The group funded by the "Bernstein Award" will become an integral part of the National Network for Computational Neuroscience. Future announcements of the "Bernstein Award" are in the scope of the Ministry's planning.

The grant is provided for a scientific project of a young research group headed by a postdoc regardless of nationality. The project will be conducted at a German university or research institution – within or outside the Bernstein Centers. It is a prerequisite for funding that the university or research institution concerned employs the young researcher during the funding period and supports him/her with the basic equipment in terms of laboratory space and other infrastructure. A statement made to that effect by the receiving institution must be included with the project outline to be submitted.

Deadline for applications is April 15th, 2015.

For more detailed information about the "Bernstein Award" including application conditions please visit

<http://www.nncn.de>
or

http://www.gesundheitsforschung-bmbf.de/_media/Bernstein_Award_2015_Call_for_proposals.pdf



Faculty Positions Chemical Science

The Physical Sciences and Engineering (PSE) Division (<http://pse.kaust.edu.sa>) at King Abdullah University of Science and Technology (KAUST) invites qualified applicants to apply for faculty positions at all ranks (Assistant, Associate, and Full Professor) in the Chemical Science Program.

KAUST offers superb research facilities which include the Analytical, the Nanofabrication and Thin film and the Imaging and Characterization core laboratories, generous assured research funding and internationally competitive salaries. The science produced in PSE is about understanding, modeling, and manipulating matter at all scales: nano, meso, and macroscopic levels; in all forms: bulk, thin films, divided colloids, fluid flows, earth as system etc. and in interaction with external stimuli: light, heat, fluids, etc. or stresses. The knowledge created serves to design and engineer materials, technologies, and systems.

The Chemical Science Program is concerned with chemistry in all its facets including those addressed in KAUST Research Centers, particularly in Catalysis, Membrane, Solar Energy, and Clean Combustion (<http://chems.kaust.edu.sa>).

The Chemical Science program is currently recruiting in the following areas:

Experimental Polymer Physics: With emphasis on the dynamics and molecular rheology of polymeric systems including, but not limited to, branched polymers, copolymers, functionalized and responsive polymers, nano composites, melts and solutions.

Polymer Engineering/Processing: With emphasis on a) the design, characterization, properties and modification of polymeric materials, b) the compounding and processing of polymeric materials and c) the structure property relationships and applications.

Heterogeneous Catalysis: Candidates are expected to have a strong expertise on "catalysis by design" especially on multistep reactions, on the association of various types of catalytic concepts or tools e.g. -acid base, -oxidation, -cascade, -confinement effect, -green and sustainable chemistry – in situ, in operando spectroscopies.

Organometallic Catalysis for Polymer Synthesis: The main objectives of this position will be the development of "new concepts in polymerization catalysts towards major breakthroughs". An appointment in this area is needed to develop also a better knowledge of elementary steps of polymerization with transition, rare earth or non-transition elements. New polymeric materials with new catalysts and a sustainable approach are domains of strong appeal.

Analytical Chemistry NMR: Candidates should develop new NMR techniques and apply these either to the investigation of biomolecules such as proteins, nucleic acids or polymers or to explore novel materials using solid-state NMR. Structural characterization, dynamic processes and the evaluation of reaction dynamics as well as mechanisms or understanding of the complex interplay between solutes and solvents are examples of relevant research topics. The candidate should be able to contribute to cutting-edge science in a strongly interdisciplinary setting and demonstrate the ability to participate in collaborative research. KAUST has established outstanding NMR facilities with including a 950 MHz NMR and a DNP-NMR. A successful candidate will have full access to these facilities and expected to take an active role in their development.

Catalytic Reactions Engineering (Chemical and Biological Engineering Program): This position should be focusing on "reactor design" and establishment of a "scale up platform". It will complement the existing areas of expertise in Chemical Science Program and put a greater focus on bridging chemistry and chemical engineering: "from the bench to the processes". Strong experience with industrial partners is needed.

New Methods of Organic Synthetic Chemistry: This position should be focused on initiating an organic chemistry research program focusing on new methods of organic synthesis from different feed stocks e.g. petrochemicals and natural products.

Applicants should have a proven track record to establish a high impact research program and have a commitment to high quality teaching at the graduate level.

To learn more about the PSE Division and complete the online application form, visit <http://apptkr.com/546726>

Application requirements include the following:

- Updated curriculum vitae with a full list of publications
- Statement of research
- Statement of teaching interests
- Contact details of at least four potential referees

Applications received by January 31, 2015 will receive full consideration and positions will remain open until filled.

www.kaust.edu.sa



Cairns
Singapore
Townsville

Careers in the Tropics

Lecturer/Senior Lecturer – Zoology/Ecology

Ref. No. 14283 – Townsville

The College of Marine and Environmental Sciences has an enviable international research reputation, and is a leading Australian University in the ISI field of Ecology and Environment. We are seeking to appoint a Lecturer in the Terrestrial Ecosystems and Climate Change group, to contribute to and complement our current teaching and research profile. The appointee will have a strong interest in teaching and research in the tropics. He/she will have demonstrated experience and success in tertiary teaching, student supervision and research. The appointee will be required to teach in appropriate areas of zoology, ecology and/or quantitative biology, including their area of special expertise. Preference may be given to applicants with interests in one or more of the following: terrestrial vertebrate ecology, ornithology, mammalogy, wildlife biology, plant-animal interactions, conservation, quantitative methods, and/or terrestrial invertebrate biology.

The Terrestrial Ecosystems and Climate change group is one of the top disciplines in James Cook University for winning competitive research grants, and belongs to JCU's flagship research College. JCU is an excellent base for research in tropical zoology and ecology because: it has excellent infrastructure; there is ready access to a wide array of environments (rainforest, savannah, streams, wetlands, mountains and islands); there is a rich intellectual environment in the region, including CSIRO (on campus), Wet Tropics Management Authority, Australian Institute of Marine Science, Great Barrier Reef Marine Park Authority, several government departments and successful cognate disciplines of JCU; and it has the all the attributes of a western-style university in a safe political and healthy environment.

Employment Type: Appointment will be full-time on a continuing basis.

Salary: Lecturer - Academic Level B - \$84,700 - \$99,942 per annum; Senior Lecturer - Academic Level C - \$102,988 - \$118,228 per annum. Level of appointment and commencing salary will be in accordance with qualifications and experience. Benefits include a generous superannuation scheme with 17% employer contributions, five weeks annual recreation leave, flexible working arrangements and attractive options for salary packaging. Applications close on 11 January 2015.

Applications must be lodged electronically using the online facility located at <http://www.jcu.edu.au/jobs/>

For more information go to:
jcu.edu.au/jobs

JCU is committed to equal opportunity, diversity and sustainability.

CRICOS Provider Code 00171

Cairns
Singapore
Townsville

Careers in the Tropics

Lecturer/Senior Lecturer – Marine Biology

Ref. No. 14282 – Townsville

The College of Marine and Environmental Sciences is a recognised world leader in coral reef research. We are seeking to appoint a Lecturer in the Discipline of Marine Biology, within the Marine Ecosystems and Impacts Group, to complement our current teaching and research profile. The appointee will have a strong interest in teaching and research focussed on marine invertebrate biology and ecology in the tropics. He/she will have demonstrated experience and success in tertiary teaching, graduate student supervision and research. This is a joint research and teaching appointment, and the appointee will be required to teach undergraduate and postgraduate subjects in marine biology, ecology, and/or quantitative biology. Preference may be given to applicants with interests in coral biology and ecology, and/or marine invertebrate biology.

The Marine Ecosystems and Impacts group is one of the top research disciplines in James Cook University, and belongs to JCU's flagship research College. JCU provides an excellent base for research on coral reefs because it has excellent infrastructure including aquarium facilities and high-performance computing facilities, and has ready access to a wide array of marine environments within the Great Barrier Reef World Heritage Area and the Pacific and Indian Oceans. JCU has a rich intellectual environment including as the administering organisation for the ARC Centre of Excellence for Coral Reef Studies, together with internal Centres that have an aquatic/maritime focus. Further, the Australian Institute of Marine Science, the Great Barrier Reef Marine Park Authority and several government departments are all located within the region.

Employment Type: Appointment will be full-time on a continuing basis.

Salary: Lecturer - Academic Level B - \$84,700 - \$99,942 per annum; Senior Lecturer - Academic Level C - \$102,988 - \$118,228 per annum. Level of appointment and commencing salary will be in accordance with qualifications and experience. Benefits include a generous superannuation scheme with 17% employer contributions, five weeks annual recreation leave, flexible working arrangements and attractive options for salary packaging. Applications close on 11 January 2015.

Applications must be lodged electronically using the online facility located at <http://www.jcu.edu.au/jobs/>

For more information go to:
jcu.edu.au/jobs

JCU is committed to equal opportunity, diversity and sustainability.

CRICOS Provider Code 00171



ÉCOLE POLYTECHNIQUE
FÉDÉRALE DE LAUSANNE

Faculty Position in Bioengineering at the Ecole polytechnique fédérale de Lausanne (EPFL)

The Institute of Bioengineering (bioengineering.epfl.ch) and School of Life Sciences (sv.epfl.ch) at EPFL (www.epfl.ch) invite applications for a **faculty position in Bioengineering**. Appointments at all levels (tenure track assistant/associate/full) will be considered. We seek exceptional individuals who will develop and lead a research program at the forefront of the discipline and who will also be committed to excellence in undergraduate and graduate-level teaching.

Areas of interest include, but are not limited to: synthetic biology, biomolecular engineering, systems biology, stem cell biology, tissue engineering, biomaterials, immunoengineering, functional genomics, proteomics and metabolomics. Thematic links to research foci at the Institutes of the School of Life Sciences (cancer, infectious, immunological and metabolic diseases, neuroscience) are encouraged but not necessary. Start-up resources and state-of-the-art research infrastructure will be available. Salaries and benefits are internationally competitive.

Bioengineering at EPFL is well integrated between the School of Engineering and the School of Life Sciences. Close interactions with the newly founded Wyss Center, University of Lausanne, the University Hospital of Lausanne (CHUV), and the Ludwig Institute for Cancer Research are encouraged.

EPFL, with its main campus located in Lausanne, Switzerland, is a dynamically growing and well-funded institution fostering ex-

cellence and diversity. It has a highly international campus at an exceptionally attractive location boasting first-class infrastructure. As a technical university covering essentially the entire palette of engineering and science, EPFL offers a fertile environment for research collaboration between different disciplines. The EPFL environment is multi-lingual and multi-cultural, with English serving as a common interface.

Applications should include a cover letter with a statement of motivation, curriculum vitae, list of publications and patents, concise statement of research and teaching interests, and the names and addresses of at least five referees. Applications must be uploaded in PDF format to the recruitment web site:

<https://academicjobsonline.org/ajo/jobs/5137>

Formal evaluation of candidates will begin on **February 1st, 2015** and continue until the position is filled.

Enquiries may be addressed to:

Prof. Matthias Lutolf

Chairman of the Committee

e-mail: bioeng-search@epfl.ch

EPFL is committed to increasing the diversity of its faculty, and strongly encourages women to apply.

CONFIRMED SPEAKERS

Zakri ABDUL HAMID (MY)
Syahrilnizam ABDULLAH (MY)
Stylianios E ANTONARAKIS (CH)
Stephan BECK (UK)
Hany BINTI MOHD ARIFFIN (MY)
Ruth CHADWICK (UK)
Andrew CLARK (US)
Marcel DINGER (AU)
Evan EICHLER (US)
Andrew FUTREAL (US)

Richard A GIBBS (US)
Dean NIZETIC (SG)
Maude E. PHIPPS (MY)
Steve QUAKE (US)
Gerardo JIMENEZ-SANCHEZ (MX)
Maria KARAYIORGOU (US)
Kazuto KATO (JP)
Poh San LAI (SG)
Edison LIU (US)
Partha P MAJUMDER (IN)

Timothy MERCER (AU)
John E RASKO (AU)
Charles ROTIMI (US)
Michael SNYDER (US)
Himla SOODYALL (ZA)
Nicole SORANZO (UK)
Henk STUNNENBERG (NL)
Meow Keong THONG (MY)
Hub ZWART (NL)



FIVE FACULTY POSITIONS IN SYSTEMS BIOLOGY, GENOMICS, AND INFORMATICS AT OREGON STATE UNIVERSITY

Oregon State University is searching for five collaboratively-minded faculty with an enthusiasm for research and teaching at the interface between the life or environmental sciences and the quantitative or physical sciences. Appointees will be expected to develop independent and collaborative grant-funded research programs, at levels of scale from the molecular to the ecological. The research, teaching, and extension programs of the appointees are expected to integrate student success, and diversity and inclusion, as core values. This search is part of a large cohort of new faculty hires at OSU focused on interdisciplinary research, on advancement of diversity, and on advancing and equalizing student success.

To review the full position announcements, qualifications and detailed application information for any of these positions, go to <http://oregonstate.edu/jobs> and select the relevant posting number.

COMPLEX SYSTEMS IN THE LIFE AND ENVIRONMENTAL SCIENCES

Two assistant professor (9 month) positions are available in any domain where the life or environmental sciences intersect with the quantitative or physical sciences. Complex systems in the life and environmental sciences span numerous levels of scale from metabolites, macromolecules, cells, tissues, and organisms, to populations, communities and ecosystems. Increasingly, understanding these systems requires interdisciplinary collaborative research at the intersection with quantitative or physical sciences. Each appointment will reside jointly in a life or environmental sciences unit, and in a physical or quantitative sciences unit, depending on the appointee's expertise and interest. **Posting #0013430; Closes February 6, 2015. Contact: Brett Tyler (brett.tyler@oregonstate.edu).**

QUANTITATIVE SYSTEMS BIOLOGIST

Assistant Professor (9 month) position in the Department of Integrative Biology (70%) and the Departments of Mathematics or Statistics (30%). The appointee will use and develop mathematical or statistical approaches to tackle problems in systems biology in the broad sense. Research focus can be at any level of biological organization, but must involve strong quantitative approaches and integrating large data sets. Candidate will teach in the general biology curriculum and will teach courses aimed at improving the quantitative skills of biology students. **Posting #0013398. Closes January 25, 2015. Contact: Tara Bevandich (Tara.Bevandich@science.oregonstate.edu; 541-737-5336).**

MARINE EVOLUTIONARY SYSTEMS BIOLOGIST

Assistant Professor (9 month) position in the Department of Integrative Biology. The appointee will conduct research, develop an active, grant-supported research program that applies systems biology approaches to evolutionary questions in marine organisms. Research focus can be at any level of biological organization, but must involve strong quantitative approaches and cutting-edge technologies. Appointee will teach courses in genetics and evolution. **Posting #0013400. Closes January 25, 2015. Contact: Tara Bevandich (Tara.Bevandich@science.oregonstate.edu or 541-737-5336).**

GENOMICS AND BIOINFORMATICS OF CROP PLANTS

Assistant Professor (9 month) position in the Department of Horticulture. The appointee will develop a comprehensive program in research (both independent and collaborative), teaching and outreach in applied genomics and bioinformatics of plants, with a focus on discovery of new knowledge and/or creative solutions to problems related to economically important staple and specialty crops of Oregon. The research discoveries and impacts are to be communicated to peers, practitioners and citizens. **Posting #0013285; Closes January 25, 2015. Contact: Bill Braunworth (541-737-1317 or bill.braunworth@oregonstate.edu).**

Idaho State UNIVERSITY

Assistant/Associate/Full Professors, Nuclear Engineering and Health Physics 9 Month Full-Time Nuclear Eng/Health Physics Idaho Falls

Idaho State University seeks to significantly expand its research enterprise in broad areas relating to nuclear material science and engineering while contributing to the national objectives as outlined by the Department of Energy in collaboration with the Idaho National Laboratory. Up to five new faculty, open at any rank, will be recruited into this outstanding opportunity. Outstanding candidates with a strong proven background for developing research and contributing to graduate and undergraduate education in the areas of nuclear materials and nuclear fuels and various other nuclear engineering and related areas will be considered

The Department of **Nuclear Engineering and Health Physics** at Idaho State University invites applications from individuals with a background in the following areas:

- **nuclear materials** for a tenure-track position. Exceptional candidates should possess particular interest and scholarly accomplishments in **radiation damage, structural material and fuel development, and material characterization. Emphases in both experimentation and modeling, including visualization and simulation, will be strongly considered.**
- **computational thermal-hydraulics** for a tenure-track position. Exceptional candidates should possess particular interest and scholarly accomplishments in **mass/energy balance of energy systems (chemical and nuclear) and advanced analytics. Emphases in both experimentation and modeling, including visualization and simulation, will be strongly considered.**
- **light-water reactor system analysis** for a tenure-track position. Exceptional candidates should possess particular interest and scholarly accomplishments in **safety analysis (i.e. probabilistic risk assessment (PRA)), structural analysis, hybrid energy system integration, and instrumentation & control (I & C). Emphases in both experimentation and modeling, including visualization and simulation, will be strongly considered.**
- **light-water reactor system analysis** for a tenure-track position. Exceptional candidates should possess particular interest and scholarly accomplishments in **light-water reactor fuel and zircaloy cladding properties and behavior. Emphases in both experimentation and modeling, including visualization and simulation, will be strongly considered.**
- **radio- and separation chemistry** for a tenure-track position. Exceptional candidates should possess particular interest and scholarly accomplishments in **pyroprocessing, actinide chemistry, and radioanalytical analysis for safeguards applications. Emphases in both experimentation and modeling, including visualization and simulation, will be strongly considered.**

Successful candidates are expected to establish vigorous research programs and help support graduate and undergraduate research. Joint appointments with INL will be encouraged and expected. Candidates are expected to utilize the laboratory facilities located at the Center for Advanced Energy Studies (CAES) facility in Idaho Falls. The Idaho Accelerator Center (IAC) and the Research and Innovation in Science and Engineering (RISE) complex also provide excellent experimental facilities for research. These positions are primarily focused on research.

Minimum Qualifications: Ph.D. in nuclear science or engineering, materials science, mechanical engineering, chemical engineering, radiochemistry, or a related field. Exceptionally strong candidates that are "all but dissertation (ABD)" will be considered.

Preferred Qualifications: Ability to obtain unescorted access to Idaho National Laboratory research facilities. The candidates should have a distinguished record and exceptional potential for world-class research.

Please submit the following documents with your application: Full Academic Transcript History, full curriculum vitae, a one-page statement of professional interests and activities, a statement of research, and the names, and contact information (including addresses, e-mail and telephone numbers) of four references. Reference letters optional. To apply go to careers.isu.edu. Priority consideration will be given to applications received by March 31, 2015. However, the positions will remain open until filled. Salary will be \$100,000 to \$120,000 for assistant professors depending upon education and experience. Full professors will be considered at a salary commensurate with their experience and research record. All positions include a competitive benefits package.

Idaho State University is an Equal Opportunity/Affirmative Action Employer. We have an institution-wide commitment to inclusion and diversity and encourage all qualified individuals to apply. Veterans' preference. Upon request, reasonable accommodations in the application process will be provided to individuals with disabilities.



HARVARD
MEDICAL SCHOOL

MASTER OF MEDICAL SCIENCES DEGREE in IMMUNOLOGY

A comprehensive program in Basic and Clinical Immunology. Taught by renowned Harvard faculty and intended for biology graduates interested in immunology research and medicine, as well as for research-oriented clinical fellows (MD, MBBS, and equivalent degrees) from all disciplines.

Visit <http://mmscimmunology.hms.harvard.edu/> for information on our comprehensive two-year program, including extensive coursework and laboratory-based research, at Harvard Medical School.

Assistant, Associate, or Full Professor Biomedical Engineering (tenure-track)

The Department of Biomedical Engineering in the School of Engineering at the City College of New York (CCNY) of the City University of New York seeks to recruit an outstanding faculty member with expertise to complement their growing program in neural engineering. Other areas of specialization in the department include: tissue engineering, nanotechnology/biomaterials, cardiovascular engineering, and musculoskeletal biomechanics. It is expected that appointment will be made at the level of Assistant Professor, though outstanding candidates at more senior levels will be considered.

Responsibilities will focus on developing successful, extramurally funded research program as well as excellence in teaching at the graduate and undergraduate levels.

The City College of New York, in the heart of New York City, is building upon its strengths in neuroscience, which is currently comprised of more than 20 faculty from 5 different departments across the campus. Shared research instrumentation include state of the art microscopy, several EEG systems, TMS, tDCS, non-invasive optical imaging, and a research-dedicated MRI scanner scheduled to be operational by the end of 2014.

The research environment in the CCNY BME department is very strong, and builds upon internal strengths as well the New York Center for Biomedical Engineering (NYCBE) - a unique consortium between the Grove School of Engineering and seven of the premier health care and medical institutions in New York City. The research productivity of the faculty in the CCNY BME department is among the top in the nation and supported by over \$5,000,000 annual in extramural grant support. The National Research Council rankings put the department in the top 10% in the nation terms of research productivity and #1 in the nation in terms of diversity. Its commitment to diversity is reflected in its unique composition of over 50% female or minority faculty. Additional information on the department can be found at bme.cuny.cuny.edu. CCNY is the founding and flagship college of the City University of New York (CUNY).

To apply, please view Job ID 11824) at <http://www.cuny.edu/employment/jobsearch.html>, and follow all instructions.

The City College
of New York



Agricultural
Research
Service

www.ars.usda.gov

Research Microbiologist or Research Veterinary Medical Officer GS-12/13

Salary Range of \$69,497 to \$107,434

The Food Safety and Enteric Pathogens Research Unit at the National Animal Diseases Center in Ames, Iowa, is seeking a permanent full-time Research Microbiologist or a Research Veterinary Medical Officer to conduct research on the interactions between intestinal commensal microbes, notably foodborne pathogen *Salmonella* species, and mucosal immune mechanisms of swine.

The scientist is responsible for molecular-based investigations to define intestinal mucosal responses and host defense mechanisms (innate and acquired) of early life swine. Factors eliciting those responses include pre-weaning and postweaning colonization by intestinal commensal microbes (including foodborne pathogen species) and diet composition. The incumbent's knowledge and research will supplement and complement unit efforts to reduce antibiotic use in swine, and to discover alternatives to traditional antibiotics for inhibiting human foodborne pathogens (*Salmonella*, *Campylobacter*) thus improving animal health and productivity. The ultimate goal of the FSEP Unit is to reduce foodborne pathogens on the farm, the first link in the food chain to humans.

NADC is the premier research institute within the USDA for studying diseases of large animals and has recently undergone a \$500 million upgrade of laboratory facilities. NADC resources for the position include flow cytometry, mass spectroscopy, laser capture microdissection microscopy, a nucleic acid center operating Illumina, MiSeq, AP3100 sequencers, an electron microscopy/histology facility, bioinformatics resources, and both conventional and gnotobiotic large animal support. NADC researchers also have access to resources and collaborators at nearby Iowa State University. At the NADC, scientists are able to investigate microbe-host interactions at every level—molecular, microbe, and natural host.

Beginning December 4, 2014, details of this position, including salary, qualification requirements and application directions will be described in Job Announcements **ARS-D15E-0011** and **ARS-D15E-0010** posted on the USAJOBS website, www.usajobs.gov. **U.S. citizenship is required.** Applications must be received by the closing date of **Thursday, January 22, 2015.**

Contacts: **Application procedure:** Heather Lee, Heather.Lee@ars.usda.gov, 301-504-1410
Scientific information: Thad Stanton, Thad.Stanton@ars.usda.gov, 515-337-7350

USDA/ARS is an Equal Opportunity Employer and Provider.



FOR RESEARCH. FOR HEALTH.
FOR OUR FUTURE

FACULTY POSITIONS IN MYCOLOGY

The Institut Pasteur in Paris announces an international call for outstanding candidates at all levels to establish independent research groups in the Mycology Department. Preference will be given to studies on human pathogenic filamentous fungi and yeasts, fungal cell biology or population genetics and genomics. Research on model species will be also considered when connecting to fungal pathogenesis. Attractive start-up and ongoing support includes salary, equipment, and operating costs. In addition, Institut Pasteur provides access to state-of-the-art technology platforms, and to laboratories and research infrastructure in disease-endemic regions through the Pasteur International Network. Further information on the Institute and on-campus facilities can be found at <http://www.pasteur.fr>. Further information on the Mycology Department can be found at <http://www.pasteur.fr/mycology>.

The application should comprise the following (in order) in a single pdf file: i) A brief introductory letter, ii) A Curriculum Vitae, a list of 10 selected publications and a full publication list, iii) A description of past and present research activities (up to 3 pages), iv) The proposed research project (up to 6 pages, including a summary).

Junior candidates [1] should also provide:

v) The names of 3 scientists from whom letters of recommendation can be sought, together with the names of scientists with a potential conflict of interest from whom evaluations should not be requested.

Applications and requests for information should be addressed to myco_call2015@pasteur.fr by **February 27, 2015**. Short-listed candidates will be invited for interviews in the spring 2015 and decisions will be announced by the summer 2015.

[1] Institut Pasteur is an equal opportunity employer. Junior group leaders should be less than 8 years after PhD at the time of submission. Women are eligible up to 11 years after their PhD if they have one child and up to 14 years after their PhD if they have two or more children.

INDIANA UNIVERSITY

Assistant Professor – Biology IU Northwest Biology

Applications are invited for a tenure-track assistant professor position in the Biology Department at Indiana University Northwest.

Teaching focus: Sophomore-level genetics, introductory biology (e.g. BIOL L101) and upper level in area of expertise. This would include lectures, labs, and discussions. Specific teaching experience in systems that complement department strengths but fill department needs would be ideal. This could include molecular genetics, population genetics (e.g. aquatic organisms, other novel organisms), human genetics, phylogenetics and evolution, and quantitative genetics.

Research focus: Any realm of research in genetics will be considered from molecular/cellular to organismal/population. Study systems that match department facilities and the tractability of certain genetic systems should be considered (e.g. fruit flies and plants are easier to maintain given facilities than vertebrates and humans). IUN maintains a zebra fish colony in conjunction with the Northwest Center for Medical Education. The ideal candidate would be particularly interested in pursuing a vigorous research program that would be attractive to undergraduates interested in careers in biological fieldwork, laboratory research, or health professions.

Service focus: Service to the campus and candidate's profession is expected, but one emphasis will be excellence in advising undergraduate students toward their degree.

One of eight campuses of Indiana University, Indiana University Northwest is located in metropolitan Northwest Indiana, approximately 30 miles southeast of Chicago and 10 miles from the Indiana Dunes National Lakeshore. The campus has a diverse student population of over 6,000 students and offers Associate, Baccalaureate and Master degrees in a variety of undergraduate and graduate programs in arts and sciences, business and economics, education, nursing and health professions, public and environmental affairs, and social work. IU Northwest emphasizes high quality teaching, peer-reviewed research and service. As a student-centered campus, IU Northwest is committed to academic excellence characterized by a love of ideas and achievement in learning, discovery, creativity, and engagement.

Required qualifications include an earned doctorate. Post-doctoral experience is preferred. Evidence of previous teaching experience and/or future potential are helpful. Salary and benefits are competitive.

Please upload: (1) curriculum vitae; (2) letter of application; (3) statement of research and teaching; and (4) list of references with contact information to include mailing address, e-mail address, and telephone numbers. Interested candidates should review the application requirements and submit their application at <https://indiana.peopleadmin.com/postings/1308> by **January 5, 2015**. Expected start date is August 1, 2015. Questions regarding the position or application process can be directed to the **Search Committee Chair, Peter Avis, Indiana University Northwest, 3400 Broadway, Gary, IN 46408, pavis@iun.edu, (219) 980-6717**.

PENNSTATE



SENIOR FACULTY POSITION IN BIOCHEMISTRY, MOLECULAR BIOLOGY, AND GENETICS

The Department of Biochemistry and Molecular Biology at the Penn State University College of Medicine invites applications from outstanding senior scientists with Ph.D., M.D., or equivalent degrees for a full-time tenure-track position. We seek candidates at the Associate or Full Professor level who have an active and highly competitive independent research program in the area of human genetics and genomics, particularly with an emphasis of the genomics of disease related traits. The successful applicant will serve as associate director of the Penn State Institute for Personalized Medicine (<http://www2.med.psu.edu/ipm>) and should be familiar with development of protocols for Institutional Review Boards and with management of CLIA laboratories.

For additional information, please visit the following website: <http://www2.med.psu.edu/biochemistry/>.

Applicants should submit a curriculum vitae and a brief statement of research plans to **www.psu.jobs**, position #55016 and arrange for three letters of reference to be sent to Faculty Search Committee, **biochem_apply@hmc.psu.edu**. Application should be received prior to **February 1, 2015**.

Penn State is committed to Affirmative Action, Equal Opportunity and the diversity of its workforce.

BOYS TOWN National Research Hospital



Research Faculty Positions

Four full-time research faculty positions are currently available at the Boys Town National Research Hospital in Omaha, Nebraska. We seek two qualified independent investigators at any level (entry level preferred) to join our Center for Sensory Neuroscience, a multidisciplinary group of laboratories with a focus on molecular processes underlying hearing and vision. We seek an additional two qualified independent investigators at any level to join our Center for Hearing Research, a multidisciplinary group of laboratories with a focus on perception and communication in children with hearing loss. Applicants for all four positions should have a Ph.D. and at least 3 years post-doctoral experience, the talent and personal drive to establish a robust and collaborative independent research program and the ability to successfully compete for extramural support. The Hospital will provide generous laboratory space and start-up packages along with a strong mentoring program for young investigators. Salary support for these positions is provided from a mix of Hospital and state funds as well as NIH grants.

Interested parties should submit a current CV, including the names of 3-5 references, and a 2-page research statement to:

Jessica Diekmann
Boys Town Human Resources
jessica.diekmann@boystown.org
402 498-1783

<https://www.boystownhospital.org/>

Boys Town National Research Hospital is an Equal Employment Opportunity Employer. Qualified applicants will receive consideration for employment without regard to their protected veteran status. Boys Town National Research Hospital is also an equal employment opportunity employer of individuals with disabilities. Please contact us at 1-877-639-6003 if you need an accommodation to complete the application process. Boys Town National Research Hospital is an Affirmative Action Employer and participates in the E-Verify program.



Stanford MEDICINE

Assistant or Associate Professor of Comparative Medicine

The Department of Comparative Medicine at Stanford University invites applications for a tenure-track position at the ASSISTANT or ASSOCIATE Professor level. The main criterion for appointment in the University Tenure Line is a major commitment to research and teaching.

We are particularly interested in an outstanding investigator whose animal model-based research synergizes with general themes in, but not limited to, comparative genomics and genetics, cancer biology, immunology and microbiology, bioengineering, neuroscience, bioinformatics, stem cell biology, and/or regenerative medicine. We fully support the *One Health* initiative and welcome applicants whose research has translational applications.

Faculty rank will be determined by the qualifications and experience of the successful candidate. The successful applicant should have a DVM/VMD, PhD, or MD. We are particularly interested in candidates who have an active research program, a strong record of independent research and extramural funding, and a demonstrated commitment to excellence in teaching.

A joint appointment with another department at Stanford is also possible.

Applications will be reviewed beginning April 24, 2015 and accepted until the position is filled.

Submit a brief cover letter describing future research plans, a curriculum vitae and publication list, and the names of at least three (3) references to:

Ms. Alice Schroeder, compmed-stanford@lists.stanford.edu
Executive Assistant, Department of Comparative Medicine

For more information about the Department of Comparative Medicine at Stanford University, please visit: <http://med.stanford.edu/compmed/>.

Stanford University is an equal opportunity employer and is committed to increasing the diversity of its faculty. It welcomes nominations of and applications from women, members of minority groups, protected veterans and individuals with disabilities, as well as from others who would bring additional dimensions to the university's research, teaching and clinical missions.



HUMAN FRONTIER SCIENCE PROGRAM

CALL FOR LETTERS OF INTENT
FOR RESEARCH GRANTS:
AWARD YEAR 2016

HFSP supports **international** preferably **intercontinental** collaborations in **basic** life science research. Applications are invited for grants to support **innovative** approaches to understanding **complex mechanisms of living organisms**. Applicants are expected to develop novel lines of research distinct from their ongoing research. Preliminary results are not required.

Program Grants are for independent scientists at all stages of their careers while **Young Investigators' Grants** are for teams of scientists who are **all** within 5 years of establishing an independent laboratory and within 10 years of obtaining their PhDs. Both provide 3 years support for 2 – 4 member teams, with not more than one member from any one country, unless critical for the **innovative** nature of the project. Awards are dependent upon team size and successful teams will receive up to \$450,000 per year. The principal applicant must be located in one of the **HFSP** member countries but co-investigators may be located in any country.

Please read the guidelines on the website (www.hfsp.org). Teams must register via the web site by **March 19, 2015** so as to submit a letter of intent online by the **March 31, 2015** deadline.

Specific enquiries: grant@hfsp.org



RESEARCH IS ON
THE WAY TO SUCCESS
WITH YOU



Inserm is recruiting:

**93 tenure positions are offered
to researchers (m/f) dedicated
to biomedical research**

Candidates to Research Associates and Research Directors positions must have a PhD (or equivalent degree). There is no nationality restriction.

Inserm is the only French public research institute to focus entirely on human health. Its researchers are committed to studying all diseases, whether common or rare. Through its diversity of approaches, Inserm provides a unique environment for researchers. 13 000 researchers, engineers and technicians work in the 289 Inserm laboratories housed in hospitals, universities and research campuses, all over France.

Application modalities: visit our website: <http://www.eva2.inserm.fr>

Application deadline:

- Research Associates: **January 15th, 2015 - 4.00pm (GMT+1)**
- Research Directors: **February 17th, 2015 - 4.00pm (GMT+1)**

Instituts
thématiques

Inserm

Institut national
de la santé et de la recherche médicale



PRINCETON
Neuroscience
INSTITUTE

New intensive summer course: Neurotechnologies for Analysis of Neural Dynamics

Directors: David W. Tank and Michael Berry, Princeton University,

Dates: June 15 – July 12, 2015.

Online Application Form and Course Schedule: NAND.princeton.edu

Application Deadline: February 1, 2015.

This course is designed to emphasize the major ways that scientists trained in the physical and information sciences contribute to the advance of neuroscience. It will introduce students with quantitative training in the physical sciences, mathematics or engineering to the concepts and research methodologies of modern neuroscience. Topics covered will range from cellular biophysics to systems neuroscience, including particularly imaging methods for the study of single neurons, networks of neurons and human brain dynamics during execution of behavioral computations. The course will be unique in its focus on neural dynamics at several scales of complexity – cells, circuits, intact brains – and the combination of didactic lectures and laboratory exercises, including cellular biophysics, synaptic interactions and plasticity in neuronal networks, and fMRI imaging of targeted brain regions in human subjects. The course includes substantive instruction in neurotechnologies, ranging from large-scale multi-electrode and optical recording, optogenetic stimulation and mathematical analysis of neural dynamics within the datasets produced by these methods. The capstone of this course will be one-week student-designed research projects integrating concepts and methodologies encountered during the initial formal lectures and laboratory exercises.

**Arthritis
Research UK**

**Call for
applications**

The role of the microbiome in musculoskeletal health and disease

The microbiome is increasingly recognised as influencing health and disease.

To help clarify the role of the microbiome in musculoskeletal disease, applications are invited from multidisciplinary groups using innovative approaches to address novel questions in this area.

Microbiome Pathfinder Awards will support development work to enable successful applicants to apply for future follow-on programmatic support. These awards will provide support for up to £300,000 for 24 months.

The Microbiome Strategic Programme Award will provide longer term support to established multidisciplinary groups. This prestigious award will provide support for up to £2m for 5 years.

The call launches on Monday 5 January 2015.
For further details and how to apply, visit the Arthritis Research UK website www.arthritisresearchuk.org from this date.

Registered Charity England and Wales No. 207711, Scotland No. SC041156.



**Learn more and
keep your job search
out of the cheap seats.**

- Search thousands of job postings
- Create job alerts based on your criteria
- Get career advice from our Career Forum experts
- Download career advice articles and webinars
- Complete an individual development plan at “myIDP”

Target your job search using relevant resources
on **ScienceCareers.org**.

ScienceCareers

FROM THE JOURNAL SCIENCE  AAAS

Cernet

ScienceCareers

“《科学》职业”
已经与Cernet/
赛尔互联开展合
作。中国大陆的
高校可以直接联
系Cernet/赛尔互
联进行国际人才
招聘。



请访问

Sciencecareers.org/CER

获得联系信息。

Science



**University of
New Hampshire**

Assistant Professor in Climate Change Cluster (4) Positions

The UNH College of Life Sciences and Agriculture (COLSA) seeks to hire four tenure-track assistant professors with demonstrated interests and expertise in (1) Environmental Economics, (1) Agricultural Engineering, (1) Forest Ecosystem Health, and (1) Quantitative Ecology. Candidates must have a Ph.D. in the appropriate field, and demonstrated potential to develop and lead strong and productive research programs. Working under the auspices of the New Hampshire Agricultural Experiment Station, the successful candidates will be expected to compete successfully in national and regional funding initiatives, achieve national and international prominence in their fields, and provide leadership in engagement with our stakeholders. They will embrace interdisciplinary approaches, and will be expected to interface with broad segments of the science-to-policy spectrum. Successful candidates will be expected to train graduate students and to develop and teach outstanding courses at the undergraduate and graduate levels. Integrating areas of research strength with academic programs is a key goal of the UNH Academic Plan. The new faculty will be located within the College of Life Sciences and Agriculture, matched with the department that best suits their position, interests and expertise. Likely home departments are Natural Resources and the Environment (NREN) and Biological Sciences (BS).

The University actively seeks excellence through diversity among its administrators, faculty, staff, and students, and prohibits discrimination on the basis of race, color, religion, sex, age, national origin, sexual orientation, gender identity or expression, disability, veteran status, or marital status. Application by members of all underrepresented groups is encouraged.

Complete application information is available at: colsa.unh.edu/employment. Review of applications will begin on January 20, 2015 and will continue until the positions are filled. All applicants will be required to apply online at <https://jobs.usnh.edu>. Please direct all inquiries to Jane Garnett, COLSA search coordinator, 603-862-5417, Jane.Garnett@unh.edu.

*The University of New Hampshire is an Equal Opportunity/
Equal Access/Affirmative Action institution.*



SCIENCE EDUCATION IN BIOLOGY DEPARTMENT OF BIOLOGY COLORADO STATE UNIVERSITY

POSITION: The Department of Biology at Colorado State University (Fort Collins, Colorado) is recruiting a faculty member who is advancing areas of **Science Education in Biology** for a tenured/tenure-track faculty position at the rank of Assistant or Associate Professor. Relevant areas of interest include (but are not limited to) how students learn science, analysis and development of instructional approaches, and methods of assessment.

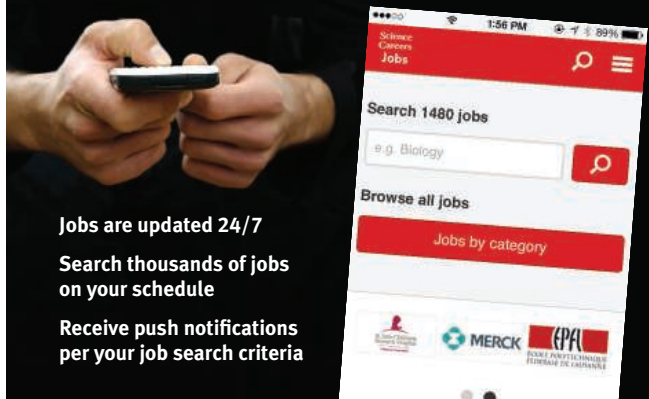
QUALIFICATIONS: Applicants must have a Ph.D. either in an area of Biology or in Science Education with an emphasis in Biology by the time of their application. Must have teaching experience in higher education, and active research demonstrated with peer-reviewed publications in science education with relevance to Biology.

DATES AND RECORDS: This position will be available as early as August 16, 2015. For full consideration, complete applications must be received by **January 19, 2015**.

For instructions on how to apply and to view full job description:
<http://www.biology.colostate.edu/employment/>

*CSU is an EO/EA/AA Employer. Colorado State University conducts
background checks on all final candidates.*

Download the Science Careers jobs app from Science



Jobs are updated 24/7

**Search thousands of jobs
on your schedule**

**Receive push notifications
per your job search criteria**

Get a job on the go.

Search worldwide for thousands of scientific jobs in academia, industry, and government. The application process is seamless, linking you directly to job postings from your customized push notifications.



Scan this code to
download app or visit
apps.sciencemag.org
for information.

Science Careers AAAS
FROM THE JOURNAL SCIENCE

ScienceCareers.org



PROFESSOR AND DEPARTMENT CHAIR DEPARTMENT OF NEUROBIOLOGY UNIVERSITY OF MASSACHUSETTS MEDICAL SCHOOL

The University of Massachusetts Medical School invites applications for the position of Professor and Chair of the Department of Neurobiology. This highly successful department has focused on fundamental mechanisms of brain function using model genetic systems (<http://www.umassmed.edu/neurobiology/>) and is now expanding its neuroscience research and scholarship capabilities. The Medical School seeks an individual of outstanding research and leadership capability who will further promote and catalyze breakthrough science in neurobiology.

The Neurobiology department occupies one floor of a state-of-the-art research building at the Medical School. Core facilities for deep sequencing, proteomics, genotyping, fluorescence-activated cell sorting, digital imaging/confocal microscopy, genomics/bioinformatics, transgenic/knockout mice, and mouse metabolic phenotyping, among many other techniques are available. The position is highly competitive with regard to start-up funds, laboratory space and salary.

Applicants should submit a cover letter explaining their interest in department leadership, curriculum vitae and contact information for three references to <https://academicjobsonline.org/ajo/5228>. Inquiries, but not application materials, may be directed to the Search Committee Chair, Dr. Michael P. Czech (michael.czech@umassmed.edu).

*As an Equal Opportunity and Affirmative Action Employer, UMass
recognizes the power of a diverse community and encourages
applications from individuals with varied experiences, perspectives, and
backgrounds.*

By Karen Perkins

For the love of ferns

I attended Hampshire College to major in music. While watering plants in the greenhouse to fulfill my community service requirement, I fell in love with a fern. ¶ Intending to make thousands of them, I discovered the college laboratory, where I tweezed the furry rhizomes of *Davallia fejeensis* into agar-filled test tubes, careful to keep my sleeve out of the Bunsen burner flame used to keep things sterile. Between frat parties and piano practice, I made a discovery: Agar prepared for growing bacteria caused the rhizomes to reprogram and become reproductive-like structures. My discovery set me on a path to research. I would stay on that path for about a dozen years.

No one in my family had ever studied science. I was already midway through college, with just a high school biology class behind me. I struggled through remedial math, then chemistry and physics. One graduate school accepted me. For the next 2 years, I taught and worked in a research lab, studying membranes. I aced my graduate courses. Membranes didn't seem to play a role in reprogramming development, so I transferred to Albert Einstein College of Medicine, to a laboratory that studied enzymes involved in transcription and DNA replication.

"Be here as often as possible," my new graduate adviser said. I went to dinner at 5 p.m. and returned at 7 p.m. "Where were you?" he demanded. From then on, I humbly apprenticed myself. I brought dinner in, studied while my gels ran, and slept on the orange vinyl couch in the women's lounge.

"You've studied enough. Let's go to a movie," one boyfriend said. I shooed him away. Another offered marriage and travel if I would quit my Ph.D. program. Ha! My experiments were my life. Finally, I married a cute medical student I met at a mixer in the research center lobby. He followed me to my postdoc at the University of California, Berkeley, where I was a Damon Runyon Cancer Research Foundation Fellow. While my husband was on call, and even when he wasn't, I buried myself in transcription factors that control developmental genes.

I applied for tenure-track positions and was offered several: Duke. Johns Hopkins. Brandeis. My husband said he would go anywhere. I committed to Hopkins and wrote my first big National Institutes of Health grant. My husband served me with divorce papers. I fell into a state of shock. Twelve years had passed since I'd fallen in love with my fern.

At Hopkins, I was unable to lift a pipette, let alone con-



"I still love ferns, but I'll let someone else figure out their genetic switches."

centrate on building a lab. I had written for scientific journals, but now I wrote madly in my own journal, using words as therapy to figure out what had gone wrong.

An old boyfriend invited me to sunny Los Angeles. Skeptically, I boarded a plane to a world of palm trees, movies, restaurants, and—surprisingly—laughter and love. These were tastes of a life I had missed. For months, I assumed my attraction to this "real" world was a transient response to the trauma of divorce. I expected my love for the lab to return. My grant was rejected by a couple of points. I moved to LA with no job prospects. I became a live-in girlfriend.

I remarried, re-divorced, practiced piano again, and raised two children. I bought a house near mountains and hiking trails. I

read. I briefly accepted a tenure-track assistant professorship at a liberal arts college, assuming I was ready for the lab again.

I wasn't. It was as a teacher that I made sense of myself. Teaching gave me a life of work but also a life of people and play. Colleges, though, want research. I resigned.

Today I teach 11th and 12th grade physiology. I have been a school board chair and a high school principal. I often work with special education and at-risk students. Many of them have trouble focusing because of traumatic life events. I can relate. I still love ferns, but I'll let someone else figure out their genetic switches. I'm okay with watering the ferns in my backyard. ■

Karen Perkins is a teacher at Palisades Charter High School in Los Angeles. For more on life and careers, visit www.sciencereers.org. Send your story to SciCareerEditor@aaas.org.